RIKEN Accelerator Progress Report

2004

vol. 38

BOOK & CD-ROM

独立行政法人理化学研究所
RIKEN

CONTENTS

2. Atomic and Solid-State Physics

Frontispiece: Figures for "Experiment on synthesis of element 113 in reaction ^{209}Bi(^{70}Zn, n)^{278}113" (p. 70)

Experiment on synthesis of element 113 in reaction ^{209}Bi(^{70}Zn, n)^{278}113
—Newly discovered 113th element— (P. 70)

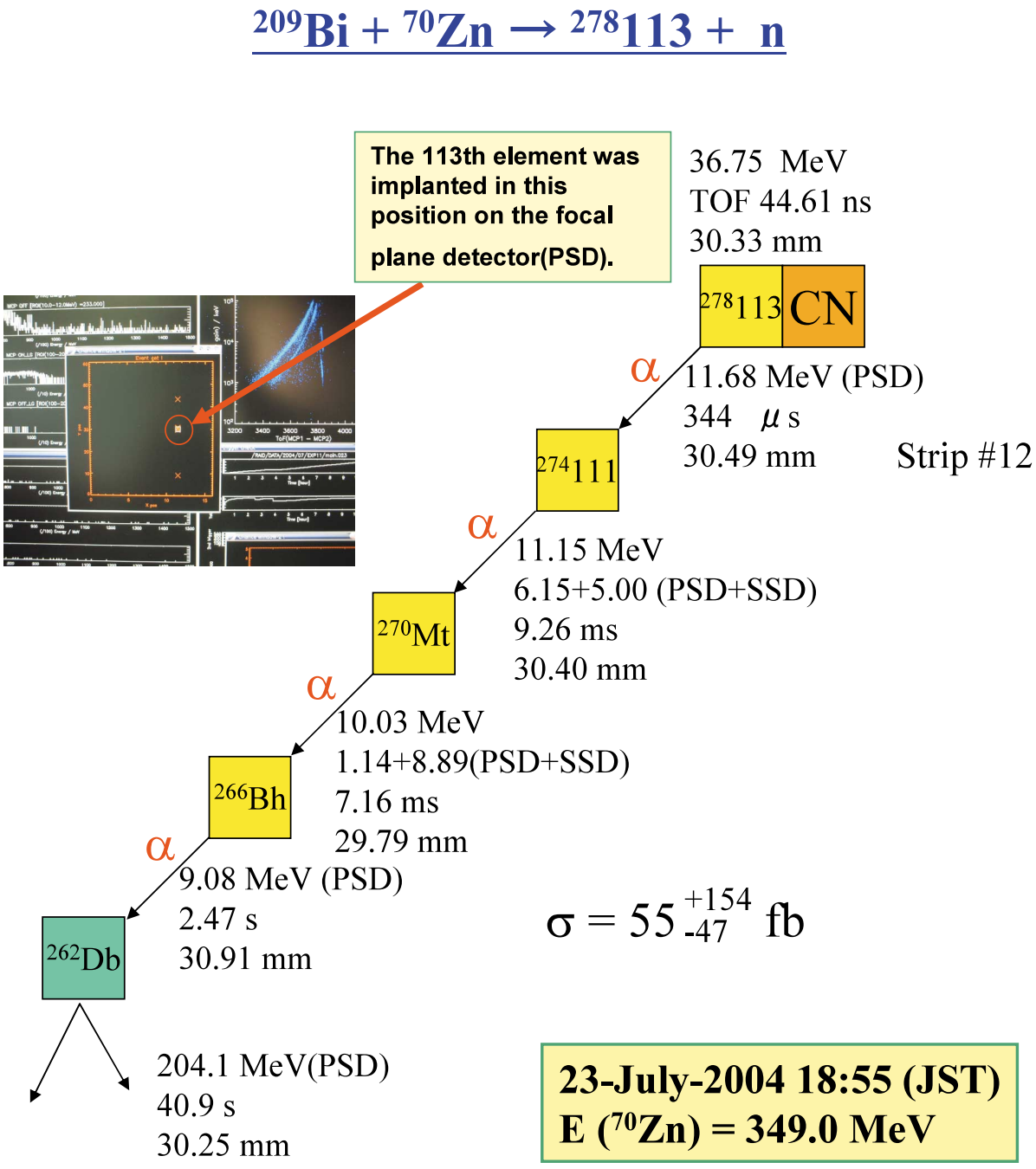

Fig. 1. The most likely candidate event for the isotope of the 113th element, ^{278}113, and its daughter nuclei was observed, for the first time, in the ^{209}Bi + ^{70}Zn reaction. The measured energies and decay times are indicated in the figure.

RIKEN Gas-filled Recoil Separator GARIS

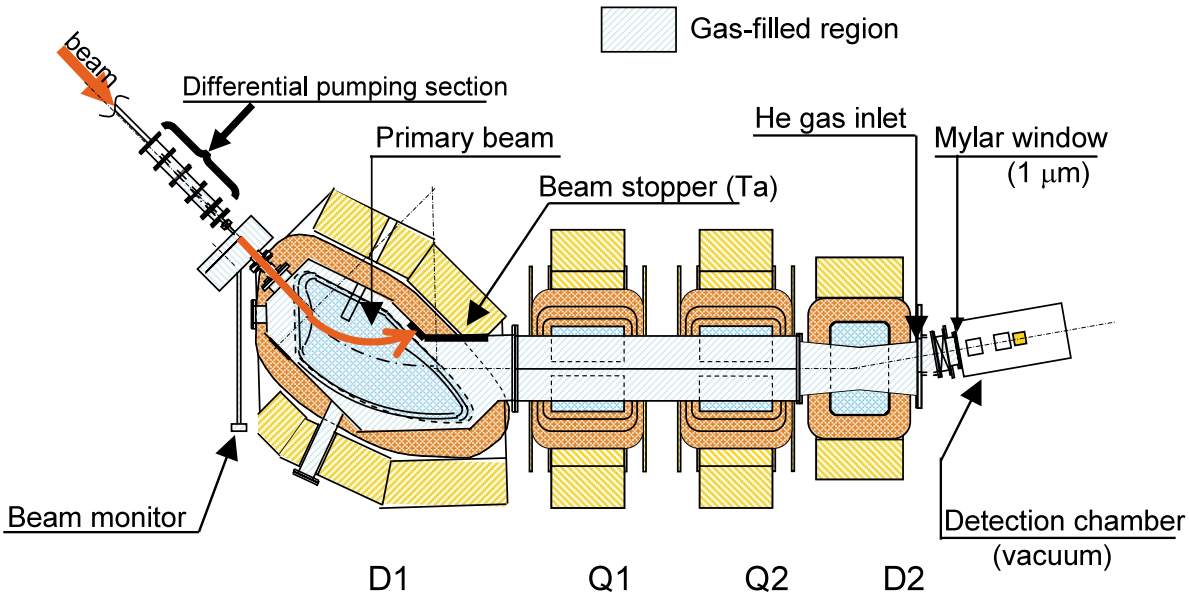

D1

Bending angle	45 degree
Pole gap	150 mm
Radius of central ray	1200 mm
Maximum field	1.54 T

Q1, Q2

Pole length	500 mm
Bore radius	150 mm
Maximum field gradient	5.2 T/m

D2

Bending angle	10 degree
Pole gap	160 mm
Pole length	400 mm
Maximum Field	1.04 T

Magnification	X	-0.76
	Y	-1.99
Dispersion		0.97 cm/%
Total length		5760 mm
Acceptance	$\Delta\theta$	$\pm$68 mrad
	$\Delta\phi$	$\pm$57 mrad
	$\Delta\Omega$	12.2 msr

Fig. 2. This figure shows a schematic view of the Gas-filled Recoil Ion Separator GARIS. The GARIS is a separator for recoiling atoms with a large transport efficiency and a low background.

Gas-cooled Rotating Target

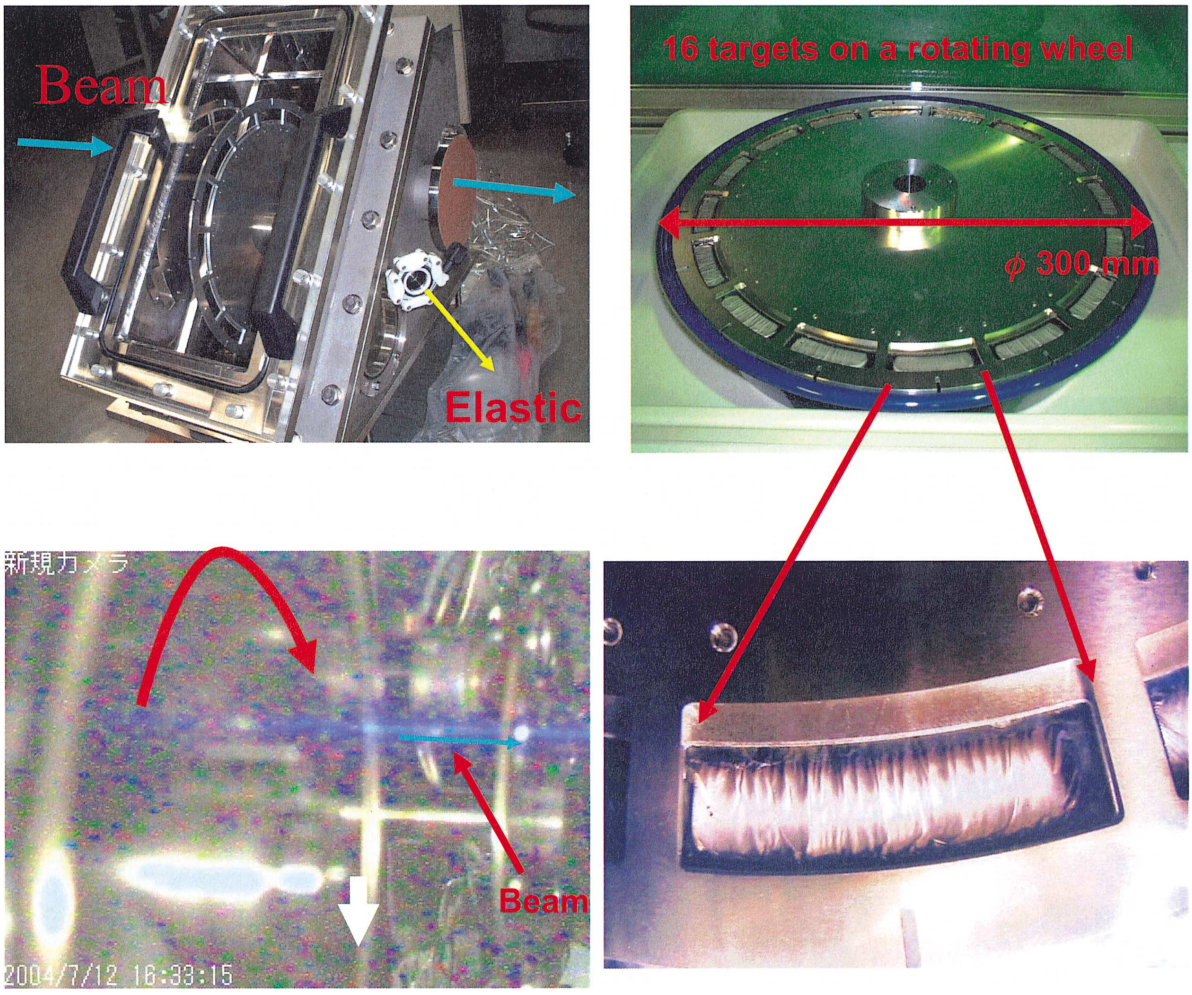

Fig. 3. These figures show the gas-cooled rotating target system. The diameter of the rotating wheel is 300 mm and the rotating speed is 3000 rpm. Helium gas in the GARIS has two important roles, charge equilibration of recoiling ions, and cooling of the target.

Focal Plane Detectors

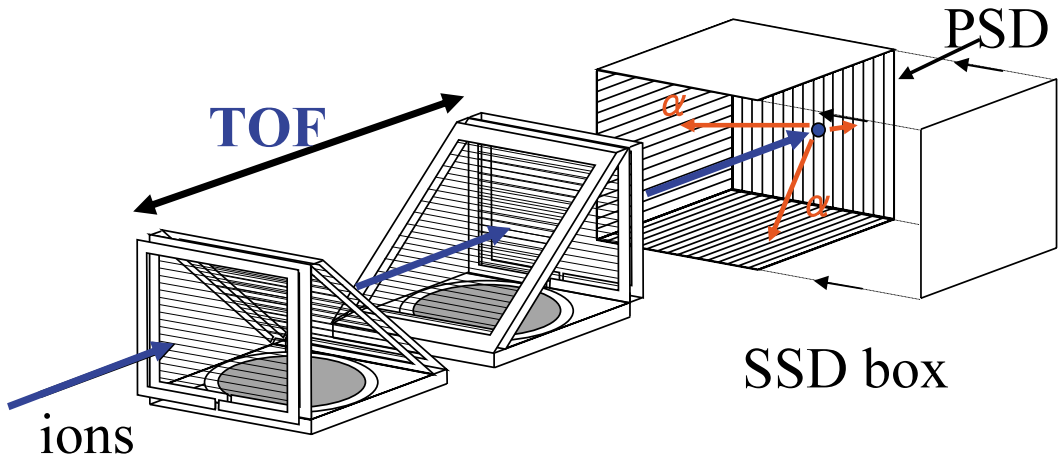

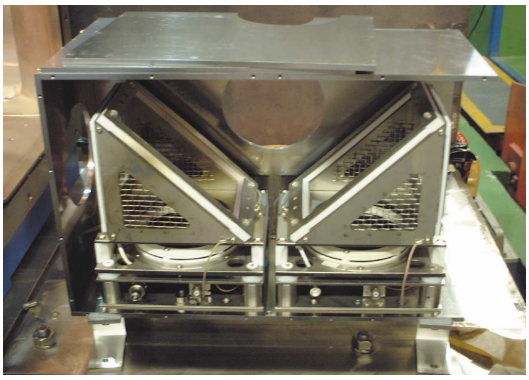

Time-of-flight detector

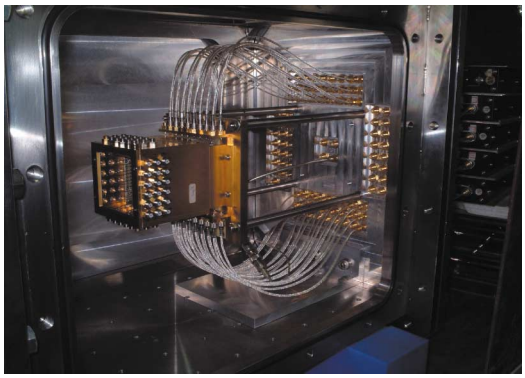

SSD detector box

Transmission	**: 94 %**
Time resolution (FWHM for a of ^{241}Am)	**: 530 ps**
Detection efficiency (For a of ^{241}Am)	**: 95 %**

PSD (x 1)	**Number of strips**	**: 16 strip (3.75 mm x 60 mm)**
	Positional resolution	**: within +/-1 mm**
	Energy resolution	**: 40 keV**
SSD (x 4)	**Energy resolution (Sum of PSD and SSD)**	**: 70 keV**

Geometrical detection efficiency (PSD+SSD) : 85 %

Fig. 4. These figures show the focal plane detectors installed in the detector chamber. The detector system consists of two Time-of-Flight (TOF) detectors and a silicon detector box. The fusion product is implanted in the Position-Sensitive semiconductor Detector (PSD) and mass information is obtained in combination with TOF and implantation energy. The decaying alpha particle accompanied by implantation is detected by PSD or PSD and the Side detector without a TOF signal.

I. PREFACE

This issue of RIKEN Accelerator Progress Report reports on progress of research activities in the RIKEN Accelerator Research Facility (RARF) up to October 2004. The research programs involve a variety of fields such as experimental and theoretical nuclear physics, nuclear chemistry, radiation biology, atomic physics, condensed matter physics, plant mutation, material characterization, application to space science, accelerator physics and engineering, laser technology, and computational technology in terms of accelerator or radiation application. These activities involved a few hundred researchers from domestic and foreign institutions together with laboratories and Centers in RIKEN. The spotlight is directed to the first production and identification of an isotope $^{278}113$ of the 113th element, which is the heaviest element ever created with confirmation by known α decay.

Major research activities of the RARF are based on the heavy-ion accelerator complex consisting of the $K = 540$ MeV RIKEN Ring Cyclotron (RRC), the energy variable heavy-ion linear accelerator (RILAC), and the $K = 70$ MeV azimuthally varying field cyclotron (AVF). Heavy-ion beams of a variety of elements with energies ranging from a few A MeV to 135A MeV are provided. Vector and tensor polarized deuterons are also available. The three accelerators have been used in various configurations. The RRC operates either with the AVF or the RILAC as the injector. The AVF has been providing beams of ions of mass numbers up to 60, whereas the RILAC can accelerate heavier ions. An energy booster called CSM (Charge State Multiplier) installed in collaboration with CNS, the University of Tokyo, is used to raise the maximum beam energy from the RILAC. This enabled to deliver high-intensity beams of intermediate mass elements such as Kr up to 64A MeV from RRC. In addition, RILAC and RRC can be operated separately, when the AVF is used to inject ions to the RRC. This allows for long runs with RILAC beams like the experiment of super-heavy element search, which lead to the synthesis of an atom of the element 113. Two thirds of the RRC research beam time is used for nuclear physics and nuclear astrophysics, and remaining one third is used for atomic physics, material science, nuclear chemistry, radiation biology and others. The AVF beam time was also used for fields other than nuclear physics.

The RARF carries many international collaborations. Among them are two large-size collaboration programs using overseas accelerator facilities: one is the muon science project at ISIS in collaboration with the Rutherford-Appleton Laboratory (RAL), and the other is the spin physics program at RHIC in collaboration with the Brookhaven National Laboratory (BNL). The pulsed muon-beam facility at ISIS has been operating steadily. At the RHIC facility, with the new AGS snake made by RIKEN, polarization of proton was improved to 40–50% and stabilized. The research group has succeeded to measure direct photon cross section, asymmetry of which is the first key to solve "spin crisis". Other smaller collaborations using foreign facilities are underway at CERN (Switzerland/France) and GSI (Germany). We have collaborated with the CNS for operating the low-energy RI beam separator (CRIB) to use the low-energy beam from the AVF. Several experiments of nuclear astrophysics and spectroscopy have been performed by using light RI beams of a few A MeV available as a CNS/RIKEN facility.

Highlights of the year for the research at RARF are as follows. (1) Besides the production of the isotope $^{278}113$, production and decay of the 112th element $^{277}112$ has been confirmed. (2) In-beam γ spectroscopy has been performed for light neutron-rich nuclei, ^{15,17}B, ^{17,19}C, ^{23}O, and ^{23,27}F, excited by proton- and α-inelastic scattering, neutron removal reactions, and nucleon transfer reactions. Many new levels have been identified, and measured transition strengths have revealed new feature of nuclear structure, such as decoupling of neutron motion. (3) Reactions involved in stellar burning processes have been studied. Radiative capture processes for ^{18}Ne, ^{22}Mg and ^{26}Si have been investigated by the Coulomb dissociation method. Several low-energy resonant states in ^{21}Na, ^{22}Mg and ^{23}Mg have been found by the thick target method utilizing the low-energy RI beams from the CRIB. (4) The nuclear moment study has been extended to the sd-shell region, and the magnetic moments for ^{23}Al, ^{30}Al and ^{32}Al have been determined. (5) A precision measurement of Coulomb and nuclear breakup of one of the one-nucleon halo nuclei ^{11}B has been made, and the breakup mechanism has been clarified in details. (6) A pilot device for a slow RI-beam facility (SLOWRI) using an rf ion guide achieved a overall efficiency of 5% for $\approx$100A MeV ^{8}Li from RIPS. The ions were trapped in a linear rf trap for precision hyperfine structure spectroscopy. (7) The reaction cross section and fragment momentum distribution for ^{23}Al, a candidate of proton halo nuclei, have been measured. (8) The rf deflector improves the fraction of the beam of interest in the cocktail secondary beams, and has been used for many experiments with proton-rich beams. For example, the $0^+ \rightarrow 2^+$ transi-

tion probabilities have been measured for the first time by Coulomb excitation for ^{46}Cr, ^{50}Fe and ^{54}Ni. (9) The TOF spectrometer for precise particle identification of the reaction products of RI-beam induced reaction has been completed. (10) It has been found that heavy-ion irradiation enhanced the activity of DNA-PK, which acts as a sensor of DNA double-strand breaks (DSBs) during non-homologous end-joining, more than X-ray irradiation. (11) New types of sterile mutants in ornamental flowers such as self-incompatibility and anther deficiency have been found by the plant-mutagenesis using ion-beam irradiation.

Other related research activities are as follows. a) An evidence of strongly bound kaonic system in K^-ppn with the total binding energy of 175 MeV has been obtained. b) A new scheme to store positrons realized with ≈30 times higher accumulation efficiency than ever realized under ultra-high vacuum condition. c) Antiprotons trapped and cooled have been extracted at 10–500 eV with high efficiency for the first time. d) New type of ion source was developed, which broke the world record of carbon intensity by factor 100.

The RI beam factory project is in progress. Construction of the experimental facility building is about to be completed. The fRC is being constructed for completion by March in 2005. The assembling of the sector magnets and vacuum systems for the IRC has been completed. The assembling of the sector magnets and the superconducting coils of the SRC is in progress. A part of the fragment separator Big RIPS has been installed, and test of super-conducting quadrupole magnets has been started. The first production of RI beams are foreseen in the year 2006.

For experimental installation of RIBF in its phase II, various research and developments are being performed. For Self-Confining Radioactive Ion Target (SCRIT), test experiments were carried out at KSR of Kyoto University. A new scheme of mass measurements using an isochronous ring has been developed. Design of a large acceptance spectrometer (SAMURAI) and a high-resolution spectrometer (SHARAQ) have progressed. For creation of highly polarized RI beams using primary beams from IRC and the RIPS, a new system using the atomic beam method is being developed.

T. Motobayashi
Director, Accelerator-based Research Group
RIKEN Accelerator Research Facility

RILAC operation

E. Ikezawa, M. Kase, O. Kamigaito, T. Nakagawa, N. Sakamoto, H. Okuno, N. Inabe, M. Wakasugi, N. Fukunishi, M. Kobayashi-Komiyama, M. Kidera, Y. Higurashi, H. Ryuto, S. Kohara, M. Fujimaki, M. Nagase, T. Kageyama, S. Yokouchi, A. Yoneda, T. Aihara,* T. Ohki,* H. Yamauchi,* A. Uchiyama,* K. Oyamada,* R. Koyama,* A. Goto, and Y. Yano

Throughout this reporting period, RILAC has been in steady operation and has supplied various ion beams for various experiments. Table 1 shows the statistics for RILAC operation from January 1 through December 31, 2004. Regular RILAC operation was discontinued from January through February, 2004, for modification works of the injection line and installation works of the cooling system. Table 2 summarizes the number of days allotted to the search for the heaviest elements, radiation chemistry, accelerator mass spectrometry, and other experiments.

Research experiments on the heaviest elements have been carried out with a gas-filled recoil isotope separator (GARIS) at the e3 beam line since 2002. In this year, the experiments were carried out 30 days in April, 9 days in May, 27 days in July, and 23 days in December. More than 1 pμA of the 5 MeV/u ^{70}Zn beam was supplied to the experiments. The total beam service time for the experiments was 1770 hours. As a result, a convincing candidate event for the isotope of the 113th element was observed for the first time on July 23, 2004.

The percentage of beam time used by the RIKEN Ring Cyclotron (RRC) was approximately 32% of the total. The ^{4}He, ^{58}Fe, ^{58}Ni, ^{70}Zn, ^{86}Kr, and ^{136}Xe ions accelerated by RILAC were injected into RRC.

Table 3 shows the statistics for the numbers of days on which RILAC ion beams were delivered using the RFQ linac with an 18 GHz ECR ion source. The ion beams of 9 elements were used for the experiments and beam acceleration tests.

We carried out the following machine improvements during this reporting period.

(1) The beam transport line of the RFQ linac with the 18 GHz ECR ion source (18 G-ECRIS) was modified. A superconducting ECR ion source (SC-ECRIS) was installed in parallel with the existing 18 G-ECRIS. Thus, the beam transport line of the Cockcroft-Walton injector with the 8 GHz ECR ion source (NEOMAFIOS), which has been used for many years, was dismantled. Figure 1 shows the layout of the beam transport line of the RFQ linac with two ECR ion sources.
(2) A new deionizer watercooling system was installed. The cooling capacity is 400 kW. This system has been used for the 18 G-ECRIS and the SC-ECRIS. In addition, five water pumps, two cooling towers, a deionizer water system, and a control circuit for the cooling system of RILAC were replaced with new ones.
(3) To enable stable operation and easy maintenance, the final stage of the rf power amplifier for the RFQ linac was improved.
(4) For the RIKEN RI beam factory project, the accelerator room of RILAC was divided into an ion

Table 1. Statistics for RILAC operation from January 1 through December 31, 2004.

	No. of Days	%
Beam time	182	49.7
Overhaul and improvement	84	23.0
Periodic inspection and repair	37	10.1
Scheduled shutdown	63	17.2
Total	366	100

Table 2. Beam time allocated to different research groups.

	No. of Days	%
Search for heaviest elements	89	48.9
Radiation chemistry	12	6.6
Accelerator mass spectrometry	14	7.7
Instrumentation	4	2.2
Accelerator research	5	2.7
Beam transport to RRC	58	31.9
Total	182	100

Table 3. Statistics for RILAC ion beams delivered using RFQ linac with 18 GHz ECR ion source.

Ion	Mass	Charge state	No. of Days
He	4	1	3
N	14	3	2
Ar	40	8, 11	18
Ti	47	9	4
Fe	58	13	14
Ni	58	9	7
Zn	70	15, 16	104
Kr	86	18	15
Xe	136	20, 27	15
		Total	182

* SHI Accelerator Service, Ltd.

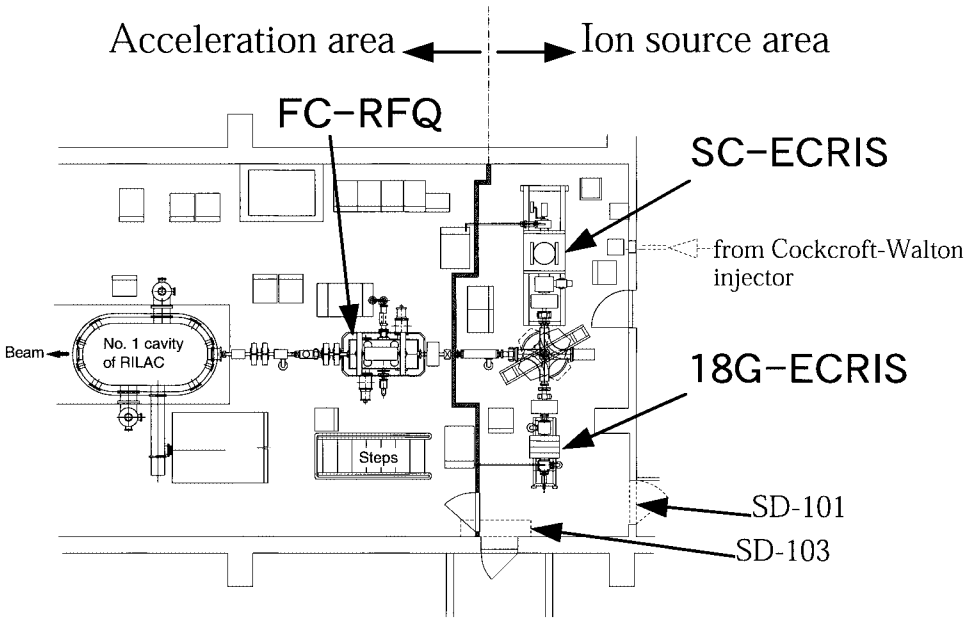

Fig. 1. Layout of beam transport line of RFQ linac with two ion sources (18 G-ECRIS and SC-ECRIS). The boundary of the ion source area and the acceleration area is also shown. SD-101 and SD-103 denote the dismantled shield doors.

source area and an acceleration area using a partition. Thus, shield doors (SD-101 and SD-103) in the ion source area were dismantled. Figure 1 shows the boundary of the ion source area and the acceleration area.

We experienced the following machine problems during this reporting period.

(1) The RFQ linac had a big vacuum leak on a cooling pipe of the stem. The No.5 cavity had a small vacuum leak on a air pressure pipe of the shorting plate. These leaky parts were soldered.

(2) A new water pump of the deionized water circuit for RILAC had a terminal breakdown after just one month of operation. Two weeks of scheduled beam time was cancelled owing the trouble.

RRC and AVF operation

M. Kase, E. Ikezawa, T. Nakagawa, O. Kamigaito, H. Ryuto, N. Fukunishi, H. Okuno, N. Sakamoto, M. Kidera, M. Wakasugi, N. Inabe, M. Kobayashi-Komiyama, T. Kageyama, M. Nagase, S. Kohara, M. Fujimaki, A. Yoneda, S. Yokouchi, Y. Higurashi, Y. Ohshiro,[*1] N. Tsukiori,[*2] R. Ohta,[*2] K. Kobayashi,[*2] M. Nishida,[*2] Y. Kotaka,[*2] K. Masuda,[*2] S. Fukuzawa,[*2] T. Nakamura,[*2], A. Goto, and Y. Yano

Table 1 shows the statistics of the RRC and AVF operation in 2004. Due to fund limitation for electric power in the fiscal year 2003, all the accelerators stopped operation in January and February 2004. And also unscheduled shutdown took place frequently during the second half of 2004 due to machine troubles. Therefore the total operation hours per year was shortened by 15% than that in the previous year.

Table 2 shows the beam service time for each beam course of RARF from E1 to E7 as shown in Fig. 1. About 80% of the total beam time was devoted to experiments using secondary beams (RI beams) produced at RIPS by projectile fragmentations. For the efficient production of RI beams, intense primary beams of heavy neutron-rich isotopes are increasingly required, such as ^{48}Ca, ^{58}Fe, and ^{86}Kr. The AVF-RRC scheme supplies relatively low intensities for these beams (only several pnA). Since RRC operation with a harmonics of 8 was successfully carried out in 2002, beams of these heavy particles have been accelerated in the RILAC-CSM-RRC scheme. The data for these beams accumulated thus far are listed in Table 3. In all cases, beam intensity drastically increased; nevertheless the beam energy are somewhat lower (63 MeV/u) than those in the AVF-RRC scheme. Since a high beam intensity sometimes overcomes the drawback of a low beam energy in RI beam production, this new scheme has been frequently used for recent RIPS experiments.

The upgrade of the AVF has been in progress in cooperation with CNS of the university of Tokyo. The flattop acceleration system was added to the AVF cavities in 2002. The power supplies will be improved in order to increase the maximum energy of light ion beam in the beginning of 2005. As results, the K-value of the AVF will be upgraded from 70 to 78 MeV.

Table 1. Operation statistics of RRC and AVF in 2004.

Operation time of RRC	5091	(5678) hr
Beam service time	3421	(3739) hr
Machine trouble	736	(239) hr
Nuclear physics experiment	78	(74) %
Non-nuclear physics experiment	22	(26) %
RILAC-RRC operation	23	(11) %
AVF-RRC operation	77	(89) %
Operation time of AVF standalone	999	(1582) hr
Beam service time	637	(1192) hr

Figures in parentheses are data obtained in 2003.

Table 2. RRC and AVF beam time for each beam course in 2004.

Target room	Total time (hr)	No. of experiments
E1	0 (100)	0 (6)
E2	134 (117)	4 (3)
E3	182 (342)	8 (13)
E4 (SMART)	189 (538)	6 (9)
E5	183 (286)	29 (40)
E6 (RIPS)	2650 (2342)	27 (25)
RRC/D (MS)	107	5
AVF (C03)[§]	192 (158)	7 (5)
E7 (CRIB)[§]	445 (1034)	9 (16)

[§] AVF stand-alone only, used for CNS of the University of Tokyo. Figures in parentheses are data obtained in 2003.

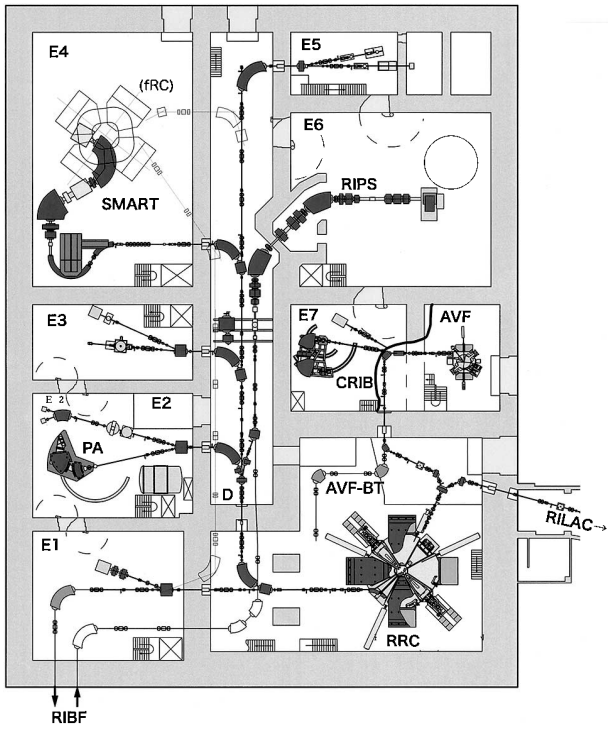

Fig. 1. Layout of beamlines of RRC and AVF.

[*1] Center for Nuclear Study, University of Tokyo
[*2] SHI Accelerator Service, Ltd.

Table 3. Upgrade of beam intensities with CSM.

Ion	AVF → RRC					RILAC → CSM → RRC				
		Stripping after AVF			Beam		Stripping after CSM			Beam
	E_{RRC} (h_{RRC}) MeV/n	$q_i \rightarrow q_f$	E_{AVF} MeV/n	effi. %	intensity pnA	E_{RRC} (h_{RRC}) MeV/n	$q_i \rightarrow q_f$	E_{CSM} MeV/n	effi. %	intensity pnA
^{40}Ar	95 (5)	+11 →+17	5.2	32	90	63 (8)	+9 →+15	3.6	26	1000
	AVF+RRC(28.1MHz)					RILAC(37.8MHz)+A1+A2+RRC				
^{48}Ca	70 (5)	+11 →+18	4.0	26	7	63 (8)	+11 →+17	3.6	29	150
	AVF+RRC(24.6MHz)					RILAC(37.8MHz)+A1+A2+RRC				
^{58}Fe	90 (5)	+13 →+24	5.0	14	4	63 (8)	+13 →+21	3.6	32	80
^{56}Fe data	AVF+RRC(27.6MHz)					RILAC(37.8MHz)+A1+A2+RRC				
^{70}Zn						63 (8)	+16 →+25	3.6	21	120
						RILAC(37.8MHz)+A1+A2+RRC				
^{86}Kr	70 (5)	+20 →+31	4.0	27	4	63 (8)	+16 →+30	3.6	11	90
^{84}Kr data	AVF+RRC(24.6MHz)					RILAC(37.8MHz)+A1+A2+RRC				

The maximum energy of the nitrogen beam becomes higher than 9 MeV/u and it extends the availability of RI beams by the CRIB in E7.

The cogeneration system (CGS) can supply a power of 6.5 MW at maximum, which is enough to cover the power consumption of the existing accelerators. The CGS operation, which had been carried out in the framework of accelerator operations, was handed over to the Facilities Maintenance Section of the RIKEN administration office at the beginning of Oct. 2004. The heat source for air-conditioning in Nishina Memorial building was switched to the absorption chiller in the CGS in March 2004 instead of three sets of mechanical chillers in order to save the power (300 kW).

A serious trouble was found in the #1 rf cavity of RRC in June 2004. The contact fingers of the upper moving box (that is, one of the coarse tuners) were damaged during the operation caused by a control-sequence problem. The scale of the damage was so large that it took about two months to repair them completely. The experiments scheduled with the RRC from the end of June to July were all cancelled. In the mean time, superheavy-element research experiments were performed instead, leading to the discovery of $Z = 113$ element on 23 July.

As the RIBF project is approaching the commissioning in 2006, the RARF needs to start relevant preparations as follows: The production of uranium ions at RILAC ion source will begin in summer 2005, and its acceleration test will start in autumn 2005. In order to realize it, we applied an official license of the uranium acceleration to 11 MeV/u with the RRC in the end of 2004. The development of a charge stripper that can withstand uranium beams is in progress.

Since the construction of the fixed-frequency Ring Cyclotron (fRC) will start in July 2005 in the E4 target room (see Fig. 1), an experiment with the SMART should come to an end in May 2005. Some magnets in SMART will be transferred to the new building of the RIBF experimental hall, and will be used there as part of a new apparatus. The extraction beamline of fRC will be built in the D, RRC and E1 rooms as shown in Fig. 1 by thin lines. The operation of RRC will be interrupted due to the construction of these beamlines from April to June 2006. In autumn 2006, the RILAC and RRC will begin to provide beams into the RIBF accelerators (fRC, IRC and SRC).

Cogeneration system operation

T. Fujinawa, E. Ikezawa, K. Yamaguchi, M. Kase, and Y. Yano

It has been passed twenty months since the Cogeneration system (CGS) was introduced in spring 2003. During this period, the CGS has been in stable operation mainly for supplying electrical power to RARF accelerators. The operation statistics in FY2003 and 2004 is shown in Tables 1 and 2. At present, the CGS operates only in the daytime during weekdays and Saturday because there is not yet a constant demand for thermal loads and because the low electricity charge rate during the night is too low. This may cause the problem that the current overall efficiency (42.5%) is not as high as that expected in 2007, when the whole facility will start to be operational. The CGS operates primarily electricity generation since less there is demand for thermal load at present. The performance of the CGS with a full refrigerator load in 2007 is shown in Table 3. The refrigerator load over 920USRT electrical output will decease from 6.5 MW, but overall efficiency will be better. The total refrigerator capacity is 9.5 MW (2700USRT[a)]) with five 1.4 MW (400USRT) and two 1.2 MW (350USRT) absorption chillers (7°C). The chilled water 670 kW (190USRT)) is used to cool the compressor-inlet air in order to increase the hot-weather capacity.

The reliability of turbine blades was improved to increase the maximum electrical output from 6.3 to 6.5 MW in august 2004. (The unit price changed from ¥8.96/kW to ¥8.86/kW this makes ¥1000/h profit & a heat recovery of ¥685.7/h.)

As an effort to increase the head load to the CGS, its cooled water line was connected to those in the Nishina memorial building and the linac buildings in the winter of 2004. In April 2004, some old chillers on these buildings stopped their operation, and the CGS commenced to supply 7°C cooled water (3.7 t/min) to these buildings instead. It is used for the air-conditioning units in the rooms of beam lines, experimental apparatus, and power supplies as well as accelerators, *i.e.*, RRC, AVF, and RILAC. It is also supplied to the heat exchanger of the vacuum cooling system in order to lower the temperature of water for compressors of cryogenic vacuum pumps of RRC and AVF with these improvements, approximately 300 kW of electric power can be saved.

CGS operation and maintenance have been carried out in the framework of accelerator operations. In October 2004, according to the RIKEN policy that energy affairs should be managed by one division, the CGS operation and maintenance was handed over to the Facilities Maintenance division.

Table 2. Total cost.

Unit rate	¥/kWh
Electrical output only	10.2
Inc heat recovery	9.68
Fixed cost	
Profit	¥
Electrical basic cost	184558500
Gas unitrate down	27669966
Loss	¥
Private generator charge by TEPCO	−38669400
Operator cost	−36000000
Consumable	−7653023
Maintenance	−38627556
Profit	91278487

Table 3. Performance of CGS expected in 2007.

Electric output at 15°C	5,790 kW
Steam production	10,300 kg/hr
Electrical efficiency	32.1%
Overall efficiency	64.4%
Refrigeration capacity	2510USRT
NO_x emission	32.3 ppm

Table 1. Statistics of CGS operation from April, 2003 to end of September, 2004.

	2003		2004		Total	
	No.of Days	%	No.of Days	%	No.of Days	%
Operation time	270	72.4	153	83.6	423	76.1
Scheduled shutdown	69	18.5	29	15.8	98	17.6
Overhaul and improvement	34	9.1	1	0.6	35	6.3
Sum	373	100	183	100	556	100
Direct cost						
Electrical output power	¥	kWh	¥	kWh	¥	kWh
	207602218	19938240	138433342	13999075	346035560	33937315[§]
	10.41 (¥/kWh)		9.89 (¥/kWh)		10.2 (¥/kWh)	
Used gas of CGS	¥	Nm^3	¥	Nm^3	¥	Nm^3
	196194230	5510220	150541736	4023150	346735966	9533370

[§] 50.8% and 16.5% of total consumption in RARF and RIKEN, respectively.

a) United States Refrigeration Tom, 1USRT = 3.52 kW

Operation of the tandem accelerator

T. Kobayashi and K. Ogiwara

The 1.7 MV tandem accelerator (Pelletron) was operated for a total of 93 days for experiments during the annual reporting period from Nov. 1, 2003 to Oct. 31, 2004. A total of 44 days was spent for machine inspection and beam test. The accelerated ion species in this period are H^+, He^+ and B^+ with energies from 2.0 to 2.3 MeV.

Experimental studies on the following subjects were performed, and are still in progress.

(1) Nuclear reaction analysis (NRA) using $^1H(^{11}B, \alpha)2\alpha$ reaction (47 days)
  (a) The state of hydrogen in Nb-based and Ta-based alloys as investigated by the channeling method
  (b) Effect of irradiation on the state of hydrogen in metals

(2) Particle-induced X-ray emission (PIXE) (28 days)
  (a) Development of a highly sensitive high-resolution in-air PIXE system for chemical state analysis
  (b) Trace element analysis of biological and environmental samples using energy dispersive X-ray spectrometry

(3) The analysis using elastic scattering (18 days)
  (a) Rutherford backscattering spectrometry (RBS) analysis of polymers and carbon materials containing metallic nanoparticles.
  (b) Elastic recoil detection (ERD) analysis of diamond-like carbon (DLC) thin films and ion-implanted polymers for determining hydrogen contents.

The total time in days, which was spent for each experiment, is shown in parentheses.

Decay modes of heavy and superheavy nuclei

H. Koura*

[Decay by proton emission, Spontaneous fission, Binding energies and masses]

In the heavy and superheavy nuclidic region, some decay modes coexist, such as α-decay, β-decay, and spontaneous fission. We have studied the estimation of partial half-lives of these decay modes[1] with the use of some decay models and the KUTY mass formula,[2,3] and discussed the most probable decay modes for each nucleus in that region. In addition to these decay modes, proton emission is also a possible decay mode outer from a proton-drip line in that region. In this report, we estimate proton-emission half-lives with the use of a single-proton potential. We take the modified Woods-Saxon potential[4] which is used for calculating the KUTY mass formula. The central and spin-orbit parts are expressed as

$$V_{\rm cen}(r) = V_0 \frac{1}{\{1+\exp\,[(r-R_v)/a_v]\}^{a_v/\kappa}} \times \left\{1 + V_{\rm dp}\frac{1}{1+\exp\,[-(r-R_v)/a_v]}\right\}, \quad (1)$$

and

$$V_{ls}(r)\boldsymbol{l}\bullet\boldsymbol{s} = V_{ls0}\frac{1}{2m}\frac{1}{r} \times \frac{d}{dr}\left\{\frac{1}{1+\exp\,[(r-R_{ls})/a_{ls}]}\right\}\boldsymbol{l}\bullet\boldsymbol{s}, \quad (2)$$

where included parameters are taken to be smooth functions of Z and N, and the charge symmetry is imposed on these potentials. This potential reproduces fairly well the experimental single-particle levels of 15 doubly magic and magic-submagic nuclides in a wide nuclidic region. The proton-emission partial half-lives $T_{\rm p1/2}$ are calculated by the one-dimensional WKB method for this potential, including the central part, the spin-orbit part, and the Coulomb part. The spin-parity and centrifugal force for a single proton are estimated from this potential. Figure 1 shows some experimentally measured, and calculated $\log_{10}(T_{\rm p1/2}/({\rm s}))$ results for odd-Z nuclei. The differences between experimental $T_{\rm p1/2}$ and calculated ones are nearly within 2 in $\log_{10}$.

With the above calculation, we estimate the shortest partial half-lives among proton emission, α-decay, β-decay and spontaneous fission in the heavy and superheavy nuclidic region. To calculate the half-lives, we take Q-values of the KUTY mass formula. Figure 2 shows the most dominant decay modes for the nuclei with total half lives $T_{\rm total1/2} > 10^{-9}$ s. In this figure

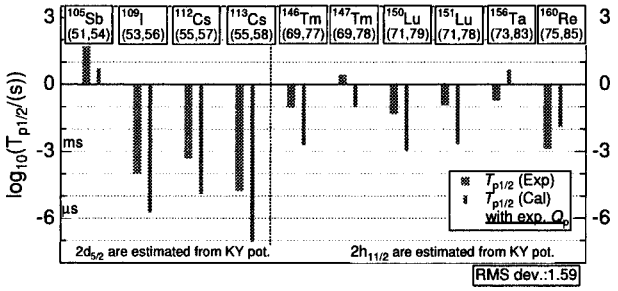

Fig. 1. Experimental and calculated $\log_{10}(T_{\rm p1/2}/({\rm s}))$.

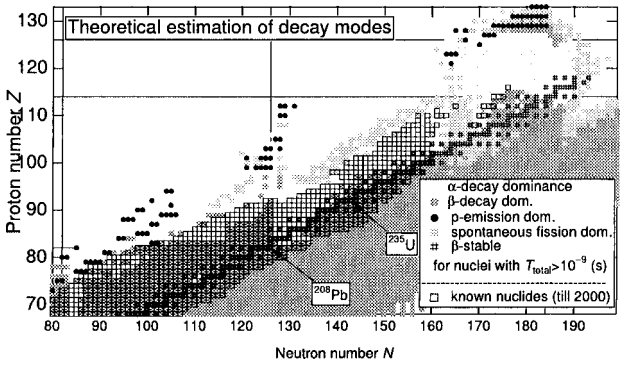

Fig. 2. Shortest partial half-lives among α-decay, β-decay, spontaneous fission and proton emission. The Q values of KUTY's formula are used for calculations of α-decay, β-decay and proton emission. The known nuclei are also shown.[5]

we can see some proton-emitting nuclei with $N \lesssim 100$ near the proton-drip line. This tendency is roughly similar to that of some experimental results. In the region of $100 \lesssim N \lesssim 110$ and $120 \lesssim N \lesssim 130$, proton emission is expected to be dominant, although these nuclei are far from known nuclei. On the other hand, in the region of $110 \lesssim N \lesssim 120$ and $130 \lesssim N \lesssim 160$, proton-emitting nuclei are not expected, because these spontaneous fission half-lives seem to be very short, or less than 10^{-9} s in this region.

* Advanced Science Research Center, Japan Atomic Energy Research Institute

References

1) H. Koura: RIKEN Accel. Prog. Rep. **37**, 11 (2004).
2) H. Koura et al.: Nucl. Phys. A **674**, 44 (2000).
3) H. Koura et al.: RIKEN Accel. Prog. Rep. **36**, 9 (2003).
4) H. Koura et al.: Nucl. Phys. A **671**, 96 (2000).
5) T. Horiguchi et al.: Chart of the Nuclides 2000, Japan Atomic Energy Research Institute (2001).

Variational calculations of nuclear equation of state

M. Takano*

[NUCLEAR STRUCTURE, Nuclear matter]

Recently, studies of the equation of state (EOS) for asymmetric nuclear matter (ANM) have become important. For example, Oyamatsu and Iida[1] pointed out that future measurements of the radii of neutron-rich unstable nuclei will provide some constraints for the EOS of ANM, particularly for the proton-fraction dependence of the saturation density ρ_0.

As one of the most powerful many-body techniques for the theoretical derivation of the nuclear EOS, the variational method such as the Fermi Hypernetted Chain (FHNC) calculation, has been applied to symmetric nuclear matter (SNM) and pure neutron matter (PNM). However, in the case of ANM, there are only few examples of the variational calculations[2] because the FHNC method is complicated.

In this study, we apply a new variational method, which we proposed in Ref. 3, for calculating the EOS of ANM. The main feature of this method is to construct an approximate energy expression (AEE) which expresses the energy per particle E/N as an explicit functional of variational functions. Here, spin-isospin-dependent, central-, tensor- and spin-orbit-type two-body distribution functions are introduced as the variational functions. Since the three states of the isospin-triplet have to be treated independently in the case of ANM, there are 16 variational functions.

Spin-isospin-dependent structure functions, which are the Fourier transforms of the central-type two-body distribution functions, are also introduced for the AEE. There are several necessary conditions on the structure functions, and the AEE automatically guarantees those necessary conditions.

Once the explicit AEE is constructed, the Euler-Lagrange equations for the variational functions are derived, and fully minimized values of E/N are obtained by solving them numerically.

This variational method has been applied to liquid ^{3}He and fairly reasonable results have been obtained. In the case of nuclear matter, however, a "phenomenological refinement" is necessary, *i.e.*, the long-range part of the noncentral nuclear forces such as the tensor and the spin-orbit components must be multiplied by a damping function; without this refinement, the variational calculation gives extremely low values for E/N.[4] The damping function has an adjustable parameter, the value of which is determined so that the calculated saturation point for SNM becomes close to the empirical one.

In order to construct the AEE for ANM, which is partially isospin-polarized nuclear matter, we need to extend the formulation. This extension, from SNM and PNM[4] to ANM, is similar to the one carried out in Ref. 5, where the AEEs for spin-unpolarized and fully spin-polarized liquid ^{3}He have been extended to that for the partially spin-polarized one.

In Fig. 1, E/N for ANM calculated by this variational method with the AV18 potential is shown as a function of the proton fraction ξ. Owing to the "phenomenological refinement", $E/N = -15.2\,\mathrm{MeV}$ at $\rho_0 = 0.21\,\mathrm{fm}^{-3}$ is obtained for SNM. The result for ρ_0 is somewhat high, which may be understandable because the three-body nuclear force is not included in the calculations.

In order to discuss the EOS of ANM in detail, better reproduction of the empirical saturation point for SNM is necessary.

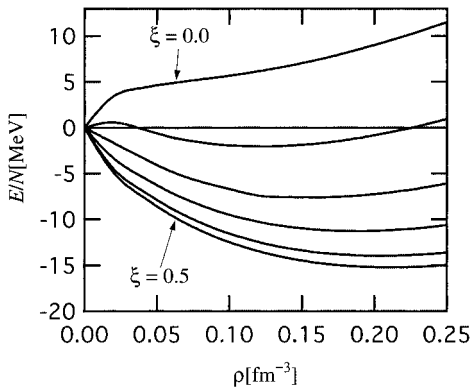

Fig. 1. Energies per nucleon for ANM with the AV18 potential.

References

1) K. Oyamatsu and K. Iida: Prog. Theor. Phys. **109**, 631 (2003).
2) I. E. Lagaris and V. R. Pandharipande: Nucl. Phys. A **369**, 470 (1981).
3) M. Takano and M. Yamada: Prog. Theor. Phys. **91**, 1149 (1994).
4) M. Takano and M. Yamada: Prog. Theor. Phys. **100**, 745 (1998).
5) M. Takano, T. Endo, R. Kimura, and M. Yamada: Prog. Theor. Phys. **109**, 213 (2003).

* Advanced Research Institute for Science and Engineering, Waseda University

Importance of prolate neutrino radiation in core-collapse supernovae

H. Madokoro, T. Shimizu, and Y. Motizuki

[shock waves, hydrodynamics, stars:neutron, supernova:general]

We study the effects of the prolate and oblate neutrino heating on the mechanism of core-collapse supernovae. It is expected that neutrino radiation becomes anisotropic when a proto-neutron star rotates and when convection occurs inside the proto-neutron star. Our purpose in this study, which follows that of previous studies,[1,2] is to understand what kind of neutrino radiation is favorable for a successful explosion through a parameter study when the total neutrino luminosity is given. The details of our results are shown in Ref. 3.

We performed 2D simulations by solving hydrodynamical equations in spherical coordinates (r, θ).[1–3] The local neutrino flux density is assumed to be $l_\nu(r,\theta) \propto T_\nu^4 \left(1 + c_2 \cos^2\theta\right)/r^2$, where T_ν is the neutrino temperature (we fix $T_\nu = 4.70\,\mathrm{MeV}$ in this study), and c_2 is a parameter which represents the degree of anisotropy in the neutrino radiation. The ratio of neutrino flux along the polar axis ($l_z \equiv l_\nu(r, \theta = 0°)$) and that on the equatorial plane ($l_x \equiv l_\nu(r, \theta = 90°)$) becomes $l_z/l_x = 1 + c_2$. The models that we examined are summarized in Table 1.

We have found that the effect of anisotropy becomes more powerful in both the prolate and oblate models as the degree of anisotropy in the neutrino radiation increases: the larger is the degree of anisotropy, the larger is the explosion energy. It was found, however, that this effect saturates at around a certain degree of anisotropy. We found that, at a later stage of evolution, model pro100 ($t < 360\,\mathrm{ms}$) or pro150 ($t > 360\,\mathrm{ms}$) shows the largest explosion energy among the prolate models, while the explosion energy of model obl167 becomes the largest among the oblate models. This means that the saturation of the effect of anisotropic neutrino radiation appears at $l_z/l_x \sim 1.1 - 1.15$ for a prolate explosion and $l_x/l_z \sim 1.2$ for an oblate explosion. We also confirmed that the explosion energy in the prolate model of $l_z/l_x = 1.1$ is larger than that in the saturated oblate model of $l_x/l_z = 1.2$. This is explicitly illustrated in Fig. 1. In other words, the prolate explosion of $l_z/l_x = 1.1$ (which corresponds to an anisotropy of $\sim 5\%$) is always more energetic than any other oblate models, even if the degree of anisotropy in the neutrino radiation becomes larger. Combined with our previous results,[1,2] we conclude that globally anisotropic (prolate) neutrino radiation is the most effective way to increase the explosion energy among the various types of explosions investigated in these studies when the total neutrino luminosity is given. Our results are suggestive of the observation that the expanding materials of SN1987A have been observed to be deformed in a prolate form.

Table 1. Simulated models.

Model	l_z/l_x	c_2
sph000	1.00	0.000
pro050	1.05	0.050
pro100	1.10	0.100
pro150	1.15	0.150
pro200	1.20	0.200
pro250	1.25	0.250
pro300	1.30	0.300
obl048	1/1.05	−0.048
obl091	1/1.10	−0.091
obl130	1/1.15	−0.130
obl167	1/1.20	−0.167
obl200	1/1.25	−0.200
obl231	1/1.30	−0.231

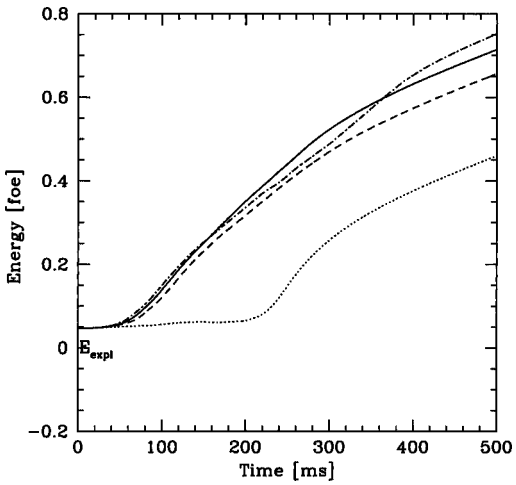

Fig. 1. Evolution of explosion energy for saturated models: pro100 (solid line), pro150 (dot-dashed line), obl167 (dashed line), and sph000 (dotted line).

References

1) T. M. Shimizu et al.: Astrophys. J. **552**, 756 (2001).
2) H. Madokoro, T. Shimizu, and Y. Motizuki: Astrophys. J. **592**, 1035 (2003).
3) H. Madokoro, T. Shimizu, and Y. Motizuki: Pub. Astron. Soc. Jpn. **56**, 663 (2004).

Study of supernova explosions with neutrino-transfer hydrodynamics

K. Sumiyoshi,[*1] H. Suzuki,[*2] S. Yamada,[*3] and H. Toki[*4]

[supernova, EOS, neutrino]

Understanding the explosion mechanism of core-collapse supernovae is a challenging problem, that requires extensive researches in nuclear physics and astrophysics. In order to reach the final answer, it is necessary to investigate the core-collapse supernovae by implementing hydrodynamics and neutrino-transfer together with reliable nuclear equation of states and neutrino-related reactions. Advances in physics of unstable nuclei in radioactive nuclear beam facilities have given chances to provide us with nuclear physics in supernovae than ever before, hence, new nuclear data supported by extensive experiments should be examined in modern supernova simulations.

We study the explosion mechanism of collapse-driven supernovae by numerical simulations with a new nuclear equation of state (EOS) based on unstable nuclei. We especially focus on the influence of the new nuclear EOS in the neutrino-transfer hydrodynamics. We follow the core-collapse, bounce and shock propagation by adopting the new EOS, which is based on the data of unstable nuclei, and the conventional one which has been used almost uniquely in recent simulations. We compare the behavior of shock and the thermal evolution of supernova core by performing numerical simulations for a long period of $\sim$1 sec after the core bounce.

A new complete set of EOS for supernova simulations (Shen's EOS) has become available[1,2] by the relativistic mean field (RMF) theory with a local density approximation. The RMF framework with the parameter set TM1 has been successful to reproduce the properties of finite nuclei including n-rich ones.[3] For comparison, we adopt also the EOS by Lattimer and Swesty.[4] The EOS is based on the compressible liquid drop model for nuclei together with dripped nucleons.

We have developed a new numerical code of neutrino-transfer hydrodynamics[5,6] for supernova simulations. The code solves hydrodynamics and neutrino-transfer at once in general relativity under the spherical symmetry. As an initial model, we adopt the profile of iron core of a $15\,M_\odot$ massive star. We perform the numerical simulations with Shen's EOS (denoted by SH) and Lattimer-Swesty EOS (LS) for comparisons.

It is remarkable that the explosion does not occur in the model SH, *i.e.* the case with the new EOS table, and the shock wave stalls in a similar manner as the model LS. The shock in SH does not reach at a significantly larger radius than in LS (Fig. 1). The shock stalls below 200 km and starts receding in two cases. We have found, however, that there are quantitative differences in core-collapse and bounce due to the differences between nuclear EOSs.[7] Having a larger symmetry energy in SH, free-proton fractions during collapse in SH are smaller than in LS. Smaller free-proton fractions lead to smaller electron capture rates if electron captures on nuclei are suppressed. The difference of EOS becomes apparent having a more compact star for LS with the central density of $6.6 \times 10^{14}\,\mathrm{g/cm^3}$ ($4.0 \times 10^{14}\,\mathrm{g/cm^3}$ for SH) at 800 ms after the bounce. The peak structure of temperature at around 10 km is formed and the peak temperature reaches at 38 and 51 MeV for SH and LS, respectively, due to the gradual compression of core having accretion. These differences of thermal structure may give influences on shock dynamics, supernova neutrinos and proto-neutron star cooling. Further details of the full numerical simulations will be published elsewhere.[6]

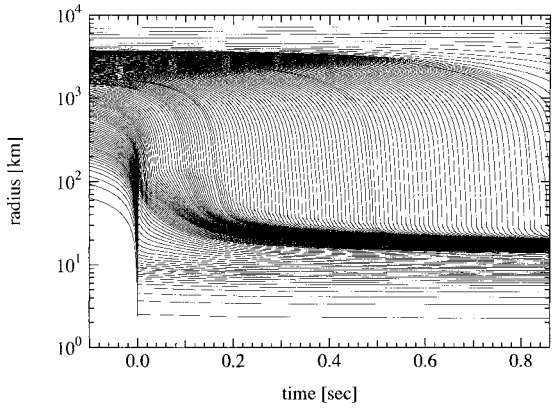

Fig. 1. Radial trajectories of mass elements of the core of $15\,M_\odot$ star as a function of time after the bounce (SH).

*1 Numazu College of Technology
*2 Faculty of Science and Technology, Tokyo University of Science
*3 Science and Engineering, Waseda University
*4 Research Center for Nuclear Physics, Osaka University

References

1) H. Shen, H. Toki, K. Oyamatsu, and K. Sumiyoshi: Nucl. Phys. A **637**, 435 (1998).
2) H. Shen, H. Toki, K. Oyamatsu, and K. Sumiyoshi: Prog. Theor. Phys. **100**, 1013 (1998).
3) Y. Sugahara and H. Toki: Nucl. Phys. A **579**, 557 (1994).
4) J. M. Lattimer and F.D. Swesty: Nucl. Phys. A **535**, 331 (1991).
5) K. Sumiyoshi, S. Yamada, H. Suzuki, H. Shen, and H. Toki: Nucl. Phys. (2005), in press.
6) K. Sumiyoshi, S. Yamada, H. Suzuki, H. Shen, S. Chiba, and H. Toki: Submitted to Astrophys. J. (2005).
7) K. Sumiyoshi, H. Suzuki, S. Yamada, and H. Toki: Nucl. Phys. A **730**, 227 (2004).

Neutron star matter in a chiral quark theory†

S. Lawley,*1 W. Bentz,*2 and A. W. Thomas*3

[MATTER AT HIGH DENSITY, Neutron matter]

Many ideas in the area of finite density phase transitions have been developed in the context of neutron star calculations, in particular the phase transitions from nuclear matter (NM) to quark matter (QM).[1] In this work we calculate both the NM and QM phases in β-equilibrium using the flavor SU(2) flavor Nambu–Jona-Lasinio (NJL) model. Recently, the problem of NM saturation has been addressed with a method to simulate confinement in the description of the nucleon as a quark-diquark bound state.[2] In the QM phase, we allow for the possibility of scalar diquark condensation (color superconductivity),[3] and the mixed phases are calculated using the method of Glendenning.[1]

The effective potential for NM is $V^{NM} = V_{vac} + V_N - V_\omega - V_\rho - V_e$, where the vacuum term V_{vac} accounts for the polarization of the quark Dirac sea due to the valence nucleons,[2] V_N represents the Fermi motion of the nucleons which are described as quark-diquark bound states, V_ω and V_ρ are contributions from the isoscalar and isovector mean vector fields respectively, and V_e is the electron contribution which is necessary for chemical equilibrium.

The effective potential for QM is $V^{QM} = V_{vac} + V_Q - V_e + V_\Delta$, where the vacuum and electron terms are as above and the term for the Fermi motion of the quarks V_Q is analogous to V_N, but refering to up and down quarks instead of protons and neutrons. Color superconducting quark matter (SQM) includes a contribution from the quark pairing arising at the Fermi surface. This is expressed by the term V_Δ, which involves the pairing gap Δ and a coupling constant (G_s) for the pairing interaction in the scalar diquark channel.

In the calculations we set the constituent quark mass to zero, as it is known to decrease rapidly with density.[3] The strength of the pairing interaction is set to $G_S = 0.25 G_\pi$, where the coupling constant in the pionic channel (G_π) is fixed by reproducing the pion mass. To construct the phase diagram we compare the NM and QM effective potentials for each baryon and isospin chemical potential μ_B and μ_I, respectively.

Figure 1 shows the phases in the plane of the chemical potentials. The charge neutral equation of state trace the lines between the positively and negatively charged regions. It begins in the NM region, proceeds along the boundary between negatively charged NM and positively charged SQM, and ends in the SQM phase. The boundary between the NM(−) phase and the SQM(+) phase, which is rather short in this case, corresponds to the NM/SQM mixed phase. The volume fractions of NM and SQM in the mixed phase are obtained by the requirement of charge neutrality. It is important to observe that the coupling constant $G_s = 0.25 G_\pi$ is sufficiently strong to support a superconducting gap which is stable for isospin asymmetric matter. Figure 2 shows the phases in the plane of the charge density ρ_C and the baryon density ρ_B. We see that charge neutral matter will have a pure NM phase in the lower density region and a pure SQM phase at high densities. Between there is a mixed phase at intermediate densities.

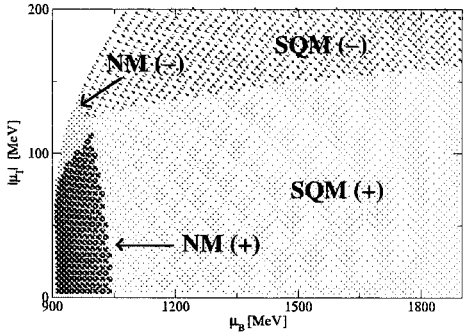

Fig. 1. Phase diagram in the plane of chemical potentials for baryon number and isospin.

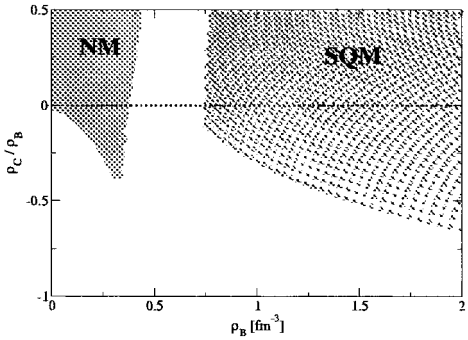

Fig. 2. Phase diagram in the plane of charge and baryon density.

References

1) N. K. Glendenning: *Compact Stars* (Springer, New York, 2000).
2) W. Bentz and A. W. Thomas: Nucl. Phys. A **696**, 138 (2001).
3) W. Bentz, T. Horikawa, N. Ishii, and A. W. Thomas: Nucl. Phys. A **720**, 95 (2003).

† Condensed from an article by S. Lawley, W. Bentz, and A. W. Thomas, to be published.

*1 Department of Physics, University of Adelaide, Australia
*2 Department of Physics, Tokai University
*3 Jefferson Laboratory, USA

Linear response theory in the continuum for deformed nuclei: Green's function vs absorbing-boundary condition†

T. Nakatsukasa* and K. Yabana*

[NUCLEAR STRUCTURE, Unstable nuclei]

The time-dependent Hartree-Fock (TDHF) theory is a dynamical theory and takes both collective and single-particle excitations into account. Its small-amplitude regime is known as the random-phase approximation (RPA) for effective density-dependent forces. The spreading width, which is partially described in the TDHF theory (one-body dissipation), is known to be important in broadening giant resonances. However, for light nuclei, the escape width is the dominant factor and becomes even more important near the drip line. In this paper, we propose a feasible method of treating the continuum in real-space TDHF calculation, that is, the absorbing-boundary condition (ABC) approach. We studied photoabsorption in molecules[1] and nuclear breakup reaction[2,3] using a similar technique.

The method, we call TDHF+ABC, is sufficiently simple and accurate for calculating nuclear responses in the continuum for spherical and deformed nuclei. Its small amplitude limit is equivalent to the continuum RPA.[4] Its advantage over the continuum RPA is its applicability to nonspherical systems. In addition, the TDHF wave function in the coordinate space provides us with an intuitive picture of the nuclear collective motion and the damping mechanism of the escape of particles. The time evolution of the TDHF states is calculated using the predictor-corrector method.[5] A technique of treating the continuum is the introduction of an absorbing complex potential outside interaction region. The potential must be properly chosen so as to achieve minimum reflection.

We study $E1$ responses in neutron-rich Be isotopes. The full Skyrme functional (SIII) is used in the calculation. A perturbative external field is chosen as $V_{\rm ext}(\mathbf{r}) = e_1 r^1 Y_{10}$, where e_1 is the $E1$ recoil charge. The time evolution is determined using the TDHF equation with the complex absorbing potential $-i\eta(\mathbf{r})$

$$i\hbar\frac{\partial}{\partial t}\psi_i(\mathbf{r},t) = \{h[\rho(t)] + \epsilon V_{\rm ext}(\mathbf{r})\delta(t) - i\eta(\mathbf{r})\}\,\psi_i(\mathbf{r},t), \qquad (1)$$

where $i = 1, \cdots, A$ and ϵ is a small parameter for validating the linear response approximation. $\eta(\mathbf{r})$ is zero in the physically relevant region of space. The TDHF equation, Eq. (1), is solved in real time from $t = 0$ to $30\,\hbar$/MeV, and then we perform the Fourier transform. The single-particle wave functions are represented in three-dimensional coordinate space. A nonuniform adaptive mesh is adopted in the calculation. See our original paper for details.

The calculated energy-weighted sum rule values are listed in Table 1. The soft $E1$ strength, $\tilde{S}(E1)$, is defined by integrating the $E1$ strength in the continuum, $dB(E1)/dE$, from $E = 0$ to 15 MeV. The enhancement of the soft dipole strength is significant for ^{14}Be. The large $\tilde{S}(E1)$ value for ^{8}Be is due to a large deformation splitting of the giant dipole resonance. For ^{12}Be, we obtain the ground state with a small prolate deformation. The lowest dipole state appears near the threshold, at $E \approx 4.5$ MeV, with $B(E1; 0^+ \to 1^-) = 0.023\,e^2$ fm^2. The corresponding experimental data[6] indicate $E = 2.68$ MeV with $B(E1) = 0.051(13)\,e^2$ fm^2.

For ^{14}Be, the calculated ground state has a superdeformed prolate shape ($\beta \approx 0.75$). The low-energy dipole state is embedded in the continuum at $E \approx 5$ MeV with a significant $E1$ strength, $B(E1) \approx 0.26\,e^2$ fm^2. The peak position is almost at the same energy as that for ^{12}Be, however, the strength is about 10 times larger. The experiment results seem to indicate a certain enhancement of the Coulomb dissociation cross section at approximately $E \approx 2$ and ≈ 5 MeV.[7]

Table 1. Energy-weighted sum rule in units of e^2 fm^2 MeV. $S(E1)_{\rm class}$ indicates the classical TRK value. $S(E1)$ is obtained using the present TDHF+ABC method. $\tilde{S}(E1)$ gives the soft $E1$ strength.

	$S(E1)_{\rm class}$	$S(E1)$	$\tilde{S}(E1)$
^{8}Be	29.7	34.0	3.14
^{10}Be	35.7	42.8	1.26
^{12}Be	39.6	48.2	2.54
^{14}Be	42.5	52.2	7.57

† Condensed from the article submitted to Phys. Rev. C **71**, 024301 (2005).

* Center for Computational Sciences, University of Tsukuba

References
1) T. Nakatsukasa and K. Yabana: J. Chem. Phys. **114**, 2550 (2001).
2) M. Ueda, K. Yabana, and T. Nakatsukasa: Phys. Rev. C **67**, 014606 (2002).
3) M. Ueda, K. Yabana, and T. Nakatsukasa: Nucl. Phys. A **738**, 288 (2004).
4) S. Shlomo and G. F. Bertsch: Nucl. Phys. A **243**, 507 (1975).
5) H. Flocard, S. E. Koonin, and M. S. Weiss: Phys. Rev. C **17**, 1682 (1978).
6) H. Iwasaki et al.: Phys. Lett. B **491**, 8 (2000).
7) M. Labiche et al.: Phys. Rev. Lett. **86**, 600 (2001).

Molecular structures of excited ^{10}Be and nucleon transfer in $\alpha + {}^6$He scattering

M. Ito,[*1] K. Yabana,[*1] K. Katō,[*2] and K. Ikeda

[NUCLEAR STRUCTURE, cluster model, unstable nuclei]

In studies on light neutron-rich nuclei, much attention has been concentrated on couplings between the clusters and the motion of the valence neutrons. From the viewpoint of these couplings, Be isotopes ($= \alpha + \alpha + n + n \ldots$) have very interesting features. In this system, the low-lying states can be understood in terms of molecular orbitals, as they are a single-particle motion around two α-cores,[1] while the "He-molecules" such as $^{12}\mathrm{Be} = {}^6\mathrm{He} + {}^6\mathrm{He}$ are observed in the excited states.[2,3] These mean that exotic structural change occurs between the "molecular orbitals" and the "valence bonds" in this system.

In order to understand this exotic structural change, we proposed a "generalized two-center cluster model" (GTCM) and applied the model to the $^{10}\mathrm{Be} = \alpha + \alpha + 2n$ system.[4] In this model, the total wave function is expressed by a linear combination of the "atomic orbitals" having $(\alpha + n) + (\alpha + n)$ and $\alpha + (\alpha + 2n)$ structures. The α particle is described by the $(0s)^4$ configuration in the harmonic oscillator (HO) potential and the valence neutrons are specified by the atomic orbitals in which the neutrons are localized at one of the α cores with $0p_i$ orbitals ($i = x, y, z$) in the same HO. The constructed atomic-orbital states are fully antisymmetrized and projected to the eigenstates of the total spin and the parity. This model naturally describes the molecular orbitals at a small α-α distance as well as the asymptotic cluster states of $\alpha + {}^6$He and $^5\mathrm{He} + {}^5\mathrm{He}$ at a large α-α distance. To describe the resonance boundary conditions, we also apply the method of the absorbing kernels in generator coordinates (AGC) on GTCM, which is a revised version of the complex absorbing potential (CAP) method for application to the microscopic cluster model.

The calculated energy surfaces and the energy spectrum are shown in Fig. 1. We obtained two bound states around the respective local minimum in the energy surfaces, which have molecular orbital configurations consistent with those in previous studies.[1] Furthermore, we have found two resonant states above the $\alpha + {}^6\mathrm{He}_{g.s.}$ threshold. The 0_3^+ state has a large component of the $\alpha + {}^6\mathrm{He}(2_1^+)$ channel, while the 0_4^+ state is the molecular-orbital state with the configuration of $(\pi_{1/2}^-)^2$. We also solve the scattering problem in this system and find a pronounced peak in the scattering matrix (S-matrix) of the transition from $\alpha + {}^6\mathrm{He}_{g.s.}$ to $\alpha + {}^6\mathrm{He}(2_1^+)$.

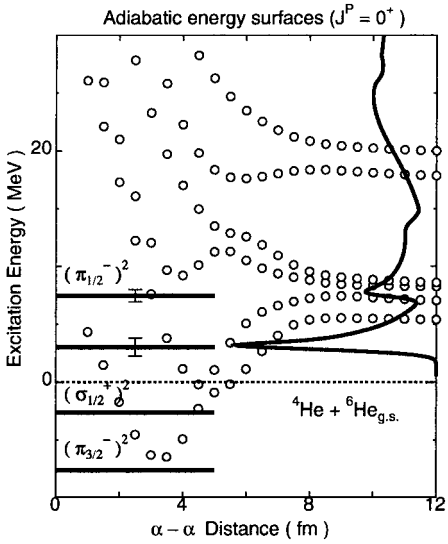

Fig. 1. Adiabatic energy surfaces (white circles) and the energy spectrum (horizontal bars) in $^{10}\mathrm{Be}$ ($J^\pi = 0^+$). The lowest and second-lowest states are the bound states having the molecular orbital configurations of $(\pi_{3/2}^-)^2$ and $(\sigma_{1/2}^+)^2$, respectively, while the highest state has a configuration of $(\pi_{1/2}^-)^2$. In the right part of the figure, the magnitude of the scattering matrix is also shown.

The strong enhancement of the S-matrix can be seen, and its position is coincident to the resonance energy of 0_3^+, which reflects the large population of the final channel in the resonant state. Conversely, the strength of the S-matrix corresponding to the 0_4^+ state is weak, because it has a molecular orbital configuration that has a different structure from the incident channel ($\alpha + {}^6\mathrm{He}_{g.s.}$) and the exit one ($\alpha + {}^6\mathrm{He}(2_1^+)$). Therefore, the excitation of the resonant states has a close connection to their intrinsic structure. For Be isotopes, unified studies on their nuclear structure and nuclear reaction are now in progress.

*1 Institute of Physics, University of Tsukuba
*2 Division of Physics, Graduate School of Science, Hokkaido University

References

1) N. Itagaki and S. Okabe: Phys. Rev. C **61**, 044306 (2000).
2) M. Freer et al.: Phys. Rev. C **63**, 034301 (2001).
3) A. Saito et al.: Prog. Theor. Phys. Suppl. No. 146, 615 (2002).
4) M. Ito, K. Kato, and K. Ikeda: Phys. Lett. B **588**, 43 (2004).

Fusion reaction of halo nuclei†

M. Ito,[*1] M. Kobayashi,[*1] K. Yabana,[*2] T. Nakatsukasa,[*2] and M. Ueda[*3]

[NUCLEAR REACTION, Unstable nuclei]

Since the discovery of the halo structure in radioactive beam experiments, much effort has been devoted to developing reaction theories appropriate for halo nuclei and to elucidating their reaction mechanisms. At medium and high incident energies, such as $E > 50\,\mathrm{MeV/A}$, the eikonal theory has been successful in describing the reaction. On the other hand, at low incident energies, $E < 50\,\mathrm{MeV/A}$, the fundamental mechanism of the reaction has not been fully elucidated thus far.

Halo nuclei consist of the core nucleus and a few halo nucleons, which are bound weakly in the projectile. At high energies, the eikonal theory suggests that the core and the halo nucleons are independently scattered by the target nucleus. The interaction between the core and the halo nucleons plays only a minor role during the reaction. We will show that the independent scattering picture also holds for the reactions at low incident energies.

To elucidate the reaction mechanism of the halo nuclei at low incident energies, we have been developing a time-dependent wave-packet approach using the three-body reaction model.[1,2)] We have shown that the fusion probability is suppressed by the presence of the neutron halo. In this paper, we present our extended analyses for both neutron and proton halo cases. The fusion probability is suppressed by the neutron halo and is enhanced by the proton halo. The reason for these opposite effects of the halo nucleons on the fusion probability is related to the spectator role of the weakly bound nucleon. This analysis provides a unified picture for the reaction mechanism of halo nuclei.

We adopt a three-body model; a halo nucleon (n) and a core nucleus (C) constitute the projectile (P) colliding with a target nucleus (T). The method is based on the time-dependent Schrödinger equation

$$i\hbar\frac{\partial}{\partial t}\Psi(\mathbf{R},\mathbf{r},t) = \left\{-\frac{\hbar^2}{2\mu}\nabla^2_{\mathbf{R}} - \frac{\hbar^2}{2m}\nabla^2_{\mathbf{r}} + V_{nC}(r) + V_{CT}(R_{CT}) + V_{nT}(r_{nT})\right\}\Psi(\mathbf{R},\mathbf{r},t), \quad (1)$$

where we denote the relative n-C coordinate as $\mathbf{r}$ and the relative P-T coordinate as $\mathbf{R}$. The reduced masses of n-C and P-T motions are m and μ, respectively. We prepare an initial wave packet boosted toward the collision, then calculate the time evolution in the coordinate space. The fusion is identified as the flux loss due to the imaginary part of the core-target potential, $V_{CT}(R_{CT})$. The energy projection before and after the time evolution gives the fusion probability as a function of energy. In Fig. 1, we show the calculated fusion probability for a neutron halo nucleus, $^{11}\mathrm{Be} = {}^{10}\mathrm{Be}+\mathrm{n}$, and a hypothetical proton halo nucleus, $^{11}\mathrm{Be} = {}^{10}\mathrm{Li}+\mathrm{p}$ (a weakly-bound s-wave proton is assumed). The target is assumed to be ^{208}Pb. The result clearly indicates the suppression of the fusion cross section for the neutron halo case and the enhancement of it for the proton halo case, compared with the one without the halo nucleon.

The time evolution of the calculated wave packet suggests a spectator role in the dynamics of the weakly-bound nucleon. For the neutron halo case, the core nucleus is scattered in the backward direction by the Coulomb repulsion between the core and the target nuclei. This leads to the Coulomb breakup of the halo neutron. Since the neutron carries approximately 10% of the incident energy, the core effectively loses its energy (^{10}Be), which results in the suppression of fusion. Conversely, in the case of the proton halo projectile, the halo proton is scattered in the backward direction by the target Coulomb field, which is much stronger than the core nucleus is. This leads to the backward proton breakup, then the charge of the projectile decreases from Z to $Z-1$, which increases the fusion probability.

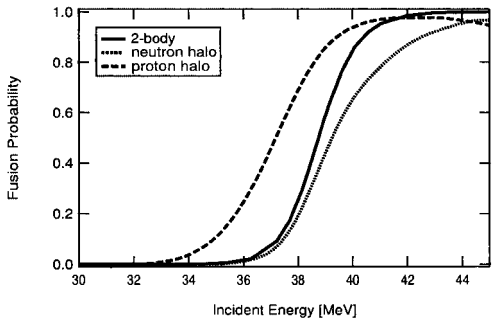

Fig. 1. Fusion probability as a function of incident energy. The '2-body' indicates the fusion probability between the core and the target nuclei without a halo nucleon.

† Condensed from articles in Nucl. Phys. A **738**, 303 (2004); Prog. Theor. Phys. Suppl. No. 154, 85 (2004).

*1 Institute of Physics, University of Tsukuba
*2 Center for Computational Sciences, University of Tsukuba
*3 Akita National College of Technology

References

1) K. Yabana: Prog. Theor. Phys. **97**, 437 (1997).
2) K. Yabana, M. Ueda, and T. Nakatsukasa: Nucl. Phys. A **722**, 261c (2003).

Microscopic study of ^{16}C + ^{208}Pb inelastic scattering

M. Takashina, Y. Kanada-En'yo,[*1] and Y. Sakuragi[*2]

[NUCLEAR REACTION, Unstable nuclei]

Recently, the opposite deformations between proton and neutron densities in C isotopes were theoretically suggested[1] by the method of antisymmetrized molecular dynamics (AMD). The author also gives a qualitative explanation[2] for the unusually small $B(E2; 2_1^+ \to 0_1^+) = 0.63\ e^2\ \mathrm{fm}^4$ in ^{16}C, which is derived from lifetime measurement.[3] According to Ref. 2, the 2_1^+ state is a rotational excited state, and the symmetric axis of neutron density is perpendicular to the rotational axis, while that of proton density is aligned to the rotational axis. Namely, the 2_1^+ state is dominated by neutron excitation.

In order to search for the possible different proton and neutron contributions to the excitation of the 2_1^+ state in ^{16}C, an inelastic scattering experiment of ^{16}C on a ^{208}Pb target was performed[4] applying the Coulomb-nuclear interference method. The analysis was carried out phenomenologically with the deformed potential model, and the M_n/M_p ratio was extracted. However, this analysis contains some assumptions, and hence, it seems inappropriate to test the validity of the AMD result by comparing the M_n/M_p ratio calculated by AMD with that evaluated in Ref. 4.

The simplest procedure to test the AMD result may be to calculate the differential cross sections of the inelastic scattering of ^{16}C on a ^{208}Pb target by the microscopic coupled-channels (MCC) method using the ^{16}C internal wave function obtained by AMD, and to compare the calculated result with the experimental reaction data measured in Ref. 4.

In the MCC calculation, the diagonal and coupling potentials are given by the double-folding model:

$$V_{\alpha(ij)\alpha'(k\ell)}(\mathbf{R}) = \int \rho_{ik}^{(a)}(\mathbf{r}_a)\rho_{j\ell}^{(A)}(\mathbf{r}_A) \times v_{NN}(\mathbf{r}_a + \mathbf{R} - \mathbf{r}_A)d\mathbf{r}_a d\mathbf{r}_A, \quad (1)$$

where $\rho_{ik}^{(a)}$ ($\rho_{j\ell}^{(A)}$) represents the transition density of the ^{16}C (^{208}Pb) nucleus between the state i (j) in channel α and the state k (ℓ) in channel α', and v_{NN} is the DDM3Y interaction.[5]

Here, we use the AMD wave function to calculate $\rho_{ik}^{(a)}(\mathbf{r}_a)$. In Ref. 2, two versions of the ^{16}C internal wave function are obtained in the variation before projection (VBP) formalism, for which the strength of the spin-orbit force is changed: (a) $u_{ls} = 900$ MeV and (b) $u_{ls} = 1500$ MeV. In addition to them, we also use the AMD wave function for which the strength of the spin-orbit force is set to (c) $u_{ls} = 2000$ MeV so as to reduce the $B(E2)$ value. The $B(E2)$ values obtained with these three wave functions are $B(E2; 2_1^+ \to 0_1^+) = 1.9$, 1.4, and 0.93 $e^2\mathrm{fm}^4$, respectively. The density distribution of the ^{208}Pb nucleus is obtained by unfolding the measured charge form factor[6] with the realistic proton charge form factor[7] and it is assumed that the shape of the neutron density is the same as that of the proton density, namely $\rho_n(\mathbf{r}) = (N/Z)\rho_p(\mathbf{r})$.

The Coulomb potential is also given by the double-folding model. The double-folded Coulomb potential is written in the same form as Eq. (1), except for certain inputs: the proton transition densities and Coulomb force are substituted in place of the matter transition densities and v_{NN}, respectively. The imaginary part of the nuclear potential is assumed to be the same as the real part multiplied by a factor N_I. In the current calculation, we choose $N_I = 1.2$. We have found that the N_I dependence of the calculated differential cross sections was very weak.

The results of the MCC calculations with the AMD internal wave functions of cases (a) and (b) reproduce the experimental data well without introducing any normalization factor for the calculated differential cross sections, while the result with the wave function of case (c) underestimates the measured differential cross sections. The present result indicates that the AMD wave functions of cases (a) and (b) are better than that of case (c).

References

1) Y. Kanada-En'yo and H. Horiuchi: Phys. Rev. C **55**, 2860 (1997).
2) Y. Kanada-En'yo: Phys. Rev. C **71**, 014310 (2005).
3) N. Imai et al.: Phys. Rev. Lett. **92**, 062501 (2004).
4) Z. Elekes et al.: Phys. Lett. B **586**, 34 (2004).
5) M. El-Azab Farid and G. R. Satchler: Nucl. Phys. A **438**, 525 (1985).
6) H. de Vries et al.: At. Data Nucl. Data Tables **36**, 495 (1987).
7) T. Janssens et al.: Phys. Rev. **142**, 922 (1966).

[*1] Institute of Particle and Nuclear Studies, High Energy Accelerator Research Organization (KEK)
[*2] Department of Physics, Osaka City University

Nuclear radius deduced from proton diffraction by a black nucleus†

A. Kohama, K. Iida, and K. Oyamatsu*

[Nuclear reaction, Proton elastic scattering, Nuclear radius]

Size of atomic nuclei, one of the most fundamental nuclear properties, remains to be determined precisely. Most commonly, the size is deduced from electron and proton elastic scattering off nuclei.[1,2] The charge radii are well determined due to our full understanding of the underlying electromagnetic interactions, while deduction of the matter radii from the proton-nucleus scattering data depends on scattering theory, which is more or less approximate in the sense that the nucleon-nucleon interactions involved are not fully understood. During the past three decades there have been many efforts to deduce the matter density distributions, which are based on various scattering theories incorporating empirical nucleon-nucleon scattering amplitudes, such as Glauber theory and nonrelativistic and relativistic optical potential methods. A systematic analysis of the data for a large number of nuclides, however, is still missing.

In this work, we propose a new method of deducing the root-mean-square (rms) matter radii, which is powerful enough to allow us to perform such a systematic analysis. This method, in which we assume that the target nucleus is completely absorptive to the incident proton and hence acts like a "black" sphere,[3] is far simpler than the conventional methods, since, in the present method, one has only to analyze the proton elastic scattering data around a maximum in the small-angle regime.

In this method, a nucleus is viewed as a black sphere of radius a. A diffraction pattern of protons by this sphere is equivalent to that of the Fraunhofer diffraction by a circular hole of the same radius embedded in a screen. We determine a in such a way that the c.m. scattering angle [$\theta_{\rm c.m.} \equiv 2\sin^{-1}(q/2p)$] of the first maximum for the Fraunhofer diffraction agrees with that measured by proton-nucleus elastic scattering, θ_M. (Here, we define the zeroth peak as that whose angle corresponds to $\theta_{\rm c.m.} = 0$.) We remark that the diffraction patterns for $\theta_{\rm c.m.} \gg \theta_M$ are distorted by multiple scattering effects, which are beyond the scope of the black sphere picture. The radius, a, and the angle, θ_M, are then related by

$$2pa\sin(\theta_M/2) = 5.1356\cdots. \tag{1}$$

It is useful to identify this radius multiplied by $\sqrt{3/5}$ with the root-mean-square matter radius of the target nucleus:

$$r_{\rm BS} \equiv \sqrt{3/5}a. \tag{2}$$

The factor $\sqrt{3/5}$ comes from the assumption that the density distribution of the black sphere is uniform. Combining Eq. (2) with Eq. (1), we may thus write

$$r_{\rm BS} = \frac{3.9780\cdots}{2p\sin(\theta_M/2)}. \tag{3}$$

For most of stable isotopes of masses heavier than 50, the values of $r_{\rm BS}$ that can be determined from Eq. (3) agree well with the values of the rms matter radius, r_m, deduced from elaborate scattering theories in previous works, at proton incident energies higher than ∼800 MeV as shown in Fig. 1.

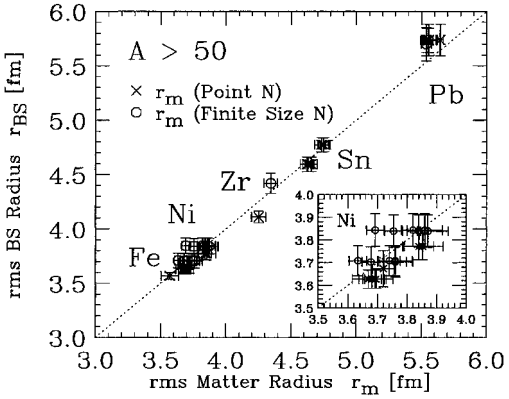

Fig. 1. $r_{\rm BS}$ *vs.* r_m for stable nuclei of masses above 50, such as ^{54}Fe, ^{58,60,62,64}Ni, ^{90}Zr, ^{116,124}Sn, and ^{208}Pb. The values of $r_{\rm BS}$ and r_m are derived from the data for proton incident energies higher than ∼800 MeV. The uncertainties of $r_{\rm BS}$ come from those of θ_M. The crosses (×) denote the rms matter radii of the point nucleon distributions, and the circles (○) denote those folded with the nucleon form factor. The dotted line represents $r_{\rm BS} = r_m$. Inset: $r_{\rm BS}$ *vs.* r_m for Ni isotopes.

References

1) C. J. Batty, E. Friedman, H. J. Gils, and H. Rebel: Adv. Nucl. Phys. **19**, 1 (1989).
2) B. Frois, C. N. Papanicolas, and S. E. Williamson: in *Modern Topics in Electron Scattering*, edited by B. Frois and I. Sick (World Scientific, Singapore, 1991), p. 352.
3) G. Placzek and H. A. Bethe: Phys. Rev. **57**, 1075 (1940).

† Condensed from the article in Phys. Rev. C **69**, 064316 (2004)

* Department of Media Theories and Production, Aichi Shukutoku University

Variation after parity projection calculation with Skyrme interaction for light nuclei†

H. Ohta,[*1] K. Yabana,[*2] and T. Nakatsukasa[*2]

[NUCLEAR STRUCTURE]

Among theories beyond the static mean field, the variation after the projection (VAP) method is one of the simplest ones. Yet, practical applications with realistic effective interactions, such as the Skyrme interaction, have not been fully investigated even for projection with respect to just the parity. The variation after the parity projection (VAPP) with a symmetry-violating intrinsic state leads to the ground state including certain octupole correlations. In addition, one can obtain a negative-parity excited state which is either a collective or non-collective excitation. In this paper, we propose an algorithm for the calculation of the VAPP with the Skyrme interaction on three-dimensional (3D) Cartesian coordinates. Calculations with the simple BKN interaction were reported previously.[1)]

In ordinary mean-field calculations, one finds self-consistent solutions with the axial and reflection symmetries for most nuclei. However, in VAPP calculations, the self-consistent solutions violate these symmetries. This symmetry violation in the intrinsic state is a consequence of the correlation beyond the mean field, which can be regarded as the octupole correlation. This is similar to the cluster correlation in light systems. In Table 1, we show the deformation parameters of the ground and excited states. The VAPP with the Skyrme interaction (SGII) leads to a cluster structure of $\alpha + {}^{16}\mathrm{O}$ in ^{20}Ne. The positive-parity solution has a substantial β_{30} deformation, which is consistent with the $\alpha + {}^{16}\mathrm{O}$ cluster structure. There are two solutions in the negative-parity sector. The lowest energy solution has a small β_{32} deformation as well as a prolate deformation. The next solution has a large β_{30} deformation as well as β_2. The former solution is characterized by $K^\pi = 2^-$ and the latter solution by $K^\pi = 0^-$. The $K^\pi = 0^-$ state can be interpreted as a parity partner of the ground state. Clustering is stronger in the negative-parity solution.

Table 1. Calculated and experimental excitation energies (E_x) for ^{20}Ne. We also show the quadrupole and octupole deformations in the intrinsic states.

K^π	0^+ $(J=0)$	2^- $(J=2)$	0^- $(J=1)$
E_x	g.s.	4.91 (MeV)	6.42 (MeV)
E_x (exp)	g.s.	4.97 (MeV)	5.78 (MeV)
β_2	0.535	0.589	0.694
γ	0.0	0.0	0.0
β_{30}	0.314	0.0	0.576
β_{32}	0.0	0.178	0.0

The angular momentum projection after the variation gives rotational spectra and transition strengths (Table 2). The calculated $B(E2)$ values agree well with experimental data, except for the terminating spin, $J = 8\,\hbar$. Since, in this work, each rotational band is constructed from a single intrinsic state, the angular momentum dependence of $B(E2; J_i \to J_f)$ is similar to that of the rotational model.

We also carry out the VAPP calculation for ^{12}C. To obtain a reasonable agreement with experiments, we must reduce the spin-orbit force in the SGII interaction (and most versions of the Skyrme as well). Introducing a reduction factor of 0.8 for the spin-orbit force, we are able to reproduce experimental positive- and negative-parity bands. It turns out that the ground state has a large β_{33} deformation with an oblate shape, which is consistent with the 3α clustering structure.

Table 2. Calculated intraband $B(E2)$ strengths for the $K^\pi = 0^+$ and $K^\pi = 2^-$ bands in ^{20}Ne. The first column indicates the initial and final spins/parities. For comparison, we show the values of the rotational model ($B(E2)_{\mathrm{rot}}$). The values in brackets are adjusted to experimental values. The experimental values[2)] are listed in the last column.

$J_i^\pi \to J_f^\pi$	$B(E2)_{\mathrm{cal}}$ ($e^2\mathrm{fm}^4$)	$B(E2)_{\mathrm{rot}}$ ($e^2\mathrm{fm}^4$)	$B(E2)_{\mathrm{exp}}$ ($e^2\mathrm{fm}^4$)
$2^+ \to 0^+$ $(K=0)$	41.6	(57.0)	57 ± 8
$4^+ \to 2^+$	59.9	81.4	71 ± 7
$6^+ \to 4^+$	67.5	89.7	66 ± 8
$8^+ \to 6^+$	75.1	93.9	24 ± 8
$3^- \to 2^-$ $(K=2)$	97.6	101	113 ± 29
$4^- \to 3^-$	73.5	75	77 ± 16
$4^- \to 2^-$	32.9	(34)	34 ± 6
$5^- \to 4^-$	52.6	53	< 808
$5^- \to 3^-$	53.1	53	84 ± 19
$6^- \to 5^-$	39.7	39	32 ± 13
$6^- \to 4^-$	67.0	66	$55\ ^{+23}_{-13}$

† Condensed from the article in Phys. Rev. C **70**, 014301 (2004).

*1 Institute of Physics, University of Tsukuba
*2 Center for Computational Sciences, University of Tsukuba

References

1) S. Takami, K. Yabana, and K. Ikeda: Prog. Theor. Phys. **96**, 407 (1996).
2) O. Häusser et al.: Nucl. Phys. A **168**, 17 (1971).

Direct inclusion of the tensor contribution in the cluster model and mechanism of the appearance of cluster structure in light nuclei

N. Itagaki,[*1] S. Aoyama,[*2] S. Okabe,[*3] and K. Ikeda

[NUCLEAR STRUCTURE, CLUSTER MODEL]

Recently, theoretical investigations of light nuclei based on a realistic nucleon-nucleon interaction have become feasible. For example, it is surprising that the quantum Monte Carlo calculation has microscopically shown the appearance of an α-α cluster structure in ^{8}Be based on a realistic nucleon-nucleon interaction.[1] Despite this situation, it should be mentioned that cluster models are still useful in describing very exotic cluster structures or intruder states of excess neutrons. Therefore, what we are going to do is to refine further the effective interactions used in the conventional cluster models to include the nature of the original nucleon-nucleon interaction, keeping a large model space for describing both exotic cluster and standard shell structures.

One of the key issues concerning the effective interactions used in the conventioanl cluster models that must be improved is the direct treatment of tensor terms, which has been renormalized in the central part of the effective interaction used in most cluster studies. Recently, several attempts of directly taking into account the tensor part of the interaction in microscopic cluster models have been started,[2] and a strong contribution has been discussed, for example, in the ^{4}He nucleus. However, if the tensor interaction is directly treated, the central part of the effective interaction has to be modified completely. Therefore, we perturbatively include a weakened tensor interaction as a first step, which is fitted to reproduce the tail part of the one-pion exchange potential (OPEP) with its inner part being weakened. By adding this tensor interaction, the long-range nature of the pion exchange potential is taken into account. In addition to the tensor term, we adopt the Volkov interaction for the central part and the G3RS potential for the spin-orbit part, and the strenght of the triplet-even channel of the Volkov interaction is reduced to adjust the binding energies of two- and three-nucleon systems.

The energy convergence of ^{4}He is shown in Fig. 1 as a function of the number of wave functions of antisymmetrized molecular dynamics (AMD). Both the results of the studies with and without the tensor interaction are presented. The energy obtained without the tenser terms converges around -23.3 MeV, but the binding energy becomes larger by about 4.4 MeV by introducing the present tensor term. The expectation value of the tensor interaction is -6.4 MeV; however, the increase in the kinetic energy by 2.0 MeV compared to the case without the present tensor term compensates it.

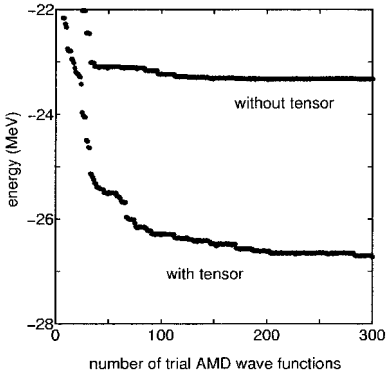

Fig. 1. The energy convergences of ^{4}He as a function of number of trial AMD Slater determinants (horizontal axis).

Furthermore, we can study the validity of one of the most fundamental bases of the mechanism of the appearance of a cluster structure. In the 1960s, a microscopic α-α potential was derived based on the meson theory,[3] and it was found that an α-α structure has a large relative distance, since the contribution of OPEP vanishes from the direct terms, when each α-cluster is described as the $(0s)^4$ configuration. Therefore, an interaction between α-clusters is weak and a cluster structure appears in ^{8}Be. Using such a microscopic potential, it has been possible to reproduce the phase shift of α-α scattering. This idea has been generalized as the threshold rule, which has been proposed as a mechanism to explain the appearance of exotic clustering. Using our interaction, the contribution of the tensor interaction becomes important at an α-α distance of 3 fm, and it does not eliminate the clustering of the system. The picture of the "weak interaction" between two ^{4}He nuclei is still valid, although the model space of the wave function is much extended compared to the $(0s)^4$ configuration.

*1 University of Tokyo
*2 Niigata University
*3 Hokkaido University

References

1) R. B. Wiringa, S. C. Pieper, J. Carlson, and V. R. Pandharipande: Phys. Rev. C **62**, 014001 (2000).
2) S. Sugimoto, K. Ikeda, and H. Toki: Nucl. Phys. A **740**, 77 (2004).
3) I. Shimodaya, R. Tamagaki, and H. Tanaka: Prog. Theor. Phys. **27**, 793 (1962).

Cluster-shell competition in light nuclei†

N. Itagaki,[*1] S. Aoyama,[*2] S. Okabe,[*3] and K. Ikeda

[NUCLEAR STRUCTURE, Cluster model, Unstable nuclei]

Nuclei are quantum many-body systems consisting of protons and neutrons, and these nucleons have been known to form some self-consistent mean field and to perform independent-particle motions. The nuclear shell-model, which is one of the standard models for the nuclear structure, is based on this assumption, and the strong spin-orbit interaction in the mean field has been known to be a key mechanism that fully explain the observed magic numbers. On the other hand, the α-particle, which corresponds to the doubly closed shell of the lowest s-shell in the shell model, is strongly bound, and since the relative α-α interaction is weak, strongly interacting four nucleons (α-particle) become a subunit of the nuclear structure in some light nuclei, contrary to the mean-field models.

If an α-cluster is expressed as the lowest $(s_{1/2})^4$ configuration, it is a spin-zero system, and non-central interactions do not contribute to it. However, the dissolution of the α-cluster should be taken into account in the systems, where the spin-orbit interaction, which is a characteristic interaction in the mean-field picture, strongly acts. Therefore, it is intriguing to study the cluster-shell competition for a unified understanding of the nuclear structure.

The antisymmetrized molecular dynamics (AMD) has been proposed to demonstrate this effect and extensively applied to calculating the properties of light stable and neutron-rich nuclei,[1)] and we superimpose many AMD wave functions based on AMD — superposition of selected snapshots (AMD triple-S).[2)] Here, the Gaussian centers for each nucleon are randomly generated and only their imaginary parts are optimized by solving the cooling equation. Then, we select important Slater determinants from the trial AMD wave functions. For the central part of the interaction, we use the Volkov effective $N-N$ potential with $M = 0.60$ and $B = H = 0.125$. For the spin-orbit term, we introduce the G3RS potential with a strength of $V_0 = 2000$ MeV.

The energy convergence of ^{12}C is shown in Fig. 1, here, the horizontal axis is the number of trial AMD wave functions. The basis states from 1 to 100 have various configurations of 3α, and those from 101 to 600 have a α+α+$2p$+$2n$ model space (relative α-α distances of 2, 3, and 4 fm). Here, the decrease in energy from the 3α-model is 5.2 MeV due to the strong spin-orbit interaction. Furthermore, the shell model-like wave functions of the α+$4p$+$4n$ model space are added (from 601 to 800), where two of α-clusters are broken. However, the decrease in energy by adding these basis states is only about 1 MeV, and it is considered that the contribution of the spin-orbit interaction is almost taken into account when one of the α-clusters is broken.

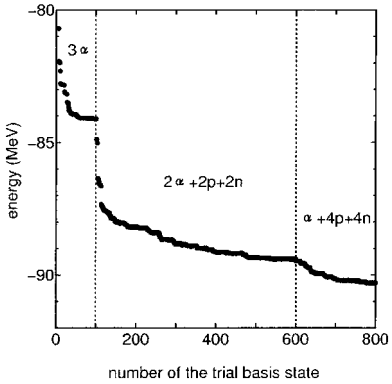

Fig. 1. The energy convergence of ^{12}C (0^+) with respect to the number of trial AMD basis states.

On the other hand, the calculated second 0^+ state (observed at $E_x = 7.65$ MeV) mainly has the 3α-component. In stellar nucleosynthesis, the second 0^+ state above the 3α threshold plays a crucial role in forming ^{12}C. It is formed as a triple-α resonance state and decays first to the 2^+ state and next to the ground 0^+ state by emitting γ-rays. The B(E2, $0^+_2 \rightarrow 2^+_1$) value strongly affects the abundance of ^{12}C; however, it has been about one-half in the conventional 3α model based on the resonating group method (RGM).[3)] In the present case, the mixing of 3α and α-breaking components affects the B(E2) value and it becomes consistent with the experimental value.

It can be summarized that for nuclei ^{8}Be, ^{10}Be, and ^{10}B, the increase in binding energy when the breaking of one of the α-clusters is taken into account is about 2 MeV, and essentially the α+α structure is the dominant configuration of the ground states. However, the increase is very large in ^{12}C (5.2 MeV).

References

1) Y. Kanada-En'yo and H. Horiuchi: Prog. Theor. Phys. **93**, 115 (1995).
2) N. Itagaki, A. Kobayakawa, and S. Aoyama: Phys. Rev. C **68**, 054302 (2003).
3) M. Kamimura: Nucl. Phys. A **351**, 456 (1981).

† Condensed from the article in Phys. Rev. C **70**, 054307 (2004)

*1 University of Tokyo
*2 Niigata University
*3 Hokkaido University

Effects of ground-state correlations beyond RPA in light exotic nuclei

N. Dinh Dang and N. Vinh Mau*

[NUCLEAR STRUCTURE, random-phase approximation, ground-state correlations, exotic nuclei]

The random-phase approximation (RPA) has been a powerful tool in the theoretical study of many-body systems such as atomic nuclei. An essential ingredient of the RPA is the use of the quasiboson approximation (QBA), which considers fermion pairs as boson operators, just neglecting the Pauli principle between them. Within the QBA a set of linear equations, which is usually called the RPA equation, is derived, which makes computationally demanding problems become tractable. The success of RPA depends on the validity of the QBA, which turns out to be very good in medium and heavy nuclei.

With increasing interest in light exotic nuclei, the particle-particle (*pp*) RPA has been applied recently to the calculations for ^{14}C, ^{12,14}Be, and ^{11}Li.[1] However, in light systems, due to strong ground-state correlations (GSC) beyond RPA[2] the validity of the QBA becomes questionable.

In the present study we used the renormalized *pp* RPA (RRPA) to take into account the effects of GSC beyond RPA due to Pauli principle between fermion pairs in the calculations for ^{12,14}Be. The calculations were based on the set of RRPA equations for the systems with a core ± 2 neutrons. As the inputs the calculations used the Gogny interaction and neutron states up to an energy $\epsilon_c \simeq 10$ MeV. The continuum states are discretized using a box with a radius of 20 fm. The parameter of the particle-phonon coupling in the one-neutron potential was fitted to reproduce the experimental $1p_{1/2}$, $2s$, $1d_{5/2}$ single-neutron energies for ^{12}Be. The inversion of $1p_{1/2}$ and $2s$ shells was assumed with $2s$ shell being the last occupied one with an energy given by the one-neutron separation energy, while the energy of the $1p_{1/2}$ shell was fitted to 0.7 MeV in order to reproduce approximately within RPA the experimental two-neutron separation energy in ^{14}Be, which is equal to $S_{2n} = 1.34 \pm 0.11$ MeV.

The results of calculations show that GSC beyond RPA have strong effects on the ground-state and correlation energies in these light exotic nuclei. In ^{12}Be the GSC shift up the ground-state energy by 13.6%, from -3.614 MeV (RPA result) to -3.122 MeV (RRPA result), and the correlation energy by 21%, from -2.1 MeV (within RPA) to -1.66 MeV (within RRPA). Quite stronger effects are obtained in ^{14}Be, where the ground-state energy increases by 50%, from -1.391 MeV (within RPA) up to -0.695 (within RRPA), and the correlation energy increases by around 25%, from -2.22 MeV (within RPA) up to -1.66 MeV (within RRPA). We also found that the violation of particle number due to using the GSC factor of the type introduced in Ref. 3 is negligible ($\sim 0.1\%$).

References

1) J. C. Pacheco and N. Vinh Mau: Phys. Rev. C **65**, 044004 (2002).
2) F. Catara, N. Dinh Dang, and M. Sambataro: Nucl. Phys. A **579**, 1 (1994).
3) J. Dukelsky and P. Schuck: Phys. Let. B **464**, 164 (1999).

* Institut de Physique Nucléaire, France

Particle-number conservation in the self-consistent random-phase approximation

N. Dinh Dang

[NUCLEAR STRUCTURE, random-phase approximation, ground-state correlations]

The random-phase approximation (RPA) is usually derived within the quasiboson approximation, neglecting the Pauli principle between fermion-pair operators. As a result, the RPA equation yields imaginary solutions at a certain critical value of the interaction parameter. Several approaches have been developed to remove this inconsistency of the RPA. The popular one among them is the renormalized RPA (RRPA),[1,2] which avoids the collapse of RPA. However, the tests carried out within exactly solvable models showed that there is still a large discrepancy between the solution obtained within the RRPA and the exact one. Recently, the self-consistent RPA (SCRPA)[3] has included the expectation values of the products of two fermion pairs in the correlated ground state as screening corrections. As a result, within a particle-hole (ph) symmetric multilevel-pairing model with double degeneracy (the so-called picket-fence model), the SCRPA yielded the solutions very close to the exact ones for the correlation energy of the system with Ω particles, as well as the energy of the first excited state of the system with $\Omega + 2$ particles.[3] Realistic nuclear single-particle spectra are in general ph non-symmetric. It is, therefore, worthwhile to reexamine carefully the SCRPA before applying it to realistic nuclei.

This work shows that, within a multilevel-pairing model with double degeneracy, the expressions for occupation numbers used in the original version of SCRPA[3] violate the particle number for non-symmetric particle-hole (ph) spectra. A renormalization is introduced to restore the particle number, which leads to the expressions of occupation numbers similar to those derived by Hara *et al.* for the ph case.[1] The results of calculations within the ph symmetric case show that this number-conserving SCRPA yields the energies of the ground state and first excited state of the system with $\Omega + 2$ particles relative to the ground state of the system with Ω particles in close agreement with those obtained within the original SCRPA. However it gives a slightly larger correlation energy (see Fig. 1).

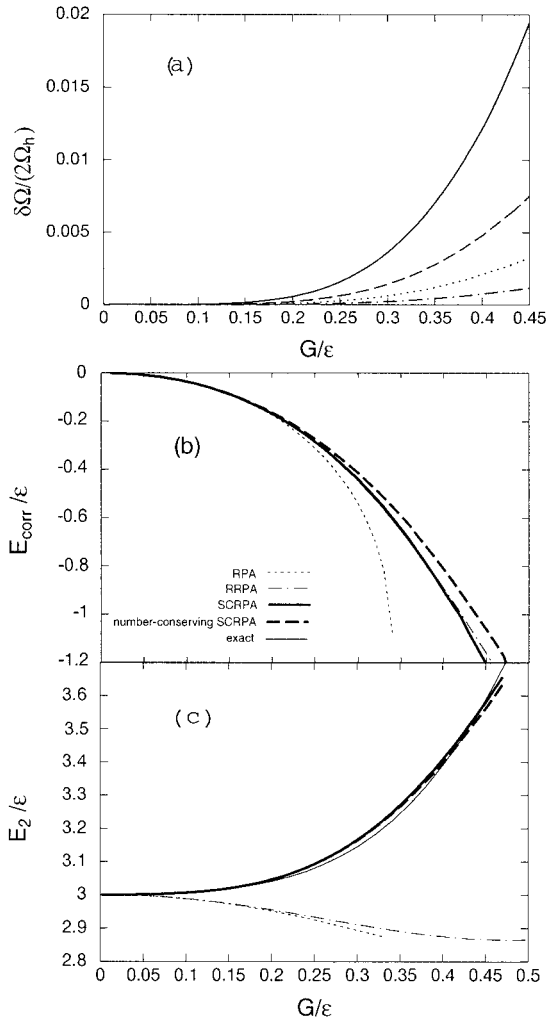

Fig. 1. (a) Particle-number violations within SCRPA for ph non-symmetric cases with particle number $\Omega = 10$ and number of hole levels $\Omega_h = 1$ (solid line), 2 (dashed line), 3 (dotted line), and 4 (dash-dotted line) as functions of interaction parameter G (in units of the level distance ϵ). (b) Correlation energy $E_{\rm corr}$ in the system with 10 particles, and (c) first-excited-state energy E_2 of the system with 12 particles relative to the ground-state of the system with 10 particles obtained within RPA (dotted line), RRPA (dash-dotted line), SCRPA (thick solid line), number-conserving SCRPA (thick dashed line), and exact (thin solid line) calculations.

References

1) K. Hara: Prog. Theor. Phys. **32**, 88 (1964); K. Ikeda, T. Udagawa, and H. Yamamura: Prog. Theor. Phys. **33**, 22 (1965).
2) F. Catara, N. Dinh Dang, and M. Sambataro: Nucl. Phys. A **579**, 1 (1994).
3) J. Dukelsky and P. Schuck: Phys. Let. B **464**, 164 (1999).

^{8}Be in the charge- and parity-projected Hartree-Fock method

S. Sugimoto, K. Ikeda, and H. Toki*

[NUCLEAR STRUCTURE, Mean field model, ^{8}Be]

Recently, we have developed a new mean-field-type model that can treat the tensor force by breaking the parity and charge symmetries of single-particle states.[1,2] We call this model the charge- and parity-projected Hartree-Fock (CPPHF) method, because the charge and parity projections are performed before the variation. We applied the CPPHF method to the case of the alpha particle and found that it is effective in treating the tensor correlation and both the charge and parity projections are important in obtaining a finite energy from the tensor force in the alpha particle.[2]

The cluster aspects of nuclei are very interesting and generally appear in a light mass region. ^{8}Be is a typical alpha-clustering nucleus and studied extensively using various methods. Some of these studies show that the tensor force is important in alpha clustering. The recent exact calculations clearly show that ^{8}Be consists of weakly bounded two alpha clusters and the large amount of the attractive energy comes from the one-pion-exchange potential.[3] This indicates that the tensor force is important in alpha clustering, because the one-pion-exchange potential has a strong tensor part. Therefore, it is interesting to study ^{8}Be using the CPPHF method to study the effect of the tensor force on alpha clustering.

In the present study, we use the wave function of the alpha particle obtained in the CPPHF method, Φ_α, and calculate the energy surface of two alpha particles as a function of relative distance. The parity and charge projections are performed for each alpha particle as

$$\Psi^{^8\mathrm{Be}}(1,\ldots,8) = N\mathcal{A}_{1-8}\big[P^{\mathrm{p}}_{1-4}P^{\mathrm{c}}_{1-4}\Phi_\alpha(1,\ldots,4) \times P^{\mathrm{p}}_{5-8}P^{\mathrm{c}}_{5-8}\Phi_\alpha(5,\ldots,8)\big]. \quad (1)$$

In the above equation, $\mathcal{A}_{1-8}$ is the antisymmetrization operator for eight particles, P^{p}_{a-b} and P^{c}_{a-b} are the parity and charge projection operators for the particle numbers a to b, and N is the normalization factor. As for the Hamiltonian, we use the Volkov No. 1 force for the central part[4] and the G3RS force for the tensor part.[5] We multiply X_{TE} for the ^{3}E part of the central force and X_{T} for the $\tau_1 \cdot \tau_2$ part of the tensor force.

In Fig. 1, we show the energy surfaces for three cases. The solid line indicates the energy surface for the case with no tensor force and $X_{\mathrm{TE}} = 1.0$ in the parity-projected Hartree-Fock calculation, the dashed line with $X_{\mathrm{T}} = 1.5$ and $X_{\mathrm{TE}} = 0.95$ in the parity-projected Hartree-Fock calculation, and the dotted line with $X_{\mathrm{T}} = 1.5$ and $X_{\mathrm{TE}} = 0.8$ in the charge- and parity-projected Hartree-Fock calculation. X_{T} and X_{TE} are determined to reproduce the binding energy of the alpha particle. Here, the parity-projected Hartree-Fock calculation means that we only perform the parity projection when we calculate the alpha particle and ^{8}Be. From the figure, we can see that when the tensor correlation is introduced to the calculation of the alpha particle, the energy surface steeply goes up compared with the no-tensor-force case. This effect is mainly caused by a large increase in kinetic energy due to the decrease in relative distance. The large increase in kinetic energy is probably due to the p-state mixing in the single-particle states in the alpha particle induced by the tensor force. In this sense, we can say that the tensor correlation significantly affects the inner region of the energy surface of ^{8}Be.

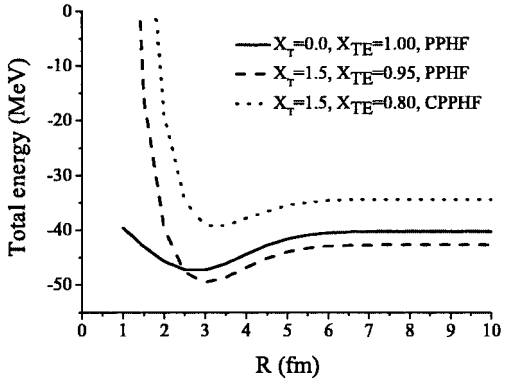

Fig. 1. Energy surface for ^{8}Be as a function of the relative distance between alpha particles, R.

References
1) H. Toki, S. Sugimoto, and K. Ikeda: Prog. Theor. Phys. **108**, 903 (2002).
2) S. Sugimoto, K. Ikeda, and H. Toki: Nucl. Phys. A **740**, 77 (2004).
3) R. B. Wiringa, S. C. Pieper, J. Carlson, and V. R. Pandharipande: Phys. Rev. C **62**, 014001 (2001).
4) A. Volkov: Nucl. Phys. **74**, 33 (1965).
5) R. Tamagaki: Prog. Theor. Phys. **39**, 91 (1968).

* Research Center for Nuclear Physics (RCNP), Osaka University

Systematic study of $E2$ transition strengths of C isotopes

Y. Kanada-En'yo*

[NUCLEAR STRUCTURE, Unstable nuclei, Cluster]

Recently, the life time of the 2_1^+ state of ^{16}C has been measured.[1] It indicates the abnormally small $E2$ transition strength as $B(E2; 2_1^+ \to 0_1^+) = 0.63e^2\,\mathrm{fm}^4$ in ^{16}C, compared with those for other C isotopes (^{10}C, ^{12}C and ^{14}C). As well known, $B(E2)$ has a close relation to the intrinsic deformation of the nucleus. Considering the excitation energy $E_x(2_1^+) = 1.766\,\mathrm{MeV}$ of ^{16}C, this nucleus is expected to have a deformed structure. In case of normal stable nuclei, $B(E2)$ values tend to be large in the deformed nuclei. It means that the hindrance of the $B(E2; 2_1^+ \to 0_1^+)$ in ^{16}C seems to contradict with the large deformation expected from the excitation energy $E_x(2_1^+)$.

In the theoretical work on C isotopes,[2] it was suggested that the different shapes between proton and neutron densities may cause the suppression of $B(E2)$. In this paper, we perform systematic analysis of the deformations of proton and neutron densities in even-even C isotopes based on calculations of antisymmetrized molecular dynamics (AMD),[3] and discuss the $E2$ transition strengths in neutron-rich C isotopes in relation to the deformations.

We applied the simplest version of AMD to even-even C isotopes. The excitation energies of 2_1^+ and the $E2$ transition strengths are shown in Table 1. Systematics of the experimental $B(E2)$ values in the series of C isotopes is well described by the calculations. The results indicate that the neutron shape drastically changes with the increase of neutron number, while the proton shape is rather stable. It is suggested that the difference between proton and neutron shapes may appear in ^{16}C and ^{18}C as well as ^{10}C. Namely, the oblate nature of the proton shape still remains, though the neutron structure is prolate or triaxial in these isotopes. We analyze the $E2$ transition strength in relation to the deformation. The unusually small $B(E2; 2_1^+ \to 0_1^+)$ in ^{16}C, which has been recently measured, was described by the coexistence of the oblate proton shape and the prolate neutron shape. In other words, the deviation between the proton and neutron shapes is important in the hindrance of $B(E2)$. According to the present prediction, the $B(E2; 2_1^+ \to 0_1^+)$ in ^{18}C is as small as that in ^{16}C, while the $B(E2)$ is larger in ^{20}C. The present results also show the enhancement of the neutron skin structure in neutron-rich C. It was found that the stable proton structure in C isotopes plays an important role in the neutron skin structure as well as in the systematics of $B(E2)$.

Table 1. Excitation energies (MeV) of the 2_1^+ states and $B(E2; 2_1^+ \to 0_1^+)$ ($e^2\mathrm{fm}^4$) in C isotopes calculated by AMD method. The adopted interaction consists of the central force of MV1 ($m = 0.576$) and the spin-orbit force of GSRS ($u_{ls} = 1500\,\mathrm{MeV}$), and Coulomb.

		^{10}C	^{12}C	^{14}C
cal.	$E_x(2_1^+)$	1.95	1.66	3.75
exp.	$E_x(2_1^+)$	3.354	4.439	7.012
cal.	$B(E2)$	5.4	6.8	5.9
exp.	$B(E2)$	12.4 ± 0.2	8.2 ± 0.1	3.74 ± 0.5
		^{16}C	^{18}C	^{20}C
cal.	$E_x(2_1^+)$	0.65	0.87	0.88
exp.	$E_x(2_1^+)$	1.766	1.59[§1]	1.59[§1]
cal.	$B(E2)$	1.4	0.6[§2]	5.0
exp.	$B(E2)$	0.63	–	–

[§1] The experimental data for ^{18}C and ^{20}C are taken from Ref. 4.

[§2] The theoretical $B(E2)$ in ^{18}C is sensitive to the strength of spin-orbit force (see Ref. 5).

The present results tend to underestimate the excitation energies $E_x(2_1^+)$ in general, though the systematic behavior of $E_x(2_1^+)$ in the series of C is reproduced. One of the reason for the underestimation of $E_x(2_1^+)$ may be the paring effect, which is not sufficiently taken into account in the simplest AMD. Such extension of the framework as the variation after projection and superposition will improve the results. Here, we would like to mention that the neutron excitation is dominant in the 2_1^+ states of ^{16}C and ^{18}C. Therefore, the excitation energy $E_x(2_1^+)$ is related to the neutron structure rather than proton structure. In the analysis of the ^{208}Pb+^{16}C inelastic scattering,[6] the dominant contribution of the neutron excitation in the 2_1^+ state is supported by the experimental data.

* Institute of Particle and Nuclear Studies, High Energy Accelerator Research Organization (KEK)

References

1) N. Imai et al.: Phys. Rev. Lett. **92**, 062501 (2004).
2) Y. Kanada-En'yo and H. Horiuchi: Phys. Rev. C **55**, 2860 (1997).
3) Y. Kanada-En'yo and H. Horiuchi: Prog. Theor. Phys. Suppl. No. 142, 205 (2001); Y. Kanada-En'yo, M. Kimura, and H. Horiuchi: C. R. Physique **4**, 497 (2003).
4) M. Stanoiu et al.: Eur. Phys. J. A **20**, 95 (2004).
5) Y. Kanada-En'yo: Phys. Rev. C. **71**, 014310 (2005).
6) Z. Elekes et al.: Phys. Lett. B **586**, 34 (2004).

Study of unstable nuclei with an extended cluster-orbital shell model

H. Masui,[*1] T. Myo,[*2] K. Katō,[*3] and K. Ikeda

[Nuclear structure, Unstable nuclei, Cluster model]

The recent development of experiments for unstable nuclei shows different aspects from the stable nuclei.[1] The observed ^{23}O r.m.s radius is large compared with the empirical low $A^{1/3}$. An experimental analysis using the Glauber theory suggests that ^{23}O is not a simple ^{22}O core plus one valence neutron structure[2] from the analysis of the spin parity of the ground state, which is $5/2^+$. However, there is another experimental analysis, which shows that the ground state of ^{23}O is $1/2^+$.[3] Therefore, a theoretical study with a high accuracy and an ability of describing the halo structure is required.

To study such a complex halo structure, we develop a method using the cluster-orbital shell model (COSM) and extend it so as to be able to treat the dynamics of the total system. For treating the dynamics of the core, we introduce the degrees of freedom for the width parameter b. The energy of the core and the potential between the core and valence nucleons, which is constructed microscopically, are connected to each other by the core b width parameter.

The energy of the core can be calculated analytically, if we use the lowest configuration for the core.[4] In this formalism, the core-N potential is a folding-type potential using the core density. Hence, the change in b affects the shape and strength of the core-N potential. The optimum value of b can be determined by combining the core and core-N parts. To reproduce the asymptotic shape of the core-N wave function, the radial part is expressed by a linear combination of Gaussian basis functions. Using such Gaussian basis functions, the motion of valence nucleons is solved by the stochastic variational method (SVM).[5] We call this approach "Neo-COSM".

We use the effective nucleon-nucleon potential, Volkov No. 2 with the exchange parameter $m = 0.58$. For valence nucleons, we artificially introduce the Heisenberg and Bertrett parameters as $h = b = 0.07$ to adjust the ground-state energy of ^{18}O.

First, we perform the calculation at a fixed b. For oxygen isotopes, the binding energies and r.m.s. radii of the isotopes are well reproduced. On the other hand, for $N = 8$ isotones (the ^{16}O+Xp systems), the calculated r.m.s. radii do not reach the observed values, while the calculated binding energies of the isotones are well reproduced. The results for the r.m.s. radii at a fixed b are shown in Fig. 1 (a).

The difference between the ^{16}O+Xn and ^{16}O+Xp systems suggests that we need to introduce a new mechanism or improve the description of the system, which includes the improvement of the interaction. Therefore, to reproduce the difference, we performed the Neo-COSM calculation by changing the core b parameter. The energy of the core is calculated analytically. Hence, b is determined by searching the minimum point of the energy in the total system. By performing the above calculation, the obtained r.m.s. radii are qualitatively improved from the fixed-b Neo-COSM calculation, as shown in Fig. 1 (b).

In summary, we developed a new method of studying the particular structures of neutron- and proton-rich nuclei. The essential point of our method is that we treat the total system by introducing the degrees of freedom of the core b parameter in the COSM.

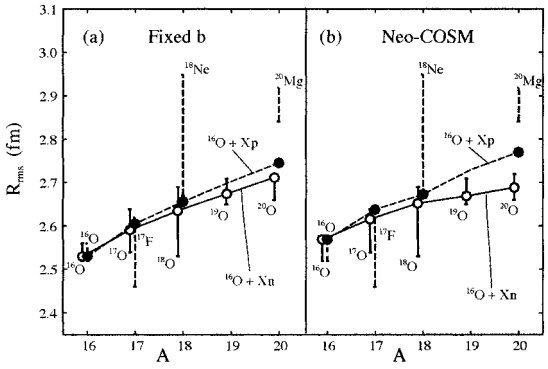

Fig. 1. Calculated r.m.s. radii using (a) fixed b and (b) Neo-COSM. Experimental values[1] are shown with error bars.

References

1) A. Ozawa et al.: Nucl. Phys. A **693**, 32 (2001).
2) R. Kanungo et al.: Phys. Rev. Lett. **88**, 142502 (2002).
3) D. Cortina-Gil et al.: Phys. Rev. Lett. **93**, 062501 (2004).
4) T. Ando, K. Ikeda, and A. Tohsaki-Suzuki: Prog. Theor. Phys. **64**, 1608 (1980).
5) V. I. Kukulin and V. M. Krasnopol'sky: J. Phys. G **3**, 795 (1977).

*1 Information Processing Center, Kitami Institute of Technology
*2 Research Center for Nuclear Physics, Osaka University
*3 Department of Physics, Hokkaido University

Dominance of intruder state in ^{30}Na†

Y. Utsuno,[*1] T. Otsuka,[*2] T. Glasmacher,[*3] T. Mizusaki,[*4] and M. Honma[*5]

[NUCLEAR STRUCTURE, Shell model, Unstable nuclei]

Recently, it has been clarified in which nucleus the $N = 20$ magic structure disappears. In the so-called "island of inversion" picture,[1] the region with the disappearance was restricted to nine $N \geq 20$ nuclei, whereas a recent Monte Carlo shell-model (MCSM) calculation[2] has indicated that certain $N = 19$ isotopes should have the ground state dominated by the intruder state, from a comparison with the experimentally determined[3] electromagnetic moments of Na isotopes. In the present study, we examine what the dominance of the intruder state in an $N = 19$ isotope ^{30}Na means in terms of the $N = 20$ shell gap on the basis of the MCSM calculation. The numerical computations have been carried out with the Alphleet and Alphleet-2 parallel computer systems as a RIKEN-CNS collaboration project on large-scale nuclear structure calculations.

In order to examine the importance of the narrow $N = 20$ shell gap given by the present shell-model Hamiltonian,[4] we artificially widen the shell gap from the original interaction, shifting the strength of the monopole interaction with a control parameter x as

$$\delta V^{T=1,0}_{0d_{5/2},0d_{3/2}}(x) = -0.3x, +0.7x\,\mathrm{MeV}, \qquad (1)$$

where V^T_{ij} denotes the monopole interaction between i and j orbits with isospin coupled to T.[4] Figure 1 shows some quantities as functions of the shell gap. As presented in Figs. 1 (a) and (b), both the quadrupole moment and the magnetic moment of ^{30}Na suddenly deviate from values close to the experimental values at the shell gap ~ 4 MeV. This is accounted for by the sudden transition of the dominant ground-state component from the intruder state to the normal state as indicated in Figs. 1 (c) and (d). Compared with the cases of ^{29}Na and ^{31}Na, the transition in ^{30}Na occurs very sharply and the dominance of the intruder state in this nucleus is thus a rather sensitive probe for the shell gap. The present result supports the argument that the shell evolution[5] is caused by the spin-isospin dependence of the effective interaction.

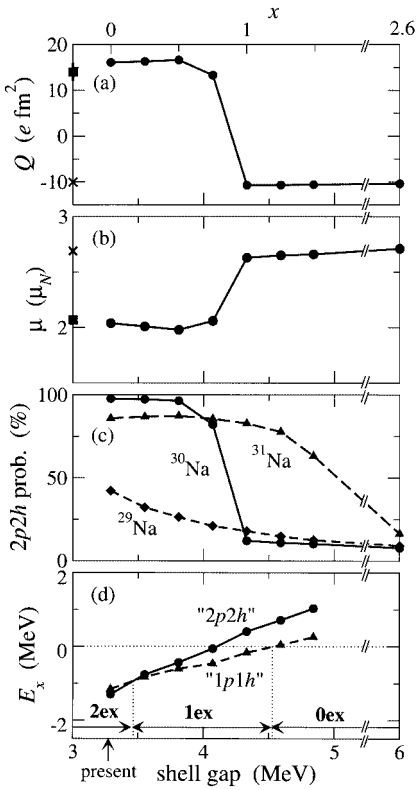

Fig. 1. (a) Quadrupole moment and (b) magnetic moment of ^{30}Na. The horizontal axis shows the shell gap. The value of the shell gap is controlled by a parameter x in Eq. (1), shown by the upper horizontal axis. The moments determined by the experiment[3] and *sd*-shell-model are denoted by the squares and crosses, respectively. (c) $2p2h$ probabilities in the (positive-parity) ground states of $^{29-31}$Na. (d) Energies of the $2p2h$- and $1p1h$-dominant lowest states of ^{30}Na (denoted by "$2p2h$" and "$1p1h$", respectively) measured from that of the $0p0h$-dominant lowest state. The range of the shell gap giving the $npnh$ ground state ($n = 0, 1, 2$) is indicated by $n$ex.

References

1) E. K. Warburton, J. A. Becker, and B. A. Brown: Phys. Rev. C **41**, 1147 (1990).
2) Y. Utsuno, T. Otsuka, T. Mizusaki, and M. Honma: Prog. Theor. Phys. Suppl. No. 146, 488 (2002).
3) M. Keim: AIP Conf. Proc. **455**, 50 (1998); M. Keim et al.: Eur. Phys. J. A **8**, 31 (2000).
4) Y. Utsuno, T. Otsuka, T. Mizusaki, and M. Honma: Phys. Rev. C **60**, 054315 (1999).
5) T. Otsuka, R. Fujimoto, Y. Utsuno, B. A. Brown, M. Honma, and T. Mizusaki: Phys. Rev. Lett. **87**, 082502 (2001).

† Condensed from article in Phys. Rev. C **70**, 044307 (2004)

*1 Japan Atomic Energy Research Institute
*2 Department of Physics and Center for Nuclear Study, University of Tokyo
*3 National Superconducting Cyclotron Laboratory and Department of Physics and Astronomy, Michigan State University, USA
*4 Institute of Natural Sciences, Senshu University
*5 Center for Mathematical Sciences, University of Aizu

Low-lying collective vibrational excitations induced by pairing anti-halo effect

M. Yamagami

[Nuclear structure, low-lying vibrational excitations, pairing correlations]

A special interplay of loosely-bound neutrons with small orbital angular momentum ℓ and selfconsistent pairing correlations based on the Hartree-Fock-Bogoliubov (HFB) theory in low-lying collective vibrational excitations is studied.[1] In general, vibrational excitations are microscopically represented by the coherent superposition of one-particle one-hole ($1p$-$1h$) states. In stable nuclei with the deep Fermi energy, $1p$-$1h$ states among tightly-bound states mainly contribute to low-lying vibrational excitations, and these $1p$-$1h$ states spatially concentrate around the surface region. In contrast, in neutron drip line region, the contributing configurations are $1p$-$1h$ states among tightly-bound, loosely-bound, resonant and non-resonant continuum states. Because loosely-bound low-ℓ neutrons have an appreciable probability to be outside the core nucleus, $1p$-$1h$ excitations from loosely-bound low-ℓ neutrons to the nearby continuum states have a spatially extended structure. Such coupling to the continuum states gives rise to a soft excitation with a large transition strength as a non-resonant single-particle excitation.[2] Therefore the realization of the localization of $1p$-$1h$ states is nontrivial in neutron drip line nuclei, and such spatially extended $1p$-$1h$ states may cause qualitative differences in low-lying collective vibrational excitations.

In this study, we emphasize the change in the spatial structure of quasiparticle wave functions in loosely-bound low-ℓ neutrons by selfconsistent pairing correlations, namely, "the pairing anti-halo effect in hole wave functions" (see Fig. 1), and "the broadening effect in particle wave functions". Consequently, the spatial structure of $1p$-$1h$ states changes, and "the extended localization of $1p$-$1h$ states among low-lying quasiparticle states", that can enhance low-lying collectivity, is realized.

By performing HFB plus quasiparticle random phase approximation (QRPA) calculations with Skyrme interaction, we investigate low-lying 2^+ states in neutron-rich Ni isotopes. In Fig. 2, the $B(E2, 0_1^+ \rightarrow 2_1^+)$ values obtained by HFB plus QRPA calculations are shown. For comparison, the results obtained by resonant BCS plus QRPA and RPA calculations are also shown. While approaching the neutron drip line, the calculated $B(E2)$ values exhibit a different behavior; the $B(E2)$ values in HFB plus QRPA increase, but decrease in resonant BCS plus QRPA, and are much smaller in RPA. The main qualitative difference among these calculations is the realization of the extended localization of $1p$-$1h$ states among the low-lying $s_{1/2}$, $d_{3/2}$ and $d_{5/2}$ quasiparticle states in the HFB theory.

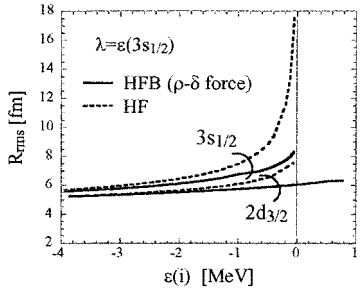

Fig. 1. The r.m.s radii of the (hole) $3s_{1/2}$ and $2d_{3/2}$ states with/without HFB pairing correlations are shown as functions of the single-particle energies. The Woods-Saxon potential is used for the mean-field. The density-dependent pairing force is used in the HFB calculation.

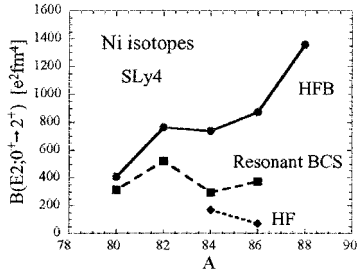

Fig. 2. The $B(E2, 0_1^+ \rightarrow 2_1^+)$ values in neutron-rich Ni isotopes obtained by HFB plus QRPA, resonant BCS plus QRPA, and RPA calculations with Skyrme SLy4 force.

Finally the effects of quadrupole deformation in low-lying vibrational excitations in neutron drip line nuclei are examined. We discuss the roles of the breaking of the rotational symmetry and the mixing of isoscalar and isovector modes in association with the possibility of new types of vibrational excitation; collective soft dipole modes with a pear- or banana-shape vibration.

References

1) M. Yamagami: Proc. 5th Japan-China Joint Nuclear Physics Symp., Fukuoka, 2004-3, edited by Y. Gono, N. Ikeda, and K. Ogata (Kyushu University, 2004) p. 218; preprint nucl-th/0404030.
2) H. Sagawa, N. Van Giai, N. Takigawa, M. Ishihara, and K. Yazaki: Z. Phys. A **351**, 385 (1995).

A search for a unified effective interaction for Monte Carlo shell model calculations (VI)

M. Honma,[*1] T. Otsuka,[*2,*3] and T. Mizusaki[*4]

[Shell model, Effective interaction]

The Monte Carlo shell model[1] (MCSM) has enabled us to apply the nuclear shell model to various problems in a huge model space and with many valence nucleons which are not accessible by conventional methods. However, the effective interaction for a practical use in such a huge model space is unknown. As shown in our previous reports,[2] we have been investigating a possibility to construct an effective interaction which can be used for a unified description of many nuclei in a huge model space with a reasonable predictive power, and have published a possible solution GXPF1[3] for pf-shell nuclei.

In this report, we discuss our recent trial to describe heavier nuclei around $A = 60$–100 in the shell-model framework. A reasonable choice of the model space is to include the orbits $p_{3/2,1/2}$, $f_{5/2}$ and $g_{9/2}$, taking ^{56}Ni as an inert core. One advantage of such a model space is that it is free from the spurious center of mass motions. The largest M-scheme dimension of this model space reaches about 13 billions, which is beyond the current basis-size limitation in the conventional diagonalization method, and therefore, the MCSM can play a role. Considering the connection with the pf-shell, it is more natural to take the $pf + g_{9/2}$ space including also the $f_{7/2}$ orbits, which is in fact in a scope of our future investigation.

In order to obtain an effective interaction for this model space, we have carried out the similar fitting calculations as in the case of the pf-shell. Starting from a microscopic interaction,[4] we have varied 32 linear combinations of Hamiltonian parameters (133 two-body matrix elements and four single-particle energies) by the least-squares fit to the 310 experimental data out of 69 nuclei with $A = 63$–96. In the latest iteration, we have attained the rms error of 213 keV.

Since the closed ^{56}Ni core is severely broken[3] in Ni isotopes around $N = 34$ due to the strong proton-neutron interaction, it is not practical to describe Ni isotopes in the present model space. Keeping in mind a future inclusion of $f_{7/2}$ orbit in the model space, we exclude the data of Ni isotopes for the fit. Also, in the present model space, there are many nuclei in which strong E2 transitions among low-lying states are observed, suggesting large deformation. Such nuclei are found in the middle of the model space, corresponding to isotopes from Se to Zr around $N \sim Z$ line. Because of the missing $f_{7/2}$ orbit and upper $N_{\rm osc} = 4$ orbits such as the $d_{5/2}$, the present model space is not suitable for the description of such states. We excluded them from the data to be fitted. Thus, our targets of the present approach are mainly: (1) $Z \sim 32$ region, (2) $N \sim 50$ region, and (3) $Z \geq 40$ region.

As an example, the systematics of low-lying states of Ge isotopes are shown in Fig. 1. We can find reasonable agreement between the experimental data and the shell-model results throughout the isotope chain. However, the description becomes worse for $N > 40$, suggesting the effects of missing $f_{7/2}$ orbit.

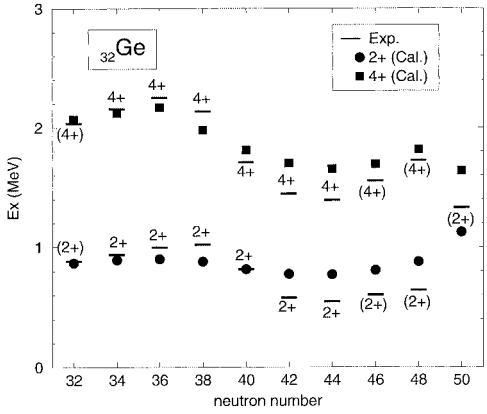

Fig. 1. Energy levels of yrast 2^+ and 4^+ states for Ge isotopes. The experimental data are shown by horizontal bars, while symbols show shell-model values obtained by a code MSHELL.[5] Data are taken from Ref. 6.

*1 Center for Mathematical Sciences, University of Aizu
*2 Department of Physics, University of Tokyo
*3 Center for Nuclear Study, University of Tokyo
*4 Institute of Natural Sciences, Senshu University

References

1) T. Otsuka et al.: Phys. Rev. Lett. **81**, 1588 (1998).
2) M. Honma et al.: RIKEN Accel. Prog. Rep. **33**, 16 (2000); RIKEN Accel. Prog. Rep. **34**, 15 (2001); RIKEN Accel. Prog. Rep. **35**, 12 (2002); RIKEN Accel. Prog. Rep. **36**, 21 (2003); RIKEN Accel. Prog. Rep. **37**, 17 (2004).
3) M. Honma et al.: Phys. Rev. C **65**, 061301(R) (2002); Phys. Rev. C **69**, 034335 (2004).
4) M. Hjorth-Jensen: private communications.
5) T. Mizusaki: RIKEN Accel. Prog. Rep. **33**, 14 (2000).
6) Data extracted using the NNDC WorldWideWeb site from the ENSDF database.

Hartree-Fock calculation of three-dimensional nuclear rotation

Y. Hashimoto[*1] and T. Horibata[*2]

[NUCLEAR STRUCTURE, tilted axis rotation, wobbling motion]

A typical mode of collective motion of a deformed nucleus is the uniform rotation about the shortest principal axis, where the moment of inertia is the largest. In general, there are other classes of rotational motion: One is a mode in which the nucleus rotates about an axis which is not any of the principal axes, called *tilted axis rotation* (TAR).[1,2] Another is the nonuniform rotational motion called the *wobbling motion* in which the angular velocity is not uniform but time-dependent and the rotational axis is tilted away from the principal axes.[3,4] Recent experimental data support the existence of the wobbling motion.[5]

Kerman and Onishi (referred to as KO)[6] presented a framework to study the general mode of rotational motion as wobbling motion with the use of Hartree-Fock (HF) calculation. Based on this framework, Horibata and Onishi (referred to as HO)[1] found an intrinsic state corresponding to TAR as the Hartree-Fock-Bogoliubov (HFB) solution. In the calculations performed by HO, the P+QQ model was used together with a truncated single-particle space. Then the KO theory was applied in the modern framework of HF or HFB based on spatial mesh and density-dependent local effective interactions as the Skyrme force.

In this brief report, we present the numerical results obtained by Hartree-Fock calculations with a simplified density-dependent local effective interaction of the rotational motion where the axis of rotation is tilted away from the shortest principal axis.

The energy of the model Hamiltonian that we used in the present calculation is given as

$$E = \int d^3x \Bigg\{ \sum_{\tau=p,n} \sum_j \psi^{(\tau)}{}_j(x)^* \left(-\frac{\hbar^2}{2m}\nabla^2 \right) \psi_j^{(\tau)}(x) + a_2 D(x)^2 + a_3 D(x)^3 + \frac{1}{2} D(x) V_Y(x) + \frac{1}{2} D_p(x) V_c(x) \Bigg\}, \quad (1)$$

where V_Y (V_C) is the Yukawa (Coulomb) potential, and a_2 and a_3 are parameters. $D(x)$ and $D_p(x)$ indicate the total nucleon density and proton density, respectively. In this report, we show the results for a case with $N = Z = 12$. The pairing effects are neglected. As the numerical basis in the HF calculation, the Lagrange mesh is used.[7] As explained in the paper by HO, the HF equation is solved with six constraints, namely, three angular momenta, $\langle J_x \rangle = j_x$, $\langle J_y \rangle = j_y$ and $\langle J_z \rangle = j_z$, for a given set of ($j_x$, j_y, j_z) and three principal axis conditions, $\langle yz \rangle = 0$, $\langle zx \rangle = 0$ and $\langle xy \rangle = 0$.

The ground state is triaxially deformed. The shortest axis of the deformed density distribution is taken as the x-axis, and the longest, the z-axis. The tilt angle θ is defined as $j_x = j_0 \cos\theta$, $j_y = 0$ and $j_z = j_0 \sin\theta$ for a given angular momentum j_0. In Fig. 1, we show the variation in energy $E(j_0, \theta)$ in Eq. (1) against the tilt angle θ for several angular momenta j_0. At the minimum point of each of the curves, the angular momentum vector $\vec{j} = (j_x, j_y = 0, j_z)$ is parallel to the angular velocity vector $\vec{\omega} = (\omega_x, \omega_y = 0, \omega_z)$, indicating the possibility of TAR.[1]

In Fig. 1, each of the curves for angular momenta larger than $j_0 \sim 4$ becomes irregular at a point of the tilt angle. For the tilt angle greater than the value at this point, the nucleus takes an almost axially symmetric shape and the cranked HF solution for the tilted axis is not easy to find numerically.

Because the pairing effects are not considered in the present calculation and the effective interaction is not realistic, the results in Fig. 1 are preliminary. Refinements of the numerical method are now in progress.

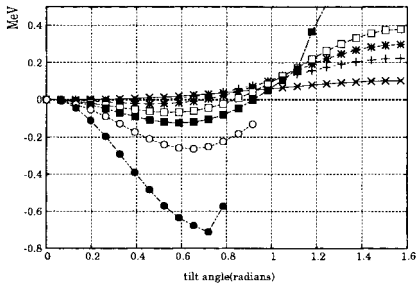

Fig. 1. Variation in energy against tilt angle for angular momenta from $j_0 = 2$ (crosses) to $j_0 = 6$ (filled circles).

*1 Institute of Physics, University of Tsukuba
*2 Faculty of Software and Information Technology, Aomori University

References

1) T. Horibata and N. Onishi: Nucl. Phys. A **596**, 251 (1996).
2) S. Frauendorf: Rev. Mod. Phys. **73**, 463 (2001).
3) A. Bohr and B. R. Mottelson: *Nuclear Structure*, Vol. II (Benjamin, Reading, New York, 1975).
4) I. Hamamoto and G. B. Hagemann: Phys. Rev. C **67**, 014319 (2003).
5) S. W. Ødegård et al.: Phys. Rev. Lett. **86**, 5866 (2001).
6) A. K. Kerman and N. Onishi: Nucl. Phys. A **361**, 179 (1981).
7) D. Baye and P. H. Heenen: J. Phys. A **19**, 2041 (1986).

Symmetry in random matrix theory

N. Shimizu[*1] and T. Otsuka[*1,*2]

[Nuclear Shell Model, Quantum Chaos]

Although quantum chaos has been studied for a long time, the properties of the ground state have not been known well, and its survey is a challenging topic. In the nuclear shell model, Johnson *et al.* discovered the "$J = 0$ dominance" of the ground state provided by a random Hamiltonian matrix.[1] The $J = 0$ dominance indicates that the ground-state spin (J) of even-even nuclei obtained by a random Hamiltonian matrix favors zero. In the *sd*-shell with six neutrons, the ground-state spin becomes $J = 0$ in the probability of 76% with randomly generated two-body matrix elements, whereas only 9.8% of the Hilbert space of six neutrons in the *sd*-shell is $J = 0$.

After this discovery, many works have been performed to investigate the ground-state properties provided with the random interaction (*e.g.*, see Ref. 2). However, the origin of the $J = 0$ dominance is still unclear. We propose the following ansatz for describing the $J = 0$ dominance.

- A certain type of random interaction mixes various states strongly in a chaotic manner without preference, in the eigenstates of a many-body system.
- In this situation, maximum binding can be achieved by the wave function being invariant with respect to the transformation of coordinates, because all orientations should be equal.
- The highest symmetries are then assigned to the ground state; the distortion of the wave function results in the loss of binding energy.

Concerning a rotational symmetry, the consequence of this ansatz is the $J = 0$ dominance of the ground state which is consistent with the work by Johnson *et al.*[1] In this report, we show two cases of the realization of other highest symmetries provided by random interaction for the verification of this ansatz.

First, we show the isospin distribution of the ground state in Table 1. The random interaction is provided by a two-body random ensemble (TBRE),[3] where two-body matrix elements of the Hamiltonian are random numbers obeying the Gaussian distribution. The system consists of N_ν neutrons and N_π protons in the orbits $d_{3/2}$, $d_{5/2}$, and $s_{1/2}$.

Table 1 shows the probability that the isospin of the ground state will be the lowest value ($P(T_{\min})$) as compared to the ratio of the dimensions of the $T_{\min}$ subspace to those of the entire Hilbert space (H. space).

Table 1. Probability that the isospin of the ground state will be the lowest value ($P(T_{\min})$) as compared to the ratio of the dimensions of the Hilbert space (H. space). See the text for details.

(N_ν, N_π)	(2,2)	(2,4)	(2,6)	(4,4)	(4,6)	(6,6)
$P(T_{\min})$ (%)	71.4	87.6	96.3	86.2	96.2	91.0
H. space (%)	38.4	52.1	82.9	27.8	60.2	25.5

The highest symmetry state in the ansatz corresponds to the lowest isospin state ($T_{\min}$) in terms of the rotational transformation of the isospin space. We see that the $P(T_{\min})$ is much higher than the ratio of the dimensions of the $T_{\min}$ subspace.

Second, the probability that the ground state will have a positive parity ($P(J^+)$) and the positive parity state ratio in the Hilbert space (H. space) are shown in Table 2. The system consists of N_ν neutrons in the orbits $p_{3/2}$, $p_{1/2}$, $f_{5/2}$, and $g_{9/2}$. The probability is obtained by 1000 runs of TBRE Hamiltonians. In this case, the highest symmetry state in the ansatz corresponds to the state with a positive parity. Although the parity positive state ratio of the entire Hilbert space is almost the same as the parity negative state ratio, the probability that the ground state will have a positive parity is higher than 80%.

These results are shown to be consistent with our ansatz, because the ground state provided by random interaction is likely to have the highest symmetry states, which correspond to the lowest isospin and positive parity states. You can see further discussion of this work in Ref. 3.

This work is a part of the RIKEN-CNS collaboration project on large-scale nuclear structure calculation.

Table 2. Probability that the parity of the ground state will be positive ($P(J^+)$) as compared to the ratio of the dimensions of the Hilbert space (H. space). See the text for details.

N_ν	2	4	6	8	10
$P(J^+)$ (%)	81.6	86.4	81.0	82.6	84.4
H. space (%)	44.2	52.1	50.4	50.1	50.0

*1 Department of Physics, University of Tokyo
*2 Center for Nuclear Study, University of Tokyo

References

1) C. W. Johnson, G. F. Bertsch, and D. J. Dean: Phys. Rev. Lett. **80**, 2749 (1998).
2) Y. M. Zhao, A. Arima, N. Shimizu, K. Ogawa, N. Yoshinaga, and O. Scholten: Phys. Rev. C **70**, 054322 (2004).
3) N. Shimizu and T. Otsuka: AIP Conf. Proc. **726**, 43 (2004).

Strange tribaryons as $\bar{K}$-mediated dense nuclear systems

Y. Akaishi, T. Yamazaki, and A. Doté*

[strange tribaryon, kaonic nuclei, dense nuclei]

We discuss implications of recent discoveries of strange tribaryons in ^{4}He(stopped-K^-, p)S^0(3115)[1] and ^{4}He(stopped-K^-, n) S^1(3140)[2] in the framework of deeply bound $\bar{K}$ nuclear states. The isospin structure of strange tribaryon system is shown in Fig. 1. S^1(3140) corresponds to an originally predicted shrunk $T = 0$ $ppnK^-$,[3,4] whereas S^0(3115) can be identified to $T = 1$ $pnnK^-$, which is an isobaric analog state of $pppK^-$, also predicted before.[5,6] In the $T = 1$ state, the nuclear core is a non-existing $(NNN)_{T=3/2}$ one with a peculiar density distribution as shown in the figure. We point out that the observed total binding energies can be accounted for by including the relativistic effect and by invoking a medium-enhanced $\bar{K}N$ interaction by 15% (see Fig. 2), which may occur as an effect of chiral symmetry restoration in such a high density nuclear medium. The experimental observation as a whole supports the predicted shrinkage of $\bar{K}$-mediated nuclear systems.

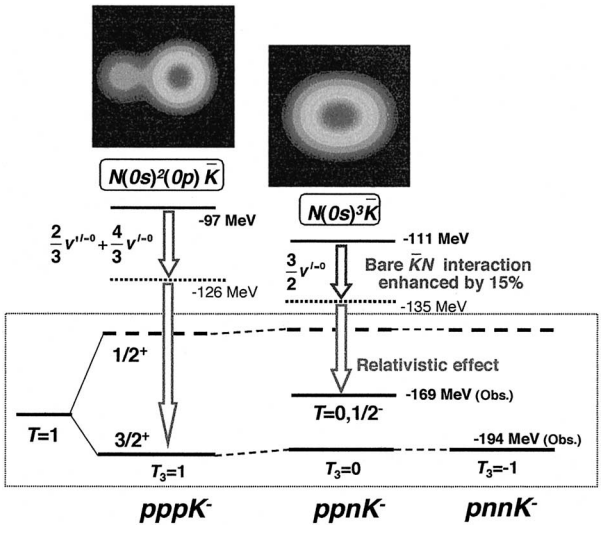

Fig. 1. Spin-isospin structure of the strange tribaryon system $[(NNN)\bar{K}]^Q_{(T,T_3)}$. The previously calculated nucleon-density contours and energy levels with E_K values are shown on top. The observed S^0(3115) and S^1(3140) are identified as the $(T, T_3) = (1, -1)$ and $T = 0$ states, respectively.

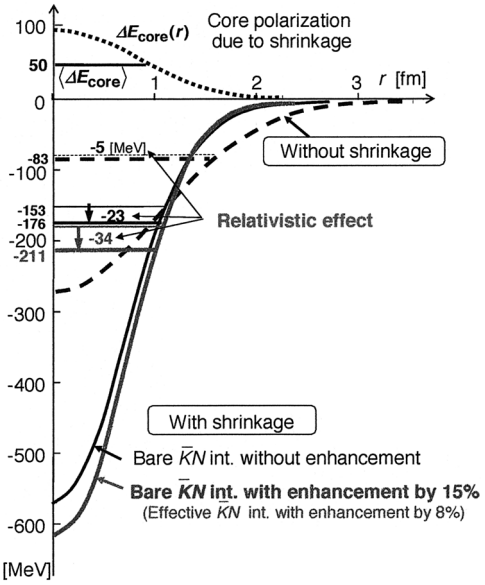

Fig. 2. Calculated $\bar{K}$-core potentials, $U_{\bar{K}\text{-core}}(r)$, for the $T = 0$ $ppnK^-$ state in three cases: without shrinkage, with shrinkage with the original bare $\bar{K}N$ interaction and with an enhanced bare $\bar{K}N$ interaction by 15%. The relativistic effects on the $\bar{K}$-core binding energies ($E_{\bar{K}\text{-core}}$) are indicated by arrows. Also shown is the nuclear core energy, $\Delta E_{\rm core}(r)$, with an average value ($< \Delta E_{\rm core} >$).

References

1) T. Suzuki et al.: Phys. Lett. B **597**, 263 (2004).
2) M. Iwasaki et al.: nucl-ex/0310018, submitted to Phys. Lett. B.
3) Y. Akaishi and T. Yamazaki: Phys. Rev. C **65**, 044005 (2002).
4) A. Doté, H. Horiuchi, Y. Akaishi, and T. Yamazaki: Phys. Lett. B **590**, 51 (2004).
5) T. Yamazaki and Y. Akaishi: Phys. Lett. B **535**, 70 (2002).
6) A. Doté, H. Horiuchi, Y. Akaishi, and T. Yamazaki: Phys. Rev. C **70**, 044313 (2004).

* Institute of Particle and Nuclear Studies, High Energy Accelerator Research Organization (KEK)

Spin dependent nuclear structure functions†

I. C. Cloet,*1 W. Bentz,*2 and A. W. Thomas*1

[NUCLEAR STRUCTURE FUNCTIONS, Spin dependence, Effective Quark Theories]

One of the most prominent phenomena in deep inelastic scattering of leptons off nuclei is the EMC effect, which concerns the spin-independent nuclear structure functions.[1] In a recent work,[2] this effect has been successfully described in terms of the self consistent scalar and vector fields which couple to the quarks inside the nucleons. Concerning the spin-dependent nuclear structure functions, on the other hand, only little is known about them both experimentally and theoretically, except for very light nuclei. In this work we will investigate the medium modifications of the spin-dependent structure functions of a nucleon bound in the nuclear medium, and present a simple model calculation of the spin-dependent counter part of the EMC ratio.

As an effective chiral quark theory, we use the Nambu-Jona-Lasinio model to describe the single nucleon as a bound state of a quark and a scalar diquark, and to describe nuclear matter in terms of self consistent scalar and vector mean fields which act on the quarks within the nucleons.[3] It has been shown that this approach describes the nuclear matter saturation properties. By using the quark-diquark wave function and the density dependent effective masses obtained in this model, we calculate the spin-dependent light-cone momentum distributions of the quarks in the nuclear medium by using the familiar convolution approach. In principle, the spin-dependent smearing function representing the Fermi motion of the nucleons should be calculated for a given valence nucleon orbit, but as a first step we employ the same function as for the spin-independent case. In the pure quark-scalar diquark description, only the up quark contributes to the polarization of the proton. In order to describe also the down quark contribution, one should include also the axial vector diquark channel.

The results for the polarized up quark distribution ($\Delta u(x)$) at the saturation density of our nuclear matter equation of state are shown in Fig. 1 for the low energy scale $Q_0 = 0.4\,\mathrm{GeV}$. The dotted line shows the distribution in a free nucleon, the dashed line shows the result including the mean scalar field, the dotted-dashed line shows the result including the Fermi motion of nucleons, and the solid line also includes the mean vector field. It is clear from this figure that the mean vector field plays an important role to deplete the distribution in the medium, which is reminiscent

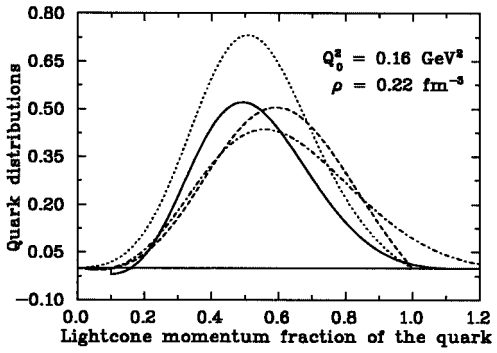

Fig. 1. Medium modifications of the polarized up quark distribution. For explanation of the lines, see text.

of the spin-independent case. Figure 2 shows the ratio of the in-medium $\Delta u(x)$ to the free nucleon value at $Q^2 = 10\,\mathrm{GeV}^2$, which represents a first estimate of the "spin-dependent EMC effect" in this simple model. It is interesting to observe that there is a plateau for $0.2 < x < 0.8$ with an average value of about 0.7, which is smaller than the well known spin-independent EMC ratio. We can therefore expect that the medium modifications are more important for the case of the spin-dependent structure functions than for the spin-independent ones.

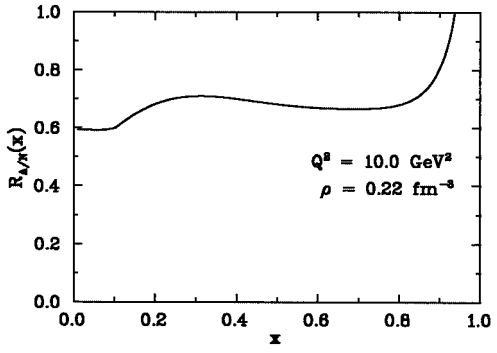

Fig. 2. Ratio of the in-medium polarized up quark distribution to the free nucleon value.

References

1) M. Arneodo: Phys. Rep. **240**, 240 (1994).
2) H. Mineo, W. Bentz, N. Ishii, A. W. Thomas, and K. Yazaki: Nucl. Phys. A **735**, 482 (2004).
3) W. Bentz and A. W. Thomas: Nucl. Phys. A **696**, 138 (2001).

† Condensed from an article by I. C. Cloet, W. Bentz, and A. W. Thomas, to be published.

*1 Jefferson Laboratories, USA
*2 Department of Physics, Tokai University

Chiral symmetry in light-cone field theory†

F. Lenz,[*1] M. Thies,[*1] K. Ohta,[*2] and K. Yazaki[*3]

[Hadron Physics, Chiral Symmetry, Light-Cone, Ward-Takahashi Identity]

We completed our work on chiral symmetry in light-cone quantization, a part of which had been reported last year.[1)] This work was previously published,[2)] and we report here its condensed form.

We study symmetry properties of systems with a spontaneously broken chiral symmetry in the light-cone formulation of field theories. The structure of a vacuum, which is crucial for describing dynamical symmetry breaking in a standard formulation, is kinematically determined in the light-cone formulation and is thus independent of symmetry realization. We attempt to understand how a dynamically broken phase can be compatible with a trivial vacuum.

As in a standard field theory, we describe symmetry properties from chiral Ward-Takahashi (WT) identities.[3,4)] Functional techniques are most convenient for such a purpose. We define a fermionic light-cone field theory by a generating functional containing only the unconstrained degrees of freedom, *i.e.*, with the "bad" components of the spinors being eliminated. Such a fermionic theory is nonlocal irrespective of dynamics. It reflects the dependence of light-cone energy on the inverse of light-cone momentum in the dispersion relation of a free particle. We note that the same dispersion relation determines the vacuum kinematically.

In the standard derivation of the relevant WT identities, one considers soft space-time-dependent modulations of global symmetry transformations.[5)] In a symmetry broken phase, these transformations generate soft excitations approaching zero energy excitations with increasing modulation wavelength, which are called Nambu-Goldstone (NG) bosons.[6,7)] From the WT identities, one identifies the creation operator of the NG bosons in the limit of vanishing momentum and one establishes a series of relations between composite NG bosons and the fundamental fermionic degrees of freedom. In an application to the light-cone theory, this standard procedure fails due to the nonlocality of a light-cone Hamiltonian. The infinite nonlocality range induced by the inverse of light-cone momentum destroys the connection between soft modulations and low excitation energies. This is akin to the suppression of NG particles in the presence of long-range interactions in gauge theories.

We demonstrate the failure of the standard procedure and show that the excitation of massive particles is not suppressed in the limit of long- wavelength modulations. To adjust the procedure to the light-cone Hamiltonian, we have to introduce nonlocal transformations of fermion fields. We carry out this by deriving the general form of the light-cone WT identities and by explicitly constructing the nonlocal symmetry transformations for various model field theories. We derive Gell-Mann-Oakes-Renner-like relations[8)] and consider the connection between a fermion propagator and the structure function of the NG bosons.[5)]

References

1) F. Lenz, K. Ohta, M. Thies, and K. Yazaki: RIKEN Accel. Prog. Rep. **36**, 44 (2003).
2) F. Lenz, K. Ohta, M. Thies, and K. Yazaki: Phys. Rev. D **70**, 025015 (2004).
3) J. C. Ward: Phys. Rev. **78**, 182 (1950).
4) Y. Takahashi: Nuovo Cimento **6**, 371 (1957).
5) V. A. Miransky: *Dynamical Symmetry Breaking in Quantum Field Theory* (World Scientific, Singapore, 1993).
6) Y. Nambu: Phys. Rev. Lett. **4**, 380 (1960).
7) J. Goldstone: Nuovo Cimento **19**, 154 (1961).
8) M. Gell-Mann, R. J. Oakes, and B. Renner: Phys. Rev. **175**, 2195 (1968).

† Condensed from the article in Phys. Rev. D **70**, 025015 (2004)

*1 Institute for Theoretical Physics, University of Erlangen, Germany
*2 Institute of Physics, University of Tokyo
*3 College of Arts and Sciences, Tokyo Woman's Christian University

Tensor analyzing power for the $\vec{d} + \alpha$ backward scattering

T. Uesaka,[*1] T. Ikeda,[*2] T. Kawabata,[*1] H. Okamura,[*3] K. Itoh,[*2] H. Sakai,[*4] K. Yako,[*4] T. Saito,[*4] H. Kuboki,[*4] M. Sasano,[*4] and K. Sekiguchi

[^{4}He(d, ^{4}He)^{2}H reaction, D-state, tensor analyzing power]

Short-range structures of light nuclei have a close connection to the high-momentum behavior of nuclear interactions which can not be fully described, for the moment, neither by meson exchange theories nor by non-perturbed quantum chromodynamics. Information on the short-range structure of light nuclei, especially spin-dependent one, is crucial to establish a better understanding of nuclear interactions. The $d + \alpha$ backward scattering, which is the $d + \alpha$ elastic scattering at $\theta \sim 180°$, at intermediate energies can be a candidate for a possible probe to the short-range structure of ^{4}He nucleus. Since the reaction in the backward region is considered to be dominated by two-nucleon transfer processes, the polarization observables as well as the cross sections are expected to be sensitive to the ^{4}He form factor of d-d or d-pn partition. In particular, tensor analyzing powers, A_{yy} and A_{xx}, can provide an information on the D-state admixture in the short-range region. In this report, the measurement of the cross section and analyzing powers, A_y, A_{yy}, and A_{xx}, for the $d+\alpha$ backward scattering at the deuteron energies of 140 MeV and 270 MeV is described. In addition to the $d + \alpha$ backward scattering, data for the ^{4}He(d, ^{3}He)^{3}H reaction were also measured in the same experimental conditions. The data are used to estimate the contribution from the sequential transfer of two nucleons, $d + \alpha \rightarrow {}^3\mathrm{He} + {}^3\mathrm{H} \rightarrow \alpha + d$.

The experiment was carried out at the E4 experimental area of RIKEN Accelerator Research Facility. A cryogenic ^{4}He gas target[1)] placed in the scattering chamber was cooled down to ~ 6 K. The target density and thickness were 8.1 mg/cm^3 and 4.3 mg/cm^2, respectively. Polarized deuteron beams with energies of 140 and 270 MeV were used to bombard the target. α particles emitted at forward angles in the laboratory system were analyzed in the magnetic spectrograph SMART[2)] and detected with multiwire drift chambers and three-layers of plastic scintillation counters located in the focal plane. Timing and pulse height information of the plastic scintillation counters was used to identify the particle. Momentum and scattering angle of the particle were reconstructed from the particle trajctory determined from the timing data of drift chambers with a help of ion-optical parameters of SMART. The energy resolution was obtained to be 800 keV (FWHM), which is high enough to resolve the $d + \alpha$ backward events from $pn - \alpha$ events.

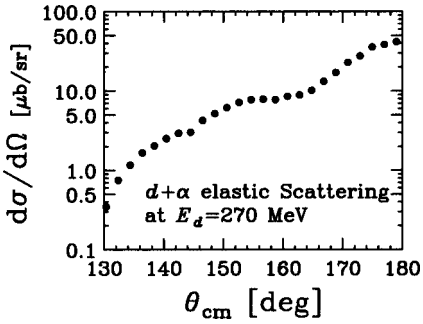

Fig. 1. Differntial cross section for the $d + \alpha$ elastic scattering at backward angles and at 270 MeV.

Figure 1 shows the preliminary results of the differential cross sections for the $d + \alpha$ backward scattering at 270 MeV. The statistical uncertainty of each data point is 1–5% depending on the angle and is smaller than the symbol in the figure. The data obviously exhibits a 180°-peak distribution which is typical for the nucleon transfer processes.

Tensor analyzing powers, A_{yy} and A_{xx} are shown in Fig. 2. Both A_{yy} and A_{xx} take large values of $A_{yy} = +0.2 \sim +0.7$ and $A_{xx} = -0.7 \sim +0.2$, respectively. Finite values of tensor analyzing powers present a clear manifestation of the D-state admixture in ^{4}He at finite momenta. Detailed theoretical analysis to estimate contributions from the D-state of deuteron and the reaction mechanism will be evaluated through analysis of the $d+\alpha$ elastic scattering and the ^{4}He(d, ^{3}He)^{3}H reactions.

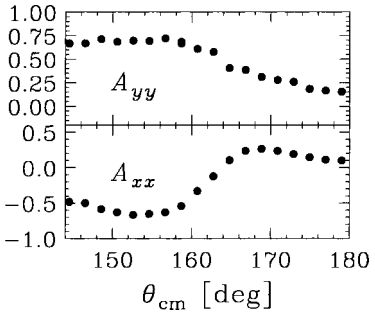

Fig. 2. Tensor analyzing powers for the $d + \alpha$ elastic scattering at backward angles.

*1 Center for Nuclear Study, University of Tokyo
*2 Department of Physics, Saitama University
*3 Tohoku University
*4 Department of Physics, University of Tokyo

References

1) T. Ikeda et al.: CNS-REP-61, 86 (2004).
2) T. Ichihara et al.: Nucl. Phys. A **569**, 287c (1994).

Absolute calibration of proton polarization via $\vec{p}$+^{4}He elastic scattering

S. Sakaguchi,[*1] T. Wakui,[*1] T. Uesaka,[*1] K. Itoh,[*2] T. Kawabata,[*1] H. Kuboki,[*3] Y. Maeda,[*1] H. Sakai,[*1,*3] Y. Sasamoto,[*1] M. Sasano,[*3] K. Sekiguchi, K. Suda,[*1] Y. Takahashi,[*3] and K. Yako[*3]

[polarized solid proton target]

We have recently succeeded in developing a polarized solid proton target which is distinctive in its applicability in a low magnetic field of 80 mT and at a high temperature of 100 K.[1)] The target was used, for the first time, in an experiment to measure the asymmetry of $\vec{p}$+^{6}He elastic scattering in 2003.[2)] During the scattering experiment, proton polarization was monitored with NMR. The NMR signal is usually calibrated using a known thermal equilibrium (TE) signal as a polarization standard. For our target, however, there is difficulty in measuring the TE signal. The TE polarization of a proton is quite small in a low magnetic field of 80 mT and at a high temperature of 100 K. In addition, the NMR sensitivity of our system is not sufficiently high, since the system is specialized to the scattering experiments. It is impractical to measure the proton thermal equilibrium signal with the present NMR system. We thus decided to use an alternative method to determine the absolute value of the proton polarization by using a nuclear reaction. For the determination, we carried out a measurement of the spin-dependent asymmetry of $\vec{p}$ + ^{4}He elastic scattering, since polarization P is described as

$$P = \frac{1}{A}\frac{N_{\mathrm{L}} - N_{\mathrm{R}}}{N_{\mathrm{L}} + N_{\mathrm{R}}}, \tag{1}$$

where A is the analyzing power, and $N_{\mathrm{L}}/N_{\mathrm{R}}$ are left/right yields. Details of the experiment are reported in this paper.

The experiment was performed in the E3 experimental area at the RIKEN Accelerator Research Facility. The energy and the typical intensity of the ^{4}He beam were 80 MeV/nucleon and 200 kcps, respectively.

For the material of the target, we used a single crystal of naphthalene doped with 0.01 mol% pentacene. The thickness of the target was 113 mg/cm^2. Protons in the target were polarized by the cross-polarization method.[3)] The target was operated at 88 mT and 100 K. Figure 1 shows the time development of the NMR signal amplitude, which is proportional to proton polarization. Proton polarization first increased in the "up" direction from 0 to 29.2 h. The polarization was once broken at 29.2 h, and increased in the opposite "down" direction from 37.8 to 52.0 h. Polarization measurement for both cases of spin "up/down" was carried out for the elimination of spurious asymmetry, which will be described later. The target was irradiated with a ^{4}He beam from 14.8 to 29.2 h and from 41.5 to 52.0 h. A decrease in polarization was observed after the beam irradiation started at 14.8 h. The small polarization in the case of spin "down" might be due to the beam irradiation effect. Polarization measurement using elastic scattering was carried out from 17.0 to 29.2 h and from 41.5 to 52.0 h.

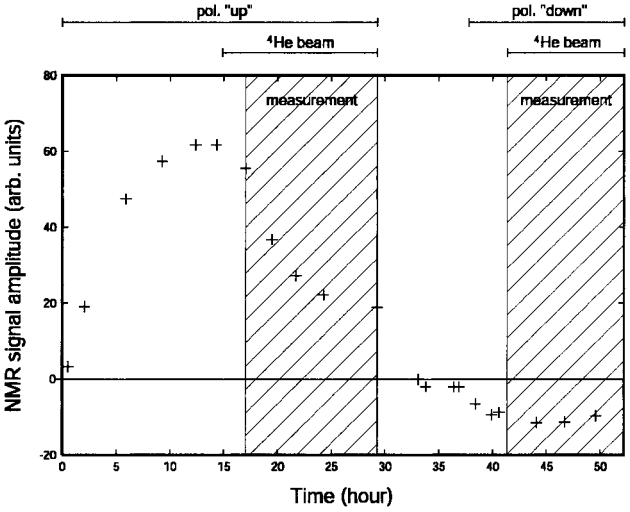

Fig. 1. Time development of proton polarization measured by pulsed NMR. The vertical axis denotes the NMR signal amplitude, which is proportional to the proton polarization. The origin of the horizontal axis denotes the time when laser irradiation was started for the increase of polarization in the "up" direction.

Figure 2 shows the schematic view of the experimental setup. For the detection of leading particles (mainly ^{4}He), we used a forward-counter placed approximately 1 m downstream of the target. The forward-counter consisted of a multiwired drift chamber (MWDC) and three layers of plastic scintillation detectors placed downstream of the MWDC. The MWDC was used to determine the trajectory of the leading particles. The plastic scintillation detectors were used to identify the leading particle by the standard ΔE-E method. The thicknesses of the scintillators are 5 mm in the first layer and 30 mm in the other two layers.

For the detection of recoiled protons, a pair of backward-counters was used. One was for the left-

*1 Center for Nuclear Study, Graduate School of Science, University of Tokyo
*2 Department of Physics, Saitama University
*3 Department of Physics, University of Tokyo

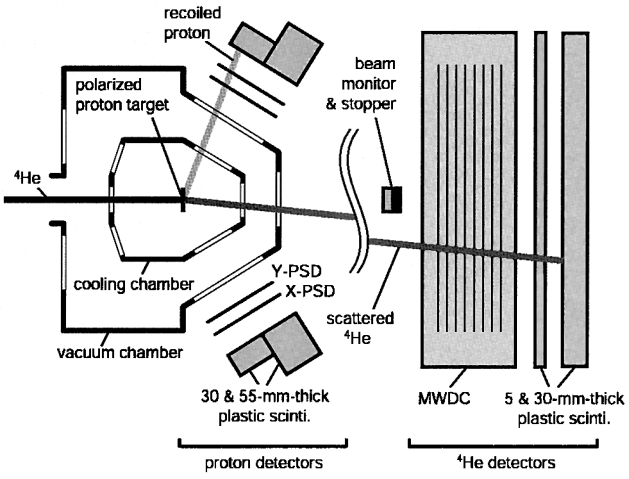

Fig. 2. Schematic view of experimental setup. The distances from the target to plastic scintillators for ^{4}He and protons are approximately 1 m and 180 mm, respectively.

hand event and the other was for the right-hand event. Each counter consisted of two 5-mm strip silicon detectors (X-PSD, Y-PSD) and plastic scintillation detectors. The PSD had a $50 \times 50\,\mathrm{mm}^2$ active area divided into 10 strips on the front face. Two PSDs with an orthogonal strip direction located 120 mm and 140 mm from the target determined the scattering angles of the recoiled protons in both vertical and horizontal directions. The identification of recoiled particles was performed with the ΔE data from the PSDs and E data from the plastic scintillation detectors. To discriminate background events, scattered ^{4}He particles and recoiled protons were detected in coincidence.

For the elimination of spurious asymmetry resulting from asymmetric geometry, we counted the number of elastic scattering events with left and right detectors in both cases where the polarizations were up and down. We then obtained yields as $N_{\mathrm{L}}^{\uparrow}$, $N_{\mathrm{R}}^{\uparrow}$, $N_{\mathrm{L}}^{\downarrow}$, and $N_{\mathrm{R}}^{\downarrow}$ where indices L/R represent left/right and $\uparrow/\downarrow$ represent up/down proton polarizations, respectively. The elimination of spurious asymmetry and derivation of the polarization were carried out using those yields by a calculation method described in Ref. 4.

The $\vec{p}$+^{4}He elastic scattering events are clearly identified by the identification of a proton and ^{4}He, and with conditions of kinematical consistency. Differential cross sections are deduced for each strip of the X-PSD from 38° to 70° in the center-of-mass system. The results obtained in 5 strips are shown in Fig. 3. From 44° to 56°, our results are consistent with the previously reported data[5] obtained under an ordinary kinematics condition. In the forwardmost strip, which corresponds to the angular range from 37.9° to 41.7°, the obtained cross section is about half the previously reported value. This is due to the fact that a number of the recoiled protons stop before reaching the plastic scintillators. Consequently, the corresponding events are not taken into account in the present analysis where E data of the plastic scintillator is required. Note that, in the angular range, energies of recoiled protons are as low as $< 10\,\mathrm{MeV}$ at the entrance of the detectors, owing to energy loss in the target material, cooling nitrogen gas, window foils and so on. In the future analysis, the energy loss correlation between X-PSD and Y-PSD is to be used for particle identification. Those events can then be reliably used to obtain the $\vec{p}$+^{4}He elastic scattering yield. The proton polarization will be determined from the elastic scattering yields for spin up/down.

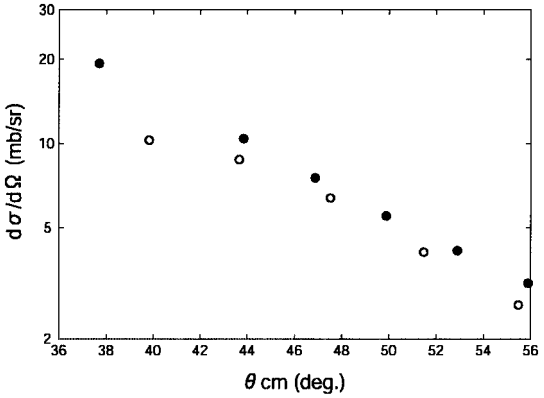

Fig. 3. Differential cross sections of p+^{4}He elastic scattering. The open circles show the present data, and the closed circles the previously reported data.[5]

References
1) M. Hatano et al.: RIKEN Accel. Prog. Rep. **36**, 48 (2003).
2) M. Hatano et al.: RIKEN Accel. Prog. Rep. **37**, 44 (2004).
3) T. Wakui et al.: RIKEN Accel. Prog. Rep. **36**, 171 (2003).
4) G. G. Ohlsen: Rep. Prog. Phys. **35**, 717 (1972).
5) H. Togawa et al.: RCNP Ann. Rep. **1987**, 1.

Breakup reactions of ^{11}Li

T. Nakamura, A. M. Vinodkumar,[*1] T. Sugimoto,[*1] N. Fukuda, Y. Kondo,[*1] M. Miura,[*1] N. Aoi, N. Imai,[*2] T. Kubo, T. Kobayashi,[*3] T. Gomi, A. Saito, H. Sakurai,[*4] S. Shimoura,[*5] D. Bazin,[*6] H. Hasegawa,[*7] H. Baba,[*7] T. Motobayashi, K. Watanabe,[*3] Y. X. Watanabe,[*2] T. Yakushiji,[*3] Y. Yanagisawa, K. Yoneda,[*6] and M. Ishihara

[NUCLEAR REACTIONS: Coulomb Dissociation, Halo Nuclei]

Strong E1 excitation to the low-lying continuum (soft E1 excitation) is one of the characteristic features of halo nuclei. This excitation has been well understood for one-neutron halo nuclei, such as ^{11}Be and ^{19}C, by the E1 direct breakup mechanism as shown in our previous ^{11}Be works using Coulomb dissociations.[1–3] On the other hand, the soft E1 excitation for the two-neutron halo case as in ^{11}Li is not well understood, mainly due to discrepancies among three previously obtained experimental results on the Coulomb dissociation at MSU,[4] RIKEN,[5] and GSI.[6]

We have thus studied the Coulomb dissociation of ^{11}Li on a Pb target at an incident energy of approximately 70 MeV/nucleon to obtain the data with much higher statistics and much less ambiguity caused by crosstalk events in detecting two neutrons. Nuclear breakup with a light target was also studied, part of which has already been reported.[7] A secondary beam of ^{11}Li was produced by fragmentation of a 100 MeV/nucleon primary ^{18}O beam in a thick Be production target and separated using the RIPS radioactive beam line at RIKEN. The ^{11}Li beam bombarded a Pb target of thickness 346 mg/cm^2 with an average energy of 70 MeV/nucleon. The momentum of the beam ion was obtained by tracing the trajectory with two PPAC's and by measuring the time of flight (TOF) using a thin plastic scintillator and an RF signal. The outgoing particles, a ^{9}Li ion and two neutrons, were emitted in a narrow kinematical cone at forward angles. The trajectory of the ^{9}Li ion was bent using a large-gap dipole magnet, tracked with a drift chamber, and then the ^{9}Li ion hit a hodoscope. The momentum of the ^{9}Li ion was thus obtained using the tracking information in combination with the TOF. The momentum of neutrons was obtained using the TOF and position information at the neutron detector arrays, which were composed of 54 rods of plastic scintillators arranged into two layers. The details of the experimental setup can be seen in the previous report.[8] The momentum vectors of outgoing particles were then combined to extract the invariant mass of the excited ^{11}Li nuclei.

Figure 1 shows the preliminary spectrum of the relative energy ($E_{\rm rel}$) of the three outgoing particles, ^{9}Li and two neutrons. A large peak at $E_{\rm rel} \sim 0.5$ MeV is observed. The cross section amounts to 2.74 ± 0.07 (stat.) barns for $E_{\rm rel} \leq 3$ MeV (preliminary). The $B(E1)$ strengths were obtained to be 1.5 ± 0.1 e^2 fm^2 for $E_{\rm rel} \leq 3$ MeV using the conventional equivalent photon method. The observed $B(E1)$ spectrum peaked at lower excitation energies with higher strengths, compared with the results of the previous experiments. Further analysis, such as on two neutron correlations, is now in progress.

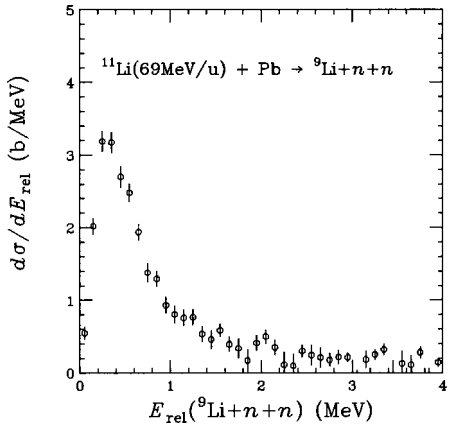

Fig. 1. Relative energy spectrum of the three outgoing particles ($^9{\rm Li}+n+n$) in the breakup of ^{11}Li on Pb.

References

1) T. Nakamura et al.: Phys. Lett. B **331**, 296 (1994).
2) N. Fukuda, T. Nakamura et al.: Phys. Rev. C **70**, 054606 (2004).
3) T. Nakamura et al.: Phys. Rev. Lett **83**, 1112 (1999).
4) K. Ieki et al.: Phys. Rev. Lett **70**, 730 (1993).
5) S. Shimoura et al.: Phys. Lett. B **348**, 29 (1995).
6) M. Zinser et al.: Nucl. Phys. A **619**, 151 (1997).
7) T. Nakamura et al.: RIKEN Accel. Prog. Rep. **35**, 57 (2002).
8) A. M. Vinodkumar et al.: RIKEN Accel. Prog. Rep. **37**, 50 (2004).

*1 Department of Physics, Tokyo Institute of Technology
*2 High Energy Accelerator Research Organization (KEK)
*3 Department of Physics, Tohoku University
*4 Department of Physics, University of Tokyo
*5 Center for Nuclear Study, University of Tokyo
*6 National Superconducting Cyclotron Laboratory, Michigan State University, USA
*7 Department of Physics, Rikkyo University

Coulomb and nuclear breakup of a halo nucleus ^{11}Be†

N. Fukuda, T. Nakamura,[*1] N. Aoi, N. Imai,[*2] M. Ishihara, T. Kobayashi,[*3] H. Iwasaki,[*4] T. Kubo, A. Mengoni,[*5] M. Notani,[*6] H. Otsu,[*3] H. Sakurai,[*4] S. Shimoura,[*7] T. Teranishi,[*8] Y. X. Watanabe,[*2] and K. Yoneda[*9]

[NUCLEAR REACTIONS: Pb(^{11}Be, ^{10}Be n) X, C(^{11}Be, ^{10}Be n) X, Halo nuclei, Coulomb breakup, Nuclear breakup]

We have investigated the Coulomb and nuclear breakup of ^{11}Be on Pb and C targets at energies of 69 MeV/nucleon and 67 MeV/nucleon, respectively. By measuring the momentum vectors of the incoming ^{11}Be ion, of the outgoing ^{10}Be ion, and the neutron in coincidence, we have extracted the relative energy spectra as well as the angular distributions of the scattering of the ^{10}Be + n c.m. system on both targets.

The obtained angular distribution of the ^{10}Be + n c.m. on Pb has been found to be well described by the first-order $E1$ Coulomb breakup mechanism, in particular for the very forward angular regions corresponding to large impact parameters in the semiclassical point of view. The experimental relative energy spectrum selected for $b \geq 30$ fm (or $\theta \leq 1.3°$) is in perfect agreement with the 1st-order pure $E1$ Coulomb calculation with the direct breakup mechanism, leading to a spectroscopic factor for the halo configuration $^{10}\mathrm{Be}(0^+) \otimes \nu 2s_{1/2}$ of 0.72 ± 0.04.

The $E1$ non-energy-weighted sum, corresponding to the integrated $B(E1)$ strength, has been compared to the value calculated with the cluster sum rule, leading to a root-mean-square distance of 5.77 ± 0.16 fm for the neutron in its halo state. The energy-weighted cluster sum rule has been applied to the present case. The energy-weighted $E1$ strength has been found to be $70\% \pm 10\%$ of the value calculated with this sum rule. It is interesting to note that this value agrees with the value of $\alpha^2 = 0.72(4)$.

The inelastic breakup scattering of ^{11}Be on a C target has been investigated experimentally. We have observed two peaks corresponding to the $E_\mathrm{x} = 1.78$ MeV and 3.41 MeV states. The angular distributions for these states show $L = 2$ excitation patterns, leading to their spin-parity assignments of $J^\pi = (3/2, 5/2)^+$. The amplitude of the angular distribution provided the deformation lengths for these states as well. The energy levels and the transition densities have been compared with those from shell model calculations for the low-lying positive parity states of ^{11}Be in the p-sd model space with the WBT effective interaction. We have found that the energy levels and deformation lengths are rather well reproduced. The comparison with the shell model calculation also suggests $J^\pi = 5/2^+$ and $J^\pi = 3/2^+$ as preferred assignments for the $E_\mathrm{x} = 1.78$ MeV and 3.41 MeV states, respectively. The deformation lengths are also well reproduced by the shell model calculation with Bernstein's prescription and the conventional values of effective charges.

The angular distributions have been investigated further to elucidate the reaction mechanism. We have found that the $L = 1$ Coulomb component is strong at very forward angles in contrast with the $L = 2$ pattern in the angular distribution around the 1.78 MeV resonance. In fact, the relative energy spectrum for $\theta \leq 0.5°$ is well reproduced by the pure $E1$ direct breakup model. This result shows that Coulomb breakup occurs at forward angles even on a light target such as carbon.

Finally, we have estimated the nuclear breakup and/or higher order effects by subtracting the calculated pure $E1$ Coulomb component for the Pb target. By making a comparison of the subtracted spectrum with the C target, the scaling factor Γ of the nuclear contribution for the Pb target to the C target is estimated. The scaling factor needed to reproduce the data at $E_\mathrm{rel} \geq 2$ MeV has been found to be $\Gamma = 2.1(5)$, which is consistent with Serber-type models. This value is smaller than $\Gamma = 5.4$ extracted from data at higher energies. This incident energy dependence can be qualitatively explained in the eikonal picture.

† Condensed from the article in Phys. Rev. C **70**, 054606 (2004)

*1 Department of Physics, Tokyo Institute of Technology
*2 High Energy Accelerator Research Organization (KEK)
*3 Department of Physics, Tohoku University
*4 Department of Physics, University of Tokyo
*5 Applied Physics Division, Italian National Agency for New Technologies, Energy and the Environment, Italy
*6 Physics Division, Argonne National Laboratory, USA
*7 Center for Nuclear Study, University of Tokyo
*8 Department of Physics, Kyushu University
*9 National Superconducting Cyclotron Laboratory, Michigan State University, USA

Coulomb and nuclear breakup of ^{14}Be

T. Sugimoto,[*1] T. Nakamura,[*1] N. Fukuda, M. Miura,[*1] Y. Kondo,[*1] N. Aoi, H. Baba,[*2] D. Bazin,[*3] T. Gomi, H. Hasegawa,[*4] Y. Hashimoto,[*1] N. Imai,[*5] T. Kobayashi,[*6] T. Kubo, T. Motobayashi, M. Ohara,[*1] A. Saito,[*2] H. Sakurai,[*7] S. Shimoura,[*2] A. M. Vinodkumar,[*1] K. Watanabe,[*6] Y. X. Watanabe,[*5] T. Yakushiji,[*6] Y. Yanagisawa, K. Yoneda,[*3] and M. Ishihara

[NUCLEAR REACTIONS: C(^{14}Be, ^{12}Ben), C, Pb(^{14}Be, ^{12}Be$2n$), Coulomb breakup, Nuclear breakup]

We studied the nuclear structure of two-neutron halo nucleus ^{14}Be using Coulomb- and nuclear-breakup reactions. In the case of one-neutron halo nuclei such as ^{11}Be, the low-lying E1 strength, observed characteristically in the Coulomb breakup of halo nuclei, is well understood as being the direct-breakup mechanism. The B(E1) distribution was used to extract a spectroscopic factor of the halo configuration of ^{11}Be.[1,2] In the case of the two-neutron halo, however, the excitation mechanism is not well understood due to the experimental and theoretical difficulties. To study the excitation mechanism, we performed an experiment on Coulomb breakup of ^{14}Be. In addition, we performed a nuclear-breakup experiment to study the first 2^+ state, since it is related to the deformation of ^{14}Be.

The experiment was performed at the RIPS beam line. The secondary ^{14}Be beam was produced by fragmentation of the ^{18}O primary beam at 100A MeV. The secondary beam was identified event-by-event by the standard $B\rho$-TOF-ΔE method. The secondary lead and carbon target (346 mg/cm^2 and 377 mg/cm^2, respectively) were bombarded by ^{14}Be with a central energy of 70A MeV. ^{14}Be was broken up into charged particles and neutrons. The charged particles and neutrons were measured simultaneously. The experimental details are presented in a former report.[3]

Figure 1 shows the relative-energy spectrum of the $^{12}\mathrm{Be} + 1n$ system measured with the carbon target. The relative-energy resolution is estimated as $\Delta E_{\mathrm{rel}} = 0.25\sqrt{E_{\mathrm{rel}}}$ MeV. In the spectrum, a broad peak at 0.2 MeV is observed. Assuming the peak to be a $2s$ continuum state, we fitted the experimental data using a theoretical model,[4] where the peak energy is related to the scattering length a ($E_{\mathrm{peak}} \leq \hbar^2/2\mu a^2$). The fitting parameter obtained ($a = -4.7$ fm) is consistent with the previous work.[5] Although another peak at 2.1 MeV was reported,[5–7] no clear peak was observed in our data.

We also analyze three-body (^{12}Be+$2n$) decay events in the Coulomb breakup. To eliminate crosstalk events in the neutron counters, we developed a new algorithm which enables us to reject more than 95% of crosstalk events. Figure 2 shows the relative-energy spectrum of the $^{12}\mathrm{Be} + 2n$ system measured with the lead target. The estimated relative-energy resolution was $\Delta E_{\mathrm{rel}} = 0.38\sqrt{E_{\mathrm{rel}}}$ MeV. Further analysis is in progress.

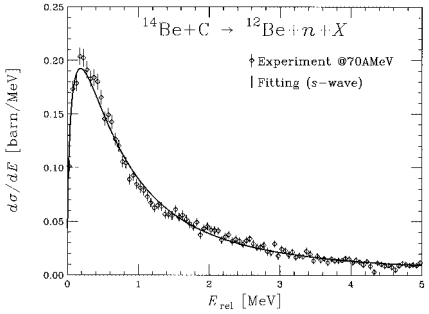

Fig. 1. Relative-energy spectrum of $^{12}\mathrm{Be} + 1n$ system.

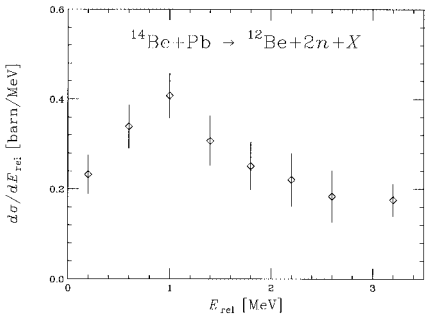

Fig. 2. Preliminary result of the relative-energy spectrum of $^{12}\mathrm{Be} + 2n$ system.

*1 Department of Physics, Tokyo Institute of Technology
*2 Center for Nuclear Study, University of Tokyo
*3 National Superconducting Cyclotron Laboratory, Michigan State University, USA
*4 Department of Physics, Rikkyo University
*5 High Energy Accelerator Research Organization (KEK)
*6 Department of Physics, Tohoku University
*7 Department of Physics, University of Tokyo

References
1) T. Nakamura et al.: Phys. Lett. B **331**, 296 (1994).
2) N. Fukuda et al.: Phys. Rev. C **70**, 054606 (2004).
3) T. Sugimoto et al.: RIKEN Accel. Prog. Rep. **37**, 59 (2004).
4) G. F. Bertsch et al.: Phys. Rev. C **57**, 1366 (1998).
5) M. Thoennessen et al.: Phys. Rev. C **63**, 014308 (2000).
6) A. V. Belozyorov et al.: Nucl. Phys. A **636**, 419 (1998).
7) J. L. Lecouey: Few-Body Systems **34**, 21 (2004).

Lifetime of the first excited state of ^{12}Be

N. Imai, N. Aoi, H. J. Ong,[*1] H. Sakurai,[*1] K. Demichi,[*2] H. Kawasaki,[*2] H. Baba,[*2] Zs. Dombrádi,[*3] Z. Elekes, N. Fukuda, Zs. Fülöp,[*3] A. Gelberg,[*4] T. Gomi,[*2] H. Hasegawa,[*2] K. Ishikawa,[*6] H. Iwasaki,[*5] E. Kaneko,[*2] S. Kanno,[*2] T. Kishida, Y. Kondo,[*6] T. Kubo, K. Kurita,[*2] S. Michimasa,[*5] T. Minemura, M. Miura,[*6] T. Motobayashi, T. Nakamura,[*6] M. Notani,[*3] T. K. Onishi,[*1] A. Saito,[*2] S. Shimoura,[*5] T. Sugimoto,[*6] M.K. Suzuki,[*1] E. Takeshita,[*2] S. Takeuchi, M. Tamaki,[*5] K. Yoneda, H. Watanabe, and M. Ishihara

[Doppler-shift attenuation method, ^{197}Au(^{12}Be, ^{12}Be*)^{197}Au E=40.3 MeV/u]

We applied the Doppler-shift attenuation method (DSAM)[1] to measure the lifetime of the first excited 2_1^+ state located at 2.10 MeV of ^{12}Be in flight. This is the first application of DSAM to the intermediate-energy RI beam. The lifetime is inversely proportional to the $B(E2)$ value. To measure $B(E2)$ of unstable nuclei, the Coulomb excitation method at the intermediate energy has been applied. However, this technique is not suitable for small Z nuclei since the nuclear excitation competes with the Coulomb excitation. In order to determine $B(E2)$ of ^{12}Be, we adopted DSAM, which has been used with thin targets where energy losses of the beams are negligible.

In the present experiment, a thick target was used so that the velocity of the ^{12}Be beam was degraded by as much as 20% in the target. The target also plays a role in exciting the beam to the 2_1^+ state. Due to the change in beam velocity, the Doppler-shifted de-excitation γ-ray energy was spread over a certain region. The energy of the γ-rays emitted inside the target was distributed continuously, while that of γ-rays emitted outside was constant since the excited nucleus no longer changed its velocity. In the energy spectrum, one can distinguish the γ-rays emitted inside the target from those emitted outside. The ratio of the γ-ray yield from inside the target to that from the outside depends on the lifetime. Hence, measurement of the γ-ray energy spectrum allows one to determine the lifetime.

A radioactive beam of ^{12}Be was produced by the projectile fragmentation of a 100 MeV/u ^{18}O beam with a 1850 mg/cm^2 thick Be target. The ^{12}Be beams were separated by the RIPS beam line[2] and bombarded on a 1930 mg/cm^2 thick Au target. At the final focal plane of RIPS, the energies of the beams were 40.3 MeV/u. The typical secondary beam intensity was 400 kHz. The scattering angle was measured using three parallel-plate avalanche counters, two of which were located upstream and the third one downstream of the target. Identification of the scattered particle was carried out using a plastic scintillator hodoscope. It consisted of a 2-mm-thick ΔE plane and a 5-mm-thick E plane. The de-excitation γ-rays from the inelastically excited ^{12}Be were detected using four clover Ge detectors (Clovers) manufactured by ORTEC. Each Clover was located 30 cm upstream of the target at 150 degrees with respect to the beam direction.

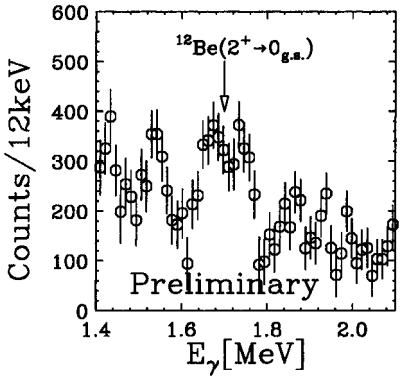

Fig. 1. Obtained energy spectrum of γ-rays. A broad peak around 1.7 MeV corresponds to the $2_1^+ \rightarrow 0_{\rm g.s.}^+$ transition in ^{12}Be.

The projectile fragmentation reaction also produced the isomeric 0^+ state at 2.24 MeV in ^{12}Be, which partly decays to the ground state via the 2_1^+ state.[3] We also measured the γ-rays without the target in order to estimate the effect of the cascade transition from the isomeric state. The energy spectrum measured without the target was subtracted from that measured with the target. The resultant spectrum is shown in Fig. 1.

The lifetime will be determined by comparison of the measured spectrum with that of the simulation. The simulated energy spectrum was obtained by a Monte Carlo method. In the simulation, we took into account the geometry, the measured beam profile, and the angular distribution of the γ-rays. Further analysis is in progress.

*1 Department of Physics, University of Tokyo
*2 Department of Physics, Rikkyo University
*3 ATOMKI, Hungary
*4 University of Köln, Germany
*5 Center for Nuclear Study, University of Tokyo
*6 Department of Physics, Tokyo Institute of Technology

References

1) S. Devons et al.: Proc. Phys. Soc. A **68**, 18 (1955).
2) T. Kubo et al.: Nucl. Instrum. Methods Phys. Res. B **70**, 309 (1992).
3) S. Shimoura et al.: Phys. Lett. B **560**, 31 (2003).

In-beam γ-ray spectroscopy of neutron-rich boron isotopes ^{15}B and ^{17}B via inelastic scattering on ^{12}C

Y. Kondo,[*1] T. Nakamura,[*1] N. Aoi, H. Baba,[*2] D. Bazin,[*3] N. Fukuda, T. Gomi, H. Hasegawa,[*4] N. Imai,[*5] M. Ishihara, T. Kobayashi,[*6] T. Kubo, M. Miura,[*1] T. Motobayashi, A. Saito,[*2] H. Sakurai,[*7] S. Shimoura,[*2] T. Sugimoto,[*1] K. Watanabe,[*6] Y. X. Watanabe,[*5] T. Yakushiji,[*6] Y. Yanagisawa, and K. Yoneda[*3]

[NUCLEAR REACTIONS: C(^{15}B,^{15}B*), C(^{17}B,^{17}B*), in-beam γ-ray spectroscopy]

We have observed a new γ transition in ^{17}B and known two transitions in ^{15}B using in-beam γ-ray spectroscopy with inelastic scattering on ^{12}C.

The experiment was performed at the RIKEN Accelerator Research Facility using the in-flight radioactive-isotope beam separator, RIPS.[1)] A ^{22}Ne beam at 110 MeV/nucleon bombarded a primary Be target of 1.1 g/cm^2 thickness to produce the secondary ^{15}B and ^{17}B beams. The secondary carbon target of 377 mg/cm^2 thickness was placed at the third focal plane (F3). The average kinetic energies of the ^{15}B and ^{17}B beams were 72 MeV/nucleon in the center of the target. The position and angle of the incident beam at the secondary target were measured using two parallel-plate avalanche counters (PPACs). De-excitation γ rays were detected using about a half-set of the DALI system,[2)] composed of thirty-six blocks of NaI(Tl) scintillators surrounding the secondary target. The outgoing boron isotopes were analyzed using a magnetic spectrometer equipped with a drift chamber and a plastic scintillator hodoscope. The particle identification of the outgoing boron isotopes was performed by combining the ΔE and TOF information from the hodoscope with the magnetic rigidity information from the drift chamber.

The observed γ transition in ^{17}B has been assigned as the decay from the first excited state at $E_{\rm x} = 1.07 \pm 0.01$ MeV to the ground state. For ^{15}B, we have observed two γ transitions, which are assigned as a cascade decay from the second excited state ($E_{\rm x} = 2.71$ MeV) to the ground state via the first excited state ($E_{\rm x} = 1.30$ MeV), using a γ-γ coincidence analysis and by comparing the two observed γ-ray energies with those obtained from a recent study using a fragmentation reaction.[3)] With the help of DWBA analysis the angular distributions of inelastically scattered ^{15}B and ^{17}B isotopes have been found to exhibit $\Delta L^\pi = 2^+$ characteristics.

The deformation lengths for the transitions have been deduced to be 1.20 ± 0.08 fm for ^{17}B and 1.17 ± 0.12 fm for ^{15}B using differential cross sections analyzed with the ECIS code. These values are compared with calculated deformation lengths using the shell model. Figure 1 shows the comparison of the experimental deformation lengths with the calculated ones as a function of the neutron effective charge e_n with a fixed proton effective charge of $e_p = 1.3e$. The comparison clearly indicates $e_n \approx 0$, which is different from the conventional values of effective charges $e_p = 1.3e$ and $e_n = 0.5e$ in *sd*-shell region.[4)] The measurements of the Q moment for ^{15}B[5)] and ^{17}B[6)] indicated the quenching of the neutron effective charge for these neutron-rich boron isotopes.

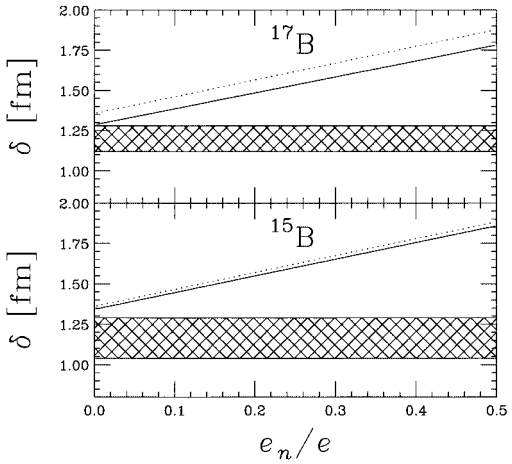

Fig. 1. Dependence of deformation length δ on neutron effective charge e_n of ^{17}B (top) and ^{15}B (bottom). Hatched zones indicate experimental values. Solid and dotted lines indicate shell model calculation using PSDWBT and PSDMK interactions, respectively.

*1 Tokyo Institute of Technology
*2 Center for Nuclear Study, University of Tokyo
*3 National Superconducting Cyclotron Laboratory, Michigan State University, USA
*4 Rikkyo University
*5 High Energy Accelerator Research Organization (KEK)
*6 Tohoku University
*7 University of Tokyo

References

1) T. Kubo et al.: Nucl. Instrum. Methods Phys. Res. B **70**, 309 (1992).
2) T. Motobayashi et al.: Phys. Lett. B **346**, 9 (1995).
3) M. Stanoiu et al.: Eur. Phys. J. A **22**, 5 (2004).
4) B. A. Brown and B. H. Wildenthal.: Ann. Rev. Nucl. Sci. **38**, 29 (1988).
5) H. Izumi et al.: Phys. Lett. B **366**, 51 (1996).
6) H. Ogawa et al.: Eur. Phys. J. A **13**, 81 (2002).

Anomalously hindered $E2$ strength $B(E2; 2^+ \rightarrow 0^+_{\text{g.s.}})$ in ^{16}C†

N. Imai, H. J. Ong,[*1] N. Aoi, H. Sakurai,[*1] K. Demichi,[*2] H. Kawasaki,[*2] H. Baba,[*2] Zs. Dombrádi,[*3] Z. Elekes,[*3] N. Fukuda, Zs. Fülöp,[*3] A. Gelberg,[*4] T. Gomi,[*2] H. Hasegawa,[*2] K. Ishikawa,[*5] H. Iwasaki,[*6] E. Kaneko,[*2] S. Kanno,[*2] T. Kishida, Y. Kondo,[*5] T. Kubo, K. Kurita,[*2] S. Michimasa,[*6] T. Minemura,[*3] M. Miura,[*5] T. Motobayashi, T. Nakamura,[*5] M. Notani,[*3] T. K. Onishi,[*1] A. Saito,[*2] S. Shimoura,[*6] T. Sugimoto,[*5] M. K. Suzuki,[*1] E. Takeshita,[*2] S. Takeuchi, M. Tamaki,[*6] K. Yoneda,[*3] H. Watanabe,[*3] and M. Ishihara

[NUCLEAR REACTIONS: ^{9}Be(^{16}C, ^{16}C*)^{9}Be $E = 34.6$ MeV/u; RSM]

In a recent paper, we reported an anomalously small B($E2$) value of ^{16}C. This B($E2$) value was determined by the lifetime measurement of the first excited state in ^{16}C.[1)] The lifetime τ is inversely proportional to the B($E2$) value of the nucleus. To measure τ, we adopted the recoil shadow method (RSM).[2)] This is the first application of the RSM to the τ measurement of the excited state of the radioactive-isotope (RI) beam. In the RSM, the emission point of the de-excitation γ ray is located and the γ-ray intensity is recorded as a function of the flight distance of the de-exciting nucleus. By utilizing an intermediate-energy RI beam, the flight velocity of the de-exciting nucleus is close to half the light velocity even after the secondary reaction. With such a high velocity, the flight distance at τ of 100 ps corresponds to a macroscopic length of about 1.7 cm. The present RSM provides a wide range of applications, extending to $\tau \approx 20$ ps.

A ^{16}C beam was produced by the projectile fragmentation of a 100 MeV/u ^{18}O beam with a thick 1850 mg/cm^2 Be target. The ^{16}C beam was separated by the RIPS beam line[3)] and bombarded onto a thick 370 mg/cm^2 Be target. In the middle of the target, the energy of the beam was 34.6 MeV/u. The typical secondary beam intensity was 200 kHz.

The de-excitation γ rays from the inelastically excited ^{16}C nuclei were detected by an array of thirty-two NaI(Tl) detectors. The array was divided into two rings, R1 and R2. R1 (R2) was composed of 14 (18) NaI(Tl) detectors and placed at 121 (102) degrees from the center of the target position with respect to the beam axis. To implement the RSM concept, we placed a lead slab of 5 cm thickness immediately downstream of R2. The slab had a columnar hole with a diameter of 5 cm at the center, where the beam passed through. The upstream surface of the slab was defined as $z = 0.0$ cm. The target was placed at $z = 0.0$ cm. Due to the screening effect of this slab, the effective γ-ray efficiencies of R1 and R2 are different. The magnitude of the difference depends on the point of γ-ray emission along the beam axis. Thus, τ can be deduced from the γ-ray yield ratio (R1/R2).

The measurement was also performed with another target position, $z = 1.0$ cm, to verify the deduced τ. The τ value was determined by comparing of the measured R1/R2 ratio with the simulated ratios as a function of τ. The simulation was carried out by the Monte Carlo method considering the measured emittance of the beams, scattering angles, and the calculated angular distribution of de-excitation γ rays. From the overlapped regions of the experimental R1/R2 ratio and the simulation, the τ values were determined to be 92 ± 22 ps and 63 ± 17 ps for the data obtained at the two target positions. As the final value, we adopted the weighted average of these two values. The uncertainty mentioned above is attributed to the statistical error. By incorporating the systematic error, which was mainly derived from the geometrical uncertainty of 1 mm, we determined $\tau = 77 \pm 14$(stat) ± 19(sys) ps. The central value of τ corresponds to B($E2$) = 0.63 e^2fm^4 or 0.26 Weisskopf units.

This B($E2$) value is an order of magnitude smaller than that obtained using an empirical formula based on the homogeneous quantum liquid drop model.[4)] Considering the fact that the model reproduces the experimental B($E2$) value of even-even nuclei with $\pm 50\%$ discrepancy except for a few nuclei, the present large difference from the model indicates an anomalous ^{16}C structure.

References

1) N. Imai et al.: Phys. Rev. Lett. **92**, 06251 (2004).
2) H. Backe et al.: Z. Phys. A **285**, 159 (1978).
3) T. Kubo et al.: Nucl. Instrum. Methods Phys. Res. B **70**, 309 (1992).
4) S. Raman et al.: At. Data Nucl. Data Tables **78**, 1 (2001).

† Condensed from the article in Phys. Rev. Lett **92**, 062501 (2004)

*1 Department of Physics, University of Tokyo
*2 Department of Physics, Rikkyo University
*3 ATOMKI, Hungary
*4 University of Köln, Germany
*5 Department of Physics, Tokyo Institute of Technology
*6 Center for Nuclear Study, University of Tokyo

Lifetime measurement of 2_1^+ state in ^{18}C

H. J. Ong,[*1] N. Imai, D. Suzuki,[*1] T. Nakao,[*1] H. Iwasaki,[*1] H. Sakurai,[*1] T. K. Onishi,[*1] M. K. Suzuki,[*1] S. Ota,[*2] S. Takeuchi, Y. Togano,[*3] Y. Kondo,[*4] N. Aoi, H. Baba,[*5] S. Bishop, J. Cook,[*6] Y. Ichikawa,[*1] M. Ishihara, T. Kubo, K. Kurita,[*3] T. Motobayashi, T. Nakamura,[*4] T. Okumura,[*4] and Y. Yanagisawa

[NUCLEAR REACTIONS: ^{9}Be(^{18}C,^{18}C)^{9}Be, lifetime measurement, MRSM]

The measurement of the reduced $E2$ transition probability from the first excited 2_1^+ state to the ground ($0_{\rm g.s.}^+$) state $B(E2)$ in an even-even nucleus is an important tool for studying proton collectivity. Recently, anomalously small $B(E2)$ has been reported for the neutron-rich ^{16}C nucleus.[1] The result indicates a surpressed proton contribution to the transition strength. Extended studies on other neighboring nuclei such as ^{18}C may be helpful in understanding this exotic phenomenon.

We have performed an experiment using a modified recoil shadow method (RSM)[1] to measure the lifetime of the 2_1^+ state in ^{18}C. The mechanism of γ-ray emission is governed by the electromagnetic theory and the lifetime of a γ-ray-emitting nuclear state is inversely proportional to $B(E2)$. Hence, the lifetime measurement is a direct method of determining $B(E2)$.

The experiment was performed at the RIKEN Accelerator Research Facility. A secondary beam of ^{18}C was obtained in a fragmentation reaction using a 110-MeV/nucleon ^{22}Ne beam with an intensity of 150 pnA incident on a 924-mg/cm^2 ^{9}Be target. The secondary beams, consisting of ^{18}C, ^{17}C and ^{17}B, were separated with the RIKEN Projectile-fragment Separator (RIPS).[2] The total beam intensity of the secondary beams was approximately 50 kcps at the final focal plane (F3). The time-of-flight (TOF) of the secondary beams between the second focal plane (F2) and F3 were measured using two 1-mm-thick plastic scintillators (PLs) placed at F2 and F3. The energy of the secondary beams deposited in the PLs (ΔE) was also measured. Particle identification was performed by means of the TOF-ΔE method. The purity of the ^{18}C beam was approximately 88%. The energy of the ^{18}C beam at F3 was deduced to be about 80 MeV/nucleon from the TOF information. A 370-mg-thick secondary Be target was placed 1.5 m downstream of the PL at F3 to excite the ^{18}C nuclei.

Scattered particles were detected using a plastic scintillatorhodoscope placed 4 m downstream of the secondary target. The hodoscope, which was mounted in a vacuum chamber, consisted of thirteen 5-mm-thick ΔE- and sixteen 60-mm-thick E- plastic scintillators. The ΔE and E counters were set perpendicular to each other, dividing the hodoscope into 13×16 segments. The position information obtained from the segmentation of the hodoscope was used to determine the scattering angle. The TOF between the secondary target and the hodoscope was measured using the timing information of the hodoscope and that of the PL at F3. The ^{18}C nuclei were stopped in the E counters. Particle identification of the scattered particles was performed by the TOF-ΔE and TOF-E methods.

To implement the MRS method, we placed a thick γ-ray shield around the target. The shield was a 5-cm-thick lead slab with an outer frame of 24×24 cm^2 and an inner hole of 5.4 cmϕ. The de-excitation γ-rays were detected in coincidence with the scattered ^{18}C using a modified DALI2 detector array.[3] The modified DALI2 consisted of 150 NaI(Tl) scintillators, which were divided into thirteen layers surrounding the target. Depending on the lifetime, the detection efficiency of the γ rays varies in each layer due to the presence of the lead shield. Measurements were also performed without the lead slab to reduce the systematic error due to the geometrical ambiguity of DALI2.

By comparing the measured full-energy peak yields in each layer with those obtained from GEANT simulations,[4] the lifetime of the 2_1^+ state in ^{18}C can be determined. Data analysis is in progress.

References

1) N. Imai et al.: Phys. Rev. Lett. **92**, 062501 (2004).
2) T. Kubo et al.: Nucl. Instrum. Methods Phys. Res. B **70**, 309 (1992).
3) S. Takeuchi et al.: RIKEN Accel. Prog. Rep. **36**, 148 (2003).
4) GEANT3: *Detector Description and Simulation Tool* (CERN, Geneva, 1993).

[*1] Department of Physics, University of Tokyo
[*2] Department of Physics, Kyoto University
[*3] Department of Physics, Rikkyo University
[*4] Tokyo Institute of Technology
[*5] Center for Nuclear Study, University of Tokyo
[*6] National Superconducting Cyclotron Laboratory, Michigan State University, USA

Low-lying excited states of ^{17}C and ^{19}C

Z. Elekes,[*1] Zs. Dombrádi,[*1] R. Kanungo, H. Baba,[*2] Zs. Fülöp,[*1] J. Gibelin,[*3] Á. Horváth,[*4] E. Ideguchi,[*5] Y. Ichikawa,[*5] N. Iwasa,[*6] H. Iwasaki,[*5] S. Kanno,[*2] S. Kawai,[*2] Y. Kondo,[*2] T. Motobayashi, M. Notani,[*5] T. Ohnishi,[*5] A. Ozawa, H. Sakurai,[*5] S. Shimoura,[*5] T. Suzuki,[*2] E. Takeshita,[*2] S. Takeuchi, I. Tanihata,[*7] Y. Togano,[*2] C. Wu,[*8] Y. Yamaguchi,[*2] Y. Yanagisawa, A. Yoshida, and K. Yoshida

[NUCLEAR STRUCTURE, Unstable nuclei, proton inelastic scattering, ^{17,19}C, bound excited states]

Theoretical calculations predict two low-lying excited states of both ^{17}C and ^{19}C,[1–3] but only one excited state has been found in ^{17}C.[4,5] Recently, indications of two γ transitions of ^{17}C have been reported,[6] suggesting that both predicted excited states are bound in ^{17}C. In addition, a γ peak in ^{19}C was also observed.[6] To obtain more information on the excited states in neutron rich odd carbon nuclei we have studied them by the (p,p$'\gamma$) process in inverse kinematics. The experiment was carried out at the RIKEN radioactive isotope separator RIPS.[7] A ^{22}Ne primary beam of 100 pnA intensity and 110 A·MeV energy hits a ^{9}Be production target of 0.8 cm thickness. For optimizing the ^{19}C beam, the secondary cocktail beam included 20% ^{19}C and 25% ^{17}B. By tuning the ^{17}C beam, practically 100% purity could be achieved. On an event-by-event basis, the identification of the incoming beam was performed by energy-loss, time-of-flight (TOF) and magnetic rigidity ($B\rho$) measurements. The secondary beam bombarded a liquid hydrogen target of 3 cm diameter.[8] The DALI2 setup[9] surrounded the liquid hydrogen target to detect de-excited γ rays. A silicon telescope with layers of 0.5, 2 and 2 mm thicknesses was inserted in air atmosphere to identify scattered particles. To produce γ ray spectra, one fold events in the NaI(Tl) array were selected (Fig. 1). In the (a) panel, two peaks are clearly visible at 72(4) and 197(6) keV which can be associated with the prompt decays of excited states of ^{19}C. Figure 1 (b) shows two distinct peaks at 210(4) and 331(6) keV confirming two low-lying excited states of ^{17}C. In the (c) panel of the ^{1}H(^{17}C,^{17}C) reaction, the higher energy peak is clearly visible, while the 210 keV peak is very faint, if it exists at all, and is situated on the Compton background of the 331 keV peak. The counting statistics in Fig. 1 (b) allowed us to perform a γ-γ coincidence analysis, which showed that the two observed transitions of ^{17}C are not in coincidence. The analyses of the spectra and the cross sections are now in progress.

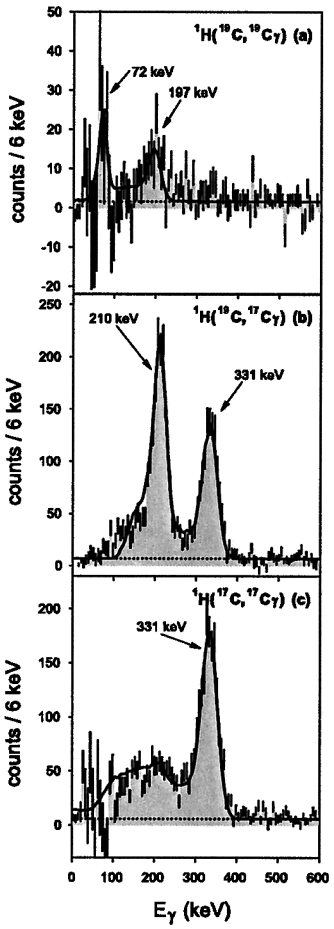

Fig. 1. Doppler-corrected spectra of γ rays emerging from ^{1}H(^{19}C,^{19}C) (a), ^{1}H(^{19}F,^{17}C) (b), and ^{1}H(^{17}C,^{17}C) (c) reactions.

*1 Insitute of Nuclear Research, ATOMKI, Hungary
*2 Rikkyo University
*3 Institut de Physique Nucléaire, France
*4 Eötvös Lóránd University, Hungary
*5 University of Tokyo
*6 Tohoku University
*7 Argonne National Laboratory, USA
*8 Peking University, China

References

1) P. Descouvemont et al.: Nucl. Phys. A **675**, 559 (2000).
2) V. Maddalena et al.: Phys. Rev. C **63**, 024613 (2001).
3) R. Fujimoto: Ph.D. Thesis, University of Tokyo (2003).
4) L. K. Fifield et al.: Nucl. Phys. A **383**, 505 (2000).
5) H. G. Bohlen et al.: Nucl. Phys. A **738**, 333 (2004).
6) M. Stanoiu et al.: Eur. Phys. J. A **20**, 95 (2004).
7) T. Kubo et al.: Nucl. Instrum. Methods Phys. Res. B **70**, 309 (1992).
8) H. Akiyoshi et al.: RIKEN Accel. Prog. Rep. **32**, 167 (1999).
9) H. Hasegawa et al.: RIKEN Accel. Prog. Rep. **35**, 169 (2002).

Decoupling of valence neutrons from the core in ^{16}C†

Z. Elekes,[*1] Zs. Dombrádi,[*1] A. Krasznahorkay,[*1] H. Baba,[*2] M. Csatlós,[*1] L. Csige,[*1] N. Fukuda, Zs. Fülöp,[*1] Z. Gácsi,[*1] J. Gulyás,[*1] N. Iwasa,[*3] H. Kinugawa,[*2] S. Kubono,[*4] M. Kurokawa, X. Liu, S. Michimasa, T. Minemura,[*4] T. Motobayashi, A. Ozawa,[*5] A. Saito,[*4] S. Shimoura,[*4] S. Takeuchi, I. Tanihata,[*6] P. Thirolf,[*7] Y. Yanagisawa, and K. Yoshida

[NUCLEAR STRUCTURE, Unstable nuclei, ^{16}C deformation]

Recent calculations[1] have suggested different deformations for proton and neutron distributions in carbon isotopes. We applied the Coulomb-nuclear interference method to study proton and neutron contribution to the excitation of the first 2^+ state. The experiment was carried out in RIKEN. The ^{16}C beam with 52.7 A·MeV at $4{\cdot}10^5$ particles/s was transmitted to a ^{208}Pb target of 50 mg/cm^2 thickness. The scattered particles were identified using a plastic scintillator hodoscope. For tracking the beam, four parallel plate avalanche counters (PPAC's) were used. The angular resolution was 0.28 ° at 1σ. The de-exciting γ-rays in coincidence with the ^{16}C particles were detected using an array of 68 NaI(Tl) scintillator detectors. The resulting angular distribution is showed the minimum from the Coulomb-nuclear interference at approximately 2.6° (Fig. 1). For the analysis of the angular distribution, we used the coupled channel code ECIS95.[2] The optical model parameters were taken from Ref. 3. The standard collective form factors were applied. Two parameters for the coupling potential, the "Coulomb deformation" length $\delta_{\rm C}$ and the "matter deformation" length $\delta_{\rm M}$, characterizing respectively the Coulomb and nuclear interactions between the target and projectile, have been determined by a χ^2-minimization analysis. Two χ^2-minima can be found at $\delta_{\rm M}/\delta_{\rm C} = 0.67$ and $\delta_{\rm M}/\delta_{\rm C} = 3.1$ with reduced $\chi^2 = 1.6$. The resultant $\delta_{\rm M}$ and $\delta_{\rm C}$ are connected to the neutron and proton transition matrix elements $M_{\rm n}$ and $M_{\rm p}$ via the Bernstein formula.[4] The deduced ratio is $M_{\rm n}/M_{\rm p} = 7.6 \pm 1.7$. The proton matrix element corresponds to an electromagnetic transition probability of B(E2) $= 0.28 \pm 0.06$ Weisskopf units (W.u.), while the neutron matrix element is slightly higher than the single-particle matrix element. Our B(E2) being significantly less than 1 W.u. is consistent with the result of a recent direct lifetime measurement, which gives B(E2) $= 0.26 \pm 0.05$ W.u.,[5] and is the smallest transition probability ever observed, while the deduced $M_{\rm n}/M_{\rm p}$ ratio is the highest thus far. Our experimental results clearly show that a very small proton deformation, or more strictly a very small amount of proton excitation, contributes to the 2_1^+ state in ^{16}C. The excitation is dominated by neutron transitions. In a simple shell-model picture (two valence neutrons $+^{14}$C core), we estimated the amount of core polarization and the neutron effective charge is found to be $e_{\rm n} = 0.15e$, much smaller than usual in the shell-model calculations in the region ($e_{\rm n} = 0.5$). This small value obtained for the effective charge in ^{16}C can be considered as an indication of the decoupling of the valence neutrons from the ^{14}C core.

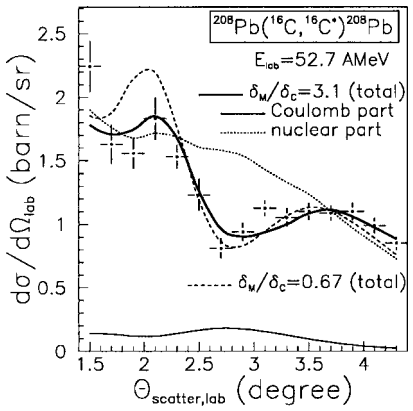

Fig. 1. Differential cross sections for the inelastic scattering exciting the 2_1^+ state in ^{16}C. The thick solid line represent the best fit with ECIS calculation which was smoothed by the angular resolution of the experimental setup (thin solid line: Coulomb part, dash-dotted line: nuclear part). Dashed line is plotted with $\delta_{\rm M}/\delta_{\rm C} = 0.67$ local minimum value.

References
1) Y. Kanada-En'yo et al.: Phys. Rev. C **55**, 2860 (1997).
2) J. Raynal: Phys. Rev. C **23**, 2571 (1981).
3) J. Barrette et al.: Phys. Rev. C **62**, 0340306 (2000).
4) A. M. Bernstein et al.: Phys. Rev. Lett. **42**, 425 (1979).
5) N. Imai et al.: Phys. Rev. Lett. **92**, 2501 (2004).

† Condensed from the article in Phys. Lett. B **599**, 17 (2004)

*1 Institute of Nuclear Research, ATOMKI, Hungary
*2 Rikkyo University
*3 Tohoku University
*4 University of Tokyo
*5 University of Tsukuba
*6 Argonne National Laboratory, USA
*7 Ludwig-Maximilians-Universität, Germany

Density distribution of ^{17}B studied via its reaction cross section measurement†

Y. Yamaguchi,[*1] C. Wu,[*2] A. Ozawa,[*3] T. Suzuki,[*4] D. Q. Fang,[*5] M. Fukuda,[*6] N. Iwasa,[*7] T. Izumikawa,[*8] R. Kanungo, R. Koyama,[*8] T. Ohnishi, T. Ohtsubo,[*8] W. Shinozaki,[*8] T. Suda, M. Takahashi,[*8] and I. Tanihata[*9]

[NUCLEAR STRUCTURE, ^{17}B, density distribution, halo structure]

The reaction cross section (σ_R) for the neutron-rich nucleus ^{17}B on a carbon target has been measured at an energy of 77A MeV by the transmission method. An enhancement of σ_R at intermediate energy compared with that at high energy was observed.[1)] Based on the assumption of the core (^{15}B) plus valence two-neutron picture, the density distribution ($\rho(r)$) of ^{17}B was deduced through the energy dependence of σ_R using a finite-range Glauber-model calculation. The finite-range Glauber-model calculation seems a useful tool for determining the association of σ_R and $\rho(r)$ in a wide-energy region.[2)] We parameterized a finite-range parameter by fitting the energy dependence of σ_R for the ^{12}C + ^{12}C system, including new data from Ref. 3. We employed the finite-range Glauber-model calculation under the optical-limit (OL) approximation (1) as well as the few-body (FB) approach (2).

(1) We assumed the $\rho(r)$ of ^{17}B to be a HO-type function for the core (^{15}B) plus a square of Yukawa tail function for the valence two neutrons, and calculated σ_R with a finite-range parameter. The width parameter of the HO-type function of the core, chosen to be 1.679 fm so as to reproduce σ_I of ^{15}B,[4)] is common to both protons and neutrons. By fitting the measured σ_R with a free parameter, which is an asymptotic slope of the square of Yukawa tail function, the best fit was obtained with $\chi^2 = 8.03$.

(2) Note that a few-body (FB) Glauber-model calculation may be more suitable for describing a weakly bound system, like a halo nucleus.[5,6)] Thus, we applied the FB calculation to a three-body system (core + neutron + neutron) of ^{17}B. The minimum χ^2 was 2.53 with a free parameter, which is a fraction of the wave function with the valence two-neutron configuration of $(2s_{1/2})^2_{J=0}$ or $(1d_{5/2})^2_{J=0}$.

We have applied the two methods mentioned above. In the present analysis, the FB approach reproduces the experimental data better than the OL approach from the point of the minimum χ^2 value. However, many more assumptions are involved in the FB approach, in which the wave function is assumed to be a product of the halo neutron wave function and the core wave function. Moreover, the slope of the tail is fixed by the weak binding energy of the valence two-neutron (S_{2n}).[7)] In contrast, an advantage of the OL approach is the fact that the slope of the tail is independently determined from S_{2n}. Thus, it is difficult to decide which method is better for ^{17}B density distribution. Therefore, we include, as the final $\rho(r)$ of ^{17}B, all the distributions obtained from these two methods, shown in Fig. 1. It is clearly demonstrated that a long neutron tail with a significant amplitude exists in the density distribution of ^{17}B. It was proved that the neutron tail in the density distribution is essential for ^{17}B to reproduce the measured reaction cross sections.

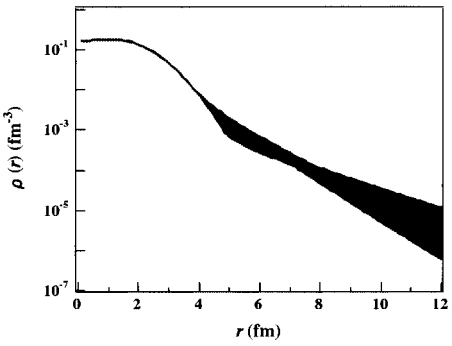

Fig. 1. Final density distribution of ^{17}B with significant amplitude of long neutron tail.

References
1) Y. Yamaguchi et al.: RIKEN Accel. Prog. Rep. **37**, 52 (2004).
2) T. Zheng et al.: Nucl. Phys. A **709**, 103 (2002).
3) M. Fukuda: private communication.
4) A. Ozawa et al.: Nucl. Phys. A **608**, 63 (1996).
5) J. S. Al-Khalili et al.: Phys. Rev. C **54**, 1843 (1996).
6) Y. Ogawa et al.: Prog. Theor. Phys. Suppl. No. 142, 157 (2001).
7) G. Audi et al.: Nucl. Phys. A **624**, 1 (1997).

† Condensed from the article in Phys. Rev. C **70**, 054320 (2004)

*1 Center for Nuclear Study, University of Tokyo
*2 Peking University, China
*3 University of Tsukuba
*4 Saitama University
*5 Chinese Academy of Sciences, China
*6 Osaka University
*7 Tohoku University
*8 Niigata University
*9 Argonne National Laboratory, USA

Isoscalar electric multipole strength in ^{14}O

H. Baba,[*1] S. Shimoura,[*1] T. Minemura, Y. U. Matsuyama,[*2] A. Saito,[*1] H. Akiyoshi, N. Aoi, T. Gomi, Y. Higurashi, K. Ieki,[*2] N. Imai, N. Iwasa,[*3] H. Iwasaki,[*1] S. Kanno,[*2] S. Kubono,[*1] M. Kunibu,[*2] S. Michimasa, T. Motobayashi, T. Nakamura,[*4] H. Sakurai,[*5] M. Serata,[*2] E. Takeshita,[*2] S. Takeuchi, T. Teranishi,[*6] K. Ue,[*5] K. Yamada, and Y. Yanagisawa

[NUCLEAR REACTIONS: ^{14}O(α,α'), 60 A MeV; Inelastic α Scattering]

Intermediate energy RI beams enable us to investigate excited unstable nuclei using inverse kinematics and measuring decaying particles and γ rays. We performed the measurement of inelastic α scattering on the light unstable nuclei ^{14}O. For light stable nuclei, isoscalar electric multipole strength has been systematically studied[1,2] using an inelastic scattering of 60 A MeV α and the isoscalar monopole ($E0$) and dipole ($E1$) resonance have been discussed, which are relevant to the incompressibility of nuclear matter.

In the present experiment, we aimed at measuring the excitation energy spectrum and the isoscalar multipole strength in a wide energy range by the invariant-mass method for various particle decay channels and the multipole decomposition (MD) analysis.[3]

The experiment was performed at the RIKEN projectile fragment separator (RIPS). A beam of 60 A MeV ^{14}O was produced by the fragmentation reaction and bombarded on a 120-mg/cm^2 thick liquid-helium secondary target. Outgoing particles were measured using a ΔE-$E1$-$E2$ plastic hodoscope located 4 m downstream of the target. To obtain de-excitation γ rays from the outgoing particles, an array of sixty-eight NaI(Tl) scintillators were set around the secondary target. The excitation energy was constructed from the momentum vectors of decay products by the invariant-mass method. We measured the decay channels of $^{14}O^* \rightarrow {}^{13}N + p$, $^{12}C + p + p$, $^{10}C + \alpha$, $^{12}C_1^* + p + p$, and $^{10}C_1^* + \alpha$.

In order to obtain the multipole strength distributions, the MD analysis with the distorted wave Born approximation (DWBA) method has been extensively used. In this analysis, the DWBA calculations for inelastic α scattering were performed using the computer code ECIS97[4] with external optical and transition potentials. We employed a single-folding model with a density-dependent nucleon-α interaction[5] and isoscalar transition densities[6,7] to obtain optical and transition potentials.

Figure 1 shows the decomposed multipole strength distributions of $L = 0$–3, and $L \geq 4$ obtained from the MD analysis. The integrated strengths up to 25.0 MeV were identified corresponding to 37.7 ± 8.4, 72.4 ± 8.3, 15.9 ± 3.8, and 9.6 ± 3.7% of the isoscalar $E0$, $E1$, $E2$, and $E3$ EWSR, respectively. In addition to the fragmented strength distributions as seen in light stable nuclei,[1,2] substantial continuum strengths below 10 MeV for the isoscalar $E0$ and $E1$ response were newly observed which may be due to the low threshold of the proton in ^{14}O.

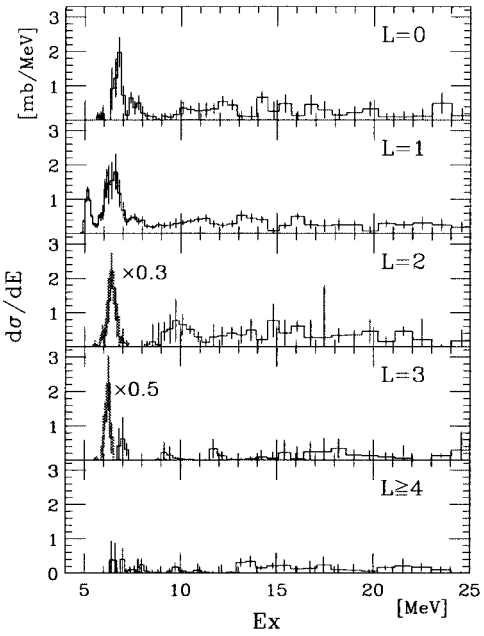

Fig. 1. Decomposed strength distributions of ^{14}O obtained by sum of measured decay channels.

*1 Center for Nuclear Study, University of Tokyo
*2 Department of Physics, Rikkyo University
*3 Department of Physics, Tohoku University
*4 Department of Applied Physics, Tokyo Institute of Technology
*5 Department of Physics, University of Tokyo
*6 Department of Physics, Kyushu University

References
1) B. John et al.: Phys. Rev. C **68**, 014305 (2003).
2) Y.-W. Lui et al.: Phys. Rev. C **64**, 064308 (2001).
3) M. Itoh et al.: Phys. Lett. B **549**, 58 (2002).
4) J. Raynal: ECIS97, unpublished.
5) A. Kolomiets et al.: Phys. Rev. C **61**, 34312 (2000).
6) G. R. Satchler: Nucl. Phys. A **472**, 215 (1987).
7) M. N. Harakeh and A. E. L. Dieperink: Phys. Rev. C **23**, 2329 (1981).

E1 strength of the subthreshold $3/2^+$ state in ^{15}O studied by Coulomb excitation†

K. Yamada, T. Motobayashi, H. Akiyoshi, N. Aoi, Zs. Fülöp,[*1] T. Gomi, Y. Higurashi, N. Imai,[*2] N. Iwasa,[*3] H. Iwasaki,[*4] Y. Iwata,[*5] H. Kobayashi,[*6] M. Kurokawa, Z. Liu,[*7] T. Minemura,[*2] S. Ozawa,[*8] H. Sakurai,[*4] M. Serata,[*6] S. Shimoura,[*9] S. Takeuchi, T. Teranishi,[*10] Y. Yanagisawa, K. Yoshida, and M. Ishihara

[Nuclear astrophysics, CNO cycle, Coulomb excitation]

The ^{14}N(p,γ)^{15}O reaction at low energies is particularly essential in the hydrogen-burning stage of a massive main-sequence star as this reaction, being the slowest in the main CNO cycle under stellar conditions, dominates the rate of energy generation through the entire cycle. The behavior of the low-energy (p,γ) capture yield is influenced by the tails of a few discrete levels. The s-wave resonance located 504 keV below the p + ^{14}N threshold, which corresponds to the $3/2^+$ state at 6.793 MeV excitation energy in ^{15}O, has attracted much attention. Schröder *et al.* extracted the radiative width of the $3/2^+$ state to be $\Gamma_\gamma = 6.3$ eV.[1)] A recent R-matrix analysis yielded the width $\Gamma_\gamma = 1.75 \pm 0.60$ eV,[2)] based on the same data as those used in Ref. 1. A recent lifetime measurement showed the mean life of $1.60^{+0.75}_{-0.72}$ fs for the $3/2^+$ state,[3)] which corresponds to a width $\Gamma_\gamma = 0.41^{+0.34}_{-0.13}$ eV. The widths of 1.75 eV and 0.41 eV lead to negligible contribution of the $3/2^+$ state to the ^{14}N(p,γ)^{15}O reaction rate, while the width of 6.3 eV increases the astrophysical S-factor at zero energy by approximately 50% compared with that estimated without any resonance effect. In this article we report on a measurement of the radiative width for the $3/2^+$ state in ^{15}O by intermediate-energy Coulomb excitation. Because this method is independent of those employed in the earlier experiments, this study is expected to provide complementary information and help resolve the conflicting situation mentioned above.

An ^{15}O beam was produced by the projectile fragmentation of an ^{16}O beam, and was isotopically separated by RIPS. The beam was focused onto a lead target of 1480 mg/cm^2 thickness. The average energy in the middle of the target was about 85 A MeV. The typical ^{15}O intensity was about 4×10^5 counts per second. ^{15}O was identified by measuring the time-of-flight (TOF) using a plastic scintillator and cyclotron RF signals. Reaction particles were identified by measuring the energies deposited in the ΔE and E plastic-scintillator hodoscope placed 5.0 m downstream from the target, and the TOF between the plastic scintillator and the hodoscope. An array of 64 NaI(Tl) scintillators was placed around the lead target and was used to detect de-excitation γ-rays. The Doppler shift was corrected event by event using the γ-ray emission angle.

The γ-ray spectrum obtained by the 63-degree detectors was analyzed with the following six components: four line shapes from the transitions in ^{15}O (5.241 MeV ($5/2^+ \rightarrow 1/2^-_{\rm g.s.}$), 6.176 MeV ($3/2^- \rightarrow 1/2^-_{\rm g.s.}$), 6.793 MeV ($3/2^+ \rightarrow 1/2^-_{\rm g.s.}$), and 7.276 MeV ($7/2^+ \rightarrow 1/2^-_{\rm g.s.}$)) obtained by the Monte-Carlo calculation; a target excitation component, and a continuous background component. The target excitation component was determined from the energy spectrum obtained by the backward-angle array detectors at 127 degrees. From the fit, the resulting cross section was found to be 0.55 ± 0.35 mb for the 6.8 MeV component. The radiative width for the $3/2^+$ state, $\Gamma_\gamma = 0.95 \pm 0.60$ eV, was derived from the cross section for the 6.8 MeV component with the help of a distorted-wave calculation assuming pure E1 Coulomb excitation. However, contributions from other γ-transitions feeding the 6.8 MeV state could cause reduction of the Γ_γ value. Considering that the amount of this effect cannot be derived experimentally, it is appropriate to provide an experimental radiative width of $0.95^{+0.60}_{-0.95}$ eV.

The present result provides an independent support to the recent studies that yielded small Γ_γ values, $0.41^{+0.34}_{-0.13}$ eV,[3)] and 1.75 ± 0.60 eV.[2)] However, the prediction of 6.3 eV by Schröder *et al.*[1)] is not compatible with the present Coulomb excitation result. This suggests that the role of the $3/2^+$ subthreshold state is considerably small and negligible for the low-energy ^{14}N(p,γ)^{15}O cross section. Thus, a possible increase in the S-factor toward zero energy is not favorable in contrast to the prediction in Ref. 1.

† Condensed from the article in Phys. Lett. B **579**, 265 (2004)

*1 ATOMKI, Hungary
*2 High Energy Accelerator Research Organization (KEK)
*3 Department of Physics, Tohoku University
*4 Department of Physics, University of Tokyo
*5 National Institute of Radiological Sciences
*6 Department of Physics, Rikkyo University
*7 Institute of Modern Physics, China
*8 Japan Atomic Energy Research Institute
*9 Center for Nuclear Study, University of Tokyo
*10 Department of Physics, Kyushu University

References

1) U. Schröder et al.: Nucl. Phys. A **467**, 240 (1987).
2) C. Angulo and P. Descouvemont: Nucl. Phys. A **690**, 755 (2001).
3) P. F. Bertone et al.: Phys. Rev. Lett. **87**, 152501 (2001).

Study of ^{22}O(d,p)^{23}O reaction in inverse kinematics

Z. Elekes,[*1] Zs. Dombrádi,[*1] S. Bishop, Zs. Fülöp,[*1] J. Gibelin,[*2] T. Gomi, Y. Hashimoto,[*3] N. Imai, N. Iwasa,[*4] H. Iwasaki,[*5] G. Kalinka,[*1] Y. Kondo,[*3] K. Kurita,[*6] M. Kurokawa, N. Matsui,[*3] T. Motobayashi, T. Nakamura,[*3] T. Nakao,[*5] T. Ohnishi, T. Okumura,[*3] S. Ota,[*7] A. Perera, A. Saito,[*5] H. Sakurai,[*5] Y. Satou,[*3] D. Sohler,[*1] T. Sumikama, D. Suzuki,[*6] M. Suzuki,[*6] H. Takeda,[*5] S. Takeuchi, Y. Togano,[*6] and Y. Yanagisawa

[NUCLEAR STRUCTURE, Unstable nuclei, transfer reaction, single-particle energies]

The structure of atomic nuclei is known to be largely dominated by single-particle shell effects. For instance, basic nuclear properties such as binding energies and shapes depend strongly on the underlying shell structure. The study of nuclei beyond the valley of stability is motivated by the understanding of the way single-particle energies evolves when we owe move away from stable nuclei to neutron and proton drip lines. This would make more precise predictions of the limit of the existence of nuclear species. In the case of light nuclei, the rapid change in the location of the neutron drip line between O and F species is still not understood. The neutron drip line seems to be reached at $N = 16$ in O isotopes whereas in the neighboring F isotopes, it has been found to extend up to $N = 22$.[1)] Obviously, the understanding of how the shell structure evolves from O to F nuclei should shed light on how nuclear force could accommodate the binding of up to 6 neutrons in ^{31}F by the addition of a single proton. The situation can be partly understood by assuming a sufficiently large $N = 16$ shell gap between the $s_{1/2}$ and $d_{3/2}$ neutron orbits, making the $d_{3/2}$ orbit unbound in oxygen, but bound in F nuclei. To understand the problems related to the $N = 16$ subshell closure at the neutron drip line, measurement of the energy of the single-particle states in ^{23}O is required. Since the first excited state in ^{23}O is expected to be unbound, the only way to measure its energy is to search for a resonance in the cross section of a well-chosen reaction. For this purpose, we studied the ^{2}H(^{22}O,^{23}O)^{1}H reaction in which a neutron and an ^{22}O nucleus is emitted after the ^{23}O excited state was formed.

In the experiment, a 94 A·MeV energy primary beam of ^{40}Ar with 60 pnA intensity hit a ^{9}Be production target of 0.5 cm thickness. The reaction products were momentum- and mass-analyzed by the RIPS[2)] fragment separator. The secondary beam mainly included neutron-rich ^{25}Ne and ^{22}O nuclei. The RIPS was operated at 6% momentum acceptance. The total intensity was approximately 1500 cps having an average ^{22}O intensity of 600 cps. The identification of incident beam species was performed by energy loss and time-of-flight.[1)] The secondary beam was transmitted to a CD_2 target of 30 mg/cm^2 at the final focus of RIPS. The reaction occurred at an energy of 34 A·MeV. The position of the incident particles was determined by two PPACs placed at F3 upstream of the target. The scattered particles were detected and identified by a 2×2 matrix silicon telescope placed 96 cm downstream of the target. The telescope consisted of three layers with thicknesses of 0.5, 0.5, 2 and 2 mm. The first two layers were made of stripped detectors measuring the x and y positions of the fragments. On the basis of ΔE-E information, isotope separation was carried out among the different oxygen isotopes. The protons emitted backward during the reaction were detected by 156 CsI(Tl) scintillator crystals read out by photodiodes. 80 NaI(Tl) scintillator detectors also surrounded the target to detect de-exciting γ rays emitted by the inelastically scattered nuclei. The neutrons coming from the breakup of the excited ^{23}O nuclei were detected by a neutron wall consisting of four layers placed 2.5 m downstream of the target. The schematic view of the experimental setup is shown in Fig. 1. The analysis of the data is now in progress.

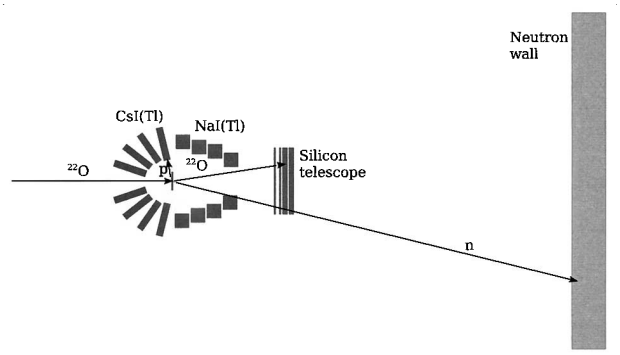

Fig. 1. Schematic view of experimental setup.

*1 Institute of Nuclear Research, ATOMKI, Hungary
*2 Institut de Physique Nucléaire, France
*3 Tokyo Institute of Technology
*4 Tohoku University
*5 University of Tokyo
*6 Rikkyo University
*7 Kyoto University

References
1) H. Sakurai et al.: Phys. Lett. B **448**, 180 (1999).
2) T. Kubo et al.: Nucl. Instrum. Methods Phys. Res. B **70**, 309 (1992).

Proton single particle states in ^{23}F

S. Michimasa, S. Shimoura,[*1] H. Iwasaki,[*2] M. Tamaki,[*1] S. Ota,[*3] N. Aoi, H. Baba,[*1] N. Iwasa,[*4] S. Kanno,[*5] S. Kubono,[*1] K. Kurita,[*5] M. Kurokawa, T. Minemura, T. Motobayashi, M. Notani,[*6] H. J. Ong,[*2] A. Saito,[*1] H. Sakurai,[*2] S. Takeuchi, E. Takeshita,[*5] Y. Yanagisawa, and A. Yoshida

[NUCLEAR REACTIONS: ^{4}He(^{22}O,^{23}F*), ^{4}He(^{23}F,^{23}F*), ^{4}He(^{24}F,^{23}F*), Single-particle state, In-beam γ-ray spectroscopy]

We have measured de-excited γ rays from ^{23}F produced by the proton transfer reaction ^{4}He(^{22}O,^{23}F*), the inelastic scattering ^{4}He(^{23}F,^{23}F*) and the neutron knockout reaction ^{4}He(^{24}F,^{23}F*). The ^{23}F isotope locates in the vicinity of the exotic magic number of $N = 16$.[1] In the region, numerous experimental works were performed to investigate neutron contributions to the exotic phenomenon. Here, we considered the proton shell structure in the neutron-rich nucleus ^{23}F, and searched proton single-particle states in ^{23}F on the basis of the difference in population strength among the above-mentioned reactions.

The experiment was performed at the RIPS beam line in RIKEN. ^{40}Ar ions were accelerated up to 63 MeV/nucleon using the linear accelerator scheme of RFQ-RILAC-CSM-RRC. The maximum intensity of the primary beam was achieved up to 800 pnA. The primary target was ^{9}Be with a thickness of 1 mm. The secondary beam was a cocktail of ^{22}O, ^{23}F and ^{24}F, and produced by their projectile fragmentation reaction. The averaged beam energies of ^{22}O, ^{23}F and ^{24}F were 35, 41.5 and 36 MeV/nucleon, and these intensities were 2×10^3, 6×10^2 and 3×10^2 cps, respectively. The secondary beam bombarded a liquid helium target[2] of 100 mg/cm^2 with havar foil windows. Reaction products were identified using a telescope consisting of 9 SSDs and 36 NaI(Tl) scintillators.[3] The scattering angles of the reaction products were measured using three PPACs. The resolution of the scattering angle were estimated to be 0.25 degrees (σ) in laboratory coordinates. Furthermore, de-excitation γ rays from the reaction products were detected using 150 NaI(Tl) scintillators[4] surrounding the secondary target.

In the analysis, we examined coincidences of multiple γ rays in the above-mentioned reactions and preliminarily reconstructed the γ-decay scheme in ^{23}F as shown in Fig. 1. Level energies with underlines show newly observed excited states in the present experiment. The bar graphs on the right side of the excitation energies show the relative cross sections to populate these excited states. In these relative cross sections, one can observe that the 4.06-MeV state is strongly populated by the proton transfer reaction, but hardly populated by the other reactions. This strongly suggests that the 4.06-MeV state has a single-particle nature. The angular distribution of scattered ^{23}F ions for the 4.06-MeV state was compared with DWBA calculations. The measured angular distribution was found to agree with the $\ell = 2$ transition. Therefore, the 4.061-MeV state was preliminarily assigned to have $J^\pi = 3/2^+$ or $5/2^+$.

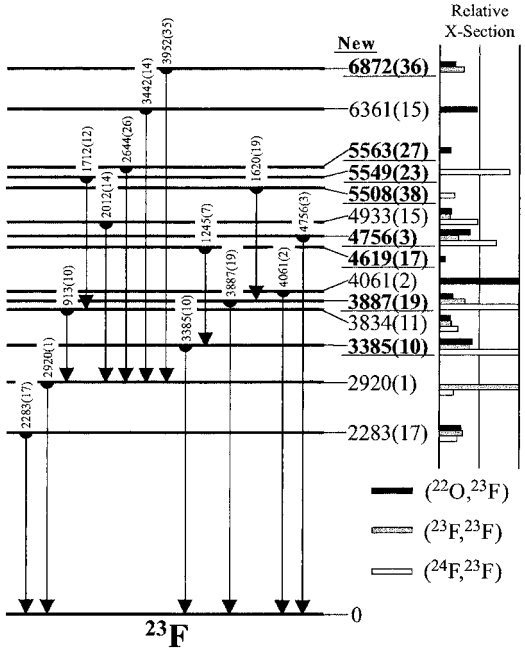

Fig. 1. Proposed level and γ-decay scheme in ^{23}F. Level energies with underlines show newly observed excited states in the present experiment. The bars on the right side of excitation energies show the relative cross sections to populate these states.

*1 Center for Nuclear Study, University of Tokyo
*2 Department of Physics, University of Tokyo
*3 Department of Physics, Kyoto University
*4 Department of Physics, Tohoku University
*5 Department of Physics, Rikkyo University
*6 Argonne National Laboratory, USA

References
1) A. Ozawa et al.: Phys. Rev. Lett. **84**, 5493 (2000).
2) H. Akiyoshi et al.: RIKEN Accel. Prog. Rep. **34**, 193 (2001).
3) M. Tamaki et al.: CNS-REP-59, 76 (2003).
4) S. Takeuchi et al.: RIKEN Accel. Prog. Rep. **36**, 148 (2003).

Bound excited states in ^{27}F†

Z. Elekes,[*1] Zs. Dombrádi,[*1] A. Saito,[*2] N. Aoi, H. Baba,[*2] K. Demichi,[*2] Zs. Fülöp,[*1] J. Gibelin,[*3] T. Gomi, H. Hasegawa,[*2] N. Imai,[*4] M. Ishihara, H. Iwasaki,[*4] S. Kanno,[*2] S. Kawai,[*2] T. Kishida, T. Kubo, K. Kurita,[*2] Y. Matsuyama,[*2] S. Michimasa, T. Minemura, T. Motobayashi, M. Notani,[*4] T. Ohnishi,[*4] H.J. Ong,[*4] S. Ota,[*5] A. Ozawa,[*6] H. K. Sakai,[*2] H. Sakurai,[*4] S. Shimoura,[*4] E. Takeshita,[*2] S. Takeuchi, M. Tamaki,[*4] Y. Togano,[*2] K. Yamada, Y. Yanagisawa, and K. Yoneda

[NUCLEAR STRUCTURE, Unstable nuclei, ^{27}F bound excited states]

It is known that the last bound oxygen neutron-rich nucleus is ^{24}O, while when adding one more proton to the oxygen isotopes even ^{31}F is bound.[1] A straightforward way of understanding this phenomena is to assume that the $\nu d_{3/2}$ neutron orbit is unbound in oxygen isotopes, while the additional proton in the fluors can make this state bound. This assumption is sufficient for explaining the existence of ^{27,29}F, but for understanding the bound nature of ^{31}F, additional assumptions are required. In terms of the shell model, a sudden lowering of multiparticle multihole states may be an explanation.[2] If this is valid, the traces of this lowering must also be apparent in the lighter F isotopes. In ^{27}F, the first excited state is expected to be unbound in the usd[3] approximation; while allowing for particle-hole excitations to the fp shell, a bound excited state in ^{27}F is expected. To identify such states, we studied the ^{27}F(p,p$'\gamma$) reaction.

In the present experiment, a 94 A·MeV energy primary beam of ^{40}Ar with 60 pnA intensity hit a ^{181}Ta production target of 0.5 cm thickness. The reaction products were momentum- and mass-analyzed by using the RIPS[4] fragment separator. The secondary beam included neutron-rich ^{24}O, ^{25,26,27}F, ^{27,28,29,30}Ne and ^{29,30,31,32}Na nuclei. The RIPS was operated at 6% momentum acceptance. The total intensity was approximately 100 cps having an average ^{27}F intensity of 4 cps. The identification of incident beam species was performed by means of energy loss, time-of-flight and magnetic rigidity ($B\rho$) analyses.[5] ^{27}F particles could be fully separated from other nuclei. The secondary beam was transmitted to a liquid hydrogen target[6] at the final focus of RIPS. The average areal density of the hydrogen was 210 mg/cm^2. The position of the incident particles was determined by two PPACs placed at F3 upstream of the target. The scattered particles were detected and identified by a PPAC and a silicon telescope, respectively. The telescope consisted of three layers with thicknesses of 0.5, 0.5 and 1 mm. The Z identification was performed by using of the TOF-energy-loss method. Based on ΔE-E information, isotope separation was carried out among the different fluorine isotopes. ^{27}F nuclei represented a distinct peak and they were well separated from other products that emerged due to neutron removal reactions in the liquid hydrogen target. The new DALI2 setup, including 146 NaI(Tl) scintillator detectors,[7] surrounded the target to detect the de-exciting γ rays emitted by the inelastically scattered nuclei. The ^{27}F spectrum showed two peaks at 504(15) and 777(19) keV. The experimental data can be compared with the predictions of the shell model calculations. According to the *sd* shell model,[9] a $5/2^+$ ground state is expected with the $1/2^+$ state as the first excited state at 1997 keV, which means that both levels of ^{27}F appear at energies which are too low. Extending the model space to the *sdpf* shells,[8] a lowering to 1.1 MeV of the $1/2^+$ excited state is calculated in ^{27}F. Although an excited state with a similar energy can be constructed by placing the two γ rays of ^{27}F on top of each other, on the basis of the expected decay properties, a state directly feeding the ground state is a more probable candidate for the spin 1/2 state. In spite of the ∼300 keV energy difference, the 777 keV transition may be a reasonable candidate for the decay of the $1/2^+$ state of the *sdpf* shell model prediction. The large energy deviation between at least one of the predicted and observed excited states suggests that these states intrude from a configuration outside of the model space, or that the predicted energies strongly deviate from the observed ones due to some additional correlations not included in the models.

References
1) H. Sakurai et al.: Phys. Lett. B **448**, 1147 (1990).
2) Y. Utsuno et al.: Phys. Rev. C **64**, 011301 (2001).
3) T. Otsuka et al.: Eur. Phys. J. A **15**, 151 (2002).
4) T. Kubo et al.: Nucl. Instrum. Methods Phys. Res. B **70**, 309 (1992).
5) H. Sakurai et al.: Phys. Lett. B **448**, 180 (1999).
6) H. Akiyoshi et al.: RIKEN Accel. Prog. Rep. **32**, 167 (1999).
7) H. Hasegawa et al.: RIKEN Accel. Prog. Rep. **35**, 169 (2002).
8) Y. Utsuno, et al.: Phys. Rev. C **60**, 054315 (1999).
9) B. A. Brown: http://www.nscl.msu.edu/ brown/ sde.htm

† Condensed from the article in Phys. Lett. B **599**, 17 (2004)

*1 Insitute of Nuclear Research, ATOMKI, Hungary
*2 Rikkyo University
*3 Institut de Physique Nucléaire, France
*4 University of Tokyo
*5 Kyoto University
*6 University of Tsukuba

In-beam gamma spectroscopy of ^{25}Ne *via* ^{26}Ne breakup

J. Gibelin,[*1,*2] N. Aoi, H. Baba,[*2] D. Beaumel,[*1] Y. Blumenfeld,[*1] Z. Elekes, N. Fukuda, T. Gomi, K. Ishikawa,[*3] Y. Kondo,[*3] T. Kubo, V. Lima,[*1] T. Motobayashi, T. Nakamura,[*3] A. Saito, Y. Satou,[*3] E. Takeshita,[*2] S. Takeuchi, T. Teranishi,[*4] Y. Togano,[*2] A. M. Vinodkumar[*3], Y. Yanagisawa, and K. Yoshida

[Gamma spectroscopy, ^{25}Ne]

The Coulomb excitation of ^{26}Ne has been studied in a recent experiment performed at RARF. We report here on the bound states of ^{25}Ne populated in the breakup of ^{26}Ne.

A ^{26}Ne beam was produced by the RIKEN Projectile fragment Separator (RIPS) after a 2-mm-thick Be production target was bombarded with a 95 A MeV ^{40}Ar beam. We obtained a secondary ^{26}Ne beam with an energy of 58 A MeV, an average rate of 10 kcps and a purity of 80%. The main contaminant was ^{29}Mg. The beam impiged on a 230 mg/cm^2 Pb target.

Particle identification was performed using a wall of silicon detectors placed 1.2 m downstream of the target. It consisted of two layers of 8 silicon strip detectors (SSD) and a layer of 3-mm-thick Si(Li) (8 pieces) from the charged-particle detector MUST.[1)] Energy calibration was performed using a ^{25}Ne beam of 0.1% momentum resolution at three different energies (50, 55 and 60 A MeV).

^{25}Ne nuclei were identified with the E-ΔE correlation. ΔE is the sum of energy loss in SSD and E the sum of ΔE and the residual energy in Si(Li). After selecting Ne isotopes, we project this 2D histogram onto a 1D histogram representing the mass number A of the Ne isotopes. From the range formula,[2)] we wrote A as $A = \lambda.\left(E^{\zeta+\eta\,\Delta E} - (E-\Delta E)^{\zeta+\eta\,\Delta E}\right)+\kappa$. We adjusted the four coefficients λ, κ, ζ, η to obtain independence from incident energy and a resolution of $\delta A/A \approx 10\%$, see result in Fig. 1.

In-beam gamma rays were detected using the 4π-gamma-detector DALI2,[3)] which consists of 152 NaI detectors, placed around the target. For 2 MeV γ-rays, its efficiency is typically 10% with an energy resolution of 7% (FWHM).

Finally, an hodoscope for neutron detection was placed 3.5 m downstream of the target. Its total intrinsic efficiency is $\sim$ 30% for neutrons at 50 A MeV.

The Doppler-corrected gamma distribution in coincidence with ^{25}Ne fragments detected by the silicon wall is plotted in Fig. 2 (left). The accuracy of the calibration is tested by comparing the energies of the first 2^+ state of: ^{26}Ne at 2018.2 $\pm$ .1 keV and ^{24}Ne at 1981.6 $\pm$ .4 keV. We obtained 2010 $\pm$ 60 keV and 1983 $\pm$ 75 keV, respectively.

The resolution of 125 keV (FWHM) is not sufficient to separate the states at 1613 and 1703 keV in ^{25}Ne. However, we confirm the state at 2050 $\pm$ 80 keV initially measured at 2030 $\pm$ 50 keV in the ^{26}Mg(^{7}Li,^{8}B)^{25}Ne transfer reaction[4)] but unseen in the ^{26}Mg(^{13}C,^{14}O)^{25}Ne transfer reaction[5)] and β decay from ^{25}F.[6)]

No contribution of the 2188 keV γ-ray from the 3891.2 keV state is observed.

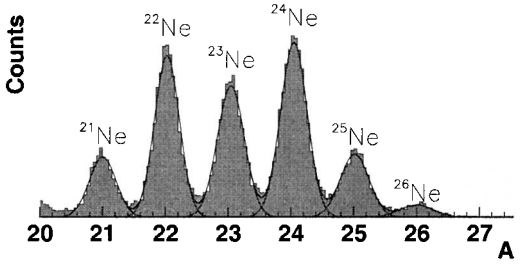

Fig. 1. Projected E-ΔE histogram onto A, neon isotope mass number, in coincidence with neutron events in neutron detectors.

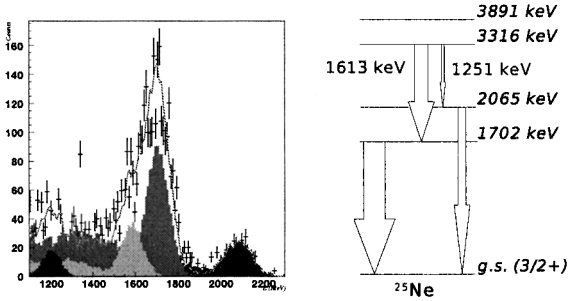

Fig. 2. **Left:** Doppler-corrected gamma ray spectrum in coincidence with ^{25}Ne fragments after exponential background substraction. Superimposed histograms: results of simulations using GEANT 3. **Right:** Known levels of ^{25}Ne.

*1 Institut de Physique Nucléaire, France
*2 Department of Physics, Rikkyo University
*3 Department of Physics, Tokyo Institute of Technology
*4 Center for Nuclear Study, University of Tokyo

References

1) Y. Blumenfeld et al.: Nucl. Instrum Methods Phys. Res. A **421**, 471 (1999).
2) F. S. Goulding: *Treatrise on Heavy-Ion Science*, 7, (Plenum, New York, 1985), p.285.
3) S. Takeuchi et al.: RIKEN Accel. Prog. Rep. **36**, 148 (2003).
4) R. H. Wilcox et al.: Phys. Rev. Lett. **30**, 866 (1973).
5) C. L. Woods et al. Nucl. Phys. A **437**, 454 (1985).
6) A. T. Reed et al.: Phys. Rev. C **60**, 024311 (1999).

First excited state in ^{23}Al with Coulomb dissociation method

T. Gomi, T. Motobayashi, Y. Ando,[*1] N. Aoi, H. Baba,[*2] K. Demichi,[*1] Z. Elekes,[*3] N. Fukuda, Zs. Fülöp,[*3] U. Futakami,[*1] H. Hasegawa,[*1] Y. Higurashi, K. Ieki,[*1] N. Imai,[*4] M. Ishihara, K. Ishikawa,[*5] N. Iwasa,[*6] H. Iwasaki,[*7] S. Kanno,[*1] Y. Kondo,[*5] T. Kubo, S. Kubono,[*2] M. Kunibu,[*1] K. Kurita,[*1] Y. U. Matsuyama,[*1] S. Michimasa, T. Minemura, M. Miura,[*5] H. Murakami,[*1] T. Nakamura,[*5] M. Notani,[*8] S. Ota,[*9] A. Saito,[*2] H. Sakurai,[*7] M. Serata,[*1] S. Shimoura,[*2] T. Sugimoto,[*5] E. Takeshita,[*1] S. Takeuchi, Y. Togano,[*1] K. Ue,[*7] K. Yamada, Y. Yanagisawa, K. Yoneda, and A. Yoshida

[NUCLEAR REACTIONS, ^{208}Pb(^{23}Al,^{22}Mg p)^{208}Pb, Coulomb dissociation]

The first excited state in ^{23}Al is important as a resonant state in the stellar ^{22}Mg(p,γ)^{23}Al reaction. This stellar reaction is relevant to nucleosynthesis in explosive hydrogen burning, which occurs in novae and X-ray bursts. The energy of the first excited state is known to be 0.528 MeV;[1)] however, there is no experimental data for the radiative width that has a direct effect on the astrophysical reaction rate.

A Coulomb dissociation method for radioactive nuclei has an attractive feature, that is, a high experimental efficiency. Using this method, one can determine the radiative width and extract the transition multipolarity from the distribution of the scattering angle of ^{23}Al.

The experiment was performed at the RIPS beam line. A secondary beam of ^{23}Al at 50 MeV/nucleon bombarded an 88 mg/cm^2 Pb target. The products of the breakup reaction, ^{22}Mg and a proton, were detected respectively using a silicon counter telescope and a plastic scintillator hodoscope located 50 cm and 3 m downstream of the target. The silicon telescope consisted of four layers of detectors of 0.5 mm thickness. Each layer consisted of eight detectors with an effective area of 50×50 cm^2. These eight detectors formed a 3×3 matrix with a hole in the center. The detectors in the first and second layers consisted of 5-mm-wide strip electrodes, which enabled position measurement in the horizontal and vertical directions. A stack of sixty-eight NaI(Tl) scintillators (DALI) was placed around the target to measure de-excitation γ-rays from ^{22}Mg in the excited state, the contribution of which should be subtracted to extract the Coulomb dissociation cross section of interest. The details of the experimental setup can be found in Ref. 2.

The relative energies of ^{22}Mg and the proton were determined from the invariant mass, which was extracted from the momenta of particles. We identified the breakup reaction through the first excited state in ^{23}Al, and extracted the angular distribution of the scattered ^{23}Al as shown in Fig. 1. The scattering angle was defined as the angle of the p-^{22}Mg center of mass with respect to the beam direction in the laboratory coordinates. For comparison, the theoretical angular distribution obtained by distorted-wave calculation when we assumed an E2 transition is shown. In this calculation, we used the optical potential parameters determined for the ^{17}O + ^{208}Pb reaction.[3)] The calculated distribution matches well with the experimental data. This is consistent with the theoretical prediction that the spin and parity of ^{23}Al are $5/2^+$ for the ground state and $1/2^+$ for the first excited state. Further analysis is now in progress.

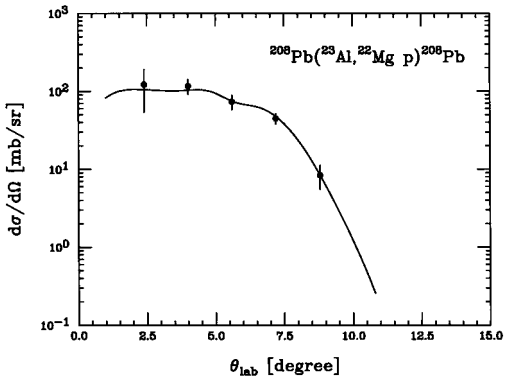

Fig. 1. Angular distribution of the scattered ^{23}Al. The filled circles show the experimental data. The solid curve represents the result of a distorted-wave calculation with the angular-momentum transfer $l = 2$.

References
1) J. A. Caggiano et al.: Phys. Rev. C **64**, 025802 (2001).
2) T. Gomi et al.: RIKEN Accel. Prog. Rep. **36**, 82 (2003).
3) J. Barrette et al.: Phys. Lett. B **209**, 182 (1988).

*1 Rikkyo University
*2 Center for Nuclear Study, University of Tokyo
*3 ATOMKI, Hungary
*4 High Energy Accelerator Research Organization (KEK)
*5 Tokyo Institute of Technology
*6 Tohoku University
*7 University of Tokyo
*8 Argonne National Laboratory, USA
*9 Kyoto University

Measurement of momentum distribution and reaction cross section for proton-rich nucleus ^{23}Al

Y. G. Ma,[*1] D. Q. Fang,[*1] X. Z. Cai,[*1] W. Q. Shen,[*1] Z. Y. Sun,[*2] Z. Z. Ren,[*3] W. Guo,[*1] Y. B. Wei,[*1] K. Wang,[*1] T. Z. Yan,[*1] C. W. Ma,[*1] J. G. Chen,[*1] J. H. Chen,[*1] G. L. Ma,[*1] Q. M. Su,[*1] W. D. Tian,[*1] C. Zhong,[*1] J. X. Zuo,[*1] M. Hosoi,[*4] T. Izumikawa,[*5] R. Kanungo, S. Nakajima,[*4] T. Ohnishi, T. Ohtsubo,[*5] A. Ozawa,[*6] T. Suda, K. Sugawara,[*4] T. Suzuki,[*4] A. Takisawa,[*5] K. Tanaka, T. Yamaguchi,[*4] and I. Tanihata[*7]

[Measured fragment momentum distribution, measured reaction cross section, proton halo structure]

Recently, the measurement of the momentum distribution has confirmed the existence of a proton halo in ^{26,27,28}P.[1] Reaction cross sections (σ_R) of $N = 10 \sim 15$ isotones were measured in Lanzhou on the HIRFL-RIBLL.[2] A remarkable enhancement of σ_R for ^{27}P and ^{23}Al is observed as compared with their neighboring nuclei. This result, together with the small proton separation energy, strongly suggests the existence of a proton halo in ^{27}P and ^{23}Al.[2,3] For ^{23}Al, it is interesting to investigate the possible cause for the appearance of the proton halo. In the ground state of ^{23}Al, the last proton may occupy the level $1d_{5/2}$ or $2s_{1/2}$ in the spherical shell model. When the last proton occupies $1d_{5/2}$, a large centrifugal barrier tends to suppress the formation of a halo. If there exist deformations in the nuclei, the situation may become more complex because both prolate and oblate deformations can appear. Here it is unclear which case the nucleus ^{23}Al will belong to. The experimental ground state spin and parity of this nucleus is not yet available. Thus a correct description of the proton halo in ^{23}Al may present a new challenge to the existing theoretical models. ^{23}Al is between the halo nuclei ^{17}Ne and ^{26,27}P. It may play an important role for the study of proton halos in $2s$-$1d$ shell nuclei. It bridges the gap between ^{17}Ne and ^{26,27}P. Since the momentum distribution and σ_R measurement are very useful methods for halo structure investigation, we have performed this experiment for further clarification of the halo structure in ^{23}Al.

The experiment was performed at the Riken Projectile Fragment Separator (RIPS). The primary beam of 135 A MeV ^{28}Si was used to produce the secondary beam of ^{23}Al. Before the carbon target (377 mg/cm^2) installed at F2, particle identification was carried out by using the $B\rho$-ΔE-TOF method. The TOF was determined from a delay-line PPAC at F1 and a plastic scintillator (0.5 mm thick) at F2. ΔE was measured using the newly constructed Ion Chamber ($200\phi \times 780$ mm). After the carbon target, the TOF-ΔE-E method was used for particle identification. Another plastic scintillator (1.5 mm thick) at F3 gave the stop signal of the TOF from F2 to F3. The Ion Chamber ($90\phi \times 650$ mm) was used to measure ΔE. E was measured by the $3''\phi \times 6$ cm NaI(Tl) detector with veto counters.[4]

The measurement of σ_R was carried out by using a transmission-type method. σ_R was determined by the ratios between the incident and outgoing particles without reaction from both target-in and target-out measurements. The longitudinal momentum distributions of fragments from the breakup reactions were determined from the TOF between the two plastic scintillators installed at F2 and F3. The position information from F1-PPAC was used to derive the incident momentum.[5] The particle identification for fragments ^{22}Mg at F3 is shown in Fig. 1. This spectrum was obtained after substructing fragments with different charges by the TOF and ΔE methods. The detailed analysis of momentum distribution and σ_R data are in progress.

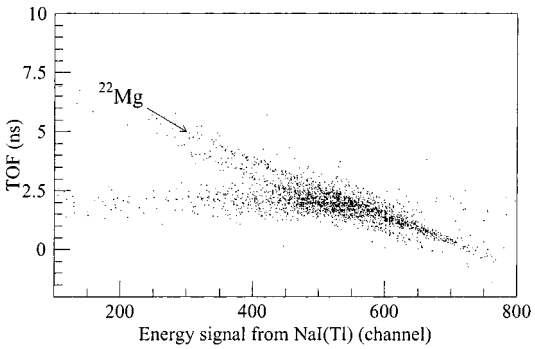

Fig. 1. Particle identification plot for fragments ^{22}Mg at F3 by using TOF from F2 to F3 and energy information from NaI(Tl).

*1 Shanghai Institute of Applied Physics, China
*2 Institute of Modern Physics, China
*3 Department of Physics, Nanjing University, China
*4 Department of Physics, Saitama University
*5 Department of Physics, Niigata University
*6 Department of Physics, University of Tsukuba
*7 Argonne National Laboratory, USA

References

1) A. Navin et al.: Phys. Rev. Lett. **81**, 5089 (1998).
2) D. Q. Fang et al.: Eur. Phys. J. A **12**, 335 (2001).
3) X. Z. Cai et al.: Phys. Rev. C **65**, 024610 (2002).
4) T. Suda et al.: RIKEN Accel. Prog. Rep. **35**, 171 (2002).
5) R. Kanungo et al.: Phys. Rev. Lett. **88**, 142502 (2002).

Proton resonant states in ^{23}Al using a radioactive beam of ^{22}Mg

J. J. He,[*1] S. Kubono,[*1] T. Teranishi,[*1,*2] M. Notani,[*1,*3] H. Baba,[*1] S. Nishimura, J. Y. Moon,[*4] M. Kurata-Nishimura, S. Michimasa,[*1] H. Iwasaki,[*5] Y. Yanagisawa, N. Hokoiwa,[*2] M. Kibe,[*2] J. H. Lee,[*4] S. Kato,[*6] Y. Gono,[*2] and C. S. Lee[*4]

[Proton Resonant State, Nuclear Astrophysics]

The stellar ^{22}Mg(p, γ)^{23}Al reaction is an important reaction in the Hot NeNa-cycle, because it influences the production of ^{22}Na in nova ejecta.[1–3] The higher energy proton resonant states ($E_x \geq 1.77$ MeV) also contribute to the X-ray burst and supernova events. In addition, the proton resonance information in ^{23}Al is very important from the nuclear-structure point of view. In the present study, we directly investigated proton resonant states in ^{23}Al by resonant elastic scattering of an ^{22}Mg RI beam on a thick hydrogen target.

The experiment was performed in the CNS radioactive ion beam separator (CRIB).[4,5] The experimental procedure and setup were described previously[6] in detail. This report will only show the recent results.

Figure 1 shows the experimental proton spectrum for ^{22}Mg+ p scattering at $\theta_{cm} = 180°$. The proton threshold in ^{23}Al is known to be 0.123 MeV.[2] Therefore, the excitation energy in ^{23}Al is calculated by $E_x = E_{cm} + 0.123$ MeV. It should be pointed out that the spectrum was obtained by assuming elastic scattering of ^{22}Mg+ p. Therefore, in a case of inelastic scattering, the E_{cm} energy in the figure must be corrected. The inelastic scattering contributions were evaluated by comparing the experimental scattering data at three different angles. From a detailed analysis of kinematics, it has been concluded that via proton emission, the excited state at 3.00 MeV decays to the ground state in ^{22}Mg, while the excited states at 3.14, 3.24 and 3.93 MeV decay to the first excited state in ^{22}Mg. A new level scheme of ^{23}Al is proposed in Fig. 2.

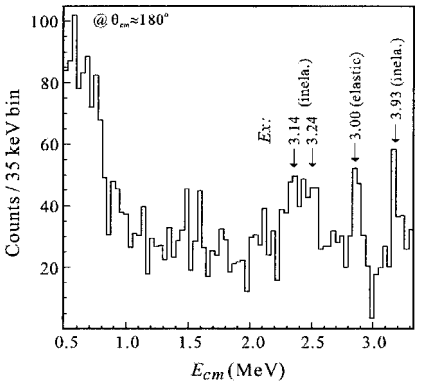

Fig. 1. Experimental proton spectrum for ^{22}Mg+p scattering (elastic and inelastic) at $\theta_{cm} = 180°$.

The experimental results were analyzed using the R-matrix code SAMMY-M6-BETA,[7] which enables multilevel R-matrix fits to neutron and charged-particle cross-section data using Bayes' equations. A preliminary R-matrix fit was performed for the resonant state at $E_x = 3.00$ MeV, and a d-wave fit reproduces the experimental data very well. Therefore, we assign this state with the spin-parity of $(3/2^+, 5/2^+)$. Three other excited states (at 3.14, 3.24 and 3.93 MeV) in the ^{23}Al nucleus decay to the first excited state in ^{22}Mg probably *via* d-wave proton emissions. The spin-parity of these three excited states is tentatively assigned as $J^\pi = (7/2^+)$. It is concluded that the excited states at 3.00 and 3.93 MeV are the newly observed excited states in ^{23}Al, and one of the excited states at 3.14 and 3.24 MeV could correspond to the previously observed state at 3.204 MeV.[2] Further analysis of the resonant properties of these states is in progress.

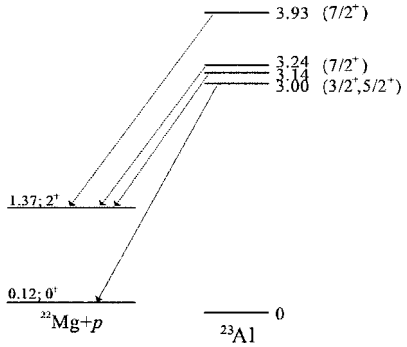

Fig. 2. Level scheme in ^{23}Al proposed by the present experiment.

*1 Center of Nuclear Study, University of Tokyo
*2 Department of Physics, Kyushu University
*3 Argonne National Laboratory, USA
*4 Department of Physics, Chung-Ang University, Korea
*5 Department of Physics, University of Tokyo
*6 Department of Physics, Yamagata University

References

1) I. Iyudin et al.: Astron. Astrophys. **300**, 422 (1995).
2) J. A. Caggiano et al.: Phys. Rev. C **64**, 025802 (2001).
3) M. Wiescher et al.: Astron. Astrophys. **160**, 56 (1986).
4) S. Kubono et al.: Eur. Phys. J. A **13**, 217 (2002).
5) T. Teranishi et al.: Phys. Lett. B **556**, 27 (2003).
6) J. J. He et al.: CNS Annu. Rep. **2003**, 34 (2004).
7) N. M. Larson: ORNL/TM-9179/R5, Oak Ridge National Laboratory (2000).

Study of proton resonant states in ^{22}Mg using radioactive beam of ^{21}Na

J. J. He,[*1] S. Kubono,[*1] T. Teranishi,[*1,*2] M. Notani,[*1,*3] H. Baba,[*1] S. Nishimura, J. Y. Moon,[*4] M. Nishimura, S. Michimasa,[*1] H. Iwasaki,[*5] Y. Yanagisawa, N. Hokoiwa,[*2] M. Kibe,[*2] J. H. Lee,[*4] S. Kato,[*6] Y. Gono, and C. S. Lee[*4]

[Proton Resonant State, Nuclear Astrophysics]

Observation of the characteristic ^{22}Na (E_γ = 1.275 MeV) activity with satellite γ telescopes such as COMPTEL only yielded the upper limit, which is substantially below the predicted abundances.[1–3] This discrepancy may be explained by the insufficiency of the theoretical models, but there are still considerable uncertainties with respect to the nuclear physics aspects. A better understanding of this issue requires accurate experimental data on the proton resonant states in ^{22}Mg. We have investigated the proton resonant states in ^{22}Mg using the resonant elastic scattering of a ^{21}Na RI beam on a thick hydrogen target.

The experiment was performed using the CNS radioactive-ion-beam separator (CRIB).[5,6] An 8.11 A MeV primary beam of ^{20}Ne^{8+} bombarded a water-cooled ^{3}He gas target (0.36 mg/cm^2), and a ^{21}Na beam was produced by the ^{3}He(^{20}Ne, ^{21}Na)X reaction. The secondary ^{21}Na beam was separated in CRIB and used in the experiment as described elsewhere[4] in detail.

A thick $(CH_2)_n$ foil (7.9 mg/cm^2) was used in the experiment. A carbon target (9.3 mg/cm^2) was also used in a separate run for evaluating the background contribution. At the secondary target position, the average intensity of ^{21}Na was 1.5×10^4 particles/s with a purity of 8.3%, and the mean energy was 4.00 MeV/nucleon with a width (FWHM) of 0.16 MeV/nucleon. The ^{21}Na particles were stopped in the target, and only the recoiled products were measured using the ΔE-E Si telescopes. The identification of beam particles and recoiled protons is also described in Ref. 4.

The center-of-mass energies (E_{cm}) were deduced using the elastic scattering kinematics of ^{21}Na + p and considering the energy loss of particles in the target. Contribution from the inelastic scattering ^{21}Na(p, p'γ(0.33))^{21}Na is not considered in the present report. At θ_{cm} = 180°, the typical energy resolutions (FWHM) in E_{cm} are approximately 20 keV at E_{cm} = 0.5 MeV and 45 keV at E_{cm} = 3.5 MeV. The systematic uncertainties in E_{cm} are approximately ±12 keV at 1.0 MeV and ±20 keV at 3.5 MeV.

Figure 1 shows the experimental center-of-mass energy spectrum for the ^{21}Na + p scattering at θ_{cm} = 170° ∼ 180°. After correction for the number of ^{21}Na beam particles and the stopping cross sections (dE/dx) of the beam particles in the target material, the differential cross sections (dσ/dΩ) of ^{21}Na+p elastic scattering can be deduced.[7] The proton threshold in ^{22}Mg is known to be 5.50 MeV.[8] Therefore, the excitation energy in ^{22}Mg can be calculated by E_x= E_{cm}+5.50 MeV. Some excitation energies are indicated on the figure. The arrows indicate possible excited states in ^{22}Mg which were observed previously.[8]

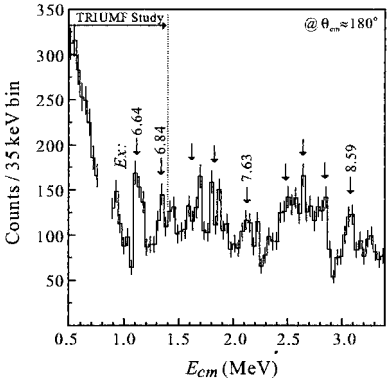

Fig. 1. Experimental center-of-mass energy spectrum for ^{21}Na+p elastic scattering at θ_{cm} = 180° (without dead-layer region).

The experimental results are being analyzed by the R-matrix code SAMMY-M6-BETA,[9] which enables multilevel R-matrix fits to neutron and charged-particle cross-sectional data using Bayes' equations. The resonance properties such as E_r, Γ_p and J^π can be deduced from the analysis.

*1 Center for Nuclear Study, University of Tokyo
*2 Department of Physics, Kyushu University
*3 Argonne National Laboratory, USA
*4 Department of Physics, Chung-Ang University, Korea
*5 Department of Physics, University of Tokyo
*6 Department of Physics, Yamagata University

References
1) I. Iyudin et al.: Astron. Astrophys. **300**, 422 (1995).
2) M. Wiescher and K. Langanke: Z. Phys. A **325**, 309 (2002).
3) C. Ruiz et al.: Phys. Rev. C **65**, 042801 (2002).
4) J. J. He et al.: CNS Annu. Rep. **2003**, 34 (2004).
5) S. Kubono et al.: Eur. Phys. J. A **13**, 217 (2002).
6) T. Teranishi et al.: Phys. Lett. B **556**, 27 (2003).
7) S. Kubono: Nucl. Phys. A **693**, 221 (2001).
8) A. A. Chen et al.: Phys. Rev. C **63**, 065807 (2002).
9) N. M. Larson: ORNL/TM-9179/R5, Oak Ridge National Laboratory, (2000).

Coulomb excitation of ^{20}Mg

N. Iwasa,[*1] S. Bishop, Z. Elekes,[*2] J. Gibelin,[*3,*4] M. Hosoi,[*5] K. Ieki,[*3] K. Ishikawa,[*6] H. Iwasaki,[*7] S. Kawai,[*3] S. Kubono,[*8] K. Kurita,[*3] M. Kurokawa, N. Matsui,[*6] T. Minemura,[*9] H. Morikawa,[*3] T. Nakamura,[*6] M. Niikura,[*8] M. Notani,[*8] S. Ota,[*8,*10] A. Saito,[*8] H. Sakurai,[*7] S. Shimoura,[*8] K. Sugawara,[*5] T. Sugimoto,[*6] H. Suzuki,[*7] T. Suzuki,[*5] E. Takeshita, S. Takeuchi, I. Tanihata[*11], T. Teranishi,[*12] Y. Togano,[*3] K. Yamada,[*3] K. Yamaguchi,[*3] Y. Yanagisawa, and T. Motobayashi

[NUCLEAR REACTIONS: ^{20}Mg+Pb, Coulomb excitation]

The Coulomb excitation and carbon inelastic scattering of ^{20}Mg were studied by reverse kinematics for deducing the excitation energy of the first 2^+ state $E(2_1^+)$ in ^{20}Mg and the reduced transition probability B(E2).

A radioactive ^{20}Mg beam was produced by the fragmentation of a ^{24}Mg beam at 135 A MeV in 1.35-mm-thick nickel target, and was isotopically separated using the RIKEN projectile-fragment separator (RIPS) in cooperation with the RF deflector.[1)] Particle identification of the secondary beam was performed event-by-event by the $B\rho$-TOF-ΔE method. Using the nickel target instead of a 6-mm-thick beryllium target, the number of contaminant particles was greatly reduced and the purity of ^{20}Mg was improved by a factor of 6. A further purity improvement of a factor of 3 was achieved using the RF deflector. Typical ^{20}Mg-beam intensity was 0.5 kcps, which was about 12% of the total secondary-beam intensity.

A lead target with a thickness of 226 mg/cm^2 placed at the final focus was bombarded by the ^{20}Mg beam. The beam energy at the center of the target was 58 A MeV. The beam spot size and incident angle were measured with two PPACs placed 1.50 and 1.20 m upstream of the target. Scattered ^{20}Mg was measured using nine silicon-counter telescopes arranged in a 3×3 matrix located 65 cm downstream of the target. Each telescope consisted of six layers of ion-implanted silicon detectors with an effective area of 50×50 mm^2 and a thickness of 500 μm. For the first and second layers, strip detectors with 5-mm strip pitch were used for measuring the scattering angle of ^{20}Mg in the vertical and horizontal directions, respectively. The scattered ^{20}Mg stopped at the fourth or fifth layers. Particle identification of the scattered ^{20}Mg was performed by the ΔE-E method. Deexcitation γ rays were detected with an array of 68 NaI(Tl) scintillators (DALI)[2)] surrounding the target. Each scintillator crystal has a rectangular shape with dimensions of $6 \times 6 \times 12$ cm^3. The energy resolution was measured to be 9% (FWHM) for 0.661 MeV γ rays from a ^{137}Cs source. Detection efficiency was measured for ^{137}Cs, ^{60}Co, and ^{22}Na calibrated sources, and the obtained results agreed with the results of Monte Carlo simulations using GEANT3 within the errors.

Figure 1 shows the Doppler-corrected γ-ray energy spectrum measured in coincidence when both beam particles and reaction products were identified as ^{20}Mg. Only the events with the γ detection multiplicity equal to 1 were employed to obtain the spectrum. The γ line at 1.61 ± 0.06 MeV was clearly observed for the first time. This γ line was also observed in the ^{20}Mg+C reaction. It was tentatively assigned to the transition of $2_1^+ \rightarrow 0_1^+$. The first 2^+ energy was determined to be 1.61 ± 0.06 MeV in the present experiment.

Further analysis of the data is in progress.

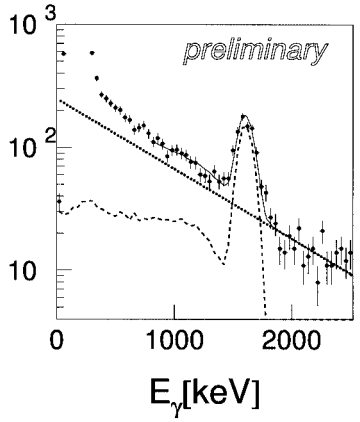

Fig. 1. Doppler-corrected γ energy spectrum measured in coincidence with ^{20}Mg. The solid curve represents the best fit by simulated line shape (dashed curve) and exponential background (dotted curve).

*1 Department of Physics, Tohoku University
*2 ATOMKI, Hungary
*3 Department of Physics, Rikkyo University
*4 Institut de Physique Nucléaire, France
*5 Department of Physics, Saitama University
*6 Department of Physics, Tokyo Institute of Technology
*7 Department of Physics, University of Tokyo
*8 Center for Nuclear Study, University of Tokyo
*9 High Energy Accelerator Research Organization (KEK)
*10 Department of Physics, Kyoto University
*11 Argonne National Laboratory, USA
*12 Department of Physics, Kyushu University

References

1) K. Yamada et al.: RIKEN Accel. Prog. Rep. **35**, 147 (2002).
2) T. Motobayashi et al.: Phys. Lett. B **346**, 9 (1995).

Elastic resonance scattering of ^{23}Mg+p

T. Teranishi,[*1] S. Kubono,[*2] J. J. He,[*2] M. Notani,[*2] T. Fukuchi,[*2] S. Shimoura,[*2] S. Nishimura, M. Nishimura, S. Michimasa, Y. Wakabayashi,[*1] N. Hokoiwa,[*1] Y. Gono,[*1] A. Odahara,[*3] H. Baba,[*4] J. Y. Moon,[*5] J. H. Lee,[*5] C. S. Lee,[*5] J. C. Kim,[*5] H. Ishiyama,[*6] Y. X. Watanabe,[*6] T. Hashimoto,[*7] T. Ishikawa,[*7] M. H. Tanaka,[*6] H. Miyatake,[*6] V. Guimarães,[*8] R. Lichtenthäler,[*8] H. Sato,[*9] T. Kawamura,[*9] and S. Kato[*9]

[unstable nuclei, nuclear astrophysics]

^{24}Al levels above the proton threshold of E_x = 1.871 MeV may play important roles in the astrophysical reaction of ^{23}Mg(p,γ)^{24}Al, which is one of the breakout paths from the Ne-Na cycle.[1] J^π values have not yet been precisely determined for many ^{24}Al levels. There are almost no experimental data of Γ for ^{24}Al resonance levels.[2] We performed an experiment on ^{23}Mg+p elastic resonance scattering, aiming at deducing new information on J^π and Γ for the ^{24}Al levels.

The ^{23}Mg+p experiment was performed in inverse kinematics with a secondary ^{23}Mg beam and a proton target. The ^{23}Mg beam was produced by the ^{24}Mg(d,t)^{23}Mg reaction in inverse kinematics. The primary ^{24}Mg beam was accelerated using an AVF cyclotron up to 7.5 MeV/nucleon with an intensity of 60 pnA. The deuterium gas target had a thickness of 0.33 mg/cm^2 and was confined in a cell by two Havar window foils of 2.2 μm. After the CRIB separator,[3,4] the ^{23}Mg secondary beam had an energy of 4.0 MeV/nucleon and an intensity of 3.2 $\times$ 10^4 particles/sec.

A thick-target technique[5,6] was used to measure the excitation function efficiently. A polyethylene sheet of 8.2 mg/cm^2 was set as a proton target. Due to the energy-loss process of the beam in the target, a wide center-of-mass energy ($E_{\rm CM}$) range was scanned without changing the beam energy before the target. While the beam particles were completely stopped in the target, most of the recoil protons went out from the target with small energy losses. The recoil protons were detected by the two sets of silicon detectors at laboratory angles of $\theta_{\rm LAB}$ = 0° and 17°. Each set consisted of ΔE and E layers with thicknesses of 75 and 1500 μm, respectively. Protons were identified with the information of ΔE, E, and timing. The $E_{\rm CM}$ and center-of-mass angle ($\theta_{\rm CM}$) were determined by measuring the energy and angle of protons.

Preliminary spectra of ^{23}Mg+p at $\theta_{\rm LAB}$ = 0° and 17° are shown in Fig. 1. The solid line represents the cross sections deduced from the Coulomb and hard-sphere scattering amplitudes. The deviation of the experimental cross sections from the solid line is seen in a region of $E_{\rm CM} > 1.6$ MeV both at 0° and 17°. These deviation patterns at 0° and 17° are similar to each other, indicating the presence of several resonance levels. The quantitative analysis of these patterns is in progress. Certain J^π values will be determined by R-matrix analysis. The Γ for these levels will also be evaluated for the first time.

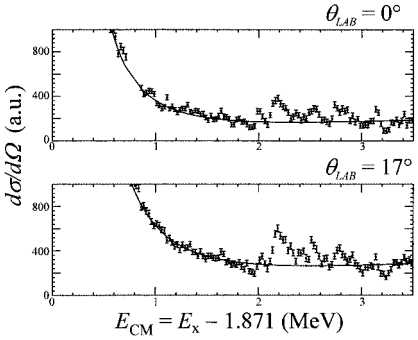

Fig. 1. Preliminary excitation functions for ^{23}Mg+p at $\theta_{\rm LAB}$ = 0° and 17°. The solid curves represent the cross sections deduced from the Coulomb and hard-sphere scattering amplitudes.

References
1) S. Kubono et al.: Nucl. Phys. A **588**, 521 (1995), and references therein.
2) P. M. Endt: Nucl. Phys. A **633**, 1 (1998).
3) T. Teranishi et al.: Nucl. Phys. A **718**, 207c (2003).
4) S. Kubono et al.: Eur. Phys. J. A **13**, 217 (2002).
5) K. P. Artemov et al.: Sov. J. Nucl. Phys. **52**, 408 (1990).
6) S. Kubono: Nucl. Phys. A **693**, 221 (2001), and references therein.

*1 Department of Physics, Kyushu University
*2 Center for Nuclear Study, University of Tokyo
*3 Nishinippon Institute of Technology
*4 Department of Physics, Rikkyo University
*5 Department of Physics, Chung-Ang University, Korea
*6 Institute of Particle and Nuclear Studies, High Energy Accelerator Research Organization (KEK)
*7 Department of Physics, Tokyo University of Science
*8 Department of Physics, University of São Paulo, Brazil
*9 Department of Physics, Yamagata University

Measurements of magnetic moments of ^{30}Al and ^{32}Al

D. Kameda,[*1] K. Asahi, H. Ueno, A. Yoshimi, G. Kijima,[*1] H. Miyoshi,[*1] K. Shimada,[*1] T. Haseyama, D. Nagae,[*1] G. Kato,[*1] S. Emori,[*1] M. Tsukui,[*1] H. Watanabe,[*2] Y. Kobayashi, and M. Ishihara

[NUCLEAR STRUCTURE, Neutron-rich isotopes, Spin polarization, β-NMR method]

We measured the magnetic moments of ^{30}Al($I^\pi = 3^+$, $T_{1/2} = 3.60$ s) and ^{32}Al($I^\pi = 1^+$, $T_{1/2} = 33$ ms) by the β-NMR method with the spin-polarized radioactive nuclear beams which were produced in the RIKEN Projectile-fragmentation Separator RIPS.

The average intensity for the primary beam of 95 A MeV ^{40}Ar^{17+} was 54 particle nA. The ^{30}Al fragments produced by use of a 0.13 g/cm^2 thick $^{\rm nat}$Nb target were separated from other nuclides in RIPS. In order to obtain spin-polarized fragments, selections were also made on the emission angle, $\theta = 1.3°$–$5.7°$, and the outgoing momentum, $p = 12.4$–12.7 GeV/c. In the case of ^{32}Al, a 0.37g/cm^2 thick $^{\rm nat}$Nb target was employed and a momentum region, $p = 12.2$–13.0 GeV/c, was selected. The purities of the secondary beams were 93% for ^{30}Al and 86% for ^{32}Al.

The spin-polarized fragments were implanted in a single crystal α-Al_2O_3 (corundum) to which a static magnetic field $B_0 \approx 0.5$ mT was applied. The crystal sample was mounted on a holder for which the angle between the c-axis of the crystal and the B_0 field was maintained at $(54 \pm 1)°$, the "magic angle" where the quadrupolar splitting for ^{30}Al and ^{32}Al in the crystal vanishes. The holder temperature was maintained below 100 K so that a sufficiently long spin-lattice relaxation time was achieved. β-rays from the stopper were detected with counter telescopes consisting of three plastic scintillators located above and below the stopper.

The obtained β-NMR spectra for ^{30}Al and ^{32}Al are shown in Figs. 1 and 2, respectively. The vertical bars show statistical errors only. The horizontal bars indicate the frequency regions over which the RF field was swept. The solid circles represent the centers of the individual frequency regions. In Fig. 1 (2), a significant asymmetry change is observed at 3831 (7446) kHz with the deviation from zero by 4.0 (4.4) σ. Thus, the resonance frequencies for ^{30}Al and ^{32}Al were obtained to be (3830.8 ± 20.7) kHz and (7445.7 ± 64.0) kHz, respectively. The errors indicated here are tentative ones which were determined from the width of the swept frequency. The magnetic moments obtained are $|\mu(^{30}\mathrm{Al})| = (3.012 \pm 0.021)\mu_{\rm N}$ and $|\mu(^{32}\mathrm{Al})| = (1.959 \pm 0.019)\mu_{\rm N}$, where $\mu_{\rm N}$ denotes the nuclear magneton. Fitting analyses for the spectra,

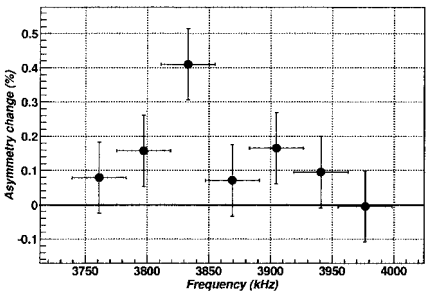

Fig. 1. β-NMR spectrum for ^{30}Al. The β-ray asymmetry change in the β-ray up/down ratio is plotted against the frequency regions over which the RF field was swept.

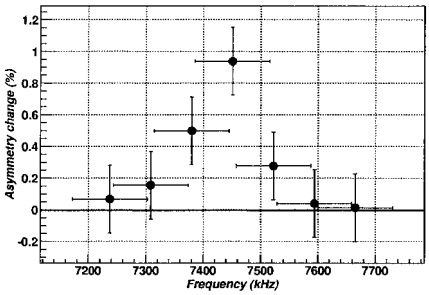

Fig. 2. β-NMR spectrum for ^{32}Al.

which are now in progress, would improve the accuracy of the tentative results.

A shell model calculation with the USD effective interaction[1)] for sd-shell model space is in good agreement with the present results within 6%. On the other hand, the magnetic moment of ^{30}Na, which has the same neutron number as ^{32}Al, was found[2)] to be 23% smaller than the shell model prediction using the USD interaction. The present result shows sharp contrast to the ^{30}Na result[2)] at the border of the "island of inversion"[3)] where the $N = 20$ shell gap vanishes.

References

1) B. H. Wildenthal: Prog. Part. Nucl. Phys. **11**, 5 (1984).
2) M. Keim et al.: Eur. Phys. J. A **8**, 31 (2000).
3) E. K. Warburton et al.: Phys. Rev. C **41**, 1147 (1990).

[*1] Department of Physics, Tokyo Institute of Technology
[*2] Department of Nuclear Physics, Australian National University, Australia

Production of spin-polarized ^{33}Si beam for g-factor measurement

G. Kijima,[*1] K. Asahi, H. Ueno, D. Kameda,[*1] H. Miyoshi,[*1] A. Yoshimi, H. Watanabe,[*2] T. Haseyama, M. Uchida,[*1] K. Shimada,[*1] D. Nagae,[*1] G. Kato,[*1] S. Emori,[*1] M. Tsukui,[*1] S. Oshima,[*1] M. Takemura,[*1] T. Arai,[*1] and Y. Kobayashi

[NUCLEAR STRUCTURE, ^{33}Si, β-NMR method, g-factor]

It was revealed in our earlier study that spin polarization is produced as a function of the emission angle $\theta_{\rm L}$ and momentum $p_{\rm F}$ of fragments.[1,2] Taking advantage of spin-polarized radioactive-isotope beams in the β-NMR method,[3] the nuclear moments of light unstable nuclei have been determined.[4] In this method, however, g-factor search could not be performed separately from the production of spin polarization in principle. For the g-factor measurement of ^{33}Si, the parameter sets of $\theta_{\rm L}$ and $p_{\rm F}$ have been investigated for the production of spin-polarized ^{33}Si fragments in a wide range of g factor values prior to the g-factor determination.

A beam of ^{33}Si was produced from the fragmentation of an ^{40}Ar projectile at an energy of 95 A MeV on a 385 mg/cm^2-thick Nb target. The ^{33}Si beam was isotope-separated using a projectile-fragment separator RIPS with its $\theta_{\rm L}$ and $p_{\rm F}$ selected accordingly. The ^{33}Si beam was then introduced to the final focus and implanted into a 0.3 mm-thick α-Al_2O_3 single-crystal stopper in a β-NMR apparatus located at the final focus of RIPS. The single crystal was cut so that the c-axis of the hexagonal crystal structure was oriented parallel to its surface. The stopper was kept under vacuum and oriented at the magic angle (54.7°) with respect to an external magnetic field B_0, where the quadrupolar level splitting of the magnetic sublevels vanishes. A B_0 of $\sim$ 700 mT was applied in order to preserve the spin polarization.[5] A radio-frequency oscillating field B_1 $\sim$ 1 mT was applied to the stopper in the direction perpendicular to B_0. The α-Al_2O_3 stopper was cooled to a temperature of $T < 100$ K, where a long spin-lattice relaxation time is expected[6] compared with its β-decay lifetime $\tau = 8.91$ sec. We employed β-NMR measurements[3] with the adiabatic fast passage (AFP) technique.[7] In this method, the resonance is observed through a change in the β-ray asymmetry AP, where A is the β-decay parameter and P the spin polarization.

An obtained NMR spectrum is shown in Fig. 1, where all data obtained with various parameter sets of $\theta_{\rm L}$ and $p_{\rm F}$ are plotted. The deviation of up/down ratios, which are divided by those obtained without B_1, from unity indicates the occurrence of the spin alteration by the AFP-NMR. Within a search region of the frequency range 3501.2 – 4598.0 kHz, we found that two data points showed substantialy high AP values of $\sim$ 0.2% with 3.3σ and 4.2σ statistics as depicted by hole circles in Fig. 1. The left (right) data point was obtained for the ^{33}Si fragments produced at $\theta_{\rm L} = 1.3°$ $-5.7°$ ($0.5°$ $-5.7°$) and $p_{\rm F} = 12.8 - 13.6(13.3 - 13.7)$ GeV/c. The two data points exhibit the same sign and similar magnitudes of polarization. These facts indicate that they have a resonance frequency in the common frequency region. These asymmetry changes, however, could not be confirmed in a precision measurement. Two factors can be considered to account for this imprecison:

i) A resonance frequency was not included in the two data points and ^{33}Si was not spin-polarized. Two data points accidentally deviated from unity with 3.3σ and 4.2σ statistics.
ii) It was found after the experiment that B_0 was not completely stabilized due to trouble in the current stabilization system of the power supply. The adiabatic conduction for the spin reversal was not met in the AFP-NMR.

The latter would be reasonable, but it could not be proved with only the present data. An experiment for the confirmation of the observed ^{33}Si spin polarization and its g-factor measurement are under preparation.

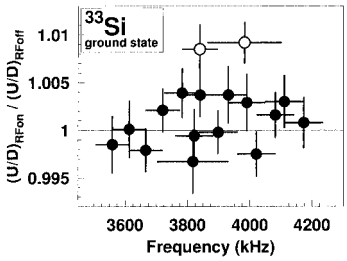

Fig. 1. Obtained β-NMR spectrum for ^{33}Si in various parameter sets of $\theta_{\rm L}$ and $p_{\rm F}$. The data points are accompanied by the statistical errors and widths of swept frequency in the AFP-NMR. For details, see the text.

References
1) K. Asahi et al.: Phys. Lett. B **251**, 488 (1990).
2) H. Okuno et al.: Phys. Lett. B **335**, 29 (1994).
3) K. Sugimoto et al.: J. Phys. Soc. Jpn. **21**, 213 (1966).
4) K. Asahi et al.: Nucl. Phys. A **704**, 88c (2002).
5) J. W. Hugg: Phys. Rev. C **30**, 1328 (1984).
6) R. L. Mieher: Phys. Rev. Lett. **4**, 57 (1960).
7) A. Abragam: *The Principle of Nuclear Magnetism* (Clarendon, Oxford, 1961).

*1 Department of Physics, Tokyo Institute of Technology
*2 Department of Nuclear Physics, Australian National University, Australia

Investigation of first excited state in ^{27}P for astrophysical interest

Y. Togano,[*1] T. Gomi,[*1] T. Motobayashi, Y. Ando,[*1] N. Aoi, H. Baba,[*1] K. Demichi,[*1] Z. Elekes, N. Fukuda, Zs. Fülöp,[*2] U. Futakami,[*1] H. Hasegawa,[*1] Y. Higurashi, K. Ieki,[*1] N. Imai, M. Ishihara, K. Ishikawa,[*3] N. Iwasa,[*4] H. Iwasaki,[*5] S. Kanno,[*1] Y. Kondo,[*3] T. Kubo, S. Kubono,[*5] M. Kunibu,[*1] K. Kurita,[*1] Y. U. Matsuyama,[*1] S. Michimasa,[*5] T. Minemura, M. Miura,[*3] H. Murakami,[*1] T. Nakamura,[*3] M. Notani,[*5] S. Ota,[*6] A. Saito,[*1] H. Sakurai,[*7] M. Serata,[*1] S. Shimoura,[*5] T. Sugimoto,[*3] E. Takeshita,[*1] S. Takeuchi, K. Ue,[*7] K. Yamada,[*1] Y. Yanagisawa, K. Yoneda,[*8]and A. Yoshida

[^{208}Pb(^{27}P,p^{26}Si)^{208}Pb, Coulomb dissociation, Nuclear astrophysics]

The Coulomb dissociation of ^{27}P has been studied to investigate the ^{26}Si(p,γ)^{27}P reaction. The gamma decay width of the first excited state in ^{27}P was extracted for astrophysical interest.

The ^{26}Si(p,γ)^{27}P reaction is suggested to be one of the important reactions in the rp process.[1] In particular, this reaction is on the path of the reaction flow of the rp process in X-ray bursts.[2] In extremely high temperature and density environments such as X-ray bursts and novae, resonances below 1 MeV play an important role. The resonance structure of ^{27}P was once studied via the ^{28}Si(^{7}Li,^{8}He)^{27}P reaction.[3] However, there is no experimental information of the strength on the resonances. Here, we report on the gamma decay width, which is relevant to the strength of the resonances, of the first excited state in ^{27}P.

An experiment was performed at the RIPS beam line in the RIKEN Accelerator Research Facility. The secondary beam of ^{27}P at 57 MeV/nucleon was produced by the fragmentation of the 115-AMeV ^{36}Ar beam on a ^{9}Be target. The ^{27}P beam bombarded a 125 mg/cm^3 thick natural Pb target. The details of the experimental setup are described in Ref. 4.

Supposing the spin and parity of the first excited state in ^{27}P is $3/2^+$ from the level scheme of the mirror nucleus ^{27}Mg, the transition between the first excited state and the ground state ($1/2^+$) is induced by M1/E2 multipolarities. Since the E2 component was strongly enhanced in the Coulomb dissociation,[5] the experimental cross section may be exhausted via the E2 excitation. To extract the total gamma decay width, the M1 component was estimated using the mixing ratio E2/M1 = 0.048 from the mirror transition in ^{27}Mg.[6] The gamma decay width of the first excited state was determined preliminarily to be 0.36 meV with an uncertainty of 15%. This value is ten times smaller than that estimated on the basis of a shell model calculation by Caggiano *et al.*[3] This indicates that the ^{26}Si(p,γ)^{27}P reaction does not contribute significantly to the amount of ^{26}Al in novae.[3]

The gamma decay width depends on the mixing ratio. The relationship between the gamma decay width and E2/M1 mixing ratio is presented in Fig. 1. The solid and dashed lines represent our result and margin of experimental error, respectively. The closed circle represents the value obtained with the E2/M1 mixing ratio of the first excited state in ^{27}Mg corresponding to the result mentioned above (0.36 meV). The diamond indicates the value obtained with the E2/M1 mixing ratio calculated using a simple single-particle model.[7] The dot-dashed line denotes the gamma decay width calculated by the shell model.[3] The upper and lower limits of the gamma decay width are determined to be 29 meV and 1.6×10^{-2} meV, assuming the decay occurs with pure M1 and E2 multipolarities, respectively. Further analysis is now in progress.

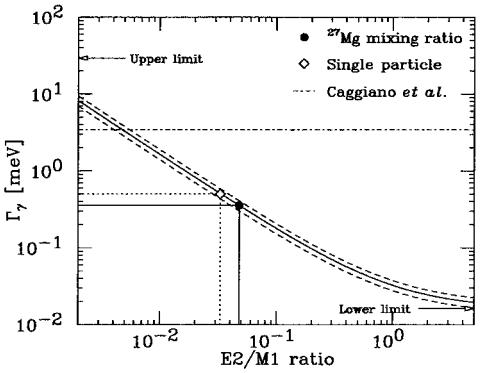

Fig. 1. Relationship between gamma decay width and E2/M1 mixing ratio.

*1 Rikkyo University
*2 Institute of Nuclear Research, ATOMKI, Hungary
*3 Tokyo Institute of Technology
*4 Tohoku University
*5 Center for Nuclear Study, University of Tokyo
*6 Kyoto University
*7 University of Tokyo
*8 National Superconducting Cyclotron Laboratory, Michigan State University, USA

References

1) H. Herndl et al.: Phys. Rev. C **52**, 1078 (1995).
2) H. Schatz et al.: Nucl. Phys. A **718**, 247c (2003).
3) J. A. Caggiano et al.: Phys. Rev. C **64**, 025802 (2001).
4) Y. Togano et al.: RIKEN Accel. Prog. Rep. **37**, 69 (2004).
5) T. Motobayashi et al.: Phys. Rev. Lett. **73**, 2680 (1994).
6) M. J. A. Voigt et al.: Nucl. Phys. A **186**, 365 (1972).
7) A. Bohr and B. R. Mottelson: *Nuclear Structure*, Vol.1 (World Scientific, Singapore, 1988).

Study of astrophysically important resonance states in ^{26}Si and ^{27}P using radioactive ion beams

J. Y. Moon,[*1] C.-S. Lee,[*1] J.-H. Lee,[*1] C. C. Yun,[*1] J. C. Kim,[*2] M. Youn,[*2] S. Kubono,[*3] T. Teranishi,[*4] J. J. He,[*3] M. Notani,[*3] S. Nishimura, M. Kurata-Nishimura, S. Kato,[*5] V. Guimarães,[*6] and R. F. Lichitenthaler[*6]

[Nucleoastrophysics, radioactive ion beam, ^{26}Si, ^{27}P]

As described in our previous report,[1)] spectroscopic properties, such as excitation energy, decay width and spin-parity of levels above the proton threshold in ^{26}Si and ^{27}P, are very crucial to determining the production rate of ^{26}Al (g.s.) in stellar sites under the explosive hydrogen burning stage, which is a source of cosmic gamma-rays of 1.809 MeV. We performed an experiment on ^{25}Al + p and ^{26}Si + p elastic scatterings to obtain such information. In this report, preliminary results of R-matrix analysis are presented.

This experiment has been carried out with the radioactive beams obtained using the CNS radioactive ion beam separator (CRIB)[2,3)] and thick target method.[4,5)] A ^{24}Mg^{8+} primary beam accelerated by the RIKEN AVF cyclotron (K = 70) was used to bombard a ^{3}He gas target at 7.434 A MeV. The thickness of the ^{3}He gas target was 0.32 mg/cm^2. With ^{3}He(^{24}Mg, np)^{25}Al and ^{3}He(^{24}Mg, n)^{26}Si, two kinds of radioactive beam of ^{25}Al and ^{26}Si were produced and used for measuring ^{1}H(^{25}Al, p)^{25}Al and ^{1}H(^{26}Si, p)^{26}Si elastic scatterings, respectively. More details of the experimental setup were described in Ref. 1.

Using a $(CH_2)_n$ target whose thickness of 8.13 mg/cm^2 was sufficient to stop the secondary beams, namely, ^{25}Al of 3.4407 A MeV and ^{26}Si of 3.9575 A MeV, we could scan up to E_x = 8.8243 MeV for ^{26}Si and E_x = 4.7109 MeV for ^{27}P above the proton threshold. The energy resolutions of the 0°- and 17°-detection systems[1)] that were used to detect the recoiled protons were 36 keV and 53 keV (FWHM) in the center of mass (C.M.), respectively. Figure 1 shows the proton excitation function for each case, obtained at 0° corresponding to 180° in the C.M. frame where the interference patterns of the potential and resonance scatterings are significant. The energy region above $E_{C.M.}$ = 2.8 MeV was omitted in the analysis, because there existed a large proton contaminant from the elastic scattering due to hydrogen atoms in the mylar layers of a PPAC in the F2 chamber. In the ^{26}Si + p elastic scattering, R-matrix analysis is performed using the code SAMMY M6-beta[6)] to determine the energy, decay width and spin-parity of resonance states. The energy and decay width are used as varied parameters. A small bump (a) at approximately $E_{C.M.}$ = 2.2 MeV is assumed to be due to two resonance states from the comparison of our results with those of the shell model and with the level structure of mirror nucleus ^{27}Mg (Table 1). The shell model calculation was

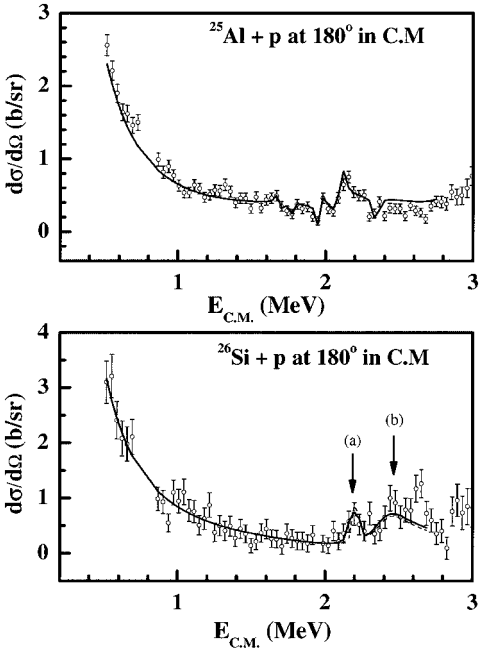

Fig. 1. Elastic scattering spectra obtained from this work. In the lower figure, the solid line represents the case with a state at E_x = 3.073 MeV in R-matrix analysis and the dashed line for the case without it. See text for details.

Table 1. Resonance states in ^{27}P determined in this work (tentatively) and their comparison with those determined using ^{27}Mg and shell model calculations.

J^π	^{27}Mg	Shell model	This work[§]
7/2+	3.109	3.150	3.073(202)
3/2+	3.109	3.163	3.109(66)
3/2−	3.560		3.323(33)

[§] Excitation energy in MeV and fitting uncertainty shown in this work.

[*1] Department of Physics, Chung-Ang University, Korea
[*2] Department of Physics, Seoul National University, Korea
[*3] Center for Nuclear Study, Graduate School of Science, University of Tokyo
[*4] Department of Physics, Kyushu University
[*5] Department of Physics, Yamagata University
[*6] Instituto de Física, Universidade de São Paulo, Brazil

carried out in the sd model space with the Wildenthal (USD) Hamiltonian[7] using the code Oxbash.[8] From the R-matrix fitting based on this assumption and preliminary analysis, the two states of $E_x = 3.073\,\mathrm{MeV}$ and $E_x = 3.109\,\mathrm{MeV}$ in ^{27}P whose excitation energy is $E_x = E_{C.M.} + 0.897\,\mathrm{MeV}$ are assigned with spin-parities of $J^\pi = 7/2+$ and $3/2+$, respectively, and the state of $E_x = 3.323\,\mathrm{MeV}$ assigned with $J^\pi = 3/2-$ contributed to the bump (b). It should be noted that the reduced χ^2 (χ^2 divided by the number of data) increases from 0.88 to 1.030 when only one resonance is assumed at approximately $E_x = 3.1\,\mathrm{MeV}$. In the case of ^{25}Al + p elastic scattering, interference patterns are also found. Detailed analysis is being performed to clarify the above resonance states.

References

1) J. Y. Moon et al.: RIKEN Accel. Prog. Rep. **37**, 65 (2004).
2) T. Teranishi et al.: Phys. Lett. B **556**, 27 (2003).
3) Y. Yanagisawa et al.: Nucl. Instrum. Methods Phys. Res. A **539**, 74 (2005).
4) K. P. Artemov et al.: Sov. J. Nucl. Phys. **52**, 408 (1990).
5) S. Kubono: Nucl. Phys. A **693**, 221 (2001), and references therein.
6) N. M. Larson: ORNL/TM-9179/R5, Oak Ridge National Laboratory (2000).
7) B. H. Wildenthal: Prog. Part. Nucl. Phys. **11**, 5 (1984).
8) B. A. Brown et al.: MSU-NSCL report number 1289 (1988).

Systematic behavior of B(E2) for $T_z = \pm 1$ even-even nuclides studied by Coulomb excitation of ^{46}Cr, ^{50}Fe, and ^{54}Ni

K. Yamada, T. Motobayashi, N. Aoi, H. Baba,[*1] K. Demichi,[*2] Z. Elekes,[*3] J. Gibelin,[*4] T. Gomi, H. Hasegawa,[*2] N. Imai,[*5] H. Iwasaki,[*6] S. Kanno,[*2] T. Kubo, K. Kurita,[*2] Y. U. Matsuyama,[*2] S. Michimasa, T. Minemura,[*5] M. Notani,[*7] T. K. Onishi,[*6] H. J. Ong,[*6] S. Ota,[*8] A. Ozawa,[*9] A. Saito,[*1] H. Sakurai,[*6] S. Shimoura,[*1] E. Takeshita,[*2] S. Takeuchi, M. Tamaki,[*1] Y. Togano,[*2] Y. Yanagisawa, K. Yoneda,[*10] and I. Tanihata[*7]

[Nuclear structure, B(E2), Coulomb excitation, Matrix element]

The proton-rich ^{46}Cr, ^{50}Fe, and ^{54}Ni nuclei were studied by intermediate-energy Coulomb excitation in order to investigate the evolution of the nuclear collectivity at the beginning of the *pf* shell as reported previously.[1] The $B(\mathrm{E2}; 0^+_{\mathrm{g.s.}} \rightarrow 2^+_1)$ values of ^{46}Cr, ^{50}Fe, and ^{54}Ni were extracted from the Coulomb excitation cross sections with the help of DWBA analysis to be 929 ± 199 e^{2}fm^4, 1359 ± 261 e^{2}fm^4, and 590 ± 168 e^{2}fm^4, respectively. The excitation energy $E(2^+)$ was also determined for the first 2^+ excited state in ^{54}Ni to be 1374 ± 30 keV. The complete systematics of B(E2) and $E(2^+)$ for the $T_z = \pm 1$ even-even nuclides up to $Z = 28$ have been established by the present study.

The proton and neutron matrix elements, $|M_{\mathrm{p}}|$ and $|M_{\mathrm{n}}|$, were separately extracted from the B(E2) values by combining the ones known for their mirror nuclei,[2] for which we used the Bernstein's mirror nucleus method,[3] which is based on the equality between M_{p} and M_{n} in the mirror pair under the assumption of isospin symmetry. The resultant $|M_{\mathrm{p}}|$ values are respectively 4.4 ± 0.5 W.u., 5.0 ± 0.5 W.u., and 3.1 ± 0.4 W.u. for ^{46}Cr, ^{50}Fe, and ^{54}Ni, while the $|M_{\mathrm{n}}|$ values were extracted to be 4.4 ± 0.1 W.u., 4.4 ± 0.1 W.u., and 3.2 ± 0.1 W.u., respectively.

The double ratio $(|M_{\mathrm{n}}|/|M_{\mathrm{p}}|)/(N/Z)$ is a measure of the collectivity of the 2^+_1 states. In even-even nuclei in which both proton and neutron shells are open, the ratio is generally close to unity, while nuclei with closed shells systematically deviate from unity. Figure 1 shows the ratios for all $T_z = -1$ even-even nuclides in the Z = 10–28 region. The results obtained for both ^{46}Cr and ^{50}Fe are close to unity and are consistent with the picture of a collective nucleus. The ratio for ^{54}Ni, which is close to unity, indicates the weakness of the $Z = 28$ shell closure.

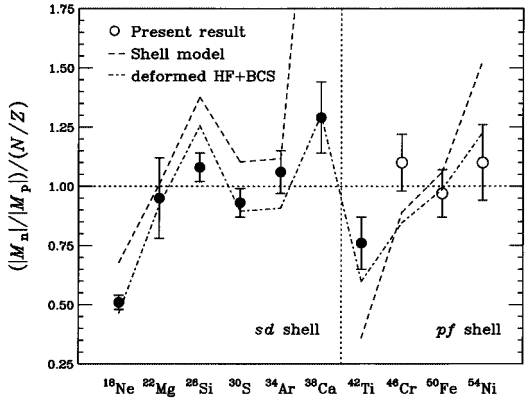

Fig. 1. The ratio of $|M_{\mathrm{n}}|$ and $|M_{\mathrm{p}}|$ normalized by N/Z for $T_z = -1$ even-even nuclides in the Z = 10–28 region.

In Fig. 1, the ratios are compared with theoretical predictions from the conventional shell-model calculations using the USD interaction for the *sd*-shell region[4] and the GXPF1 interaction for the *pf*-shell region[5] (dashed lines) and from the deformed Hartree-Fock + BCS calculation[6] using the SIII interaction (dot-dashed line). The experimental results exhibit smaller extents of single-particle natures compared with the shell-model predictions in the vicinity of the shell closures 20 and 28, suggesting the importance of collective aspects which should be taken into account. On the other hand, the behavior of the experimental data is well reproduced by the deformed HF + BCS prediction. However, this prediction considerably underestimates the amplitude of the matrix elements: for example, the predicted $|M_{\mathrm{p}}|$ values are smaller by a factor of approximately 20 for ^{38}Ca and ^{42}Ti. The present result requires a more elaborate treatment of the nuclear collectivity in this mass region.

*1 Center for Nuclear Study, University of Tokyo
*2 Department of Physics, Rikkyo University
*3 Institute of Nuclear Research of the Hungarian Academy of Sciences, Hungary
*4 Institut de Physique Nucléare, France
*5 High Energy Accelerator Research Organization
*6 Department of Physics, University of Tokyo
*7 Argonne National Laboratory, USA
*8 Department of Physics, Kyoto University
*9 Department of Physics, University of Tsukuba
*10 National Superconducting Cyclotron Laboratory, Michigan State University, USA

References

1) K. Yamada et al.: RIKEN Accel. Prog. Rep. **37**, 76 (2004).
2) S. Raman et al.: At. Data Nucl. Data Tables **78**, 1 (2001).
3) A. M. Bernstein et al.: Phys. Rev. Lett. **42**, 425 (1979).
4) B. A. Brown et al.: Phys. Rev. C **26**, 2247 (1982).
5) M. Honma et al.: Private communication.
6) H. Sagawa et al.: Private communication.

Proton inelastic scattering on ^{74}Ni

S. Kanno,[*1] N. Aoi, W. F. Mueller,[*2] H. Sakurai,[*3] D. Bazin,[*2] M. D. Bowen,[*2] C. M. Campbell,[*2] J. M. Cook,[*2] D.-C. Dinca,[*2] A. Gade,[*2] T. Glasmacher,[*2] H. Iwasaki,[*3] T. Kubo, T. Motobayashi, T. Nakamura,[*4] H. Olliver,[*2] H. Suzuki,[*3] S. Takeuchi, J. R. Terry,[*2] and K. Yoneda[*2]

[NUCLEAR STRUCTURE, ^{74}Ni(p,p'γ), 104 MeV/u, Inelastic Scattering, Unstable nuclei]

Proton inelastic scattering on the very neutron-rich nucleus ^{74}Ni was studied using a liquid hydrogen target (LH_2[1)]) and a radioactive beam of ^{74}Ni at 104 MeV/nucleon.

Among Ni isotopes, the excitation energies of the first 2^+ states ($E_x(2^+)$'s) are known for the nuclei lighter than ^{72}Ni. They are higher than those in the neighboring nuclei, reflecting the magicity at Z=28. In the present experiment, $E_x(2^+)$ and the deformation parameter of a more neutron-rich Ni isotope ^{74}Ni is measured by proton inelastic scattering aiming at exploring the evolution of the magicity at Z=28 in a very neutron-rich region.

The proton inelastic scattering with a LH_2 target has the highest sensitivity to the present experiment. One of the advantages is the large number of nuclei in the target material. The other is the low background due to the absence of γ rays originating from the target nuclei. These advantages enable us to perform the experiment with an extremely weak secondary beam of ^{74}Ni.

The experiment was performed at the National Superconducting Cyclotron Laboratory (NSCL) at Michigan State University. The ^{74}Ni nucleus was produced by the projectile fragmentation of a ^{86}Kr primary beam (140 MeV/nucleon, 20 pnA) on a ^{9}Be production target (188 mg/cm^2). The fragments were collected and analyzed with the A1900 fragment separator[2)] and transmitted to the S800 spectrograph.[3)]

The ^{74}Ni intensity was typically 0.5 particle/sec with a purity of 0.73%. The other nuclei in the secondary beam and their intensities were as follows : ^{73}Ni (0.3), ^{75}Cu (7.1), ^{76}Cu (3.5), ^{77}Zn (16.7), ^{78}Zn (9.1), ^{79}Ga (12.7), ^{80}Ga (5.7), ^{81}Ge (0.1) and ^{82}Ge (0.5), where the values in the parentheses are the intensities in the units of count/sec. The LH_2 target was placed at the target position of S800 which was tuned to the focusing mode. The LH_2 target system was previously developed at Kyushu-Rikkyo-RIKEN. We used aluminum for the cell window for instead of haver foil to increase the number of fully stripped particles that reach the focal plane of S800.

The plastic scintillator at the extended focal plane of A1900 is used for the time-of-flight (TOF) start signal. At the object point of S800, PIN Si detectors for determinig the energy-loss (ΔE) of the secondary beam were located, and at the focal plane, a pair of Cathode Readout Drift Chambers (CRDC's) for determining Bρ, an ion-chamber with 140 Torr P10 gas for determining ΔE, and three plastic scintillators for determining TOF-stop signal were placed in vacuum.[4)] The high resolving power of these detectors enable us to distinguish the isotopes of $A \sim 74$.

The particle identification of the secondary beam was carried out event-by-event using the TOF and ΔE of PIN Si. A flight path length of 60 m is sufficient to distinguish ^{74}Ni nuclei from other beam fragments.

Scattered ^{74}Ni nuclei were detected by the ion-chamber and CRDCs. We obtained the atomic number (Z) of the scattered particles from TOF and ΔE of the ion-chamber. Using this Z-gate, we obtained the mass number (A) from TOF and Bρ.

An array of 21 NaI(Tl) scintillators (the APEX array[5)]) surrounded the target for detecting γ rays. Each scintillator has a length of 55 cm with a trapezoidal cross section and a height of 6 cm and a width of 5 or 7 cm. Three of the original 24 NaI(Tl) detectors were removed to allow the insertion of the LH_2 target from the top. Two photomultiplier tubes were optically coupled to each scintillator. Both the interaction point X_γ and energy E_γ can be deduced from the output signals from the pair of photomultiplier tubes. Since X_γ is used for event-by-event Doppler-shift correction of the γ rays from the excited ^{74}Ni moving with $v/c \approx 0.44$, the position, energy and efficiency calibrations of each NaI(Tl) scintillator were made using standard ^{22}Na, ^{60}Co and ^{137}Cs sources.

Excitation to the 2^+ state was identified by measuring the de-excitation γ rays in coincidence with the incoming and scattered ^{74}Ni ions. Further analysis are now in progress.

*1 Rikkyo University
*2 Michigan State University, USA
*3 University of Tokyo
*4 Tokyo Institute of Technology

References

1) H. Akiyoshi et al.: RIKEN Accel. Prog. Rep. **32**, 167 (1999).
2) D. J. Morrissey et al.: Nucl. Instrum. Methods Phys. Res. B **204**, 90 (2003).
3) D. Bazin et al.: Nucl. Instrum. Methods Phys. Res. B **204**, 629 (2003).
4) J. Yurcon et al.: Nucl. Instrum. Methods Phys. Res. A **422**, 291 (1999).
5) B. C. Perry et al.: Nucl. Instrum. Methods Phys. Res. A **505**, 85 (2003).

Excitation function measurement of neutron-rich Ti isotope by secondary fusion reaction

M. Niikura,[*1] E. Ideguchi,[*1] T. Fukuchi,[*1] H. Baba,[*1] N. Hokoiwa,[*2] C. Ishida,[*3] H. Iwasaki,[*4] T. Koike,[*5] T. Komatsubara,[*6] T. Kubo, M. Kurokawa, S. Michimasa, K. Miyakawa,[*6] K. Morimoto, T. Ohnishi, S. Ota,[*7] A. Ozawa,[*6] S. Shimoura,[*1] T. Suda, M. Tamaki,[*1] I. Tanihata,[*8] Y. Wakabayashi,[*2] and K. Yoshida

[NUCLEAR REACTION, ^{9}Be(^{46}Ar, xn)$^{55-x}$Ti, Unstable nuclei, Fusion reaction]

We have studied high-spin states of ^{50}Ti in search for a well-deformed rotational band due to the presence of deformed shell gaps[1] in $N = 28$ and $Z = 22$. Excited states in ^{50}Ti were previously studied using the ^{48}Ca $(\alpha, 2n)$ ^{50}Ti reaction[2]; however, no rotational bands were observed. Since deformed collective states may approach yrast in higher excited states, it is necessary to populate spin states higher than those in a previous study. This can be achieved by heavy-ion fusion reactions, but the lack of beam and target combinations with stable isotopes has prevented experimental studies thus far. The usage of neutron-rich radioactive (RI) beams can relax this experimental constraint and enables the investigation of high-spin states in ^{50}Ti populated in the secondary fusion reaction ^{9}Be $\left(^{46}\mathrm{Ar}, x\mathrm{n}\right)$ $^{50-x}$Ti. We have measured the excitation function of Ti isotopes produced by this reaction, in order to determine the optimum beam energy for producing high-spin states in ^{50}Ti at a maximum cross section.

The experiment was performed at the RIPS facility in RIKEN.[3] A low-energy ^{46}Ar beam was produced by fragmentation using a ^{48}Ca primary beam, and its energy was reduced to ∼6 MeV/nucleon using degraders placed at the first (F1) and second (F2) focal planes. The secondary beam was transported to the final (F3) focal plane, where a 10-μm thick ^{9}Be target was placed for the fusion reaction. The incident beam energy was measured event-by-event by TOF deduced from the timing information of a plastic scintillator placed at F2 and PPAC's placed at F3. Due to the energy struggling in the degraders and the beam-line detectors, the energy-broadened beam of 2–7 MeV/nucleon at the center of the target was obtained.

Gamma rays from the excited states of the reaction products $^{49\text{-}52}$Ti were detected by the GRAPE system.[4] We have successfully observed high-spin states in ^{50}Ti[3] and confirmed the known γ rays de-excited from the first excited states: 1539, 1549, 1432, and 1051 keV for $^{49\text{-}52}$Ti, respectively.[2,5–7] Based on the assumption that all γ-ray cascades decay through these transitions, their relative γ-ray yields normalized by beam intensities are proportional to the production cross section of each isotope. Figure 1 (b) shows the relative γ-ray yields gated using each incident beam energy.

In Fig. 1 (a), the results of a statistical model calculation using the CASCADE code[8] are shown. The calculated production cross section compares well with the peak beam energy and the trend of the measured excitation function for the ^{9}Be $\left(^{46}\mathrm{Ar}, 5\mathrm{n}\right)$ ^{50}Ti reaction.

By taking into account the angular momentum in the reaction as well as the excitation function, the optimum energy for producing the high-spin states in ^{50}Ti was estimated to be ∼4.5 MeV/nucleon. Further analysis is now in progress.

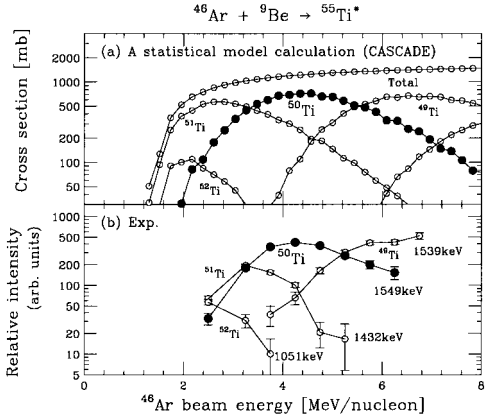

Fig. 1. Calculated (a) and measured (b) excitation functions of Ti isotopes.

*1 Center for Nuclear Study, University of Tokyo
*2 Department of Physics, Kyushu University
*3 Department of Physics, Royal Institute of Technology, Sweden
*4 Department of Physics, University of Tokyo
*5 Department of Physics, Tohoku University
*6 Institute of Physics, University of Tsukuba
*7 Department of Physics, Kyoto University
*8 Argonne National Laboratory, USA

References

1) E. Ideguchi et al.: Phys. Rev. Lett. **87**, 222501 (2001).
2) J. Styczen et al.: Nucl. Phys. A **327**, 295 (1979).
3) E. Ideguchi et al.: RIKEN Accel. Prog. Rep. **38**, 72 (2005).
4) S. Shimoura: Nucl. Instrum. Methods Phys. Res. A **525**, 188 (2004).
5) M. Behar et al.: Nucl. Phys. A **366**, 61 (1981).
6) S. E. Arnell et al.: Phys. Scr. **6**, 222 (1972).
7) R. V. F. Janssens et al.: Phys. Lett. B **546**, 55 (2002).
8) F. Pühlhofer: Nucl. Phys. A **280**, 267 (1977).

Search for high-spin isomers in $N = 51$ isotones

Y. Wakabayashi,[*1,*2] A. Odahara,[*3] Y. Gono, T. Fukuchi,[*2] S. Kubono,[*2] T. Teranishi,[*1] S. Ota,[*4] H. Yamaguchi,[*2] A. Saitoh,[*2] E. Ideguchi,[*2] S. Nishimura, J. J. He,[*2] H. Fujikawa,[*2] G. Amadio,[*2] M. Notani,[*5] Y. Yanagisawa, S. Michimasa, S. Shimoura,[*2] H. Watanabe,[*6] T. Kishida, H. Baba,[*2] and M. Kurata-Nishimura

[High-spin isomer, γ-γ Coincidence, Unstable nuclear beams]

High-spin isomers are known in $N = 83$ isotones systematically.[1)] They are considered to be shape isomers. In order to search for the same type of isomers in other mass regions, we selected $N = 51$ isotones which have similar single-particle orbits near the Fermi level to those of $N = 83$ isotones.[1)]

We developed a ^{17}N secondary beam using the low-energy radioactive-isotope beam separator (CRIB)[2)] of the Center for Nuclear Study, University of Tokyo, for high-spin isomer search in $N = 51$ isotones. Since the nuclei with $Z < 40$ of $N = 51$ isotones are close to the stability line, they can only be produced by light-ion-induced reactions such as (p,α,Xn) by which it is difficult to produce high spin states of these nuclei. Therefore, it is effective to use radioactive-isotope beams. By means of the γ-ray spectroscopy method, high-spin isomers in ^{90}Y, ^{89}Sr and ^{88}Rb were searched for.

The experiment for isomer search was performed in Sep. 2003 using CRIB. In this experiment, seven γ rays from ^{92,93}Nb produced by the secondary fusion reactions of ^{82}Se(^{17}N, 7n,6n) ^{92,93}Nb have been observed. However, those of the relevant nuclei, such as those of ^{90}Y, which have production cross sections smaller than those of ^{92,93}Nb by one order of magnitude, could not be observed. This is because the background level of the amount of thermal-neutron capture γ rays was 200 times higher than the expected counts of peak area coming from the relevant nuclei, such as a 1535 keV γ ray of ^{90}Y. Therefore, it is essential to reduce the thermal-neutron capture γ rays.

A test experiment for isomer search was performed in May 2004. A ^{9}Be primary target of 2.3 mg/cm^2 was bombarded by an ^{18}O^{8+} primary beam of 126 MeV to obtain a ^{17}N beam. The beam current was 0.4 pμA at the primary target position. A PPAC was set at a dispersive focal plane (F1) for beam monitoring. Another PPAC and a Si detector of 1.5 mm thickness were installed for particle identification at an achromatic focal plane (F2). A PPAC and a Si detector were also placed just upstream and downstream of a ^{82}Se secondary target of 4.9 mg/cm^2, respectively, to separate the secondary fusion reaction products from the ^{17}N beam. This separation could be achieved by the particle identification performed using energy signals of the Si detector and time information between the signals from F3PPAC and the Si detector. Two clover Ge detectors were set at 40 mm from the ^{82}Se secondary target to measure γ rays emitted from the secondary fusion reaction products.

Figure 1 shows time spectra between F3PPAC and Ge detectors. Spectrum (a) was obtained without any gate. Kinetic energies of recoiling fusion products are lower than 15 MeV. Therefore, spectrum (b) was obtained by setting a gate for this region of the Si energy spectrum. The time relations between signals from F3PPAC and the Si detector could provide an additional condition to select events related to the secondary fusion reaction products. The time period corresponding to those reaction products is that obtained by setting a gate for a part lower than 15 MeV of the Si energy spectrum. Spectrum (c) was obtained by setting gates for both the Si energy spectrum and the time spectrum between F3PPAC and the Si detector selected under the gating condition mentioned above. They indicate that the peak to background ratio has been greatly improved by adding gate conditions. Consequently, the relevant γ rays can be measured using the present setup.

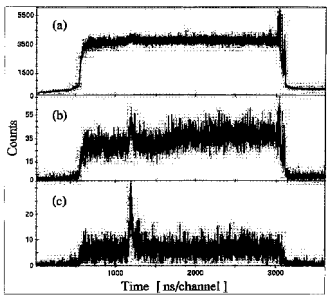

Fig. 1. Time spectra between F3PPAC and Ge detectors. Gating conditions of spectra (a), (b) and (c) are given in the text.

*1 Department of Physics, Kyushu University
*2 Center for Nuclear Study, University of Tokyo
*3 Nishinippon Institute of Technology
*4 Department of Physics, Kyoto University
*5 Physics Division, Argonne National Laboratory, USA
*6 Department of Nuclear Physics, The Australian National University, Australia

References

1) Y. Gono et al.: Eur. Phys. J. A **13**, 5 (2002), and references therein.
2) S. Kubono et al.: Eur. Phys. J. A **13**, 217 (2002), and to be published in Nucl. Instrum. Methods Phys. Res. B.

Experiments on synthesis of isotope ^{277}112 by ^{208}Pb + ^{70}Zn reaction

K. Morita, K. Morimoto, D. Kaji, T. Akiyama,[*1] S. Goto,[*2] H. Haba, E. Ideguchi,[*3] H. Koura,[*4] H. Kudo,[*2] T. Ohnishi, A. Ozawa,[*5] T. Suda, K. Sueki,[*5] H. Xu,[*6] T. Yamaguchi,[*1] A. Yoneda, A. Yoshida, and Y.-L. Zhao[*7]

[^{277}112, production and decay, gas-filled recoil ion separator]

We studied isotope ^{277}112 using the ^{208}Pb(^{70}Zn, n) reaction, as an extension of the previous studies on ^{271}Ds ($Z = 110$)[1] and ^{272}Rg ($Z = 111$).[2] Previously, the isotope was studied by Hofmann *et al.*,[3] where only two decay chains originating from ^{277}112 were reported. Therefore, it is important to confirm these events. During the irradiation of ^{208}Pb targets by ^{70}Zn projectiles, we observed two decay chains that can be assigned to subsequent decays originating from ^{277}112. The result has provided a confirmation of the discovery of ^{277}112 and its daughter nucleus ^{273}Ds.

A ^{70}Zn ion beam of 349.5 MeV was extracted from RILAC. The absolute accuracy of the beam energy was ±0.6 MeV. A typical beam intensity on the target was 1.7×10^{12} s^{-1}. Targets were prepared by vacuum evaporation of ^{208}Pb, enrichment 98.4%, onto carbon backing foils of 30 μg/cm^2 thickness. The thickness of the lead layer was about 450 μg/cm^2. The lead layer was covered by 10 μg/cm^2-thick carbon layer to protect the target from sputtering. Energy loss of the beam in the target was estimated to be 5.4 MeV using a stopping power table. Beam energy at the half-depth of targets was estimated to be 345.9 MeV. Sixteen targets were mounted on a rotating wheel 30 cm in diameter. The wheel was rotated at 2000 rpm during irradiation. The reaction products were separated in-flight from the beam by a gas-filled recoil ion separator, GARIS,[1] and were guided into a detector box placed at the focal plane of GARIS. The separator was filled with helium gas at a pressure of 86 Pa. The value of the magnetic rigidity of GARIS in the evaporation residue measurement was set at 2.09 Tm. The total dose of ^{70}Zn was 4.4×10^{18}. All the other experimental conditions were almost identical to the ones adopted in the experiment for the ^{209}Bi(^{64}Ni, n)^{272}111 reaction.[2]

We observed two events of implantation of evaporation residues (ER) in a position-sensitive semiconductor detector (PSD) followed by four sequential α-decays terminated by spontaneous fission (SF) decays. The probabilities of accidental coincidences between the implantation and individual decays are estimated by the same method as that described in Ref. 4. The maximum value is evaluated to be 3.0×10^{-4} for α_4 decay in the second chain. Decay energies, time intervals, and positions of the observed decay chains, as well as the energy and position of ER, are summarized in Table 1.

Decay energies of α_1 in the present work, 11.09 ± 0.07 MeV and 11.32 ± 0.04 MeV, differ from the values obtained at GSI, 11.45 MeV and 11.17 MeV, by about 0.10 MeV. Decay energies of α_2 and α_3 in the present work agree well with the values obtained at GSI. Decay energies of α_4 in the present work were 8.71±0.04 MeV and 8.70 ± 0.04 MeV, while the values obtained at GSI were only partially measured in both chains.

Based on the comparison between the decay times and the energies of the decay chain members observed in the present work and those observed in the work done by the GSI group, the present result has provided a confirmation of the discovery of ^{277}112 and its daughter nucleus ^{273}Ds. The production cross section of isotope ^{277}112 by the ^{208}Pb(^{70}Zn, n) reaction was deduced to be $0.44^{+0.59}_{-0.29}$ pb using the transmission efficiency of 0.8 for GARIS.[1]

Table 1. Summary of the observed events. ±: energy resolution in FWHM. ΔT: time difference between events. Position: measured from the bottom of the detector.

	chain 1	chain 2	Nuclide
	E (MeV) ΔT Position	E (MeV) ΔT Position	
ER	34.42 - 23.3 mm	35.13 - 18.5 mm	
α_1	11.09 ± 0.07 1.10 ms 23.6 mm	11.32 ± 0.04 1.22 ms 18.3 mm	^{277}112
α_2	11.14 ± 0.04 0.52 ms 23.5 mm	11.15 ± 0.07 0.040 ms 20.2 mm	^{273}Ds
α_3	9.17 ± 0.04 14.2 s 23.3 mm	9.25 ± 0.07 0.270 s 19.0 mm	^{269}Hs
α_4	8.71 ± 0.04 23.0 s 23.5 mm	8.70 ± 0.04 79.9 s 18.1 mm	^{265}Sg
SF or α_5	197.3 2.97 s 23.4 mm	156.3 8.30 s 18.5 mm	^{261}Rf

*1 Saitama University
*2 Niigata University
*3 Center for Nuclear Science, University of Tokyo
*4 Japan Atomic Energy Research Institute
*5 University of Tsukuba
*6 Institute of Modern Physics, China
*7 Institute of High Energy Physics, China

References

1) K. Morita et al.: Eur. Phys. J. A **21**, 257 (2004).
2) K. Morita et al.: J. Phys. Soc. Jpn. **73**, 1738 (2004).
3) S. Hofmann et al.: Eur. Phys. J. A **14**, 147 (2002).
4) K. Morita et al.: J. Phys. Soc. Jpn. **73**, 2593 (2004).

Experiment on synthesis of element 113 in reaction ^{209}Bi(^{70}Zn,n)^{278}113†

K. Morita, K. Morimoto, D. Kaji, T. Akiyama,[*1] S. Goto,[*2] H. Haba, E. Ideguchi,[*3] R. Kanungo, K. Katori, H. Koura,[*4] H. Kudo,[*2] T. Ohnishi, A. Ozawa,[*5] T. Suda, K. Sueki,[*5] H. Xu,[*6] T. Yamaguchi,[*7] A. Yoneda, A. Yoshida, and Y.-L. Zhao[*8]

[^{278}113, new element, production and decay, gas-filled recoil ion separator]

Finding the new isotopes of very heavy elements, including new elements, and studying their decay properties are interesting subjects in both nuclear physics and nuclear chemistry. Since 2002, we have investigated the production and decay of ^{271}Ds ($Z = 110$) and ^{272}111 using ^{208}Pb(^{64}Ni, n) and ^{209}Bi(^{64}Ni, n) reactions, respectively,[1,2] at the RIKEN Linear Accelerator Facility (RILAC). Subsequently, we studied the isotope of the 112th element using the ^{208}Pb(^{70}Zn, n)^{277}112 reaction. Our results clearly confirmed the production of the isotopes reported by Hofmann and coworkers,[3–8] and provided new spectroscopic information on the isotopes and their daughter nuclei. As an extension of our previous work, we performed experiments aimed at synthesizing an isotope of larger atomic number, $Z = 113$, using the ^{209}Bi + ^{70}Zn reaction.

The experiment was designed to produce the isotope ^{278}113 by the one-neutron evaporation channel in the ^{209}Bi + ^{70}Zn complete fusion reaction. On the basis of a systematic study of the most probable reaction energies for the one-neutron evaporation channel in the ^{208}Pb(^{64}Ni, n)^{271}Ds, ^{209}Bi(^{64}Ni, n)^{272}111, and ^{208}Pb(^{70}Zn, n)^{277}112 reactions, a reaction energy of 349.0 MeV at the half-depth of the targets was adopted to maximize the relevant cross section for producing ^{278}113. The reaction products were separated in-flight from the beam using a gas-filled recoil ion separator, GARIS, and were guided into a detector box placed at the focal plane of GARIS. The magnetic rigidity (Bρ) of GARIS for evaporation residue measurement was set at 2.09 Tm. The experimental setup is almost the same as the one used in experiments for ^{271}Ds and ^{272}111 except for the targets. The detail of the experimantal setup is given in Morita *et al.*[1)]

As a result, the convincing candidate event of the isotope of the 113th element, ^{278}113, and its daughter nuclei, ^{274}111 and ^{270}Mt, were observed, for the first time, in the ^{209}Bi + ^{70}Zn reaction at a beam energy of 349.0 MeV with a total dose of 1.7×10^{19}. The alpha decay energies and decay times of the candidates, ^{278}113, ^{274}111, and ^{270}Mt, were (11.68 ± 0.04 MeV, 0.344 ms), (11.15 ± 0.07 MeV, 9.26 ms), and (10.03 ± 0.07 MeV, 7.16 ms), respectively. The production cross section of the isotope was deduced to be 55^{+150}_{-45} fb (10^{-39} cm^2). The decay chain is shown in Fig. 1, together with decay energies (E_α and/or E_{SF}) and decay times.

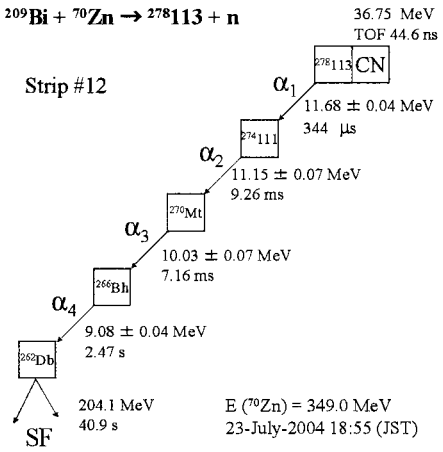

Fig. 1. Decay chain observed in irradiation of ^{209}Bi targets by ^{70}Zn projectiles. Measured energies and decay times are indicated in the figure.

References
1) K. Morita et al.: Eur. Phys. J. A **21**, 257 (2004).
2) K. Morita et al.: J. Phys. Soc. Jpn. **73**, 1738 (2004).
3) S. Hofmann: Rep. Prog. Phys. **61**, 639 (1998).
4) S. Hofmann et al.: Z. Phys. A **350**, 281 (1995).
5) S. Hofmann et al.: Z. Phys. A **354**, 229 (1996).
6) S. Hofmann and G. Münzenberg: Rev. Mod. Phys. **72**, 733 (2000).
7) S. Hofmann et al.: Eur. Phys. J. A **14**, 147 (2002).
8) S. Hofmann: J. Nucl. Radiochem. Sci. **4**, R1 (2003).

† Condensed from the article in J. Phys. Soc. Jpn. **73**, 2593 (2004)

*1 Saitama University
*2 Department of Chemistry, Niigata University
*3 Center for Nuclear Study, University of Tokyo
*4 Japan Atomic Energy Research Institute
*5 University of Tsukuba
*6 Institute of Modern Physics, China
*7 Department of Physics, Saitama University
*8 Institute of High Energy Physics, China

Electron scattering from unstable nuclei by a novel SCRIT method (II)

T. Suda, T. Emoto, S. Ito, T. Koseki, K. Kurita,* H. Morikawa,* M. Nakamura, T. Ohnishi, H. Takeda, M. Wakasugi, and Y. Yano

[electron scattering, RI, SCRIT]

Electron scattering is one of the most precise probes for studying the internal structure of atomic nuclei, and will surely play an essential role in the structure studies of radioactive isotopes (RI) when an electron-RI (eRI) scattering experiment becomes possible.

We propose a novel scheme for the eRI scattering experiment, SCRIT (Self-Confining RI Target). This novel method provides a localized RI target on the electron beam in an electron storage ring. According to numerical simulations, a sufficiently high luminosity for elastic electron scattering, 10^{27} /cm^2/s, is expected for 10^7/s ion injection with a 500-mA electron beam current.[1)]

To study the feasibility of this SCRIT scheme, a prototype was designed and constructed in 2003. The SCRIT prototype consists of an Cs ion source, an ion transport line, SCRIT electrodes for ion trapping, an electron detector[2)] and a luminosity monitor. In the beginning of 2004, it was successfully installed in an existing electron storage ring, KSR, of Kyoto University.

The following are the experiments we carried out this year.

- SCRIT prototype in KSR: Immediately after the installation and baking of the prototype, a series of test experiments were carried out with electron beams. No serious effects on the KSR performances, such as the beam lifetime and the maximum storaged current, were observed as a result of the SCRIT prototype installation.
- Electron detector installation: An electron detector, consisting of a drift chamber, 12 plastic scintillators and 9 calorimeters, was installed. Prior to the installation, all the calorimeters were energy-calibrated using a monoenergetic (60 MeV) electron beam. The electron detector was confirmed to work well using a storaged electron beam of 80 mA. In particular, the drift chamber, placed very close to the high-current electron beam, functioned normally using He+C_2H_6 (50 : 50) gas. Figure 1 shows an example of one event during the measurement at a storaged current of 50 mA. The trajectory of an electron scattered at the SCRIT electrodes is clearly reconstructed.
- Luminosity monitor installation: Bremsstrahlung from trapped ions is to be measured for luminosity determination. A bremsstrahlung detector consisting of seven BaF_2 crystals was placed downstream of a straight section of KSR, where the SCRIT prototype was installed. Prior to the installation, all BaF_2 crystals were also energy-calibrated. The background attributed to the short beam lifetime of 1000 seconds was found to be quite high, $\sim$ a few KHz, compared with the expected bremsstrahlung rate of the trapped ions, $\sim$500 Hz. Background reduction is essential for luminosity determination. The modification of the beam transport line, i.e., the installation of new beam pipes and a severer collimation system, are underway.

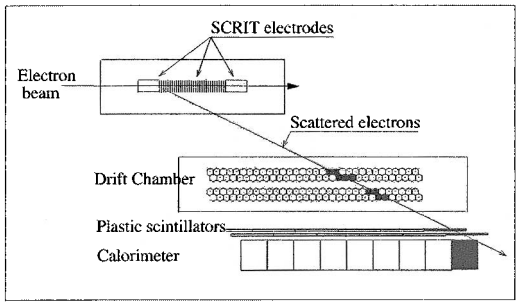

Fig. 1. Trajectory of a scattered electron measured using the drift chamber.

- Confirmation of ion trapping: Although no direct evidence of Cs ion trapping was observed in the luminosity monitor, the trapping of Cs ions in SCRIT was confirmed by the detection of ions extracted from the trapping potential. It was demonstrated that SCRIT can trap an order of 10^7 ions for 10 seconds. It is suggested on the basis of our numerical simulation that the luminosity of an order of 10^{25}/cm^2/s is achieved.

The next step that should be carried out is the accurate determination of luminosity. In addition to the bremsstrahlung monitor, new monitors, which measure characteristic X-rays from the trapped Cs ions and Möller electrons from the collision between an electron beam and electrons in Cs ions, are planned to be installed.

* Rikkyo University

References

1) M. Wakasugi, T. Suda, and Y. Yano: Nucl. Instrum. Methods Phys. Res. A **532**, 216 (2004).
2) T. Suda et al.: RIKEN Accel. Prog. Rep. **37**, 81 (2004).

Production of low-energy RI beam ^{46}Ar for secondary fusion reaction

E. Ideguchi,[*1] M. Niikura,[*1] C. Ishida,[*2] T. Fukuchi,[*1] H. Baba,[*1] N. Hokoiwa,[*3] H. Iwasaki,[*4] T. Komatsubara,[*5] T. Koike,[*6] T. Kubo, M. Kurokawa, S. Michimasa, K. Miyakawa,[*5] K. Morimoto, T. Ohnishi, S. Ota,[*7] A. Ozawa,[*5] S. Shimoura,[*1] T. Suda, M. Tamaki,[*1] I. Tanihata,[*8] Y. Wakabayashi,[*3] and K. Yoshida

[NUCLEAR REACTION, ^{9}Be(^{46}Ar, xn)$^{55-x}$Ti, Unstable nuclei, Fusion reaction]

In-beam gamma-ray spectroscopy by fusion reactions has been one of the most efficient methods for the study of nuclear structure at a high spin since a large angular momentum can be brought in to the reaction. However, nuclei produced by fusion reaction using stable isotopes are limited in many cases to the proton-rich side relative to the β-stability line. To study high-spin states of neutron-rich nuclei by heavy-ion-induced fusion reaction, it is necessary to use neutron-rich secondary beams. In the study of ^{50}Ti, a secondary fusion reaction, ^{46}Ar+^{9}Be, can be used to investigate high-spin states where deformed collective states due to the presence of deformed shell gaps[1)] in $Z = 22$ and $N = 28$ may approach the yrast state.

To actualize the method, a low-energy neutron-rich secondary beam has been developed. An ^{46}Ar beam was produced at the RIPS Facility[2)] in RIKEN by fragmentation reaction. A primary ^{48}Ca beam with an energy of 63 MeV/nucleon was provided by the RIKEN Ring Cyclotron with a maximum intensity of 100 pnA, and it was impinged on a ^{9}Be target of 1.0 mm thick. An aluminum wedge with a mean thickness of 221 mg/cm^2 placed at the momentum-dispersive focal plane (F1) was used to achieve a clear isotope separation and to lower the energy of the fragment to 30 MeV/nucleon. By operating RIPS at the maximum values of momentum acceptance and solid angle, a typical intensity of 7.3×10^5 counts per second was obtained at the achromatic focal plane (F2). Particle identification of the secondary beam was performed by the time-of-flight (TOF)-ΔE method. The purity of the ^{46}Ar beam was found to be 90% by this method.

^{46}Ar beam energy was further lowered using an aluminum rotatable degrader of 0.5 mm thick at F2. It was adjusted to 4.1 ± 0.9 MeV/nucleon, which was estimated by the statistical model calculation (CASCADE)[3)] for an optimum production of ^{50}Ti *via* secondary fusion reaction, ^{9}Be(^{46}Ar, 5n)^{50}Ti.

The ^{46}Ar beam was transported to the final focal plane (F3) and irradiated on the secondary ^{9}Be target of 10 μm thickness to induce the secondary fusion reaction. The intensity of the ^{46}Ar beam at F3 was about 3.2×10^5 counts per second.

Gamma rays emitted in the fusion reaction were measured using a CNS segmented-Ge array, GRAPE.[4)] Doppler correction was carried out on the basis of the position, incident angle and energy of the beam obtained using beam profile information deduced from two PPAC counters[5)] placed upstream of the target as well as TOF between the plastic signal at F2 and PPACs. Figure 1 shows the gamma-ray energy spectrum after Doppler correction. Gamma rays due to ^{49,50,51}Ti[6–8)] are clearly observed.

Data analysis of the secondary fusion experiment is still in progress.

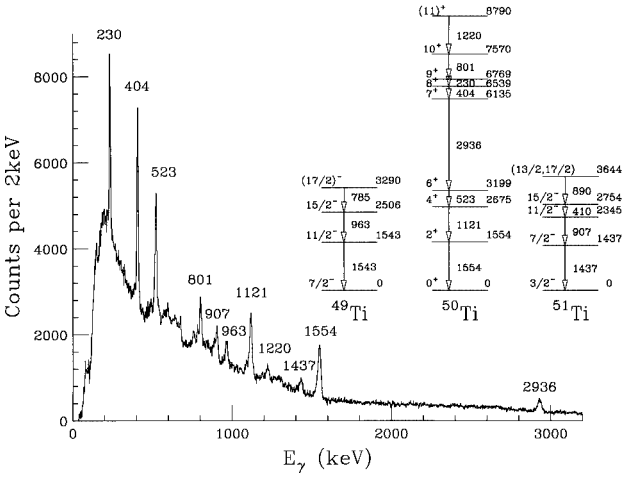

Fig. 1. Doppler-corrected gamma-ray spectrum observed in ^{46}Ar + ^{9}Be fusion reaction.

*1 Center for Nuclear Study, University of Tokyo
*2 Department of Physics, Royal Institute of Technology, Sweden
*3 Department of Physics, Kyushu University
*4 Department of Physics, University of Tokyo
*5 Institute of Physics, University of Tsukuba
*6 Department of Physics and Astronomy, State University of New York at Stony Brook, USA
*7 Department of Physics, Kyoto University
*8 Argonne National Laboratory, USA

References

1) E. Ideguchi et al.: Phys. Rev. Lett. **87**, 222501 (2001).
2) T. Kubo et al.: Nucl. Instrum. Methods Phys. Res. B **461**, 309 (1992).
3) F. Pühlhofer: Nucl. Phys. A **280**, 267 (1977).
4) S. Shimoura et al.: CNS Annu. Rep. **2003**, 87 (2004).
5) H. Kumagai et al.: Nucl. Instrum. Methods Phys. Res. A **470**, 562 (2001).
6) M. Behar et al.: Nucl. Phys. A **366**, 61 (1981).
7) J. Styczen et al.: Nucl. Phys. A **327**, 295 (1979).
8) S. E. Arnell et al.: Phys. Scr. **6**, 222 (1972).

Production of ^{39}Ar at the CRIB facility

Zs. Fülöp,[*1] H. Yamaguchi,[*2] Z. Elekes,[*1] S. Kubono,[*2] G. Amadio,[*2] H. Fujikawa,[*2] J. J. He,[*2] S. Michimasa, J. Niikura,[*2] S. Nishimura, A. Saito,[*2] T. Teranishi,[*3] Y. Wakabayashi,[*3] and Y. Yanagisawa

[NUCLEAR STRUCTURE, Half-life, Unstable nuclei]

The half-life is one of the basic properties of nuclei; consequently, it is well known for the majority of isotopes. However, there are many questions not only for isotopes far from the valley of stability, but also for isotopes having half-lives of around a hundred years or more, in which the determination of the decay curve is getting difficult and the measurement should be very long. Alternative methods such as accelerator mass spectrometry (AMS) and half-life determinations based on geochemical considerations improve the situation, but also have limitations. Recently, we have developed a novel, fast and absolute implantation method, by which the isotope in question is produced as a radioactive beam, and implanted into a stopper, and its specific activity is measured after the irradiation. The advantage of the implantation method is that it allows absolute half-life determination with minimum systematic error and maximum versatility. It is also important that the measurement gives reasonable error without years of data gathering. The first measurement with this technique aimed at the half-life of ^{44}Ti and the results[1,2] confirmed the recent data.

^{39}Ar is a 100% beta-decaying isotope with a half-life of 269 years. It can be produced by the ^{39}K(n,p)^{39}Ar reaction underground[3] and by cosmic-ray-induced spallation reactions.[4] The determination of the ^{39}Ar concentration in rocks and groundwater gives valuable data for geochemical studies. By comparing the concentration of ^{37}Ar ($T_{1/2} = 35$ d) with that of ^{39}Ar in meteorites, the cosmic ray distribution in the solar system can be estimated.[4] As shown in Table 1, apart from an early study[5] with large errors, there is only one measurement on the half-life of ^{39}Ar. Stoenner *et al.*[6] determined the half-life by mass spectrometry and activity determination and gave a result of 269 ± 3 y, upgrading their preliminary value of 325 y.[7]

Table 1. Half-life measurements and compilations for ^{39}Ar.

half-life	error	method	reference
265 y	30 y	mass spectr. + activity	5
325 y	?	relative to ^{37}Ar	7
269 y	3 y	relative to ^{37}Ar	6
269 y	3 y	compilation	8
268 y	8 y	re-evaluation of[6]	9

*1 ATOMKI, Hungary
*2 Center for Nuclear Study, University of Tokyo
*3 Kyushu University

This value is widely accepted and cited in compilations.[8] It should be noted, however, that according to Holden[9] the error in the original data is underestimated by a factor of three and having reanalyzed the errors, 268 ± 8 y was proposed. The half-life of ^{39}Ar is too long to obtain its decay curve. For example, in the case of ^{32}Si ($T_{1/2} = 170$ y), a measurement of four years was necessary to give a result. Since argon is a noble gas, the AMS technique is also difficult to apply, because a negative ion source is needed.[10,11] The implantation method, however, is suitable for the ^{39}Ar half-life measurement, because it is not necessary to determine the decay curve, but only to detect the activity of the implanted isotopes. As a first step towards the determination of ^{39}Ar half-life, the production of ^{39}Ar was tested at the CNS low-energy in-flight type RI beam separator, CRIB. The ^{39}Ar particles were produced by (^{3}He,^{4}He) reaction in inverse kinematics using a 4.5 MeV/nucleon ^{40}Ar with a ^{3}He gas target. The ^{39}Ar products were separated at charge states of 15^+ and 16^+ by the CRIB separator, and further separation was provided by a Wien filter. Two PPACs and a silicon detector served as detectors for particle identification and position determination. The ^{39}Ar particles were completely separated from ^{40}Ar at a beam rate of 10^4 cps, and the ^{39}Ar content was around 500 cps. In summary, the achieved intensity allows the preparation of ^{39}Ar samples by implantation to investigate its half-life.

References

1) Zs. Fülöp et al.: in *Proc. Nuclei in the Cosmos* V, edited by N. Prantzos and S. Harissopulos (Editions Frontieres, Paris, 1998), p.281.
2) T. Hashimoto et al.: Nucl. Phys. A **686**, 591 (2001).
3) T. Florkiwski: J. Phys. G **17**, S513 (1991).
4) R. C. Reedy et al.: Science **219**, 127 (1983).
5) H. Zeldes et al.: Phys. Rev. **86**, 811 (1952).
6) R. W. Stoenner et al.: Science **148**, 1328 (1965).
7) R. W. Stoenner et al.: J. Geophys. Res. **65**, 3025 (1960).
8) P. M. Endt: Nucl. Phys. A **521**, 1 (1990).
9) N. E. Holden: Pure Appl. Chem. **62**, 941 (1990).
10) W. Kutschera: Annu. Rev. Nucl. Part. Sci. **40**, 411 (1990).
11) I. Ahmad et al.: ANL Ann. Rep. 2001, **ANL-02/15**, 79 (2002).

Magnetic-field effect in muon-catalyzed dt fusion in liquid and solid D/T mixtures

K. Ishida, T. Matsuzaki, M. Iwasaki, Y. Matsuda, K. Nagamine,[*1] N. Kawamura,[*1] H. Imao,[*2] M. Kato,[*3] H. Sugai,[*3] and G. H. Eaton[*4]

[Muon-catalyzed fusion]

In muon-catalyzed fusion (μCF), a high fusion yield can be achieved with a high λ_c (cycling rate of μCF process) and low W (muon loss per cycle). Here, W is dominated by muon-to-alpha sticking with the muon being captured by the Coulomb field of an α particle produced by fusion, which occurs with a small but non-negligible probability of less than 1% per fusion. μCF has been studied under a variety of D/T target conditions to understand the basic processes and to increase the fusion yield. Although the effect of magnetic field in μCF is one of the important practical parameters, there have been only a few theoretical studies on, for example, the convoy muon effect[1)] and field-induced transition in $\alpha\mu$,[2)] and there have been no experimental studies. Thus, we started measurements of the magnetic-field dependence of μCF at the RIKEN-RAL Muon Facility.

A preliminary study with a liquid D/T target was reported in the last progress report.[3)] The experiment was carried out under four magnetic-field settings (0, 1.2, 2.4 and 3.3 T) for liquid D/T with a tritium concentration of 30%. Fusion neutrons and various muonic X-rays were detected. This time, we changed the target condition to solid at 16 K and 8 K to study how the field dependence is affected by the target density and temperature.

Figure 1 shows the observed magnetic field dependence of the cycling rate, the muon loss probability, and the yield of $\alpha\mu$ K_α X-rays per fusion. Our new data on solid D/T generally show the same tendencies as those of liquid D/T. Within the statistical error of $\pm$5%, no significant dependence on the magnetic field of either the cycling rate or the muon loss probability was observed, while the $\alpha\mu$ K_α X-ray yield increased with the field by as much as 30%. The result is opposite to the prediction based on the convoy effect,[1)] which predicts decreasing muon-to-alpha sticking and X-ray yield as the field is increased. However, the stimulated transition[2)] enhances 2s-2p mixing in $\alpha\mu$ and increases the K_α emission by competing with further excitation or stripping from the 2s state. Thus it is consistent with, or at least does not contradict with, our results.

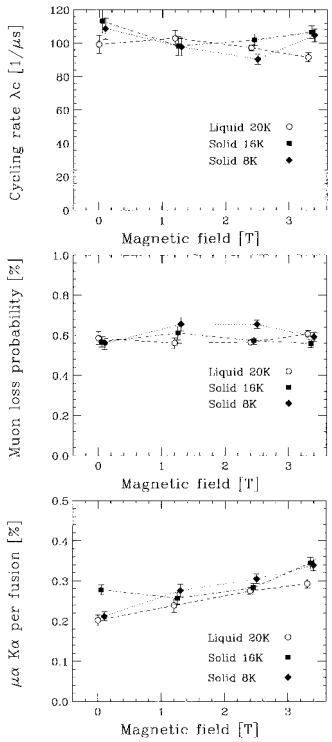

Fig. 1. Preliminary result on field dependence of μCF cycling rate (λ_c), muon loss per cycle (W), and the yield of $\alpha\mu$ K_α X-rays per fusion for three target conditions, 20 K liquid, 16 K solid and 8 K solid.

In this process, however, its effect on the muon-sticking loss is not zero but small because the initial sticking to the $\alpha\mu$ 2s state is calculated to be less than 20% of the total initial sticking and the loss is dominated by initial muon sticking to the $\alpha\mu$ 1s state.

In summary, our result implies a field effect that enhances the sticking K_α X-ray emission but does not simply increase the overall sticking. The field-stimulated transition is one of the candidates of the cause of such an effect.

References

1) B. Müller, H. E. Rafelski, and J. Rafelski: Phys. Rev. A **40**, 2839 (1989).
2) V. S. Melezhik and P. Schmelcher: Phys. Rev. A **59**, 4264 (1999).
3) K. Ishida et al.: RIKEN Accel. Prog. Rep. **37**, 91 (2004).

*1 Muon Science Laboratory, Institute of Materials Structure Science, High Energy Accelerator Research Organization (KEK)
*2 Department of Physics, University of Tokyo
*3 Tokai Research Establishment, Japan Atomic Energy Research Institute (JAERI)
*4 Rutherford Appleton Laboratory, UK

Muon catalyzed t-t fusion and muon transfer experiments using liquid and solid T_2 targets

T. Matsuzaki, K. Nagamine,[*1] K. Ishida, N. Kawamura,[*1] H. Imao,[*1,*2] Y. Matsuda, M. Iwasaki, M. Kato,[*3] H. Sugai,[*3] M. Tanase,[*3] S. N. Nakamura,[*4] K. Kudo,[*5] A. Uritani,[*5] H. Harano,[*5] and G. H. Eaton[*6]

[Muon catalyzed t-t fusion, muon transfer reaction, ^{3}He acccumulation in solid T_2]

Muon catalyzed t-t fusions (t-t μCF) take place spontaneously when negative muons stop in a tritium (T_2) target. The negative muons form tμ atoms by binding to triton nuclei (t), and the tμ atoms then collide with T_2 molecules to form ttμ molecules. The t-t fusions occur in the framework of ttμ molecules, and induce a three-particle decay consisting of an α-particle and two neutrons. After the t-t μCF process, muons are liberated and participate in the next t-t μCF reaction.

$$t + t + \mu \rightarrow (tt\mu) \rightarrow \alpha + n + n + \mu + Q(11.33\,\mathrm{MeV}) \quad (1)$$

For some probability, the muon is captured by the α-particle and muonic X-rays are emitted, thus terminating the t-t μCF cycle. This phenomenon is termed muon sticking.

$$t + t + \mu \rightarrow (tt\mu) \rightarrow (\mu\alpha) + n + n + Q \quad (2)$$

The 6.76 keV radiative photons are generated in association with the muon transfer process from tμ atoms to the accumulated ^{3}He nuclei through intermediate ($t^3He\mu$) mesomolecule formation,[1)] where ^{3}He is the decay product of tritium. The muon transfer process is described as

$$t\mu + {}^3He \rightarrow (t^3He\mu)^* \rightarrow t + ({}^3He\mu) + \gamma(6.76\,\mathrm{keV}). \quad (3)$$

We conducted the experiment at the RIKEN-RAL Muon Facility.[2)] A high-purity tritium gas (T: 99.4%, H: 0.6%, D: $<$ 100 ppm), produced by Ontario Power Generation Inc. in Canada, was imported to RAL. Tritium gas was purified in an in situ tritium gas-handing system[3)] to remove any ^{3}He impurities originating from tritium β-decay. The tritium gas (inventory of 1479 Ci) was liquefied and solidified in a target. For the photon and neutron detections, a Si(Li) X-ray detector (70 mm^2 $\times$ 3.5 mm thickness) and three calibrated NE213 liquid scintillators (2 inchϕ $\times$ 2 inch) were used. Typical delayed photon spectra obtained for solid and liquid T_2 targets are respectively shown in Fig. 1 and Fig. 2. We clearly observed K_α (8.21 keV) and K_β (9.6 keV) muonic X-rays originated from $\mu\alpha$ atoms formed in the muon sticking processes. In addition, we can see characteristic radiative photons at 6.76 keV in Fig. 1, originating from the radiative decay of excited intermediate $t^3He\mu$ mesomolecules in muon transfer process from tμ atoms to accumulated ^{3}He nuclei in solid T_2 targets. In contrast, the 6.76 keV photon was not observed at all in liquid target runs (Fig. 2), indicating that ^{3}He does not accumulate at all in liquid T_2. By analyzing photon and neutron data, we will clarify important parameters in t-t μCF and muon transfer processes, including their temperature-dependent behavior. This analysis is currently in progress.

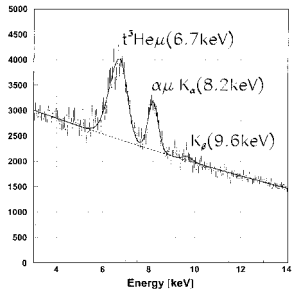

Fig. 1. A typical photon spectrum for solid T_2 targets.

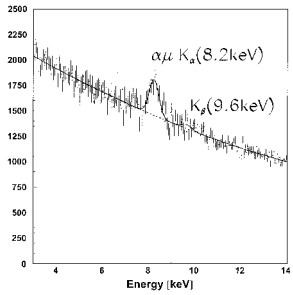

Fig. 2. A typical photon spectrum for liquid T_2 targets.

*1 Meson Science Laboratory, Institute of Materials Structure Science, High Energy Accelerator Research Organization (KEK)
*2 Faculty of Science, University of Tokyo
*3 Department of Radioisotopes, Japan Atomic Energy Research Institute (JAERI)
*4 Department of Physics, Tohoku University
*5 Quantum Radiation Division, Metrology Institute of Japan, National Institute of Advanced Industrial Science and Technology (AIST)
*6 ISIS, Rutherford Appleton Laboratory (RAL), UK

References

1) T. Matsuzaki, K. Nagamine, K. Ishida, and K. Kawamura: Phys. Lett. B **527**, 43 (2002).
2) T. Matsuzaki, K. Ishida, K. Nagamine, I. Watanabe, G. H. Eaton, and W. G. Williams: Nucl. Instrum. Methods Phys. Res. A **465**, 365 (2001).
3) T. Matsuzaki, K. Nagamine, M. Tanase, M. Kato, and K. Kurosawa: Nucl. Instum. Methods Phys. Res. A **480**, 812 (2002).

Dimuon measurement in indium-indium collisions at the CERN/SPS

H. Ohnishi and J. M. Heuser

[heavy-ion collisions, quark-gluon plasma, charm quark]

The use of high-energy heavy-ion collisions is known to be one of the possible ways of creating nuclear matter with high energy density. Normal nuclear matter may then undergo a phase transition to a new state of matter, the quark-gluon plasma (QGP). The observed J/ψ suppression pattern in high-energy heavy-ion collisions at CERN's Super Proton Synchrotron (SPS) seems to provide the first signal of color deconfinement through parton condensation. Simultaneously, an enhancement of dimuons in the Intermediate Mass Region (IMR, $1.5 < M_{\mu\mu} < 2.5$ GeV) is observed, with the main contributions expected to be from decays of charm mesons and dimuons originating from Drell-Yan processes. So far, however, there have been no indications that this color condensate subsequently leads to a medium in thermal equilibrium, *e.g.*, the QGP.

One of the relevant issues that the NA60 experiment intends to address is the origin of the enhancement of IMR dimuons. Two hypotheses are proposed: enhancement of charm meson production in heavy-ion collisions, and thermal dimuon production from the created medium, which is direct evidence of QGP formation. To clarify this issue, we must be able to isolate the considerable yield of dimuons coming from decays of charm mesons. Due to the long life time of charm mesons, the origin of muons coming from charm meson decays will be offset from the primary vertex. Therefore, we need to perform secondary vertex measurements that provide approximately 50 μm resolution.

The NA60 experiment comprises four main detector components: the vertex spectrometer, hadron absorber, zero-degree calorimeter and muon spectrometer. The vertex spectrometer consists of a 16-plane tracking telescope in a 2.5 T magnetic field, built from radiation tolerant silicon pixel detectors developed for the ALICE experiment at the Large Hadron Collider. A vertex telescope tracks the large number of charged particles created from collisions of heavy-ion or proton beams on nuclear targets. Only muons pass through the hadron absorber and are tracked by the muon spectrometer. In the offline analysis, muons reconstructed in the muon spectrometer are matched in both spatial and momentum coordinates with one of the charged tracks measured using the vertex telescope. In this way, complete muon tracks are identified from the target region to the muon spectrometer. This track matching allows us to significantly improve the dimuon mass resolution since we can analyze the muon kinematics before the scattering in the hadron absorber.

During the NA60 run in 2003, beams of indium ions were collided at 158 GeV/nucleon with indium targets. The analysis of the data is in progress, and the mass resolution at the ϕ mass is found to be 23 MeV. The advantage of muon matching is that we can identify the origin of the muon. The resolution of the offset of the tracks from the collision vertex is analyzed with dimuons from J/ψ decays and yields the design value of 50 μm for the vertex telescope.[1] This is consistent with the expected performance evaluated in Monte Carlo simulations.

To demonstrate the identification of the charm decay contribution, dimuons are separated into two sub samples. One is the prompt sample, where both muons originate from the collision vertex. The other is the offset sample, where the origin of both muons is located away from the collision vertex. Figure 1 (a) shows the dimuon mass distributions of the prompt and offset samples, and Fig. 1 (b) shows their ratio. Large reductions in the dimuon yields at the dimuon masses dominated by the ω, ϕ and J/ψ peaks are clearly visible in the prompt sample. A clear excess is seen in the offset dimuon sample in the mass window where the charm decay contribution is dominat. Further analysis is under way to extract the production cross section of the charm quark.

From August to November 2004, we recorded data with 400 GeV protons colliding with Be, Al, Cu, In, Pb, W and U targets. We expect about 500 k dimuons from J/ψ and almost the same amount of signal from charm mesons at IMR in the data. These will be good references for the results from indium-indium collisions and will help clarify the reason for the enhancement of IMR dimuons, that is, whether it is due to IMR dimuons originating from QGP or to the enhancement of charm meson production in heavy-ion collisions.

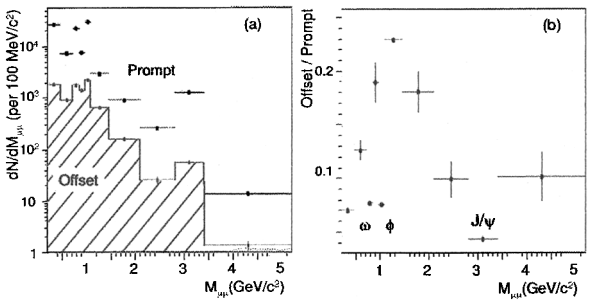

Fig. 1. (a) Dimuon mass distributions of prompt and offset muon pairs. (b) Ratio of the mass distributions with and without track offset requirement.

Reference

1) H. Ohnishi et al: To be published in J. Phys. G.

Experimental signature of in-medium mass modification of $\rho/\omega/\phi$ mesons at normal nuclear density

R. Muto, H. En'yo, M. Naruki,* F. Sakuma,* T. Tabaru, and S. Yokkaichi, for the KEK-PS E325 Collaboration

[QCD, chiral symmetry, normal nuclear density, mass modification, vector meson]

KEK-PS E325 experiment measured the invariant mass spectra of e^+e^- pairs in 12 GeV p + A interactions at KEK Proton-Synchrotron. The aim of this experiment was to detect the in-medium mass modification of vector mesons at a normal nuclear density, which was theoretically expected as a precursor of chiral phase transition.

In our earlier publication, we reported the signature of mass modification of ρ/ω mesons.[1] From the observed modification, however, it was not easy to differentiate the effects of ρ mesons from those of ω mesons on the invariant mass spectrum. In this report, we focus on the analysis of another vector meson, ϕ. There is no other resonance near the ϕ meson mass, thus we are able to examine the possible mass modification more clearly.

The decrease in ϕ meson mass at a normal nuclear density was expected to be about 20–40 MeV/c^2 according to the calculation by Hatsuda and Lee.[2] If such a mass modification occurs, the observed spectrum becomes the summation of two components, a mass peak of normal in-vacuum decays and a low-mass tail from in-medium decays. A large amount of the tail was expected for a large target nucleus, because the decay probability inside the nucleus was high. Experimentally, we compared the mass spectra of carbon and copper targets to examine the nuclear mass dependence of the modification tails.

We reanalyzed all the data with an improved track reconstruction technique. Through this process the statistics of the ϕ meson were almost doubled. We also performed event generation using cascade code JAM[3] and detailed detector simulation using Geant4.[4] To analyze the shape of the ϕ meson peaks, it is important to understand the detector response precisely. We found that the invariant mass spectrum of $K_s \to \pi^+\pi^-$ was well reproduced by this simulation.

Using the mass shape of the ϕ meson obtained from this simulation, together with a quadratic curve for the background shape, the mass region from 0.85 GeV/c^2 to 1.2 GeV/c^2 was analyzed. When we included all the data points in the fitting, the reduced χ^2's were 1.33 (DOF = 49) for the carbon target and 2.18 (DOF = 49) for the copper target. The χ^2's were improved to 1.30 (DOF = 40) and 1.61 (DOF = 40) for the carbon and copper targets, respectively, by excluding the region from 0.95 GeV/c^2 to 1.01 GeV/c^2, where the modification tails could appear. The fitting results excluding the excess region are shown in Fig. 1.

We conclude that the ϕ meson mass shape of the copper data is not reproducible with the expected detector resolution at a 99% confidence level, although the carbon data is reproducible. A possible reason for this is the ϕ meson mass modification in nuclei.

In these analyses, we used approximately 220,000 cpu·hours of the excellent cpu power of RIKEN CC-J and RIKEN Super Combined Cluster System (RSCC).[5] We are grateful for the support from these computing facilities.

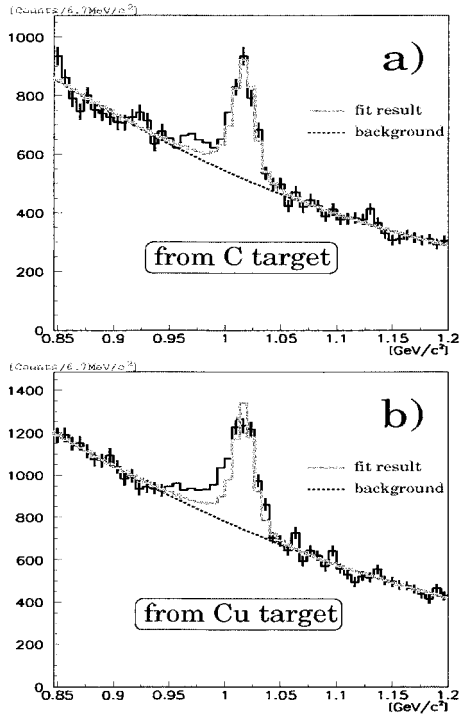

Fig. 1. Invariant mass spectra of the e^+e^- pair for a) the carbon target and b) the copper targets. Gray lines show the best fitting result of the simulated mass shape, and dotted lines, the quadratic background. Fitting was performed excluding the region from 0.95 GeV/c^2 to 1.01 GeV/c^2 (shown as regions without error bars).

* Department of Physics, Kyoto University

References
1) R. Muto et al.: RIKEN Accel. Prog. Rep. **37**, 85 (2004).
2) T. Hatsuda and S. H. Lee: Phys. Rev. C **46**, R34 (1992).
3) Y. Nara et al.: Phys. Rev. C **61**, 024901 (1999).
4) S. Agostinelli et al.: Nucl. Instrum. Methods **506**, 250 (2003).
5) S. Yokkaichi et al.: RIKEN Accel. Prog. Rep. **38**, 247 (2005).

Time-delay-matrix analysis of resonance scattering: General theory and Coulomb-three-body systems with diverging background

I. Shimamura and A. Igarashi*

Resonance analysis of multichannel atomic and molecular scattering and photoionization calculations has traditionally been based on the Breit-Wigner (BW) formula for the eigenphase sum $\delta(E)$[1)]

$$\tan[\delta(E) - \delta^0(E)] = (\Gamma/2)/(E_\mathrm{r} - E), \quad (1)$$

where δ^0 is the background eigenphase sum. This formula is fitted to calculated $\delta(E)$ to extract resonance parameters, *i.e.*, positions E_r and widths Γ.

Later, the derivative $d\delta(E)/dE$ with respect to energy E turned out to be more useful than $\delta(E)$ itself for resonance analysis. For one thing, resonances stand out more clearly in $d\delta/dE$ than in δ. For another, $d\delta/dE$ is related to the lifetime $\hbar/\Gamma$ of the resonance state, leading to transparent physical interpretation. Smith's lifetime or delay-time matrix $Q(E)$ satisfies[2)]

$$Q(E) = i\hbar S dS^\dagger/dE = -i\hbar(dS/dE)S^\dagger = Q^\dagger(E) \quad (2)$$

in terms of the S matrix. If S takes a BW form

$$S_{ij} = e^{i\phi_i}\left(\delta_{ij} - \frac{i\Gamma_i^{1/2}\Gamma_j^{1/2}}{E - E_r + i\Gamma/2}\right)e^{i\phi_j}, \quad (3)$$

where $\Gamma \equiv \sum_i \Gamma_i$, and where the background phases ϕ_i and ϕ_j and partial widths Γ_i and Γ_j are assumed to be constants, the trace of Q has a Lorentzian profile, *i.e.*, $\mathrm{Tr}\,Q(E) = \hbar\Gamma/[(E-E_\mathrm{r})^2 + (\Gamma/2)^2]$,[3)] and the diagonal elements are given by $Q_{ii} = (\Gamma_i/\Gamma)\mathrm{Tr}\,Q$. If δ^0 in (1) is assumed to be constant, this Lorentzian form satisfies

$$\mathrm{Tr}\,Q(E) = 2\hbar\, d\delta(E)/dE. \quad (4)$$

This has the same form as the relation of the phase shift with the time delay in single-channel scattering.

However, the BW formula (3) is too restrictive for analysis of atomic/molecular resonances. It assumes the background S matrix to be diagonal (*i.e.*, inelastic scattering is forbidden, which is impractical) and independent of E (which can be generalized for E-dependent background).

We have proved (4)[4)] for *any E-dependent $S(E)$* or $\delta(E)$, *i.e.*, for E-dependent background, for overlapping resonances, off any resonances, or for the case of no resonances existing. The proof is very general, being based only on relation (2). It applies not only to atomic/molecular physics but also to nuclear physics and any other field of physics where S is defined.

An interesting case is the nonrelativistic interaction of a charged particle A with a hydrogenlike atom BC(nl), where an asymptotic dipole term $\sim\mu r^{-2}$ exists. If it is overcritically attractive, $\delta(E)$ diverges toward a threshold E_th of BC(nl), violating the Wigner threshold law. Then a resonance just above E_th may have a background $\delta^0(E)$ with a strong negative slope, which *washes away the effect of an S-matrix pole and produces "negative time delay" or "time advance."* For such cases we have proposed a fitting formula[5)]

$$\mathrm{Tr}\,Q(E) = \frac{\hbar\Gamma}{(E-E_\mathrm{r})^2 + (\Gamma/2)^2} - \frac{C_1}{E - E_\mathrm{th}} + C_0, \quad (5)$$

which turns out to fit very well even for huge background overcoming the Lorentzian term. The height of this term is related to its width by Γ. *If the height needs to be scaled by a constant in a fitting to computed* $\mathrm{Tr}\,Q(E)$, *it suggests errors in the computation.*

As an example, Fig. 1 shows results for $^3P^\mathrm{o}$ positron scattering by positronium Ps just above the Ps($n = 3$) threshold.[5)] The effect of an S-matrix pole is seen in one of the eigenvalues $q_i(E)$ of $Q(E)$, but $\delta(E)$ decreases monotonically and $\mathrm{Tr}\,Q(E)$ (average time delay) is negative due to the overcritical dipole potential.

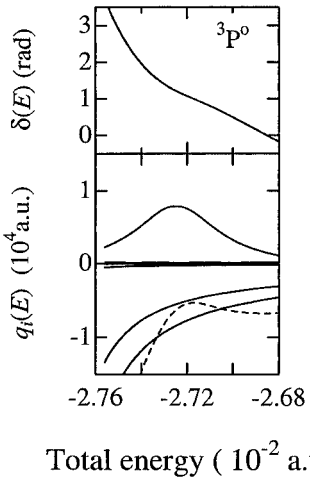

Fig. 1. Positron-positronium $^3P^\mathrm{o}$ eigenphase sum $\delta(E)$ and the trace ($= 2\hbar d\delta/dE$) (– – –) and eigenvalues $q_i(E)$ (——) of the Q matrix plotted *vs.* energy E.

* Department of Applied Physics, Miyazaki University

References

1) A. U. Hazi: Phys. Rev. A **19**, 920 (1979).
2) F. T. Smith: Phys. Rev. **118**, 349 (1960).
3) L. Celenza and W. Tobocman: Phys. Rev. **174**, 1115 (1968).
4) A. Igarashi and I. Shimamura: Phys. Rev. A **70**, 012706 (2004).
5) A. Igarashi and I. Shimamura: J. Phys. B: At., Mol. Opt. Phys. **37**, 4221 (2004).

Apparent discrepancy between the complex-rotation and hyperspherical results now resolved: $e^+ + \mathrm{He}^+$ scattering

A. Igarashi* and I. Shimamura

In Coulomb-three-body scattering, e.g., e^- or e^+ scattering by H or He^+, the correlation between the two light particles is crucial. Its standard treatment used to be to include in the wave function the distance r_{12} between the light particles, as in the Hylleraas coordinates.[1,2] Later, it has been superseded by the hyperspherical (HS) coupled-channel (CC) method,[3–5] which is far more powerful from both numerical accuracy and transparent physical interpretation. The HS coordinates have been useful also for complete solutions of the long-standing problem of breakup in e^-+H scattering using the well-known exterior complex scaling, and the time-dependent Schrödinger equation.[6]

The HS coordinates are five-dimensional hyperangles and a hyperradius $\rho = (r_1^2+r_2^2)^{1/2}$, r_1 and r_2 being distances of the two light particles from the nucleus. The ρ plays a role similar to the ion-atom distance in the molecular-base theory of ion-atom collisions; scattering may be described using adiabatic HS potentials $V_{ii}(\rho)$ and the nonadiabatic couplings $V_{ij}(\rho)$.

The system $He^{2+}e^-e^+$ is interesting because of a few distinct kinds of asymptotic channels; channels $e^+ + \mathrm{He}^+$ with a *repulsive* Coulomb potential $\propto r^{-1}$, and channels $\mathrm{He}^{2+} + \mathrm{Ps}(nl)$ with *attractive* polarization potential $\propto r^{-4}$ if the positronium Ps is in $1s$ state, or with *either attractive or repulsive* dipole potential $\propto r^{-2}$ if $n \geq 2$. Many avoided crossings occur between attractive and repulsive HS potentials with different n, producing rich physics clearly describable using adiabatic HS states.[5] Overcritical dipole potentials lead to infinite series of Feshbach resonances and a strange threshold law violating the Wigner law,[7] the cross section oscillating infinite times close to the threshold.

By solving 42 HSCC equations for S-wave $e^+ + \mathrm{He}^+$ scattering we calculated positions E_r and widths Γ of 9 narrow resonances from the rapidly rising eigenphase sum $\delta(E)$,[5] 3 of which had been detected by the bound-state-type complex-coordinate rotation method (CRM).[8] We also obtained 10 narrow P-wave resonances from 73 HSCC equations,[5] of which 4 had been detected by the CRM.[8] The agreement between the HSCC and CRM values is excellent when both exist.

CRM also found two S-matrix poles with large Γ in each partial wave $L \leq 6$.[8] In both HSCC[4] and conventional CC calculations,[9] $\delta(E)$ increased only weakly in the energy region of the lower "broad resonance" and *decreased monotonically* (meaning *negative time delay*) in the higher region. This disaccord between the bound-state-type and scattering approaches, however, has been resolved by our time-delay matrix analysis,[5] described in Ref. 7.

S-matrix poles at $E = E_r - i\Gamma/2$ can produce resonance scattering, *provided that* Γ *is small enough* for the poles to affect the actual process occurring at real E. A counterexample is the case of shorter lifetime $\hbar/\Gamma$ than the nonresonant collision time. Another counterexample occurs for a strong background that makes $\delta(E)$ hardly increase in the region of width $\sim\Gamma$ near E_r; see Fig. 1 in the preceding report.[7] A very similar behavior of $\delta(E)$ is found in the higher "broad resonance" region in $e^+ + \mathrm{He}^+$ scattering.[5] This was responsible for the seemingly inconsistent HSCC and CRM results; fitting of HSCC time-delay matrix resulted in S-matrix poles consistent with CRM.

The strong background overcoming the S-matrix-pole effect is due to the long-range dipole potential $V_d(r)$, and is lost unless the scattering equations are solved up to very large r. We treated $V_d(r)$ analytically, and hence up to $r \to \infty$ in effect. In recent time-dependent CC calculations[10] a boundary was set at a fairly small r $(= a)$, only within which the time delay was calculated, naturally resulting in a positive value. Also, the peak height of the delay time contradicted their widths,[7] which may be due to the flux loss at the artificial absorption potential set at $r = a$.

* Department of Applied Physics, Miyazaki University

References

1) C. Schwartz: Phys. Rev. **124**, 1468 (1961).
2) I. Shimamura: J. Phys. Soc. Jpn. **30**, 1702 (1971); J. Phys. Soc. Jpn. **31**, 217 (1971); J. Phys. Soc. Jpn. **31**, 852 (1971); V. I. Korobov and I. Shimamura: Phys. Rev. A **56**, 4587 (1997).
3) J.-Z. Tang and I. Shimamura: Phys. Rev. A **50**, 1321 (1994); Phys. Rev. A **51**, R1738 (1995); Phys. Rev. A **52**, R3413 (1995).
4) A. Igarashi and I. Shimamura: Phys. Rev. A **56**, 4733 (1997); A. Igarashi, I. Shimamura, and N. Toshima: Phys. Rev. A **58**, 1166 (1998); New J. Phys. **2**, 17 (2000); A. Igarashi, M. Kimura, and I. Shimamura: Phys. Rev. Lett. **89**, 123201 (2002).
5) A. Igarashi and I. Shimamura: Phys. Rev. A **70**, 012706 (2004); J. Phys. B **37**, 4221 (2004).
6) T. Rescigno et al.: Science **286**, 2474 (1999); C. W. McCurdy et al.: Phys. Rev. A **65**, 042714 (2002); J. Colgan et al.: Phys. Rev. A **65**, 042721 (2002).
7) I. Shimamura and A. Igarashi: RIKEN Accel. Prog. Rep. **38**, 79 (2005).
8) Y. K. Ho: Phys. Rev. A **53**, 3165 (1996); Y. K. Ho and Z.-C. Yan: Phys. Rev. A **66**, 62705 (2002).
9) B. H. Bransden *et al.*: J. Phys. B **34**, 2267 (2001).
10) N. Yamanaka *et al.*: Phys. Rev. A **70**, 062701 (2004).

Electron capture in H^++NH_2 collisions between 0.5 and 1.5 keV

H. Suno,[*1] M. Kimura,[*2] R. J. Buenker,[*3] and L. Pichl[*4]

Electron capture in collisions of ions with atoms in keV-energy regions is one of the most important processes in experimental and theoretical atomic physics as well as in applications to astrophysics and fusion research. Relatively comprehensive studies have been carried out for various atomic targets and charged projectiles in a wide range of collision energies (meV to keV), but those for molecular targets are still rare, both experimentally and theoretically.

This report concerns a theoretical investigation of the electron capture process in the collision of H^+ ions with NH_2 molecules in the region below 1.5 keV. These hydronitrogen molecules, NH_2, exist in various atmospheric and astrophysical environments. They also play a key role in various molecular reactions involving nitrogen atoms in the universe. Since an exact quantum-mechanical treatment of the NH_3^+ system would be difficult, we consider four different trajectories for collision dynamics: (i) the proton approaches the N atom along the bisector of the H-N-H bond angle, passing the midpoint of the H-H line; (ii) it travels along the same line as in (i), but in the opposite direction; (iii) the proton approaches the N atom on the H-N-H plane and perpendicularly to the bisector of the H-N-H bond angle; (iv) the proton approaches the N atom perpendicularly to the H-N-H plane.

Adiabatic potential-energy curves are calculated by the multireference single- and double-excitation configuration-interaction (MRD-CI) method,[1,2] with configuration selection and energy extrapolation employing the Table-CI algorithm.[3] *Ab initio* calculations are performed for each of the four configurations mentioned above. Scattering dynamics is studied on the basis of the fully quantum formulation of a molecular-orbital expansion method. The total scattering wave function is described in an adiabatic representation as an expansion in products of electronic and nuclear wave functions and the electron translation factor. The substitution of the total scattering wave function into the stationary Schrödinger equation and transformation to the diabatic representation[4] yield the coupled equation

$$\left[\frac{1}{2\mu}\triangle_R I - V^d(R) + EI\right] X^d(R) = 0, \qquad (1)$$

where μ is the reduced mass of the system, I the identity matrix, V^d the diabatic potential-energy matrix, and $X^d(R)$ the nuclear wave function in the diabatic representation. The coupled Eq. (1) is solved numerically to obtain the scattering S^l matrix for each partial wave l.[5] The differential cross section is then given by

$$\frac{d\sigma(\theta)}{d\Omega} = \frac{1}{4k^2}\left|\sum_l (2l+1)\{\delta_{if} - S^l_{if}\}P_l(\cos\theta)\right|^2, \qquad (2)$$

where $k = (2\mu E)^{1/2}$ is the momentum of the projectile and θ the scattering angle in the center of mass coordinates.

Differential cross sections for electron capture are shown in Fig. 1 for all four molecular configurations (i)–(iv), for scattering angles of 0°-180° at 1.5 keV. For all cases, the differential cross sections oscillate rapidly when $\theta \leq 5°$, while they are all relatively smooth when $5° \leq \theta \leq 25°$. We noted that the magnitude of the differential cross section for case (i) is nearly the same as that for case (ii) in the region $\theta \leq 60°$. For all cases, oscillatory structures are present when $\theta \geq 60°$.

In conclusion, the dependences on the molecular orientation — the steric effects — are conspicuous in H^++NH_2 collisions.

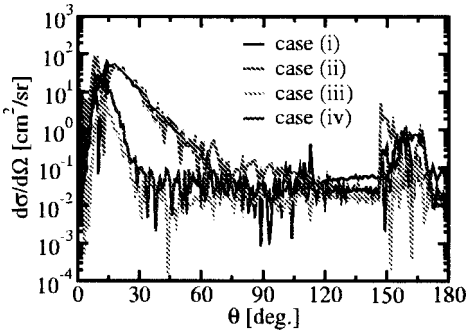

Fig. 1. Differential cross sections for electron capture for the four molecular configurations (described in the text) at 1.5 keV.

References

1) R. J. Buenker and S. D. Peyrimhoff: Theor. Chim. Acta **35**, 33 (1974).
2) R. J. Buenker: Int. J. Quantum Chem. **29**, 435 (1986).
3) R. J. Buenker: Proc. Workshop on Quantum Chemistry and Molecular Physics, Wollongong, Australia, edited by P. Burton (University Press, Wollongong, 1980).
4) M. Kimura and N. F. Lane: Adv. At. Mol. Opt. Phys. **26**, 79 (1989).
5) B. H. Bransden: *Atomic Collision Theory* (Benjamin, New York, 1983).

*1 National Institute for Fusion Science
*2 Graduate School of Sciences, Kyushu University
*3 Theoretische Chemie, Bergische Universität-Gesamthoscschule Wuppertal, Germany
*4 University of Aizu

Charge transfer processes by proton in collisions with C_2H_4 molecule below 10-keV

R. Suzuki,[*1] S. N. Rai,[*2] H.-P. Liebermann,[*3] R. J. Buenker,[*3] L. Pichl,[*4] and M. Kimura[*5]

Charge transfer and direct elastic scattering in collisions of proton with C_2H_4 molecules are studied by using a molecular representation within a semiclassical as well as fully quantum-mechanical approaches[1] below 10 keV. The coordinate system for the projectile and the target molecule of the $[H + C_2H_4]^+$ collision system is shown in Fig. 1. The C=C bond is placed along the X-axis with its midpoint at the origin of coordinate system, and C-H bonds all lie in the XY-plane. Calculations are carried out at three different molecular configurations (X, Y, Z-direction configuration), in which proton approaches (X) parallel, and (Y) perpendicular to the C=C axis in the molecular plane, and (Z) perpendicular to this plane. The adiabatic potentials[2] of the system are shown in Fig. 2.

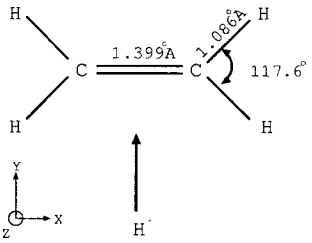

Fig. 1. Schematic diagram indicating the molecular axis orientation for the $[H + C_2H_4]^+$ collision system.

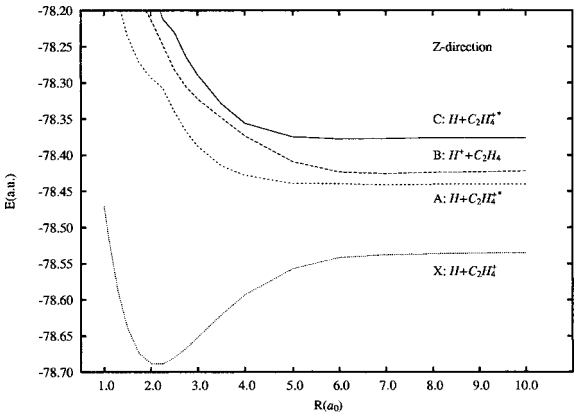

Fig. 2. The adiabatic potentials of the $[H + C_2H_4]^+$ system for the Z-direction. The proton moves along the Z-axis toward the midpoint of the C=C bond.

*1 Computer Center, Hitotsubashi University
*2 Computer Center, Bijni Complex, North-Eastern Hill University, India
*3 Fachbereich C-Mathematik und Naturwissenschaften, Bergische Universität Wuppertal, Germany
*4 Foundation of Computer Science Laboratory, University of Aizu
*5 Graduate School of Sciences, Kyushu University

Differential cross sections from the initial state B to the charge transferred state C for (X), (Y), (Z) at 1.5 keV are shown in Fig. 3. We find that charge transfer in the (Z) takes place preferentially over that in the (X) and (Y) at scattering angles above 15°, while the results for (X) and (Y) are comparable in magnitude below 10°, although (Y) dominates slightly at still smaller angles. Total charge transfer cross sections are shown in Fig. 4. The results for the (Z) and (Y) differ by a factor of four above 500 eV, while those for (X) lie between these values. Below 500 eV, the results for (X) and (Z) are similar in magnitude, while that for the (Y) sharply decreases.

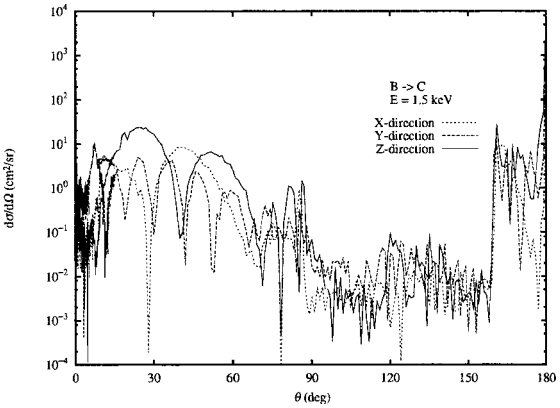

Fig. 3. Differential cross sections from the initial state B to the charge transferred state C.

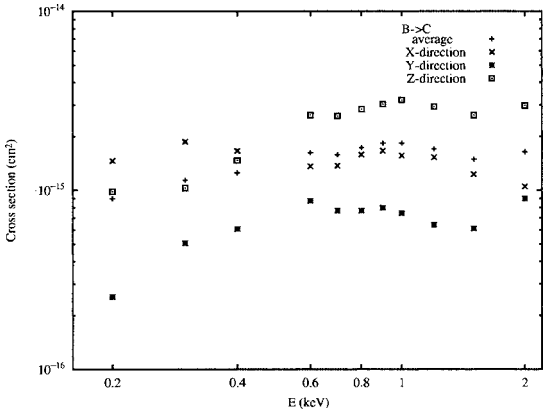

Fig. 4. Total cross sections from the initial state B to the charge transferred state C.

References

1) M. Kimura et al.: Phys. Rev. A **54**, 5019 (1996).
2) S. N. Rai et al.: Int. J. Qantum Chem. **95**, 866 (2003).

Transient field of ^{24}Mg ions in Gd at high velocities

H. Ueno, A. Yoshimi, Y. Kobayashi, W. Sato,[*1] H. Watanabe,[*2] H. Miyoshi,[*3] K. Shimada,[*3] D. Kameda,[*3] G. Kato,[*3] T. Haseyama, S. Emori,[*3] G. Kijima,[*3] M. Tsukui,[*3] and K. Asahi

Transient field (TF) is an effective magnetic field acting on ions passing through ferromagnetic foils. Because of large TF strengths, a large number of nuclear magnetic moments have been measured for short-lifetime excited states on stable nuclei. Such measurements have been carried out using stable-ion beams at velocities $v \ll Zv_0$, since the velocity dependence of the TF strength $B_{\rm TF}$ is well known in this region.[1)] Taking into account the fact that radioactive-isotope beams produced in the projectile-fragmentation reaction have high velocities $v \geq Zv_0$, it is important to determine the velocity dependence of $B_{\rm TF}$ at a velocity of approximately Zv_0 or higher, where Z and v_0 denote the atomic number and the Bohr velocity.

The experimental setup, which was developed to carry out the TF experiments with high-velocity beams,[2,3)] was used for the present measurement of TF strength at the velocities $v \sim Zv_0$. A ^{24}Mg beam obtained from the $K = 70$ RIKEN AVF cyclotron was used to bombard a target at the energy $E = 7.5A$ MeV. The target consisted of two layers, Au and Gd, with thicknesses of 8.1 and 8.4 mg/cm^2, respectively, allowing us to determine TF strength at the beam velocity $v = 14.2v_0$. The typical beam current was $I = 0.1$ pnA. The $I^\pi = 2^+$ first excited state of ^{24}Mg at the excitation energy $E_{\rm x} = 1.369$ MeV, whose g-factor and lifetime are $g = +0.51(2)$ $\mu_{\rm N}$ and $\tau = 1.35(3)$ ps, respectively, was populated by Coulomb scattering from Au consisting of the upstream layer of the target. The γ-rays emitted from the excited projectiles were detected coincidentally with scattered particles with a pair of NaI(Tl) detectors placed symmetrically at the angle $\theta_{\rm L} = \pm 50^\circ$ relative to the beam axis.

For a small precession of the nuclear moment, $B_{\rm TF}$ strength can be determined by combining the obtained γ-ray angular distribution $W(\theta_{\rm L})$ and double ratio $R^{\uparrow}_{\rm LR}/R^{\downarrow}_{\rm LR}$ of the photo-peak counting rates measured using a pair of NaI detectors in an external magnetic field of $B_{\rm ext} = 450$ Gauss in the "up" and "down" directions.[4)] For the reduction in the systematic error due to beam-profile fluctuation, the $B_{\rm ext}$ direction was changed periodically every 15 seconds. The obtained photo-peak counting rates measured at several angles shown in Fig. 1 were fitted using the Doppler-corrected angular distribution function. The obtained typical γ-ray spectrum is also shown in Fig. 1. We have thus determined a preliminary value of $B_{\rm TF} = 1.2(2)$ kT.

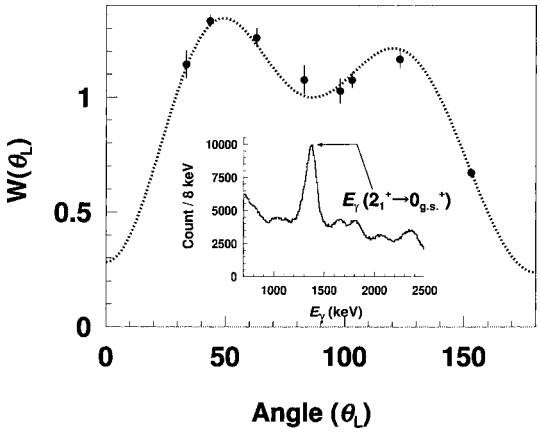

Fig. 1. A measured γ-ray angular distribution and a typical γ-ray spectrum for the de-excitation γ rays from the 2^+_1 excited state of ^{24}Mg. The dotted curve shows the result of peak-fitting analysis.

At lower velocities $v \ll Zv_0$, TF strength is approximately given by[1)]

$$B_{\rm TF} = a \cdot Z \cdot v/v_0, \tag{1}$$

where a is the strength parameter. The a value was found to be 17 T for Gd.[5)] Although the present data shows a large attenuation compared with the $B_{\rm TF}$ strength obtained from Eq. (1), it is still larger than the prediction of previous models,[6)] where a sharp decrease in TF strength is predicted at velocities $v \geq Zv_0$. The present result supports a recent model,[7)] with which a rather constant or even increasing trend of $B_{\rm TF}$ strength is predicted at velocities $v \geq Zv_0$. Moreover, this observation is in agreement with other measurements obtained at similar velocities.[8,9)]

In the present experiment, several targets having various thicknesses of Au layers were also used, which allowed us to determine the velocity dependence of TF strength at a velocity of approximately $\sim Zv_0$. The data analysis of these targets is in progress now.

*1 Department of Chemistry, Osaka University
*2 Department of Nuclear Physics, Australian National University, Australia
*3 Department of Physics, Tokyo Institute of Technology

References

1) J. L. Eberhardt et al.: Hyperfine Interact. **3**, 195 (1977).
2) H. Ueno et al.: Hyperfine Interact. **136/137**, 211 (2001).
3) A. Yoshimi et al.: Nucl. Phys. A **738**, 519 (2004).
4) M. Forterre et al.: Phys. Rev. C **11**, 1976 (1975).
5) G. Jakob et al.: Z. Phys. D **32**, 7 (1994).
6) G. Hagelberg et al.: Z. Phys. D **17**, 17 (1990).
7) F. Hagelberg et al.: Phys. Rev. C **48**, 2230 (1993).
8) K.-H. Speidel et al.: Z. Phys. A **339**, 265 (1991).
9) J. Cub et al.: Nucl. Phys. A **549**, 304 (1992).

Seismological analyses of acoustic emission in solids by 95 MeV/u Ar ions

T. Kambara, K. Kageyama,* Y. Kanai, T. M. Kojima, Y. Nakai, A. Yoneda, and Y. Yamazaki

Radiation penetrating in solids can produce defects which generate stress and strain, and thus acoustic waves in ultrasonic frequencies. We have analyzed experimental acoustic waveforms from solids irradiated with fast heavy ions to study dynamical processes in irradiation effects.

An experimental procedure was reported previously[1,2] where polycrystalline metals (Al and Cu) and single-crystal BaF_2 were irradiated with a single-bunch beam of 3.8-GeV Ar ions from the RIKEN Ring Cyclotron. Figure 1 shows the geometrical arrangement, where an ion beam impinges on a sample plate with a thickness of $D \approx 10$ mm, and stops at a depth L. For L we take the range of the 3.8-GeV Ar ion estimated with the TRIM code;[3] the L's are 4.24 mm for Al, 1.53 mm for Cu and 3.06 mm for BaF_2. The maximum of the energy deposition by the ions, the Bragg peak, is close to the end of the range, therefore the source of the wave is assumed to be at the end of the ion range and the point on the back plane just above it is called the epicenter (E). A piezoelectric sensor is on the back of the plate at a distance x from E, at an azimuth angle $\theta = \arctan[x/(D-L)]$, and a distance $r = (D-L)/\cos\theta$ relative to the source. The sensor is sensitive only to the component of the displacement perpendicular to the surface.

Seismological formulations are employed in the analyses. In a bulk solid, there are two modes of acoustic waves, the compressional wave (P wave) and shear wave (S wave). Since the P wave is always faster than the S wave, they can be identified by their arrival time. The dynamics of the source of the waves is described by a 3×3 moment tensor. The waves at different positions are determined by the moment tensor and a Green function. Here we use a Green function for infinite, isotropic and homogeneous elastic media. In ion-beam irradiations, axial symmetry permits two types of source motion; an isotropic expansion and a uniaxial expansion in the beam direction. The isotropic expansion can generate only isotropic P waves. On the other hand, the uniaxial expansion generates P and S waves which have a common time-dependent waveform but different angular dependence and the maximum amplitude of the S wave is larger than that of the P wave.

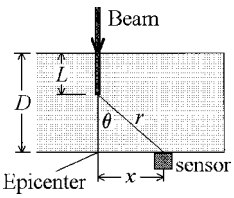

Fig. 1. Geometrical relationship between irradiated sample, beam, and sensor.

Under the present experimental conditions, the P-wave amplitude from an isotropic expansion, which is observed by the sensor, is proportional to $\cos^2\theta$. In the case of uniaxial expansion, the observed P-wave amplitude is proportional to $\cos^4\theta$ and the S-wave amplitude to $\cos^2\theta\sin^2\theta$, therefore the observed P-wave amplitude has maxima at $\theta = 0°$ and 180°, while the S wave has maxima at 45° and 135°. Since the S wave is not generated by an isotropic expansion, an S wave observed at $\theta \approx 45°$ should be a clear indication of the anisotropy of the deformation at the source.

The experimental waveforms show clear P-wave signals for all the samples but no obvious structure at the S-wave arrival time. Figure 2 shows the height of the first peak in the observed P wave as a function of θ for the three samples. The solid line in the figure is a $\cos^2\theta$ curve which is expected from the isotropic expansion. There is good agreement between the experimental plots and the curve. This angular dependence and the fact that the S wave is not observed in the waveforms at $\theta \approx 45°$ indicate that the deformation due to the irradiation is almost isotropic in the present case.

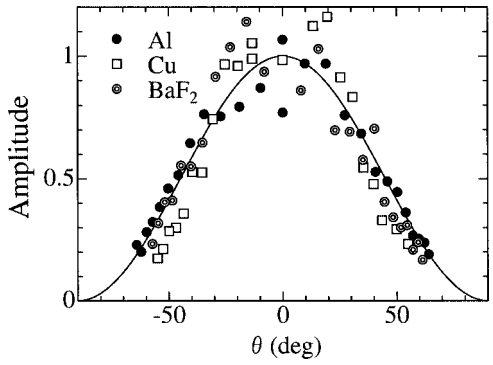

Fig. 2. Onset peak height of acoustic P wave by sensor plotted against azimuth angle. Curve is amplitude estimated for P wave from isotropic expansion.

* Department of Engineering, Saitama University

References

1) T. Kambara et al.: Nucl. Instrum. Methods Phys. Res. B **193**, 371 (2002).
2) T. Kambara et al.: RIKEN Accel. Prog. Rep. **36**, 97 (2003).
3) J. F. Ziegler, J. P. Biersack, and U. Littmark: *The Stopping and Range of Ions in Solids* (Pergamon Press, New York, 1985).

Effect of GeV ion irradiation on magnetic property of equiatomic FeRh alloys

M. Fukuzumi,[*1] Y. Chimi,[*2] N. Ishikawa,[*2] F. Ono,[*3] T. Kambara, and A. Iwase[*1]

It is well known that equiatomic FeRh alloy shows a first-order magnetic transition near the room temperature, where a low-temperature antiferromagnetic (AF) phase transforms to a high-temperature ferromagnetic (FM) phase.[1)] Below the transition temperature, this alloy shows atiferromagnetic down to liquid-helium temperature. In this paper, we report that GeV heavy ion irradiation stabilizes the ferromagnetic phase of FeRh alloy even at 5 K.

Specimens used for the present experiment were Fe-50at.%Rh alloys, the dimensions of which were 5.0 mm × 5.0 mm × 0.3 mm. The X-ray profiles of the specimens showed that most peaks could be identified as corresponding to a B2 ordered structure. The specimens were irradiated at room temperature with 3.5 GeV (26 MeV/u) Xe ions at the fluence of 1×10^{12}/cm^2, 2.5×10^{12}/cm^2 or 5×10^{12}/cm^2 using the RIKEN Ring Cyclotron. After irradiation, the magnetization of the specimens was measured as a function of temperature under the magnetic field of 0.6 T using a Quantum Design SQUID magnetometer.

Figure 1 shows the temperature dependence of magnetization for the unirradiated specimen and those irradiated with Xe ions. The figure indicates a large change in magnetization near 300 K. This magnetization change corresponds to the magnetic transition from AF to FM phase. For the irradiated specimens, besides a large change in magnetization near room temperature, we can see a finite magnetization at low temperatures. As the projected range of 3.5 GeV Xe ions is smaller than the specimen thickness, the irradiated region is localized only near the surface, and some part of the specimen remains unirradiated. Therefore, the large change in magnetization near room temperature for the irradiated specimens indicates the AF-FM transition in the unirradiated region, and the finite the magnetization at the low temperatures means that the ferromagnetic phase is induced near the surface by irradiation. The irradiation-induced magnetization is still observed even at 5 K. In Fig. 2, the values of the magnetization at 5 K are plotted as a function of ion fluence. As can be seen in the figure, the magnetization increases with increasing ion fluence.

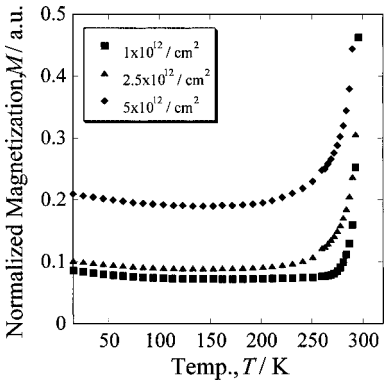

Fig. 1. Temperature dependence of magnetization for unirradiated and 3.54 GeV Xe ion-irradiated Fe-50at.%Rh specimens under magnetic field of 0.6 T.

Although the reason why the ferromagnetic phase is stabilized below room temperature by the Xe ion irradiation still remains uncertain, the magnetic property of non-equiatomic Fe-Rh alloys may give us a clue to the solution. The magnetic properties of Fe-Rh alloys strongly depend on the composition of Fe and Rh.[2)] The increase in Fe content by only 1–2% makes Fe-50at.%Rh alloys ferromagnetic even at low temperatures. Such a non-equiatomic Fe-50at.%Rh alloy includes some lattice disordering such as Rh atom vacancies and anti-site defects. Therefore, the present result suggests that irradiation-induced lattice disordering plays an important role in the stabilization of the ferromagnetic phase of Fe-50at.%Rh alloy.

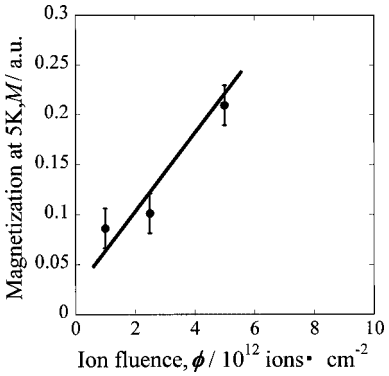

Fig. 2. Magnetization at 5 K as a function of ion fluence.

References

1) J. S. Kouvel and C. C. Hartelius: J. Appl. Phys. Suppl. No. 33, 1343 (1962).
2) L. Pal, G. Zimmer, M. P. Horvath, and J. Paitz: J. de Phys. **32**, C1-861 (1971).

*1 Osaka Prefecture University
*2 Japan Atomic Energy Research Institute
*3 Okayama University

Single-event burnout of super-junction power MOSFETs

N. Ikeda,[*1] S. Kuboyama,[*1] K. Oka,[*1] H. Ohira,[*2] H. Otomo,[*2] O. Shimada,[*2] N. Inabe and M. Kase

A power MOSFET (metal-oxide-semiconductor field-effect transistor) is a key device in a power circuit that has a low ON-resistance and a fast switching. A MOSFET to be used in space is required to have radiation hardness. Protons, heavy ions and other particles in space could cause single-event effects and lead to semiconductor device malfunction or failure. Single-event burnout (SEB) is the main concern regarding power MOSFETs. SEB is triggered by a heavy ion passing through the device when it is off. A transient current by such an ion turn on a parasitic bipolar transistor, which results in the burning out of the device and its possible destruction.[1)]

Recently, a new type of MOSFET called Super-Junction MOSFET (SJ-MOSFET) has been realized for high voltage usage. SJ-MOSFET has a new structure and has a considerably lower ON-resistance than standard MOSFETs. Although it is an attractive feature, no one has examined its SEB tolerance which is very important for space application.

JAXA (Japan Aerospace Exploration Agency) has conducted $^{58}Ni^{19+}$ irradiation tests of a 600 V SJ-MOSFET using the RIKEN Ring Cyclotron to determine its SEB tolerance. A standard MOSFET with almost the same specification was also irradiated as a reference. Energy, LET and the projected range of ions in a device were 673 MeV, 19 MeV/(mg/cm^2), and 122 μm, respectively.

The EPICS (Energetic Particle Induced Charge Spectroscopy) system developed by JAXA was introduced to observe SEB, and the spectra of collected charges were examined in the same manner as previous study.[2)] Typically, two peaks are observed in the spectra, which are here called the first peak and the second peak. A larger charge collection of the second peak implies less SEB tolerance.

Figure 1 shows the spectra of collected charges and the number of SEB occurrences of both types of MOSFET. SEB was observed at lower V_{DS} in the SJ-MOSFET (390 V) than in the standard MOSFET (410 V). Figure 2 shows the collected charge of the second peak to V_{DS} of both types of MOSFET. Although the collected charges of the SJ-MOSFET were smaller at lower V_{DS} than those of the standard MOSFET, they were almost the same in quantity and the gradient of the curve of the SJ-MOSFET was larger at higher voltages. These results suggest that the SJ-MOSFET is less immune to SEB.

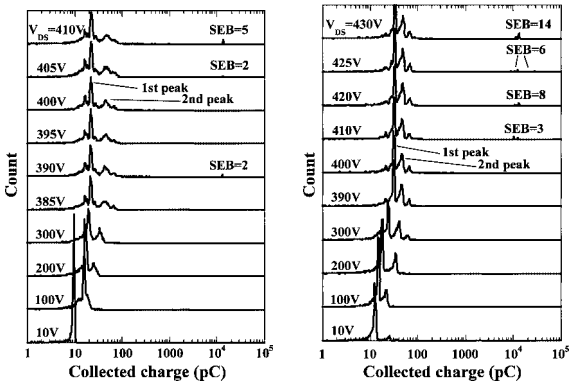

(a) SJ-MOSFET (b) standard MOSFET

Fig. 1. SEB spectra and number of SEB occurrences of an SJ-MOSFET and a standard MOSFET. SEB occurred at lower V_{DS} in SJ-MOSFET.

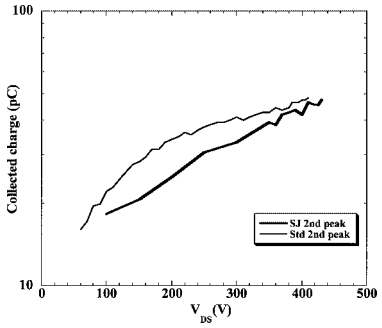

Fig. 2. Collected charges of second peak to V_{DS} of both types of MOSFET. Collected charge of the second peak of SJ-MOSFET was almost the same as that of standard MOSFET at high voltage, and the gradient of the curve was larger in SJ-MOSFET at high voltage.

References

1) JAERI and NASDA Joint Research Report, Vol. 2 (1999), p. II-9.
2) N. Ikeda et al.: RIKEN Acce. Prog. Rep. **37**, 98 (2003).

*1 Japan Aerospace Exploration Agency
*2 Ryoei Technica Company

Ion-track continuum: Its finding and material dependence

K. Kimura,* M. Koshimizu,* K. Asai,* H. Ryuto, and M. Kase

We have observed ultrafast luminescence (UFL, $\tau <$ 100 ps) from incipient heavy-ion track cores in insulator crystals such as alkali halides, metal oxides, and alkaline-earth halides, from measurements of decay curves and time-resolved spectra (TRS) with a time resolution of 85 ps.[1] UFL can be detected using not only fast sensitive detection techniques but also an appropriate beam condition to suppress the formation of energetic secondary electrons, that is, to make the track-core effects prominent. UFL is the first observed collective-behavior of an ion track. UFL was characterized by the insensitivity to temperature, nonlinearity of excitation-density dependence, and so on. Of these characteristics, the material dependence is described in this report. This is an important characteristic that distinguish UFL from the known radiation-induced continuum such as Bremsstrahlung, Cerenkov radiations, transition radiations, and intra band transitions. UFL in insulators is observable only because of extremely dense-energy deposition given by heavy ions, but seams impossible to observe using other sources, such as a laser or electron beam. Therefore, we refer to UFL as the ion-track continuum hereafter. Figures 1 and 2 show three-dimensional displays of wavelength-dependent decay curves of luminescence in Xe-ion bombarded single crystals of RbI and MgO at close to 4.2 K, respectively. There exists commonly the short-lived continuum extending from the vacuum UV to the visible range. Experimental results suggest that the continuum originates from radiative recombination forced by interaction among adjoining e-h pairs.[1,2] The structure of the continuum can be explained by self-hole trapping. Untill the group of ejected electrons returns to the group of holes located along the track center, holes can be trapped since the hole trapping is so fast as to be complete in 2 ps.[2] The recombination luminescence of e-h pairs decreases the energy gap according to the depth of the hole-trapping, namely according to the Stokes shifts. Also, the continuum has higher density of states at the trapped holes to make a structure. Actually, the continuum has peaks at wavelengths close to self-trapped excitons (STE). Thus, the continuum may look like the hot luminescence band of the STE. This fact is distinct in alkali halides in which knowledge about the STE is complete.[2] As for RbI, STEs are known to have peaks at 318, 400, and 539 nm. The ion-track continuum has an evident peak around 318 nm although the continuum and STE luminescence are superposed and also projections near 400 and 539 nm although they are weak. MgO has an intense band at 180 nm in the vacuum

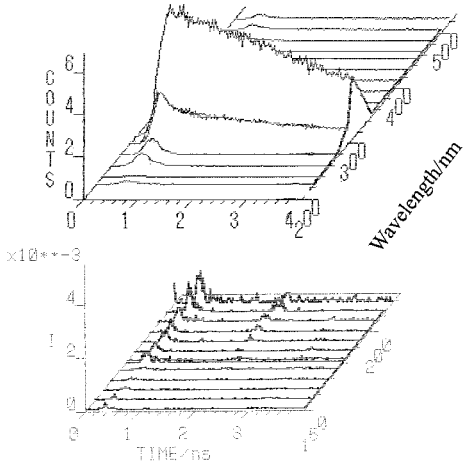

Fig. 1. Wavelength-dependent luminescence decay curves of Xe-ion bombarded single crystals of RbI at 6 K.

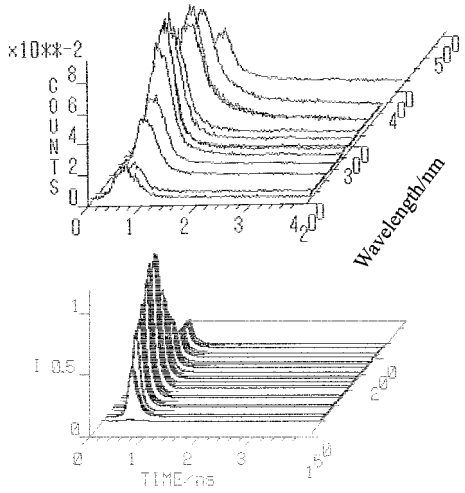

Fig. 2. Wavelength-dependent luminescence decay curves of Xe-ion bombarded single crystals of MgO at 6 K.

UV region (Fig. 2). This band can be ascribed to the ion-track continuum. Moreover, was found the important fact that the continuum precedes the free-exciton formation of which luminescence at 162.4 nm is principal in case of photon- or electron excitations. This result is proved from the fact that Xe-irradiation gives the continuum but no free exciton luminescence and also the fact that at room temperature, Ar-irradiation gives the intense 180-nm band but the free-exciton band disappeared. According to the results obtained for alkali halides, the 180-nm band implies the hole-trapping with the depth corresponding to Stokes shift, although the depth is much shallower compared with

* Department of Applied Chemistry, Tohoku University

alkali halides. Some references suggest that STE luminescence exists at 180 nm[3,4], although its intensity is negligibly small. On the other hand, the 180-nm band is different on some points from e-h plasmas known for semiconductors: the shift of the latter much smaller and is not Stokes shift but due to binding energy between e-h pairs. The former emission occurs at much higher density of e-h pairs. Now, a significant procedure to predict final products emerged. In case of excitation beyond ionization, one can predict radiative or non-radiative relaxation processes or products formations by considering likely reactions between holes and lattice during the travel of ejected electrons, that is independent of any source such as photons, electrons, or ions. For examples, in MgO, the hole is $O^-$and the valence state is O^{2-} ; For RbI, the hole I^0 and the valence I^-.

Lastly, the largest efficiency of alkali halides are given by iodides such as RbI and CsI, and with decreasing mass of the halogens, the efficiencies decrease by three orders of magnitude untill fluorides. The efficiency is almost independent of the type of metal ions. This independence may be due to large spin-orbit coupling of heavy halogens. On the other hand, the ion-track continuum can be scarcely observed for SiO_2, and cannot be observed at all for diamonds. Holes in ionic crystals X^- is isolated, that is, the hole has no network of phonons, whereas holes in a covalent crystal keeps bonds with surrounding and then has a network of phonons. The network works as energy dispersion paths such that excess energy is not necessary to rely photoemission.

References

1) K. Kimura, J. Kaneko, S. Sharma, W. Hong, and N. Itoh: Phys. Rev. B **60**, 12626 (1999); K. Kimura, S. Sharma, and A. Popov: Radiat. Meas. **34**, 99 (2001); Nucl. Instrum. Methods Phys. Res. B **191**, 48 (2002).
2) K. Kimura: Nucl. Instrum. Methods Phys. Res. B **212**, 123 (2003).
3) Z. A. Rachiko and J. A. Valbis: Phys. Stat. Sol. (b) **98**, 161 (1979).
4) M. Kirm, S. Vielhauser, G. Zimmerer, A. Lushchik, and Ch. Lushchik: Surf. Rev. Lett. **9**, 1363 (2002).

Time-resolved luminescence spectra of ion-irradiated alpha-alumina in VUV region

M. Koshimizu,* K. Kimura, H. Ryuto, K. Asai,* and M. Kase

The irradiation effects of heavy ions in insulators have been attracting considerable interest. It has been pointed out that self-trapped excitons (STEs) play a crucial role in the irradiation effects, particularly in the formation of an ion track.[1] In our previous study on MgO, however, it was shown that the luminescence band due to free excitons disappeared and the intensity of the peak possibly due to dense e-h pairs with some lattice relaxation increased at higher excitation density,[2] indicating that the formation of excitons from e-h pairs does not occur before relaxation of holes accompanying lattice deformation. In order to further investigate the influence of the hole relaxation on the dynamics of the electron-lattice system under high-density excitation, we analyzed the high-density excitation effects in alpha-alumina, where the relaxation of holes or excitons has been discussed by many researchers.

Time-resolved luminescence spectra of alpha-alumina under irradiation of Xe ions at the energy of 2.0 MeV/nucleon in the VUV region are shown in Fig. 1. The time-resolved spectra at various temperatures are characterized by two decaying components. The fast component has a lifetime of approximately 100 ps, which is independent of temperature. Also, its intensity seems rather insensitive to temperature. On the other hand, the temperature-dependence of the slow component is complicated. Below 15 K, the lifetime of the slow component increases with increasing temperature, whereas it decreases as the temperature increases above 77 K, and the slow component almost disappears at 300 K. The fast component is broadly distributed beyond 200 nm and has a peak at a longer wavelength than the slow component.

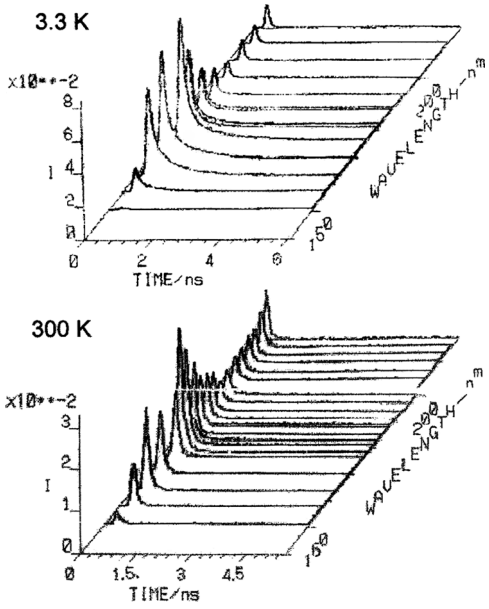

Fig. 1. Time-resolved luminescence spectra of alpha-alumina at 3.3 and 300 K.

The characteristics of the fast component are exactly analogous to the fast luminescence band observed for MgO[2] and other alkali-halides[3–5] under heavy-ion irradiation. The possible origin of these bands is the dense e-h pairs analogous to the electron-hole plasma in semiconductors, accompanied by some lattice relaxation similar to polarons. A gigantic oscillator strength is expected for such dense e-h pairs analogous to the case of semiconductors, which explains the extremely fast decay of these bands. These bands cannot be seen in the case of electron irradiation.

The temperature dependence of the slow component, on the other hand, is similar to the previous result under electron irradiation, where the efficiency of the band at 7.5 eV reached the maximum value at approximately 40 K.[6] The origin of this band is certainly ascribed to the STEs[6] or self-shrunk excitons,[7] which are STEs when electrons or holes do not individually undergo self-trapping. However, the decay rate of the slow component is even faster than the fastest component of the STE band observed under electron irradiation. This difference is possibly due to nonradiative annihilation due to STE-STE interaction, which is reported for ion-irradiated BaF_2.[8]

Interestingly, the peak of the fast band of alpha-alumina is rather clear compared to that of alkali-halide, and is located on the longer-wavelength side of the STE band. This result strongly suggests that the the origin of the fast band is accompanied by a similar lattice deformation to that of the STE.

*1 Department of Applied Chemistry, Tohoku University

References

1) N. Itoh and A. M. Stoneham: Nucl. Instrum. Methods Phys. Res. B **146**, 362 (1998).
2) K. Kimura, M. Koshimizu, K. Asai, and M. Kase: RIKEN Accel. Prog. Rep. **37**, 99 (2004).
3) K. Kimura et al.: Radiat. Meas. **34**, 99 (2001).
4) K. Kimura et al.: Nucl. Instrum. Methods Phys. Res. B **191**, 48 (2002).
5) K. Kimura: Nucl. Instrum. Methods Phys. Res. B **212**, 123 (2003).
6) J. Valbis and N. Itoh: Radiat. Eff. Defects Solids **116**, 171 (1991).
7) M. Kirm et al.: Phys. Rev. B **60**, 502 (1999).
8) K. Kimura et al.: Phys. Rev. B **58**, 6981 (1998).

Coincidence measurements between L X-rays and final charge states of Ar ions after passing Ni microcapillary

Y. Kanai, Y. Nakai, Y. Iwai, T. Ikeda, M. Hoshino, K. Nishio,* H. Masuda,* and Y. Yamazaki

A slow highly charged ion passing through a microcapillary target captures target valence electrons into high-n orbitals while keeping inner shell vacancies.[1] To study the production and decay processes of such highly excited ions, we have measured the L X-ray spectra in coincidence with the final charge states of Ar ions after passing a Ni microcapillary by changing the number of initial inner-shell (L-shell) vacancies.[2,3] The experiments were carried out at the Slow Highly Charged Ion Facility at RIKEN.[4] 2.8 keV/u Ar^{qi+} (q_i = 14, 13, 11 and 9) ions from a 14.5 GHz ECR ions source were used. The beams impinged on a Ni microcapillary target[5] along the capillary axis. A Si(Li) X-ray detector, which was placed at 90° to the beam axis, detected the X-rays emitted from the excited Ar ions after passing the microcapillary target. We have obtained L X-ray spectra, their shapes and energy positions, and X-ray yields as functions of delay time t_d, as well as integrated delayed X-ray yields, in coincidence with the final charge states q_f of Ar ions. The integrated delayed X-ray yield η (t_d, q_f) is given

$$\eta(t_d, q_f) = \int_{t_d}^{T} \zeta(t, q_f) dt, \quad (1)$$

where $\zeta(t, q_f)$ is the intensity of the L X-rays emitted from the ions with q_f at t after passing the target, and T is the maximum observable delay time where T = 14 ns in our experiments.

In this report, we summarize our experimental results:

(1) the peak energy of the coincidence X-ray spectrum $d\eta/dE$ shifts to a lower energy region with decreasing final charge states q_f, *i.e.*, with increasing number of electrons being stabilized $N_s = (q_i - q_f)$, and does not depend on the delay time t_d,

(2) the shape of the X-ray spectrum does not depend on t_d,

(3) the integrated delayed X-ray yields $\eta(t_d, q_f)$ for single-electron-stabilized ions ($N_s = 1$) decrease more rapidly than those for multielectron-stabilized ions ($N_s \geq 2$), except for $q_i = 9$,

(4) the integrated delayed X-ray yields show a long decay time ($\sim$ ns), and

(5) the integrated delayed X-ray yields for t_d = 0 ns are almost the same as those for the ions, which have multiple L-shell holes at the moment of the X-ray emission.

Experimental results (1) and (2) indicate that the core charge states q_c of Ar ions at the moment of the L X-ray emission depend only on the final charge state q_f; $q_c = q_f + 1 = q_i - (N_s - 1)$, and do not depend on the delay time t_d after the target. These may be explained by the fact that the $(N_s - 1)$ of the L-shell holes are filled by a cascade of Auger processes rapidly ($\ll$ ns) and then the N_sth hole is filled by emitting L X-rays.

Experimental result (3) may be attributed to the radiative decay time of the N_sth electron from the excited state to the M shell as follws. The observed decay time τ_o of X-ray intensity is given by $\tau_o = \tau_A + \tau_d + \tau_{\text{L X-ray}}$, where τ_A is the decay time for a cascade of Auger processes to fill the $(N_s - 1)$ holes leaving one electron in an excited state (n_0, l_0), τ_d is the decay time for a cascade of radiative transitions from the (n_0, l_0) state to $n = 3$ states, $\tau_{\text{L X-ray}}$ is the decay time of the N_sth L-shell hole filled by the M-shell electron by emitting L X-rays. In general, the Auger cascade processes of multiply excited states are rapid, which is also indicated by our experimental results (1) and (2). Thus, τ_o can be reduced to $\tau_o \sim \tau_d + \tau_{\text{L X-ray}}$. It is difficult to explain the difference between the observed decay time for $N_s = 1$ and that for $N_s \geq 2$ using the difference in $\tau_{\text{L X-ray}}$; because there is no reason that the $\tau_{\text{L X-ray}}$ for $N_s = 1$ must be always shorter than that for $N_s \geq 2$. Therefore, we consider that τ_d is different between the $N_s = 1$ and $N_s \geq 2$ cases.

If the excited state (n_0, l_0) has small angular momenta, such as s, p and d, the excited electron rapidly decays into the L-shell hole by emitting X-rays. Thus, our observed $\sim$ ns decay time (experimental result (4)) should be related to the higher angular momentum excited states $l_0 \gg 1$.

Based on the image mentioned above, (a) if the N_sth electron is left in the excited state by the final Auger transition, the Ar ion emits L X-rays. On the other hand, (b) if the N_sth electron fills an L-shell hole by the final Auger transition, the Ar ion does not emit L X-rays. The branching ratio between processes (a) and (b) depends on the electronic configuration before the final Auger transition. Experimental result (5) indicates that the branching ratio is almost the same for the ions with multiple L-shell holes at the moment of the L X-ray emission.

* Department of Applied Chemistry, Tokyo Metropolitan University

References

1) S. Ninomiya et al.: Phys. Rev. Lett. **78**, 4557 (1997).
2) Y. Kanai et al.: RIKEN Accel. Prog. Rep. **36**, 109 (2003).
3) Y. Kanai et al.: RIKEN Accel. Prog. Rep. **37**, 104 (2004).
4) Y. Kanai et al.: Phys. Scr. T **92**, 467 (2001).
5) Y. Masuda et al.: Appl. Phys. Lett. **71**, 2770 (1997).

Coincidence measurements of X rays and final charge states of N ions transmitted through Ni microcapillaries

Y. Iwai, Y. Kanai, Y. Nakai, T. Ikeda, M. Hoshino, H. Oyama, K. Ando, H. Masuda,[*1] K. Nishio,[*1] H. A. Torii,[*2] K. Komaki,[*2] and Y. Yamazaki

K X rays emitted from 2.1 keV/u N ions which passed through a thin Ni microcapillary foil were measured in coincidence with a final charge state q_f in the cases of incident charge states of $q_i = 7$ and 6. Ninomiya et al. measured X rays in coincidence with a final charge state q_f for N^{6+} ions incident on the microcapillary target.[1)] They found that the K-hole lifetimes were ∼ns even when several electrons were in the L shell. In this work, N^{7+} ions as well as N^{6+} ions were selected as projectiles so that the relaxation dynamics with different numbers of inner-shell vacancies can be studied.

Ions (2.1 keV/u $N^{6,7+}$) are supplied by a 14.5 GHz Caprice electron cyclotron resonance ion source in RIKEN.[2)] The microcapillary target was ∼1 mm^2 in area with a thickness of ∼1 μm and had a multitude of straight holes of ∼200 nm in diameter.[3)] A windowless Si(Li) X-ray detector was installed at 90 degrees with respect to the incident ion beam. A shield located between the ion beam and the detector was movable along the ion beam and was used to limit the detection region of delayed X rays. When the shield is located at z, the detector can capture X rays emitted at time 17 ns $> t > z/v$, where v is the projectile velocity. The ions passed through the microcapillary target were charge-state analyzed with an electrostatic deflector and detected by a channel electron multiplier.[4)]

The solid and open circles in Fig. 1 are for the coincidence spectra with the X-ray detector for (q_i, q_f) = (7,6) setting the shield at 0 mm and 1 mm, respectively. The solid line shows the spectrum measured with a high-resolution spectrometer for $q_i = 7$ immediately downstream of the Ni microcapillary foil.[5)] It is then concluded that the coincidence X rays with (7,6) were primarily attributed to 2p - 1s transition.

Figure 2 shows the coincidence X-ray yields as a function of the shield position. It is seen that the X-ray yield for (7,5) was almost the same with that for (6,5), and the same is true for (7,4) and (6,4), i.e., the coincidence X-ray yields did not depend on the number of K-shell holes of the incident ions but on the final charge state q_f. The coincidence X-ray yield for (7,6) decreased faster than those with other (q_i, q_f)-combinations. The solid line in Fig. 2 shows the integrated K X-ray yield obtained via the cascade calculation of one electron ion initially populated according to the report of visible light measurement.[6)] It is seen that the calculation can crudely reproduce the experimental result for (7,6).

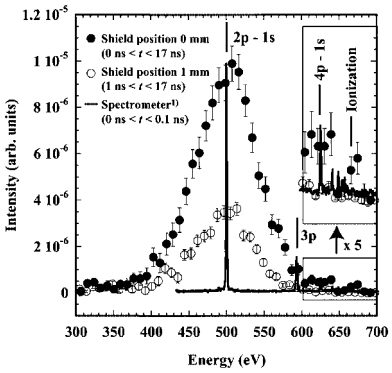

Fig. 1. Energy spectra of nitrogen K X rays with (q_i, q_f) = (7,6). A spectrum of X rays measured with a high-resolution soft X-ray spectrometer is shown for comparison.[5)] The bars with transition terms show transition energies.

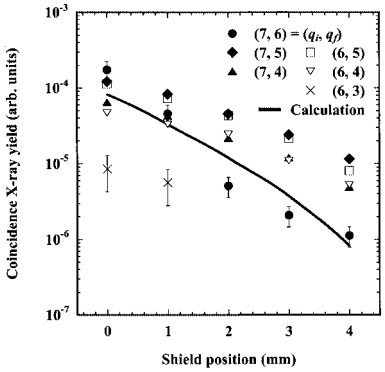

Fig. 2. Integrated coincidence X-ray yields as a function of the shield position for incident and final charge state combinations. The solid line shows the integrated K X-ray yield obtained via cascade calculation.

*1 Department of Applied Chemistry, Graduate School of Engineering, Tokyo Metropolitan University
*2 Institute of Physics, Graduate School of Arts and Sciences, University of Tokyo

References
1) S. Ninomiya et al.: Phys. Rev. Lett. **78**, 4557 (1997).
2) Y. Kanai et al.: Phys. Scr. T **92**, 467 (2001).
3) H. Masuda et al.: Appl. Phys. Lett. **71**, 2770 (1997).
4) Y. Kanai et al.: Nucl. Instrum. Methods Phys. Res. B, in print.
5) Y. Iwai et al.: Nucl. Instrum. Methods Phys. Res. B **193**, 504 (2002).
6) Y. Morishita et al.: Phys. Rev. A **70**, 012902 (2004).

Single and double electron capture processes in slow N^{5+}-He collisions

Y. Miyamoto,* M. Hoshino, N. Tanaka,* K. Yamashita,* Y. Kanai, M. Kitajima,* Y. Nakai, H. Tanaka,* and Y. Yamazaki

The angle-resolved energy gain spectra of N^{5+}-He collisions have been measured at an impact energy of 140 eV/q. Several experimental[1–6] and theoretical[7] works on N^{5+}-He collisions have been reported for single electron capture above 1 keV/q. Partial cross sections for single electron capture have been determined by vuv photon emission spectroscopy.[8–10] It has been found that the dominant final states are $N^{4+}(1s^2 3s\ ^2S)$, $N^{4+}(1s^2 3p\ ^2P)$ and $N^{4+}(1s^2 3d\ ^2D)$. However, there has been no state-selective measurement of double capture in the low energy region. Therefore, we measured the state-selective angular distributions at 140 eV/q.

The experiment was carried out using a crossed-beam apparatus, which was positioned at the beam line BL2 of the 14.5 GHz Caprice-type ECRIS in the slow highly charged ion beam facility. Details of our experimental setup have been described elsewhere.[11,12] The typical current and energy resolution of the energy selected N^{5+} beam at 140 eV/q were 50 pA and 1 eV/q, respectively.

The angle-resolved energy gain spectra for single and double electron capture were measured at the scattering angle θ of 0°–10° with a 0.5° step. From these energy gain spectra we constructed a 2D contour map of the scattered ion intensity with respect to the energy gain ΔE and scattering angle θ of projectiles in the laboratory system. The kinematic relationship between ΔE and θ can be derived from the energy and momentum conservation for a Q-value, where the Q-value is the energy release of the reaction. When the Q-value is specified, a unique curve is drawn on the 2D contour map. This curve shows the relationship between ΔE and θ of the scattering ions in a certain final channel.

Figure 1 shows the 2D contour map of N^{3+} ions produced in N^{5+}-He collisions at the energy of 140 eV/q. Solid curves show the relationship between ΔE and θ for the final channels $N^{3+}(1s^2 2s3l)$, $N^{3+}(1s^2 2s4l)$, $N^{3+}(1s^2 2p3l)$, $N^{3+}(1s^2 2s5l)$, $N^{3+}(1s^2 2s8l)$ and $N^{3+}(1s^2 2p4l)$. In Fig. 1, double electron capture into the $N^{3+}(1s^2 2snl)$ state (n = 3–5) and the $N^{3+}(1s^2 2pn'l)$ state (n' = 3, 4) are observed. At smaller scattering angles, electron capture into the $N^{3+}(1s^2 2s3l)$ state, the N^{3+} $(1s^2 2s4l)$ state and the $N^{3+}(1s^2 2p4l)$ state show strong intensities. At large scattering angles electron capture into the $N^{3+}(1s^2 2s5l)$ state shows strong intensities. The intensities of the peaks of each final state markedly change with changing scattering angle. By adopting the classical over-barrier model,[13] the final states can be predicted as $N^{4+}(1s^2 3l)$ and $N^{3+}(1s^2 2l3l')$ for single and double electron capture, respectively. However, there are discrepancies between the model and our results and we observed many more final states than predicted by the model.

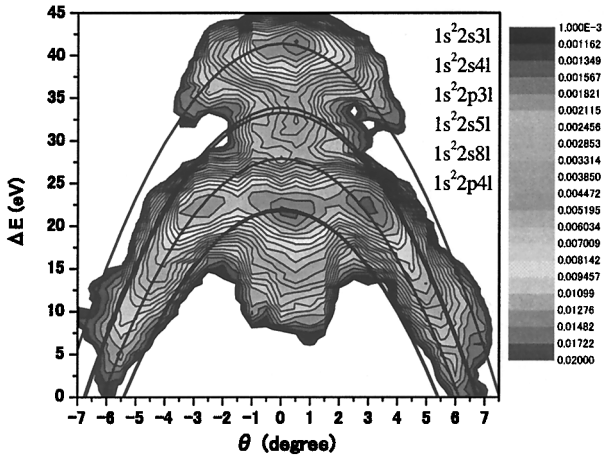

Fig. 1. 2D contour map of N^{3+} ions from double electron capture for N^{5+}-He at collision energy of 140 eV/q.

References

1) K. Okuno et al.: Phys. Rev. A **28**, 127 (1983).
2) W. Waggoner et al.: Phys. Rev. A **37**, 2386 (1987).
3) T. Iwai et al.: Phys. Rev. A **26**, 105 (1982).
4) L. D. Gardner et al.: Phys. Rev. A **20**, 766 (1979).
5) D. H Grandall: Phys. Rev. A **16**, 958 (1977).
6) K. Ishii et al.: Phys. Rev. A **70**, 042716 (2004).
7) M. C. Bacchus-Montabonel: Phys. Rev. A **40**, 6088 (1989).
8) J. P. M. Beijers et al.: Phys. Rev. A **49**, 363 (1944).
9) P. H. Cotte et al.: Nucl. Instrum. Methods Phys. Res. B **9**, 743 (1985).
10) D. Dijkkamp et al.: J. Phys. B **18**, 4763 (1985).
11) Y. Kanai et al.: Phys. Scr. T **92**, 467 (2001).
12) M. Hoshino et al.: Nucl. Instrum. Methods Phys. Res. B **205**, 568 (2003).
13) A. Neihaus.: J. Phys. B **19**, 2925 (1986).

* Department of Physics, Sophia University

Theoretical study of electron capture in collisions of C^{4+} with He

L. Pichl,[*1] R. Suzuki,[*2] M. Hoshino, Y. Li,[*3] R. J. Buenker,[*3] M. Kimura,[*4] and Y. Yamazaki

Although the theoretical formalism of ion-atom collisions has been well established for a long time,[1] various cross-section calculations for electron capture relevant to fusion research, plasma diagnostics or astrophysics remain to be performed. The system of C^{4+} colliding with He is theoretically interesting because of its exothermic initial channel which intersects with numerous single- and double-capture states at shorter distances, and also the unusual dominance of double electron capture process. In addition, the single capture states exhibit long-range Coulomb asymptotics that effects the boundary conditions. The CHe^{4+} system also serves as a particular benchmark for measurements and theory calculations.[2]

In order to compare to recent measurements in RIKEN[3] which reported angular differential cross sections for double electron capture (energy 240, 320 and 440 eV) we have computed the electronic potential energy curves and radial couplings in the singlet state manifold. These are used in subsequent close-coupling calculations. Because of the relatively high energy, a large number of partial waves is required. Since the asymptotic energy level separation compares to the kinetic energy, a common trajectory approximation does not apply. The calculated values of angular-differential cross sections are sensitive to the details of the potential energy curves.

The electronic potential energy curves (PEC) and radial couplings were computed with the multi-reference single- and double-excitation configuration interaction method (MRD-CI[4]). A standard gaussian basis set has been used ([5s4p3d2f1g] for C and [4s3p2d1f] for He) and augmented by diffuse functions. The energy selection threshold and number of configurations is $0.1\,\mu E_h$ and 500,000, respectively. Radial couplings are calculated by using numerical derivatives of the CI wave functions. The PEC and couplings define the diabatic representation of the system. Our ab initio results are shown in Fig. 1; the electronic states are assigned to carbon ions in increasing order (at R = 100 a.u.) as $1s^22s^1(He^+)$, $1s^22s^2$ (main double capture channel), $1s^22p^1(He^+)$, $1s^22s^12p^1$, $1s^22p^2$, $1s^22p^2$, $1s^22s^13s^1$, $1s^23s^1(He^+)$, and $1s^2$(He) (the initial state for electron capture in C^{4+}|He collision). Note the long-range series of sharp near-diabatic crossings along the initial channel in the figure.

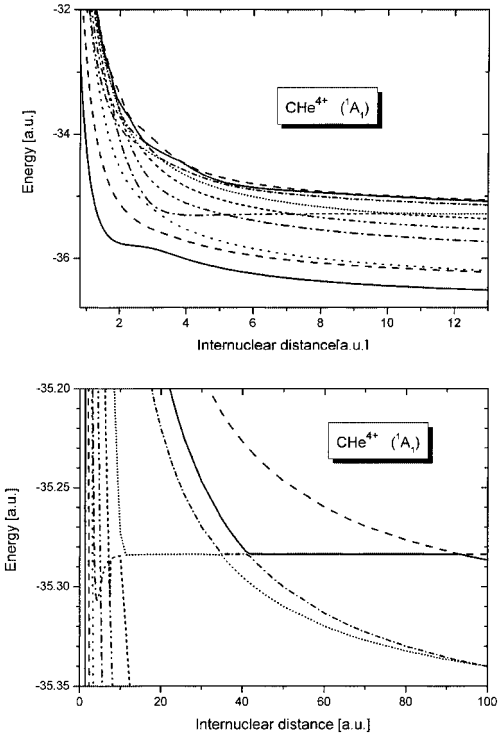

Fig. 1. Potential energy curves of CHe^{4+} system.

Our first results of quantal scattering calculations indicate a good qualitative agreement with the experimental angular-differential cross sections.[3] Stueckelberg oscillations are seen as a result of interference between electronic states. The double capture cross sections appear to include both the direct mechanism as well as a sequence of the single capture processes. A comparison with other theoretical calculations is in progress.

References

1) M. Kimura and N. F. Lane: Adv. At. Mol. Opt. Phys. **26**, 79 (1989).
2) N. Keller, L. R. Andersson, R. D. Miller et al.: Phys. Rev. A **48**, 3684 (1993).
3) M. Hoshino, M. Kitajima, Y. Kanai, Y. Nakai, H. Tanaka, and Y. Yamazaki: Phys. Scr. T **92**, 339 (2001).
4) R. J. Buenker and R. A. Phillips: J. Mol. Struct. Theochem **123**, 291 (1985).

*1 Department of Computer Software, University of Aizu
*2 Computer Center, Hitotsubashi University
*3 Bergische Universitaet Wuppertal, Germany
*4 Graduate School of Sciences, Kyushu University

Multiple-electron processes in close single collisions of Ne^{q+} ($q = 1$, 2, and 3) with Ar at 5 keV

M. Hoshino, T. Kambara, Y. Kanai, R. Schuch,* and Y. Yamazaki

A simplified description of electron transfer in highly charged ion (HCI)-atom collisions is given by the classical over barrier model,[1] which has been successfully describing single electron transfer in peripheral collisions, where most of the cross section can be found. A very small amount of the differential cross section is at a large scattering angle. Therefore, multiple electron processes, which include not only electron capture but also ionization processes, can be expected to become dominant.

To study the multiple electron processes in large-angle scattering, we have measured the charge state correlation between the scattered and recoil ions as a function of incident charge states in collisions of 5 keV Ne^{q+} ($q = 1, 2$, and 3) with Ar atoms. The corresponding distance of the closest approach is estimated to be about 0.6 a.u. using the screened Coulomb potential,[2] which is by one order of magnitude smaller than the critical distance of electron capture from the classical over barrier model.

The experiment was carried out at the slow highly charged ion-beam facility. A 5 keV Ne^{q+} ($q = 1, 2$, and 3) beam from the 14.5 GHz Caprice ECR ion source was collimated on a localized Ar target from a needle. We used the experimental apparatus reported last year.[3] The scattered Ne and recoil Ar ions were detected at 27° and 70° as expected from the kinematics of elastic scattering, which corresponds to 40° in the CM system. Each ion detection telescope consists of a time-of-flight (TOF) drift tube and a two-dimensional position-sensitive detector with a microchannel plate. For each coincidence event, the positions of the scattered and recoil ions and the difference of the TOF values (ΔTOF) between these ions were recorded. With the drift tube biased on the electrostatic potential, one can modulate the ion velocity and determine the outgoing charge states using ΔTOF.

In Fig. 1, the charge state distributions of Ne and Ar ions are shown for $q = 1, 2$, and 3. For $q = 1$, the fraction of pure ionization ($q_{\mathrm{Ne}} = 1$) was found to be the largest. In the case of $q = 2$, the recoil charge states showed broader distributions, and single-electron capture with target ionization channels ($q_{\mathrm{Ne}} = 1$ and $q_{\mathrm{Ar}} > 1$) were the main channels. In $q = 3$, a single-electron capture with triple target ionization channel was the major channel. Double-electron capture channel ($q_{\mathrm{Ne}} = 1$) and pure target ionization channel

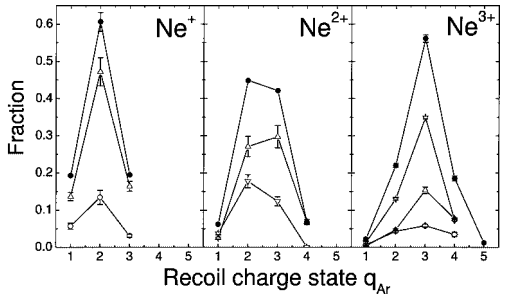

Fig. 1. Charge state distributions of Ne and Ar ions in Ne^{q+} ($q = 1, 2$, and 3)-Ar collisions at 5 keV. ●: total, ○: $q_{\mathrm{Ne}} = 0$, △: $q_{\mathrm{Ne}} = 1$, ▽: $q_{\mathrm{Ne}} = 2$, ◇: $q_{\mathrm{Ne}} = 3$.

($q_{\mathrm{Ne}} = 3$) were also observed.

Figure 2 shows the mean charge states of both the scattered ($\overline{q}_{\mathrm{Ne}}$) and recoil ($\overline{q}_{\mathrm{Ar}}$) ions as functions of incident charge state q, and the number of emitted electrons ($q_e = \overline{q}_{\mathrm{Ne}} + \overline{q}_{\mathrm{Ar}} - q$). The mean charge states of the scattered and recoil ions increase with q, while the number of emitted electrons q_e appears almost independent of q.

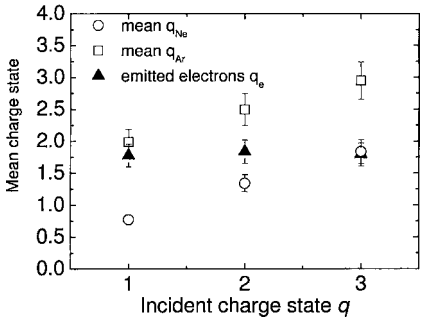

Fig. 2. Incident charge dependence of the mean charge state of the scattered and recoil ions, and the emitted electron number for $q = 1, 2$, and 3.

References

1) A. Niehaus: J. Phys. B **19**, 2925 (1986).
2) E. Everhart, G. Stone, and R. J. Carbone: Phys. Rev. **99**, 1287 (1955).
3) M. Hoshino et al.: RIKEN Accel. Prog. Rep. **37**, 105 (2004).

* Atomic Physics, Stockholm University, Sweden

Scheme for highly charged ion cooling with positron and electron

N. Oshima, M. Niigaki, A. Mohri, Y. Kanai, Y. Nakai, K. Komaki,* and Y. Yamazaki

The developments of electron cyclotron resonance (ECR) ion source and electron beam ion source (EBIS) have opened a new research field of slow highly charged ions (HCIs). However, the accessible kinetic energy (1–10 eV/q) is still not necessarily satisfactorily low, and there are strong demands to develop an efficient technique to store and cool HCIs to 0.1 eV/q.[1–6)]

Electron and positron cooling techniques are useful methods to produce cold HCI beams. Charged particles in a strong magnetic field lose their kinetic energies *via* synchrotron radiation, the rate of which is inversely proportional to the particle mass cubed, *i.e.*, the rates for positrons and electrons are more than 10^{10} times faster than those of ions. Actually, only electrons and positrons can be cooled *via* synchrotron radiation within some reasonable time for a magnetic field available on earth. Heavy particles can accordingly be cooled sympathetically if they are stored simultaneously with electrons and/or positrons in a strong magnetic field.

In principle, positrons are better coolants than electrons because HCIs are not lost due to recombination during cooling. On the other hand, the number of electrons (10^9–10^{10}) in a trap[4)] can be practically a few orders of magnitude larger than the number of positrons (10^7–10^8),[7)] and the electron cooling scheme has a great advantage with respect to cooling time and accordingly the loss due to recombination with residual gases. In order to selectively utilize the favorable features of positrons and electrons and suppress disadvantages, a new scheme to cool HCIs is considered utilizing electrons and positrons simultaneously.[5,8)]

The considered cooling procedure is schematically shown in Fig. 1, which consists of the (a) formation of electron and positron plasmas,[4,7)] (b) simultaneous cooling of pulse-injected HCIs with electron and positron plasmas, and (c) extraction of cooled HCIs by the ramping of trapping potential.

Our simple evaluation showed that the required cooling time of HCIs from 10 keV/q to 0.1 eV/q with the new scheme could be on the order of 1 second, which is 10 times faster than the that by pure positron cooling.[8)] Therefore, the loss of HCIs due to recombination with residual gases can be decreased by one order of magnitude. A numerical calculation also showed that the probability of HCI loss due to recombination with electrons is negligibly small in our scheme.[8)]

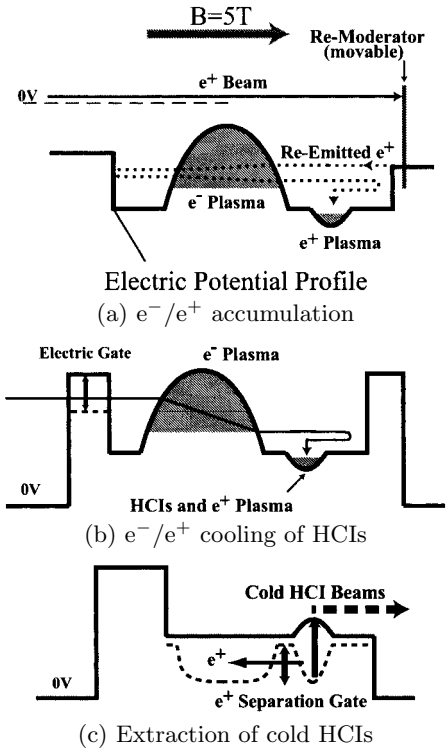

Fig. 1. Procedure of HCI cooling scheme with electron and positron plasmas.

References

1) Y. Yamazaki ed.: Production of Ultra Slow Highly-Charged Ions, RIKEN Rev., No. 31 (2000).
2) Y. Kanai et al.: Physica Scr. T **92**, 467 (2001).
3) W. Quint et al.: Hyperfine Interact. **132**, 457 (2001).
4) N. Oshima et al.: Nucl. Instrum. Methods Phys. Res. B **205**, 178 (2003).
5) N. Oshima et al.: J. Phys. Conference Series **2**, 127 (2004).
6) J. Bernard et al.: Nucl. Instrum. Methods Phys. Res. A **532**, 224 (2004).
7) N. Oshima et al.: Phys. Rev. Lett. **93**, 15001-1 (2004).
8) N. Oshima et al.: Nucl. Instrum. Methods Phys. Res. B (to be published).

* Department of Physics, University of Tokyo

Confinement of nonneutral plasma in superconducting quadrupole magnet for antihydrogen synthesis

A. Mohri, Y. Kanai, Y. Nakai, and Y. Yamazaki

Cold antihydrogen atoms ($\bar{\mathrm{H}}$'s) have been produced at CERN. They were synthesized from positrons (e^+'s) and antiprotons ($\bar{p}$'s) in a nested trap that consisted of three separate Penning traps. Charged particles of both polarities can be stored and manipulated in the nested trap with a uniform magnetic field, but $\bar{\mathrm{H}}$'s synthesized in the trap cannot be trapped because of the lack of magnetic field gradient. For high-precision spectropy of $\bar{\mathrm{H}}$'s and accurate determination of the magnetic moment of $\bar{p}$'s to test the CPT symmetry, it is essential to confine $\bar{\mathrm{H}}$'s and to extract $\bar{\mathrm{H}}$ beams out of the trapping region.

A new scheme of cold $\bar{\mathrm{H}}$ synthesis with a recombination trap consisting of a magnetic cusp and an electrostatic quadrupole (MCEO)[1] is experimentally being studied using a superconducting quadrupole magnet, which can generate the magnetic field strength necessary for synchrotron radiation cooling of e^+'s and a field gradient that is sufficiently strong to control the motion of $\bar{\mathrm{H}}$'s. A nonneutral e^+ plasma confined in MCEO induces the electric field. When $\bar{p}$'s are guided into the central region, they are trapped in the induced electric field and mixed with the positrons. These two kinds of particle are expected to recombine and form $\bar{\mathrm{H}}$'s. In a magnetic field, $\bar{\mathrm{H}}$'s are split into four hyperfine states. $\bar{\mathrm{H}}$'s in the low-field seeking states are decelerated while going to a higher magnetic field, but those having sufficient energy to overcome the magnetic potential barrier can be focused at a location apart from the cusp center. This scheme allows the extraction of an almost 100% polarized $\bar{\mathrm{H}}$ beam of considerable intensity.

A magnet with a bore of 16 cm radius generates a field strength of 3.5 T and a gradient of 35 T/m at maximum. Here, the field configuration enables the extraction of a focused spin-polarized beam of $\bar{\mathrm{H}}$'s in the ground state. Figure 1 shows magnetic field lines in a vacuum tube and also the equipotential surfaces of an electric octupole produced with electrodes.

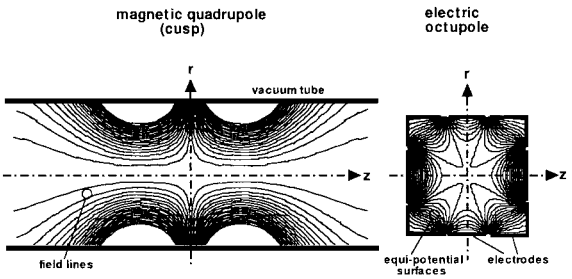

Fig. 1. Field lines of the magnetic cusp and equipotential surfaces of the electric octupole used for MCEO.

Experiments using this MCEO trap were first performed on nonneutral electron confinement in a warm bore to establish the control method of particle accumulation in the trap and also to elucidate the dynamics of electrons trapped in a high magnetic field, such as diffusion across the magnetic field and cooling by synchrotron radiation. Figure 2 illustrates the setting of components inside the vacuum tube. Pulsed electrons are injected with the electron gun into the MCEO trap and the total number of trapped electrons is measured by dumping them to the Faraday cup. The number of trapped electrons does not change for a time longer than 100 s. This means that the electron plasma is confined in the trap without touching the surrounding walls for a long time[2]. The electric field needed to trap positively charged ions (or $\bar{p}$'s) depends on the spatial density distribution of the trapped electrons (or e^+'s). Experiments to find the electron density distribution are now under way.

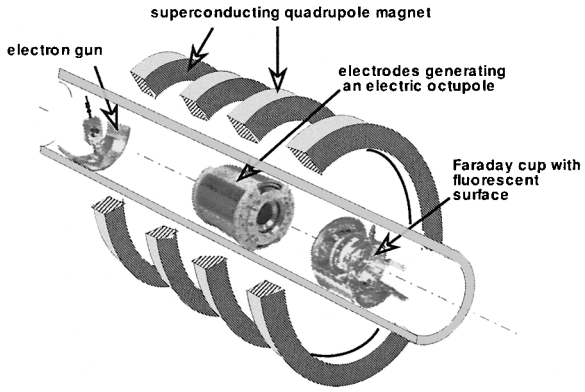

Fig. 2. MCEO trap using a superconducting quadrupole magnet. An electron gun, electrodes for the octupole and a Faraday cup with fluorescent screen are housed in the vacuum tube.

References

1) A. Mohri and Y. Yamazaki: Europhys. Lett. **63**, 207 (2002).
2) A. Mohri, Y. Kanai, Y. Nakai, and Y. Yamazaki: Proc. 31st European Physical Society Conf. on Plasma Physics, London, UK, 2004-7 (European Physical Society, 2004), P4-225.

Precision spectroscopy of Zeeman splittings of $^9Be^+$ 2 $^2S_{1/2}$ hyperfine structure levels (III)

T. Nakamura,[*1] M. Wada, K. Okada,[*2] I. Katayama,[*1] S. Ohtani,[*3] and H. A. Schuessler[*4]

We have been conducting precision measurements of the ground-state hyperfine structure (hfs) of trapped $^9Be^+$ ions in a strong magnetic field using a combined trap[1] and laser-microwave multiple resonance spectroscopy methods.[2] The main purpose of our project is to study the nuclear structure of unstable nuclei through the Bohr-Weisskopf effect, which is deduced from a comparison of the hfs constant A, which is normalized by the nuclear g_I-factor, among the isotopes. The hfs constant A and the nuclear g_I-factor in units of the electronic g_J-factor were determined from two pairs of transition frequencies, the nuclear spin-flip transitions ν_n and the electron spin-flip transitions ν_e, at different optical pumping conditions, σ_+ and σ_-.

We achieved high accuracies of 10^{-9} and 10^{-7} for the measurement of A and g'_I/g_J, respectively, at the external magnetic field $B_0 = 0.47\,\mathrm{T}$.[2] Although the present accuracy is sufficient for our primary purpose, we have worked on improving the accuracies. Our measurement values are slightly inconsistent with a previously reported values by the NIST group[3] at different strengths of the magnetic field. Fortson and Fletcher proposed theories on a possible quadratic dependence of the hfs constant A and the nuclear g_I-factor on the strength of the external magnetic field.[4,5] Since our experimental method allows the measurement of the constant at an arbitrary strength of the magnetic field, the dependence on the magnetic field can be determined with a high accuracy.

In our previous resonance detection scheme, a drift of the magnetic field strength had a significant effect on the obtained accuracies. Therefore, we modified the measurement sequence to measure the nuclear spin-flip transition and the electron spin-flip transition, simultaneously. The coherent time of each measurement cycle was also increased to decrease the line width of the resonance curve. We measured using the new scheme two pairs of transition frequencies at the $B_0 = 0.58\,\mathrm{T}$ as shown in Fig. 1. From these frequencies, we obtained new values of $A = -625\,008\,836.07(11)\,\mathrm{Hz}$ and $g'_I/g_J = 2.134\,780\,406(35) \times 10^{-4}$. All previously reported values including our recently obtained values are plotted as the function of B_0 in Fig. 2. It should be pointed that the NIST values (a) were obtained from frequencies at different field strengths, $B_0 = 0.68\,\mathrm{T}$ and $0.82\,\mathrm{T}$ for $\sigma_\pm$, so that the values are not applicable to discussing the B_0 dependence. Also our previous measurements at $B_0 = 0.47\,\mathrm{T}$ are not sufficiently accurate. Therefore, we now measure at different B_0 values with high accuracies to determine the dependence of A and g'_I/g_J on the strength of the magnetic field.

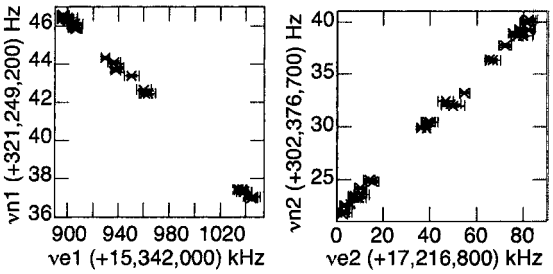

Fig. 1. Measured two pairs of transition frequencies, nuclear spin-flip transitions ν_n and electron spin-flip transitions, ν_e for σ_+ (left) and σ_- (right) at $B_0 = 0.58\,\mathrm{T}$. The linear correlations in two graphs indicate good experimental consistency.

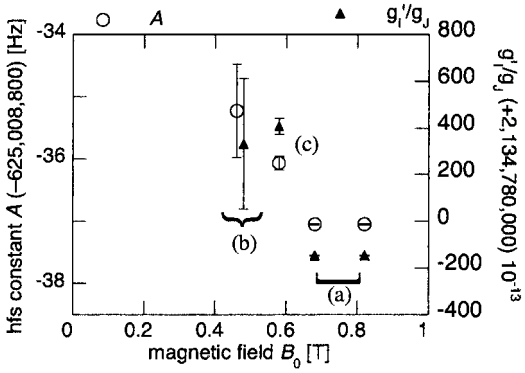

Fig. 2. Magnetic field dependence of the A and g'_I/g_J. (a) NIST values (see text), (b) our previously reported values at $B_0 = 0.47\,\mathrm{T}$,[2] and (c) our presently obtained values at $B_0 = 0.58\,\mathrm{T}$.

References

1) T. Nakamura et al.: J. Appl. Phys. **89**, 2922 (2001).
2) T. Nakamura et al.: Opt. Commun. **205**, 329 (2002).
3) D. J. Wineland et al.: Adv. At. Mol. Phys. **19**, 135 (1983).
4) G. D. Fletcher et al.: Phys. Rev. Lett. **58**, 2535 (1987).
5) N. Fortson: Phys. Rev. Lett. **59**, 988 (1987).

*1 Institute of Particle and Nuclear Studies, High Energy Accelerator Research Organization (KEK)
*2 Department of Physics, Sophia University
*3 Institute for Laser Science, University of Electro-Communications
*4 Department of Physics, Texas A&M University, USA

Laser-induced fluoresence spectra of alkaline-earth ion-helium exciplexes produced in cold helium environment

Y. Fukuyama, Y. Moriwaki,* and Y. Matsuo

Superfluid He (He II) is expected to be a suitable medium in the study of short-lived radioactive nuclei because it can instantly stop atoms and ions that are produced in a fragmentation reaction with a high kinetic energy (∼100 MeV/u).[1] In addition, various laser spectroscopic methods can be achieved in He II because He II is transparent in a wide wavelength region from radio frequency to vacuum ultraviolet. The high-resolution laser spectroscopy of atoms in He II will reveal nuclear properties such as electromagnetic moments. However, in a cold He environment, there are few spectroscopic studies on impurities, although the study on impurities itself has a long history. In addition, it is known that certain atoms and ions form exciplexes with He atoms in liquid He and cold He gas.[2] To perform a laser spectroscopic study of unstable nuclei in He II, it is necessary to investigate spectroscopic properties of atoms and ions in a cold He environment. In this paper, we describe the laser-induced fluoresence (LIF) detection of impurity ions such as Ba^+ in a cold He gas and report the first observation of Ba^{+*}-He exciplexes in the same environment at 3–30 K.[3]

The experimental setup is illustrated in Fig. 1. The experimental apparatus consisted of a cryostat chamber, an ablation laser, an excitation laser, and a detection system. The bottom part of the cryostat chamber contained liquid He. The space above the liquid He was filled with cold He gas. A small solid Ba sample was placed in an open quartz container, which was fixed above the liquid level, to prevent the disturbance of direct He gas flow. Barium ions were produced in the cold He gas by ablating the solid Ba sample with the third-harmonic pulse of the Nd:YAG laser output (355 nm, ∼10 mJ/pulse). Typically, 10^{10} ions were dispersed in the cold He gas. Then, the Ba^+ ions were irradiated using a pulsed dye laser (455 nm, 1 μJ/pulse). A LIF from ions and exciplexes was detected with a photomultiplier tube through a 25 cm grating monochromator, and the signal was averaged with a boxcar integrator and stored in a computer.

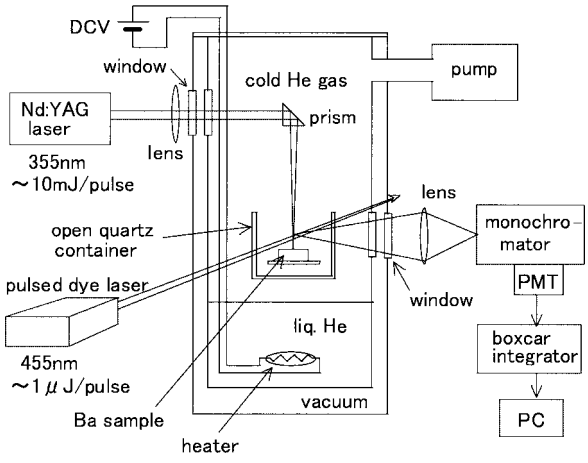

Fig. 1. Experimental setup.

We observed LIF spectra of Ba^+ in the cold He gas by exciting Ba^+ ions from the $6s\ ^2S_{1/2}$ ground state to the $6p\ ^2P_{3/2}$ excited state (D2 excitation). The typical spectrum observed at the temperature of 25 K and the pressure of 6700 Pa is shown in Fig. 2. The observed spectrum was composed of a sharp line of D1 transition ($6s\ ^2S_{1/2}$–$6p\ ^2P_{1/2}$) of Ba^+ at 20262 cm^{-1} and a broad fluorescence band over a range of 20500–21800 cm^{-1}. The broad fluorescence band was observed only in the temperature and pressure ranges of 3–30 K and 2000–27000 Pa, respectively. This broad fluorescence band of the Ba^{+*}-He exciplex was composed of four components that were assigned as transitions from different vibrational levels (v = 0, 1, 2 and 3) in the $6p\ ^2\Pi_{3/2}$ state to the bound free $6s\ ^2\Sigma_{1/2}$ state. We also performed *ab initio* calculations to determine the pair potential of the Ba^+-He system and calculated emission spectra based on the Franck-Condon approximation. The observed emission spectra of Ba^{+*}-He exciplexes were reasonably in good agreement with the calculated ones.

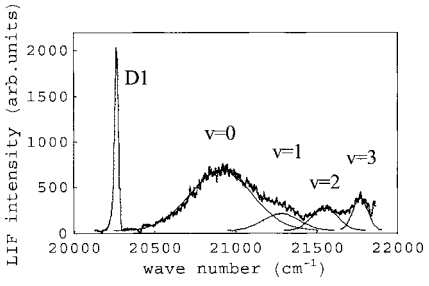

Fig. 2. LIF spectra of Ba^+ ion and Ba^{+*}-He exciplex.

References

1) Y. Fukuyama et al.: RIKEN Accel. Prog. Rep. **35**, 101 (2002).
2) H. Günther and B. Tabbert: Z. Phys. B **98**, 297 (1995).
3) Y. Fukuyama et al.: Phys. Rev. A **69**, 042505 (2004).

* Department of Physics, Toyama University

Long electronic spin relaxation time of Cs atoms in superfluid helium

T. Furukawa,[*1] Y. Matsuo, A. Hatakeyama,[*2] Y. Fukuyama, T. Kobayashi, H. Izumi,[*1] Y. Arakawa,[*1] I. Wakabayashi,[*1] K. Kawai,[*1] S. Morinobu,[*1] and T. Shimoda[*1]

We have been studying optical pumping of impurity atoms in superfluid helium (He II) with the aim of establishing a versatile method for determining the nuclear moments of unstable nuclei from their hyperfine structure.[1)] The broadened absorption line spectrum of the atom in He II is very promising for pumping a wide variety of atomic species. The electronic spin relaxation time of the atoms in He II is the key quantity for successful of optical pumping. Kinoshita *et al.*[2)] succeeded in polarizing the alkali metal atoms (Rb and Cs) in He II by optical pumping, but no quantitative measurement of the relaxation time has been carried out to date.

We have measured for the first time the longitudinal spin relaxation time T_1 of Cs atoms in a holding magnetic field B_0 of approximately 5 G in He II, using the "relaxation in the dark" method.[3,4)] This method is based on the fact that the laser-induced fluorescence (LIF) signal observed with circularly polarized "pumping" light, tuned to the wavelength of the $D1$ excitation line of Cs atoms in He II, is proportional to the number of depolarized atoms. The LIF intensity I is described as

$$I \propto N_{\mathrm{Cs}} \times (1 - P_z), \tag{1}$$

where N_{Cs} is the number of Cs atoms and P_{z} is the electronic spin polarization of the atoms.[4,5)] The details of the method are as follows. At the beginning of the measurement, Cs atoms were injected locally into the optical detection region in He II by the laser sputtering technique.[6)] The injected Cs atoms were optically pumped and polarized with irradiation of the pumping laser light. After the pumping of Cs atoms, LIF was not observed from polarized atoms. Next, the pumping laser light was switched off during the dark period τ. The optical pumping of Cs atoms was interrupted and Cs atoms were gradually depolarized by the perturbing field from the surrounding helium atoms during this period. When the pumping laser light was irradiated again after the dark period, the LIF signals were revived. In the liquid He II, the number of injected Cs atoms in the measurement region of He II, N_{Cs} in Eq. (1), gradually decreased due to the diffusion of the atoms. In order to compensate for the effect of the time-variant N_{Cs}, we depolarized the Cs atoms compulsorily by irradiating the linear polarized D1 excitation laser light immediately after the measurement of $I(\tau)$, and we measured the LIF intensity I_0, namely the intensity from the atoms of $P_{\mathrm{z}} = 0$. From Eq. (1), the intensity I_0 was proportional only to the number of Cs atoms N_{Cs}. We determined the polarization $P_{\mathrm{z}}(\tau)$ from the ratio of these two LIF intensities, as

$$P_z(\tau) = 1 - \frac{I(\tau)}{I_0}, \tag{2}$$

which is independent of N_{Cs}

Then, we obtained the polarization $P_{\mathrm{z}}(\tau)$ for each dark period up to 1.4 s, and we determined the spin relaxation time T_1 deduced from the polarization $P_{\mathrm{z}}(\tau)$. Figure 1 shows the relative polarization $P_{\mathrm{z}}(\tau)/P_{\mathrm{z}}(0)$ as a function of τ. From a single component exponential fit, the spin relaxation time of $T_1 = 2.56(19)$ s was determined at the helium temperature of about 1.6 K and a holding magnetic field B_0 of approximately 5 G. This extraordinary long spin relaxation time is even longer than that in solid helium (bcc phase) of about 1–2 s.[4,5)] This result encourages us to take advantage of He II as a suitable environment for trapping unstable nuclear beams and for performing laser spectroscopy for the measurement of nuclear moments.

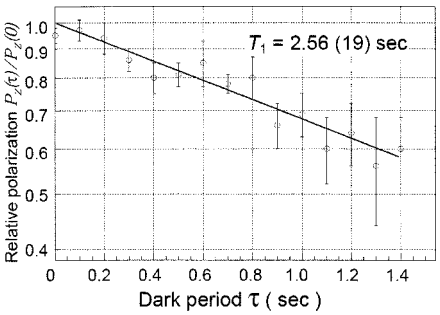

Fig. 1. Spin relaxation of Cs atoms in He II as function of dark period τ.

References

1) T. Furukawa et al.: Ann. Rep. Osaka University Laboratory of Nuclear Studies **2002**, 27.
2) T. Kinoshita, Y. Takahashi, and T. Yabuzaki: Phys. Rev. B **49**, 3648 (1994).
3) W. Franzen et al.: Phys. Rev. **115**, 850 (1959).
4) M. Arndt et al.: Phys. Rev. Lett. **74**, 1359 (1995).
5) S. Lang et al.: Phys. Rev. A **60**, 3867 (1999).
6) A. Fujisaki et al.: Phys. Rev. Lett. **71**, 1039 (1993).

*1 Department of Physics, Graduate School of Science, Osaka University
*2 Institute of Physics, Graduate School of Arts and Sciences, University of Tokyo

Development of optical detection technique for single spin in diamond N-V center

G. Kato,[*1] T. Arai,[*1] D. Nagae,[*1] K. Shimada,[*1] M. Tsukui,[*1] H. Miyoshi,[*1] D. Kameda,[*1] S. Emori,[*1] M. Uchida,[*1] M. Kurosawa,[*2] A. Yoshimi, H. Ueno, T. Haseyama, Y. Kobayashi, E. Yagi, K. Kawasaki,[*1] and K. Asahi[*1]

The exclusively long relaxation times that are achieved for nuclear spins in solids suggest a promising nuclear spin system for quantum bits. However, to realize nuclear spin qubits, the observation and operation of a single nuclear spin are inevitably required. A ^{15}N nuclear spin in a diamond N-V center would provide such an opportunity.

The N-V center consists of a nitrogen atom substituting for a carbon atom and a nearest-neighbor vacancy as illustrated in Fig. 1 (a).[1)] The N-V centers are produced in type Ib diamond by high-energy electron irradiation and subsequent annealing. The N-V center has a ^{3}A ground state and a ^{3}E excited state with a very short lifetime (see Fig. 1 (b)). The notably luminous optical transition between these states[2)] would provide a means of detecting a single nuclear spin in the N-V center: After repetition of the optical excitation and de-excitation, the electronic spin state is oriented preferentially to the population of the $m_s = 0$ state. Once the orientation of electronic spins is achieved, the application of a microwave for the ESR transition between the hyperfine-split levels leads to an intensity change in the optical transition, thus enabling a high-sensitivity detection of ESR (optically detected ESR). Furthermore, by incorporating an NMR transition with ESR the polarization of nitrogen nuclear spins is induced. We are investigating the method of examining this nuclear polarization process by detecting β-rays from the unstable nuclei ^{17}N.

As the first step toward the operation of the spin ensemble, we performed an ESR experiment on type Ib diamond. Among the nitrogen-related defect centers that are known in the type Ib diamond, the P1 center is understood as a structure with a nitrogen atom substituting for a carbon atom.[3)]

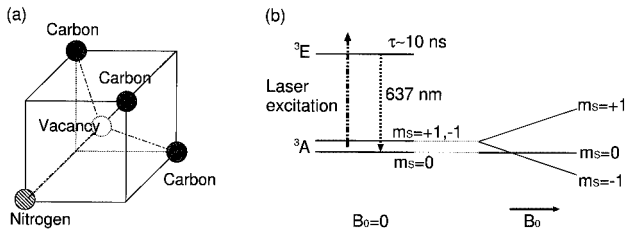

Fig. 1. Crystalline structure (a) and energy levels and excitation scheme (b) of N-V center.

*1 Department of Physics, Tokyo Institute of Technology
*2 Department of Physics, Tokyo University of Science

The ESR spectrum obtained for the type Ib diamond (Sumitomo HT-HP synthetic diamond) is presented in Fig. 2. The spectrum was obtained under the condition that the applied magnetic field B_0 was parallel to the [100] direction of the diamond crystal. In terms of the hyperfine coupling (hfc) constant A, the resonance frequencies are expressed as $h\nu = g_e\mu_B(B_0 + Am_I)$. The hyperfine interaction between ^{14}N (nuclear spin $I = 1$) and an unbound electron gives rise to three resonance lines. From this spectrum, we obtained the hfc constant $A = 3.4 \pm 0.1$ mT. Because this value agrees well with the A value known for the P1 center ($A = 3.36$ mT[3)]), we consider that the obtained ESR spectrum originates from the substitutional nitrogen structure. To confirm the substitutional nitrogen structure of the P1 center, the β-NMR method can be used. For the magnetic moment ^{17}N, $|\mu(^{17}\mathrm{N})| = (0.352 \pm 0.002)\mu_\mathrm{N}$,[4)] the hfc constant is calculated as $A_{^{17}\mathrm{N}} \sim 5.8$ mT.

Until now, we have investigated the ESR spectrum on the P1 center of a type Ib diamond sample. We have also started producing the N-V center. Several type Ib diamond samples were irradiated with 2 MeV electron beams (doses from 5×10^{12} e/cm^2 to 1×10^{16} e/cm^2) and annealed for 1 h at $T = 1173$ K and 923 K. Analyses of these samples by ESR,[5)] FT-IR[5)] and fluorescence[1,2)] measurements are under way. We also plan to observe the magnetic resonance of the N-V center by optical detection.

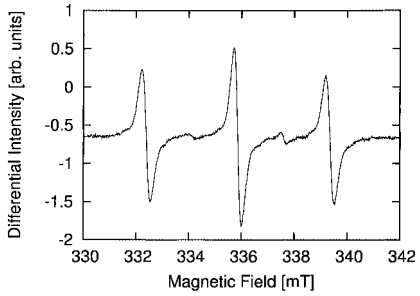

Fig. 2. ESR spectrum of P1 center in type Ib diamond.

References

1) F. T. Charnock and T. A. Kennedy: Phys. Rev. B **64**, 041201 (2001).
2) A. Gruber et al.: Science **276**, 2012 (1997).
3) W. V. Smith et al.: Phys. Rev. **115**, 1546 (1959).
4) H. Ueno et al.: Phys. Rev. C **53**, 2142 (1996).
5) A. Lenef et al.: Phys. Rev. B **53**, 13427 (1996).

Channelling studies on the lattice location of B atoms in graphite†

E. Yagi, T. Iwata,* T. Urai, and K. Ogiwara

Boron has a favourable effect on graphitization of carbon. A number of properties of graphite are influenced by the presence of boron. For example, the boron atom is expected to act as an acceptor, when it substitutes a carbon atom. Regarding where boron atoms are located in a graphite crystal lattice, experimental results on the B concentration dependence of lattice parameters,[1,2] a density,[1] and electronic properties[3,4] suggest that boron occupies a substitutional site. In the present study, to obtain additional direct information on the lattice location of boron atoms, channelling experiments are performed. There exist ⟨0001⟩ axial channels surrounded by C atomic rows in the c-direction as shown in Fig. 1 by broken lines and also {0001} planar channels between c-planes in perpendicular to the c-direction.

Specimens are highly-oriented pyrolytic graphite (HOPG) crystals doped with 0.32 at.% B. B atoms were detected with a proton beam, utilizing a resonant nuclear reaction ^{11}B(p,α)$\alpha\alpha$ around 0.624 MeV (the resonance width (FWHM) is about 0.3 MeV); the B atoms were detected by measuring the α-particles, whose energy extended up to about 5 MeV.

Channelling experiments were performed at room temperature with a 0.666 MeV proton beam for the ⟨0001⟩ channel. Backscattered protons (C-angular profiles) and emitted α-particles (B-angular profiles) were measured at angles of 160° and 150°, respectively, as a function of the incident angle with respect to the c-axis. Measurement for the {0001} channel was also tried, but it was unsuccessful, due probably to difficulties in preparation of the surface suitable for channelling experiments. Figure 2 shows the angular profiles. In this case, in order to compare the C- and B-angular profiles for approximately the same depth region (from the surface to 1.75 μm), Al foil 13 μm thick was placed in front of the α-particle detector as an energy absorber. Both angular profiles exhibit the same dips, indicating that most of B atoms are shadowed behind the ⟨0001⟩ C atomic rows. As such sites, there are three types of sites; (1) a substitutional site, (2) a centre of a hexagon (a b'-site in Fig. 1) and (3) any site between two c-planes on the ⟨0001⟩ atomic row (d- and d'-sites in Fig. 1). The first two types of sites are on the c-plane. The latter two sites (d- and d'-sites) are interstitial sites. As the measurement for the {0001} channel was unsuccessful, it is impossible to make distinction between these two groups of sites. It is widely accepted that the d'-site is stable, whereas the b'- and d-sites are unstable because of a large repulsive force from adjacent atoms. On the other hand, from the calculation by the molecular dynamical method, Taji, Yokota, and Iwata found that the stable site for the interstitial C atom is not the d'-site, but a site displaced from the d'-site toward the channel centre between two c-planes, i.e., the e-site in Fig. 1.[5] If the B atoms are located at either d'-site or e-site, the c-spacing should increase with B concentration, in contrast with the results of the X-ray diffraction. Hence, it is concluded that most of B atoms are located at substitutional sites.

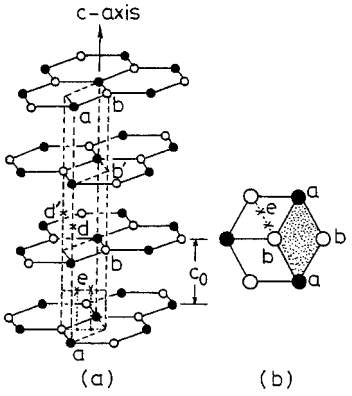

Fig. 1. (a) The crystal structure of graphite. (b) The projection of the ⟨0001⟩ channel onto the plane perpendicular to the c-axis.

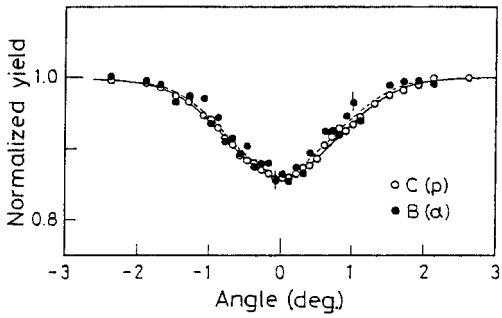

Fig. 2. The channelling angular profiles of backscattered protons and emitted α-particles obtained with a 0.666 MeV proton beam at room temperature.

References

1) C. E. Lowell: J. Am. Ceram. Soc. **50**, 142 (1967).
2) P. Wagner and J. M. Dickinson: Carbon **8**, 313 (1970).
3) D. E. Soule: Proc. 5th Conf. on Carbon, Vol.1, (Pergamon Press, New York, 1962), p.13.
4) S. Marinkovic: in *Chemistry and Physics of Carbon*, Vol.19, edited by P. A. Thrower (Marcel Dekker, New York, 1984), p.1.
5) Y. Taji, T. Yokota, and T. Iwata: J. Phys. Soc. Jpn. **55**, 2676 (1986).

† Condensed from the article in J. Nucl. Mater. **334**, 9 (2004)

* Japan Atomic Energy Research Institute

μSR study on magnetism of organic Mott insulator having two-dimensional triangular lattice

S. Ohira, Y. Shimizu[*1,*2], K. Kanoda[*2] and G. Saito[*1]

κ-(BEDT-TTF)$_2X$ is a strongly correlated electron system having a 2D layer structure of BEDT-TTF (ET) molecules, where X is a monovalent anion. They have been known to exhibit a superconducting (SC) or antiferromagnetic (AFM) phase as the ground state.[1] However, it has been suggested that one of the Mott insulators, κ-(ET)$_2$Cu$_2$(CN)$_3$, shows no long-range magnetic ordering.[2,3] The ET dimers form a nearly isotropic triangular lattice in this salt. The ground state of the 2D triangular lattice system with spin-1/2 is theoretically suggested to be a spin liquid state,[4] while it is experimentally still unclear since the existing materials are few. Because the salt also shows the SC transition under moderate hydrostatic pressures,[2] this can be a candidate to have the spin liquid ground state which neighbors the SC phase. We carried out a ZF-μSR measurement on this salt down to 1.5 K to clarify its magnetic property.

The experiment was carried out at the RIKEN-RAL Muon Facility in the Rutherford Appleton Laboratory (RAL) down to 1.5 K. 200 mg of the polycrystalline sample was packed into a silver foil and fixed onto the sample holder.

Muon spin relaxation due to nuclear dipole fields was observed down to 1.5 K (Fig. 1). It is noted that the relaxation is slightly enhanced at 1.5 K. The time spectra are well fitted with $A(t) = Ae^{-\lambda t}e^{-(\sigma t)^2}$, where λ is the muon spin relaxation rate for describing the dynamically fluctuating internal field, and σ is the distribution width of the internal field at the muon site. The fitting results below 100 K are shown in Fig. 2. λ shows a slight increase below $\sim$4 K with decreasing temperature. Because the enhancement of the relaxation is quite small, this behavior differs from the critical slow-down effect associated with the magnetic transition. In our previous experiment, no magnetic transitions were observed from 20 mK to 1.5 K. Our μSR studies strongly suggest the possibility of the quantum spin liquid ground state neighboring the SC phase in this salt.

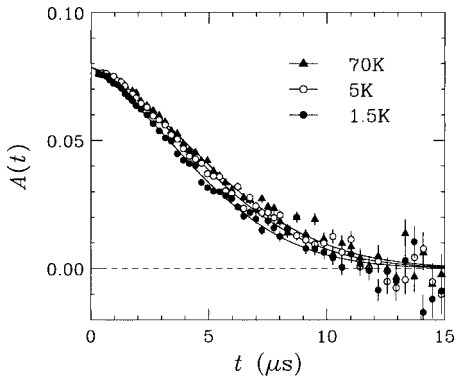

Fig. 1. ZF-μSR time spectra of κ-(ET)$_2$Cu$_2$(CN)$_3$.

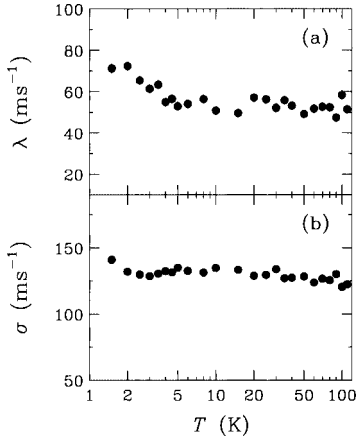

Fig. 2. Temperature dependences of (a) the relaxation rate λ and (b) the distribution width of the internal field at the muon site σ.

The anomaly in the relaxation rate at around 4 K is also observed in the ^{1}H NMR measurement.[3] The proton spin-lattice relaxation rate, T_1^{-1}, starts to increase below 4 K and exhibits a broad peak at $\sim$1 K. It is expected that some spin dynamics changes below around 4 K. More detailed studies at low temperatures are currently in progress.

References

1) K. Kanoda et al.: Physica C **282–287**, 299 (1997); K. Kanoda, Hyperfine Interact. **104**, 235 (1997).
2) T. Komatsu et al.: J. Phys. Soc. Jpn. **65**, 1340 (1996).
3) Y. Shimizu et al.: Phys. Rev. Lett. **91**, 107001 (2003).
4) L. Capriotti et al.: Phys. Rev. Lett. **82**, 3899 (1999).

*1 Division of Chemistry, Kyoto University
*2 Department of Applied Physics, University of Tokyo

Plans for superheavy-element chemistry in RIKEN: Development of gas-jet transport system coupled to GARIS

H. Haba, D. Kaji, K. Morimoto, S. Motomura, S. Enomoto, and K. Morita

Recently, the investigation of the chemical properties of superheavy elements (SHEs) with atomic number $Z \geq 104$ is one of the most interesting and challenging subjects in nuclear and radiochemistry. The increasingly strong relativistic effect on the valence electrons of SHE atoms is expected to induce deviations in chemical properties from the periodicity based on their lighter homologues in the periodic table. The production rates of the SHE nuclides are extremely low, *i.e.*, atoms per minute for elements 104 and 105, down to atoms per day for elements 106 to 108, and their half-lives are less than ∼1 min. This situation forces us to perform rapid and effective chemical experiments with single atoms.

The experimental studies on the chemical properties of SHEs have been performed for elements 104 to 108, and very recently for element 112.[1)] To perform rapid and effective chemical separations of SHE, the gas-jet transport technique has been commonly used to deliver SHE atoms from the target chamber to various chemical separation apparatuses. Nuclear reaction products recoiling out of the target are stopped in the recoil chamber filled with helium gas. After being stopped in the gas, the reaction products become attached to the aerosol particles such as potassium chloride and carbon. The gas and activity-laden aerosol particles are sucked through a capillary tube to a distant site by applying a vacuum to the downstream end of the capillary tube, where the aerosol particles are collected on a foil or filter and can be made rapidly available for chemical separation.

The SHE atoms are produced at extremely low rates among much larger amounts of background activities which hinders the detection of decays of the SHE nuclides of interest. In addition, recently available high-intensity beams of more than 1 pμA give rise to a serious problem in that the plasma formed by the beams significantly decreases the gas-jet transport efficiency. For these reasons, there is a recognized need for physical preseparation of the SHE atoms before chemical separation. It has been proposed that the kinetic separator for nuclear physics research on SHEs could be coupled to the chemistry system with the aid of the gas-jet transport technique. Since 2002, related workshops have been held to discuss the merits and design of such devices.[a)] This method enables one to study the chemical properties of various compounds by directly introducing complexing reagents into the chamber, since one no longer has to deal with the harsh ionizing conditions caused by the beam. Furthermore, background activities that cannot be effectively separated from SHEs, such as that from Po or Rn isotopes, are largely removed by the recoil separator. The first experiment with the recoil transfer chamber coupled to the Berkeley Gas-filled Separator (BGS) was a great success.[2)] The isotope of ^{257}Rf physically separated from the large background caused by β-particles was unambiguously identified with a liquid scintillator after a liquid-liquid solvent extraction into 0.25 M dibutyl-phosphoric acid in toluene from 6 M HNO_3 with SISAK. At Gesellschaft für Schwerionenforschung (GSI), the components of the former HElium Charge-exchange Kaleidoscope (HECK) separator are being used to set up a dedicated separator for chemistry experiments.[a)]

In the RIKEN Linear Accelerator Facility, a gas-

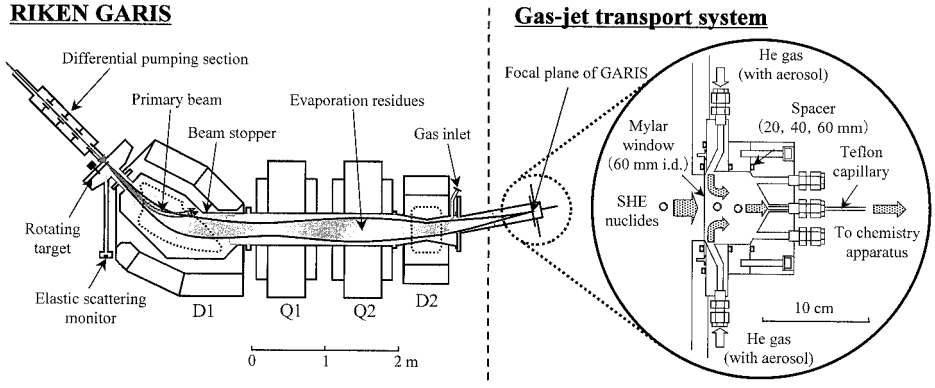

Fig. 1. Overview of gas-jet transport system coupled to GARIS.

[a)] 3rd Workshop on Recoil Separator for Superheavy Element Chemistry, GSI, Darmstadt, Germany, 2004-8 (http://www-w2k.gsi.de/tasca04/).

filled recoil separator, GARIS, is now in operation to search for the heaviest SHE nuclides. Recently, the isotopes of ^{271}Ds, ^{272}Rg, and ^{278}112 found at GSI were confirmed by better statistics and new spectroscopic information,[3,4] and a new isotope of element 113, ^{278}113, was successfully synthesized.[5] We plan to initiate SHE chemistry in RIKEN using GARIS. An overview of the gas-jet transport system coupled to GARIS is shown in Fig. 1. In this work, the gas-jet chamber was installed in the focal plane of GARIS (see Fig. 2). The gas-jet chamber at an inner pressure of ∼100 kPa should be isolated from the beam duct of GARIS at ∼100 Pa by a very thin Mylar-vacuum window. For this purpose, we use a stainless-steel honeycomb grid with 93% transparency and having 0.5 mm thickness and 60 mm diameter, which can support the Mylar foil to 2.5 μm thickness. As shown in Fig. 1, the recoiling SHE nuclides preseparated with GARIS are passed through the Mylar window and are stopped in a volume of helium gas. The helium gas, often seeded with aerosol particles, is introduced into the chamber through the four inlets (4 mm i.d.) and is sucked out through a Teflon capillary tube (1.6 mm i.d.) into a chemistry apparatus. The entire inner wall of the chamber is fabricated from chemically inert Teflon or Dyflon to enable the direct introduction of chemical reagents into the chamber. The volume of the chamber is optimized for the range of product nuclei of interest with spacers of 20, 40, and 60 mm thicknesses.

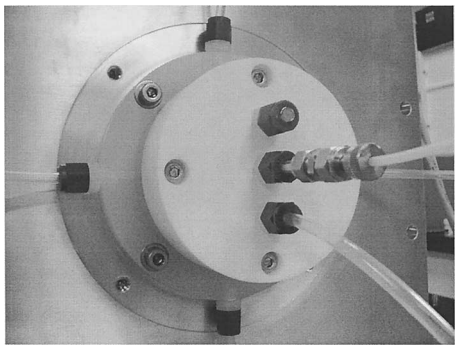

Fig. 2. A picture of gas-jet chamber coupled to GARIS.

We have also developed a rotating wheel system for the measurement of α and spontaneous fission decays of the SHE nuclides. This is a compact version of the Measurement system for the Alpha-particle and spontaneous fissioN events ON-line (MANON) developed in JAERI.[6] The product nuclei transported by the gas-jet system are deposited on Mylar foils of ∼1 μm thickness and 20 mm diameter placed at the periphery of a 40-position stainless steel wheel with a 210 mm diameter. The wheel is stepped at desired intervals to position the foils between six pairs of Si PIN photodiodes (Hamamatsu S3204-09) for α-particle detection. Each detector has an active area of 18×18 mm^2 and a 40% counting efficiency for α-particles. The α-particle energy resolution is approximately 30 keV FWHM. All events are registered in an event-by-event mode.

We will appraise the performance of the present gas-jet system using the Po and Fr isotopes produced in the ^{40}Ar-induced reactions on ^{nat}Dy and ^{169}Tm, respectively. The gas-jet efficiency will be systematically measured with the rotating wheel system by varying the experimental conditions such as the helium flow rate, pressure and volume of the chamber, thickness of Mylar vacuum window, and aerosol material. Using the GARIS + gas-jet transport system, we intend to study the chemical properties of the heaviest SHEs such as Sg, Hs, and element 112. For this purpose, experiments to measure the excitation functions for the ^{232}Th(^{40}Ar,$\alpha 3n$)^{265}Sg, ^{232}Th(^{40}Ar,$3n$)^{269}Hs, and ^{238}U(^{48}Ca,$3n$)^{283}112 reactions are planned in the near future.

References

1) M. Schädel: *The Chemistry of Superheavy Elements* (Kluwer Academic Publishers, Dordrecht, 2003).
2) J. P. Omtvedt et al.: J. Nucl. Radiochem. Sci. **3**, 121 (2002).
3) K. Morita et al.: J. Phys. Soc. Jpn. **73**, 1738 (2004).
4) K. Morita et al.: Eur. Phys. J. A **21**, 257 (2004).
5) K. Morita et al.: J. Phys. Soc. Jpn. **73**, 2593 (2004).
6) H. Haba et al.: Radiochim. Acta **89**, 733 (2001).

Radioactive tracers produced at RIKEN accelerator research facility and future RI beam factory

H. Haba and S. Enomoto

Due to its high sensitivity, the radioactive tracer technique has been successfully applied for investigations of the behavior of elements in the fields of chemistry, biology, medicine, engineering, and environmental sciences. Since the discovery of the multitracer technique at RIKEN in 1991,[1)] we have produced multitracers and conducted application studies in collaboration with many researchers in various fields.[2)] Recently, a new multitracer production system, which consists of a gas-jet-coupled multitarget system for short-lived radioactive tracers and a gas- and water-cooled target system for intense beam irradiations, has been installed at the $K = 540$ MeV RIKEN Ring Cyclotron (RRC).[3)] Single radioactive tracers such as ^{48}V, ^{67}Cu, and ^{206}Bi produced using the $K = 70$ MeV AVF Cyclotron have also been available. The Radioactive Isotope (RI) beam facility, called the RI Beam Factory (RIBF), is now under construction at RIKEN. The world's most intense RI beams over the entire range of atomic masses up to that of uranium are expected to open new frontiers in nuclear and radiochemistry as next-generation producers of radioactive tracers. In this paper, we briefly review the present status and prospects of the production of unique radioactive tracers at the RIKEN Accelerator Research Facility (RARF) and at the future RIBF.

By using the falling ball system,[1)] radionuclides of a large number of elements were simultaneously produced from metallic targets such as Ti, Fe, Cu, Ge, Ag, and Au irradiated with a 135 MeV nucl.$^{-1}$ ^{14}N (or ^{12}C, ^{16}O) beam from RRC. After the irradiation, these radionuclides were chemically separated from the target material,[1,4–6)] and then the carrier-free and salt-free multitracer solution was applied to various experiments with the aid of γ-ray spectrometry with Ge detectors. Since the first production of a multitracer in 1991, the beam intensity of RRC has been increased up to approximately 1 particle μA (pμA) for the 135 MeV nucl.$^{-1}$ ^{14}N beam, which is one order of magnitude higher than the acceptable intensity for the falling ball system. This forced us to develop an efficient target-cooled system and to place heavy shields surrounding the target chamber. In addition, technical developments for the preparations of radioactive tracers with short half-lives ($\lesssim 1$ h) and of elements lost during chemical separation were strongly desired. Thus, we have developed a new multitracer production system on the E3b beam line of RRC as an alternative to the falling ball system. A schematic of this system is shown in Fig. 1. It consists of a gas-jet-coupled multitarget chamber (1st chamber) and a simple gas- and water-cooled target chamber (2nd chamber). The beams from RRC are collimated to a 7 mm diameter with a 4-sector Ta slit. Then, the beam passes through a HAVAR vacuum window of 6 μm thickness and enters 30 multitarget of approximately 1 μm thickness with 10 mm spacings in the first chamber. The number and spacing of the targets are variable depending on the ranges of product nuclei recoiling out of the target. The recoiling multitracers are stopped in He gas, attached to aerosols such as KCl and C, and are continuously transported through a Teflon capillary (2.0 mm i.d., 10 m long) to a chemistry laboratory just beneath the E3 irradiation room, where the multitracers can be collected on a glass filter. In the second chamber, the beam enters the thick metallic targets such as Ti, Ag, and Au, which are each approximately 200 μm in thickness, and finally enters a water-cooled carbon beam stopper. After the irradiation, the long-lived multitracers were chemically separated with the aid of almost the same procedure as applied previously.[1,4–6)] The advantages of the present system are as follows. (1) The multitracers are separated from the target material without chemical separation and transported to the chemistry room within a few seconds. Thus, radionuclides with short half-lives of less than 1 minute are available for experiments. (2) The targets of almost all elements can be prepared by electrodeposition or vacuum-evaporation techniques. The composition of the radionuclides in the multitracer can be optimized by changing the target material and its array. (3) The

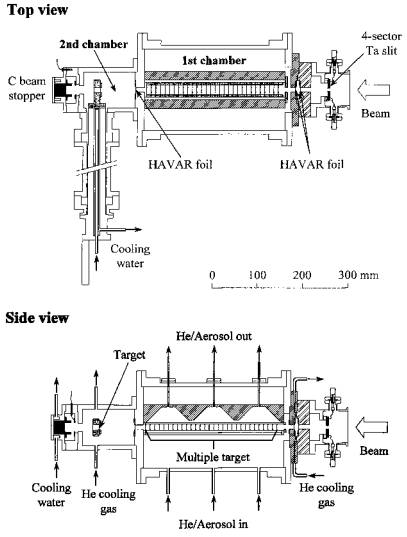

Fig. 1. Schematic of the new multitracer production system installed on the E3b beam line of the $K = 540$ MeV RIKEN Ring Cyclotron.

Table 1. Examples of the single radioactive tracers produced using the RIKEN $K = 70$ MeV AVF Cyclotron.

Nuclide	Half-life (d)	Target	Reaction	Decay mode	γ-ray energy (intensity)
^{7}Be	53.29	LiF	^{7}Li(p,n)	EC	477.6 (10.5)
^{48}V	15.9735	Ti	^{48}Ti(p,n)	EC, β^+	983.5 (100), 1312.1 (97.5)
^{54}Mn	312.3	Cr	^{54}Cr(p,n)	EC, β^+	834.8 (100)
^{65}Zn	244.26	Cu	^{65}Cu(p,n)	EC, β^+	1115.5 (50.6)
^{67}Cu	2.576	ZnO[§]	^{70}Zn(p,α)	β^-	93.3 (16.1), 184.6 (48.7)
^{85}Sr	64.84	RbCl	^{85}Rb(p,n)	EC, β^+	514.0 (95.7)
^{88}Y	106.65	$SrCO_3$	^{88}Sr(p,n)	β^+	898.0 (93.7), 1836.1 (99.2)
^{89}Zr	3.267	Y	^{89}Y(p,n)	β^+	909.1 (99.9)
^{92m}Nb	10.15	Zr	^{92}Zr(p,n)	EC, β^+	934.4 (99.1)
^{95m}Tc	61	Mo[§]	^{95}Mo(p,n)	EC, β^+	204.1 (63.2), 582.1 (29.9)
^{109}Cd	462.6	Ag	^{109}Ag(p,n)	EC	88 (3.61)
^{175}Hf	70	Lu	^{175}Lu(p,n)	EC	343.4 (84)
^{177}Ta	2.357	Hf	^{177}Hf(p,n)	EC, β^+	112.9 (7.2)
^{203}Pb	2.161	Tl_2O_3	^{203}Tl(p,n)	EC	279.2 (80.8)
^{206}Bi	6.243	PbO	^{206}Pb(p,n)	EC, β^+	881.0 (66.2), 803.1 (98.9)

[§] The isotope enrichments of ^{70}Zn and ^{95}Mo are 99.5% and 96.8%, respectively.

radionuclides of interest are readily concentrated by using a gas-jet coupled liquid chromatography apparatus based on ion exchange or solvent extraction. (4) The targets are continuously cooled with He gas and water during the irradiation. A beam intensity of $\sim$1 pμA is acceptable, though the maximum for the falling ball system was approximately 0.1 pμA due to the irradiation in a vacuum chamber. Recently, the performance of the gas-jet system was investigated with 50 radionuclides of 18 elements produced in the 135 MeV nucl.$^{-1}$ ^{14}N induced reaction on ^{nat}Cu.[3)]

Although the multitracers produced from the Ti, Ag, and Au targets have been commonly used, it is quite difficult to identify γ-ray peaks for certain elements such as Cu, Nb, Cd, and Ta depending on decay properties such as half-lives and γ-ray energies and on chemical separation. In addition, after successful screening experiments with the multitracers, researchers often hope to focus on certain elements and use their single tracers to increase detection sensitivities. Thus, we have started to provide single radioactive tracers produced by simple reactions such as (p,n) and (p,α) using a proton beam derived from the RIKEN $K = 70$ MeV AVF Cyclotron. The target nuclei of suitable chemical forms were irradiated with a He- and water-cooled target chamber. The 15 single tracers now available at RARF are listed in Table 1 together with their half-lives, target materials, nuclear reactions, decay modes, and major γ-ray energies and intensities.[7)] Among them, all tracers except for ^{54}Mn and ^{109}Cd are commercially unavailable in Japan at present.

In recent years the advent of RI beams has opened up a number of fascinating new fields. To further develop the new fields of science, the RIBF is under construction at RIKEN.[8,9)] This system consists of three ring cyclotrons, $K = 570$ MeV fixed frequency Ring Cyclotron (fRC), 980 MeV Intermediate stage Ring Cyclotron (IRC), and 2500 MeV Superconducting Ring Cyclotron (SRC), and will boost the energies of the output beams from the existing RRC up to 440 MeV nucl.$^{-1}$ for light ions and 350 MeV nucl.$^{-1}$ for heavy ions up to ^{238}U. These energetic heavy-ion beams are converted into RI beams *via* projectile fragmentation or in-flight fission of ^{238}U by the superconducting isotope separator, BigRIPS. Thus, RIBF can derive 3000 kinds of RI beams with the world's highest intensity. The beam intensities for radioisotopes near the stable line, which have relatively long half-lives ($\lesssim$ 1 min) and are practically available for radioactive tracer studies and for radiopharmaceutical diagnosis and therapy, are over 10^{10} atoms s^{-1}.[10)] We can catch the RI beams directly with suitable materials such as water, acids, physiological saline, and radiopharmaceuticals. We can select a radionuclide of interest with suitable decay properties for its application. Since they are mass-separated from other fragment isotopes, no chemical separations may be required for preparations of tracer solutions. These tracer solutions should be infinitely pure and carrier free compared with those produced by conventional cyclotrons or reactors with the aid of chemical separation. As examples, RIBF can generate the isotopes of ^{28}Mg and ^{67}Cu, which are not readily available at present, with intensities of 2.1×10^9 and 4.6×10^{10} atoms s^{-1}, respectively.[10)] These result in 1.2 GBq for ^{28}Mg and 11 GBq for ^{67}Cu after one-day irradiation. Thus, the RI beams derived from the future RIBF are expected to open new frontiers in nuclear and radiochemistry as next-generation producers of radioactive tracers.

References

1) S. Ambe et al.: Chem. Lett. **1991**, 149.
2) Y. Yano and S. Enomoto: RIKEN Rev., No.35 (2001).
3) H. Haba et al.: RIKEN Accel. Prog. Rep. **37**, 132 (2003).
4) S. Ambe: RIKEN Rev., No.13, 3 (1996).
5) S. Ambe et al.: Anal. Sci. **7**, Suppl., 317 (1991).
6) S. Ambe et al.: Radiochim. Acta **89**, 63 (2001).
7) R. B. Firestone and V. S. Shirley: *Table of Isotopes*, 8th ed. (John Wiley & Sons, New York, 1996).
8) T. Kubo: Nucl. Instrum Methods Phys. Res. B **204**, 97 (2003).
9) I. Tanihata: Nucl. Phys. A **734**, 271 (2004).
10) T. Suda: private communication.

Extraction behavior of Zr and Hf into TBP from hydrochloric acid: Development of TBP resin for reversed-phase extraction chromatography of element 104, rutherfordium

H. Haba, K. Tsukada,* K. Akiyama,* M. Asai,* A. Toyoshima,* Y. Ishii,* S. Enomoto, and Y. Nagame*

The extraction behavior of the first transactinide element, rutherfordium (Rf), into tributylphosphate (TBP) has been investigated together with its lighter group-4 homologues Zr and Hf and the actinide pseudo-homologues Th(IV) and Pu(IV).[1] The extraction of Rf into TBP is considered to proceed according to the following two reactions.

$$\mathrm{M(OH)}_x\mathrm{Cl}_{4-x} + x\mathrm{HCl} \longleftrightarrow \mathrm{MCl}_4 + x\mathrm{H_2O} \quad (1)$$

$$\mathrm{MCl}_4 + y\mathrm{TBP\ (aq.)} \longleftrightarrow \mathrm{MCl}_4 \cdot y\mathrm{TBP\ (org.)} \quad (2)$$

Thus, from the extraction behavior of Rf into TBP, we can expect to obtain information, such as chloride complexation and hydrolysis, and the stability of TBP complexes. Czerwinski *et al.*[2] first examined the extraction behavior of Zr, Hf, Th, Pu, and Rf into 0.25 M TBP in benzene in 8–12 M HCl. Their results showed that the extractability of these elements increases or remains high as a function of HCl concentration and that the extractability decreases in the order of Zr > Rf > Hf. Kacher *et al.*[3] performed some additional extractions of Rf into TBP/benzene using Ti, Zr, and Hf, and revised the extraction sequence by Czerwinski *et al.*[2] as Zr > Hf > Rf > Ti at about 8 M HCl. On the other hand, a reversed-phase chromatographic separation of Rf, Zr, and Hf at 8 M HCl was performed by Günther *et al.*[4] using microcolumns containing TBP on an inert support, and the order of Zr > Rf > Hf was obtained. Recently, we have investigated the adsorption behavior of Rf, Zr, and Hf on a strongly basic anion-exchange resin from 4.0–11.5 M HCl using an automated ion-exchange separation apparatus coupled with a detection system for alpha spectroscopy (AIDA).[5] Using AIDA, we plan to perform a reversed-phase extraction chromatography of Rf in the TBP-HCl system to clarify the conflicting results mentioned above.[3,4] As the first step, we developed a TBP resin for microcolumns of AIDA (1.6 mm i.d. × 7.0 mm or 1.0 mm i.d. × 3.5 mm) and investigated its performance by the batch method using radiotracers ^{89}Zr and ^{175}Hf.

The carrier-free radiotracers of ^{89}Zr and ^{175}Hf were produced in the ^{89}Y(p,n) and ^{175}Lu(p,n) reactions, respectively, using a 14-MeV proton beam from the RIKEN K70 MeV AVF Cyclotron. A support material used was MCI GEL CHP20Y, supplied by Mitsubishi Chemical Corporation, a styrene-divinylbenzen copolymer with a particle size of about 30 μm. The resin was washed several times alternately by the batch method with methanol and acetone, and was dried at 110°C in a vacuum oven. The resin in a beaker was suspended in methanol with stirring, and TBP was dropped. After stirring hermetically for 12 h, methanol was evaporated to dryness at room temperature, and dried to a constant weight at 110°C. The TBP weight percentages (wt.%) were 5–60%. The TBP resin (5–30 mg) and 3 mL of 6.0–11.9 M HCl containing 50 μL of ^{89}Zr and ^{175}Hf tracer solution in 6 M HCl were placed in a polypropylene tube and shaken for 4 h at 20°C. After centrifugation, 1 mL of the aqueous phase was pipetted into a polyethylene tube and subjected to γ-ray spectrometry using a Ge detector. As a standard sample, 50 μL of the tracer solution was diluted to 1 mL with 6.0 M HCl in another polyethylene tube. The distribution coefficient K_d in mL g^{-1} was obtained using $K_\mathrm{d} = A_\mathrm{r}V_\mathrm{s}/A_\mathrm{s}W_\mathrm{r}$, where A_r and A_s are the radioactivities in the resin and the solution, respectively, and V_s is the volume of the acid solution and W_r is the mass of the dry resin.

In Fig. 1 (a), the variations of the K_d values of

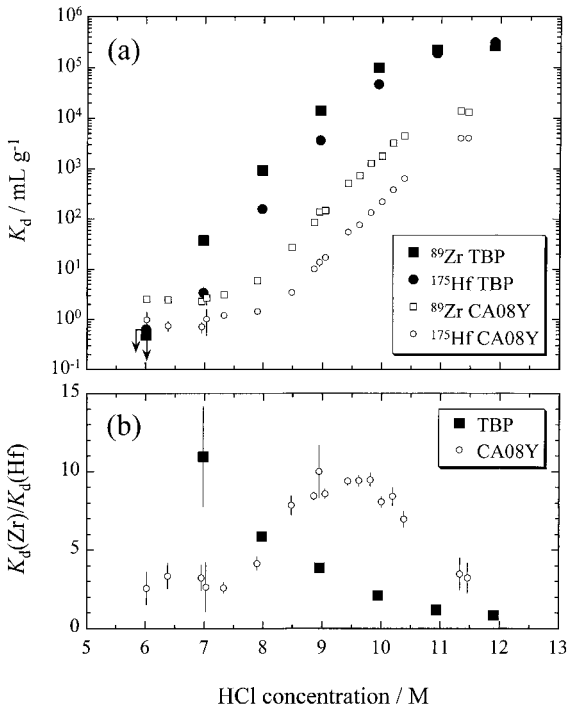

Fig. 1. Variations of (a) K_d values of ^{89}Zr and ^{175}Hf on 26-wt.% TBP resin and of (b) the separation factor K_d(Zr)/K_d(Hf) as a function of HCl concentration, compared with those on the anion-exchange resin CA08Y.[5]

* Advanced Science Research Center, Japan Atomic Energy Research Institute

^{89}Zr and ^{175}Hf on the 26-wt.% TBP resin are indicated by closed squares and closed circles, respectively, as a function of HCl concentration ([HCl]) compared with those on the anion-exchange resin CA08Y.[5] As shown in Fig. 1, the K_d values of Zr on the TBP resin are larger than those of Hf, and both increase steeply up to 3×10^5 mL g^{-1} with [HCl]. This range of the K_d values fully covers that of CA08Y, with which the anion-exchange separation of Rf was successfully performed using AIDA.[5] On the other hand, the separation factors $K_d(\mathrm{Zr})/K_d(\mathrm{Hf})$ are indicated in Fig. 1 (b) by closed squares. The $K_d(\mathrm{Zr})/K_d(\mathrm{Hf})$ values decrease with [HCl] from ∼10 at 7.0 M, and become constant at about 11.0 M. A difference in the extractability among the group-4 elements may be clearly found at ∼7 M, where a good separation between Zr and Hf is achieved. In separate experiments, we also investigated the variations of K_d values as a function of wt.% of the resin. The K_d values increase smoothly with wt.% in the studied wt.% range of 5–60%. We can adjust the extractability of the TBP resin by varying its wt.%.

Using the TBP resin developed in the present work, we will conduct the on-line extraction chromatography of ^{261}Rf, ^{85}Zr, and ^{169}Hf at the JAERI Tandem Facility. In addition, the detailed structural data of Zr and Hf in HCl and in TBP are essential for discussing the experimental results of Rf and performing the theoretical molecular orbital calculations. We will measure the extended X-ray absorption fine structure (EXAFS) spectra of the Zr and Hf complexes at the High Energy Accelerator Research Organization Photon Factory. Furthermore, relativistic molecular orbital calculations will be performed for chloride and TBP complexes of Rf, Zr, and Hf to discuss chloride complexation and the stability of TBP complexes in detail and to obtain information on the electronic structure of Rf such as the influences of relativistic effects.

References

1) M. Schädel: *The Chemistry of Superheavy Elements* (Kluwer Academic Publishers, Dordrecht, 2003).
2) K. R. Czerwinski et al.: Radiochim. Acta **64**, 29 (1994).
3) C. D. Kacher et al.: Radiochim. Acta **75**, 127 (1996).
4) R. Günther et al.: Radiochim. Acta **80**, 121 (1998).
5) H. Haba et al.: J. Nucl. Radiochem. Sci. **3**, 143 (2002).

Development of on-line solvent extraction system for heavy actinide elements

Y. Kitamoto,* D. Saika,* K. Matsuo,* Y. Tani,* H. Hasegawa,* W. Sato,* N. Takahashi,* T. Yoshimura,* H. Haba, S. Enomoto, and A. Shinohara*

It is theoretically expected that the chemical properties of the heaviest elements such as heavy actinide and trans- actinide elements deviate from the periodicity exhibited among their lighter homologues due to the influence of the relativistic effect. However, a limited number of atoms (one or a few typically) are available at a time because of their short lifetime and small production cross section in heavy-ion-induced nuclear reactions. In the experimental conditions, rapid chemical operations and measurements need to be performed many times. Therefore, we are developing an automated rapid chemical apparatus for the chemical studies of the heavy actinide elements. The apparatus using solvent extraction and the anion-exchange method is schematically shown in Fig. 1. In this work, the distribution of lanthanide elements in the solvent extraction by thenoyltrifluoroacetone (TTA) was studied with the apparatus as a simulation for actinide elements.

A batch experiment was performed with radiotracers of ^{153}Gd, ^{169}Yb and ^{170}Tm. The tracers were dissolved in a 0.5 M acetic buffer (pH 4.46) as an aqueous phase. TTA was dissolved in toluene and adjusted to 0.01–0.1 M (organic phase). A one milliliter portion of each solution was mixed and shaken for 20 minutes. After centrifugation, 0.8 mL aliquots of both phases were collected separately and subjected to γ-ray spectroscopy with a Ge detector.

An on-line experiment was performed using the E3b course of the RIKEN Accelerator Research Facility. The ^{nat}Pb targets (2 μm in thickness×30 sheets) were irradiated with 135 MeV/nucleon ^{14}N ions with an intensity of 50 pnA on average. The nuclides produced by the ^{nat}Pb (^{14}N, X) nuclear reactions were transported through a capillary tube with a gas jet to the hot laboratory within a few seconds.

They were collected on a dissolver unit and dissolved in a mixture of methanol and nitric acid at a volume ratio of 90 to 10%. They were then fed into an anion-exchange column (MCI GEL CA08Y, Mitsubishi Chemical Corporation, 2.0 mm i.d. × 60 mm). Lanthanide elements were held on the column, while their coproducts such as transition elements were eluted. An acetic buffer solution (0.5 M, pH 4.46) was fed into the column in order to elute the lanthanide elements. The eluent was mixed with a 0.024–0.046 M TTA-toluene solution with a static mixer and stirred ultrasonically for 2 minutes. After centrifugation, 0.8 mL aliquots of both phases were collected separately and subjected to γ-ray spectroscopy with a Ge detector. The yields of lanthanide elements for the gas-jet transportation, dissolution and anion exchange were 10%, 20–50% and 20–30%, respectively. Almost all of transition elements were removed by the anion exchange. The elapsed time during the chemical operation before the γ-ray measurement was approximately 12 minutes.

The distribution ratio (D) in the solvent extraction is represented as

$$D = A_{\mathrm{org}} V_{\mathrm{aq}} / A_{\mathrm{aq}} V_{\mathrm{org}},$$

where A_{org} and A_{aq} are activities [Bq] in organic and aqueous phases, respectively, and V_{org} and V_{aq} are volumes [mL] in organic and aqueous phases, respectively. The extraction of trivalent lanthanide elements by HTTA from the aqueous solution is represented by

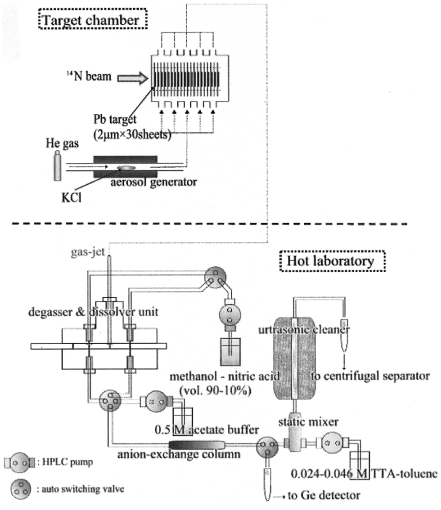

Fig. 1. Automated rapid chemical operation apparatus for solvent extraction.

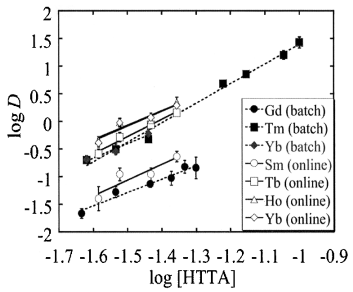

Fig. 2. Variation fo log D with log [HTTA], where D = [Ln(TTA$_3$)]/[Ln^{3+}]. The slopes of all lines are approximately.

* Department of Chemistry, Osaka University

the reaction:

$$\mathrm{Ln}^{3+}_{\mathrm{aq}} + 3\mathrm{HTTA}_{\mathrm{org}} \rightleftarrows \mathrm{Ln(TTA)}_{3\ \mathrm{org}} + 3\mathrm{H}^{+}_{\mathrm{aq}}.$$

A linear relationship with a slope of three is expected for the plot of log D (where $D = [\mathrm{Ln(TTA)_3}]/[\mathrm{Ln}^{3+}]$) as a function of log $[\mathrm{HTTA}]_{\mathrm{org}}$.

The experimental result is shown in Fig. 2. The variations of the distribution ratio for the lanthanide elements against the concentration of HTTA in both the on-line and the batch experiments are shown by the closed symbols and open symbols, respectively. The least square fits to each element are shown by various lines. It was found that the slopes of the log D-log[HTTA] plots for each element were approximately three and the distribution ratio in the on-line experiments agrees with that of the batch experiments.

Reactions of ^{57}Mn implanted into solid oxygen (II)

Y. Kobayashi, H. Nonaka,[*1] J. Miyazaki,[*1] K. M. Kubo,[*2] H. Ueno, A. Yoshimi, H. Miyoshi,[*3] D. Kameda,[*3] K. Shimada,[*3] D. Nagae,[*3] G. Kato,[*3] and Y. Yamada,[*1]

We have performed an in-beam Mössbauer spectroscopic experiment using a short-lived ^{57}Mn beam, in order to study the electronic structures, especially exotic high oxidation states, of ^{57}Fe atoms decaying from ^{57}Mn implanted into solid oxygen. From our previously obtained in-beam Mössbauer spectra of ^{57}Fe ($\leftarrow$ ^{57}Mn) implanted into $KMnO_4$ between 11 K and 155 K, the ^{57}Fe atoms occupying Mn sites in a $[MnO_4]^-$ tetrahedron were found to be in an unusually high valence state of Fe (VIII).[1)] In more reactive matrices, Fe species with extraordinarily higher oxidation states are expected to be produced. In this study, we carry out an implantation Mössbauer study of ^{57}Fe ($\leftarrow$ ^{57}Mn) in solid O_2. We determine novel Fe oxide species produced from the decay of ^{57}Mn with a high translational energy and compare them with those obtained by the rare-gas matrix isolation technique with laser-ablated Fe atoms.[2)] The ^{57}Fe atoms decaying from ^{57}Mn have an extremely higher energy than the laser-ablated Fe atoms upon implantation and decay, which provides important information on chemistry under extreme conditions and on the production of novel species.

^{57}Mn particles were produced as RI beams following the nuclear projectile fragmentation of ^{58}Fe beams ($E = 62\,A$ MeV) with a Be target using RIPS, and subsequently implanted into a solid O_2 sample. An enriched ^{58}Fe ferrocene (^{58}Fe $(C_5H_5)_2$) compound was employed as an ion source to obtain a larger ^{57}Mn yield.

The in-beam ^{57}Fe ($\leftarrow$ ^{57}Mn) Mössbauer spectrum of solid O_2 obtained at 18 K is shown in Fig. 1. The total measuring time was 18 hr. The quality of this complicated spectrum was sufficient for detailed analysis. This was the reason why the number of ^{57}Mn particles (approximately 5×10^6 particles/s) increased 20 times that obtained in our previous experiments.

The oxidation of Fe is a fundamentally and chemically interesting subject because it is related to the corrosion of materials and catalytic reactions. The simplest oxidation of Fe is the reaction between an Fe atom and an oxidizing gas. Yamada *et al.* investigated the reaction of laser-ablated Fe atoms with O_2 gas by the rare-gas matrix isolation technique at low temperatures.[2)] Reaction products were determined by conventional Mössbauer spectroscopy, IR spectroscopy, and ab-initio molecular orbital calculations. They concluded that Fe_n clusters, FeO, Fe (O_2), FeO_3, (O_2) Fe (O_2), and OFeO species were produced and isolated in the Ar matrix. Our present result could be analyzed using their Mössbauer parameters. Fe (O_2) (A in Fig. 1), FeO (B), and Fe^{2+} species with a low-spin state (C), and an exotic high oxidation state (probably Fe^{8+}, D) are preliminarily assigned. The observations obtained by in-beam Mössbauer measurements will be reported elsewhere.

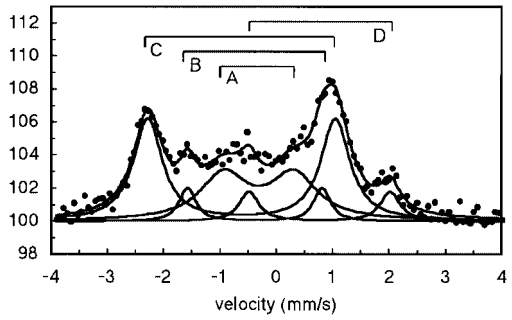

Fig. 1. In-beam Mössbauer spectrum of ^{57}Fe ($\leftarrow$ ^{57}Mn) implanted into solid oxygen at 18 K.

References

1) Y. Kobayashi et al.: J. Radioanal. Nucl. Chem. **255**, 403 (2003).
2) Y. Yamada et al.: Appl. Radiat. Isot. **52**, 157 (2000).

*1 Department of Chemistry, Science University of Tokyo
*2 International Christian University
*3 Tokyo Institute of Technology

Development of ^{83}Kr Mössbauer Spectroscopy

M. K. Kubo,[*1] Y. Kobayashi, Y. Kawaguchi,[*1] Y. Yamada,[*2] and H. Haba

Krypton is a rare gas (Rg) element and thus has limited chemical reactivity. Immediately after the discovery of the reaction of xenon and fluorine to yield xenon fluorides, the first krypton compound KrF_2 was synthesized in 1963.[1] Since then, continuous research efforts have been made in preparing various krypton, xenon and argon compounds to investigate the nature of chemical bonds in these Rg compounds. For Kr compounds, only those containing fluorine had been known until the discovery of HKrCl in 1995[2] using *ab initio* calculations. There have been a few attempts to synthesize novel Rg compounds containing Rg-C bonds.[3] In these attempts, the matrix-isolation-laser-excitation (MILE) technique was adopted. A Rg matrix is condensed onto a CsI substrate with a reactant compound, *e.g.*, hydrogen cyanide at low temperatures. After condensation, the matrix is irradiated with a laser beam to excite the reactant compound to form a stable Rg compound. The compounds formed are confirmed by IR spectroscopy. In MILE experiments, a Rg atom can form a chemical bond with only one reactant molecule, because the reactant concentration is kept low (molar ratio of Rg / reactant $\geq$ 1000). In 2003, compounds with xenon and acetylene were prepared.[4] Krypton compounds with similar structures are believed to exist, but have not been experimentally confirmed.

We have been applying the ion implantation method to produce novel and rare chemical compounds of iron using the RIKEN cyclotron in combination with emission Mössbauer spectroscopy as a characterization method.[5] By the method, we prepare various solid targets to react with incoming ions. We may observe the reactions of krypton with various solid materials using the RIKEN cyclotron.

Fortunately, krypton has the Mössbauer active nuclide ^{83}Kr. Mössbuaer spectroscopy will provide information on the electronic states of krypton, such as the valence state and electric field gradient at the Kr nucleus, complementary to IR spectroscopy which gives atom-atom bond parameters. Particularly, aiming at the production of compounds consisting of a krypton and two or more reactant molecules beyond the scope of the dilute MILE condition, we have started a new project on ^{83}Kr Mössbuaer spectroscopy using the RIKEN cyclotron. As the first step, we are setting up a Mössbauer spectrometer for ^{83}Kr using a radioisotope source ^{83}Rb ($T_{1/2} = 86.2$ d).

The nuclear level scheme of ^{83}Kr is shown in Fig. 1. The Mössbauer level of ^{83}Kr is the first excited state

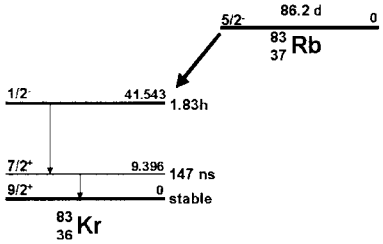

Fig. 1. Energy levels of ^{83}Kr.

at 9.396 keV. Above this level, there is the metastable state ^{83m}Kr with a half-life of 1.83 h. ^{83}Kr Mössbauer studies have been carried out since the 1960's. Most of the former studies used ^{83}Rb as the radiation source embedded in solid matrices.[6] We propose to use ^{83m}Kr as the radiation source separated from ^{83}Rb to reduce the radiation background arising from ^{83}Rb. By depositing carrier-free ^{83m}Kr on a cold plate and using it as the source, we will be able to obtain Mössbauser spectra of good quality.

Our plan for ^{83m}Kr source preparation is as follows: A $CaBr_2$ target is irradiated with an α particle beam of 25 MeV. After the irradiation, the target is dissolved in water. By adding an $(NH_4)_2CO_3$ solution to precipitate and separate $CaCO_3$, the solution is passed throuth a cation exchange resin column on which ^{83}Rb is adsorbed. Within one day, ^{83}Rb and ^{83m}Kr attain radiochemical equilibrium. The column is dried and attached to a gas handling line leading to the end nozzle facing the cryostat cold head. A slow stream of helium gas carries ^{83m}Kr to the cold head to be used as the Mössbauer source.

We carried out α particle beam irradiation and are now verifying the processes of the chemical separation.

References

1) J. J. Turner and G. C. Pimentel: Science **140**, 974 (1963).
2) M. Pettersson, J. Lundell, and M. Räsänen: J. Chem. Phys. **102**, 6423 (1995).
3) For example, M. Pettersson, J. Lundell, L. Khriachtchev, and M. Räsänen: J. Chem. Phys. **109**, 618 (1998).
4) L. Khriachtchev et al.: J. Am. Chem. Soc. **125**, 4695 (2003); V. I. Feldman et al.: J. Am. Chem. Soc. **125**, 4698 (2003).
5) For example, Y. Yamada et al.: RIKEN Accel. Prog. Rep. **37**, 112 (2004).
6) S. Bukshpan et al.: Int. J. Appl. Radiat. Isot. **27**, 15 (1976).

[*1] Department of Chemistry, International Christian University
[*2] Department of Chemistry, Tokyo University of Science

Effects of carnosine (β-alanyl-L-histidine) on the absorption of iron in rats

K. Igarashi, S. Kimura,* and S. Enomoto

Iron deficiency is probably the most frequent nutritional disorder in the world. One of the main causative factors is the poor absorption of iron, because nonheme iron, the main form of dietary iron, has a low intestinal absorption efficiency compared with heme iron. Furthermore, the absorption of nonheme iron is affected by the inhibitors such as phytic acid and polyphenols. Therefore, the enhancement of nonheme iron absorption is important for improving iron nutrition.

It is well-established that the bioavailability of nonheme iron from food is enhanced by vitamins, organic acid, meat, poultry and fish. Ascorbic acid and citric acid maintain iron in a more soluble and absorbable form, and prevent its binding to inhibitory ligands.[1] Although meat stimulates nonheme iron absorption, the factor in meat responsible for enhancing nonheme iron absorption is yet to be identified.

Carnosine (β-alanyl-L-histidine) is observed in millimolar concentrations in the skeletal muscles and brains of animals. It has been proposed to serve as a natural antioxidant *in vivo*.[2] Recently, the pharmacological activity of the carosine-metal complex has been studied.[3]

Thus, to investigate the effects of carnosine for the absorption of nonheme iron, we determined the change in serum iron concentration in rats administered ferrous sulfate and carnosine using a cannulation system.

Eight-week-old male Wistar rats were purchased and housed in stainless-steel cages. The method of cannula preparation was as described by Taguchi *et al.* and Spannagel *et al.*[4–6] After treatment, the rats were placed in Bollman-type restraint cages modified to provide the minimum restraint possible. Three days after surgery, the rats were administered 5 mg iron/rat as ferrous sulfate with or without carnosine at a dose of 30 mg into the stomach simultaneously. Then the blood was collected at regular intervals, plasma and blood cells were separated by centrifugation (3000 rpm for 15 min). To determine the bioavailability of iron, serum iron concentration was measured using a kit by the Nitroso-PSAP method.[7]

The changes in serum iron concentration in rats are shown in Fig. 1. The serum iron concentration in rats administered with ferrous sulfate reached its maximum from 30 to 60 min, and decreased thereafter. On the other hand, the serum iron concentration in rats administered with ferrous sulfate in the presence of carnosine significantly increased at 15 min, and remained constant up to 45 min after treatment. The serum iron concentration in rats administered with ferrous sulfate in the presence of carnosine was significantly higher than that in rats administered with ferrous sulfate after treatment for 15 min, indicating that the rats administered ferrous sulfate with carnosine promoted the uptake of iron into the body. Although we further determined the iron incremental area to investigate iron absorption, no significant difference was observed between ferrous sulfate-administered rats and ferrous sulfate-administered rats with carnosine.

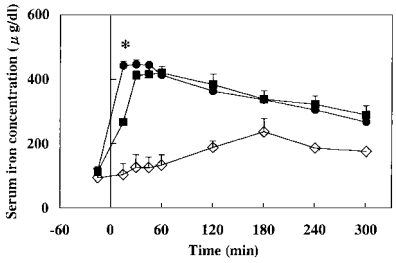

Fig. 1. Changes in serum iron concentration in rats. ◇: control, ■: ferrous sulfate, ●: ferrous sulfate with carnosine. * Significant differences were observed between ferrous sulfate-administered rats and ferrous sulfate-administered rats with carnosine.

These results suggest that carnosine may facilitate the velocity of iron absorption of ferrous sulfate. However, the stability constant of carnosine for iron was lower than that for other metals. It is assumed that carnosine has a mechanism for facilitating the velocity of iron absorption other than its chelating property.

References

1) I. M. Zijp et al.: Crit. Rev. Food Sci. Nutr. **40**, 371 (2000).
2) M. A. Babizhayev et al.: Biochem. J. **304**, 509 (1994).
3) M. Seiki et al.: Folia Pharmacologica Japonica **95**, 257 (1990).
4) S. Taguchi et al.: Jpn. J. Clin. Physiol. **24**, 241 (1994).
5) A. W. Spannagel et al.: Am. J. Physiol. **270**, G128 (1996).
6) K. Igarashi et al.: RIKEN Accel. Prog. Rep. **37**, 115 (2003).
7) M. Saito et al.: Bunseki Kagaku **30**, 635 (1981).

* Graduate School of Human Life Sciences, Showa Women's University

Cannulation study on the absorption of iron in rats: Effect of L-catechin as a polyphenol

K. Igarashi, S. Kimura,* and S. Enomoto

Polyphenols are widely present in the human diet. The consumption of polyphenols in the USA is estimated at 1 g/d,[1] and as much as 0.5 g/d is consumed from tea in the UK.[2] Several thousand molecules have been identified in various plant species, where they have several functions. Tannins give astringency or bitterness, and anthocyanins give color to red fruits such as strawberries and grapes. Others such as isoflavone phytoestrogens in soy bean are restricted to a given food source. Recent studies have shown that polyphenols are reducing agents similar to vitamin C, vitamin E and carotenoids. They may prevent various diseases associated with oxidative stress, such as cancers, cardiovascular diseases and inflammations.

On the other hand, polyphenols are inhibitors of the iron absorption. Phenolic compounds bearing catechol groups (*e.g.*, catechin) or galloyl groups (*e.g.*, gallic acid) have iron-binding properties. Tea, coffee, cocoa, red wine, many vegetables, grains, herbs and spices contain such phenolic compounds and all have an in vitro inhibitory effect on the iron absorption.

Iron is one of the essential trace elements for humans. The dietary form of iron plays a role in absorption and also in iron balance. Heme iron is absorbed as an intact porphyrin structure by specific receptors in the brush border mucosa[3] and therefore heme iron is not affected by other constituents of diet. While nonheme iron is present in foods as ferric and ferrous salts. In intestinal lumen, iron is released and rapidly chelated by other constituents in food. There are two types of chelator. One class called enhancers forms soluble low-molecular-weight chelates that are absorbed easily and the other class called inhibitors forms insoluble high-molecular-weight chelates that are unavailable for absorption.

Thus, we determined the effects of catechin on the absorption of iron in rats. We used a cannulation system for investigating iron absorption in rats administered with polyphenol because it is effective in determining the biological response to infused samples in the stomach of conscious rats.

Eight-week-old male Wistar rats were purchased and housed in stainless-steel cages in a temperature- and light-controlled room. The methods of cannula preparation and animal treatment were shown previously.[4] Three days after surgery, the rats were administered catechin and ferrous sulfate into the stomach simultaneously. Then blood was collected at regular intervals, and plasma and blood cells were separated by centrifugation (3000 rpm. for 15 min). To determine the bioavailability of iron, serum iron concentration was measured using a kit by the Nitroso-PSAP method.[5]

The serum iron concentration in ferrous sulfate-administered rats increased to 412 μg/dl from 15 to 30 min. It maintained the same level up to 60 min and then gradually decreased. The serum iron concentration of rats administered ferrous sulfate and catechin reached 457μg/dl after administration for 15 min, and remained constant up to 30 min. The serum iron concentration of rats administered ferrous sulfate and catechin was significantly high compared with that in rats administered ferrous sulfate at 15 min. No significant difference was observed between ferrous sulfate-administered rats and ferrous sulfate-administered rats in the presence of catechin, indicating that the absorption of iron was not inhibited by catechin in the rats administered with ferrous sulfate.

The result of this study demonstrates that catechin does not affect the iron absorption of ferrous sulfate. However, catechol groups are considered to be the phenolic constituents mainly responsible for the iron binding capacity of condensed tannins. Although Brune et al. reported that the binding property of a galloyl group was higher than that of a catechol group,[6] it is thought that the result of this study is due to the amount of catechin being very small compared with that of ferrous sulfate.

References

1) J. Kuehanau: World Rev. Nutr. Diet **24**, 117 (1979).
2) G. V. Stagg et al.: J. Sci. Food Agric. **26**, 1439 (1975).
3) R. Grasbeck et al.: Biochim. Biophys. Acta **700**, 137 (1982).
4) K. Igarashi et al.: RIKEN Accel. Prog. Rep. **37**, 115 (2004).
5) M. Saito et al.: Bunseki Kagaku **30**, 635 (1981).
6) M. Brune et al.: Eur. J. Clin. Nutr. **43**, 547 (1989).

* Graduate School of Human Life Sciences, Showa Women's University

Influence of pantothenic deficiency on intestinal flora in rats

M. Hasama,[*1] Y. Iizuka,[*2] N. Iwasaki,[*2] S. Enomoto, and S. Kimura[*1]

Pantothenic acid (PA), which is a component of coenzyme A (CoA) and acyl-carrier protein, is an essential nutrient for many animals. The majority of PA in food is present as a component of CoA that participates in the metabolism of carbohydrate, liquid and protein. CoA has been associated with more than 70 enzymatic reactions *in vivo*. Human PA deficiency is rare, because it is widely distributed in food.

In clinical medicine, disulfide pantetheine, pantethine (PaSS), is used as a remedy for atonic constipation and a postoperative paralyzed intestine. Because PaSS is known to increase intestinal motility, a possible mechanism of increasing intestinal motility by PaSS is thought to be defined by several factors. One factor is the energy production of muscle contraction. Muscle contraction depends on ATP and is closely associated with CoA. On the other hand, intestinal floras such as *Lactobacillus* also play an important role in intestinal motility. *Lactobacillus* requires PA and PaSS as essential nutrients. *Lactobacillus* and its metabolic substance are closely associated with intestinal motility. These facts indicate that PA and PaSS are important vitamins that support intestinal motility.

In this study, we determined whether PA deficiency decreases intestinal motility in rats, and discussed its mechanism by changing the intestinal flora and reducing the energy metabolism.

We observed that the food transit time in PA-deficient rats was significantly delayed (control, 7.3 ± 2.7 hr; PA deficiency, 11.8 ± 2.0 hr, $p < 0.01$). In addition, the number of contractions in the PA deficient rat cecum was significantly reduced (control, 715 ± 36 counts/hr; PA deficiency, 215 ± 23 counts/hr, $p < 0.01$). These results suggest that PA deficiency obviously affects intestinal motility and delays food transport in the large intestine.

Decreasing intestinal motility in PA-deficient rats affects the alternation of the intestinal flora. However, the cultivation of the intestinal flora by anaerobic culture is very difficult. Thus, we measured the concentrations of materials produced such as fatty acids and organic substances produced by a bacterium.

Table 1 shows the concentrations of various organic acids in the cecum. The concentrations of main short fatty acids (SCFAs), such as propionate, acetate, and *n*-propionate, decreased, while that of succinate increased in PA-deficient rats. Approximately 95% of SCFAs in the large intestine are immediately absorbed from large intestinal epithelial cells and recycled as nutritional sources.[1)] Approximately 4.7% of the total energy in rats induce the uptake of SCFAs, which are metabolized by intestinal floras.[2)] Decreasing SCFA concentration in PA-deficient rats is associated with the loss of energy in the intestine.

Table 1. Concentrations of various organic acids in rat cecum.

	Control	PA deficiency
Organic Acid	μmol/cecum	
Acetate	62.87 ± 26.32	$22.25 \pm 6.96^{\S 1}$
Propionate	30.10 ± 13.34	$11.06 \pm 5.81^{\S 2}$
n-Butirate	27.16 ± 13.09	9.48 ± 4.33
SCFA Total	93.02 ± 33.28	$33.41 \pm 8.52^{\S 1}$
Succinate	13.33 ± 8.21	$70.06 \pm 32.17^{\S 1}$

Each value represents the mean ± S.D. of data from eight rats. $^{\S 1}$ and $^{\S 2}$ indicate significant differences between control group and pantothenic acid (PA) deficiency group. $^{\S 1}$ $p < 0.01$, $^{\S 2}$ $p < 0.05$.

As described above, PA is an essential nutrient for intestinal floras. In particular, *Lactobacillus bifidus* requires pantetheine, which is a PA derivative. Citrate lyase (EC4.1.3.6), which produces acetate and oxalo acetate from citrate, is extracted from *Klebsiella aerogene* and *Streptococcus diacetilactis*.[3)] Citramalate lyase (EC4.1.3.22), which produces acetate and pyruvate from citra-maleate, is purified from *Clostridium tetanomorphum*.[4)] These enzymes interact with 4′-phospho-pantetheine, which is a PA-derivative. The above-mentioned bacteria are considered to require PA and its derivative.

Our results indicate that PA is effective for the control of intestinal floras. In the PA- and PA-derivative-deficient situations, the amount of good bacteria such as *L. bifidus* is low. This phenomenon is speculated to be caused by decreasing SCFA concentration.

In this study, succinate in the intestine was found to suppress intestinal motility. An organic acid in the cecum was determined to increase the concentration of succinate in PA-deficient rats.

Therefore, we conclude that the animal of good bacteria such as *L. bifidus* is low in the intestine of PA-deficient rats. This phenomenon changes the concentration of organic acids, decreases the production of SCFAs and increases the concentration of succinate, resulting in a decrease in intestinal motility.

*1 Graduate School of Human Life Science, Showa Women's University
*2 Tokyo R&D Center, Daiichi Pharmaceutical Co., Ltd.

References

1) W. V. Engelhardt, K. Roennau, G. Rechkemmer, and T. Sakata: Anim. Feed Sci. Technol. **23**, 43 (1989).
2) N. I. McNeil: Am. J. Clin. Nutr. **39**, 338 (1984).
3) P. Dimroth and H. Eggerer: Proc. Natl. Acad. Sci. USA **72**, 3458 (1975).
4) M. Singh, J. B. Robinson, and P. A. Srere: J. Biol. Chem. **252**, 6061 (1977).

Effect of pantotenic acid and pantethine in aging rats

M. Hasama,* R. Sato,* E. Mizukami,* K. Okiyama,* S. Enomoto, and S. Kimura*

Atonic constipation is a serious problem for elderly people. In this situation, a disulfide type of pantetheine, pantethine (PaSS), is widely used to increase intestinal motility in clinical medicine. Because synthesis from pantothenic acid (PA) to coenzyme A (CoA) is decreased,[1] the biosynthetic reaction rate of pantetheine from PA influences aging.[2]

In this study, to identify the interaction of PA deficiency in aging, we determined the effect of PA and PaSS on aging rats. We raised PA-deficient Wistar male rats for 23 months and divided them into three groups; PA deficient, PA intake and PaSS intake groups. After raising them for one more month, we measured each rat's heart CoA concentration. As shown in Fig. 1, the CoA concentration in the PA intake group slightly increased in contrast to that of the PA deficient group. On the other hand, the CoA concentration in the PaSS intake group increased significantly and aided recovery from PA deficiency. These results suggest that the reaction from PA to pantetheine is the rate-limiting reaction in aging animals.

We observed the food transit time (TT) to identify the degree of intestinal motility. TT indicates the time from intake to excretion. The TT delays in normal rats take an average of 7–9 hours. PA-deficient aging rats had a TT of over 10 hours. Note that TT in the PA intake group did not decrease, in contrast to that in the PaSS intake group where it decreased. Intestinal motility recovery takes place with PaSS wherein the biosythesis of CoA is high, but not with PA; CoA concentration correlates with intestinal motility. This result supports those in clinical medicine wherein PaSS affects atonic constipation.

In addition, we observed a concentration of organic acid patterns in aging rat cecum. As shown in Fig. 2,

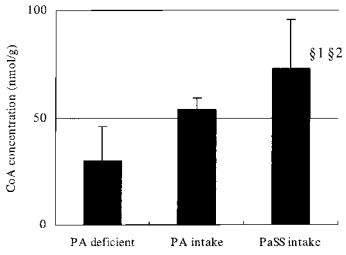

Fig. 1. Concentration of CoA in hearts of aging rats.
PA: pantothenic acid, PaSS: pantethine, §1 indicates significant difference between PA deficient group and PaSS intake group ($p < 0.01$). §2 indicates significant difference between PA intake group and PaSS intake group ($p < 0.05$).

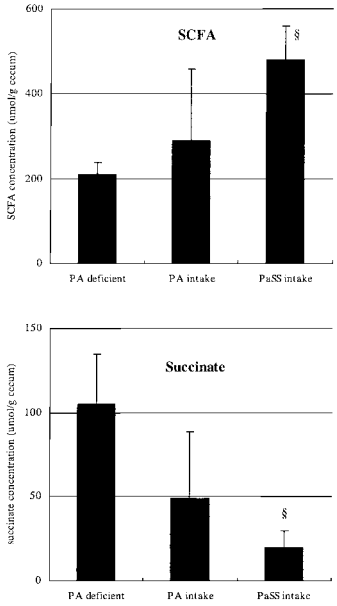

Fig. 2. Concentration of short chain fatty acid (SCFA) and succinate in cecum of aging rats.
PA: pantothenic acid, PaSS: pantethine, § indicates significant difference between PA deficient group and PaSS intake group ($p < 0.01$).

the PaSS intake group incurred an increase in short chain fatty acid (SCFA) concentration, but the PA intake group did not. On the other hand, the PaSS intake group incurred a decrease in succinate, but the PA intake group did not. In our previous study, PA deficiency caused a decrease in SCFA and an increase in succinate because the amount of good bacteria such as *L. bifidus* decreased. With the intake of PaSS, aging rats recovered from PA deficiency and utilized the good bacteria in there intestinal flora.

In conclusion, PaSS is more effective than PA in aiding the recovery of PA-deficient aging rats. These results showed that the biosynthesis reaction rate from PA to pantetheine was delayed.

These results are for the case of rats, however, we can speculate that for elderly people, CoA concentration likewise decreases. Our results indicate that atonic constipation in elderly people is closely related to PA deficiency.

References

1) S. Kimura: in *Vitamin*, edited by Japanese Society of Vitaminology (Asakura Shoten, Tokyo, 2000), p.255.
2) E. Coriandori: Naturwissenschaften **47**, 183 (1960).

* Graduate School of Human Life Science, Showa Women's University

Brain uptake behavior of ^{24}Na, ^{28}Mg, ^{43}K and ^{47}Ca by intranasal administration

Y. Kanayama,* H. Haba, S. Enomoto, and R. Amano*

Olfactory receptor neurons are in contact with the environment in the nasal cavity and the olfactory bulbs of the brain. Therefore, when certain kinds of proteins, viruses or metals are administered into the nasal cavities, the axonal transport of the olfactory neuron plays an important role in the pathway that directly enter the brain bypassing the blood-brain barrier.[1] Recently, we demonstrated that K^+-mimic ions, Rb^+, Cs^+, and Tl^+ are transported into the olfactory bulbs and delivered to other brain regions by intranasal administration.[2,3] However, the underlying mechanisms and physiological roles of the axonal transport of these K^+-mimic ions are poorly understood. Previously, we attempted simultaneous tracing of $^{24}Na^+$, $^{28}Mg^{2+}$, $^{43}K^+$, and $^{47}Ca^{2+}$ for clarifying their olfactory transport using the multitracer from a Ti target.[4]

The multitracer was obtained from a Ti foil target irradiated with a heavy-ion beam of 135 MeV/nucleon for 1 hour using the RIKEN Ring Cyclotron and prepared as a physiological saline solution.[4] The multitracer solution was intranasally administered to ICR mice (8-week-old, male). Six, 12, 24 and 48 h after the administration, mice were sacrificed, and then blood (BL), liver (LV), ethmoturbinals and brain samples were obtained. The brain was separated into 3 regions, the olfactory bulb (OB), the forebrain including the lateral olfactory tract, olfactory tubercles, and piriform cortex (FB), and the rest of the brain (RB). Activities were measured by γ-ray spectrometry using high-purity Ge detectors. The uptakes and uptake rates of each obtained sample were given as a percentage of the administered dose (%dose and %dose/g, respectively). The mean and standard deviation for three mice were determined for each set of elapsed time points.

Figure 1 shows the uptake behaviors of $^{24}Na^+$, $^{28}Mg^{2+}$, $^{43}K^+$ and $^{47}Ca^{2+}$ in the blood, liver, and brain regions following the intranasal administration of the multitracer. At 6 h, the brain regional distributions of ^{24}Na, ^{28}Mg and ^{43}K showed similar levels to those of our preliminary study.[4] The highest ^{43}K uptake rate was found in the OB at 6 h and decreased until 24 h. Meanwhile the uptake rate in the FB slightly increased until 12 h. In contrast, no regional difference was observed in the brain uptake rates of ^{24}Na throughout 48 h.

As for the alkaline earth metal ions, ^{28}Mg and ^{47}Ca

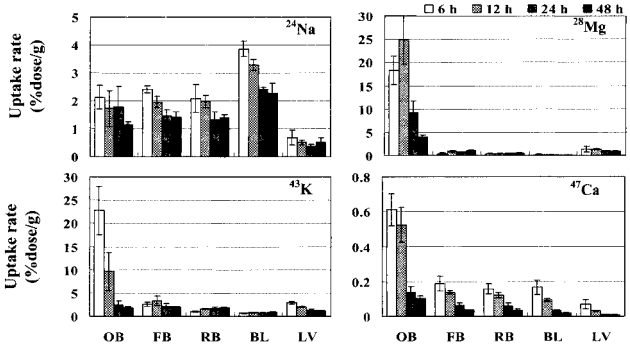

Fig. 1. Uptake rates of $^{24}Na^+$, $^{28}Mg^{2+}$, and $^{43}K^+$ in the blood, liver, and brain regions 6, 12, 24 and 48 hours after intranasal administration. IN: intranasal administration; OB: the olfactory bulbs; FB: the fore brain; RB: the rest of the brain.

were highly accumulated in the ethmoturbinals, which was virtually the access site, and also in the bone in the sample itself. There was a large difference in the uptake rate in the OB between ^{28}Mg and ^{47}Ca. Although the ^{47}Ca uptake in the ethmoturbinals maintained a high level until 48 h, the ^{28}Mg uptake rate decreased with time in the ethmoturbinals and increased at 12 h in the OB. The ^{28}Mg uptake rate showed a generally high level in the OB. However, unlike ^{43}K, the ^{28}Mg uptake rate in the OB increased until 12 h. On the other hand, ^{47}Ca uptake was at a very low level suggesting that most of the administered ^{47}Ca absorbed and bound to the bone in the ethmoturbinals.

The results indicate that Mg^{2+} and K^+ are directly transported from the nostril to the brain via the olfactory pathway, and their transport mechanism might be different due to their different transport speed.

References

1) S. Mathison, R. Nagilla, and U. B. Kompella: J. Drug Target. **5**, 415 (1998).
2) Y. Kanayama, T. Tsuji, S. Enomoto, and R. Amano: RIKEN Accel. Prog. Rep. **36**, 123 (2003).
3) Y. Kanayama, R. Amano, K. Washiyama, T. Irie, S. Enomoto, K. Kawai, and N. Tonami: Eur. J. Nucl. Med. Mol. Imaging. **30** Suppl. 2, S296 (2003).
4) Y. Kanayama, H. Haba, R. Hirunuma, S. Enomoto, and R. Amano: RIKEN Accel. Prog. Rep. **37**, 135 (2004).

* School of Health Sciences, Faculty of Medicine, Kanazawa University

Preliminary study on ^{88}Y olfactory transport: Animal experiment

M. Ono,* Y. Kanayama,* H. Haba, S. Enomoto, and R. Amano*

Some materials are transported from the nose, which is connected to the external environment, directly to the brain, which is the central organ of life activity. The substance transportation system is termed olfactory transport. However, the brain possesses a special mechanism, the blood brain barrier (BBB), that protects the brain from harmful substances in the blood stream, while supplying the brain with the required nutrients for normal functioning. In the olfactory transportation system, a material is directly transported via an olfactory nerve from the nasal cavity to the brain without passing through the BBB. Recently, the importance of the olfactory transportation system in the transportation of new medicines into the brain has been recognized by the medical field and its importance as a new pathway for heavy metals or radioactive materials in humans has been recognized by the toxicology field.

In a RIKEN multitracer screening experiment, we found that nasally administered ^{83}Rb is transported directly into the brain. A single-tracer experiment using ^{86}Rb[1] showed that the pathway was the olfactory transportation system. To search for other elements related to olfactory transport besides Rb^+, we again carried out a multitracer screening in detail. Previously, we also found that ^{88}Y may be transported via the olfactory transportation system.[2] In this study, we attempted to clarify this result using the ^{88}Y radioactive tracer.

Yttrium-88 was produced using ^{88}Sr(p, n)^{88}Y and a $SrCO_3$ target with 13.3 MeV protons at the RIKEN AVF Cyclotron. Carrier-free ^{88}Y was isolated by the solvent extraction method. The extracted ^{88}Y sample was added to 200 μl of HCl and the acid was removed by evaporation. The residue was then dissolved with distilled water and dried. The ^{88}Y injection solution was prepared by dissolving the residue with 0.9% physiological saline. ICR mice (7 weeks old, male) were used in this experiment. The mice were divided into two groups, the intranasally administered (IN) group and the intravenously administered (IV) group, which was the control group ($n = 4$). In intranasal administration, 10 μl of ^{88}Y solution was administered to both nasal cavities. Each mouse was sacrificed under anesthesia either 6, 24 or 48 hours after the administration, and the extracted brain was divided into three parts: the olfactory bulb (OB), the section including the piriform cortex (Pir) and the rest of brain (RB). We measured γ rays using a well-type scintillation counter after weighing each part, and calculated the uptake rate (%dose/g).

As shown in Fig. 1, in the OB region of the IN group the uptake rate is higher than that of the IV group in all the observation periods. The result shows the same tendency as the previous results from multitracer screening.[2] ^{88}Y olfactory transportation was confirmed in this experiment, but the uptake rate was lower than the previous results. This is due to a chemical property of $Y : Y^{3+}$ easily hydrolyses and becomes colloidal at approximately pH 7.

Y is one of the rare-earth elements and generally resemble the series of elements of the lanthanide and actinide groups. It is considered that actinide elements are similarly transported via the olfactory transportation system. Knowledge of their transport and in the influence on the central nervous system has become increasingly important from the viewpoint of environmental radioactivity and toxicology.

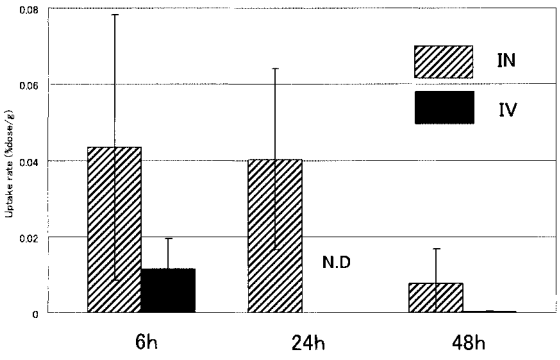

Fig. 1. Uptake rates of ^{88}Y in olfactory bulb. The bar and the line represent the mean ± S.D. of four mice.

References

1) Y. Kanayama, R. Amano, K. Washiyama, T. Irie, S. Enomoto, K. Kawai, and N. Tonami: Eur. J. Nucl. Med. Mol. Imaging. **30** Suppl. 2, S296 (2003).
2) M. Ono, R. Amano, and S. Enomoto: Proc. 6th Workshop on Environmental Radioactivity, Tsukuba, 2004-3, (KEK, 2004) p. 291.

* School of Health Sciences, Faculty of Medicine, Kanazawa University

Analysis of skin distribution of ^{65}Zn in hairless mice treated with ^{65}Zn-labeled zinc compounds by oral supplementation

H. Yasui,* H. Nishimura,* H. Haba, R. Hirunuma, S. Enomoto, and H. Sakurai,*

An increase in ultraviolet light (UV) exposure on human skin has been shown to enhance severe dermal damage (phototoxicity), inflammation, and premature skin-photoaging.[1] The harmful effects of UVA exposure are associated with the generation of reactive oxygen species (ROS).[2] In our efforts to find agents for reducing the skin damage of live mice under UVA exposure, we have found the potency of zinc(II) ion with regard to the suppression of ROS generation in the skin.[3] Zinc (Zn) is known to be one of the most important essential trace elements existing ubiquitously in all living systems.[4] Among the many pharmacological and nutritional roles of Zn(II), its anti-inflammatory activity is the most striking.[4] On the basis of these results regarding the physiological role of Zn(II), we have further examined whether orally administered $ZnCl_2$ and a Zn(II)-picolinate complex, $Zn(pic)_2$, suppress ROS generation in the skin. First, we report herein the skin distribution of orally supplemented $ZnCl_2$ or $Zn(pic)_2$ in terms of monitoring ^{65}Zn levels after the administration of ^{65}Zn-labeled compounds.

^{65}Zn in the chemical form of $ZnCl_2$ in 0.5 mol/L HCl, was obtained from RIKEN (Wako, Japan). ^{65}Zn solution was gently dried and then the residue was redissolved in a physiological saline solution (activity concentration = 370 kBq/mL). $ZnCl_2$ dissolved in the saline solution was mixed with 148 kBq of ^{65}Zn, and the preparation was completed to a final volume of 4 mL with the saline solution. While $Zn(pic)_2$ and picolinic acid (5% of complex) dissolved in the saline solution were mixed with 148 kBq of ^{65}Zn, the saline solution was added to the preparation for a final volume of 4 mL, and then the preparation was labeled with ^{65}Zn by leaving the preparation at 25°C overnight. The radioactivity administered to each mouse was 370 kBq of ^{65}Zn/kg of body weight. Male hairless mice (5 weeks old), weighing 25 g, were given the saline solution of $^{65}ZnCl_2$ or $^{65}Zn(pic)_2$ by single oral administration using gavage at a dose of 10 mg Zn/kg of body weight. After administration, each group of mice was maintained in polyethylene cages with a stainless-steel grated floor and fresh chip sawdust below the floor to prevent the urine and feces from coming into contact with mice and thus to avoid coprophagy. At 0–72 hr after treatment, the mice were sacrificed under anesthesia with ether and organs such as skin were removed. The organs were immediately weighed and transferred to polyethylene tubes for a gamma counter. The radioactivities due to ^{65}Zn amounts in organs were counted by an Aloka ARC-360 autowell gamma system (Tokyo, Japan) using the peak area of 1115.5 keV due to ^{65}Zn nucleus (half-life of ^{65}Zn, 244.26 day).

Figure 1 shows the time-dependent distribution of ^{65}Zn in the skin of hairless mice treated with ^{65}Zn-labeled $ZnCl_2$ (open circle) or $Zn(pic)_2$ (closed circle) by single oral administration at a dose of 10 mg Zn/kg of body weight, using the gavage. Interestingly, ^{65}Zn levels in the skin of mice treated with $^{65}Zn(pic)_2$ were significantly higher than those of mice treated with $^{65}ZnCl_2$ at 24 and 72 hrs as well as at 12 hr after administration, indicating that the actions of Zn on the skin are more enhanced and prolonged by the supplementation of $Zn(pic)_2$ than those of $^{65}ZnCl_2$. These findings will be useful in developing orally active Zn compounds for reducing UVA-induced ROS generation in the skin and thus for preventing skin damage after UVA exposure.

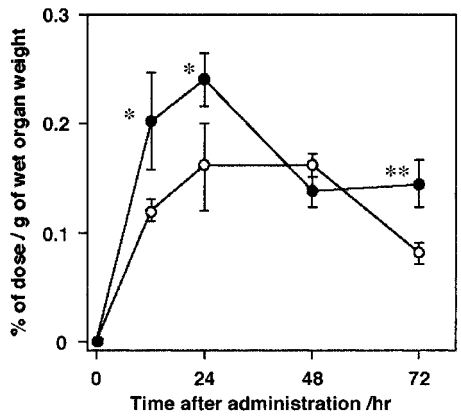

Fig. 1. Time-dependent distribution of ^{65}Zn in skin of hairless mice after single oral administration of ^{65}Zn-labeled $ZnCl_2$ (open circles) or Zn $(pic)_2$ (closed circles). Significance levels: * $p < 0.05$ and ** $p < 0.01$ of Zn $(pic)_2$ group *vs.* $ZnCl_2$ group at the same sampling time.

References

1) H. Masaki, Y. Okano, and H. Sakurai: Biochim. Biophys. Acta **1428**, 45 (1999).
2) J. Krutmann: J. Dermatol. Sci. **23**, S22 (2000).
3) H. Nishimura, H. Yasui, and H. Sakurai: Biomed. Res. Trace Elem. **14**, 239 (2003).
4) B. L. Vallee and K. H. Falchuk: Physiol. Rev. **73**, 79 (1993).

* Department of Analytical and Bioinorganic Chemistry, Kyoto Pharmaceutical University

Excretion rate of bio-trace elements in bile of rat under oxidative stress of Se-deficiency

K. Endo, K. Yamasaki, M. Tsukada, A. Okajo, K. Matsumoto, C. Honda,*
K. Matsuoka,* R. Hirunuma, and S. Enomoto

Reactive oxygen species (ROS) are formed as a result of an inevitable production process of the metabolism of an aerobic organism. The excessive ROS may possibly cause senility, cancer, and disease. On the other hand, it is known that living organisms have antioxidant systems. Their antioxidant enzymes contain metals as active centers. It is also known that Se plays a protective role against oxidative stress *in vivo*. Our previous study showed that the concentration of Selenium (Se) in the diet influences the concentration of Se in the blood, liver, and spleen.[1)] Bile is excreted to a duodenum from the liver in the detoxication of heavy metals. Under oxidative stress of Se-deficiency, it is expected that the composition and the excretion of heavy metals in bile will be changed.

In this experiment, we examined the kinetics behaviors of metal ions which are related *in vivo* redox regulation systems such as Se, iron (Fe), manganese (Mn), cobalt (Co), and zinc (Zn) in the bile of Se-deficient (SeD) rats using the multitracer (MT) technique.

Wistar mother rats, which were on 15th day after pregnancy, were fed on a SeD diet (Oriental Yeast Co., Ltd.) and ultrapure water. Newly born rats were kept with their own mother for four weeks. Then the young rats were weaned, and fed on the SeD diet and ultrapure water until the experiments were performed. The male rats were used for experiments at 8 weeks of age as SeD groups. Normal male Wistar rats of the same age as the SeD group were purchased and used as a normal control group.

The MT was prepared from silver foil irradiated with N-14 beams of 135 MeV/nucleon at the RIKEN-ring cyclotron. A saline solution containing MT was injected intravenously to SeD and normal rats. The biliary duct of a Wister rat was cannulated with a polyethylene tube under Nembutal anesthesia. After administration of MT solution, their bile was collected in a polyethylene tube every 10 min for 60 min. γ-Ray spectra of the bile samples were measured with a high-purity Ge semiconductor detector equipped with a multichannel analyzer.

The excretions (%) of Se, Sr, Mn, and Co were determined. The initial excretion rate for an element was estimated by the ratio of the corresponding radioactivity of the bile of the first 10 min collection to the radioactivity of the total injected MT solution. The results of the excretion of each element into bile are shown in Fig. 1. The excretion rate of Se was high for normal rats for about 10 min after the MT administration, and was evidently decreased for SeD rats to 1/6 of that found for normal rats. As and V showed relatively slow excretion rates for normal rats, and were not measured for SeD rats. On the other hand, the excretion rates of Sr, Mn and Co into bile increased to about 1.6, 7, 12 times greater than those of normal rats, respectively.

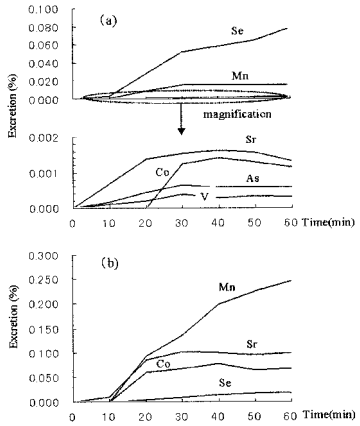

Fig. 1. Excretion (%) of metal ions into bile of (a) normal and (b) Se-deficient rats.

The radioactivities of the nuclides increased to plateau values about 20 min after administration. The excretion rate of Se into bile in a SeD rat was about 1/5 slower than that in a normal rat. Although the excretion rates of metal ions into bile for SeD and normal rats were measured within 60 min of administration, none of the radioactivities of Fe and Zn were found in this time range. This indicates that both elements were absorbed and accumulated in the liver and other organs, while other elements were excreted into bile. It is known that Fe(III) binds to transferine in blood and that the complexes are transferred to the liver, spleen, and/or bone marrow by blood circulation, where Fe is stored as ferritin or hemocyderine. In the liver, heme-iron is metabolized, and the Fe is excreted into bile, and reabsorbed at the duodenum. It is known that the biological half-life of Fe is long (the effective half-life is approximately 42 days). Therefore, the radioactivities of ^{59}Fe were not observed within the time range used in this work. In blood, nearly 70% of Zn binds to albumin, and 30% of the metal binds to α-macro-globulin, and in liver it is stored as Zn-metallothionein. Zn is used for the active centers of many enzymes. Therefore, ^{65}Zn is also not excreted into bile soon after administration of MT.

* Showa Pharmaceutical University

Reference

1) K. Matsumoto et al.: Accel. Prog. Rep. **33**, 116 (2000).

Distributions of technetium and rhenium in radish plants grown in nutrient solution culture†

K. Tagami,* S. Uchida,* N. Ishii,* R. Hirunuma, H. Haba, and S. Enomoto

Among technetium isotopes, ^{99}Tc is of potential long-term importance in the environment because of its long half-life (2.1×10^5 y) and its high fission yield from ^{235}U and ^{239}Pu (approximately 6%). Thus, knowledge of the behavior of ^{99}Tc from the soil to plant systems is of special interest. However, the amount of ^{99}Tc in the natural environment is at ultratrace levels even in the soil,[1] and therefore, the behavior of ^{99}Tc in the environment is unclear. Rhenium can be considered as a potential chemical analogue of Tc, although no data are available for terrestrial plant samples because Re is one of the rarest elements in the earth's crust. If a terrestrial plant absorbs Re at a rate as high as that reported for Tc and their uptake behaviors are similar, Re can be used as a chemical analogue of Tc. However, no study from this viewpoint has been carried out yet.

Radish seedlings were grown in a nutrient solution for about 1 month. Then, each plant was transplanted to a 120 mL plastic vessel containing 40 or 60 mL of new nutrient solution. In Run-A, $^{95m}TcO_4^-$ and multitracers[2] including $^{183}ReO_4^-$ were added to the nutrient solution to obtain 2.7×10^{-17} mol/mL (2.1 Bq/mL) ^{95m}Tc and 1.6×10^{-17} mol/mL (1.1 Bq/mL) ^{183}Re solutions, while ^{99}Tc and a multielement solution, XSTC-8 (SPEX), were added in Run-B. The concentrations of ^{99}Tc and satable Re in Run-B, which are 0.69×10^{-12} mol/mL and 54×10^{-12} mol/mL, respectively, were markedly higher than those in Run-A. The plant samples were in contact with the solution through their fine roots for 1–3 d. Then, the plants were carefully removed from the solution. After rinsing and drying their fine roots, the plants were separated into leaves, and fleshy and fine root parts. Each sample part was weighed and oven-dried (60°C, 72 h). The activities of the radioisotopes in the nutrient solution and the plants (Run-A) were measured using a Ge detecting system (Seiko EG&G Ortec). In Run-B, the concentrations of stable Re and ^{99}Tc were measured by ICP-MS (Agilent 7500a, Yokogawa analytical systems).

The amount of nutrient solution taken up by the plants increased with time for both runs, while the relative concentration ratios (C/C_0) of Tc and Re in the nutrient solution obtained after and before the exposure period did not change as shown in Fig. 1. That is, the uptakes of Tc and Re by the plants were the same as that of water. Comparing the results of Run-A and Run-B, the concentration of Re, which was about 80-fold that of Tc in Run-B, did not decrease the rate of Tc uptake. Cataldo *et al.*[3] reported that an excess amount of ReO_4^- did not reduce the rate of TcO_4^- absorption, thus Re could not be a biological analogue of Tc. However, from the results of the present study, one possible explanation for the failure of ReO_4^- to inhibit Tc uptake is that the ReO_4^- uptake mechanism is the same as that of TcO_4^-, thus the plants cannot recognize any difference between the two elements.

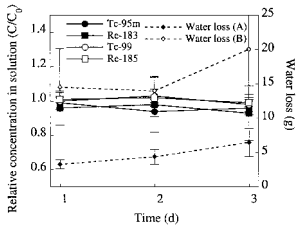

Fig. 1. Relative concentration ratios (C/C_0) of isotopes in nutrient solution and water loss from the vessel by radish.

The distribution ratio of an isotope, defined as the 'amount in a plant part' divided by the 'total absorbed amount', is shown in Fig. 2 for the samples collected on 3 d after transplanting. In each experiment, the distributions of Tc and Re in the plants were almost the same. Both TcO_4^- and ReO_4^- absorbed by the fine roots were translocated rapidly to the leaves and fleshy roots. The behaviors of other elements were different from those of Tc and Re.

From these results, we assumed that Tc and Re behave similarly in radish plants. The results strongly suggest that Re could be used as a chemical analogue of Tc in soil solutions for studies of plant uptake.

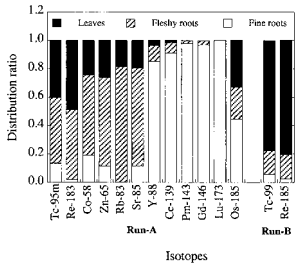

Fig. 2. Distribution ratios of isotopes in fine roots, fleshy roots and leaves of radish plants after 3 d contact.

References

1) K. Tagami and S. Uchida: J. Nucl. Radiochem. Sci. **3**, 1 (2002).
2) F. Ambe: J. Radioanal. Nucl. Chem. **243**, 21 (2000).
3) D. A. Cataldo, R. E. Wildung, and T. R. Garland: Plant. Physiol. **73**, 849 (1983).

† Condensed from the article in Appl. Radiat. Isot. **61**, 1203 (2004)

* National Institute of Radiological Sciences

Comparison of leaching and sorption behavior of various ions in soil-water system based on ICP-MS and multitracer analyses

S. Mitsunobu,* Y. Takahashi,* R. Hirunuma, H. Haba, and S. Enomoto

Soil contamination whose source is natural or anthoropogenic is still widely found in the world. As an example of natural phenomena, it has been reported that more than ten million people are suffering from pollution of groundwater concentrated high arsenic in Bangladesh and India.[1)] However, the detailed mechanism for the high concentration of arsenic has not been understood completely. To understand the mechanism of reactions in the soil-water system, we performed both leaching and sorption experiments to understand soil-water distribution of various elements to study how the difference of initial states can affect the soil-water distribution of elements. In this study, the distribution experiments of various ions were conducted in both directions, that is, starting from dissolved ions (sorption experiments) and from ions in soil (leaching experiments). Multitracer method was used in sorption experiments, which include many radioisotopes in a solution. On the other hand, leaching experiments were conducted by ICP-MS for the stable isotopes originally contained in the soil samples.

The soil was sampled from paddy field in National Institute of Agro-Environmental Science, Tsukuba, Japan. For the leaching experiments, 20 g of air-dried soil put into 50 ml styrene tube was mixed with water containing 0.010 M NaCl as supporting salt. In order to observe dissolution of element to liquid phase in various redox caused by soil condition, degree of water saturation, pH, and temperature were varied. Similar experiments were conducted for sorption experiments using multitracer. Ionic strength of the solution added to the soil was adjusted to 0.010 M by NaCl. The temperature was maintained at room temperature (293 – 296 K).

For the sorption experiments, each element remaining in solution (R_S) was simply obtained from the percentage of multitracer in water relative to the total amount introduced in the soil-water system. For the leaching experiments, because of the presence of various components as host phases for trace elements in soil, fraction of elements in active phase for the leaching behavior was experimentally determined by sequential extraction,[2,3)] which can identify concentration in phases such as Mn oxide, Fe oxide, organic matters, carbonate, and exchangeable cations. We use the sum of concentration in all the phases in the extraction as "active element concentration". For the leaching experiments, R_L was defined as the each element in water relative to the active element concentration. It is expected that the element is reversible in terms of the reaction with the active phase in soil-water system when R_S value is similar to R_L value.

We have obtained the leaching and sorption behavior for Mn, Fe, Co, Zn, As, Rb, and Sr. The R_S and R_L values at various elapsed times were compared for Co as an example accompanied with Eh variation depending on time (Fig. 1). Initial R_S value for Co must be 100%, while initial R_L must be 0%. As the elapsed time increased, Eh value decreased due to the development of reducing condition by bacterial activities in the soil. The R_S value decreased until after 30 hours, which turned into the increasing trend after that. The R_L values for Mn and Fe increased with time, showing the dissolution of Mn and Fe oxides during the development of the reducing condition. The increase of R_S value for Co is possibly due to the dissolution of Mn and Fe oxides which can be host phases of considerable amount of Co in the soil. R_L value for Co monotonously increased with time as Eh decreases. Finally, R_S and R_L values have become similar for Co. Considering the complex reactions in soil, it is interesting to observe the similarity for Co. This result strongly suggests that the reaction of Co involved in the active phase as defined in this study is reversible, the soil-water equilibrium of which can be attained within about 600 hours.

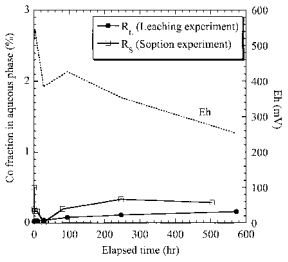

Fig. 1. Dependence of R_S, R_L, and Eh values on the elapsed time for Co. R_S and R_L: fraction remaining in the aqueous phase in the sorption and leaching experiments, respectively.

References

1) F. R. Siegel: in *Environmental Geochemistry of Potentially Toxic Metals* (Springer, Berlin, 2002), p. 32.
2) A. Tessier, P. G. C. Campbell, and M. Bisson: Anal. Chem. **51**, 844 (1979).
3) Y. Takahashi, R. Minamikawa, K. H. Hattori, K. Kurishima, N. Kihou, and K. Yuita: Environ. Sci. Technol. **38**, 1038 (2004).

* Department of Earth and Planetary Systems Science, Hiroshima University

Multitracer technique for studies of uptake and efflux of trace elements in culture cell line

T. Suzuki,[*1] K. Ishibashi,[*1] S. Ohata,[*1] N. Sato,[*1] A. Yumoto,[*1] T. Togawa,[*1] K. Nishio,[*2]
R. Hirunuma, H. Haba, S. Enomoto, and S. Tanabe[*1]

The molecular mechanism of cisplatin resistance has been revealed to be "multifunctional"; it decreases cisplatin accumulation, increases intracellular detoxification and increases the DNA repair ability. A decrease in cisplatin accumulation was observed in non-small cell lung cancer (NSCLC) cell lines resistant to cisplatin. There was a good correlation between the intracellular amount of platinum and sensitivity against cisplatin. This result suggests that the intracellular accumulation of platinum is a major determinant of the cisplatin resistance, at least in NSCLC. Previously, it was reported that cisplatin enters cells in an ATP-dependent manner. Furthermore, it was reported that cisplatin was removed by multidrug resistance proteins (MRPs) as a glutathione conjugate.[1] On the other hand, certain metals such as arsenite and cadmium were removed from cells in the same manner. Therefore, the contribution of these transporters is important for metal detoxification analysis. However, the molecular mechanisms of metal transport, such as the uptake and efflux of transporters were unclear.

In this study, to investigate the metal transport mechanisms including that of cisplatin, we determined the amounts of various metals taken up by cisplatin-resistant cell lines using a platinum tracer and multitracer. We modified the methods described by Yanagiya *et al.*[2] and used a human NSCLC cell line, PC-9, and its cisplatin-resistant subline, PC-9/CDDP. The cells were grown in RPMI1640 supplemented with 10% FBS. Pt tracer and radioactive multitracer (MT) solutions were obtained from the Au or Ag target irradiated in the RIKEN Ring Cyclotron, and used as physiological saline solutions. Then, the Pt tracer or MT solution was added to the cells in a serum-free medium and incubated at 37 °C. After incubation, the cells were separated from the medium and radioactivity was determined using a Ge detector.

As shown in Fig. 1, the accumulation of Pt in the cisplatin-resistant cell line was about 60% of that in parental cells. The amount of platinum uptake showing atrend similar to that of cisplatin uptake is interesting.

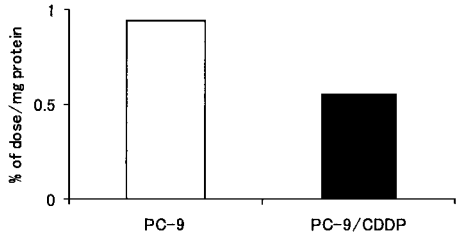

Fig. 1. Uptakes of platinum in lung cancer cell lines. The cisplatin-resistant cell line (closed column) and parental cell line (open column) were exposed to the Pt tracer for 2 h.

Furthermore, we examined the time courses of uptake of certain metals in lung cancer cell lines using MT.

Figure 2 shows the results for Be and Mn. Since the uptake behaviors of these metals are different, we examined the efflux of metals in culture cell lines using MT.

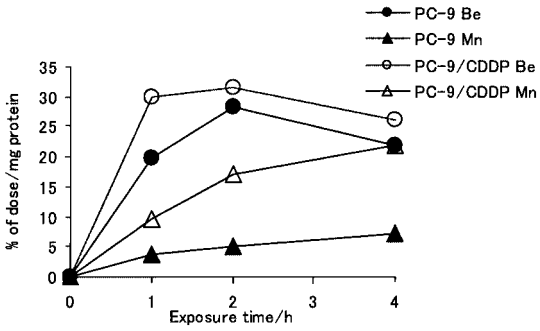

Fig. 2. Time courses of uptakes of Be and Mn in lung cancer cell lines. The cisplatin-resistant cell line and parental cell line were exposed to the multitracer for 1, 2, and 4 h.

References

1) T. Suzuki et al.: Curr. Drug Metab. **2**, 363 (2001).
2) T. Yanagiya et al.: Life Sci. **65**, PL177 (1999).

[*1] Department of Analytical Biochemistry, Meiji Pharmaceutical University
[*2] Project Ward, National Cancer Center Hospital

Iterative image reconstruction method for GREI

S. Motomura, H. Takeichi, R. Hirunuma, K. Igarashi, H. Haba, S. Enomoto, A. Odahara,*
Y. Gono, and Y. Yano

The present prototype of the γ-ray emission imaging (GREI) system is a Compton camera that includes a strip germanium telescope.[1] For image reconstruction, we have implemented two-step methods. The back-projection of a detected event is a cone surface that indicates the possible position of the γ-ray source. In the first step, an intermediate image, which is called a simple back-projection (SBP) image, is constructed by simply accumulating the back-projections over all detected events, using an algorithm analogous to the cone-surface mapping algorithm.[2] Here we assume that SBP images (n_i) are constructed by linear mapping of source distribution images (λ_j), that is:

$$n_i = \sum_j p_{ij}\lambda_j, \tag{1}$$

where p_{ij}, which is referred to as a point-spread function (PSF), is a matrix representation of the linear mapping, and $i, j = 1, \ldots, N$. In the second step, λ_j is reconstructed by the inverse mapping of n_i.

If the PSF is assumed to be shift invariant, λ_j can be reconstructed analytically. The matrix p_{ij} is diagonalized by Fourier transformation of both sides of Eq. (1), and then λ_j is obtained as follows:

$$\lambda_j = \frac{n_j}{p_{jj}}. \tag{2}$$

In most cases, the right side of Eq. (2) is multiplied by an additional filter function (w_j) to suppress statistical noise components:

$$\lambda_j = \frac{w_j n_j}{p_{jj}}. \tag{3}$$

In reality, the PSF varies depending on both i and j (shift variant). Thus we have implemented an iterative algorithm in which a shift-variant PSF can be incorporated. First, an initial image $\lambda_j^{(0)}$ is obtained by averaging the SBP image:

$$\lambda_j^{(0)} = \frac{1}{N}\sum_{i=1}^{N} n_i. \tag{4}$$

Then the $(n+1)$-th estimate ($\lambda_j^{(n+1)}$) is obtained from the n-th estimate ($\lambda_j^{(n)}$) as follows:

$$\lambda_j^{(n+1)} = \lambda_j^{(n)} + \sum_i \left(n_i - \sum_j \lambda_j^{(n)} p_{ij} \right) p_{ij}. \tag{5}$$

No additional filtering is necessary for this calculation.

To evaluate the performance of the algorithm, some images were reconstructed using a shift-invariant PSF, and the resultant images were compared with the analytically reconstructed images. Figure 1 shows the results of both the analytical and iterative reconstructions for a soybean sample administered with a multitracer solution that includes 140-kBq ^{59}Fe. The number of iterations was 1.0×10^4. The spatial resolution using the iterative algorithm was improved compared with that using the analytical algorithm. Moreover, a ripple-like artifact, which is observed on the background in Fig. 1 (b), was removed in Fig. 1 (d). The differences in the results were considered to be caused by the incompleteness inherent in the filter function used in the analytical algorithm. It is impossible to create a filter function that can remove the statistical noise components completely and preserve the signal components perfectly. The iterative algorithm is free from the restrictions caused by the filtering.

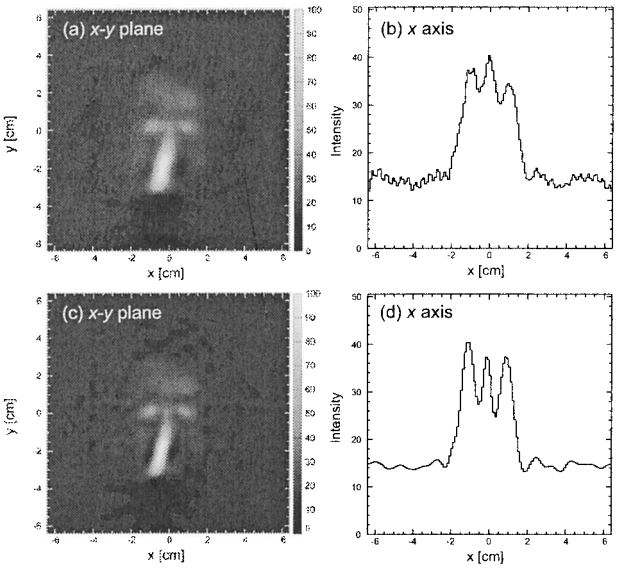

Fig. 1. Reconstructed images of ^{59}Fe administered to a soybean sample. (a), (b): Using the analytical algorithm. (c), (d): Using the iterative algorithm.

References

1) S. Motomura and S. Enomoto: J. Clin. Exper. Med. **205**, 884 (2003).
2) R. C. Rohe et al.: IEEE Trans. Nucl. Sci. **44**, 2477 (1997).

* Nishinippon Institute of Technology

Fourier analysis of back-projected images obtained by GREI system

S. Motomura, H. Takeichi, S. Enomoto, Y. Gono, and Y. Yano

In the procedure of image reconstruction for γ-ray emission imaging (GREI), a simple back-projection (SBP) image is constructed as an intermediate image.[1] In order for the source distribution image to be reconstructed from the SBP image, the information of the original source distribution must be preserved in the SBP image. If an SBP image is constructed with infinite statistics, it must have the perfect information of the source distribution. Needless to say, SBP images are actually constructed with finite statistics, thereby containing some statistical noise.

We have investigated the relationship between the statistics and the noise components in terms of Fourier power spectral densities (FPSDs). Three SBP images of a point source, which was placed 69 mm from the center of the front detector, were constructed by a Monte Carlo simulation using a GEANT[2] code with the detected event counts of 1.0×10^4, 5.0×10^4, and 1.0×10^5. The γ-ray energy was 1116 keV, which corresponds to the intrinsic γ-ray of ^{65}Zn. Figure 1 shows the FPSDs for the SBP images. One can see in Fig. 1 that the high-spatial-frequency components are dominated by the statistical noise because they are significantly dependent on the statistics. Figure 2 shows the reconstructed image with the detected event count of 1.0×10^5, where the signal components are dominant up to spatial frequencies of $0.13\,\mathrm{mm}^{-1}$ and $0.05\,\mathrm{mm}^{-1}$ in x- and z-directions, respectively. The full widths at half maximum were 4 mm in the x-direction and 10 mm in the z-direction. This result suggests that a spatial resolution of $(2f_c)^{-1}$ is obtained when the signal components are dominant up to a spatial frequency f_c.

The FPSDs of the SBP images can be utilized for optimization of the voxel dimensions. If the frequency where the statistical noise components start being dominant is chosen as the Nyquist frequency, the influence of the statistical noise can be reduced without losing the spatial resolution. An SBP image was constructed with the Nyquist frequencies of $0.20\,\mathrm{mm}^{-1}$ and $0.08\,\mathrm{mm}^{-1}$ for x- and z-directions, respectively. Then the source image was reconstructed from the SBP image (Fig. 3). The fluctuation in the background was reduced and the contrast of the image was improved by the optimization without losing the spatial resolution.

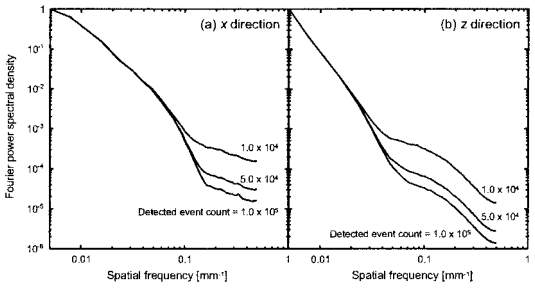

Fig. 1. Fourier power spectral densities of the SBP images obtained by Monte Carlo simulations of the present GREI system.

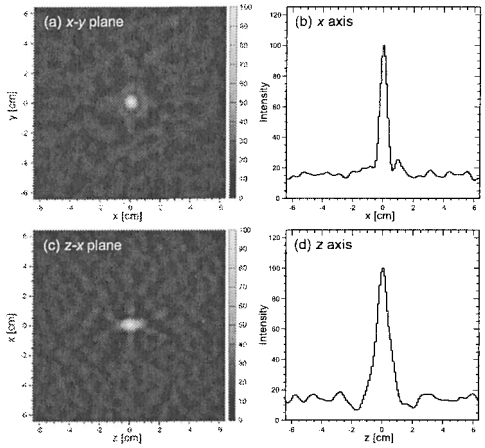

Fig. 2. Reconstructed image of the point source with the detected event count of 1.0×10^5. The voxel dimensions were 1 mm × 1 mm × 1 mm.

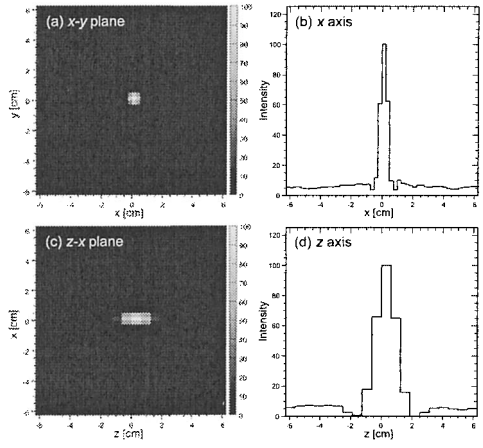

Fig. 3. Reconstructed image of the point source with the detected event count of 1.0×10^5. The voxel dimensions were 2.5 mm × 2.5 mm × 6.25 mm.

References

1) S. Motomura et al.: RIKEN Accel. Prog. Rep. **38**, 124 (2005).
2) GEANT: *Detector Description and Simulation Tool* (CERN, Geneva, 1993).

Motion correction method for γ-ray emission imaging (GREI)

H. Takeichi

In this article, a solution[a)] to the problem of body movement in biological imaging by γ-ray emission imaging (GREI),[1–3)] and its characteristic advantage are described.

An imaging dataset, or "movie," is essentially a composite of the form and motion of objects. Without constraints, it is not possible to separate them. Therefore, when information on form, or a "picture" in isolation is required, such as in emission tomography, the body movement causes a problem. This is particularly prominent in high-resolution imaging. The most simple and generic solution is to stabilize the body. In diagnosis, breath holding or electrocardiograph (ECG) gating are sometimes used. However, it is not easy for some cases such as children. Solving the problem for nonrigid parts of the body such as the heart is difficult. In contrast, solving the problem for approximately rigid parts such as the head appears tractable, by measuring the motion independently and "subtracting" it from the original composite measurement to obtain the form information.

There are three major conventional ways for biological motion measurement: mechanical, magnetic, and optical. The mechanical method uses some sort of spring and strain gauge. This is cheap, but does not appear desirable considering the design, operation, and precision. The magnetic method is to place the sample in a magnetic field, and measure the induced current in a coil that is attached to the sample. The measurement is precise and the operation is not very difficult. However, the design of the apparatus is difficult, particularly when another noninvasive biochemical measurement is performed concurrently. The optical method is to scan optical markers such as light emitting diodes that are attached to the sample with a camera, and analyze the image. The design and operation are easy. However, because the available space and the viewing angle are limited, when another noninvasive biochemical measurement is performed concurrently, it is not easy to achieve a high precision stably.

Because GREI can measure signals from multiple radioactive isotopes (RIs), motion can be monitored by attaching a few point sources that emit γ rays of different energies as references and measuring their positions concurrently. At least two references are required to obtain the six degrees of freedom: three translations and three rotations. More refrences are preferred for a precise measurement. Although the idea is very simple, this method is easy in design and operation, and has a high precision. Its three important characteristics are as follows.

First of all, unlike the optical method, no additional apparatus is required. Correction can be carried out only by computation. In an actual measurement, the only operation is to attach a few point sources to the sample. The data are acquired without any additional operations. The reference point sources can be placed at any location, as long as they are within the field of view of the imaging apparatus.

Second, because the reference is an isolated point source, the data processing is trivial. The motion can be estimated for each decay event in the list-mode data by forming a simple back projection (SBP) of the reference point sources and finding the peak in the SBP from the list-mode data around the time point of each decay event. Because the data processing is trivial, it is also easy to detect an inappropriate setting or absence of the reference by evaluating the statistical properties of the reference data.

Third and finally, because the main measurement apparatus itself is used for motion monitoring, when the measurement performance, such as the spatiotemporal resolution, of the main apparatus is improved, unlike the optical system, no corresponding additional improvement is required to the "motion measurement apparatus." A nearly identical scheme can be used at the improved performance without modification.

These characteristics mean that the method is inexpensive and practical, considering its benefit, adding some value in an application of GREI to nuclear medicine, which is described elsewhere in this volume. However, the following problems need to be considered. First, the reference point sources need to have low activity if this technique is applied in nuclear medicine, because they will be in close contact with the patient. Second, the apparatus needs to be able to acquire data sufficiently fast so that both the reference signal and the target signal are measured. Because the actual implementation of this scheme is in progress, the severity of these and other problems cannot be described at this moment.

One implication of this scheme is that GREI can be used not only for the imaging apparatus, but also for the motion measurement, or "tracking" apparatus, in radiation therapy, for example.

[a)] An application has been made for a patent for this scheme (JP 2004-151935, A).

References

1) Y. F. Yang et al.: IEEE Trans. Nucl. Sci. **48**, 656 (2001).
2) Y. F. Yang et al.: Nucl. Instrum. Methods Phys. Res. A **482**, 806 (2002).
3) S. Motomura et al.: Proc. IEEE Nuclear Science Symp. and Medical Imaging Conf. (NSS-MIC), Rome, Italy, 2004-10 (IEEE Nuclear & Plasma Sciences Society, 2005), in press.

RIKEN Accel. Prog. Rep. **38** (2005)

Current issues on application of γ-ray emission imaging GREI in nuclear medicine

H. Takeichi and S. Motomura

In this article, important problems of the nuclear medicine apparatus, solutions to overcome these issues by γ-ray emission imaging (GREI), and the remaining problems shall be briefly summarized.

Nuclear medicine consists mainly of diagnosis and treatment. In diagnosis, scintigraphy, single photon emission computed tomography (SPECT), and positron emission tomography (PET) are commonly used. By SPECT, the distribution of the tracer radioactive isotope (RI) is imaged using a scintillation detector and a mechanical collimator. By PET, the distribution of the tracer RI is imaged using a scintillator and a coincidence detector. The imaging performance is determined mainly by the detection scheme and the image reconstruction method. Various types of scintillator of various sensitivities and decay times are used. For image reconstruction, analytical filtered back projection (FBP) used to be frequently applied. However, with the increasing computational power of computers, more accurate iterative methods, such as maximum-likelihood expectation maximization (ML-EM) and its fast variation ordered subset expectation maximization (OSEM), are used more frequently nowadays.

Scatter and absorption in the body largely influence the image quality. Irrespective of the source of the photon, γ rays emitted from the body are scattered inside the body. Because the scattered γ rays no longer convey the accurate energy and position information, they blur the image, which is observed when the energy window is not narrow. When the energy loss is great or complete and the γ ray is not in the energy window, the γ ray is not observed. Indeed, this is one of the reasons for the large dose in diagnostic nuclear medicine. In the case of PET, because the paired annihilation γ rays "penetrate" the body, just like a transmission computed tomography (TCT), the activity detected for each pair of opposing detectors is independent of the position of the source along the line of response. Therefore, it is possible to correct for the attenuation accurately by a transmission scan using a known source outside the body to obtain the attenuation coefficients, which is called the μ-map, prior to the examination. In contrast, in the case of SPECT, because the emission is unidirectional, it is by itself impossible to separate completely the actual activity of the source and the influence of the attenuation, which depends on the structure and composition of the body, from the measurement. The uniformity of the structure and composition is often assumed, which is not quite correct. This is one of the main hindrances in quantitative SPECT measurement. Moreover, as the spatial resolution increases, body movements cause image blurring, as well. Even for a short examination period, it is not easy to limit body movements on the order of 10^0 or 10^{-1} mm.

By GREI,[1–3] the distribution of the tracer RI is imaged using germanium (Ge) detectors and Compton kinematics. It provides solutions to the problems as follows.

By GREI, a broad range of γ rays is measured simultaneously and independently at a high energy resolution. The high energy resolution trivially eliminates scatter artifacts only by setting up a narrow energy window. Attenuation correction can be carried out by two methods. One is to concurrently conduct the target emission imaging and reference transmission imaging using a planar source behind the body. Unlike the commercially available CT/SPECT, the image registration is a negligible problem, as an identical apparatus collects the two datasets similarly at the same time, with the only difference in the γ ray energy. The other, more promising method is to measure γ rays of multiple energies from an identical nuclide. Because the attenuation coefficient depends on the γ ray energy and the distributions should be identical, by simply comparing the two independent measurements for two energies, an approximated μ-map is easily obtained. The μ-map is in complete alignment with the target measurement in this case too, which is advantageous in high-resolution imaging. To this end, ^{111}In appears the best candidate, because it is commercially available and emits 171 keV γ ray at 90% and 245 keV γ ray at 94%. The problem of body movements can be solved similarly using the simultaneous multiple-nuclide measurement. This is described in another article in this volume.

By SPECT the γ ray emitted from the nucleus is measured, while by PET the annihilation γ ray originating from the emitted positron is measured. Representative nuclides used for diagnostic imaging are ^{99m}Tc and ^{123}I for SPECT, and ^{18}F and ^{11}C for PET. They are short-lived, reducing the time required for examination. The SPECT nuclides generally emit only low-energy γ rays, reducing the biological effects of radiation. The SPECT nuclides are often derived from generators, while the PET nuclides are normally generated from medicinal cyclotrons. By GREI, both types of nuclides, such as ^{18}F and ^{99m}Tc or ^{123}I, which can label various substances, could be measured simultaneously, independently, and at a high spatial resolution in alignment.

Unfortunately, the current implementation of GREI[3] is not complete. The problem of image reconstruction, more specifically, the problem of position-dependent response function needs to be solved. Efficiency, spatial resolution, and the choice and arrangement of the detectors may have some room for improvements.

References

1) Y. F. Yang et al.: IEEE Trans. Nucl. Sci. **48**, 656 (2001).
2) Y. F. Yang et al.: Nucl. Instrum. Methods Phys. Res. A **482**, 806 (2002).
3) S. Motomura et al.: Proc. IEEE Nuclear Science Symp. and Medical Imaging Conf. (NSS-MIC), Rome, Italy, 2004-10 (IEEE Nuclear & Plasma Sciences Society, 2005), in press.

Response of DNA repair proteins to heavy-ion-induced DNA damages

M. Tomita, M. Izumi, T. Tsukada, N. Fukunishi, H. Ryuto, and Y. Yano

Ionizing radiation is known to induce DNA double-strand breaks (DSBs), which are the most serious form of DNA damage. If not repaired efficiently, DSBs cause cell death, chromosome translocations and genomic instability. Accelerated heavy ions with a high linear energy transfer (LET) can induce complex clustered DNA damages producing two or more DNA lesions within a few helical turns. The complexity of clustered DNA damage shows strong LET dependence, which makes it a good candidate as a prime determinant of a high biological effectiveness.[1] In mammalian cells, there are two major DSB repair pathways, namely, non homologous end-joining (NHEJ) and homologous recombination (HR).[2] The repair of DSBs by NHEJ requires DNA-dependent protein kinase (DNA-PK), XRCC4, DNA ligase IV and Artemis.[3] DNA-dependent protein kinase (DNA-PK) is composed of a Ku-heterodimer and a catalytic subunit (DNA-PKcs) and is activated to bind to the ends of double-stranded DNA. Activated DNA-PK phosphorylates the XRCC4 protein and itself *in vivo*.[3,4] Previously, we reported that the relative biological effectiveness (RBE) of DNA-PKcs-defective human M059J cells was significantly lower than that of control M059K cells,[5] suggesting that DNA-PK plays an important role in the cellular response to heavy-ion-induced DSBs. In this study, we examined the activation and nuclear localization of DNA-PK after exposure to heavy ions.

To determine whether DNA-PK can recognize heavy-ion-induced DSBs, we raised polyclonal phosphospecific antibodies recognizing DNA-PKcs at Thr2638, which is a functionally relevant site in DNA-PKcs.[6] Figure 1 (A) shows the radiation-induced foci formation of phospho-DNA-PKcs on Thr2638 assessed by immunofluorescence in human HeLa cells. We observed discrete phospho-DNA-PKcs foci formed in the cell nucleus irradiated with X rays. In addition, phospho-DNA-PKcs formed larger foci after exposure to C ions than to X rays. Figure 1 (B) shows the localization of phospho-DNA-PKcs on Thr2638 after exposure to Ar ions. HeLa cells were irradiated with Ar ions, which intersect the cell nuclei as indicated by the arrow. The linear track pattern of phospho-DNA-PKcs was clearly observed after Ar-ion irradiation. These results strongly suggest that DNA-PKcs is recruited in the vicinity of multiple DSBs locally induced by heavy ions to repair DSBs by NHEJ.

To further confirm the activation of DNA-PK in response to heavy-ion-induced DSBs, we assessed DNA-PK-dependent XRCC4 phosphorylation after irradiation. XRCC4 was phosphorylated 0.5–1 h after X-ray irradiation, and then dephosphorylated within 3 h (Fig. 2). The phosphorylation level of XRCC4 after heavy-ion irradiation was higher than that after X-ray irradiation, according to LETs. The time course of XRCC4 phosphorylation, however, showed no difference in radiation quality. A series of results obtained suggests that DNA-PK recognizes the induction of clustered DSBs by heavy ions, and phosphorylates its substrates efficiently.

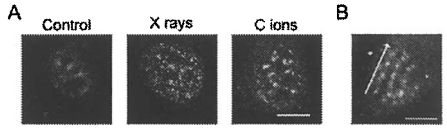

Fig. 1. Spatial distribution of phosphorylated DNA-PKcs on Thr2638 in HeLa cells after irradiation. (A) Cells were fixed 30 min after exposure to 0 or 5 Gy of X rays or C ions (80 keV/μm), and then analyzed by immmunofluorescence. (B) Cells were fixed 30 min after exposure to 0.2 Gy of Ar ions (310 keV/μm), and then analyzed by immunofluorescence. Irradiation was performed such that the rays pass through the cell nucleus, as indicated by the arrow. Bar represents 10 μm.

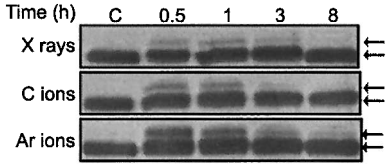

Fig. 2. Phosphorylation of XRCC4 in HeLa cells irradiated with 30 Gy of X rays, C (80 keV/μm) or Ar ions (310 keV/μm). Cells were harvested at the indicated times after irradiation, then assessed by immunoblotting. Slower migrating (upper) bands reflect phosphorylated form.[4]

References

1) D. T. Goodhead: J. Radiat. Res. **40**, Suppl. 1 (1998).
2) K. K. Khanna and S. P. Jackson: Nat. Genet. **27**, 247 (2001).
3) S. P. Lees-Miller and K. Meek: Biochimie **85**, 1161 (2003).
4) Y. Matsumoto et al.: FEBS Lett. **478**, 67 (2000).
5) M. Tomita et al.: RIKEN Accel. Prog. Rep. **37**, 145 (2004).
6) Q. Ding et al.: Mol. Cell. Biol. **23**, 5836 (2003).

Effect of heavy-ion beam irradiation on mutation induction in *Arabidopsis thaliana* (II)

H. Saito, Y. Y. Yamamoto, T. Matsuyama, N. Fukunishi, H. Ryuto, T. Abe, and S. Yoshida

To achieve an effective mutagenesis of arabidopsis (*Arabidopsis thaliana*), we examined the effect of heavy-ion beam irradiation on mutation induction. In a previous paper, we reported that although the frequencies of albino plants were significantly different between irradiations using C and Ne with different linear energy transfers (LETs), these ions with similar LETs provided similar frequencies of albino plants.[1] In the present report, therefore, we examined the effect of the several ions with similar LET on mutation induction in arabidopsis.

Dry seeds of arabidopsis ecotype Columbia were prepared for irradiation treatments as in our previous report.[1] Seeds were irradiated with ^{12}C, ^{14}N, ^{20}Ne, ^{40}Ar and ^{56}Fe ions in a dose range of 10 to 550 Gy. These ions were accelerated up to 135, 135, 135, 95 and 90 MeV/nucleon, and their LETs were ca. 23, 30, 61, 280 and 640 keV/μm, respectively. To determine the effects of LETs of heavy ions on mutation induction, the LETs of C, N, Ne and Ar ion beams were controlled to ca. 30, 61 and 280 keV/μm, 61 and 280 keV/μm, 280 keV/μm and 640 keV/μm, respectively, after passing through a set of absorbers in the range shifter. All LETs were calculated behind plant materials. The germination and culture of at least 150 M_1 seeds were carried out by the same method as in our previous report.[1] Flowering rate (FR; number of flowering plants per total number of incubated M_1 seeds) was determined one month after the transfer to soils in the present study.

In the control seeds without irradiation, the germination rate was more than 97% and all seedlings flowered until one month after transfer to soil. Germination was not affected by the irradiations with any ions at the doses tested. The effect of heavy-ion beam irradiations on FR is shown in Fig. 1. Without the range shifter for each ion (open spots), FR curves were markedly different according to the kinds of ion. Ar ions were the most effective in decreasing FR, only a few plants flowered among the seeds irradiated at a dose of 100 Gy. On the other hand, FR was not affected by irradiations with N ions up to 550 Gy. When the LETs were controlled using the range shifter (close spots), similar FRs were observed between the treatments with several ions at the same LETs. Investigations of mutation rate in the M_2 generation, such as that of frequency of albino plants, are in progress.

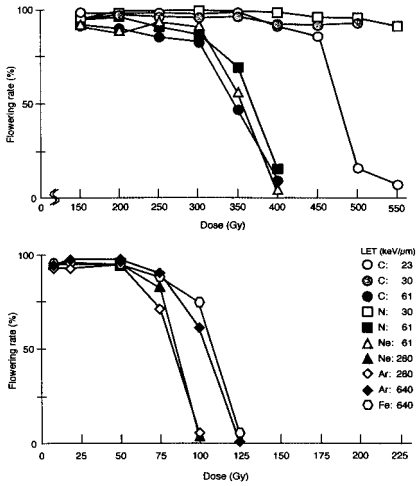

Fig. 1. Effect of heavy-ion beams on flowering rate in arabidopsis.

Reference

1) H. Saito et al.: RIKEN Accel. Prog. Rep. **37**, 147 (2004).

Establishment of *Arabidopsis thaliana* lines mutagenized by heavy ion beam irradiation

Y. Y. Yamamoto, H. Saito, H. Ryuto, N. Fukunishi, T. Abe, and S. Yoshida

For plant mutagenesis by heavy ion beam irradiation, irradiated samples (M_1) are usually grown for the next generation (M_2), and phenotypic screening is performed at M_2. The growth step requires a long time (months to years), large space, and considerable labor. Sharing M_2 resources can save such research resources of plant researchers and breeders, thus, it is desirable to establish common M_2 populations, as long as many users are expected. As the first trial, we have decided to prepare an M_2 population of *Arabidopsis thaliana*. There are several reasons for choosing *Arabidopsis*. Firstly, it is one of the most commonly used plant species for plant genetics. Secondly, the growth of *Arabidopsis* does not require a large outdoor space in a field; an *in house* growth facility is sufficient. Thirdly, considering its small genome size, a relatively small population is sufficient for saturated mutagenesis. Fourthly, the most efficient beam conditions for *Arabidopsis* mutagenesis have already been determined.[1)]

Consulting our previous report,[1)] we irradiated dry seeds of *Arabidopsis thaliana* ecotype Columbia with a Ne^{10+} beam at a dose of 150 Gy. The irradiated seeds were then grown for self-pollinated seeds. After harvesting, we grew seeds from 9 M_1 plants as one batch. We prepared around 700 M_2 batches, representing 6,000 M_1 plants. Because one M_1 plant contains two germ line cells[2)], one batch of the prepared M_2 seeds displays 18 independent germ lines. Assuming a heterozygote mutation at M_1, representation of 5 homozygous siblings at M_2 on average requires 360 seedlings per batch.

There are several long hypocotyl mutant loci that have been identified by extensive genetic studies, and among them, *hy1*, *hy2*, and *hy3*[3)] show significantly long hypocotyls when grown under white light. Examination of the appearance rate of these *hy*-type mutants in the Ne-beam-irradiated M_2 population, we found 4 independent mutant lines out of 200 M_2 batches (Table 1). This rough estimation suggests that 150 batches corresponding to 3,000 germ lines provide one mutant allele for each locus. According to this estimation, the prepared population of 700 batches would provide 4 to 5 alleles per locus. Further analysis would provide more precise information on the quality of our *Arabidopsis* M_2 population.

References

1) H. Saito, T. Matsuyama, Y. Y. Yamamoto, T. Abe, and S. Yoshida: RIKEN Accel. Prog. Rep. **37**, 147 (2004).
2) G. P. Rédei and C. Koncz: in *Methods in Arabidopsis Research*, edited by C. Koncz, N.-H. Chua, and J. Schell (World Scientific, Singapore, 1992), p.16.
3) M. Koornneef, E. Rolff, and C. J. P. Spruitt: Z. Pflanzenphysiol. **100**, 147 (1980).

Table 1. Characteristics of the *Arabidopsis* M_2 population.

Phenotype	No. of screened batches	No. of mutants	Corresponding loci in the *Arabidopsis* genome
hy[§1]	200	4[§2]	3[§3]
albino	200	41	unknown

[§1]Significantly long hypocotyl phenotype under white light. [§2]Identity of the genetic loci is not determined. [§3]*hy1*, *hy2*, and *hy3*.

Chlorophyll-deficient mutants of rice induced by C-ion irradiation

T. Abe, Y. Hayashi, H. Saito, H. Takehisa,* Y. Miyazawa,* Y. Y. Yamamoto, H. Ryuto, N. Fukunishi, T. Sato,* S. Yoshida, and T. Kameya*

High-LET radiation such as heavy ions can be controlled to deposit high energy at precise positions. Recently, heavy-ion irradiation has become a new method for mutation breeding to produce new cultivars. In the case of Arabidopsis plants, one-half of the mutants have small mutations such as base changes and small deletions involving a few bases and the other half large DNA alterations such as inversions, translocations and deletions.[1] From these results, it can be concluded that heavy ion irradiation-induced mutations show a broad spectrum and a high frequency. In a previous paper we reported the effect of heavy-ion beams on rice.[2] In this paper, we describe the mutational effect of heavy ions on rice seeds for various soaking periods.

The rice seeds (*Oryza sativa* L. cv. Nippon bare) were soaked for 1 to 3 days in water at 30°C without light. The seeds that imbibed water were exposed to C ions accelerated to 135 MeV/u by the RRC within a dose range of 20 to 40 Gy. LET values of the C ions at a dose of 20 Gy were adjusted using the absorbers from 22.6 to 60.3 keV/μm at the surface of the seeds. We irradiated 150 seeds for each soaking period. After irradiation, the seedlings were transplanted to the paddy field. M_2 seeds were harvested separately from each M_1 plant approximately 6 months after irradiation. Then seed fertility was investigated. M_2 seeds were sown on seedbeds, and grown in a greenhouse at 30°C for 11 hrs (daytime) and at 25°C for 13 hrs (night). One month later, chlorophyll-deficient mutants (CDM) were observed.

Thirty-four M_2 progenies of 744 treated lines (Table 1) and 14 M_2 progenies of 376 treated lines (Table 2) were segregated into green plants and CDM: albina (albino); xanta (yellow leaves) chlorina (pale green leaves); and striata (striped leaves) phenotypes. Mutation rates at 40 Gy irradiation were higher than those at 20 Gy irradiation for every soaking period. The optimal of CDM induction was obtained for irradiation at 40 Gy for seeds soaked for 3 days. High LET irradiation caused a decrease in seed fertility (Tabel 2). There is no difference in mutation rate at LET values of 22.6, 37.4 and 48.0 keV/μm. However, the percentages of fertile grains/panicle at LET values of 37.4 and 48.0 keV/μm decreased compared with those at 22.6 keV/μm. The rice plant is one of the most important food cereals. The sequencing of the rice genome has been completed, and the genome organization of cereals appears to be very highly conserved; rice, wheat, maize, sorghum, millet and other cereals exhibit a high degree of synteny. Therefore, new mutants of rice induced by ion-beam irradiation could be important genetic resources for research in plant functional genomics.

Table 1. Frequency of CDM in M_2 plants induced by C-ion irradiation.

Phenotype	Treatment					
Soaking period (day)	1		2		3	
Dose (Gy)	20	40	20	40	20	40
Fertile M_1 line	128	128	129	102	129	128
Seed fertility (%)	85.3	85.3	86.0	68.0	86.0	85.3
Albina/Xanta	3	4	3	2	2	5
Chlorina	1	1	2	2	1	3
Striata	0	0	0	1	1	3
Total CDM	4	5	5	5	4	11
CDM (%)	3.1	3.9	3.9	4.9	3.1	8.6

Harvest of 2002

Table 2. Frequency of CDM induced by C-ion irradiation at the dose of 20 Gy.

Phenotype LET (keV/μm)	22.6	29.9	37.4	48.0	60.3
Fertile M_1 line	119	89	81	65	22
Seed fertility (%)	79.3	59.3	54.0	43.3	14.7
Fertile grains/panicle (%)	73.2 ± 2.0	77.5 ± 2.4	65.3 ± 3.2	65.3 ± 3.6	45.2 ± 8.1
Albina/Xanta	0	1	3	1	0
Chlorina	3	0	0	0	0
Striata	3	0	1	2	0
Total CDM	6	1	4	3	0
CDM (%)	5.0	1.1	4.9	4.6	0

Harvest of 2003

References

1) A. Tanaka: Gamma Field Simposia **39**, 19 (1999).
2) T. Abe, T. Matsuyama, S. Sekido, I. Yamaguchi, S. Yoshida, and T. Kameya: J. Radiat. Res. **43**, S157 (2002).

* Graduate School of Life Sciences, Tohoku University

Biological effects of heavy-ion-beam irradiation on turfgrass

K. Watanabe,* C. Suzuki,* Y. Y. Yamamoto, T. Abe, S. Yoshida, and K. Yoneyama*

One of the turfgrass groups, bentgrass (*Agrostis* spp.), is utilized at golf courses, football grounds, and racecourses. There are major diseases of the bentgrass, such as dollar spot disease and brown patch disease. Although there are established methods of suppressing these diseases, these methods lead to pollution of the environment. Therefore, the development of the disease-resistant varieties is desirable. In order to establish procedures for mutation breeding of bentgrass, we examined the biological effects of heavy-ion-beam irradiation on it.

Dry seeds of bentgrass and wet seeds imbibed for 24 h were subjected to irradiation, and the effects of ion species as well as the dose response was observed. The energies of the ion beam were 135, 135, and 95 MeV/nucleon, and LET were 23, 63, and 240 keV/μm for $^{12}C^{6+}$, $^{20}Ne^{10+}$, and $^{40}Ar^{17+}$, respectively. The effect of each ion beam was observed 30 days after the irradiation by measuring survival rates (Fig. 1) and plant heights (data not shown). As summarized in Fig. 1, the imbibed seeds showed more sensitivity to the irradiation than the dry seeds. The order of the effectiveness of the ion species is Ar, Ne, and C, which is consistent with our previous result (1). Dose responses of the survival rate and the growth index were found to be similar (Fig. 1, data not shown).

Appearance rates of visibly recognizable mutants at the M_1 generation were also measured. Table 1 shows the mutation rates by irradiating the imbibed seeds.

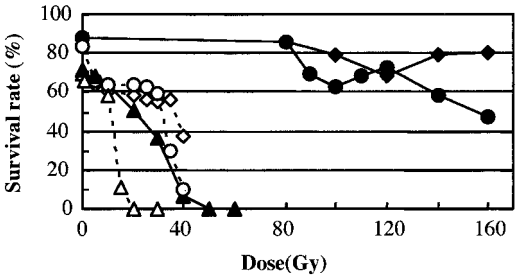

Fig. 1. Effects of C^{6+} (diamond), Ne^{10+} (circle), and Ar^{17+} (triangle) ion irradiations on survival rate. Solid and dotted lines show results of dry and imbibed seeds, respectively.

Table 1. Mutation rates of M_1 plants.

Ion species	Dose (Gy)	Germination[§1]	Mutant[§2]		Total mutant[§3] (%)
			Shrunken leaves	Striped leaves	
^{12}C	0	80	0	0	0 (0)
	20	60	0	0	0 (0)
	25	56	2	0	2 (3.8)
	30	66	1	0	1 (1.8)
	35	56	0	0	0 (0)
	40	37	3	1	4 (10.7)
^{20}Ne	0	80	0	0	0 (0)
	20	77	3	0	3 (3.9)
	25	63	2	0	2 (3.2)
	30	59	5	1	6 (10.2)
	35	30	2	0	2 (6.7)
	40	10	2	0	2 (20.0)
^{40}Ar	0	71	0	0	0 (0)
	1	66	0	0	0 (0)
	5	68	0	0	0 (0)
	10	58	2	0	2 (3.4)
	15	11	1	0	1 (9.1)
	20	0	0	0	0 (0)
	30	0	0	0	0 (0)

The results of wet seed irradiation are shown. [§1] Number of germinated seeds out of 100 irradiated seeds. [§2] The phenotype was examined 45 days after irradiation. [§3] Sum of the shrunken and striped mutants. Mutation rates indicated in the parenthesis are frequency of mutants per germinated seed.

As shown in the table, the range of doses from 20 to 40 Gy for C and Ne beams was found to be sufficient to generate mutants. However, the irradiation of C and Ne beams to the dry seeds with the dose from 80 to 160 Gy did not give so high mutation rate as that activated when irradiating for the wet seeds. Therefore, it might be necessary to examine higher doses of irradiation for the dry seeds. The obtained data, summarized in Fig. 1 and Table 1, will be utilized for effective mutagenesis of bentgrass on a large scale.

Reference

1) H. Saito, T. Matsuyama, Y. Y. Yamamoto, T. Abe, and S. Yoshida: RIKEN Accel. Prog. Rep. **37**, 147 (2004).

* Meiji University

Isolation of heavy-ion induced mutants of sweet pepper

I. Honda,* K. Kikuchi,* T. Abe, H. Saito, H. Ryuto, N. Fukunishi, and S. Yoshida

Mutant plants are very powerful tools to not only clarify the physiological mechanisms of plants but also develop new plant varieties in practical breeding programs. Many methods such as γ-ray irradiation, fast neutron bombardment and chemical treatments have long been studied, developed, and utilized to induce mutation. Recently, heavy-ion irradiation (HII) of plants has been frequently utilized as a method to induce mutations in plants. Abe[1] and Tanaka[2] extensively applied HII technology to various plant species and reported that mutation rates after HII were higher than those after γ-ray irradiation. Various mutantions induced by HII have already been reported in crops as well as in ornamental plants, however, those in vegetable plants are still limited. In this study, we attempted to isolate HII mutants of sweet pepper (*Capsicum annuum* L.).

Dry seeds of sweet pepper (*cv.* California Wonder, Takii Seed Inc.) were irradiated using ^{12}C- and ^{20}Ne-ion beams (135 MeV/u) at a dose range from 1 to 300 Gy. The effects of HII on the germination and growth of young seedlings were examined under normal cultivation conditions in soil. As shown in Fig. 1, seeds irradiated with both the heavy ions at less than 10 Gy grew well, but their growth was severely inhibited after irradiation above 100 Gy. We selected seeds irradiated with both the heavy ions at 10 Gy as suitable for isolating HII mutants. Their young plants were transplanted into a plastic pot containing a commercial soil mixture, and then cultivated in a greenhouse.

Among 108, 10-Gy ^{20}Ne-ion-irradiated plants, we found two plants, the height of one of which was significantly lower and that of the other one was slightly lower than the others, and one plant whose ovary and pericarp of young fruits were yellow. These three lines were putative HII mutants, and they were temporarily named D, SD, and Y mutants, respectively. Their seeds were collected and the inheritances of those phenotypes in their progenies were examined. As shown in Fig. 2, the heights of all the progenies of the D mutant was significantly lower and those of the SD mutant were slightly lower than those of the untreated plants. The phenotypes in terms of the heights of progenies of either mutant were not segregated. All the progenies of the Y mutant showed the viridis (yellow) phenotype even in their leaves, ovary and young pericarp and this phenotype was also not segregated. The viridis phenotype of the Y mutant progenies were not significant early in spring, but clear in summer, suggesting that the expression of those phenotypes may be affected according to temperature or day length.

These results suggest that D, SD and Y are homozygous mutants induced by HII. Reciprocal crossings between these mutants and wild-type plants were conducted to confirm and clarify that the mutational event occurred genetically. Physiological studies to clarify the mechanism of the expression of phenotypes is also necessary. In addition, seeds were obtained from 166 ^{12}C- and 105 ^{20}Ne-ion- irradiated plants. These seed stocks are useful for the isolation of other HII mutants of sweet pepper in future studies. These results may demonstrate that HII is also effective for the induction of mutation of sweet pepper, an economically important vegetable.

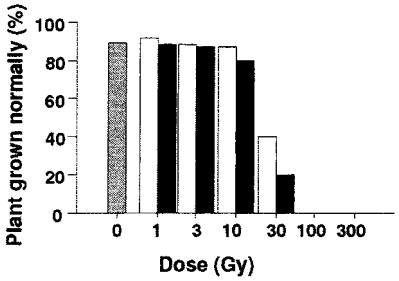

Fig. 1. Effects of heavy-ion irradiation on early growth of sweet pepper. Open and closed bars indicate the effects of ^{12}C- and ^{20}Ne-ion beam irradiation, respectively. Shaded bar indicates control (untreated).

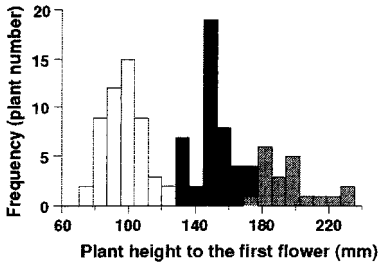

Fig. 2. Frequency distribution of heights of progenies of two putative HII dwarf mutants (D and SD). The heights are expressed as the heights of first flower. Open and closed bars indicate the frequencies of the heights of D and SD mutant progenies, respectively, and shaded bars indicate those of the control (untreated) plants.

References

1) T. Abe: Breed. Res. **5** Suppl. 2, 58 (2003).
2) A. Tanaka: Breed. Res. **5** Suppl. 2, 50 (2003).

* National Institute of Vegetable and Tea Science

Effects of heavy-ion beam irradiation on *in vitro* shoots of Japanese pear 'Nansui'

K. Osawa,[*1] I. Maruta,[*1] T. Abe, S. Tsunoda,[*1] and H. Yamanishi[*2]

'Nansui' is one of the leading Japanese pear (*Phyrus serotina* Rehd.) cultivars in Nagano prefecture, although it is known to be susceptible to black spot disease. The disease caused by the Japanese pear pathotype *Alternaria alternata* is the most serious disease to afflict 'Nansui.' The pears susceptibility is controlled by a single dominant gene.[1)] Mutants resistant to black spot disease, induced by using gamma-ray irradiation, have been sought after for a long time. Recently, some resistant mutants have been developed as new cultivars such as 'Gold Nijisseiki', 'Osa Goldd', 'Kotobuki Shinsui.'[1)] Therefore, a resistant mutant is desirable for 'Nansui.' A combination of two techniques, heavy-ion beam irradiation and tissue culture, are expected to induce a high mutation frequency. In this study, we investigated the effects of two kinds of heavy-ion beam irradiation on *in vitro* shoots of 'Nansui' and found a dose that allowed the shoots to survive and induced the black-spot-disease-resistance mutation.

In vitro-grown shoots were irradiated. Shoot tips were cut into 15-mm-long sections and placed on the shoot regeneration medium (MS medium with 1 mg/l BA and 8 g/l agar). Twenty-one to twenty-five shoot tips were placed in a plastic petri dish (9 cm in diameter). After 1 to 7 days of incubation, the shoot tips were irradiated with $^{12}C^{6+}$ ions (135 MeV/nucleon, 22.6 keV/μm) in a dose range from 5 to 100 Gy or $^{20}Ne^{10+}$ ions (135 MeV/nucleon, 63.0 keV/μm) in a dose range from 5 to 50 Gy. After irradiation, the shoots were transplanted onto a fresh medium and placed in a plant box. Eight weeks after the culture, the number of surviving and regenerating shoots were counted and shoot growth was measured.

The survival rate, shoot growth, and number of regenerating shoots decreased with the increase in dose in both C-ion and Ne-ion irradiation. The survival rate, growth and number of regenerating shoots decreased markedly at 15–25 Gy of C ions and 5–10 Gy of Ne ions (Table 1, Fig. 1, Fig. 2). The extent of shoot growth and number of regenerating shoots were suppressed by irradiation at doses higher than 25 Gy. The Ne-ion beam had a stronger effect than the C-ion beam. The difference in the effect is thought to be because LET (linear energy transfer) of Ne ions is higher than that of C ions. The values of LD_{50} for the *in vitro* shoots were found to be 15–20 Gy of the C ions and 5–10 Gy of the Ne ions. LD_{50} values of shoot tips were similar to those of dormant scions.[2)] No variegated-leaf mutants were observed after irradiation. The plants that initially had abnormally shaped leaves continued to grow normally and later produced normal leaves. Further investigation is required to determine the visible mutation rate following heavy-ion beam irradiation of fruit trees. Moreover further experiments should be performed to select mutants resistant to black spot disease.

Table 1. Effects of C- and Ne-ion beam irradiation of *in vitro* shoots of 'Nansui' on survival rate.

Ion	Dose (GY)	replications	Total shoots	Survival shoots	Survival rate (%)
Control	0	1	11	11	100
C	5	3	63	38	60
	10	4	84	76	90
	15	6	138	88	64
	20	4	96	27	28
	25	8	180	37	21
	50	7	149	27	18
	75	3	65	11	17
	100	3	53	3	6
Ne	5	3	62	42	68
	10	3	62	23	37
	15	3	75	5	7
	20	3	75	0	0
	25	6	138	4	3
	50	1	21	1	5

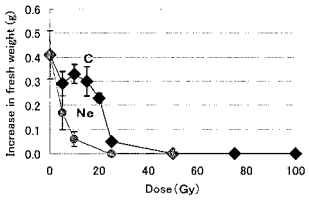

Fig. 1. Growth of *in vitro* shoots of 'Nansui' irradiated with C- and Ne-ion beams.

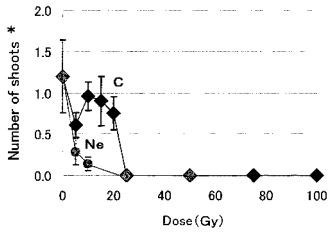

Fig. 2. Number of shoots regenerated after irradiation with C- and Ne-ion beams.
∗ Number of newly regenerated shoots from irradiated shoots.

*1 Nagano Agricultural Research Center
*2 Nagano Vegetable and Ornamental Crops Experiment Station

References
1) T. Yoshioka et al.: JARQ **33**, 227 (1999).
2) Y. Ito et al.: RIKEN Accel. Prog. Rep. **37**, 151 (2004).

Development of male sterile mutant that lacks pollen-producing ability by heavy-ion beam irradiation in pelargonium

M. Sugiyama,* T. Terakawa,* H. Saito, K. Sakamoto, Y. Hayashi, N. Fukunishi, H. Ryuto, and T. Abe

In breeding ornamental plants and flowers, mutation breeding has been a useful method because it can change the specific characteristics and shorten the period required for breeding new varieties. In particular, the induction of mutation by heavy-ion beam irradiation has attracted increasing interest in plant breeding.[1,2] In this study, we developed a mutant pelargonium that lacks pollen-producing ability by heavy-ion beam irradiation.

The stem of pelargonium (*Pelargonium tricolor* × *P. ovale* ssp. *ovale* 'Splendide') cultivated by tissue culture was cut into approximately 5 mm segments, each carrying a single axillary bud. The stem segments were placed on hormone-free 1/3 MS medium containing one-third-strength MS salts and irradiated with a ^{12}C ion beam (135 MeV/nucleon, LET 23 KeV/μm) at doses of 2.5, 5, 10, 20 Gy. Fifty segments (= fifty axillary buds) were irradiated in each experiment. The irradiated samples were transplanted onto 1/3 MS medium containing 0.05 μM naphthylacetic acid for plant elongation and rooting. Four months after the initiation of culture, the rate of surviving stem segments whose axillary buds developed relative to the total number of irradiated stem segments was determined. Then, the plants that survived were grown in a greenhouse until flowering.

The survival rates of the plant irradiated with a heavy-ion beam and the effect of irradiation on the growth of shoots are shown in Table 1 and Fig. 1, respectively. The survival rate ranged from 74 to 80%. The growth of the plant irradiated at 10 Gy and 20 Gy was slightly inhibited. A mutant was obtained by irradiation at both 5 Gy and 20 Gy (Figs. 2 (b), (d)). All the flowers formed on the mutant irradiated at 5 Gy had atrophic anthers with no pollens. On the other hand, the mutant irradiated at 20 Gy formed not only abnormal flowers whose anther was atrophic with no pollens but also normal ones, which suggests the chimerical nature of this mutant. These characteristics were stable for 2 years. In the mutant, characteristics other than the anther morphology were normal,

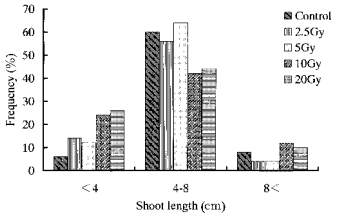

Fig. 1. Growth of pelargonium shoot irradiated with heavy-ion beam. The growth was examined four months after the irradiation.

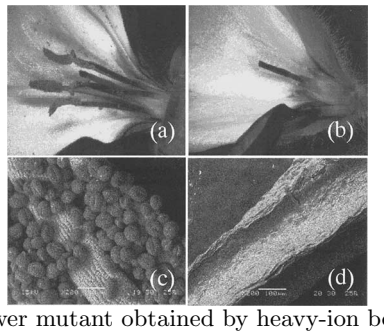

Fig. 2. Flower mutant obtained by heavy-ion beam irradiation. (a) Wild type flower, (b) mutant flower whose anther is atrophic, (c) wild-type anther with pollens and (d) mutant anther without pollens.

however, the diameter of its flower was slightly smaller than that of the wild type.

Plants that lack pollens do not discharge their gene into natural environments *via* pollination. Recently, pollen-mediated gene flow from transgenic crops to wild relatives has become an extremely important issue. A male sterile mutant that lacks pollen-producing ability induced by heavy-ion beam irradiation should be a useful material for producing transgenic plants without the above problem. The development of male sterile mutants of other plants is in progress.

References

1) M. Hamatani et al.: RIKEN Accel. Prog. Rep. **34**, 169 (2001).
2) M. Okamura et al.: Nucl. Instrum. Methods Phys. Res. B **206**, 574 (2003).

Table 1. Survival rate of plant and occurrence of mutant with atrophic anthers devoid of pollens in pelargonium irradiated with heavy-ion beam.

Dose (Gy)	Number of surviving plants	Survival rate (%)	Number of mutants	Frequency of mutants (%)
Control	32	74	0	0
2.5	32	74	0	0
5	40	80	2	5
10	39	78	0	0
20	40	80	1	2.5

* Hokko Chemical Industry Co., Ltd.

Characterization of sterile verbena cultivars produced by heavy-ion beam irradiation

H. Saito, Y. Hayashi, K. Suzuki,* T. Kanaya,* N. Fukunishi, H. Ryuto, T. Abe, and S. Yoshida

In the previous report, sterile mutant lines of the verbena cultivar 'Coral Pink' (*Verbena hybrida*) of the Temari series (Suntory Flowers Ltd., Osaka, Japan) have been successfully isolated from N-ion beam-irradiated nodal cultures.[1)] Recently, the sterile mutant of 'Sakura' of the same series has also been produced by the same method. Among these mutants, it was suggested by cross-pollination tests that sterile 'Coral Pink' produce few seeds due to exhibiting self-incompatibility. However, the characterization of sterile 'Sakura' and detailed data of the pollination tests on these mutants have not yet been reported. We report here the characteristics of sterility of these mutants and seed set following controlled pollinations.

Fertile (FC) and sterile (SC) 'Coral Pink', and fertile (FS) and sterile (SS) 'Sakura' were used. Mature pollen grains harvested at anthesis were stained with KI to examine pollen fertility. Controlled pollination tests were carried out for examining ovule fertility with emasculated flowers and fresh pollen grains. To determine the behavior of pollen tubes in the pistil, pistils with ovaries were collected at certain hours after selfing and pollen tubes stained with decolorized aniline blue were observed under UV light of a fluorescence microscope.

The pollen fertility of SC was the same as those of FC, while there are no viable pollens in SS (Table 1). The seed setting after controlled pollination tests is shown in Table 2. The seed set of SS was never observed in the self-pollinations and the reciprocal crossing, thus both male and female gametes were completely sterile. On the other hand, SC × FC and SC × FS produced seeds. Therefore, it was indicated that SC have fertile ovules. However, in the case of self-pollinated SC, FC × SC and FS × SC, few flowers produced seeds. Pollen germination on stigma was observed in pistils of self-pollinated SC, and then almost all pollen tubes accumulated on the upper regions of the ovary and ovule remained unfertilized (Fig. 1). Self-pollen tubes that arrest within the ovary, describing late-acting self-incompatibility, have been reported in teak (*Tectonia grandis*) belonging to the Verbenaceae.[2)] Results of this report may suggest that SC exhibits self-incompatibility. Detailed characterization and the genetic analysis of incompatible phenotype to clarify the mechanism of self-incompatibility in verbenas is in progress using FC, SC and wild verbena species.

Table 1. Pollen fertility in original and mutant lines of *V. hybrida*.

Lines	Fertile pollens (%)
FC	73.7 ± 5.0
SC	70.0 ± 5.9
FS	91.5 ± 1.6
SS	0

Pollen grains were stained with KI.

Table 2. Seed set following self- and cross-pollinations with original and mutant lines of *V. hybrida*.

♀\♂	FC	SC	FS	SS
FC	58/96[§1](60.4)[§2]	1/109 (0.9)	54/102 (52.9)	0/98 (0)
SC	50/107 (46.7)	1/156 (0.6)	75/121 (62.0)	0/87 (0)
FS	62/101 (61.4)	2/114 (1.8)	71/123 (57.7)	0/120 (0)
SS	0/98 (0)	0/106 (0)	0/115 (0)	0/58 (0)

§1: Number of flowers producing seeds/number of flowers pollinated.
§2: Percentage of flowers producing seeds.

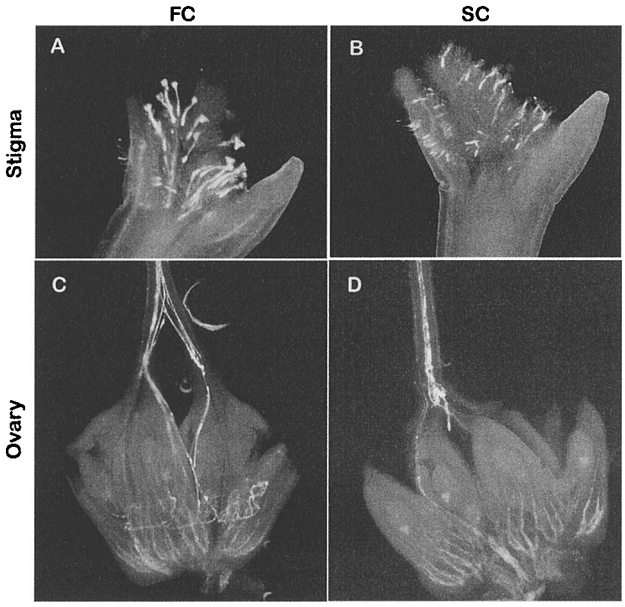

Fig. 1. Florescence micrographs of FC and SC pistils following self-pollinations. Pollen tubes show brilliant florescence. (A), (B) Germinating pollens on surface of stigma 3 h after selfing. (C), (D) Pollen tube growth in styles and ovaries 12 h after selfing.

* R&D Department, Suntory Flowers Ltd.

References

1) K. Suzuki et al.: RIKEN Accel. Prog. Rep. **35**, 129 (2002).
2) S. Tangmitcharoen and J. N. Owens: Ann. Bot. **80**, 401 (1997).

Flower color mutation in spray-type chrysanthemum (*Dendranthema grandiflorum* (Ramat.) Kitamura) induced by heavy-ion beam irradiation

K. Suzuki,* Y. Takatsu,* T. Gonai,* M. Nogi,* K. Sakamoto, N. Fukunishi, H. Ryuto, H. Saito, T. Abe, S. Yoshida, and M. Kasumi*

Developing a mutant series with different flower colors from the original variety is a useful strategy as it is then possible to use the same cultivation practices as the original. A spray-type chrysanthemum is one of the major cut flowers and the modification of flower color is performed by mutation breeding. To induce mutations in chrysanthemum effectively we investigated the effect of heavy-ion beam irradiation on the regeneration of shoots from stem segments and revealed the half lethal dose (LD_{50}) in 18 varieties.[1] In this study, we report the flower-color mutation induced by heavy-ion beam irradiation.

Stem segments were placed on a shoot regeneration medium consisting of MS basal medium supplemented with 2.0 mg/l IAA and 0.2 mg/l BA. Three to 7 days after the culture stem segments were irradiated with ^{12}C ion beams (135 MeV/nucleon, LET 23 keV/μm) at doses around LD_{50}. Regenerated shoots were taken out of stem segments and further studied for mutation in experimental fields. Among the 18 varieties studied, five red-type varieties exhibited color mutation (Table 1). However, nine yellow type, three white type and one red-type varieties did not show any color change. The nonirradiated regenerated plants did not exhibit any mutations indicating the absence of somatic mutations and the induction of color mutation by heavy-ion beam irradiation. The rate of color mutation induced was from 0.6 to 25.0% in five varieties.

A wide spectrum of flower color was exhibited by the mutants derived from the purplish-pink variety 'Chiyo.' Induced color mutants were classified into two groups, a pink-red group and a yellow-orange group. To reveal the types of pigment in petals, we extracted pigments using acetone for carotenoid and 3.0% HCl for anthocyanin. The pink-red group contained anthocyanin as well as the original petals. The yellow-orange group accumulated both anthocyanin and carotenoid. Similarly to 'Chiyo,' the color mutants derived from 'Nonko,' whose original petals contain anthocyanin, were classified into two groups, a pink-red group containing anthocyanin and a red-orange group containing both anthocyanin and carotenoid (Fig. 1 (A)). The color mutants of 'Beachball,' 'Sakiko' and 'Tomoshibi,' whose original petals contain anthocyanin, accumulated both anthocyanin and carotenoid and their colors shifted to the yellow direction (Fig. 1 (B)).

The results obtained in this study revealed that heavy-ion beam irradiation using our tissue-culture system is excellent for the mutation breeding of chrysanthemums. Further investigation is needed to evaluate flower-color mutants for developing new varieties.

Table 1. Flower-color mutation induced by heavy-ion beam irradiation.

Variety	Original flower color	Dose (Gy)	No. of plants	Color mutation Plants	(%)
Beachball	Strong red purple	7	44	2	4.5
Chiyo	Purplish pink	0	67	0	0.0
		10	57	8	14.0
		20	5	1	20.0
Nonko	Deep red purple	3	327	2	0.6
		7	8	2	25.0
Sakiko	Deep purplish pink	1	150	2	1.3
Tomoshibi	Storong red purple	3	77	1	1.3

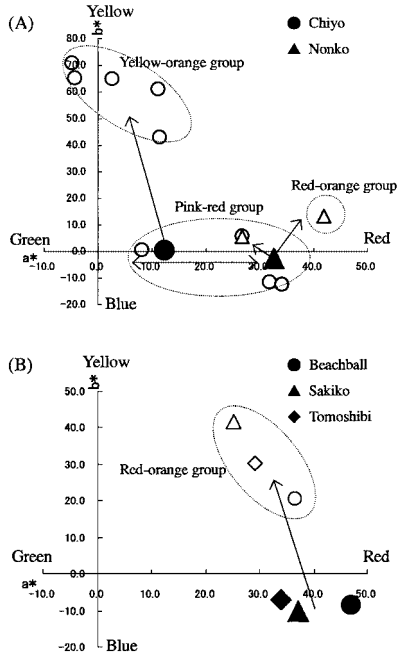

Fig. 1. Flower color analysis of the mutants derived from five varieties using spectrophotometer NF333 (Nippon Denshoku). Mutants were grouped into two (A) categories and one (B) category. Black symbols indicate original varieties.

* Plant Biotechnology Institute, Ibaraki Agricultural Center

Reference

1) K. Suzuki et al.: RIKEN Accel. Prog. Rep. **37**, 152 (2004).

Development of PHENIX silicon pixel detectors in ALICE-RIKEN collaboration

J. M. Heuser, H. En'yo, K. Fujiwara,* H. Kano, H. Ohnishi, and A. Taketani

For the silicon vertex tracker upgrade of the PHENIX experiment at RHIC,[1,2] we develop and produce pixel detectors in collaboration with the ALICE experiment at CERN. ALICE is the dedicated heavy-ion experiment presently under construction at the Large Hadron Collider. We participate in the ongoing production and tests of pixel detectors for the ALICE inner tracker,[3] a detection system similar in design and purpose to the planned PHENIX upgrade, and prepare the production of PHENIX specific pixel sensor modules based on the ALICE technology. We profit from the expertise of more than ten years with the development and application of hybrid pixel detector systems at CERN, and promote the development and construction of two pixel detector layers for the silicon vertex tracker that will be installed in the PHENIX experiment for the eighth physics run at RHIC in 2007/2008.

The upgrade of PHENIX with a silicon vertex tracker will enable the so far inaccessible direct measurement of heavy-quark production through precision vertex tracking with pixel, "strip-pixel" and "mini strip" detectors in a multi layer barrel and end-cap arrangement closely surrounding the interaction region. The two internal barrel pixel detector layers are of particular importance. They resolve the high track densities in heavy-ion collisions due to their high spatial resolution in two dimensions, and provide secondary vertex detection capability in this environment.

The key components of the hybrid pixel detector technology developed at CERN are the front-end readout chip and the interconnection technique between the chip and the two-dimensionally segmented sensor. The front-end chip ALICE1LHCb, produced in an intrinsically radiation-tolerant 0.25 μm CMOS technology, contains 256×32 pixels of $50 \times 425\,\mu\mathrm{m}^2$ size. The pixels provide a binary output reporting their charge detection. The chip is read out at 10 MHz and presents the pixels' hit status in 256 32-bit words on a bus. Several chips can be chained to build larger detector areas.

For the PHENIX application, four chips are mounted on a sensor substrate of approximately 6 cm length ("ladder"), utilizing a cutting-edge industrial flip-chip process with a 20-μm-diameter solder ball interconnection ("bump bond") for every pixel (Fig. 1 (a)). Two ladders are combined into a module, the basic detector unit controlled and read out individually (Fig. 1 (b)). Every of the 10 or 20 azimuthal sectors of the two barrels comprises two modules, mounted with their readout sides pointing in opposite directions (Fig. 1 (c)).

* Niigata University

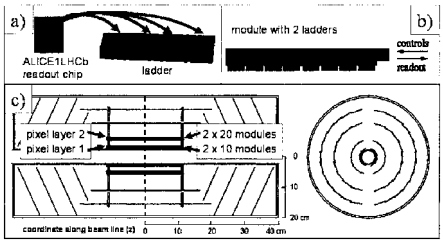

Fig. 1. The pixel detector of the PHENIX silicon vertex tracker comprises (a) 120 sensor ladders on (b) 60 modules, mounted in (c) the two internal barrel layers.

For the production of PHENIX ladders, we selected the good die from 8" ALICE1LHCb wafers with 86 chips each,[4] utilizing a wafer probe station with a specific test system. Simultaneously, the sensors were fabricated on high-resistivity 6" wafers with nine sensor ladders each. We await the final processing steps after the validation of the flip-chip tests presently performed for the ALICE experiment. The flip-chip assembly of the ladders is imminent and will be carried out as part of the ALICE ladder production.

The eight chips of a module will be wire-bonded to a thin aluminum-Kapton bus running on top of the sensors. At 10 MHz, the highest clock frequency reliably applicable to the ALICE1LHCb chips, groups of two chips must be read out in parallel to match the PHENIX readout requirement of 40 (80) μs, four times faster than in ALICE. A pixel bus with four parallel data structures is presently under development,[5] to be read out in 50 μs with two custom-designed "pilot" chips containing the ALICE data handling twice.[6]

We have been contributing to the validation and application of this pixel detector technology in ALICE test beam experiments and the fixed-target heavy-ion experiment NA60 at the CERN-SPS.[7]

References

1) J. M. Heuser: Proc. 6th Int. Workshop on Radiation Imaging Detectors (IWORID) 2004, Glasgow, UK, 2004-7, to be published in Nucl. Instrum Methods Phys. Res. A.
2) A. Drees: J. Phys. G **30**, S1109 (2004).
3) V. Manzari et al.: J. Phys. G **30**, S1091 (2004).
4) K. Fujiwara et al.: RIKEN Accel. Prog. Rep. **38**, 228 (2005).
5) A. Taketani et al.: RIKEN Accel. Prog. Rep. **38**, 233 (2005).
6) H. Kano et al.: RIKEN Accel. Prog. Rep. **38**, 237 (2005).
7) P. Nilsson et al.: Nucl. Instrum. Methods Phys. Res. A **535**, 424 (2004); H. Ohnishi and J. M. Heuser: RIKEN Accel. Prog. Rep. **38**, 76 (2005).

Development of large-area two-dimensional position-sensitive silicon detectors

R. Kanungo, H. Takeda, S. Terashima,[*1] Z. Li,[*2] W. Chen,[*2] Y. Matsuo, H. En'yo, and I. Tanihata[*3]

In various applications, one must measure precisely the position or location of an event of interest. Thus, development of position-sensitive detectors has gained considerable importance. An interesting usage of this technology in genomic science may be for testing the two-dimensional imaging of low-energy ions emitted from cDNA chips and possibly also from a slice of a cell. Imaging of elemental distributions with few tens of microns would be a significant achievement.

For studies using radioactive ion beams in nuclear physics, position-sensitive detectors find immense usage in the detection of recoiled particles in scattering experiments. One of the most important studies on this front is the measurement of density distribution.

Conventionally, proton elastic scattering has served as one of the best tools for probing the matter density of a nucleus. In the case of unstable nuclei, such scattering can be performed only in inverse kinematics, where the proton is the target nucleus. This involves detection of recoil protons with good energy and position resolution. This is necessary in order to distinguish the inelastic scattering. It is often desired that such detectors should be placed in vacuum. The silicon microstrip detectors are well suited for this purpose. The necessary detection conditions require a position resolution of $\sim 125\,\mu$m (one standard deviation) in the theta-direction. A resolution of 2 mm in the azimuthal direction was found to be sufficient for this purpose.

We report here the development of a two-dimensional position-sensitive silicon detector. As an initial step, the design was focussed on achieving the goal of proton elastic scattering described above. A significant feature of the detector is its large active area of $50\,\text{mm} \times 70\,\text{mm}$. The detector is a strip-pixel type,[1)] which employs extraction of two-dimensional position information from one side of the silicon sensor.

It consists of an X-Y array of 200×14 pixels. The pixels are 5 mm long in the Y-direction and $250\,\mu$m wide in the X-direction. Each pixel has two independent types of electrodes. Electrodes of one type are interconnected along the X (or Y) direction. This results in a readout like that from a double-sided strip detector, but from only one surface. Thus, the X-direction has 200 readout pads while there are 14 readout pads for the Y-direction.

The final detector geometry involves building up a circular-arc array with the proton target at the center. Thus, it was required to have both the X and Y pads read out in the same direction. The detector is shown in Fig. 1, which illustrates the readout pads. The silicon sensor was fabricated at Brookhaven National Laboratory, USA.

Figure 2 shows the test measurement of the sensor characteristics. The example is shown for probing a particular pad in the Y-direction. The adjacent pads were grounded for the test. The condition was not altered much when the adjacent pads remained in the floating condition. The X-direction also shows a similar trend. The current-voltage characteristics show a slightly higher value of current. This may be due to the increased surface area of the line electrodes for this large design of the sensor. A more complete view can be obtained by observing the current after integration of the pads with readout electronics.

The 200 pads in the X-direction are read out individually using the 'VA_hdr1' chip from the IDEAS company. This chip is an integrated circuit which includes a preamplifier, a shaper and a multiplexer. The driver circuit of the chip is shown in Fig. 1. The digitized signal from the sensors through the chips will be processed through CAEN, V550A ADC. The sequencer CAEN V551B is used for driving the VA chips. An interface circuit is used for coupling between the VME units and the VA chip circuit and is shown in Fig. 3. Further tests of the detectors are in progress.

The authors are thankful to Dr. J. Tojo and Dr. Y. Goto for useful discussions. Mr. S. Shimizu is gratefully acknowledged for fabricating the readout circuits. Thanks are due to Haraseiki Company, Kumamoto, for

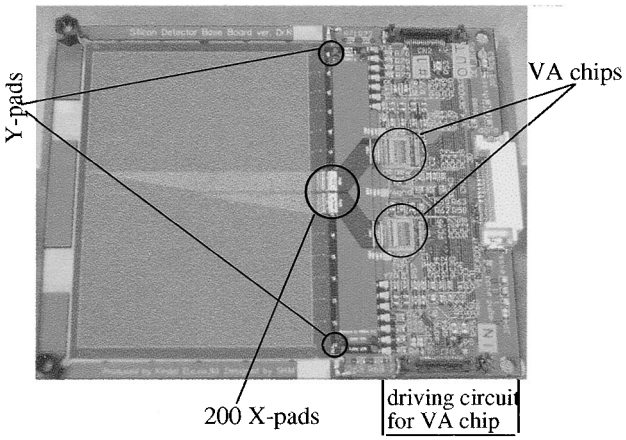

Fig. 1. The silicon strip-pixel detector with the readout VA chips and part of the associated driver circuit.

*1 Department of Physics, Kyoto University
*2 Instrumentation Division, Brookhaven National Laboratory, USA
*3 Argonne National Laboratory, USA

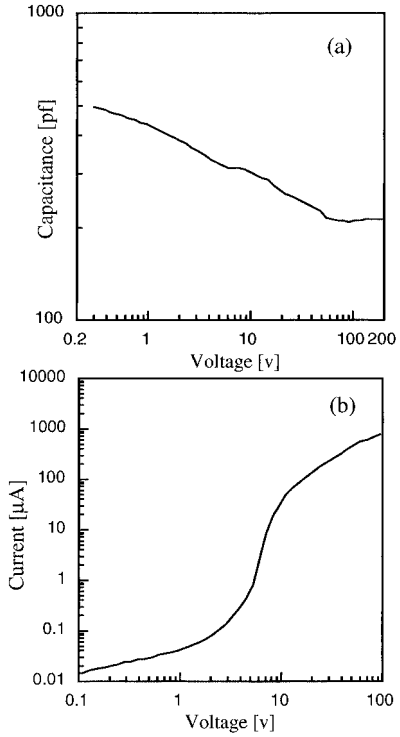

Fig. 2. The C-V (a) and I-V (b) characteristic curves measured for the detector.

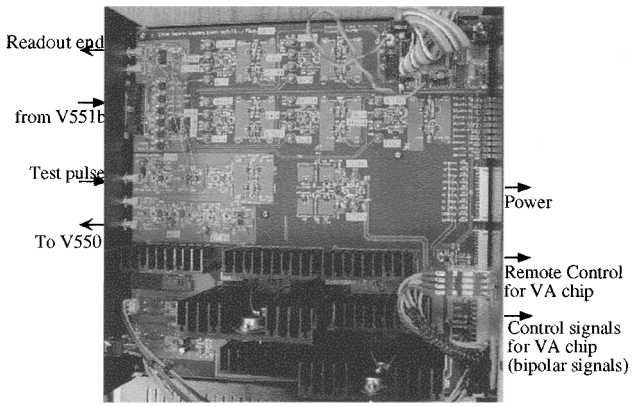

Fig. 3. View of the interface board used for coupling between the sensor readout and the VME units.

wirebonding of the sensors and chips. The help of Mr. K. Fujishiro, Kindai-denshi-elc. Company for overall integration of the detector is gratefully acknowledged.

Reference

1) Z. Li et al.: Nucl. Instrum. Methods Phys. Res. A **535**, 404 (2004).

Application of ultrathin silicon detector in low energy nuclear reaction measurement†

S. Nishimura, M. Kurata-Nishimura, J. J. He,[*1] H. Fujikawa,[*1] H. Yamaguchi,[*1] S. Kubono,[*1] Y. Tagishi,[*2] M. Yamaguchi,[*2] T. Teranishi,[*3] M. Kurokawa, T. Kishida, and T. Motobayashi

Recent progress in high-power accelerator facilities has enabled the study of nuclear reactions in the low-energy frontier, which is essential to clarify the astrophysical nucleosynthesis that occurred in the early stages of the Big Bang as well as the rapid-neutron capture process in supernovae explosions. In this scenario, the path ^{4}He(t,γ)^{7}Li(n,γ)^{8}Li(α,n)^{11}B(n,γ)^{12}B(β,ν)^{12}C is a key reaction flow for explaining the synthesis of ^{12}C and heavy elements according to full network calculations.[1)]

^{8}Li(α,n)^{11}B is recognized as an important reaction for passing through the valley of A = 8 in nucleosynthesis. Various experiments in the past decade have attempted to determine the reaction cross section of ^{8}Li(α,n)^{11}B.[2–5)] However, the results do not seem to be in qualitative agreement with each other. Moreover, the most interesting energy region of data below 1 MeV is missing due to the difficulties of particle identification of low-energy ^{11}B ions from the background particles, which mainly consists of elastically scattered ^{8}Li ions, and α particles as well as the decay products of ^{8}Li.

A new experimental approach for exploring these low-energy nuclear reactions using a monolithic silicon telescope (MST) has been studied using the simulation code GEANT4.[6)] Our feasibility study indicates that the ultrathin silicon detector could be applied to the measurements of the low-energy nuclear reaction products as a novel technique. In this article, the performance of the MST will be reported using low-energy ^{11}B and ^{7}Li ions from an accelerator together with α particles from a source (^{241}Am).

The primary beam of ^{11}B and ^{7}Li ions accelerated up to 12 MeV by the Tsukuba TANDEM Accelerator is first degraded and scattered by a $\sim$3 μm Au foil. The energies of ions are roughly adjusted by altering the angle of the Au foils and chosen by adjusting the downstream magnetic setting of a spectrometer (Q-D-Q magnets) tilted at a 35 degree angle. Two different sizes of collimator with hole sizes of 3 and 10 mm ϕ are installed in front of the MST at the end of the spectrometer. A single MST consists of two 508-μm-thick silicon detectors (E) assembled on a 14 pin IC socket. In addition, five ultrathin silicon pads (ΔE) of 1 μm thickness are arranged on the surface of each of the E layers.[7)] Two signals from the ΔE and E layers provide the dE/dx and the total energy deposited by the incident ions, simultaneously. The size of each ΔE pad is set to $3 \times 4\,\mathrm{mm}^2$ to reduce the capacitance down to 2 nF in order to reduce the noise level with the use of a standard preamplifier. The signals from the preamplifiers go to shaping amplifiers (ORTEC 641) for precise pulse height measurements. Data is gathered using a self-triggering mode on the MST, requiring a minimum energy deposit of above $\sim$100 keV in one of the ΔE pads. Figure 1 shows the compiled scatter plot between ΔE and E in arbitrary units for ^{11}B and ^{7}Li ions. The figure was created by superimposing the data taken at different magnetic settings of the spectrometer. The α particles data is also added using an ^{241}Am source under the slow pressure control of air as an energy degrader. Our result suggests that the MST has an excellent capability for identifying the low-energy ^{11}B from the ^{7}Li ions and α particles down to the energy of 0.11 MeV/u, which is the lowest separation energy of this detector as determined by the stopping range of the incident ^{11}B ions within the first ΔE layer. The bands in the low ΔE region correspond to the hit events on other pads. The incident angle dependence

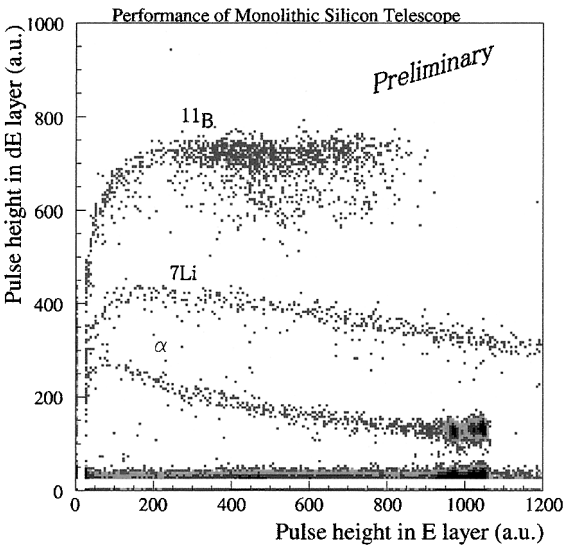

Fig. 1. Correlation between the energy deposited in ΔE and E layers by different incident ions. The clear separation among the ^{11}B and ^{7}Li, and α particles in the low-energy region evidences the excellent performance of the MST for the ^{8}Li(α,n)^{11}B reaction measurement.

† Condensed from the article in Phys. Rev. Lett. **85**, 1827 (2000)

*1 Center for Nuclear Study, University of Tokyo
*2 University of Tsukuba
*3 Kyushu University

of the energy spectrum is also measured by changing the angle of the MST with respect to the direction of the incident particles. Our preliminary results show possible channeling effects of the incident ions in the ΔE layer at the particular angle of the incident ions to the MST around 0 degrees (perpendicular). This effect disappears within 2.5 degrees and shows up again around 35∼40 degrees. Fortunately, this feature is expected to be negligible because our design of the MST allocation and its kinematics in the gas target will result in fewer occurrences of these events.

We have tested one of the MST samples and confirmed that is has adequate energy resolution and no evident crosstalk among the pads. The first experiment for the ^{8}Li(α,n)^{11}B reaction is scheduled in March, 2005 at the CRIB.

References

1) M. Terasawa et al.: Astrophys. J. **562**, 470 (2001).
2) X. Gu et al.: Phys. Lett. B **343**, 31 (1995).
3) R. N. Boyd et al.: Phys. Rev. Lett. **68**, 1283 (1992).
4) Y. Mizoi et al.: Phys. Rev. C **6206**, 5801 (2000).
5) S. Cherubini et al.: Eur. Phys. J. A **20**, 355 (2004).
6) M. Kurata-Nishimura et al.: RIKEN Accel. Prog. Rep. **37**, 183 (2004).
7) A. Musumarra et al.: Nucl. Instum. Methods Phys. Res. A **409**, 414 (1998).

Energy resolution of superconducting series junction detector for heavy ions

H. Sato, M. Kurakado, Y. Takizawa, S. Shiki, M. Ohno, S. Ariyoshi, H. M. Shimizu, K. Morita, K. Morimoto, D. Kaji, and T. Akiyama*

Superconducting tunnel junctions (STJs) as radiation detectors, particularly as photon detectors, have been developed by many groups, because STJs can realize photon detectors with good energy resolution. In addition, STJs can detect high-energy heavy ions by stopping them in a substrate. In the case of direct detection using a single junction, a large number of quasi-particles are generated in superconducting layer of the STJ. As a result, the recombination probability of the quasi-particles becomes large and the pulse height of output signal v.s. energy does not show good linearity. This situation also occurs with conventional semiconductor detectors for the detection of high energy particles. In contrast, when high-energy particles hit a substrate, phonons are generated inside the substrate and diffuse.[1,2] As a result, each single junction, which is a component of a series-junction detector, detects part of the total deposited energy. For example, if the series-junction detector consists of 10000 STJs and the incident energy is 100 MeV, it is expected that each single junction would detect 10 keV. Consequently, the series-junction detector is expected to maintain its energy resolution and linearity up to several hundreds of MeV.

We have been developing two sizes of series-junction detector, one is the small type (6 mm × 6 mm chip size)[3,4] which achieves an energy resolution of 0.5% at 5.49 MeV, and the other is the large type (12 mm × 12 mm chip size). For the detection of high-energy heavy ions, we select the large-type chip which has a detection area of 8 mm × 8 mm because the total number of single STJs in the series-array detectors is large. An example of the series-junction detector is shown in Fig. 1. The structure of each single STJ is Nb/Al/AlOx/Al/Nb and STJs are fabricated on a sapphire substrate whose thickness is 0.4 mm. A single STJ is 110 μm in diameter. 288 single STJs are connected in series and 3 series-arrays are connected in parallel. Thus, 288 × 3 = 864 STJs are included in one array and one series-junction detector consists of 864 × 4 = 3456 STJs. The detection area of the detector is surrounded by these four arrays.

An experiment was carried out for evaluating the energy resolution and linearity of a series-junction detector at the GARIS beam line at the RIKEN linear accelerator (RILAC). A cryostat was placed on the focal point of the GARIS beam line and an ^{40}Ar beam from RILAC (136 MeV, 152 MeV and 191 MeV) was introduced to the cryostat through two Al thin films

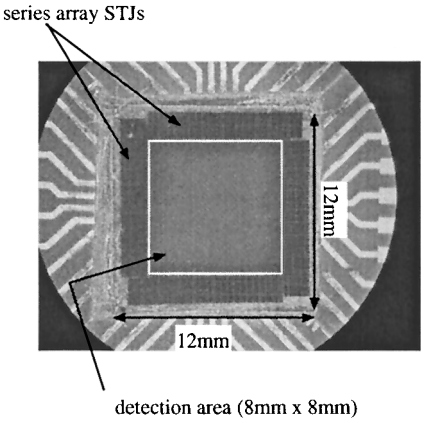

Fig. 1. Chip of series-junction detector.

(100 nm in thickness) which act as thermal shields. A series-junction detector was attached to a copper plate which had a hole (8 mm × 8 mm) in its center. The copper plate was mounted in the cryostat to be cooled to 0.4 K (Fig. 2). Each array was connected to the charge preamplifiers independently. Only coincident signals from the four arrays were acquired as true events. The accumulation of the sum of four signals from the arrays creates the energy spectrum of ^{40}Ar. However, the obtained pulse height of the signal depends on the detected position because of the nonuniformity of the character of the arrays and the difference in the phonon distribution in the substrate. This position dependence of pulse height makes the peak width broad if we simply sum all events. To pre-

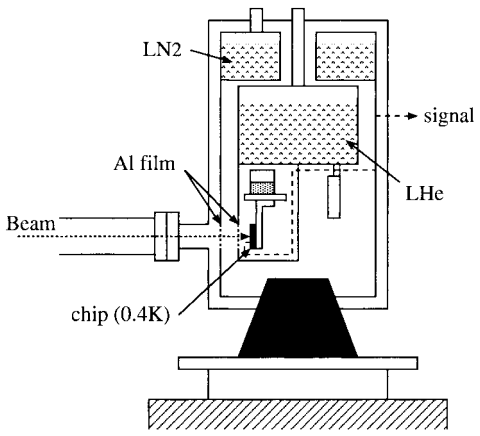

Fig. 2. Schematic view of cryostat.

* Department of Physics, Saitama University

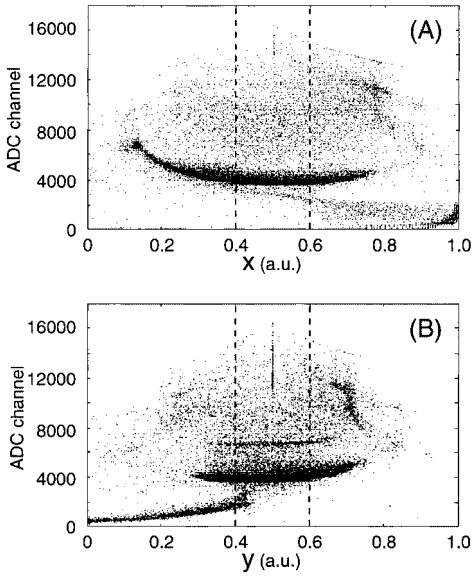

Fig. 3. Projection of obtained pulse height (ADC channel). (A) shows projection to x-axis and (B) shows projection to y-axis. Data inside of two dashed lines were used for analysis.

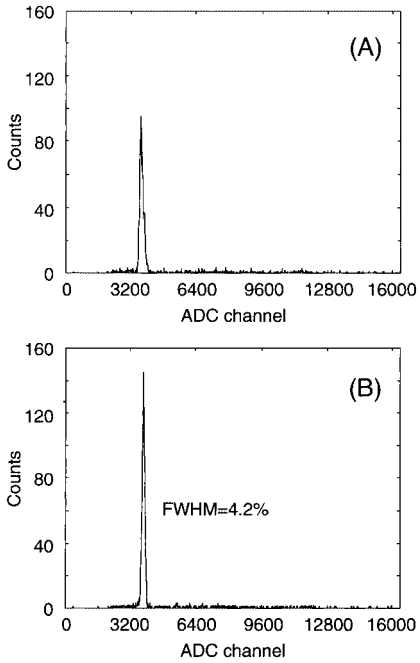

Fig. 4. Energy spectra obtained at beam energy of 191 MeV. (A) shows spectrum before applying position correction and (B) shows after applying position correction. Energy resolution of 4.2% (8.1 MeV) at FWHM was obtained.

vent this effect, a position correction method is applied to our data to obtain energy resolution and peak position channel.[5)]

The energy resolution obtained with a 191 MeV ^{40}Ar beam was calculated. From the two-dimensional scatter plot, the pulse height (sum of the signals from four arrays) distribution was projected on the x-axis and y-axis (Fig. 3). The position dependence of the pulse height was observed, as mentioned before. Thus, we cut the obtained data into a region of $0.4 < x, y < 0.6$ and the data in this region was analyzed. In order to apply the position collection method, the detection area was divided into 40×40 cells and the data of the cells which had events less than 10 counts were not used to reject inaccuracy. As a result, we obtained an energy resolution of 4.2% (8.1 MeV) at full-width at half-maximum (FWHM) (Fig. 4). On the other hand, from an analysis of all data in all region, an energy resolution of 4.9% was obtained. These values are comparable to that of conventional semiconductor detectors and show that further improvement is necessary. So we are now preparing a new design of chip to obtain better resolution.

We measured the energy spectra at three energies of ^{40}Ar beam (136 MeV, 152 MeV and 191 MeV). A peak channel was obtained by the same manner as described above for each spectrum. However, the energy peaks of 136 MeV and 152 MeV were very broad and had a distorted shape. Therefore, the obtained peak channels of 136 MeV and 152 MeV were not reliable. We consider that this does not come from detector properties but rather from experimental error. Consequently, from this experiment, we cannot judge whether the series-junction detector is free from saturation of the pulse height in the high-energy region. Further experiments are needed to resolve this problem.

References

1) M. Kurakado, A. Matsumura, T. Takahashi, S. Itoh, R. Katano, and Y. Isozumi: Proc. SPIE **1743**, 351 (1992).
2) M. Kurakado, D. Ohsawa, R. Katano, S. Itoh, and Y. Isozumi: Rev. Sci. Instrum. **68**, 3685 (1997).
3) H. Sato, M. Kurakado, Y. Takizawa, S. Shiki, and H. M. Shimizu: RIKEN Accel. Prog. Rep. **37**, 157 (2004).
4) H. Sato, Y. Takizawa, S. Shiki, C. Otani, M. Kurakado, and H. M. Shimizu: Nucl. Instrum. Methods Phys. Res. A **520**, 613 (2004).
5) M. Kurakado, S. Kamihirata, A. Kagamihata, K. Hirota, H. Hashimoto, H. Sato, H. Hotchi, H. M. Shimizu, and K. Taniguchi: Nucl. Instrum. Methods Phys. Res. A **506**, 134 (2003).

Measurements of energy resolution and position dependence of NaI(Tl) scintillators

H. Takeda, S. Terashima,* T. Murakami,* T. Ohnishi, H. Sakaguchi,* T. Suda, Y. Yasuda,* and J. Zenihiro*

Proton and neutron density distributions in nuclei provide fundamental information on nuclear physics. For stable nuclei, we have succeeded in determining neutron distributions from proton elastic scattering at intermediate energies (200–400 MeV).[1] It is suitable to extract internal information on nuclei since the *NN* cross section is minimum at such an energy region. The RI beam from the RIBF will have the same energy, thus we can use the beam to deduce nucleon density distributions in unstable nuclei.

To perform proton elastic scattering from unstable nuclei using the RI beam, we are constructing a recoiled particle detector system. An overview of this system is shown in Fig. 1. The system consists of two parts. The first part consists of a thin CH_2 target, silicon microstrip detectors[2] and Si(Li) detectors. The second part consists of a windowless solid hydrogen target,[3] drift chambers and NaI(Tl) scintillation counters. In both parts, the scattering angles and energies of the recoiled protons scattered by the RI beam in the target are measured to reconstruct the Q-value spectrum to separate elastic scattering events from inelastic ones.

NaI(Tl) scintillation counters are prepared as high-resolution calorimeters to measure the total energies of recoiled particles. Each counter consists of a $50 \times 50 \times 450\,\mathrm{mm}^3$ NaI(Tl) crystal, a 3 mm-thick aluminum housing with Pyrex optical windows and photomultipliers. A 100 μm-thick entrance window with an area of $46 \times 432\,\mathrm{mm}^2$ can be found on one of the surfaces of the aluminum housing.

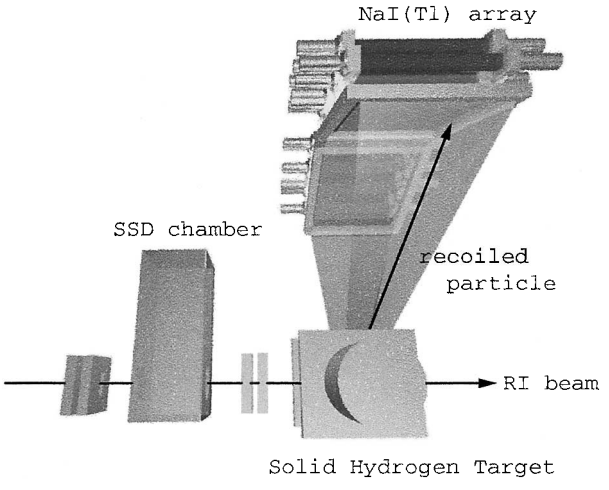

Fig. 1. Overview of the recoiled particle detector system.

* Department of Physics, Kyoto University

We measured the energy resolutions and position dependences of the NaI(Tl) counters using a 12 MeV proton beam to ensure that they satisfy the specifications required to achieve the desired resolution of the Q-value spectrum. The measurements were performed at the Tandem Van de Graaff Accelerator Laboratory, Kyoto University. A schematic view of the experimental setup is shown in Fig. 2. The 12 MeV proton beam was bombarded on Au target of $\sim$1 mg/cm^2 thickness. The scattered protons passed through a slit of 5 mm width and were measured using the NaI(Tl) scintillator. The NaI(Tl) scintillator was placed on a movable stage to change the position of the incident protons. The temperature of the NaI(Tl) scintillator was continuously monitored using a Pt resistance thermometer since the light output in the NaI(Tl) scintillator changes with temperature. The fluctuation in temperature was ± 0.8°C throughout the measurements.

The measured energies are plotted as functions of slit position in Fig. 3. The measured energies are obtained by considering the geometric means ($\sqrt{L \times R}$) of light outputs from the left and right photomultipliers to reduce the position dependence due to the absorption in the propagation of light, and are normalized to 12 MeV at the center position. Energy resolutions are obtained by the Gaussian fitting of the spectrum of the measured energies, which are 1–2% in FWHM. This result is almost consistent with the rough estimate of the number of photoelectrons emitted from the photocathode of the photomultiplier when a light collection efficiency of 20% and a quantum efficiency of the photocathode of 20% are assumed. However, there are certain unique position dependences in the measured energies as shown in Fig. 3. Such results might be due to the uneven characteristics of thallium dop-

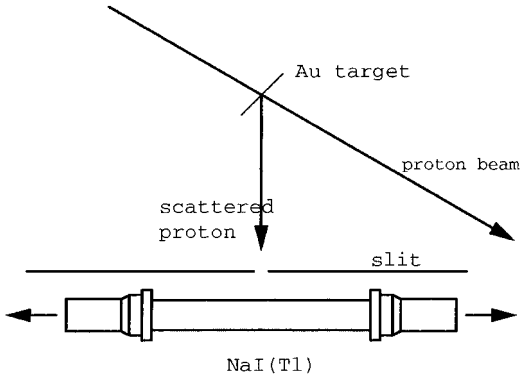

Fig. 2. Schematic view of experimental setup.

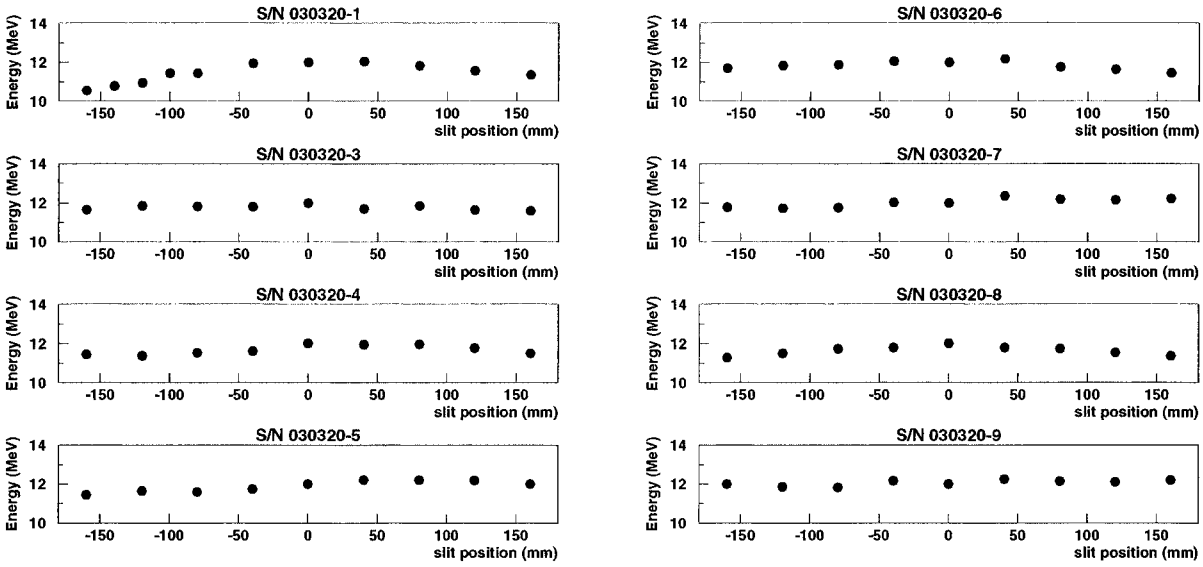

Fig. 3. Energy resolution and position dependence for each NaI(Tl) counter.

ing, entrance window thickness, reflectors inside the aluminum housing and NaI crystal itself.

Only the surface of the NaI(Tl) crystal was associated with the results here since the range of 12 MeV protons in the NaI(Tl) crystal is less than 1 mm. Further tests with a high-energy beam are necessary to investigate the position dependence deep inside the crystals. A test experiment using a 65 MeV proton beam is under preparation at the Research Center for Nuclear Physics, Osaka University. The measurement of the temperature dependence of light output is in progress.

References

1) H. Takeda et al.: AIP Conf. Proc. **610**, 648 (2002); AIP Conf. Proc. **675**, 720 (2003); Proc. Kyudai-RCNP Int. Mini-Symp. on Nuclear Many-Body and Medium Effects in Nuclear Interactions and Reactions (MEDIUM2002), Fukuoka, 2002-10 (World Scientific, Singapore, 2003), p. 269; S. Terashima et al.: RCNP Ann. Rep. **2002**, 43.
2) R. Kanungo et al.: RIKEN Accel. Prog. Rep. **38**, 140 (2005).
3) T. Ohnishi et al.: RIKEN Accel. Prog. Rep. **38**, 150 (2005).

Calibration method for fast-neutron detector wall using cosmic rays

J. Gibelin,[*1,*2] N. Fukuda, Y. Kondo,[*3] K. Kurita,[*2] T. Motobayashi, T. Nakamura,[*3] and Y. Satou[*3]

Neutron detector walls composed of multiple plastic scintillator rods play important roles in detecting fast neutrons emitted from the breakup of neutron-rich nuclei at intermediate or high incident energies.[1–3] In recent experiments at Riken,[4,5] the energy and scattering angles of the resulting fragments and neutrons were measured to deduce the excitation energy before breakup, using the invariant mass method. Breakup neutrons, with energies close to that of the beam (few tens of MeV) were detected using a neutron detector wall schematically represented in Fig. 1.

The energy of the neutrons was deduced from the time-of-flight from target (TOF), and their horizontal position from the time difference between the left and right PMTs of the rod. We report here the steps that were followed to perform the calibration of those observables. The procedures rely on the detection of cosmic-ray muon events. To record these events, the neutron detector wall was in self-triggering mode with the condition that at least 8 of the 116 scintillators were fired.

The wall was placed a few meters downstream of the target. It contained four layers of a plastic hodoscope array consisting of 29 plastic scintillator rods (16 are 1 m long and 13 are 2 m long) with a section of $6\times6\,\mathrm{cm}^2$ and a PMT at each end. A thin (5 mm) layer of plastic scintillators used as vetoes for charged particles was placed upstream of the wall.

Energy calibration of light output: To properly set the detection threshold of deposited energy in the neutron scintillator rods, a calibration of light output amplitude was required. Gamma-rays from ^{60}Co as well as muon events were used for this purpose. To eliminate the light attenuation effect in plastic scintillators, the corresponding amplitude was the geometrical mean of the light output at the right end (A_R) and at the left end (A_L): $<A>=\sqrt{A_\mathrm{L}\,A_\mathrm{R}}$.

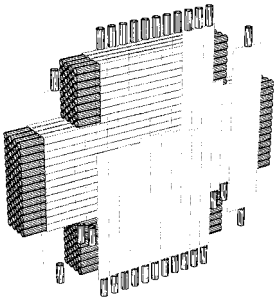

Fig. 1. Exploded view of neutron detector wall used in the experiments detailed in Refs. 4 and 5. One can see the cross-shaped layers of horizontal neutron scintillator rods equipped with one photomultiplier tube (PMT) at both ends. The thin vertical plastic scintillators on the front face are used as vetoes.

Muons reach the earth essentially vertically from the sky with a total energy of approximately 4 GeV[6] and deposit an energy of ≈ 12 MeV in one neutron plastic scintillator. Due to straggling, the deposited energy follows a Landau distribution,[7] see Fig. 2 (left), approximated by[8] $\Phi(\lambda)=\sqrt{e^{-(\lambda+e^{-\lambda})}/(2\pi)}$, where λ is proportional to the energy loss.

Time calibration: A calibration of the absolute timing of each rod was made by a run utilizing a thick brass target frame where a large amount of prompt γ-rays were emitted. For TOF measurement, $<T>=\frac{T_\mathrm{R}+T_\mathrm{L}}{2}$ defines the arrival time in one neutron detector, where T_R is the time measured for the right PMT and T_L the time measured for the left one.

Position calibration: Time difference $\Delta T=T_\mathrm{L}-T_\mathrm{R}$ provides the longitudinal position along the rods, namely the horizontal position. The maximum value of ΔT, ΔT_max, corresponds to photons that travel the entire scintillator length L. Then, $L/\Delta T_\mathrm{max}$ provides the mm↔ns correspondence.

We corrected the remaining amplitude/position dependence effect using arbitrary polynomial fitting.

For the relative position alignment between the detectors within one layer, we selected the highest multiplicity from cosmic ray events. For one event, 29 pairs of hit coordinates $(X_i,Y_i)_{i=1,29}$ were fitted to give an equation that describes the muon's trajectory: $X=\alpha Y+\beta$. For one detector and all the events we calculated the distribution of differences between the fitted trajectory and real coordinates, $\Delta_i X=X_i-(\alpha Y_i+\beta)$, which gives the position measurement's shift (for il-

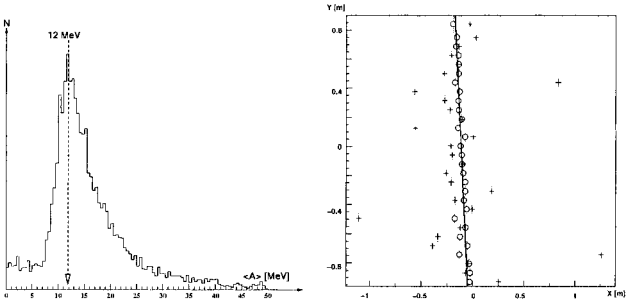

Fig. 2. Left: Landau distribution of deposited energy of muons. Right: Example of muon track before position correction (+) and after correction (○), plotted with a fitted track.

*1 Institut de Physique Nucléaire, France
*2 Department of Physics, Rikkyo University
*3 Department of Physics, Tokyo Institute of Technology

lustration see Fig. 2 (right)). The overall horizontal position resolution for muons is 2 cm (FWHM).

Finally, the absolute position with consideration of the entire setup is obtained by utilizing a proton beam run. Protons stop in the first layer at a well-known position determined using vetoes.

Slew (walk) correction description: For timing signals, leading edge (LE) discriminators were used, producing a strong time/amplitude dependence (see for example Ref. 9) termed *walk* or *slew*. For an improved resolution of TOF or position measurement, this effect must be corrected.

We confirmed that the "slew function", which describes the time/amplitude dependence from the slew effect, has the form $T_{\rm R} = T^0_{\rm R} - K_{\rm R}/\sqrt{A}_{\rm R}$ for the right side ($T_{\rm L} = T^0_{\rm L} - K_{\rm L}/\sqrt{A}_{\rm L}$ for the left), where $A_{\rm R\ or\ L}$ is the left or right light output, see Fig. 3 (left). In the following, $K_{\rm R\ or\ L}$ will be referred to as *slew coefficient* or simply *coefficient*. The rise time from the plastic scintillator is ~ 6 ns and therefore the time offset from the slew effect cannot be more than 6 ns.

The slew is corrected for each rod's end according to the above formulas. The amplitudes used for correction are strongly sensitive to the light attenuation of photons traveling through the plastic scintillator by yet another time/amplitude dependence. We eliminated this effect by selecting events from the center of the plastic rod, thus obtaining similar light attenuation at both ends.

Finally, TOF for one neutron detector is defined as:

$$< T >= \frac{1}{2}\left(T_{\rm R} + T_{\rm L} + \frac{K_{\rm R}}{\sqrt{A}_{\rm R}} + \frac{K_{\rm L}}{\sqrt{A}_{\rm L}}\right).$$

Slew correction procedure: We considered two consecutive detectors in one layer: one for correction ($\mathcal{C}$) and one for reference ($\mathcal{R}$). We define:

$$\delta T_S(A^{\mathcal{C}}_S) = T^{\mathcal{C}}_S(A^{\mathcal{C}}_S) - T^{\mathcal{R}}_S(A^{\mathcal{C}}_S)\,;\ {\rm S} = {\rm Left,\ Right}$$
$$\delta T(< A^{\mathcal{C}} >) = \left(\delta T_{\rm L}(< A^{\mathcal{C}} >) + \delta T_{\rm R}(< A^{\mathcal{C}} >)\right)/2.$$

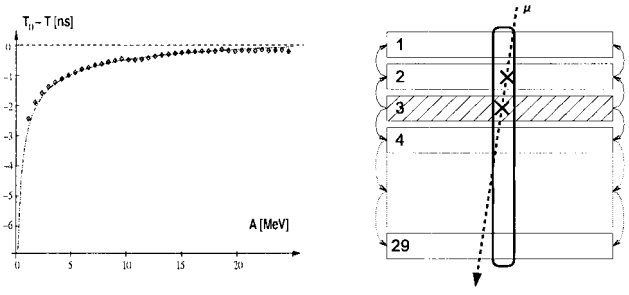

Fig. 3. Left: Experimental time shift (in ns) function of signal amplitude (in MeV) for one PMT. Right: Schematic explanation of propagation method through plastic scintillators. In this case, we start from detector 3 and propagate to both up and down, while selecting the center of the scintillators to obtain a similar light attenuation at both ends.

We fitted the $\delta T_{\rm S}$ *vs.* $A^{\mathcal{C}}_{\rm S}$ distribution using the slew function and obtained the slew coefficients.

We started from the top detector of a layer, called 1. By fitting, we obtained slew coefficients for both sides of the next rod below, called 2. Since the reference detector was not corrected yet, these coefficients included the slew effect from both the reference and corrected detectors. In the case of an $\mathcal{R}$ detector with a high slew, coefficients of the $\mathcal{C}$ detector can even be negative and the time for low-energy events appears less than that for high energy ones. We continued to propagate the correction, using 2 as a reference for 3, then 3 for 4, up to 28 as a reference for 29.

We reiterated fitting, keeping 1 untouched. The results from the fit for a given detector were added to previous values. Since previous studies showed that all the coefficient values were close to each other, we avoided possible divergences by smoothing the coefficient value distribution at each iteration. When the last detector had been fitted, we restarted the same propagation algorithm, from detector 2. This last detector is used as a reference for both 1 and 3, then 3 for 4 up to 28 as a reference for 29. We started again from 3 as a reference for 4 and 2, then 4 for 5, 2 for 1, and so on, see illustration in Fig. 3 (right).

The coefficients obtained after using all the detectors as starting points, *i.e.*, after 29 resets, were averaged to give the probable 29 ($\times 2$ sides) slew coefficients.

We validated the correction by confirming that neither δT_S nor δT depends on $A^{\mathcal{C}}_S$ or $< A^{\mathcal{C}} >$, respectively, for all detectors. Coefficients were of the order of 4 ns.MeV$^{\frac{1}{2}}$

Conclusion and results: Calibration in time and position of a large neutron detector array was performed using cosmic-ray muons. The position resolution for muons was 2 cm (FWHM) and the time resolution for γ was 850 ps.

The time resolution obtained by our method can be compared with that from "direct" correction using monoenergetic neutrons, emitted from the ^{7}Li(p,n)^{7}Be reaction, which provides after correction a resolution of 700 ps. We thus suggest that our present method can be used for improving the time resolution of neutron plastic detector walls without requiring beam time.

References

1) N. Fukuda et al.: Phys. Rev. C **70**, 054606 (2004).
2) R. Palit et al.: Nucl. Phys. A **738**, 45 (2004).
3) B. Luther et al.: Nucl. Instrum. Methods Phys. Res. A **505**, 33 (2003).
4) J. Gibelin et al.: RIKEN Accel. Prog. Rep. **37**, 63 (2004).
5) Z. Elekes et al.: RIKEN Accel. Prog. Rep. **38**, 50 (2005).
6) K. Hagiwara et al.: Phys. Rev. D **66**, 010001 (2002).
7) L. D. Landau: J. Physics **8**, (1944).
8) J. E. Moyal: Philos. Mag. **46**, 263 (1955).
9) W. R. Leo: *Techniques for Nuclear and Particle Physics Experiments* (Springer-Verlag, New York, 1994).

Development of windowless solid hydrogen target

T. Ohnishi, H. Takeda, S. Ishimoto,[*1] S. Suzuki,[*1] T. Suda, I. Tanihata,[*2] and Y. Takahashi[*3]

The requirement of a thin and flat windowless solid hydrogen target becomes more important for experiments using an RI beam, particularly, proton elastic scattering and (p, $2p$) reactions. For these experiments, the target thickness is limited to avoid energy loss, multiple scattering, and energy straggling inside the target in order to obtain high energy and angular resolutions. In addition, the number of hydrogen ion is so small that the background from the window becomes more serious. Furthermore, if the window is curved and the target thickness becomes nonuniform, the variation of the thickness has a significant effect on the resolution. Therefore, to obtain a flat target and reduce the background from the window, a windowless solid hydrogen target is needed.

The windowless solid hydrogen target has been developed recently.[1,2] Although the researchers used liquid helium for the cooling system, it is better to use a more compact cooling system so that it can be set easily on the beam line and improve the flexibility of the detector placement. Moreover, in the case of the self-supported target, the target was made only 10 mm thick.[1] So, we have developed a thin self-supported windowless solid hydrogen target using a small cryostat.

We have constructed a cooling system with a small cryostat, SUMITOMO RDK-415D. The length and diameter of the cooling system are approximately 40% and 30% smaller than those of the previous system,[1] respectively. Concerning the detector placement, the solid angle of the detector is about twice as large, because the detector can be located closer to the target. The measured cooling power of this cryostat was 1.35 W at 4.6 K.

Figure 1 shows the schematic view of the target cell. This cell was made of pure copper, and consisted of a disk and a cell plate. The disk was connected to the cryostat by a copper block. The cell plate was 7 mm thick and 50 mm wide. In its center, there was a hole of 30 mm diameter. A Pt-Co resistance thermometer sensor was inserted into a thin hole drilled in the cell plate beside the gas inlet.

The assembly for making a windowless target is shown in Fig. 2. During the solidification process, both sides of the hole were covered by Teflon-coated stainless steel plates. These plates were pressed tightly on the cell plate with stainless steel bellows which were pressurized at approximately 5 atm with helium gas. A 1-mm-thick indium gasket was used to obtain a vacuum-tight seal. Teflon-coated plates were separated from the crystal and the cell plate by evacuating helium gas inside the bellows. After separation, the plates and the bellows were pulled down linearly. The target thickness was determined by the shape of Teflon-coated plates. In the present study, we used the designed plates to fabricate a 3-mm-thick target. The effective area of 3 mm thickness had a diameter of 20 mm.

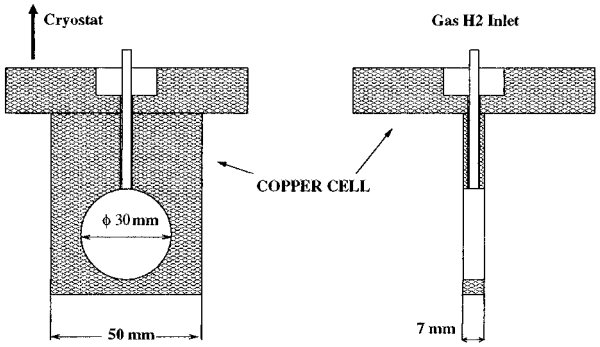

Fig. 1. Schematic view of target cell. The disk on the top of the cell was connected to the cryostat by a copper block. The diameter of hole in the wall was 30 mm. The inlet tube of hydrogen gas is also drawn.

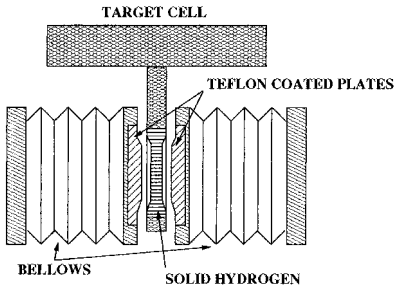

Fig. 2. Assembly of Teflon-coated stainless steel plates and stainless steel bellows. Teflon-coated plates for fabrication of the 3-mm-thick target are shown. These were pulled down lineally.

An inlet tube for hydrogen gas was a thin stainless steel tube (3 mm OD and 2 mm ID). It was directly introduced into the cell and connected only to the top of the hole to prevent the occurrence of solidification inside the tube.

The starting temperature of introducing hydrogen gas was around 4 K. The pressure of the introduced hydrogen gas was controlled and maintained constant during the solidification; it was set to 60 Torr. The cell temperature was increased to almost 6.5 K by the

[*1] High Energy Accelerator Research Organization
[*2] Argonne National Laboratory, USA
[*3] Research Center for Nuclear Physics, Osaka University

introduction of the warm gas and then decreased gradually during the process of crystal growth. When the cell temperature returned to around 4 K, the solidification was almost finished. Then, the teflon-coated plates were separated. A photograph of the crystal is shown in Fig. 3. The crystal is very transparent with no voids and is self-supported.

The measurement of the crystal thickness was carried out using the laser iconometer, KEYENCE LK-500. We measured the distance between the iconometer and the surfaces of the crystal and the cell, and scanned horizontally along the target at the vertical center. Figure 4 shows the result of the measurements. The dashed line represents the shape of the Teflon-coated plate. Compared with the dashed line, the shape of the crystal was almost the same as that of the Teflon-coated plate. With the assumption of the same shape on the back surface, the average thickness of the crystal was deduced as approximately 2.7 ± 0.2 mm (r.m.s.).

After 10 days of operation, the thickness of the crystal was the same within the error. However, a contamination was found on the surface of the crystal. This was because the pressure at the start time of the cooling, almost 10^{-5} Torr, was not sufficiently low. To avoid this problem, it is necessary to clean inside the chamber and start cooling at a pressure below 10^{-6} Torr.

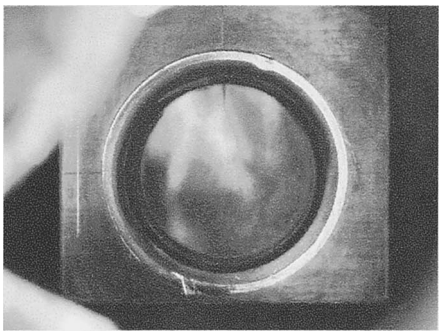

Fig. 3. Bare self-supported crystal inside the cell.

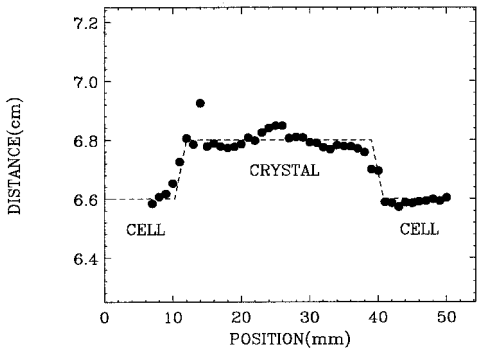

Fig. 4. Distance to surfaces of crystal and cell. The horizontal axis denotes the position along the target. The vertical axis denotes the distance from the reference point. The dashed line represents the shape of the Teflon-coated plate.

Finally, we have developed a windowless solid hydrogen target with a small cooling system. A hydrogen crystal of 20 mm diameter and 3 mm thickness was grown directory from normal hydrogen gas. The crystal was self-supported and very transparent. From the thickness measurement, the crystal had a uniform thickness. Further developments to realize a thinner target is on going.

References

1) S. Ishimoto et al.: Nucl. Instrum. Methods Phys. Res. A **480**, 314 (2002).
2) P. E. Knowles et al.: Nucl. Instrum. Methods Phys. Res. A **368**, 604 (1996).

Polarization calibration of spin-exchange-type polarized ^{3}He target at RIKEN/CNS

K. Itoh,[*1] T. Uesaka,[*2] T. Wakui,[*2] T. Kawabata,[*2] Y. Shimizu,[*3] Y. Tameshige,[*3] K. Hatanaka,[*3] Y. Sakemi,[*3] A. Tamii,[*3] K. Fujita,[*3] T. Wakasa,[*4] H. Yoshida,[*4] T. Kudoh,[*4] H. Ohira,[*4] and H. Sakai[*5]

A spin-exchange-type polarized ^{3}He target was developed at RIKEN/CNS. In 2002, this target was substantially modified to improve diagnostics capability and performance.[1] In the target system, the cell containing ^{3}He gas has the so-called "double-cell" structure. This structure consists of a target cell and an optically pumping cell, connected to each other through a pipe with an inner diameter of 10 mm. ^{3}He nuclei in the pumping cell are polarized via spin exchange with polarized Rb atoms. The polarized ^{3}He nuclei diffuses into the target cell.

The polarization of ^{3}He nuclei in the target cell is monitored by the adiabatic-fast-passage(AFP)-NMR method, which provides a relative polarization value. On the other hand, the polarization of ^{3}He nuclei in the pumping cell is obtained by measuring the frequency shift of the Rb electron spin resonance (ESR). The ESR method provides the absolute polarization value. If the difference in ^{3}He polarization between the pumping cell and the target cell is sufficiently small, the AFP-NMR signal can be calibrated by measuring the ESR frequency shift. To compare the polarization in the target cell with that in the pumping cell, the absolute polarization of ^{3}He in the target cell is measured via the $^3\vec{\mathrm{He}}(\vec{p},\pi^+)^4$He reaction, simultaneously with the ESR measurement.

The ESR frequency shift method has recently been established as the accurate polarimetry method. The ESR frequency of the Rb atoms is shifted by the presence of polarized ^{3}He gas. This is mainly due to the hyperfine interaction between a ^{3}He nucleus and a valence electron of a Rb atom. The frequency shift is given as[2]

$$\Delta\nu = A\kappa_0[^3\mathrm{He}]P_{^3\mathrm{He}}. \quad (1)$$

Coefficient A weakly depends on the strength of the static magnetic field applied to the target. $P_{^3\mathrm{He}}$ is the ^{3}He polarization and $[^3\mathrm{He}]$ is the ^{3}He density. κ_0 is the temperature-dependent coefficient measured with an uncertainty of 1.5%[2]. If the polarization of ^{3}He is 100%, the frequency shift is obtained to be 20.2 kHz using Eq. (1) for $[^3\mathrm{He}] = 7.6\times10^{19}$ atoms/cm^3, which is the density in the calibration experiments described in this report.

To observe ESR, Rb atoms are optically pumped into the F=3, m=−3 state, where F and m denote the total angular momentum and the magnetic quantum number of a Rb atom, respectively. By applying an RF field that induces ESR between the m=−3 and m=−2 states, the population in the m=−2 state is increased. Atoms in the m=−2 state absorb circularly polarized laser light and succeedingly decay back to the ground state by emitting fluorescence photons. The occurrence of ESR can thus be observed by detecting the fluorescence photons.

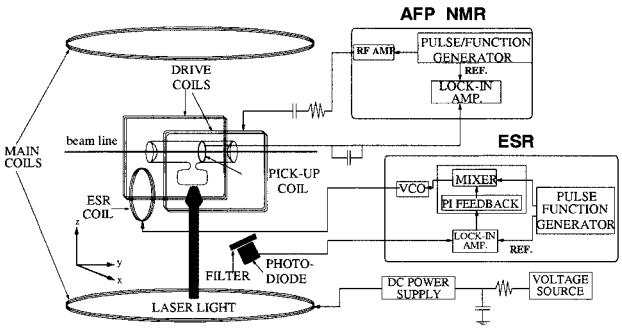

Fig. 1. Configuration of the ESR frequency shift measurement.

Figure 1 shows the experimental setup for the ESR measurement. The cell is placed in a magnetic field of ∼20 G produced by main coils. The pumping cell is illuminated by circularly polarized laser light for optical pumping. The RF field is produced using an ESR coil. The RF frequency is modulated using a voltage-controlled oscillator (VCO). The fluorescence photons are detected using a photodiode through a band-pass filter with a band width of 1.5 nm (FWHM). The detected fluorescence signal is processed using a lock-in amplifier by considering the modulation frequency. The processed signal is transmitted to a proportional-integral feedback circuit, which is used to lock the RF frequency to the ESR frequency. The locked frequency is measured as an ESR frequency using a counter.

The ESR frequency strongly depends on the strength of the magnetic field. A field fluctuation of 10 mG corresponds to an ESR frequency fluctuation of 4.5 kHz. In a previous measurement, the uncertainty of the ESR frequency was mainly due to the magnetic field fluctuation originating from the instability of a power supply.[3] The stability of the power supply was about 5×10^{-4}, leading to an ESR frequency fluctuation of ∼2.5 kHz. To improve accuracy in the determination of the ESR frequency, a high-stability power

*1 Department of Physics, Saitama University
*2 Center for Nuclear Study, University of Tokyo
*3 Research Center for Nuclear Physics, Osaka University
*4 Department of Physics, Kyushu University
*5 Department of Physics, University of Tokyo

supply has recently been installed. Using the power supply, the ESR frequency fluctuation has been decreased to less than 1 kHz.

The calibrations of the polarization obtained from the ESR frequency shift have been performed before and after the $^3\vec{\mathrm{H}}\mathrm{e}(\vec{p},\pi^+)^4\mathrm{He}$ reaction. The result is shown in Fig. 2. The mean coefficient of proportionality was deduced to be $(4.85 \pm 0.03)\times10^{-4}$ mV^{-1}. The error in the coefficient was considerably decreased from the previous measurement.[3)]

The $^3\vec{\mathrm{H}}\mathrm{e}(\vec{p},\pi^+)^4\mathrm{He}$ reaction measurement has recently been performed to calibrate the AFP-NMR signal. For the case of $\frac{\vec{1}}{2}^+ + \frac{\vec{1}}{2}^+ \rightarrow 0^- + 0^+$, one can show from the parity conservation that the polarization correlation coefficient takes $C_{y,y}$=+1.[4)] In this case, the target polarization P_y^T is written as

$$P_y^T = \frac{1}{P_y^B}\frac{\sigma_{\uparrow\uparrow}+\sigma_{\downarrow\downarrow}-\sigma_{\uparrow\downarrow}-\sigma_{\downarrow\uparrow}}{\sigma_{\uparrow\uparrow}+\sigma_{\downarrow\downarrow}+\sigma_{\uparrow\downarrow}+\sigma_{\downarrow\uparrow}}, \qquad (2)$$

where P_y^B is the beam polarization and σ is the cross section for respective combinations of the spin direction. The first and second subscripts indicate the spin directions of the beam and the target, respectively. Thus, the absolute ^{3}He polarization in the target cell can be directly deduced if the beam polarization is known.

The experiment was performed at the Research Center for Nuclear Physics (RCNP), Osaka University, using a polarized proton beam. The beam energy was 392 MeV, the beam intensity was 20 nA, and the beam polarization was about (70±2)%. The beam polarization was monitored using beam-line polarimeters, on the basis of the proton elastic and quasi-elastic scatterings from a polystyrene analyzer target. The pions were momentum analyzed using the high-resolution magnetic spectrometer Grand Raiden,[5)] and detected using two plastic scintillation counters and two vertical drift chambers (VDCs).

The excitation energy spectrum is shown in Fig. 3. The peak around E_x=0 was due to the $^3\vec{\mathrm{H}}\mathrm{e}(\vec{p},\pi^+)^4\mathrm{He}$ reaction. Small peaks at negative excitation energies and continuum were background events mainly due to the cell materials. Spin-dependent cross sections were deduced after subtracting the background. The absolute target polarization was obtained from the spin-dependent cross sections using Eq. (2). The direction of the beam polarization was reversed every second, and the direction of the target polarization was reversed every 2 hours. The polarization of the ^{3}He target was measured by the AFP-NMR method once per hour. The results of the calibration measurement are shown in Fig. 2 by closed triangles. The mean coefficient of proportionality was deduced to be $(5.92\pm0.63)\times10^{-4}$ mV^{-1}.

The results of the two different calibration measurements do not agree within the error bar. The re-examination of the systematic error in the ESR frequency measurements and the analysis of the $^3\vec{\mathrm{H}}\mathrm{e}(\vec{p},\pi^+)^4\mathrm{He}$ measurement are in progress.

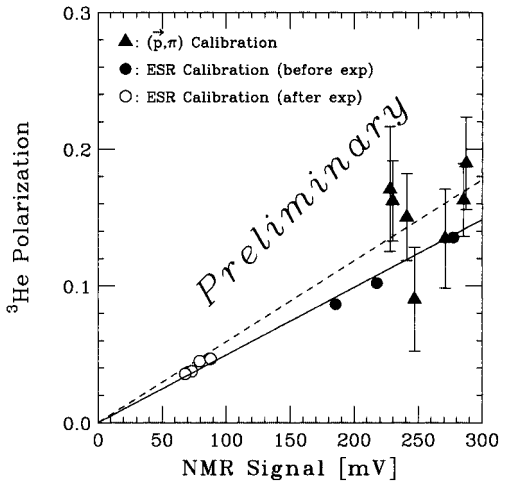

Fig. 2. Correlation of the AFP-NMR amplitude and the absolute value of ^{3}He polarization. Solid and dashed lines show the fitting results for the ESR and $^3\vec{\mathrm{H}}\mathrm{e}(\vec{p},\pi^+)^4\mathrm{He}$ measurements, respectively.

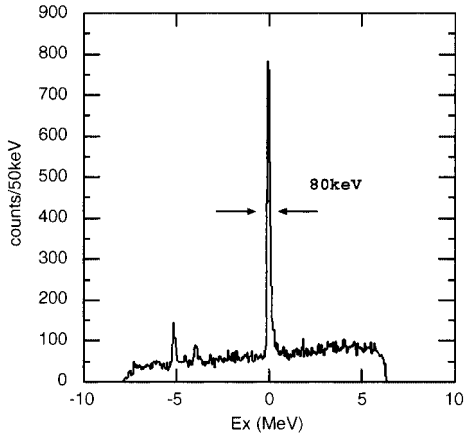

Fig. 3. Excitation energy spectrum at a beam energy of 392 MeV. The sharp peak around $E_x = 0$ is due to the $^3\vec{\mathrm{H}}\mathrm{e}(\vec{p},\pi^+)^4\mathrm{He}$ reaction.

References

1) K. Itoh et al.: CNS Annu. Rep. **2002**, 62.
2) M. V. Romalis et al.: Phys. Rev. A **58**, 3004 (1998).
3) S. Yamamoto et al.: RIKEN Accel. Prog. Rep. **34**, 198 (2001).
4) G. G. Ohlsen: Rep. Prog. Phys. **35**, 717 (1972).
5) M. Fujiwara et al.: Nucl. Instrum. Methods Phys. Res. A **422**, 484 (1999).

Relaxation of proton polarization in polarized target

T. Wakui,[*1] M. Hatano,[*2] H. Sakai,[*1,*2] T. Uesaka,[*1] and S. Sakaguchi[*1]

A polarized solid proton target has been developed using a crystal of naphthalene doped with 0.01 mol% pentacene.[1)] Among polarized solid proton targets, this target is unique in that protons can be polarized at a low magnetic field of 0.3 T and a higher temperature of 100 K.[2)] This feature allows the target to be used in a scattering experiment with an RI beam under the inverse kinematic condition. The polarized proton target has been used for an experiment with a ^{6}He beam at the RIKEN projectile fragment separator (RIPS) in July 2003[3,4)] and also for a test experiment with a ^{4}He beam at E3 in September 2004.[5)] The target system is described in Ref. 3, and the polarization procedure is described in Ref. 6.

The proton polarization, $P_{\rm p}$, during polarization buildup can be written as[7)]

$$P_{\rm p} = \frac{A}{A+\Gamma_{\rm p}}\overline{P_{\rm e}}\{1-\exp[-(A+\Gamma_{\rm p})t]\}, \qquad (1)$$

where $\overline{P_e}$ is the average population difference between two sublevels in the triplet state, $\Gamma_{\rm p}$ the total relaxation rate of proton spins, and A the buildup rate which is proportional to the laser power. The proton polarization is a result of the competition between A and $\Gamma_{\rm p}$. The relaxation rate is thus an important factor for the proton polarization.

During the buildup process, the relaxation of proton spins is caused by several sources, and $\Gamma_{\rm p}$ can be written as

$$\Gamma_{\rm p} = \Gamma_{\rm I} + \Gamma_{\rm L} + \Gamma_{\rm T}, \qquad (2)$$

where $\Gamma_{\rm I}$ is the intrinsic relaxation rate, $\Gamma_{\rm L}$ the relaxation rate caused by a cumulative effect of laser irradiation, and $\Gamma_{\rm T}$ the relaxation rate due to pentacene molecules in the photoexcited triplet state. Since pentacene molecules in the triplet state decay to the ground state with a lifetime of 100 μs, $\Gamma_{\rm T}$ disappears after stopping laser irradiation.

The intrinsic relaxation of proton spins in a target crystal below 250 K is mainly due to the fluctuating field produced by paramagnetic impurities.[8)] The relaxation rate $\Gamma_{\rm I}$ measured at 100 K ranges from 0.044 to 0.060 h^{-1}, depending on the quality of the fabricated crystal.

The relaxation due to the cumulative effect of laser irradiation has been found recently. After laser irradiation, the relaxation rate measured without laser irradiation increased compared with $\Gamma_{\rm I}$. Figure 1 shows the increase in relaxation rate, *i.e.*, $\Gamma_{\rm L}$, as a function of the product of laser power and time for laser irradiation. The relaxation rate $\Gamma_{\rm L}$ was obtained from the relaxation rate measured without laser irradiation by subtracting $\Gamma_{\rm I}$. The solid line shows the least-squares fit of a linear function. The proportionality constant was $(1.1 \pm 0.5) \times 10^{-3}$ W^{-1}h^{-2}.

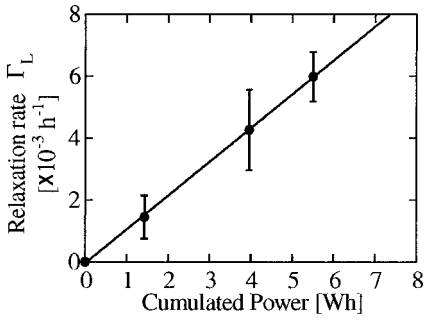

Fig. 1. Relaxation rate $\Gamma_{\rm L}$ due to cumulative effect of laser irradiation.

The relaxation due to pentacene molecules in the photoexcited triplet state is caused by the interaction between triplet and proton spins. Figure 2 shows $\Gamma_{\rm T}$ as a function of laser power. The relaxation rate $\Gamma_{\rm T}$ was obtained from the relaxation rate measured with laser irradiation by subtracting $\Gamma_{\rm I}$ and $\Gamma_{\rm L}$. The relaxation rate $\Gamma_{\rm T}$ increased almost linearly with the laser power. The linear increase would be attributed to the fact that the number of pentacene molecules in the triplet state is proportional to the laser power unless an optical transition is saturated.[9)] The solid line shows the least-squares fit of a linear function. The proportionality constant was 0.26 ± 0.06 W^{-1}h^{-1}.

In addition to the relaxation process due to these sources, we found the relaxation process caused by ion-beam irradiation. After the experiment with the ^{6}He beam, the relaxation rate measured without laser irradiation increased from 0.06 to 0.13 h^{-1}. From the measured relaxation rate, the relaxation rate due to ion-

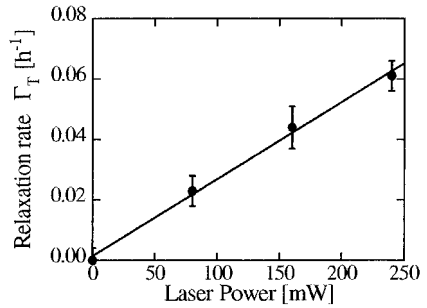

Fig. 2. Relaxation rate $\Gamma_{\rm T}$ caused by interaction between triplet and proton spins.

*1 Center for Nuclear Study, University of Tokyo
*2 Department of Physics, University of Tokyo

beam irradiation, Γ_B, was obtained as $0.065 \pm 0.11\,h^{-1}$ by subtracting Γ_L. In this experiment, the target crystal was irradiated by a ^{6}He beam of 71 MeV/u with a total dose of $1.5 \times 10^8\,mm^{-2}$. For the experiment with the ^{4}He beam, the relaxation rate Γ_B was obtained as $0.284 \pm 0.015\,h^{-1}$ in the same manner. In this experiment, the target crystal was irradiated by a ^{4}He beam of 80 MeV/u with a total dose of $7 \times 10^8\,mm^{-2}$. Although the experimental conditions such as the beam energy and the beam-spot size on the target are different in each experiment, we attempted to plot Γ_B against the total dose in a figure. Figure 3 shows Γ_B as a function of total dose. The relaxation rate Γ_B seemed to increase almost linearly with the total dose in the range of the experiments. The proportionality constant was $(4.07 \pm 0.04) \times 10^{-2}\,h^{-1}/10^8\,mm^{-2}$.

To compare the contribution of each source to the relaxation rate during a scattering experiment, we calculated the dependence of the relaxation rate on time using each proportionality constant. Figure 4 shows the result of the calculation. In this calculation, we assumed that Γ_I is $0.05\,h^{-1}$, the laser power is 200 mW, the beam intensity is 2×10^5, and the beam-spot size on the target is 10 mm ϕ. From this figure, we can see that Γ_B increases rapidly with time and becomes as large as the sum of the relaxation rates due to other sources at the irradiation time of 5 days.

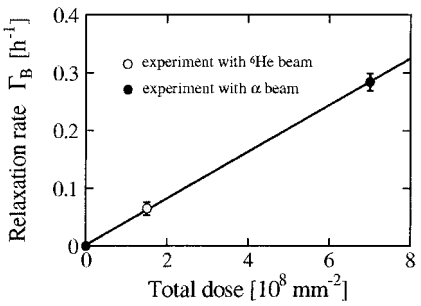

Fig. 3. Relaxation rate Γ_B caused by ion-beam irradiation.

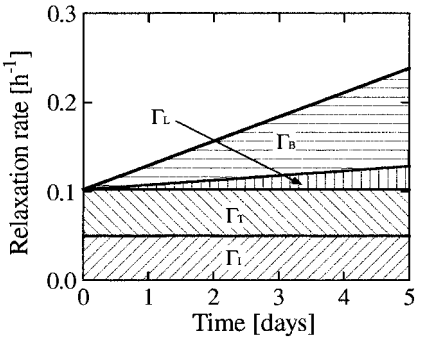

Fig. 4. Time dependence of the relaxation rate due to each source.

For a higher beam intensity, Γ_B will increase more rapidly. Since the proton polarization decreases with increasing relaxation rate, Γ_B should be reduced periodically by changing the target crystal or by annealing. We then investigated the effect of annealing after the test experiment with the ^{4}He beam. The investigation was carried out by measuring the relaxation rate without laser irradiation after annealing at different temperatures. Figure 5 shows Γ_B plotted against time. The relaxation rate Γ_B was obtained from the measured relaxation rate by subtracting Γ_I. The relaxation rate Γ_L was smaller than the error bars. For the first 63 hours, the temperature of the target crystal irradiated by the ^{4}He beam was maintained at 100 K. During the first period, the relaxation rate Γ_B remained constant at around $0.3\,h^{-1}$. The temperature of the crystal was then increased and maintained at 150 K for the next 6 hours. At 150 K, the relaxation rate Γ_B decreased, but the effect of annealing was small. For the last 16 hours, the temperature of the crystal was maintained at 200 K. The relaxation rate Γ_B clearly decreased at 200 K. From these results, the temperature of the target crystal should be increased to higher than 200 K for annealing.

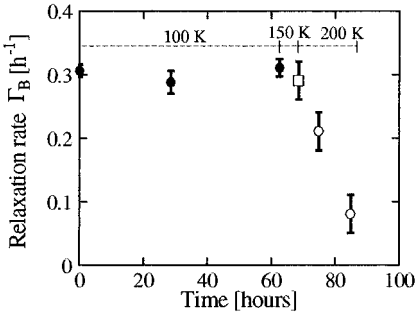

Fig. 5. History of relaxation rate Γ_B during annealing.

References

1) T. Wakui et al.: RIKEN Accel. Prog. Rep. **34**, 194 (2001).
2) A. Henstra et al.: Chem. Phys. Lett. **165**, 6 (1990).
3) T. Uesaka et al.: Nucl. Instrum. Methods Phys. Res. A **526**, 186 (2004).
4) M. Hatano et al.: RIKEN Accel. Prog. Rep. **37**, 44 (2004).
5) S. Sakaguchi et al.: RIKEN Accel. Prog. Rep. **38**, 36 (2005).
6) M. Hatano et al.: RIKEN Accel. Prog. Rep. **33**, 182 (2000).
7) M. Iinuma et al.: Phys. Lett. A **208**, 251 (1995).
8) J. U. von Schuetz et al.: Z. Naturforsch. **27**, 42 (1972).
9) T. Wakui et al.: Nucl. Instrum. Methods Phys. Res. A **526**, 182 (2004).

Development of neutron polarimeter

K. Yako,[*1] H. Sakai,[*1] H. Saenma,[*1] M. Oizumi,[*1] Y. Takahashi,[*1]
M. Sasano,[*1] T. Kawabata,[*2] and H. Kuboki[*1]

To test Bell's inequality[1] in a proton-neutron system, a beam time is scheduled for the measurement of the spin correlation between the proton and neutron in $^1S_0$ produced by the ^{6}Li$(d,pn)^6$Li$[0^+, T = 1; 3.56\,\mathrm{MeV}]$ reaction at $E = 135A\,\mathrm{MeV}$. In this measurement, the polarization of the proton is analyzed using a focal plane polarimeter[2] at SMART in the E4 experimental area, while that of the neutron is analyzed using a neutron polarimeter (NPOL), which is currently under development. The requirement of NPOL is an energy resolution of $< 1\,\mathrm{MeV}$ and a figure of merit (FOM) of $\epsilon_n (A_y^{\mathrm{eff}})^2 > 10^{-5}$, where ϵ_n and A_y^{eff} are the double scattering efficiency and the effective analyzing power of NPOL, respectively. In this year, a prototype NPOL was fabricated and tested.

Figure 1 shows a schematic view of NPOL. It consists of three planes, each of which consists of six plastic scintillators (Bicron BC408) with a size of $10 \times 60 \times 3\,\mathrm{cm}^3$. Each scintillator is viewed from both sides by photomultiplier tubes (PMTs) such that the positions are obtained from the timing information derived from the PMTs. The typical position resolution is $\pm 4\,\mathrm{cm}$ in the longitudinal direction of the scintillator. The first neutron plane serves as a neutron polarization analyzer (NA), while the two planes placed downstream of 60 cm serve as neutron catchers (NC1 and NC2). The polar angle θ and azimuthal angle ϕ of the neutron scattering in NA are determined from the position information in NA and NC. The most useful event is the elastic scattering of a neutron by a proton in NA and its detection in either NC1 or NC2.[3] To eliminate the signals due to the charged particles in the counter planes, three sets of thin plastic scintillators with a size of $20 \times 60 \times 0.5\,\mathrm{cm}^3$ are placed in front of the analyzer plane and the catcher planes.

The measurements of ϵ_n and A_y^{eff} were performed using the polarized neutron beams produced by the $\mathrm{C}(\vec{d}, \vec{n})X$ reaction at 0° at $E_d = 180\,\mathrm{MeV}$. The energy of the neutron beams was $E_n \sim 90\,\mathrm{MeV}$ and the flux was $\sim 1 \times 10^9$/s in NPOL located 21 m away from the target. The typical polarization of the deuteron beam was $p_d = 0.53 \pm 0.02$.[4] Using the polarization transfer coefficient of $K_y^y(0°) = 2/3$,[5] the polarization of the neutron beam was estimated to be $p_n = -\frac{3}{2} K_y^y p_d \approx= -0.53$.

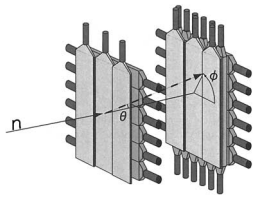

Fig. 1. Schematic view of the neutron polarimeter. The polar angle θ and the azimuthal angle ϕ are indicated.

The energy of the neutron was obtained by the time-of-light (TOF) technique. A kinematical discrimination of the $n + p$ events from the $n + \mathrm{C}$ events was performed by considering the time, position, and pulse-height information. For example, the neutron velocity between NA and NC v_{exp} obtained from the TOF and the flight path length determined by θ was compared with the velocity calculated from the incoming neutron energy and the scattering angle θ, assuming the $n + p$ kinematics (v_{NN}). The sector method was applied to obtain the left/right asymmetry,[3] where the neutrons with the scattering angles within the regions of $\theta_{\mathrm{min}} < \theta < \theta_{\mathrm{max}}$ and $|\phi| < \Phi$ ($|\phi - \pi| < \Phi$) are considered to be scattered in the right (left) direction (see Fig. 2).

The software cuts were optimized, as shown in Table 1, to obtain the maximum FOM. The results are $\epsilon_n = 2.3 \times 10^{-5}$, $A_y^{\mathrm{eff}} = 0.25 \pm 0.01$, and FOM $= 1.7 \times 10^{-6}$, where the statistical error is denoted for A_y^{eff}. The systematic uncertainty due to the uncertainty in p_n was estimated to be ± 0.01. We are preparing a new NPOL with 12 planes to achieve an FOM value of 2×10^{-5}.

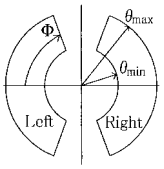

Fig. 2. Sector definition for the left/right asymmetries.

Table 1. Optimized cuts used in the neutron polarimeter.

Quantity	Cut
ϕ	$\Phi = 66.8°$
θ	$(\theta_{\mathrm{min}}, \theta_{\mathrm{max}}) = (16.0°, 36.5°)$
Pulse height in analyzer	$> 5.5\,\mathrm{MeV}_{ee}$
Pulse height in catcher	$> 4.0\,\mathrm{MeV}_{ee}$
Velocity ratio $v_{\mathrm{NN}}/v_{\mathrm{exp}}$	0.88–1.10

*1 Department of Physics, University of Tokyo
*2 Center for Nuclear Study, University of Tokyo

References
1) J. S. Bell: Physics **1**, 195 (1964).
2) T. Saito et al.: CNS Annu. Rep. **2003**, 19.
3) M. Palarczyk et al.: Nucl. Instrum. Methods Phys. Res. A **457**, 309 (2001).
4) H. Mardanpour et al.: RIKEN Accel. Prog. Rep. **38**, 157 (2005).
5) H. Sakamoto et al.: Phys. Lett. B **155**, 227 (1985).

Determination of vector- and tensor-analysing powers in elastic deuteron-proton scattering via $^{12}C(\vec{d},\alpha)^{10}B^*(2^+)$ reaction

H. Mardanpour,[*1] H. R. Amir Ahmadi,[*1] N. Kalantar-Nayestanaki,[*1] T. Kawabata,[*2] H. Kuboki,[*3] Y. Maeda,[*2] J. G. Messchendorp,[*1] S. Sakaguchi,[*2] H. Sakai[*2],[*3] N. Sakamoto, Y. Sasamoto,[*2] K. Sekiguchi, K. Suda,[*2] Y. Takahashi,[*3] T. Uesaka,[*2] and K. Yako[*3]

The measurement of the analysing powers of deuteron-proton elastic scattering at E_d = 180 and 130 MeV was carried out at RARF in May 2004. The experiment was composed of two parts. In order to measure the asymmetries of deuteron-proton elastic scattering, the first part is performed with the D-room in-beam polarimeter.[1)] Simultaneously using the same beam, the beam polarization was measured via $^{12}C(\vec{d},\alpha)^{10}B^*(2^+)$ reaction using the SMART spectrograph. The analysing powers in deuteron-proton elastic scattering were measured for beam energies of 180 and 130 MeV for 6 different angles in the center-of-mass reference frame.

In a coordinate with z-axis parallel to the beam direction, the cross section of a reaction with polarized deuteron beam of the quantization axis (Z) perpendicular to the reaction plane is expressed as:[2,3)]

$$\frac{\sigma}{\sigma_0(\theta)} = 1 + \sqrt{3}p_Z iT_{11}(\theta)\cos\phi - \frac{1}{\sqrt{8}}p_{ZZ}T_{20}(\theta) - \frac{\sqrt{3}}{2}p_{ZZ}T_{22}(\theta)\cos(2\phi), \quad (1)$$

where θ and ϕ are the polar and azimuthal scattering angles, respectively. Plastic scintillator detectors on the right, left, upper and lower (ϕ = 0°, 180°, 90°, 270°) sides of the target measure the asymmetries in the reaction of a polarized beam with a CH_2 target. The polarization state of deuteron beam switches between off-mode ($p_Z = 0$, $p_{ZZ} = 0$), mode-1 ($p_Z = \frac{1}{3}$, $p_{ZZ} = -1$), and mode-3 ($p_Z = \frac{1}{3}$, $p_{ZZ} = +1$). The quoted values for p_Z and p_{ZZ} are the theoretical maximum values.

For $\theta = 0°$, the cross section relation is simplified to

$$\sigma = \sigma_0(\theta)\left(1 - \frac{1}{\sqrt{8}}p_{ZZ}T_{20}(\theta)\right). \quad (2)$$

A measurement of the $^{12}C(\vec{d},\alpha)^{10}B^*$ reaction with the SMART spectrograph enables the unambiguous extraction of the beam polarization. The identification of the 2^+ excited state, which has a clear and background-free peak, makes it possible to determine the number of α particles (Fig. 1) corresponding to this excited state. The beam polarization can subsequently be extracted since the analysing power of

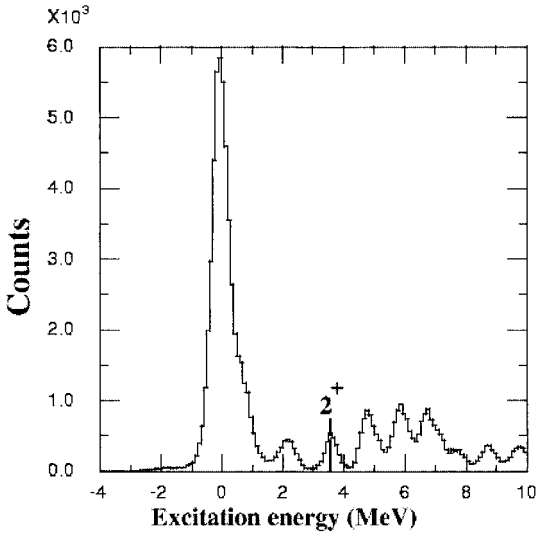

Fig. 1. Excitation energy spectrum of ^{10}B.

the 2^+ state is known exactly at zero degrees to be $T_{20}(\theta = 0) = \frac{1}{\sqrt{2}}$. Therefore, by measuring the asymmetry at $\theta = 0°$, it is possible to obtain the beam polarization. The exact measurement of beam asymmetry at $\theta = 0°$ is not possible. The asymmetry at $\theta = 0°$ is, therefore, obtained from an extrapolation of an asymmetry measurement at finite angles between $\theta = 1° - 4°$ and using a second-order polynomial fit. The asymmetries of mode-1 and mode-3 are found to be -0.200 ± 0.009 and $+0.205 \pm 0.003$, respectively. The extrapolation at $\theta = 0°$ is demonstrated in Fig. 2. These yields p_{ZZ} values of mode-1 and mode-3 of -0.801 ± 0.036 and 0.821 ± 0.012, respectively, for a polarized deuteron beam at 180 MeV, and p_Z is determined by assuming that $p_Z = \frac{1}{3} \mid p_{ZZ} \mid$.[4)]

The D-room polarimeter is composed of 6 different proton counters placed at angles listed in Table 1.

For each proton detector, the corresponding deuteron counter is located on the other side of the beam. Thus the setup makes it possible to measure the asymmetries at 6 different angles. The deuteron beam interacts with the CH_2 target placed at the center of the polarimeter.

By measuring asymmetries in the horizontal and vertical planes in the D-room polarimeter and using the obtained polarization values from SMART, the analysing powers of the $\vec{d} - p$ reaction can be calculated using the asymmetries

*1 Kernfysisch Versneller Instituute (KVI), Netherlands
*2 Center for Nuclear Study, University of Tokyo
*3 Department of Physics, University of Tokyo

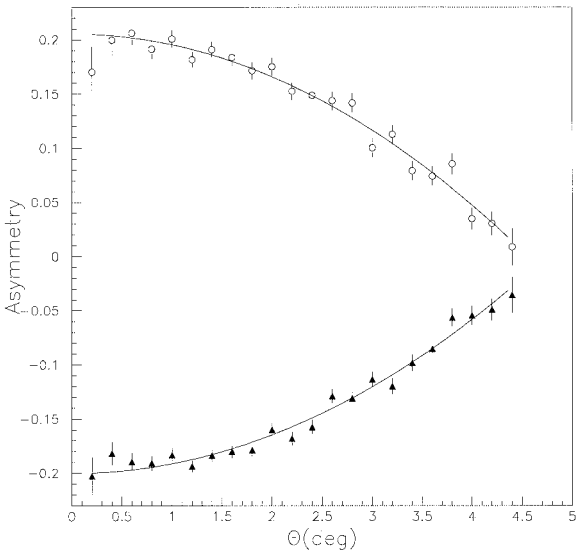

Fig. 2. Asymmetry *versus* the scattering angle of $^{12}\mathrm{C}(\vec{d},\alpha)$ $^{10}\mathrm{B}^{*}(2^{+})$ reaction. The open circles correspond to the data fitted for mode-1 and the filled triangles correspond to data fitted for mode-3.

Table 1. Positions of deuteron and proton detectors.

Label	P-lab (deg)	d-lab (deg)	θ_{CM}
P120	29.7	30.0	118.7
P5	33.3	29.6	111.2
P4	38.3	28.4	101.2
P3	41.3	27.4	95.2
P2	44.3	26.2	89.1
P1	47.3	24.9	83.2

$$L - R = 2\sqrt{3}iT_{11}p_Z, \tag{3}$$

$$R + L - U - D = -2\sqrt{3}T_{22}p_{ZZ}, \tag{4}$$

$$R + L + U + D = 4\left(1 - \frac{1}{\sqrt{8}}T_{20}p_{ZZ}\right). \tag{5}$$

Some preliminary analysing powers of the elastic deuteron-proton reaction at 180 MeV are shown in Fig. 3. The open squares and open triangles correspond to T_{20}, the filled squares and filled up triangles correspond to T_{22}, the open circles and upside down filled triangles correspond to iT_{11} for mode-3 and mode-1 polarization states, respectively.

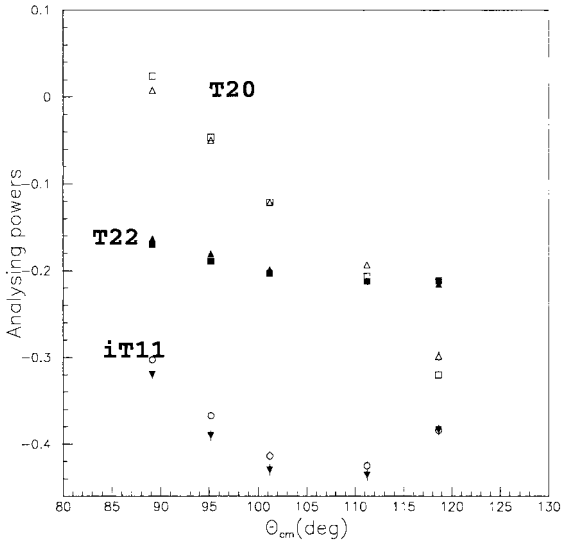

Fig. 3. Preliminary analysing powers. The open squares and open triangles correspond to T_{20}, the filled squares and filled up triangles correspond to T_{22}, the open circles and upside down filled triangles correspond to iT_{11} for mode-3 and mode-1 polarization states, respectively.

References

1) K. Sekiguchi et al.: Phys. Rev. C **65**, 034003 (2002).
2) G. G. Ohlsen: Rep. Prog. Phys. **35**, 717 (1972).
3) R. Bieber et al.: Nucl. Instrum. Methods Phys. Res. A **457**, 12 (2001).
4) K. Suda et al.: RIKEN Accel. Prog. Rep. **35**, 174 (2002).

Development of extraction and neutralization system for atomic beam resonance method

D. Nagae,[*1] K. Asahi,[*1] H. Miyoshi,[*1] K. Shimada,[*1] A. Yoshimi, M. Uchida,[*1] H. Ueno, J. Murata,[*2] Y. Kobayashi, T. Haseyama, D. Kameda,[*1] S. Emori,[*1] G. Kato,[*1] S. Oshima,[*1] G. Kijima,[*1] M. Tsukui,[*1] T. Arai,[*1] and M. Takemura[*1]

The prime tasks for realizing the RI atomic beam resonance (RIABR) method are (1) stopping the RI beam produced by an intermediate nuclear fragmentation reaction in a gas volume, (2) extraction of the stopped RIs using ions drifting in a static electric field, (3) neutralization of the RI ions, (4) transportation of the RI atoms into the spin selection system.

On-line measurements of stopped and drifting ions were performed at RIKEN using an RI beam delivered by the fragment separator RIPS. The details are described elsewhere.[1,2] In addition, we have been performing an off-line experiment in order to study the extraction and neutralization efficiencies of the developed device. A schematic view of the off-line setup is shown in Fig. 1. A new ion source was designed and installed for this experiment. A static electric field formed using many ring electrodes[2] is applied in the drift chamber in order to guide the ions towards a Laval-type glass nozzle; the ions are extracted into an active neutralization system through the nozzle.

Ions are produced by arc discharge in the nitrogen gas flow and the nitrogen ions are extracted into the ion drift chamber with an electric field together with gas flow. In the ion drift chamber, the ions are guided using an electric DC field and the gas flow toward to the nozzle. The total voltage applied to the ring electrodes is 400 V. The pressure of nitrogen gas in the ion drift chamber was maintained at approximately 150 Torr. The transported ions are detected using a Faraday cup which is located downstream of the ion source at the ground potential. The distance from the ion source was changed from 10 mm to 320 mm. The measurement result is shown in Fig. 2. The current of ions which was measured just downstream of the ion source using the Faraday cup was approximately 62.5 nA corresponding to 10^{12} particles/sec, assuming that all of the ions that were measured using the Faraday cup are single charged ions. At the end of drift chamber, the ion current was 10.2 nA (1.63×10^{11} particles/sec). The low transmission efficiency in this off-line measurement compared with the previously reported on-line result[1] is considered to be due to the large difference in neutralization cross section between the nitrogen atoms and the Al ions and Ne atoms.[1] We have not yet investigated other mechanisms for this low transmission, such as the space charge effect. In order to measure the extraction efficiency from the drift chamber, the ions extracted through the nozzle are detected using another Faraday cup located at the distance of 10 mm from the nozzle exit. We used two types of nozzle, whose diameters were 0.5 mm and 1 mm, in order to investigate the dependence of the extraction efficiency on the nozzle diameter. The current of the extracted ions that pass through the 1-mm-diameter nozzle is 4 times larger than that passes through the 0.5-mm-diameter nozzle. This value is consistent with the ratio of the cross section of the nozzle apertures, suggesting that the converging spot size of the ions at the nozzle is larger than ϕ1 mm due to incomplete focusing by the static electric field. The current of the extracted ions with the 1-mm-diameter nozzle was 0.3 nA (5.36×10^{9} particles/sec). From this result, the extraction efficiency of the nozzle was found to be 4.1×10^{-2}.

The neutralization system consists of a yttrium tube, a SUS tube and a wire, as shown in Fig. 3. A DC bias of -200 V is applied to the yttrium and

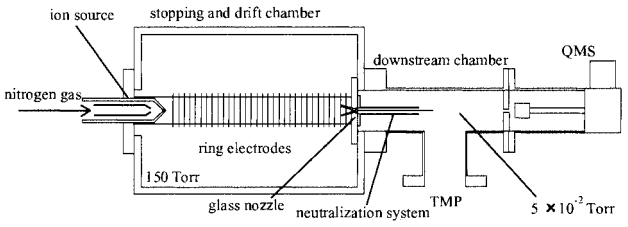

Fig. 1. Schematic view of experimental setup.

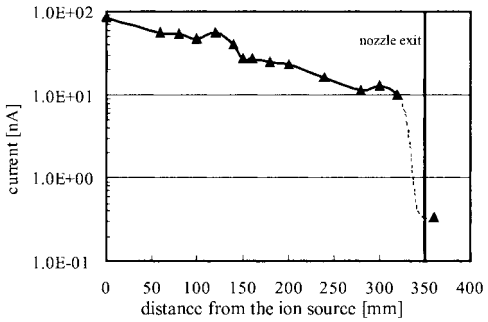

Fig. 2. The ion counts measured by replacing Faraday cups in the drift chamber (0–320 mm) and in the downstream chamber (360 mm). A 1-mm-diameter nozzle was used in this measurement. The position of the ion source exit is defined as 0 mm and that of the nozzle exit is 350 mm.

*1 Department of Physics, Tokyo Institute of Technology
*2 Department of Physics, Rikkyo University

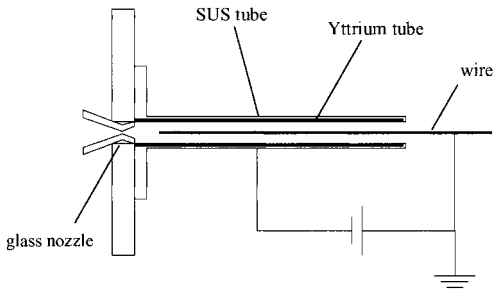

Fig. 3. The neutralization system. The length of the yttrium tube is 110 mm and the inner diameter is 8 mm.

SUS tubes, so that ions are drifted to the yttrium tube by the electric field and converted into neutral atoms by neutralization in charge-transfer collisions with the yttrium tube. After passing through the yttrium tube, the neutral atoms were detected with the quadrupole mass spectrometer (QMS422) placed in the downstream chamber.

In order to experimentally estimate the neutralization efficiency of this system, we measured the neutral atoms on the QMS under four kinds of situation, where the ion source was switched on or off, and the yttrium tube was installed or removed (SUS tube only). The procedure for determining the neutralization efficiency is as follows. The ratio (R) of the detected number of atoms with ion source on ($N_{\rm on}$) and off ($N_{\rm off}$) is described as

$$R = \frac{N_{\rm on}}{N_{\rm off}} = \frac{[1-\alpha(1-\beta)(1-\gamma)(1-\varepsilon)]N_0}{N_0}, \quad (1)$$

where N_0 is the number of atoms introduced into the ion source, α is the ionization efficiency of the ion source, β is the neutralization probability in the drift chamber, γ is the active neutralization efficiency in the neutralization system and ε is the neutralization probability of downstream of the neutralization system. Here, we define A and B for simplicity as

$$A = \alpha(1-\beta)(1-\varepsilon) \quad (2)$$

$$B = (1-\gamma). \quad (3)$$

Equation (1) is redefined with Eqs. (2) and (3) as

$$R = 1 - AB. \quad (4)$$

The ratio R with the yttrium tube and with only the SUS tube can be defined as

$$R_{\rm Y} = 1 - A_{\rm Y}B_{\rm Y}, \quad (5)$$

$$R_{\rm SUS} = 1 - A_{\rm SUS}B_{\rm SUS}. \quad (6)$$

From Eqs. (5), (6) and (3), the neutralization efficiency of the yttrium tube $\gamma_{\rm Y}$ is described as

$$\gamma_{\rm Y} = 1 - \left(\frac{1-R_{\rm Y}}{1-R_{\rm SUS}}\right)\left(\frac{A_{\rm SUS}}{A_{\rm Y}}\right)(1-\gamma_{\rm SUS}) \geq 1 - \left(\frac{1-R_{\rm Y}}{1-R_{\rm SUS}}\right)\left(\frac{A_{\rm SUS}}{A_{\rm Y}}\right). \quad (7)$$

In this experiment, nitrogen gas was used as the ion source. Argon gas was employed as a carrier gas and the gas pressure in the chamber was approximately 75 Torr. The neutral N_2 was measured with the ion source off for 120 seconds, and just after switching on the ion source the same measurement was performed for 120 seconds. The set of these two measurements was repeated and the averaged counting rates with the ion source on/off were compared in order to reduce the influence of the instability of the system parameters, such as α and gas-flow rate. The above procedure was employed for the yttrium tube and for only the SUS tube. The presently obtained data is summarized in Fig. 4. This figure shows the relative difference R between $N_{\rm off}$ and $N_{\rm on}$ normalized using $N_{\rm off}$. A notable difference between $R_{\rm Y}$ and $R_{\rm SUS}$ was observed. We are now evaluating the ionizing efficiency α and the stability of α, β, ε, in order to understand this difference and to estimate $\gamma_{\rm Y}$.

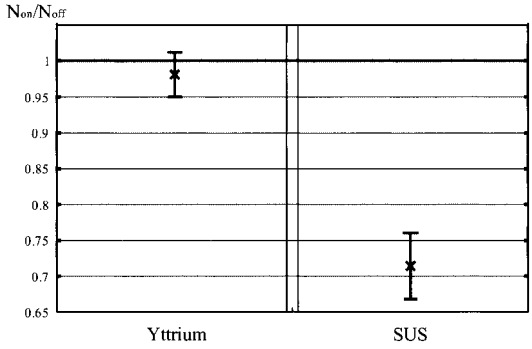

Fig. 4. The counting ratio with the ion source on/off with and without Yttrium.

References
1) H. Miyoshi et al.: RIKEN Accel. Prog. Rep. **38**, 166 (2005).
2) K. Shimada et al.: RIKEN Accel. Prog. Rep. **38**, 163 (2005).

Space-charge effects in a catcher gas cell of an rf ion guide

A. Takamine,[*1] M. Wada, Y. Ishida, T. Nakamura,[*2] T. Kambara, H. Ohyama, Y. Kanai, T. M. Kojima, Y. Nakai, N. Oshima, A. Yoshida, T. Kubo, K. Okada,[*3] T. Sonoda,[*4] K. Noda,[*5] S. Ohtani,[*6] I. Katayama,[*2] Y. Yamazaki, H. Wollnik, and V. Varentsov

A universal facility for slow radioactive ion beams (SLOWRI) is being developed[1] as part of the RIKEN radioactive ion beam factory (RIBF).[2] SLOWRI aims to provide universal slow RI-beams of high purity and small emittance by slowing down and cooling energetic RI ions using an rf ion guide.

We have tested the rf ion guide with 100 MeV/nucleon ^{8}Li beams provided by the RIKEN projectile fragment separator RIPS. A schematic of our experimental setup is shown in Fig. 1. Figure 2 shows the ion guide efficiencies η defined as the ratio between the number of extracted slow $^8Li^+$ ions to the number of thermalized ^{8}Li in the gas cell as determined from the energy distribution of ^{8}Li behind the degrader and the stopping power of the He gas. We find that, for large values of N_0, efficiency decrease as $\eta \propto N_0^{-0.53}$.

We consider that the reduction of efficiency η with the above-described dependence on the incoming beam intensity N_0 results predominantly from the space charge effects. When the incoming ^{8}Li ions are slowed down by collisions with He atoms, they form one electron-He^+ pair for every 41 eV deposited. Since the electrons have a very high mobility even a small electric field drives the electrons away to the wall of the gas cell so that ions, a significant fraction of which He^+ ions account for, are left as space charge along the track

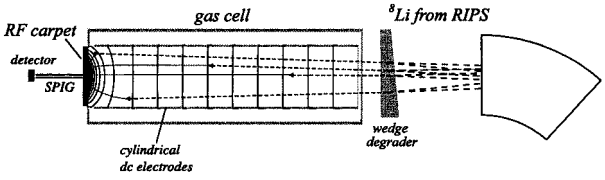

Fig. 1. Schematic of our experimental setup. Refer to Refs. 1 and 3 for details. Ions thermalized in the gas cell are tranported by linear dc field E_z toward the "rf carpet." [1] A detector of alpha-rays or of charged particles is located behind an rf six-pole beam guide (SPIG).[4] In our experiments, the gas cell was inclined by several degrees relative to the beam axis in order to hide the detector form the light high-energy ions provided by RIPS.

*1 Graduate School of Arts and Sciences, University of Tokyo
*2 Institute of Particle and Nuclear Studies, High Energy Accelerator Research Organization (KEK)
*3 Department of Physics, Sophia University
*4 Cyclotron and Radioisotope Center, Tohoku University
*5 National Institute for Radiological Science
*6 Institute for Laser Science, University of Electro-Communications

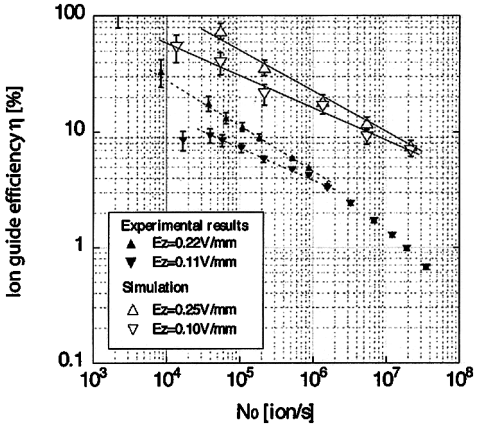

Fig. 2. Ion guide efficiency η defined as the ratio of the number of ions collected per second downstream of the SPIG and the number of thermalized ^{8}Li ions in the gas cell. Comparison of the experimental efficiencies $\eta_{\rm exp}$ and the efficiencies $\eta_{\rm sim}$ derived numerically from the trajectories shown in Fig. 3. Here, two cases of the linear dc field are shown. The dependences of $\eta_{\rm exp}$ and $\eta_{\rm sim}$ on the beam intensity were $\eta_{\rm exp} = 1.0 \times 10^3 \times N_0^{-0.40}$ and $\eta_{\rm sim} = 2.6 \times 10^3 \times N_0^{-0.25}$ when the dc field along the gas cell axis was $E_z \approx 0.2$ V/mm, for $E_z \approx 0.1$ V/mm, they were $\eta_{\rm exp} = 2.1 \times 10^2 \times N_0^{-0.29}$ and $\eta_{\rm sim} = 7.1 \times 10^2 \times N_0^{-0.27}$.

of beams in a 2000-mm-long cylinder of ≈ 80 mm diameter. On account of the contribution of ^{8}Li ions to the production of He^+ ions and an additional $\approx 50\%$ contribution from impurity ions in the incoming beam, such as ^{7}Li and ^{10}Be, an incoming beam of 10^3 to 10^7 ^{8}Li ions produces 10^9 to 10^{13} He^+ ions, namely, 10^2 to 10^6 ions per mm^3. The space charge generates a field which drives a large portion of ions, including He^+, towards the wall of the cell.

The distribution of the space-charge density $\rho(t, r, z)$ at time t and position r, z can be calculated using the continuity equations and Maxwell's equations.[5] A solution to these equations for cylindrical coordinates, neglecting the z-dependence of ρ, is

$$\rho_0 = \sqrt{\epsilon_0 Q_{\rm i}/\mu} \propto \sqrt{N_0} \tag{1}$$

$$\rho(r) = \begin{cases} \rho_0 & r \le r_0 \\ \rho_0/\sqrt{2r^2/r_0^2 - 1} & r \ge r_0 \end{cases} \tag{2}$$

$$v(r) = \begin{cases} \rho_0 r\mu/2\epsilon_0 & r \le r_0 \\ \rho_0\sqrt{2r^2/r_0^2 - 1}(\mu r_0^2/2r\epsilon_0) & r \ge r_0 \end{cases} \tag{3}$$

where ϵ_0 is the dielectric constant, $Q_{\rm i}$ is the newly

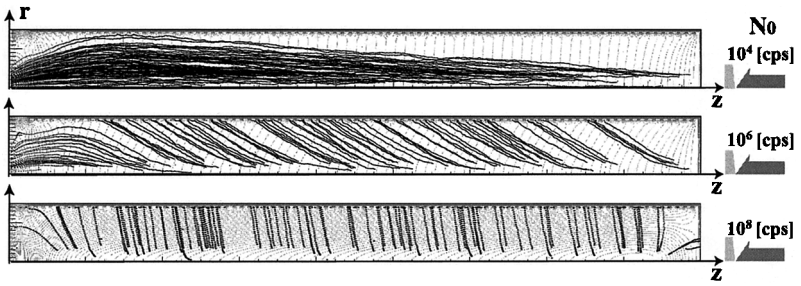

Fig. 3. The dc potential distributions (thin lines) and the ion trajectories (thick lines) in the catcher gas cell for $N_0 = 10^4$, 10^6 and 10^8 incoming energetic ^{8}Li ions. All distributions are shown as functions of the radial coordinate r and of the axial coordinate z in a cylindrical tube of 300 nm diameter and 2000 mm length.

formed charge per unit volume and unit time, and $v = \mu E$ is the velocity of He^+ in a field E, and μ being the mobility of He^+ ions in a He gas.

Knowing $\rho(r)$ for $N_0 = 10^4$, 10^5, 10^6 from Eq. (2), one can calculate the dc electric potential distributions. These are plotted in Fig. 3 together with the trajectories of the thermalized ions derived numerically from Monte Carlo simulations. The potential slopes produced by the cylindrical electrodes and the "rf carpet" electrodes are distorted by the space charge that upheaves the potential slope to a "ridge." With a higher intensity of incoming ^{8}Li ions, only ions very close to the "rf carpet" can be extracted.

One way to confirm the present space-charge model and the simple simulation is to record the He^+-current that reaches the "rf carpet" when the rf-voltage is switched off. The results of such measurements are shown in Fig. 4, together with the results of our simulations. The dependences of the He^+-ion currents are in good agreement between the results of experiments and those of simulations. The small differences that the absolute numbers of He^+ ions are $\approx 30\%$ higher in the simulations than in the experiments may be a result of the cell axis being inclined by 3° relative to the incoming beam axis in these experiments.

We also compared the simulation results with the experimentally obtained ion guide efficiency $\eta_{\rm exp}$ for $^8Li^+$ ions (Fig. 2). Reasonably good agreements are found between the dependences of the efficiencies in the experiment and in the simulation, while their absolute values differ by a factor of ≈ 4. This results mainly from the inclination of $\approx 5°$ of the gas cell relative to the beam, since in the He^+-ion current measurements, the 5° inclination reduced the He^+-ion current to $\approx 50\%$ of that with 3° inclination. The slightly faster fall off in the experiment might be explained by the fact that the transport efficiency at the "rf carpet" is reduced for higher beam intensities because a larger dc field that is caused by the increased space charge faces the "rf carpet." The most important observation is that decreases of the ion guide efficiencies are observed

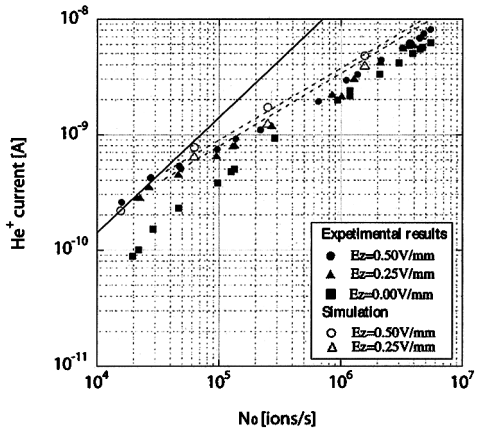

Fig. 4. The He^+ currents $I^{\rm He}_{\rm exp}$ collected experimentally in the "rf carpet" and the calculated intensities of He^+ ions $I^{\rm He}_{\rm sim}$ are shown as a function of N_0, the number of incoming ^{8}Li ions. A solid line indicates the case where the efficiency is unity. The dependence of the He^+-ion current $\mathrm{I}(N_0)$ [pA] are fitted to be $I^{\rm He}_{\rm exp} = 34 \times N_0^{0.65}$ and $I^{\rm He}_{\rm sim} = 47 \times N_0^{0.64}$ for $E_z = 0.25\,\mathrm{V/mm}$ and $I^{\rm He}_{\rm exp} = 43 \times N_0^{0.63}$ and $I^{\rm He}_{\rm sim} = 52 \times N_0^{0.64}$ for $E_z = 0.5\,\mathrm{V/mm}$.

at almost the same magnitude of intensity of incoming ^{8}Li ions. This supports our assumption that the space-charge region created by He^+ ions has a profound effect on the ion guide efficiencies in a catcher gas cell.

References

1) M. Wada et al.: Nucl. Instrum. Methods Phys. Res. B **204**, 570 (2003).
2) M. Motobayashi: Nucl. Instrum. Methods Phys. Res. B **204**, 737 (2003).
3) A. Takamine et al.: RIKEN Accel. Prog. Rep. **37**, 173 (2004).
4) H. Xu et al.: Nucl. Instrum. Methods Phys. Res. A **333**, 274 (1993).
5) A. Takamine: Master's Thesis, University of Tokyo (2004).

Development of RI Extraction System with Static Electric Field

K. Shimada,[*1] K. Asahi, H. Miyoshi,[*1] D. Nagae,[*1] A. Yoshimi, H. Ueno, Y. Kobayashi, T. Haseyama, J. Murata,[*2] M. Uchida,[*1] D. Kameda,[*1] S. Emori,[*1] G. Kato,[*1] S. Oshima,[*1] G. Kijima,[*1] M. Tsukui,[*1] T. Arai,[*1] and M. Takemura[*1]

The Radioactive Isotope (RI) extraction system with a static electric field has been developed to produce a slow RI beam for the RI Atomic Beam Resonance method (RIABR). A key issue for realizing the RIABR method is the formation of a slow neutral RI beam.[1)]

At first, we measured a drift efficiency of ^{30}Al stopping in Ne at 600 Torr.[2)] A setup of the experiment is shown in Fig. 1 of Ref. 2. The twenty electrodes installed outside of the glass chamber were 200-μm-thick discs of 8.0 cm o.d. and 5.0 cm i.d. They were connected using 300 kΩ resistors at 18 mm intervals to create a uniform electric field. The high voltage applied between the first electrode and the 19th one was 3 kV. The high voltage of the last electrode was the same as the 18th one due to trapping of the extracted ^{30}Al. We calculated the electric field using POISSON as shown in Fig. 1, and obtained a uniform axial electric field of 87 V/cm. In this calculation, the space charge created by the incident beam was not taken into account. From analyzing the experimental result,[2)] we confirmed that the electric field could drift the RI stopped in Ne gas, and obtained a drift efficiency of 0.72 (4).

We have also performed an extraction efficiency measurement. The experimental setup is shown in Fig. 2. The intensity of the collimated ^{30}Al beam was 3.7×10^4 particles/s. The upstream RI stopping chamber was the same as that described in Ref. 1 except for the applied high voltages and the size of the orifice. In this experiment, the applied high voltage was +816 V and the orifice was 0.5 mm i.d. Therefore, the electric field of the drift volume was 3.1 V/cm. Upstream, the RI-stopping chamber was fill with 600-Torr Ne. Downstream, the jet-separator (JS) chamber was evacuated to 0.12 Torr. After passing through the orifice between these two chambers, the RI and the carrier gas formed jet and diffused into volume. Nine electrodes were installed to guide ions using parallel electric field from the orifice to further downstream. We installed two scintillators. One was placed at the entrance of the stopping chamber to monitor the number of incident ^{30}Al beams. The other was a 100 mm × 100 mm × 110 mm cube with a hole of 70 mm i.d. and 80-mm-long cylinder. It was placed in the JS chamber, while a photomultiplier tube was placed outside the chamber over a glass flange. The latter could count the β-rays emitted from ^{30}Al which were extracted from the RI stopping chamber and guided to the detector. Although noise events such as from ions attached to the electrodes or nozzle were also counted, we assumed that the factor of the noise was small. We compared the counts of the two plastic scintillators with different electric fields. Figure 3 shows the obtained extraction efficiency depending on electric field strength. This result indicates that a strong electric field could guide the ions from the exit of the orifice to the detector, while carrier gas molecules were separated. The obtained maximum extraction efficiency was $4.3(1) \times 10^{-4}$.

We have been continuously investigating the configuration of the electric field, the gas pressure, and the materials of the nozzle. In experiments with an off-line ion source and an optimized configuration, we obtained an extraction efficiency as high as 4.9×10^{-3},[3)] which was 10 times higher than the on-line result. If such an efficiency could be realized in the on-line experiment, we could start the next stage of development such as the neutralization and the spin-selection system which are important for the RIABR system.

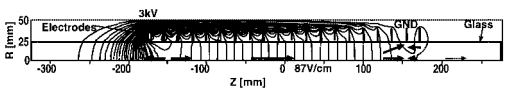

Fig. 1. Electric field of drift efficiency measurement.[2)]

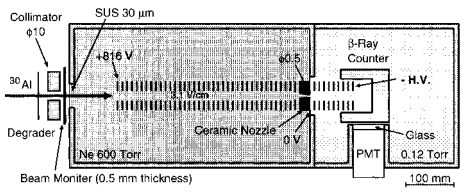

Fig. 2. Experimental setup of extraction efficiency measurement.

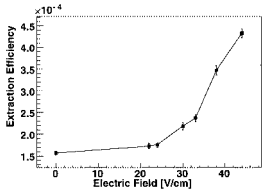

Fig. 3. Measured extraction efficiency. Electric field was limited to 44 V/cm because of discharge.

*1 Department of Physics, Tokyo Institute of Technology
*2 Department of Physics, Rikkyo University

References

1) K. Shimada et al.: RIKEN Accel. Prog. Rep. **37**, 175 (2004).
2) H. Miyoshi et al.: RIKEN Accel. Prog. Rep. **38**, 166 (2005).
3) D. Nagae et al.: RIKEN Accel. Prog. Rep. **38**, 159 (2005).

Development of linear rf trap for multireflection time-of-flight mass spectrometer

Y. Ishida, M. Wada, H. Wollnik,* and Y. Yamazaki

Using a multireflection time-of-flight mass spectrometer (MR-TOF)[1] we plan to measure masses of various short-lived nuclei, which will be provided at the slow RI-beam facility (SLOWRI) of RIKEN-RIBF.[2] At SLOWRI, energetic RI-beams from the projectile fragment separator BigRIPS are decelerated and cooled in an rf ion guide and extracted as a low-energy bunched RI-beam through an rf sextupole ion beam guide (SPIG).[3] Although a small emittance of $\leq 10\,\mathrm{eV}\cdot\mu\mathrm{s}$ of this pulsed beam is expected, ions must be well confined in the phase space to ensure a much smaller emittance of $\sim 0.1\,\mathrm{eV}\cdot\mu\mathrm{s}$ before they can be injected into the MR-TOF. While the MR-TOF can compensate the residual energy spread when the geometry and the potentials of the mirror electrodes are chosen properly,[4] a smaller initial energy spread and a smaller emittance of ions improve the total performance. Therefore, it is necessary to place an ion trap as a cooling and bunching device between the SPIG and the MR-TOF as shown in Fig. 1. Here we report on an improved experimental result using the ion trap device in addition to the previously reported MR-TOF setup[5] where an electron impact ion source was directly connected to the spectrometer.

There are two types of possible ion trap, a linear quadrupole ion trap and a circularly symmetric quadrupole trap. We chose a linear ion trap since its loading and extraction efficiency is 80% and higher than that of the circularly symmetric trap (15%) as reported by Clark *et al.*[6]

To efficiently load the pulsed ions from the SPIG and extract most of the ions from the trap without any collisions with gas molecules, our linear ion trap is divided into the loading section (b) and the extraction section (d) as shown in the inset of Fig. 1. The voltage of the endcap (a) of the trap is switched to load the pulsed ions. Ions are cooled by gas collisions with a He buffer gas of 1×10^{-3} Torr, and distributed in front of the grid (c) according to a potential formed by the voltage of segmented rods and the grid. We determined the appropriate operating parameters of this ion trap by numerically simulating the ion trajectories using SIMION.[7]

For the off-line tests of the MR-TOF with the linear trap, an electron impact ion source was attatched to the endcap. Stable nuclear ions were produced in the ion source, extracted by an electric field of $\sim 5\,\mathrm{V/mm}$ and stored in the loading section of the trap. The cooled ions were transferred to the extraction section by switching the potential of the grid. The ions were longitudinally compressed by further cooling in the extraction section. The well-confined ions were extracted by an electric field of $\sim 100\,\mathrm{V/mm}$ and then accelerated to 1500 eV. This linear trap provided ion pulses of < 10 ns duration with a repetition rate of 500 Hz.

Figure 2 shows the mass spectrum after the time

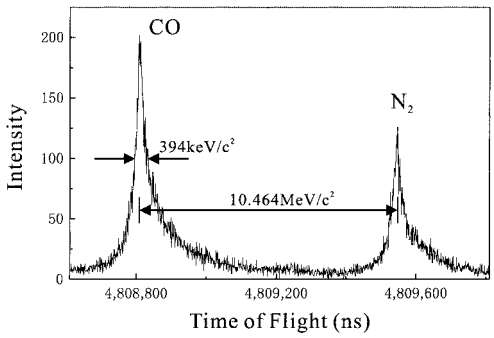

Fig. 2. Mass spectrum of CO-N_2 mass doublet after flight time of $\approx$4.8 ms.

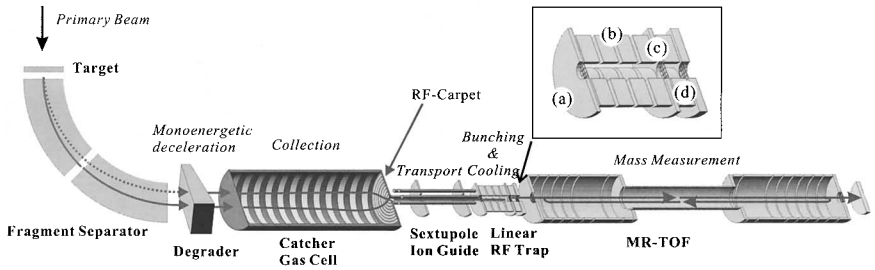

Fig. 1. Schematic drawing of overview of mass measurement system. The inset shows an enlargement of the linear RF trap, (a) an endcap, (b) a 25-mm-long loading section, (c) a grid, and (d) a 5-mm-long extraction section.

* University of Giessen, Germany

of flight of ≈4.8 ms using CO ions with a mass of 27.9949 u and N_2 ions with a mass of 28.0061 u. From this spectrum we obtained an FWHM mass resolving power of $m/\Delta m \approx 66{,}000$ for the spectrometer, which is much better than the previously reported value of $m/\Delta m = 40{,}000$.[1)] Moreover, the signal-to-noise ratio became higher.

The relative intensity of ions as a function of time of flight is shown in Fig. 3. Normalization was made on the basis of ion intensity recorded after a single pass. The fluctuation of ion intensity during this measurement is ≈5%. Since the acceptance of MR-TOF is smaller than the emittance of the ion source, rapid decreases in ion intensity up to ∼20% were observed, whereas there were almost no significant losses after ∼500 μs. This figure also shows that there was a small increase in ion intensity when the rf voltage of the trap was turned off during the TOF measurement period. Further investigation of ion loss processes will be carried out.

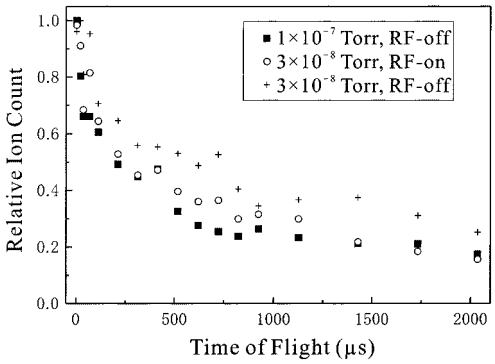

Fig. 3. Recorded ion intensity as function of ion flight time relative to intensity after one pass. Squares and crosses denote the ion count rate at residual gas pressures of 1×10^{-7} as well as 3×10^{-8} Torr with no RF power being applied to the ion trap when the ions were flying in the MR-TOF. Circles denote the ion count at 3×10^{-8} Torr when RF power was applied.

The linear ion trap developed has improved the performance of the MR-TOF. On-line test experiments of the MR-TOF combined with the rf ion-guide system are planned to be performed soon.

References

1) Y. Ishida et al.: Nucl. Instrum. Methods Phys. Res. B **219–220**, 468 (2004).
2) M. Wada et al.: Nucl. Instrum. Methods Phys. Res. B **204**, 570 (2003).
3) S. Fujitaka et al.: Nucl. Instrum. Methods Phys. Res. B **126**, 386 (1997).
4) H. Wollnik: J. Mass Spectrom. **34**, 991 (1999).
5) Y. Ishida et al.: RIKEN Accel. Prog. Rep. **36**, 184 (2003).
6) J. Clark et al.: Nucl. Instrum. Methods Phys. Res. B **204**, 487 (2003).
7) D. A. Dahl: Int. J. Mass Spectrom. **200**, 3 (2000).

Development of low-energy RI transportation system with static electric field in Ne gas

H. Miyoshi,[*1] K. Shimada,[*1] D. Nagae,[*1] A. Yoshimi, M. Uchida,[*1] K. Asahi,[*1] H. Ueno, D. Kameda,[*1] G. Kato,[*1] S. Emori,[*1] G. Kijima,[*1] M. Tsukui,[*1] T. Haseyama, J. Murata,[*2] and Y. Kobayashi

Spin-polarized low-energy radioactive isotope (RI) beams are useful not only in nuclear physics but also in materials and surface physics. We are developing a device that produces a spin-polarized low-energy RI beam on the basis of *the atomic beam resonance technique* (RIABR). A prototype, including a fragment stopping and collecting chamber, an atomic-beam forming nozzle and a spin-selecting sextupole magnet is almost completed. At present, we are testing the system with ions of stable isotopes injected from an ion source.[1)]

In this paper, we report on test experiments for the fragment stopping and collecting chamber using an RI beam delivered from the fragment separator RIPS.

The setup used for the test experiments is schematically illustrated in Fig. 1. In these experiments, we employed a neon gas as a stopping gas. The RI fragment stopping and collecting chamber is made of a glass (VIDREX). The total length of the chamber is 1500 mm, and the diameter is about 50 mm. The pressure of neon gas in the chamber was approximately 600 Torr. We chose a beam of ^{30}Al ions produced by the fragmentation of an ^{40}Ar projectile at an energy of 95 A MeV on a 3.0-mm-thick Beryllium target. The beam was collimated into a diameter of approximately 10 mm at the entrance of the chamber, and the intensity of the ^{30}Al beam was approximately 10^4 particles/sec. Using a rotary degrader, we adjusted the energy of ^{30}Al ions at the entrance of the chamber such that the ions were safely stopped in the Ne gas volume. Figure 1 also shows the detector system employed for β-ray detection. The system consisted of two layers of plastic scintillator of size 45 × 0.5 × 390 mm and 20 × 5 × 380 mm.

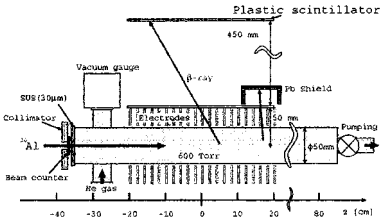

Fig. 1. Schematic view of experimental setup. The cylindrical glass chamber was surrounded by an array of 20 pieces of ring electrode with an inner diameter of 50 mm. The length of drift field is approximately 400 mm. The detailed arrangement is described elsewhere.[2)]

*1 Department of Physics, Tokyo Institute of Technology
*2 Department of Physics, Rikkyo University

We measured the β-ray counts from the radioactivities in the chamber. By comparing them with expected counts from a simulation with GEANT code,[3)] we obtained the drift efficiency. Figure 2 shows hypothetical RI distributions for immediately after the stopping of the RI ions (dashed curve) and after their drift in the electric field is completed (solid curve), that best fit the data. The drift efficiency thus obtained by fitting was 0.72. The measured and calculated ratios of counts for β-rays from the stopped and drifting RIs are summarized in Table 1.

From the measured data and calculated result, the drift efficiency for the ^{30}Al ions in a stopping gas of neon was determined to be 0.72 ± 0.04. This value corresponds to a mean neutralization cross section of 7.9×10^{-22} cm^2, assuming that the defraction efficiency is negligible. The large drift efficiency presently obtained provides a promising prospect for realizing a bright RIABR system.

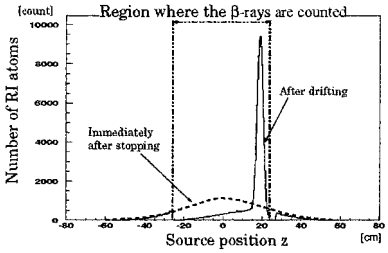

Fig. 2. Assumed distributions of RI atoms. Dashed curve indicates the RI distribution just after the stopping of the incident RI ions. Ions reach the final electrode ($z = +20$ cm) after drifting, where the efficiency for β-ray counting drops abruptly due to the presence of a Pb shield.

Table 1. Measured and calculated ratios of β-counts before and after the drift of ions. The drift efficiency of 0.72 is assumed in the calculation.

Median position of the beam [mm]	ratio	
	$\left(\frac{Drifting}{Stopping}\right)_{expt}$	$\left(\frac{Drifting}{Stopping}\right)_{calc}$
−100	0.98 ± 0.08	0.962
0	0.85 ± 0.05	0.846
+200	0.95 ± 0.07	0.969

References

1) D. Nagae et al.: RIKEN Accel. Prog. Rep. **38**, 159 (2005).
2) K. Shimada et al.: RIKEN Accel. Prog. Rep. **38**, 163 (2005).
3) GEANT3: *Detector Description and Simulation Tool* (CERN, Geneva, 1993).

Confinement of large number of antiprotons and production of ultraslow antiproton beam

N. Kuroda,[*1] H. A. Torii,[*1] K. Yoshiki Franzen,[*1] Z. Wang,[*1] S. Yoneda,[*1] M. Inoue,[*1] M. Hori,[*2] B. Juhász,[*3] D. Horváth,[*4] H. Higaki,[*5] A. Mohri, J. Eades,[*6] K. Komaki,[*1] and Y. Yamazaki[*1]

We have succeeded in storing a large number of ultraslow antiprotons, which is an important step in synthesizing antihydrogen ($\overline{p}e^+$)[1,2] and antiprotonic atoms ($\overline{p}A^+$). Such exotic atoms can only be efficiently synthesized from component particles at eV and lower energy scales, which is far below the mandatory GeV scale of accelerator-produced antiprotons.

At CERN, the Antiproton Decelerator (AD) supplies a 5.3 MeV antiproton beam. This beam energy is, however, still far above the 10 keV range at which antiprotons can readily be captured and cooled in electromagnetic traps. Although degrader foils are usually used to reduce the antiprotons energy further from the MeV to keV scale,[3–5] here the simple degrader foils were replaced by a Radio Frequency Quadrupole Decelerator (RFQD).[6,7] Thin PET foils, instead of relatively thick foils located upstream of a multiring trap (MRT),[8] were used to isolate the trap and RFQD vacuum systems. Because the antiprotons were to spend a long time in the trap, more stringent vacuum conditions were required there than in the RFQD to avoid antiproton loss by annihilation on residual gas atoms.

The MRT comprises several ring electrodes lying on the axis of a superconducting solenoid. Before the antiprotons arrived, an electron plasma was preloaded in the trap allowed to reach equilibrium, where its shape was expected to be spheroidal. This electron plasma continuously cooled the newly arrived antiprotons, since the thermal energy it received from the antiprotons was spontaneously dissipated by synchrotron radiation in a strong magnetic field with a time constant of about one second.[5,9] Approximately 1.2×10^6 $\bar{p}$s could be stored and cooled in the MRT per AD shot. This figure is ∼50 times higher than the best values obtained with thick degrader foils.[10] By stacking five AD shots in sequence,[10] ≈ 5 million antiprotons, the largest number of antiprotons ever stored and cooled, were confined in our MRT.

The joint plasma modes were observed before and after antiproton injection, which allowed us to monitor the plasma shape, density, and temperature variations nondestructively.[11] We excited axially symmetric electrostatic oscillation $(l, 0)$ modes (l = 1–4) of the joint plasma by applying pulsed white noise. The shift of these mode frequencies with time was used to monitor the antiproton cooling process. Using the observed ω_l-values (l = 2, 3, and 4) before antiproton injection and the electron number previously measured under the same conditions, the temperature-dependent dispersion relation for a cold spheroidal plasma[12,13] can be solved to give the plasma density n_e and the aspect ratio α. Using n_e and α so obtained, the temperature T_e after antiproton injection was evaluated from ω_l, which indicated a maximum plasma temperature rise of ≈ 0.6 eV. The variations of the plasma frequencies during the cooling that followed heat transfer from the antiprotons were consistently reproduced by solving rate equations which took into account the synchrotron radiation cooling of electrons with a time constant of $\sim 6/(B[\mathrm{T}])^2$ s and the energy transfer between antiprotons and the electron plasma.[13]

The antiprotons were then continuously extracted from the MRT by ramping the trap potential. The energy range of the extracted antiprotons was 10 eV–250 eV. This ultraslow antiproton beam will be used for future studies such as the investigations of antiprotonic atom formation processes under the single-collision condition[14] and of antiproton magnetic moment with $\bar{H}$ beams.[15]

[*1] Institute of Physics, University of Tokyo
[*2] Organisation Européenne Pour la Recherche Nucléaire (CERN), Switzerland
[*3] Institute of Nuclear Research of the Hungarian Academy of Science, Hungary
[*4] KFKI Research Institute for Particle and Nuclear Physics, Hungary
[*5] Plasma Research Center, University of Tsukuba
[*6] Department of Physics, University of Tokyo

References

1) M. Amoretti et al.: Nature **419**, 456 (2002).
2) G. Gabrielse et al.: Phys. Rev. Lett. **89**, 213401 (2002); Phys. Rev. Lett. **89**, 233401 (2002).
3) G. Gabrielse et al.: Phys. Rev. Lett. **57**, 2504 (1986).
4) M. H. Holzscheiter et al.: Phys. Lett. A **214**, 279 (1996).
5) G. Gabrielse et al.: Phys. Rev. Lett. **63**, 1360 (1989).
6) A. M. Lombardi, W. Pirkl, and Y. Bylinsky: Proc. 2001 Particle Accelerator Conf., Chicago, USA, 2001-6 (IEEE, 2001), p.585.
7) M. Hori et al.: Phys. Rev. Lett. **91**, 123401 (2003).
8) A. Mohri et al.: Jpn. J. Appl. Phys. **37**, 664 (1998).
9) B. R. Beck, J. Fajan, and J. Malmberg: Phys. Plasmas **3**, 1250 (1996).
10) G. Gabrielse et al.: Phys. Lett. B **548**, 140 (2002).
11) H. Higaki and A. Mohri: Phys. Lett. A **235**, 504 (1997).
12) M. D. Tinkle et al.: Phys. Rev. Lett. **72**, 352 (1994).
13) H. Higaki et al.: Phys. Rev. E **65**, 046410-1 (2002).
14) Y. Yamazaki: Nucl. Instrum. Methods Phys. Res. B **154**, 174 (1999); Hyperfine Interact. **138**, 141 (2001).
15) A. Mohri and Y. Yamazaki: Europhys. Lett. **63**, 207 (2003).

Development of collinear laser spectroscopy setup for Ni isotopes

M. Wada, V. Lioubimov,[*1] M. D. Gardner, A. Takamine,[*2] T. Nakamura,[*3] Y. Ishida, K. Okada,[*4] H. Iimura,[*5] H. A. Schuessler,[*1] and Y. Yamazaki[*2]

The root-mean-square charge radii of unstable nuclei have been determined exclusively by the isotope shift (IS) measurements of the optical transitions of singly charged ions or neutral atoms by laser spectroscopy. Many isotopes of alkaline, alkaline earth and noble gases, which all have good optical transitions and are available at conventional ISOL facilities, have been measured by collinear laser spectroscopy. However, the isotopes of other elements have not been widely investigated mainly because their beams have been difficult to be obtained.

A new facility for slow radioactive ion beams (SLOWRI) is being developed[1)] at the RIKEN radioactive ion beam factory (RIBF). SLOWRI aims to provide universal slow RI beams of high purity and small emittance with high-energy RI beams from a projectile fragment separator being slowed down to low energies and cooled in an rf ion guide. Since in these production, separation and cooling schemes there are no chemical processes, in principle, the isotopes of all atomic elements will be provided as pure, monoenergetic, small emittance, and low-energy beams. It should expand the range of applicable nuclides of laser spectroscopy. In the first few years of the RIBF project, Ni and its neighboring elements, such as Ni, Co, Fe, Cr, Cu, Ga and Ge, will be investigated. They all have possible optical transitions in the ground states of neutral atoms with presently available laser systems. The expected beam intensities of these isotopes at SLOWRI is shown in Fig. 1, together with possible resonant wavelengths for charge radius measurements.

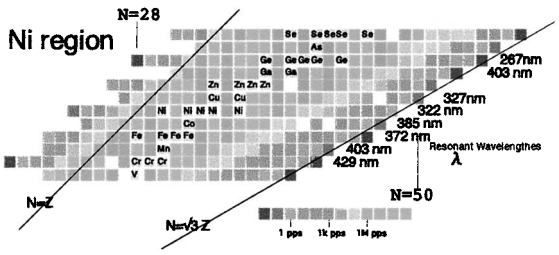

Fig. 1. Expected isotopes of Ni and their neighborhood. Possible resonant wavelengths of neutral atoms are also depicted on the right-hand side.

We set Ni isotopes as the first candidates to be investigated at SLOWRI. The level diagram of Ni atoms for a resonance ionization scheme is shown in Fig. 2. The 323.293 nm *s-p* transition from the ground state $4s\ a^3\mathrm{F}_4$ to the excited state $4p\ z^3\mathrm{G}_5$ will be used to determine the volume effect of the IS. This transition can be excited numerous times for atoms flying in the interaction region. In this excitation scheme an electron in the $J = 4$ state is excited to the $J' = 5$ state, then the electron can decay only to the $J = 4$ state, so that the electron can be excited again by the same laser radiation. This scheme notably enhances the sensitivity of spectroscopy. A fluorescence photon can be used to detect the resonance; however, the sensitivity of such photon detection is still limited. This usually requires an ion beam intensity of $> 10^4$ atoms/s. To improve the sensitivity, we will use a resonance ionization method that utilizes two more laser radiations, namely, the 511 nm radiation provided by a DISK laser with a continuous beam power of ∼5 W that excites from the $4p\ z^3\mathrm{G}_5$ state to the $5s\ f^3\mathrm{F}_4$ state and the ∼898 nm radiation provided by a titanium sapphire laser that excites to the Rydberg level. An external electric field can ionize Rydberg atoms, and then, the ion and the electron can be detected coincidentally with high sensitivity and low background. In this way, the resonance in the *s-p* transition can be detected even though the beam intensities are as low as 10 atoms/s.

In year 2004, a setup for off-line test experiments of collinear laser spectroscopy was installed with a collaboration with Texas A&M University. An ion source for test experiments will be installed in year 2005 and off-line tests will be started.

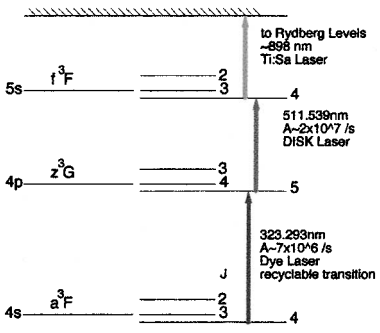

Fig. 2. Level scheme for three-step resonance ionization of Ni atoms.

*1 Department of Physics, Texas A&M University, USA
*2 Graduate School of Arts and Science, University of Tokyo
*3 Institute of Particle and Nuclear Studies, High Energy Accelerator Research Organization (KEK)
*4 Department of Physics, Sophia University
*5 Japan Atomic Energy Research Institute

Reference

1) M. Wada et al.: Nucl. Instrum. Methods Phys. Res. B **204**, 570 (2003).

Magneto-optical rotation effect in Rb for EDM experiment

A. Yoshimi, K. Asahi, S. Emori,* M. Uchida,* and S. Oshima*

A nuclear spin maser with ^{129}Xe operated at a low static field of 30 mG has been developed,[1] with which the spin precession frequency can be measured with high precision. Such a device can be utilized to search for the permanent electric dipole moment (EDM) of the atom, when it is installed with a high-performance magnetic shield and high-precision magnetometer. In the previous report, the design and construction of the 4-layer magnetic shield was reported.[2] Here, we report on the development of the atomic magnetometer that we have recently commenced.

The magneto-optical rotation effect is known to be enhanced when the light frequency is tuned to near the atomic absorption line. Recent studies on the magneto-optical rotation effect with an alkali vapor cell indicate that the sensitivity of the magnetometer based on this effect can in principle reach a shot-noise limit of $\sim 10^{-12}\,\mathrm{G}/\sqrt{\mathrm{Hz}}$.[3] The origin of the optical rotation is the difference in refractive index between left- and right-circular polarized light in the sample when a magnetic field is applied. Therefore, this leads to the rotation angle ϕ having a dispersive-shaped magnetic-field dependence.

The experimental setup is shown in Fig. 1. The cylindrical glass cell confining Rb vapor was located inside the 3-layer magnetic shield. A laser beam emitted from a laser diode with a single frequency mode passes through the cell, a linear polarizer, and a photoelastic modulator (PEM), and detected with a photodiode. The wavelength of the single-mode laser is tuned to the D1 absorption line of the Rb atom, which is being monitored by the absorption-induced emission from the reference cell the split laser beam passes through (photograph in Fig. 1). The small optical rotation of the linear polarization ($\phi \ll 1$) can be described as a change in the polarization component along a direction perpendicular to the initial polarization direction. The PEM modulates the retardation of the light phase (from $-\pi$ to $+\pi$) only in the modulating plane, so that the nonzero component of the light polarization along the axis perpendicular to the modulating axis causes a modulation of the direction of the light polarization. Therefore, the transmitted light intensity after passing through the linear-polarizing filter is modulated. The small optical rotation can be observed by phase sensitively detecting the signal using the photodiode with a lock-in amplifier, as shown in Fig. 1. A magnetic field was applied with the solenoid magnet wound inside the magnetic shield. Figure 2 shows the typically measured optical rotation signal with a commercial Rb vapor cell obtained by sweeping the magnetic field over the range of 0–3 G, which has a dispersive shape. We are now calibrating the rotation angle with precise control of a $\lambda/2$ plate. We are also investigating the dependence of the rotation signal on various parameters, such as laser power, cell temperature, and the inner coating of the cell wall, in order to explore its performance for application to the magnetometer.

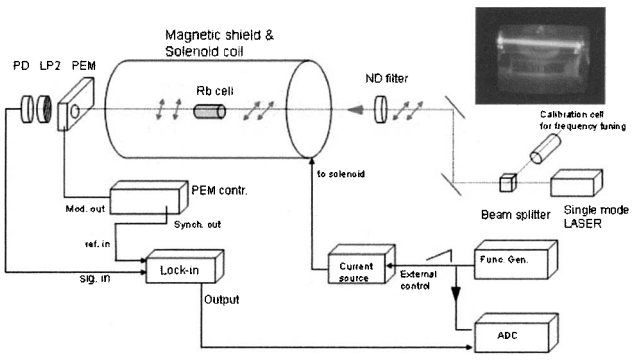

Fig. 1. Experimental setup for measuring optical rotation in Rb cell.

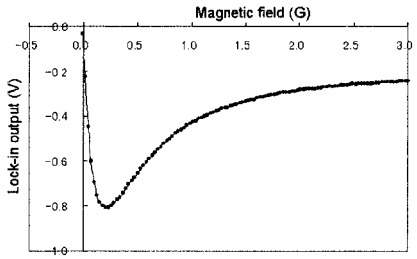

Fig. 2. Typically measured optical rotation signal.

References

1) A. Yoshimi et al.: RIKEN Accel. Prog. Rep. **36**, 173 (2003).
2) A. Yoshimi et al.: RIKEN Accel. Prog. Rep. **37**, 160 (2004).
3) D. Budker et al.: Phys. Rev. A **62**, 043403 (2000).

* Department of Physics, Tokyo Institute of Technology

Nondestructive intensity monitor for cyclotron beams

M. Wada, Y. Ishida, T. Nakamura,[*1] A. Takamine,[*2] A. Yoshida, and Y. Yamazaki[*2]

For any experiments that use beams of an accelerator, monitoring the beam intensity is always an important concern. It is particularly useful if one can continuously measure the beam current without disturbing the beams. Counting elastic scattering particle from the target is often used for such a purpose, however, the dynamic range of measurable beam intensity is limited and the calibration often changes for different experimental conditions.

We report here on the test experiments for a nondestructive current monitor of cyclotron beams using a toroidal pulse transformer. The principle of the transformer detector is shown in Fig. 1. The cyclotron beam is a single-turn "coil" of the primary side of the transformer which induces a magnetic flux in the toroidal core, then it induces a current in the secondary coil. In case a secondary coil of 5 turns is used, the transformer yields a nominal signal amplitude of

$$V_{\rm sig} = \frac{I_{\rm beam}}{5\ \text{turns}} \left(\frac{1}{50\,\Omega} + \frac{1}{50\,\Omega} \right)^{-1} = 5\,\Omega \times I_{\rm beam} \quad (1)$$

at the 50 Ω input of the amplifier. The sensitivity of 5 nV/nA, is quite low to be measured in a noisy environment. However, since the beams from the cyclotron are a chain of short pulses with a constant repetition rate of ≈ 50 ns, synchronous detection with a spectrum analyzer or a lock-in amplifier can discriminate such a low-amplitude signal from the noise.

We used a Fast Current Transformer manufactured by BERGOZ Instrumentation, France.[1)] The transformer, model FCT-082-05:1-H-INS, consists of a toroidal core made of cobalt-based nanocrystalline and amorphous alloys of 82 mm inner diameter and a five-turn coil wound by the proprietary multithread technique. The bandwidth of the FCT is 32 kHz∼700 MHz and the typical rise time is 500 ps. The fast response of the detector allows us to observe the higher harmonics of the pulsed beam. Since the duty cycle of the cyclotron beam is very low, typically $< 1/100$, it generates many harmonics and the higher order harmonics have almost the same power as the fundamental one. It is advantageous to observe higher order harmonics, since the ambient noises are in general decreases with increasing frequency.

The FCT is placed in the E6 beamline of RIKEN ring cyclotron. In order for the transformer to "see" a current passing through its center, the wall current imaging the ion beam must be diverted around the outside of the device. The beam pipe of 63.5 mm diameter is electrically interrupted by a PEEK sleeve for 4 mm width and the FCT is mounted close to the gap (Fig. 2). An aluminum box covers the FCT for electrostatic shielding as well as for electrical connection between the interrupted beam pipe outside of the FCT. The signal from the FCT is directly transported by a coaxial cable, SUHNER S10162B-11, for 70 m to the spectrum analyzer Tektronix 3056 or the lock-in amplifier, Stanford Research Systems SRS844, at control room J4.

Test experiments are performed using a cyclotron beam of 100 A-MeV $^{13}C^{6+}$ with various beam intensities. Figure 3 shows a power spectrum of the second harmonics of the 14.5 MHz pulsed beam measured by the spectrum analyzer. In this measurement, the cyclotron beam was chopped with a 10 Hz repetition cycle so that sidebands at ±10 Hz were also observed. The background level here was ∼ −115 dBm which corresponds to 0.4 μV ≈ 80 nA, which is not sufficiently small to observe low-intensity beams.

Use of a lock-in amplifier is more suitable for measurements of the absolute value of the current. A measurement for various intensities of ∼400 nA to ∼3 nA using the lock-in amplifier is shown in Fig. 4. The cyclotron beam was chopped with 0.01 Hz and a duty cycle of 50% to enhance visibility. The rf signal of the

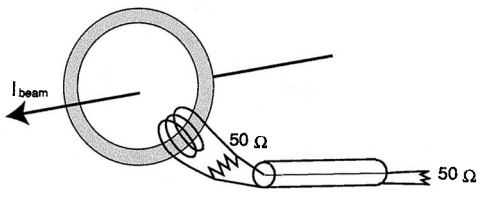

Fig. 1. Schematic diagram of toroidal current monitor. The beam current passing through the toroidal core is equivalent to the current in a one-turn coil.

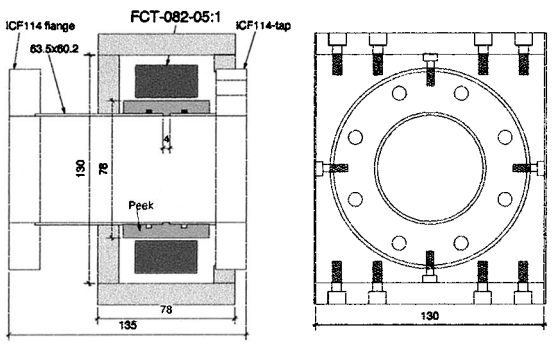

Fig. 2. Mechanical drawing of FCT monitor housing.

[*1] Institute of Particle and Nuclear Studies, High Energy Accelerator Research Organization (KEK)
[*2] Institute of Physics, Graduate School of Arts and Science, University of Tokyo

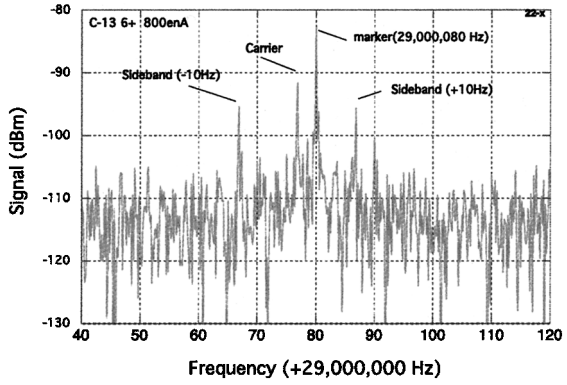

Fig. 3. Power spectrum of second harmonics of 100 A-MeV $^{13}C^{6+}$ beam of 800 enA detected by FCT. Sidebands due to a chopped beam with 10 Hz as well as the carrier signal at ∼29 MHz are observed.

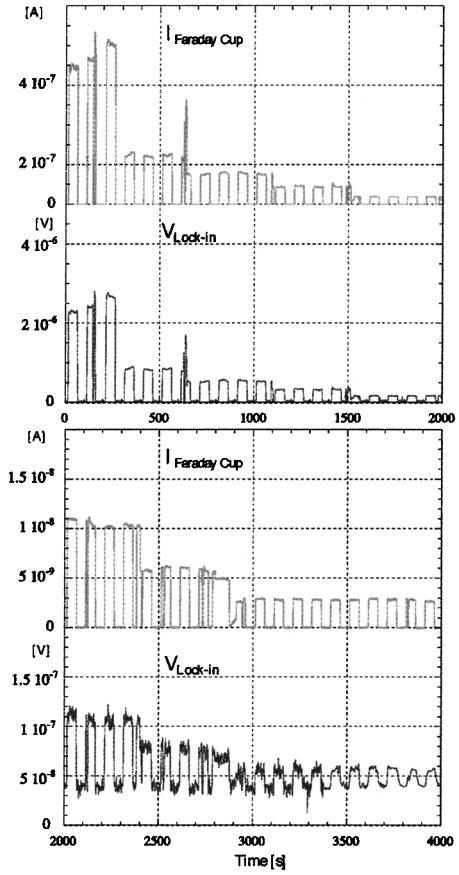

Fig. 4. Cyclotron beam intensities measured at Faraday cup and voltages of lock-in amplifier for various intensities. The time constant for the lock-in amplifier was 300 ms except for the last 5 peaks, which were at 1 s (3 peaks) and 3 s (2 peaks).

cyclotron was used for the reference signal of the lock-in amplifier with the '×2' mode which corresponds to the second harmonics. Here, the background signal was as low as ≈ 40 nV, which enabled us to measure such a low-intensity beam of 3 nA.

The proportionality of the FCT signals with a background subtraction to the Faraday cup measurements preserved for wide range of intensity (Fig. 5). The gain factor and the background voltage obtained were 6.49(4) nV/nA and 39(1) nV, respectively.

Adjustment of the phase is essential for obtaining such a low background condition. The absolute amplitude of the output signal (dBm) was as large as ∼0.45 μV even in the beam-off period, which was mainly caused by a large phase-off component $Y = -0.45\,\mu$V, while the phase-on component was $X = 0.04\,\mu$V. This large off-phase signal, but still synchronized to the cyclotron beam frequency, is supposed to be due to the rf signal of the cyclotron which may come along the beam transport line. It can be a problem if the beam bunch and the rf noise signal coincide with each other. However, such a condition should be avoided by moving the location of the FCT, since the beam velocity ($\sim 0.5c$) and the traveling velocity of the rf signal should differ.

The authors thank Mr. Julien Bergoz for useful discussions.

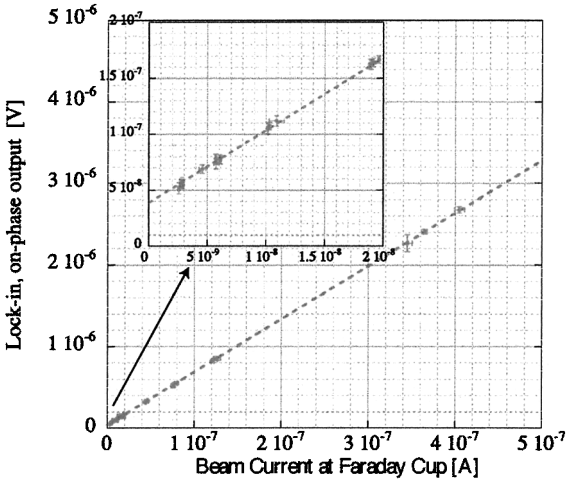

Fig. 5. 'On-phase' voltage of lock-in amplifier signal *vs.* beam current measured at Faraday cup. Insert is an enlarged graph for lower intensities. The fitting line is $y = 6.49(4) \cdot x + 39(1) \times 10^{-9}$.

Reference

1) BERGOZ Precision Beam Instrumentaion: Fast Current Transformer User's Manual.

Beam test of magnetic spectrograph PA

N. Iwasa,[*1] S. Kubono,[*2] Y. Fuchi,[*3] H. Fujikawa,[*2] N. Fukunishi, J. J. He,[*2] S. Kato,[*4] J. Moon,[*2] M. Notani,[*2] A. Saito,[*2] T. Teranishi,[*2] M. H. Tanaka,[*3] N. Yamazaki,[*2] and Y. Wakabayashi[*2]

Beam test experiments of the high-resolution magnetic spectrograph PA,[1] which was installed at the E2 experimental hall,[2] were performed. The aim of the experiments was to study achromatic beam transportation (ABT) and dispersion matching transportation (DMT) from the ring cyclotron to PA. To determine excitation energies with a resolution of 100 keV in FWHM in (^{4}He,^{8}He) reactions with a 135 MeV α beam, a momentum resolution less than 0.04% in FWHM is needed.

An α beam at 104 MeV accelerated by the ring cyclotron was transported to the target position of PA with ABT, and bombarded a 1-μm-thick gold target. PA was set at 10 degrees, and a slit was placed for restricting the solid angle to 0.1 msr. The momenta of scattered α particles were measured by a hybrid position-sensitive gas proportional counter (GPC)[3] with an active area of 400×35 mm^2 located on the focal plane of PA. The ΔE and the time of flight were measured by a plastic scintillator with a thickness of 2 mm placed behind GPC. The momenta were calibrated using the α particles with four different magnetic field settings of PA, $\Delta B/B_0 = -0.746\%$, 0%, 0.898%, and 1.804%. The momentum resolution was measured to be 0.1% in FWHM, although the intrinsic momentum resolution of PA is 0.01% using the target spot size of 1 mm.[1] Since the momentum resolution is larger than the required one, DMT is desired.

As a first step of the DMT study, a stainless-steel target with a hole of 1 mm ϕ instead of the gold target was bombarded by a faint α beam, and PA was set at 0 degrees. The target thickness is sufficient to stop the beam in the target. The position of the hole could be selected to be -5, 0, and $+5$ mm in the horizontal direction from the optical axis. The hole at 0 mm was used during this experiment. Several parameters for the beam transport line for DMT were tested.

The solid curve in Fig. 1 shows relative momentum spectra in ABT measured by GPC. The momentum resolution in ABT was measured to be 0.03% in FWHM, which is better than that of 0.1% measured at 10 degrees with the 1-μm-thick gold target. The momentum spread caused by energy straggling in the gold target was measured to be 0.03%, which agrees with the calculated energy straggling of 0.054 MeV. The remaining momentum spread of 0.08% observed at 10 degrees with a higher beam intensity was not understood. Since a 0.1 msr slit was used for PA, the momentum spread caused by the kinematics was negligible.

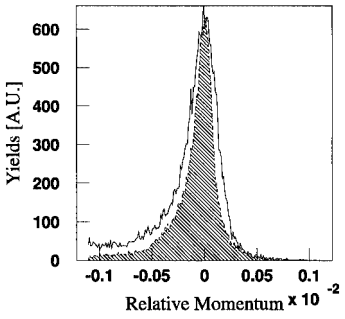

Fig. 1. Normalized momentum spectrum. The solid curve and the hatched area denote momentum distributions in achromatic beam transportation and dispersive beam transportation, respectively. Note that in the dispersive beam transportation, the momentum width was selected to be 0.01% using a dispersively focused beam and 1-mm-ϕ hole.

The hatched area in Fig. 1 shows a normalized momentum spectrum when the beam was focused dispersively on the target. The momentum resolution was measured to be 0.02% in FWHM. Note that the momentum width of the beam was selected to be 0.01% (full width) using a dispersively focused beam on the target and a 1-mm-ϕ hole. This selected momentum width was estimated from the calculated dispersion from the ring cyclotron to PA and the hole size. The measured momentum resolution is slightly larger than the calculated intrinsic momentum resolution of PA. The present momentum resolution was considered to be the best resolution measured in the RIKEN accelerator research facility, encouraging us to study dispersion matching with the spectrograph PA.

Further investigations for dispersion matching are required before studying the (^{4}He,^{8}He) reactions, because their cross sections are so small. However, the present test results indicate that the spectrograph PA can be used for the measurement of reactions that have relatively large cross sections, for example, (^{4}He,^{6}He) reactions, with a limited target size.

*1 Department of Physics, Tohoku University
*2 Center for Nuclear Study, University of Tokyo
*3 Institute of Particle and Nuclear Studies, High Energy Accelerator Research Organization (KEK)
*4 Department of Physics, Yamagata University

References

1) S. Kato, M. H. Tanaka, and T. Hasegawa: Nucl. Instrum. Methods Phys. Res. **154**, 19 (1978).
2) N. Yamazaki et al.: CNS Rep. **2000**, 14 (2001).
3) M. H. Tanaka, S. Kubono, and S. Kato: Nucl. Instrum. Methods Phys. Res. **195**, 509 (1982).

Low-energy radioisotope beam separator CRIB†

Y. Yanagisawa, S. Kubono,[*1] T. Teranishi,[*2] K. Ue, S. Michimasa, M. Notani,[*3] J. J. He,[*1] Y. Ohshiro,[*1] S. Shimoura,[*1] S. Watanabe,[*1] N. Yamazaki,[*1] H. Iwasaki,[*4] S. Kato,[*5] T. Kishida, T. Morikawa,[*2] and Y. Mizoi[*6]

Radioactive isotope (RI) beams at 5–10 MeV/nucleon are very useful for nuclear spectroscopy studies, such as particle transfer reactions. Nuclear structure studies with in-beam γ-ray spectroscopy in this energy region, are also powerful, because nuclear fusion reactions have large cross sections.

A low-energy in-flight-type RI beam separator, called CRIB, was installed in the experimental hall E7 at RARF for nuclear physics and nuclear astrophysics by the Center for Nuclear Study (CNS).[1)] This separator was developed under the CNS-RIKEN collaboration. It consists of a double achromatic system and Wien filter. It also consists of the major parts previously used for the spin transfer spectrometer DUMAS[2)] at the Research Center for Nuclear Physics (RCNP), Osaka University, and several modifications and new installations were made. It comprises a windowless gas target,[3)] a velocity filter (Wien filter) and high-power Faraday cups on inner dipole walls.

The double achromatic part of CRIB, the first half, consists basically of four components: a production target, two dipole magnet systems, and an energy degrader placed in between. It was designed to provide RI beams of 5–10 MeV/nucleon. Its compact design matches the layout of the experimental hall. A degrader of uniform thickness was adopted because it is easy to fabricate and the thickness can be accurately controlled. In addition, we constructed a velocity filter section, the second half, for better isotone separation.

During the installation of CRIB, we also renewed the beam line from the AVF cyclotron for better transport efficiency, and installed a 14 GHz ECR ion source, called Hyper ECR.[4)] The primary beam intensity was increased by one to two orders of magnitude at the production target, F0, resulting in more intense RI beam production. Recently, we have obtained an RI beam intensity of about 1×10^6 from (p,n) reactions. This value will be further increased in the near future by improving the performance of the ion source and the acceleration efficiency of the AVF cyclotron, as well as using target technology. Therefore, CRIB has a good prospect for experimental studies in both nuclear physics and nuclear astrophysics, as well as for other applications.

Current experimental programs at CRIB include (1) resonant elastic scattering experiments for nuclear structure and nuclear astrophysics studies, (2) measurements of reaction cross sections of astrophysical interest, and (3) γ-ray spectroscopy via fusion reactions. Several experiments at CRIB have already been performed successfully using ^{11}C, ^{14}O, ^{17}N, ^{22}Mg and ^{23}Al beams.[5–8)]

References

1) Y. Yanagisawa et al.: RIKEN Accel. Prog. Rep. **34**, 183 (2003).
2) T. Noro et al.: J. Phys. Soc. Jpn. **55**, 470 (1986).
3) T. Kishida et al.: Nucl. Instrum. Methods Phys. Res. A **438**, 70 (1999).
4) Y. Ohshiro et al.: RIKEN Accel. Prog. Rep. **36**, 279 (2003).
5) T. Teranishi et al.: RIKEN Accel. Prog. Rep. **35**, 73 (2002).
6) M. Notani et al.: RIKEN Accel. Prog. Rep. **36**, 64 (2003).
7) A. Odahara et al.: RIKEN Accel. Prog. Rep. **37**, 75 (2004).
8) J. J. He et al.: RIKEN Accel. Prog. Rep. **37**, 68 (2004).

† Condensed from the article in Nucl. Instrum. Methods Phys. Res. A **539**, 74 (2005)

*1 Center for Nuclear Study (CNS), University of Tokyo
*2 Department of Physics, Kyushu University
*3 Argonne National Laboratory, USA
*4 Department of Physics, University of Tokyo
*5 Department of Physics, Yamagata University
*6 Osaka Electro-Communication University

Performance of SAMURAI spectrometer in the QQQ-D mode

Y. Sasamoto,[*1] T. Uesaka,[*1] T. Kawabata,[*1] T. Kobayashi,[*2] and T. Nakamura[*3]

A large acceptance spectrometer SAMURAI[1)] is planed to be installed at RIBF. It is a superconducting dipole magnet with a circular pole of 1 m radius. The pole gap is 80 cm and the maximum magnetic field is 3 T. The spectrometer will be mainly used for spectroscopic studies of unstable nuclei with radio active beams. Several experiments concerning few body physics using a 880-MeV primary deuteron beam are also proposed. Such experiments require high momentum resolution of $\Delta p/p \simeq 3 \times 10^{-4}$, angular resolution of $\Delta\theta \simeq 3$ mr, and solid angle of $\Delta\Omega \simeq 6$ msr for 880-MeV deuteron, whose magnetic rigidity Bρ is 6.7 Tm.

In the original operation mode of SAMURAI, only the dipole magnet is used to analyze charged particles emitted from the reaction target. It is, however, difficult in this mode to achieve the high resolution required in the few-body experiment because horizontal focus can not be achieved at the detector position for particles with Bρ = 6.7 Tm. To improve the momentum resolution, a new operation mode of the SAMURAI spectrometer is studied. In the new operation mode, a triplet quadrupole magnet[2)] in the beam line is used in combination with the dipole magnet to analyze charged particles emitted from the target. The quadrupole triplet consists of the superconducting magnets with the warm bore radius is 12 cm.

In present study, the exit of the third quadrupole magnet (Q3) is located at 3.5 m upstream from the center of the dipole magnet. The target position should be close to the entrance of the first quadrupole magnet (Q1) as much as possible to obtain large acceptance. The target position is fixed at 0.8 m upstream from the entrance of the Q1. The focal plane is 3 m downstream from the center of the dipole magnet.

The computer code GIOS[3)] is used to calculate the particle trajectories in the magnet system. Figure 1 shows the layout of the spectrograph in the QQQ-D operation mode. The particle trajectories obtained from the first order calculation are also shown in Fig. 1.

Many combinations of three quadrupole fields are examined to achieve both good resolution and large acceptance simultaneously. Figure 2 shows one of the realistic solution. The ion optical properties obtained from the first order calculation are summarized in Table 1, while the magnetic field strengths are shown in Table 2. The angular acceptance is limited by the aperture of Q1. In Table 1, the acceptance is approximated by an elliptical shape not a rectangle shape. From the present study, it is found that the momentum reso-

*1 Center for Nuclear Study, Graduate School of Science, University of Tokyo
*2 Department of Physics, Tohoku University
*3 Department of Physics, Tokyo Institute of Technology

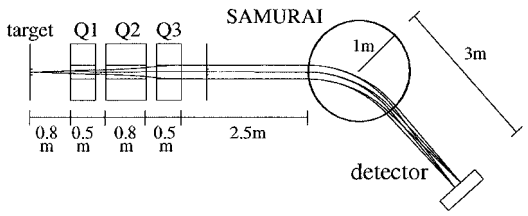

Fig. 1. Schematic layout of the SAMURAI spectrometer in the QQQ-D mode. Q1, Q2 and Q3 are quadrupole magnets, while SAMURAI is a dipole magnet. The particle trajectories with $\delta = \pm 3\%$ and $\theta = \pm 20$ and 0 mr are drawn.

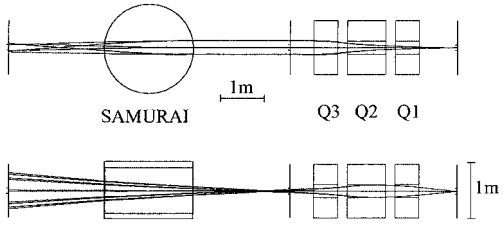

Fig. 2. Particle trajectories in the SAMURAI spectrometer in the QQQ-D mode. The trajectories with $x = \pm 1$ mm, $y = \pm 1$ mm, $\theta = \pm 20$ and 0 mr, $\phi = \pm 90$ and 0 mr, and $\delta = \pm 3\%$ are drawn. The top figure shows trajectories on the horizontal plane, while the bottom figure shows those on the vertical plane.

Table 1. Ion optical properties of the SAMURAI spectrometer in the QQQ-D mode obtained from the first-order calculation.

bending angle	48.5°
$(x\|x)$	−0.460
$(x\|\delta)$	2.249 m
$(y\|y)$	−13.36
$(y\|b)$	−2.886 m/rad
Resolving Power[§]	4.889 m
Angular acceptance (horizontal)	±20 mr
Angular acceptance (vertical)	±90 mr
Solid angle (ellipse)	5.7 msr

[§] Resolving Power $= \frac{(x|\delta)}{|(x|x)|}$

Table 2. Magnetic field strengths of the SAMURAI spectrometer in the QQQ-D mode.

Q1	−0.083 T/cm
Q2	0.912 T/cm
Q3	0.108 T/cm
SAMURAI	3.0 T

lution of $\Delta p/p \simeq 2 \times 10^{-4}$, the angular resolution of $\Delta\theta \simeq 5\,\mathrm{mr}$, and the solid angle of $\Delta\Omega \simeq 6\,\mathrm{msr}$ are expected in the first order calculation if the beam spot size is assumed to be 1 mm.

The effect of the fringing field is neglected in the present study. The third order calculation taking the fringing field into account is in progress.

References

1) T. Kobayashi et al.: RIBF International Advisory Committee 2004-11, unpublished.
2) T. Kubo: Nucl. Instrum. Methods Phys. Res. B **204**, 97 (2003).
3) H. Wollnik et al.: Proc. 7th Int. Conf. on Atomic Masses and Fundamental Constants (AMCO-7), Darmstadt-Seeheim, Germany, 1984-9, edited by O. Klepper (Lehrdruckerei, Darmstadt, 1984), p. 705; GSI Report, THD-26, 679 (1984).

Development of TOF spectrometer for use in experiments at RIPS

N. Aoi, E. Takeshita,[*1] H. Suzuki,[*2] S. Ota,[*3] T. Kubo, S. Takeuchi, K. Ieki,[*1] H. Iwasaki,[*2] K. Kusaka, H. Sakurai,[*2] S. Shimoura,[*4] T. Motobayashi, and K. Yoshida

A variety of unique structures have been revealed using the in-beam γ-ray spectroscopy technique with unstable nuclear beams. These studies have thus far been performed mainly in the mass region smaller than 40. The limitation on the mass region is mainly due to the difficulties of particle identification (PID) of scattered ions. The time-of-flight (TOF) spectrometer is being developed to extend the in-beam γ-ray spectroscopy study at RIPS toward the heavier mass region up to $A \sim 80$ by improving the PID resolution.

The TOF spectrometer is designed to have a PID resolution of $\sim$1.4% (FWHM) by combining high-energy-resolution Si detectors and high-TOF-resolution plastic scintillators with a long flight path ($\sim$4 m). The atomic number (Z) is determined from TOF and ΔE using the relation $\Delta E \propto Z^2 \mathrm{TOF}^2$, and the mass number ($A$) is determined from the TOF and E using the relation $E \propto A/\mathrm{TOF}^2$. Z and A resolutions of 0.7% and 1.4% (FWHM) are expected, assuming the relative resolutions for TOF, ΔE, and E to be 0.5% (250 ps/50 ns), 1.0%, and 1.0%, respectively. This PID resolution is much higher than the PID resolution obtained by the Si ΔE-E method (typically 2.5%) or TOF-ΔE-E method using plastic scintillator hodoscopes (typically 3.7%).

Besides the PID resolution, large angular and momentum acceptances are required, because the intensity of the beam to be used with the TOF spectrometer is very weak. Therefore, to avoid the dispersion of nuclei when they pass through the long flight path, the Superconducting Triplet Quadrapole magnet (STQ) (Fig. 1) is incorporated as a focusing element. The STQ[1)] was developed as a prototype magnet for BigRIPS,[2)] and thus, has a large bore radius (warm bore radius is 140 mm) and a large maximum field gradient (14.1 T/m). These features match the requirements of the TOF spectrometer having large angular and momentum acceptances.

Figure 2 schematically shows the configuration of the detectors in the TOF spectrometer. The TOF spectrometer is to be placed downstream of the secondary target at the third focal plane (F3) of RIPS.[3)] A PPAC and plastic scintillator are mounted, between the secondary target and the STQ. The PPAC is used to determine the scattering angle of ejectiles. Its large sensitive area of $150 \times 150\,\mathrm{mm}^2$ covers the large angular acceptance of the STQ. The plastic scintillator, which provides the start timing of TOF, has dimensions of 160 mm $\times$ 150 mm $\times$ 100 μm; a thin material was chosen to reduce the energy loss in the detector.

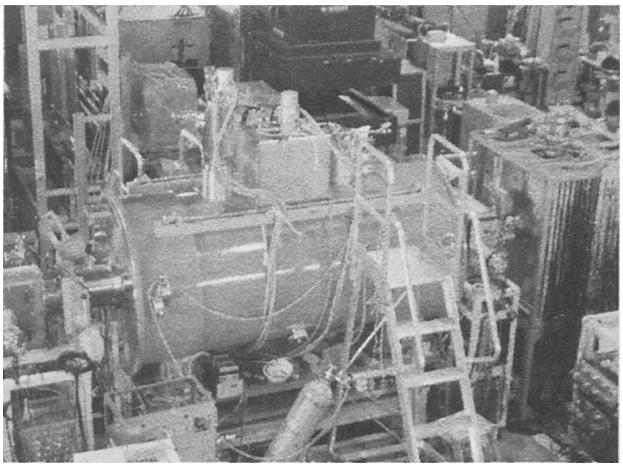

Fig. 1. The Superconducting Triplet Quadrapole magnet used for the TOF spectrometer.

Behind the STQ, two PPACs, a plastic scintillator, ΔE and E detectors are placed. The two PPACs are located at a distance of 30 cm from each other. The first and second PPACs have dimensions of $150 \times 150\,\mathrm{mm}^2$ and $100 \times 100\,\mathrm{mm}^2$, respectively. They are used to determine the position and angle of the ions being focused on the ΔE-E detectors. The plastic scintillator, placed between the two PPACs, provides the stop timing for the TOF. This configuration has the flight path length of 3.85 m between the start and stop scintillators, for which the typical TOF of ions with $E \sim 30A$ MeV is $\sim$50 ns.

The configuration of the ΔE and E counters will be optimized depending on the stopping range spread of ions. For experiments with A = 60–80 nuclei, 100 μm Si detectors and two layers of 320 μm Si detectors are used for ΔE and E measurements, respectively. The ΔE-layer consists of four sets of $50 \times 50\,\mathrm{mm}^2$ Si detectors arranged in a two-by-two matrix. The E-layers consist of round shaped Si detectors with a diameter of 134 mm. Thin ΔE detectors are used because of the small stopping range of ions, while relatively thick E-layers are used to cover the wide stopping range spread of ions. For A$\sim$30 nuclei, a NaI(Tl) scintillator array is used as an E counter instead of Si detectors to have the thick material required by the large stopping range of scattering ions.

The distance between the secondary target and the front face of the STQ is set at 1050 mm as a compromise between the angular acceptance and the space

*1 Department of Physics, Rikkyo University
*2 Department of Physics, University of Tokyo
*3 Department of Physics, Kyoto University
*4 Center for Nuclear Study, University of Tokyo

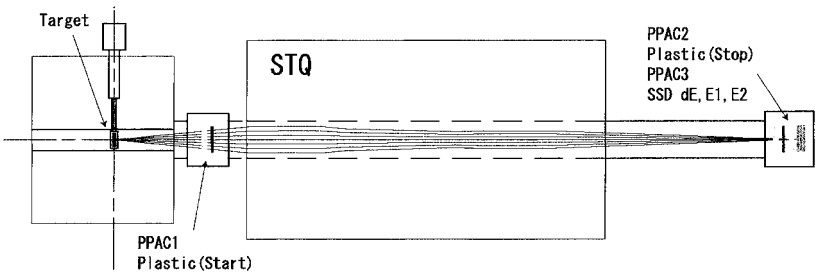

Fig. 2. Schematic view of the TOF spectrometer.

for the γ-detectors surrounding the target. With this setup, the distance between the target and the front face of the vacuum chamber for the start counters is 530 mm; here, users can place their experimental apparatus. This space is sufficiently wide to place large-scale γ-detector arrays such as DALI2[4] or GRAPE[5] surrounding the secondary target.

The features of the ion optics were investigated,[6] and it was found that the angular acceptance is 100% for angles smaller than two degrees. Taking the H(^{64}Cr,^{64}Crγ) experiment as an example, the mass of the ejectiles can be separated with $2.7\,\sigma$ and the overall acceptance of the TOF spectrometer is 95%, where the spacial, angular and momentum spreads of the beam are taken into account. The other example is the ^{4}He(^{32}Mg,^{32}Mgγ) experiment, where the mass separation is $5.4\,\sigma$ and the overall acceptance is 70%.

With the performance of the TOF spectrometer, significant improvement in the quality of experimental data is expected. All the detectors and the vacuum chambers are almost ready and the first experiment using the TOF spectrometer is scheduled for the end of 2004.

References

1) K. Kusaka et al.: IEEE Trans. Appl. Supercond. **14**, 310 (2004).
2) T. Kubo et al.: Nucl. Instrum. Methods Phys. Res. B **204**, 97 (2003) .
3) T. Kubo et al.: Nucl. Instrum. Methods Phys. Res. B **70**, 309 (1992).
4) S. Takeuchi et al.: RIKEN Accel. Prog. Rep. **36**, 148 (2003).
5) S. Shimoura et al.: CNS Annu. Rep. **2001**, 5.
6) H. Suzuki et al.: RIKEN Accel. Prog. Rep. **38**, 178 (2005).

Simulation of particle trajectories for the TOF spectrometer

H. Suzuki,[*1] E. Takeshita,[*2] N. Aoi, H. Sakurai,[*1] H. Iwasaki,[*1] T. Kubo, K. Kusaka, K. Yoshida, T. Motobayashi, and K. Ieki[*2]

The TOF spectrometer[1)] is being developed for use in in-beam γ spectroscopy at RIPS[2)] (RIken Projectile-fragment Separator) with radioactive beams. Improvement has been made with emphasis on the resolution of particle identification (PID), which enables us to identify reaction residue with a mass number of around 80. In the PID, mass number (A) identification is generally more difficult than proton number (Z) identification. In the past experiments in RIPS, PID has been performed mostly by the ΔE-E method with Si detectors. However, the resolution of Si detectors limits the mass resolution, and nuclei with $A \gtrsim 40$ are difficult to be distinguished. The TOF spectrometer employs the TOF-E method to determine A. To achieve good TOF resolution, a long flight path ($\sim$4 m) is taken, which is necessary to attain sufficient mass resolution for nuclei with $A \sim 80$. To focus the scattered particles on the small-area detectors for TOF measurement (10 cm square), Superconducting Triplet Quadrupole magnets (STQ)[3)] are used. Basic requirements of the TOF spectrometer are sufficient angular acceptance (70% at 2 degrees) and high mass resolution ($2\,\sigma$ separation at $A \sim 80$).

To estimate the transmission and mass resolution, the particle trajectories in STQ were simulated. STQ have the following characteristic features. Strong magnetic field gradients can be generated with a large duct radius (140 mm). Each magnet in STQ has a short length (500 mm or 800 mm) compared with their large bore radii (170 mm). These features enable it to have large angular acceptance for the TOF spectrometer. On the other hand, these features cause significant fringe fields. In addition, since STQ generates strong fields above the magnetic saturation point, the shapes of the magnetic field distributions change with their strengths (nonlinearity). To deal with the large fringe areas properly in the particle trajectory calculation, a code, COSY Infinity[4)] developed at Michigan State University, was used. This code can handle any distribution of magnetic fields given by users. The calculation was performed to the 3rd order.

Measured magnetic fields were used for the calculation because of the nonlinear feature of STQ. Field measurements were made at every 20 mm step along the beam axis at 120 mm in radius. The currents of the coils were set at 25%, 50%, 75%, 100%, and 120% of the nominal currents. By interpolating the discretely measured data, the magnetic fields were represented as continuous functions of currents and positions.

The field settings were determined to satisfy the focus conditions. Three conditions may be required, because the magnetic fields for three magnets can be set independently. In the present calculation, the following conditions were required: being focused in the x-direction, being focused in the y-direction, and the same magnifications of the x-direction and the y-direction. To simplify the calculation, rectangular distributions of the magnetic fields were used in place of the realistic field distributions. The lengths of the rectangular fields were taken to be the effective lengths of the original realistic ones. The strengths of the rectangular fields were determined so that the integrals of the fields were the same as those of the original realistic fields. After the field settings were determined with rectangular distributions, the transfer matrices were calculated using the realistic field distributions. The magnifications obtained with rectangular fields were -1.0 for the x-direction and the y-direction, whereas those with the realistic fields were -1.5 and -1.0, respectively. The maximum magnetic rigidity of a particle that can be focused by STQ is 5.0 Tm.

Particle trajectories were calculated using the transfer matrices, as shown in Fig. 1. In this calculation, position, angle, and kinetic energy spread of the incident particles before the target were taken into account. Energy loss and scattering in the target were also considered. Gaussian distributions were assumed for position and angle spread with $\sigma = 1$ cm and $\sigma =$ 1 degree, respectively. The kinetic energy spread is set at $\pm 6\%$. It is seen that the particles pass through STQ with wide spatial spread, and some particles hit the beam duct.

The transmission is calculated as the ratio of the number of particles that passed through the STQ to the total number of particles ejected from the target.

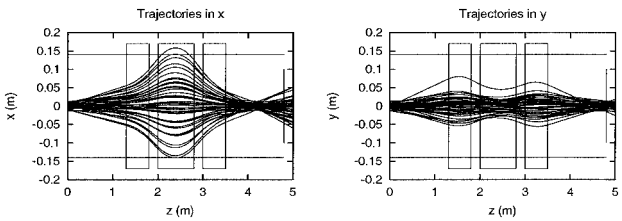

Fig. 1. The particle trajectories in the TOF spectrometer from the target to the focal plane in the x-direction (up) and the y-direction (down). The three boxes represent the quadrupole magnets. The right vertical line represents the focal plane. The two horizontal lines represent the beam duct.

[*1] University of Tokyo
[*2] Rikkyo University

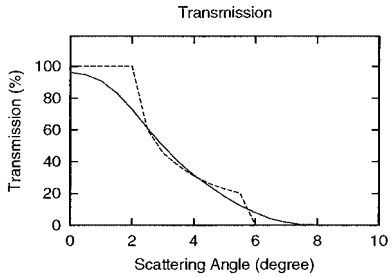

Fig. 2. The transmission of the TOF spectrometer. The dashed line shows the transmission for monochromatic particles from the point source at the center of the target. The solid line shows the transmission based on realistic conditions of the ^{64}Cr(p,p′) reaction at 30 A MeV.

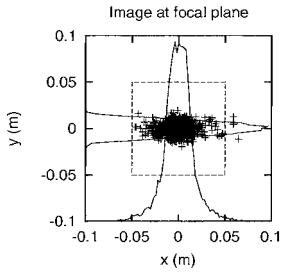

Fig. 3. The image of the particles at the focal plane. Dashed square in the figure corresponds to the active size of the detectors at the focal plane after STQ. Two histograms are projections of the image to x and y axes. The position spreads are 1.6 cm (rms) in the x-direction and 0.7 cm (rms) in the y-direction.

Figure 2 shows the transmissions as a functions of the scattering angle. The dashed line represents the transmission for monochromatic particles from the point source at the center of the target. The transmission is 100% when the scattering angle is up to 2 degrees in the lab system, and 0% at 6 degrees.

However, in the actual experiments with RI beams, the position, angle, and kinetic energy of incident particles have finite spread. The transmission under such realistic conditions is calculated and shown by the solid line in Fig. 2. Note that the scattering angle stands for the deflection angle in the target due to the reaction, and thus the outgoing angle is the sum of the incident angle and the scattering angle.

Considering the angular distributions of the differential cross section (dσ/dΩ), the overall transmission is calculated. Taking the ^{64}Cr(p,p′) reaction at 30 A MeV as an example, dσ/dΩ has a width of about 0.3 degrees (rms). The total transmission is found to be 95%. In the case of the ^{64}Cr(α,α') reaction at 30 A MeV, the widths of dσ/dΩ are about 1.2 degrees (rms). In spite of the large angle spread, a reasonably large transmission of 81% is obtained. The TOF spectrometer provides sufficient angular acceptance for the experiments.

Figure 3 shows the image at the focal plane after STQ. In this figure, the particles which did not reach the focal plane are not drawn. Of the particles that pass through STQ, 99% hit the detectors (10 cm square). To have a smaller spot size at the detector, the magnetic fields can be adjusted so that the thinnest point (waist) is at the detector position.

The spread of the flight path length shown in Fig. 1 could affect the PID resolution, and worsen the mass resolution of the PID. In the case of the ^{64}Cr(p,p′) reaction at 30 A MeV, the flight path spread is calculated to be 0.12%. Considering this effect, the A (mass number) resolution increases from 0.57% to 0.61%, where the E resolution of 0.4% (rms) with Si detectors and a TOF resolution of 0.2% (rms) with plastic scintillators are assumed. The separation capability of nuclei is also decreased from 2.8 σ to 2.5 σ. The worsening of the mass resolution is not significant. If better resolution is required, the spread of the flight path length can be corrected for by using particle tracking with position detectors. With this correction, the effect of the spread falls to 0.08% and nuclei of A∼60 are separated by 2.7 σ.

This spectrometer has satisfactory mass resolution and angular acceptance. The TOF spectrometer will contribute a great deal to the study of unstable nuclei in the medium-mass region.

References

1) N. Aoi et al.: RIKEN Accel. Prog. Rep. **38**, 176 (2005).
2) T. Kubo et al.: Nucl. Instrum. Methods Phys. Res. B **70**, 309 (1992).
3) K. Kusaka et al.: IEEE Trans. Appl. Supercond. **14**, 310 (2004).
4) K. Makino and M. Berz: Nucl. Instrum. Methods Phys. Res. A **427**, 338 (1999).

Network and computing environment for RIKEN accelerator research facility

T. Ichihara, Y. Watanabe, K. Yoshida, and A. Yoshida

The advanced computer network[1] started operation in 2002 at the RIKEN Accelerator Research Facility (RARF). Major updates undertaken this year are summarized as follows.

1) Mail Spam Filter

Recently, spam which is unsolicited junk e-mail sent to large numbers of people to promote products or services, has become a serious problem for all e-mail users. In some case more than one-hundred spam mails are sent to a person each day. Therefore the daily handling of spam mails has become a large task for individual mail users.

In order to resolve this problem, mail frontend servers for tagging spam mail have been installed. Incoming mails to the RARF mail server (rarfaxp) are first received by the mail frontend servers (rarfsmtp or rarfproxy) and spam mails are automatically identified using SpamAssassin software and tagged in the mail subject and header field.

SpamAssassin[2] is a mail filter which attempts to identify spam using a variety of mechanisms including text analysis, Bayesian filtering, DNS blacklists, and collaborative filtering databases. Using a rule base, it applies a wide range of heuristic tests to mail headers and the body of text of the mails to identify spam. To date, approximately 95–99% of spam mails have been correctly identified as spam in the RARF mail environment.

Then, each mail user can delete or separate the spam mails automatically on the basis of the tagging of the mail subject or mail header field by setting their mail client software options. As a result, each mail user is kept almost free from the spam problem by appropriate use of their mail client software.

2) ftp server (ftp.riken.jp)

An anonymous ftp server (ftp.riken.jp) is managed and operated at RARF. Recently, many research laboratories in RARF have adopt Linux as their computer operating system. In order to conduct the installation and daily management of Linux easily and efficiently, major Linux distributions are mirrored at the ftp servers. Most of the distributions are mirrored daily from the primary master server using the rsync protocol. The mirrored Linux distributions[3] include fedora core, redhat, debian, suse, scientific linux (SL), scientific linux cern (SLC), whitebox, caos (CentOS), tao, slackware, mandrake, mepis, vine, gentoo, knoppix, ubuntu, plamo and turbolinux distributions. Also the TeX archives (CTAN), GNU software and many other useful software packages are mirrored at the server.

The hardware of the server was replaced with a 2U rack-mount PC which consists of two sets of a 3.06 GHz Pentium Xeon CPU and 3.7 GB memory. Two sets of SATA Raid disks (in total, 3.0 TB) were added to the server.

Figure 1 shows the current configuration of the RARF advanced computer network. Between the RARF internal network and the external Internet, a firewall (PIX 525) has been installed to maintain security.

Figure 2 shows the current configuration of the UNIX cluster servers of RARF.

The RARF Unix cluster consists of eleven nodes of UNIX servers, four of which are True 64 UNIX (alpha), five of which are Linux and two of which are Solaris, which are connected via the Gigabit or 100 Mbps Ethernet. RARFAXP is the central server for e-mail, text processing, user home pages and general computing. RARFAX1-2, RARFLX1-3, and RARFLX10-11 are used mainly for intensive data analysis, middle-scale calculations and user terminals. RARFSUN is a gateway computer for accessing the internal private network of RARF using SSH. RARFNFS0 is a dedicated Network File Service (NFS) server which is equipped with 2.8 TB + 1.7 TB SCSI Raid5 work disks.

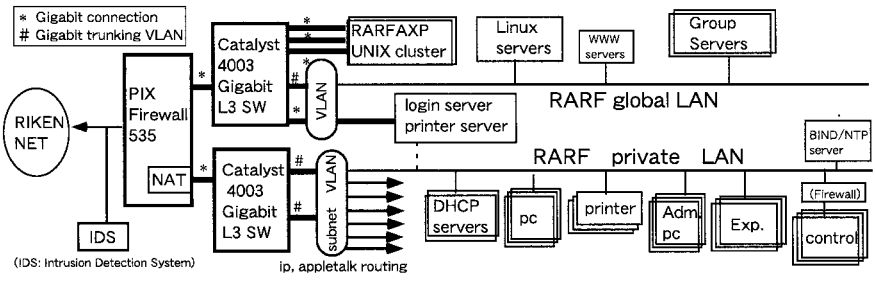

Fig. 1. Configuration of the RARF advanced computer network.

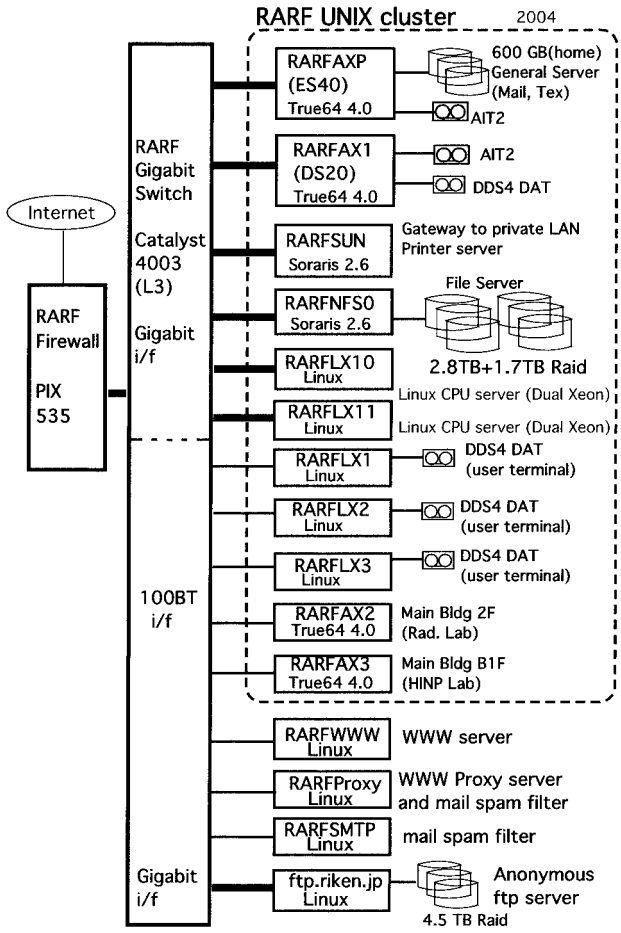

Fig. 2. Configuration of the UNIX cluster servers of RARF.

Most of the RARF users have e-mail addresses of the following patterns:

username@rarf.riken.jp or username@riken.jp.

The first one represents an e-mail address of the RARF mail server (RARFAXP) and the second one represents an e-mail address of the RIKEN mail server (postman).

References

1) T. Ichihara et al.: RIKEN Accel. Prog. Rep. **36**, 199 (2002).
2) http://spamassassin.apache.org/index.html
3) http://ftp.riken.jp/

Global analysis of fragmentation functions

S. Kretzer

Hard pQCD reactions produce highly virtual partons that will radiate off their virtualities, thus evolving into the nonperturbative states that contain observable hadrons. A quantitative understanding of this process, known widely as the fragmentation of partons, considerably widens the class of reactions that can be handled within a perturbative QCD approach.

A graph such as that shown in Fig. 1 serves as a popular illustration of QCD factorization.[1] It also displays the role of fragmentation functions $D_c^\pi(z)$ in hard scattering phenomenology when there are detected hadrons in the final state. The early Field & Feynman[2] cascade model for quark fragmentation into mesons is depicted in Fig. 2 and a later field-theoretic definition in terms of a bilocal operator[3] is shown in Fig. 3. At leading twist accuracy, these describe fragmentation (or decay) functions (now in a narrower sense of the word) that turn a single parton into a single-hadron inclusive state, with fractional momentum transfer z from the parton to the hadron. Analogous to parton densities, renormalization induces evolution of the (transposed) DGLAP type:

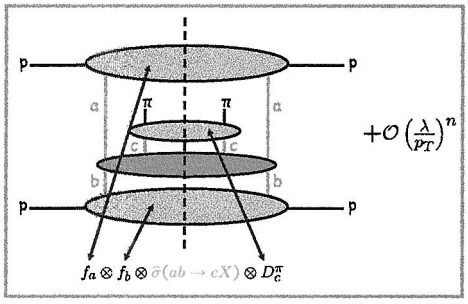

Fig. 1. Factorization in terms of parton densities and fragmentation functions.

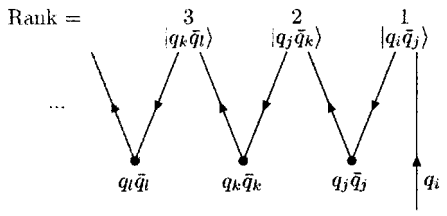

Fig. 2. Field & Feynman model of cascade fragmentation.

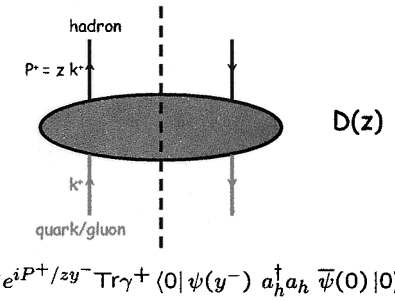

Fig. 3. Bilocal operator (right) introduced by Collins & Soper.

$$\frac{\partial D_i}{\partial \ln \mu} = \sum_{j=q,\bar{q},g} D_j \otimes P_{ij}. \tag{1}$$

Recent global analyses of fragmentation functions, determined at Next-to-Leading-Order accuracy in QCD, have been performed.[4] The individual fits are conceptually very similar, such that a comparison of the fits provides a good first estimate of the uncertainties in the functions $D_i(z)$. As explained above, the uncertainties of these functions are data driven and can be large. It can indeed be shown[5] that the electroweak couplings of up and down quarks at the Z^0 pole suggest that only flavour-insensitive combinations such as the singlet $\sum_q D_{q+\bar{q}}$ are well determined.

We have included semi-inclusive DIS data along with hadroproduction data, mainly from RHIC, in a substantial update of global analyses of fragmentation functions. Detailed results will be published soon.[6]

References

1) J. C. Collins, D. Soper, and G. Sterman: in *Perturbative Quantum Chromodynamics*, edited by A. H. Mueller, (World Scientific, Singapore, 1989), hep-ph/0409313.
2) R. D. Field and R. P. Feynman: Nucl. Phys. B **136**, 1 (1978).
3) J. C. Collins and D. E. Soper: Nucl. Phys. B **193**, 381 (1981); Nucl. Phys. B **213**, 545 (E) (1983); Nucl. Phys. B **194**, 445 (1982).
4) S. Kretzer: Phys. Rev. D **62**, 054001 (2000); B. Kniehl, G. Kramer, and B. Pötter: Nucl. Phys. B **582**, 514 (2000); Nucl. Phys. B **597**, 337 (2001); L. Bourhis, M. Fontannaz, J. P. Guillet, and M. Werlen: Eur. Phys. J. C **19**, 89 (2001).
5) S. Kretzer, E. Leader, and E. Christova: Eur. Phys. J. C **22**, 269 (2001).
6) S. Kretzer et al.: in preparation.

Single-inclusive cross sections and spin asymmetries in hadronic collisions†

W. Vogelsang

A major goal of current experiments using longitudinally polarized protons at RHIC[1] is to determine the nucleon's polarized gluon density, Δg. The tool for accessing Δg is the spin asymmetry

$$A_{\rm LL} = \frac{d\Delta\sigma}{d\sigma} = \frac{d\sigma^{++} - d\sigma^{+-}}{d\sigma^{++} + d\sigma^{+-}} \qquad (1)$$

for single-inclusive high-transverse-momentum ($p_\perp$) reactions such as $pp \to \pi X$, $pp \to$ jet X, and $pp \to \gamma X$. In Eq. (1), σ^{++} (σ^{+-}) denotes the cross section for the scattering of two protons of the same helicity (opposite helicities). The cross sections for high-$p_\perp$ reactions factorize into long-distance parts which contain the desired information on the (spin) structure of the nucleon, and short-distance parts which describe the hard interactions of the partons and are amenable to QCD perturbation theory. To make reliable predictions, it is important to know the next-to-leading order (NLO) QCD corrections to the lowest-order (LO) Born approximation for the partonic hard-scattering.

This paper gives a brief account of the calculation of (approximate) *analytical* NLO QCD corrections for the case of single-inclusive high-p_T jet production in longitudinally polarized pp collisions. For this purpose, we assume that the jet cone is narrow ("small-cone approximation," SCA). The actual calculation makes use of the fact that inclusive hadron and jet production proceed through the same set of partonic subprocesses. The NLO corrections for inclusive hadron production were obtained previously.[2] One only needs to properly add and subtract parts with two partons in the jet cone, where either one or both partons are "observed," that is, form the jet (see Fig. 1). If all contributions are appropriately taken into account, collinear singularities in the final state cancel, and therefore the dependence on the final-state factorization scale, present for the inclusive-hadron case, cancels as well.

Figure 2 shows the results for the LO and NLO inclusive jet cross sections at $\sqrt{s} = 200\,\text{GeV}$, and the associated K-factors. In Fig. 3, we show expected spin asymmetries $A_{\rm LL}$ for jet production at RHIC for various gluon polarizations.

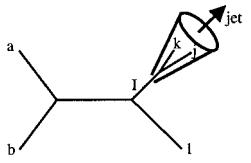

Fig. 1. Contributions to the single-inclusive jet cross section from partonic reactions where two essentially collinear partons, j and k, form a narrow jet.

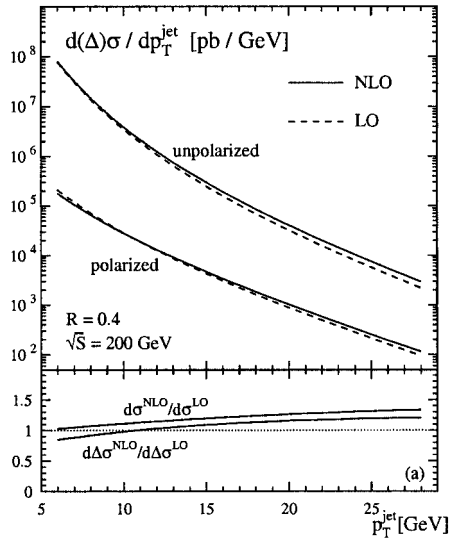

Fig. 2. Inclusive jet production cross sections in NLO (solid) and LO (dashed lines) at $\sqrt{S} = 200\,\text{GeV}$ for cone size $R = 0.4$. The lower panel shows the K-factors.

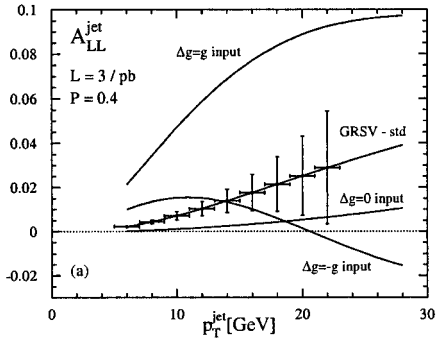

Fig. 3. NLO spin asymmetry $A_{\rm LL}$ for four different GRSV[3] sets of polarized parton distributions. The "error bars" indicate the expected statistical accuracy $\delta A_{\rm LL}^{\rm jet}$ for 40% beam polarization and integrated luminosities of $3\,\text{pb}^{-1}$.

† Condensed from the article Phys. Rev. D **70**, 034010 (2004)

References

1) See, *e.g.*, G. Bunce, N. Saito, J. Soffer, and W. Vogelsang: Annu. Rev. Nucl. Part. Sci. **50**, 525 (2000).
2) B. Jäger et al.: Phys. Rev. D **67**, 054005 (2003).
3) M. Glück et al.: Phys. Rev. D **63**, 094005 (2001).

Spin asymmetry for charged pion production at RHIC

M. Hirai* and K. Sudoh

The polarized gluon distribution $\Delta g(x)$ is an important clue to the puzzle of the nucleon spin, As a probe, inclusive π^0 production was measured by the PHENIX collaboration.[1] The cross section for the π^0 production is sensitive to $|\Delta g(x)|$, but is insensitive to its sign because the gg process dominates. Experimental uncertainties are still large. It is unclear whether $\Delta g(x)$ has a positive polarization at this stage.

To study $\Delta g(x)$ and its sign, we proposed an investigation of spin asymmetry by using charged pion production processes.[2] Spin asymmetry is defined as follows:

$$A_{\rm LL}^{\pi^+-\pi^-} \equiv \frac{\Delta\sigma^{\pi^+} - \Delta\sigma^{\pi^-}}{\sigma^{\pi^+} - \sigma^{\pi^-}} \ , \tag{1}$$

where $\Delta\sigma^{\pi^\pm}$ and $\sigma^{\pi^\pm}$ are the polarized and unpolarized cross sections for charged pion production, respectively. In each pion production, contributions from gg and qg processes dominate. The gg contribution, which is proportional to $[\Delta g(x)]^2$ and so is insensitive to the sign of $\Delta g(x)$, is independent of the charge of the measured particle and can be eliminated by using this asymmetry. The qg contribution, which is proportional to $\Delta g(x)$, becomes dominant for this quantity in the entire p_T region. Consequently, the asymmetry is sensitive to the sign of $\Delta g(x)$.

By eliminating the gg contribution, the ambiguity of the gluon fragmentation function $D_g^{\pi^\pm}$ can be removed. The subprocesses accompanying by $D_g^{\pi^\pm}$ are the $gg \to gg$ and $q\bar{q} \to gg$ processes. For instance, the polarized cross section for the $gg \to gg$ process is given by

$$\Delta\sigma_{gg}^{\pi^\pm} = \Delta g(x_a) \otimes \Delta g(x_b) \otimes D_g^{\pi^\pm}(z) \otimes \Delta\hat{\sigma}^{gg\to gg}, \tag{2}$$

where $\otimes$ denotes the convolution integral and $\Delta\hat{\sigma}$ is the partonic cross section. In the difference between cross sections for π^+ and π^-, these cross sections cancel out each other due to $D_g^{\pi^+} = D_g^{\pi^-}$. Similarly, the $q\bar{q} \to gg$ process can also be removed. In addition, contributions from $gg \to q\bar{q}$ and $q\bar{q} \to q'\bar{q}'$ processes can also be eliminated by the summation of fragmentation functions for flavors: $\sum_i D_i^{\pi^+} = \sum_i D_i^{\pi^-}$.

The asymmetry can be obtained by the difference between the $qg \to qg$ process for π^+ and π^- production. A part of the process accompanied by $D_g^{\pi^\pm}$ is eliminated, and the asymmetry is given by

$$A_{\rm LL}^{\pi^+-\pi^-} \simeq \frac{\Delta g \otimes (\Delta u_v - \Delta d_v) \otimes (D_1^\pi - D_2^\pi) \otimes \Delta\hat{\sigma}^{qg}}{g \otimes (u_v - d_v) \otimes (D_1^\pi - D_2^\pi) \otimes \hat{\sigma}^{qg}}, \tag{3}$$

where Δf_v and $f_v(x)$ are the polarized and unpolarized valence quark distributions, respectively. The following relations among the fragmentation functions are assumed due to the isospin symmetry;

$$\begin{cases} D_u^{\pi^+} = D_{\bar{d}}^{\pi^+} = D_{\bar{u}}^{\pi^-} = D_d^{\pi^-} & \equiv D_1^\pi, \\ D_u^{\pi^-} = D_{\bar{d}}^{\pi^-} = D_{\bar{u}}^{\pi^+} = D_d^{\pi^+} & \equiv D_2^\pi. \end{cases} \tag{4}$$

In Eq. (3), $(\Delta u_v - \Delta d_v)$ is well determined because its first moment is constrained by the neutron and hyperon beta decay constants. Of course, unpolarized PDFs are more precisely determined in comparison with the polarized PDFs. In addition, ambiguity of the quark fragmentation functions can be cancelled between the numerator and denominator. Therefore, the asymmetry is obtained by well-known distributions except for the undetermined $\Delta g(x)$.

Figure 1 shows the asymmetry given by Eq. (1). Solid and dotted curves are asymmetries with $\Delta g(x)$ and $-\Delta g(x)$ given by the AAC analysis,[3] respectively. In both cases, we obtain large asymmetries. In particular, the asymmetry with $-\Delta g(x)$ is negative and the absolute value is fairly large compared with that of single pion production. In the region $8 < p_T < 13\,\mathrm{GeV}$, the asymmetry is suppressed due to the qq process which provides a positive contribution and accounts for 10–15% of the asymmetry. Although $q\bar{q}^{(\prime)} \to q\bar{q}^{(\prime)}$ and $qq' \to qq'$ processes also contribute, these contributions are negligible. The main contribution is given by the qg process; therefore, the behavior of the asymmetry certainly reflects the sign of $\Delta g(x)$ Although the asymmetry might be difficult to measure experimentally, it provides a possibility of extracting additional information about $\Delta g(x)$, positively its sign, from charged pion production at RHIC.

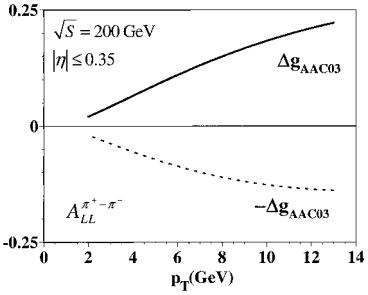

Fig. 1. Asymmetries for the difference of charged pion production with AAC $\Delta g(x)$ and $-\Delta g(x)$.

* Institute of Particle and Nuclear Studies, High Energy Accelerator Research Organization (KEK)

References

1) PHENIX Collaboration, S. S. Adler et al.: Phys. Rev. Lett. **93**, 202002 (2004).
2) M. Hirai and K. Sudoh: Phys. Rev. D **71**, 014022 (2005).
3) Asymmetry Analysis Collaboration, M. Hirai, S. Kumano, and N. Saito: Phys. Rev. D **69**, 054021 (2004).

Charm-associated $W^{\pm}$ boson production at RHIC

K. Sudoh and H. Yokoya*

The polarized parton distribution functions (PDFs) play an important role in understanding the spin structure of the nucleon. However, our knowledge of the polarized sea quark distribution and its flavor structure are still insufficient, since only the combinations $\Delta q + \Delta\bar{q}$ can be determined in the polarized deep inelastic scattering. We can extract information about $\Delta\bar{u}$ and $\Delta\bar{d}$ distributions from the conventional $W^{\pm}$ boson production in the future RHIC experiment.[1] Here, we discuss the possibility of the direct measurement of the polarized strange quark distribution Δs.

We propose charm-associated $W^{\pm}$ boson production $\vec{p} + p \to W^{\pm} + c/\bar{c} + X$ in polarized-unpolarized proton collisions at RHIC. The partonic subprocesses in leading order are composed of $\mathcal{O}(\alpha_s\alpha_w)$ $2 \to 2$ tree level channels $\Delta s'(\Delta g) + g(s') \to W^- + c$, where s' denotes the CKM combination $s' = |V_{cs}|^2 s + |V_{cd}|^2 d$. Thus, the process is sensitive to Δs. The relevant processes in W^+ production are obtained by substituting antiquarks for quarks. Note that the polarized gluon distribution Δg is also undetermined and has a large uncertainty. The Δs sensitivity is determined by the balance between the $\Delta s' \cdot g$ and $\Delta g \cdot s'$ processes.

The longitudinal single spin asymmetry is defined by

$$A_L^{W^{\pm}} \equiv \frac{[d\sigma_+ - d\sigma_-]/dp_T dy_W}{[d\sigma_+ + d\sigma_-]/dp_T dy_W} = \frac{d\Delta\sigma/dp_T dy_W}{d\sigma/dp_T dy_W}, \tag{1}$$

where $d\sigma_{+(-)}$ is the spin-dependent differential cross section with positive (negative) helicity for the incident proton, and p_T and y_W are the transverse momentum and the rapidity of $W^{\pm}$ boson, respectively.

We show the rapidity distribution of the spin asymmetry for W^- production at $\sqrt{s} = 500\,\mathrm{GeV}$ in Fig. 1, where p_T is integrated over the range: $2\,\mathrm{GeV} < p_T < 50\,\mathrm{GeV}$. For numerical calculations, we used the AAC[2] and GRV[3] parametrizations for the polarized and unpolarized PDFs, respectively. The energy scale Q^2 in PDFs is set as squared $W^{\pm}$ boson mass M_W^2, and the charm quark mass is 1.2 GeV. The unpolarized and polarized total cross sections are calculated as $\sigma \approx 4.29\,\mathrm{pb}$ and $\Delta\sigma \approx 1.11\,\mathrm{pb}$.

As mentioned above, there are two processes, $\Delta g \cdot s'$ and $\Delta s' \cdot g$, in terms of partonic initial states. In Fig. 1, the dashed line represents the contribution of the $\Delta g \cdot s'$ process to the asymmetry, while the dot-dashed line shows that of the $\Delta s \cdot g$ process. The bold line represents the total asymmetry given by the sum of the two contributions.

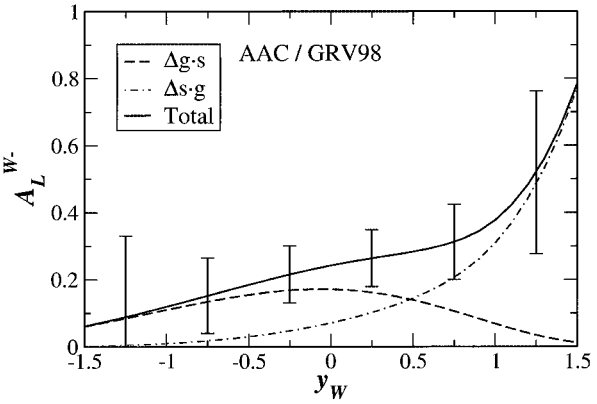

Fig. 1. Single spin asymmetry for W^- production with expected statistical errors at $\sqrt{s} = 500\,\mathrm{GeV}$ and $\mathcal{L} = 800\,\mathrm{pb}^{-1}$.

We can see that the $\Delta g \cdot s'$ process dominates in backward region ($y_W \ll 0$), whereas the $\Delta s' \cdot g$ dominates in forward region ($y_W \gg 0$), which implies that it is potentially possible to separate Δs from Δg. Moreover, the asymmetry in forward region is markedly large. However, there is a large contribution from the valence d quark distribution in the region, even though the process associated with the d quark is suppressed by the CKM parameter. W^+ production might be a promising way to access the Δs distribution through the process $\Delta\bar{s}'(\Delta g) + g(\bar{s}') \to W^+ + \bar{c}$, since the contribution from the $\bar{d}$ quark distribution is negligible.

The expected statistical errors in Fig. 1 are estimated using the designed values of the beam polarization ($P = 70\%$), the integrated luminosity ($\mathcal{L} = 800\,\mathrm{pb}^{-1}$), and the reconstruction efficiency ($\varepsilon = 10\%$), together with the unpolarized total cross sections. The error bars are large due to the small cross section. Even if ε is overestimated, the sign of Δs might be determined. These processes will provide a method of directly measuring the polarized strange quark distribution at RHIC.

References

1) For example, G. Bunce, N. Saito, J. Soffer, and W. Vogelsang: Annu. Rev. Nucl. Part. Sci. **50**, 525 (2000), and references therein.
2) Asymmetry Analysis Collaboration, Y. Goto et al.: Phys. Rev. D **62**, 034017 (2000).
3) M. Glück, E. Reya, and A. Vogt: Eur. Phys. J. C **5**, 461 (1998).

* Department of Physics, Hiroshima University

Hydrodynamic afterburner for the color glass condensate at RHIC†

T. Hirano*1 and Y. Nara*2

There has been several important findings in relativistic heavy ion collisions at BNL-RHIC:[1] (1) The relative yield of produced hadrons suggests the chemical equilibrium of the system; (2) The large magnitude of v_2 is consistent with ideal hydrodynamic calculations in the low p_T region; (3) Suppression in single hadron spectra and disappearance of the away-side peak in di-hadron spectra at high p_T indicate that semi-hard jets lose their energies while traversing a dense (possibly partonic) medium; and (4) The centrality dependence of particle yields is consistent with the Color Glass Condensate (CGC) picture. However, four distinct models are invoked for analysis of these data respectively. Each model has its intrinsic parameters for reproducing the data. Therefore, it is of particular importance to unify these approaches to achieve a comprehensive understanding of the dynamics in relativistic heavy ion collisions and to make a case for the discovery of the new state of matter, the quark gluon plasma. We have already combined three of the above approaches into a dynamical model.[2–4] Along the lines of these studies, we describe the initial stages in heavy ion collisions by employing the CGC picture and consider the resultant produced gluon distribution as an initial condition of the sequential hydrodynamic evolution.

As a first trial, we employ the simplest approach to the CGC as proposed by Kharzeev, Levin and Nardi (KLN).[5,6] The gluon distribution in the CGC collisions at the transverse point x_T can be represented by the k_T factorization formula

$$\frac{dN_g}{d^2x_\perp dy} = \frac{4\pi^2 N_c}{N_c^2-1}\int \frac{d^2p_T}{p_T^2} \cdot \int d^2k_T \alpha_s \phi_A(x_1, k_T^2; x_\perp)\phi_B(x_2, (p_T-k_T)^2; x_\perp), \tag{1}$$

where $x_{1,2} = p_T \exp(\pm y)/\sqrt{s}$, and y and p_T are the rapidity and the transverse momentum of the produced gluon respectively. For the unintegrated gluon distribution, we parametrize

$$\phi_A(x, k_T^2; x_\perp) = \begin{cases} \frac{\kappa C_F}{2\pi^3 \alpha_s(Q_s^2)} \frac{Q_s^2}{Q_s^2+\Lambda^2}, & k_T \le Q_s, \\ \frac{\kappa C_F}{2\pi^3 \alpha_s(Q_s^2)} \frac{Q_s^2}{k_T^2+\Lambda^2}, & k_T > Q_s, \end{cases} \tag{2}$$

where $C_F = (N_c^2-1)/(2N_c)$, Q_s is a saturation scale and κ is an adjustable parameter which controls the magnitude of multiplicity. The energy density distribution at an initial time τ_0, which is to be an initial condition of hydrodynamic simulations, can be obtained from Eqs. (1) and (2) on the basis of the assumption of free streaming for produced gluons in the longitudinal direction $\eta_s = y$, where η_s is a space-time rapidity. In Fig. 1, the pseudorapidity distributions of charged hadrons in Au + Au collisions at $\sqrt{s_{NN}} = 200\,\mathrm{GeV}$ are compared with the PHOBOS data.[7] The impact parameters in the hydrodynamic simulations are, from top to bottom, 2.4, 4.5, 6.3, 7.9, and 9.1 fm which are evaluated from the average number of participants at each centrality estimated using the PHOBOS data.[7] We reproduce the rapidity and centrality dependences of multiplicity very well within this hybrid approach. Therefore, the KLN k_T factorization approach in the CGC provides very good initial conditions for the hydrodynamic simulations. In summary, we have developed a dynamical model for the description of the time evolution of highly dense matter created in heavy ion collisions, on the basis of the CGC and the hydrodynamic evolution. We have shown that hydrodynamic simulations using the CGC initial conditions describe the rapidity and centrality dependences of charged hadron multiplicity at RHIC.

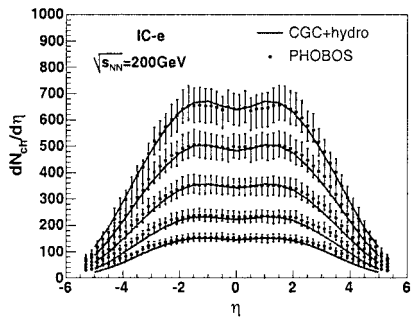

Fig. 1. Pseudorapidity distribution of charged particle in Au+Au collisions at $\sqrt{s_{NN}} = 200\,\mathrm{GeV}$

References

1) Proc. 17th Int. Conf. Ultrarelativistic Nucleus-Nucleus Collisions, Quark Matter 2004; J. Phys. G **30**, S633 (2004).
2) T. Hirano and K. Tsuda: Phys. Rev. C **66**, 054905 (2002).
3) T. Hirano and Y. Nara: Phys. Rev. C **66**, 041901(R) (2002).
4) T. Hirano and Y. Nara: Phys. Rev. C **69**, 034908 (2004).
5) D. Kharzeev and M. Nardi: Phys. Lett. B **507**, 121 (2001).
6) D. Kharzeev and E. Levin: Phys. Lett. B **523**, 79 (2001).
7) B. B. Back et al.: Phys. Rev. Lett. **91**, 052303 (2003).

† Condensed from the article in Nucl. Phys. A **743**, 305 (2004)

*1 Department of Physics, Columbia University, USA
*2 Institute für Theoretische Physik, Johann Wolfgang Goethe Universität, Germany

Global analysis of nuclear data on structure functions F_2^A and Drell-Yan processes

M. Hirai,[*1] S. Kumano,[*2] and T.-H. Nagai[*2]

Unpolarized parton distribution functions (PDFs) in the nucleon have been investigated for a long time, and they are established from small x to large x. However, their nuclear modifications are not investigated extensively. On the other hand, it is important to know the modifications accurately, for example, in heavy-ion and neutrino reactions for finding quark-gluon plasma signatures and neutrino oscillations, respectively.

We proposed optimum PDFs in nuclei by analyzing nuclear structure function ratios in 2001.[1] It was the first attempt to obtain the nuclear PDFs by a χ^2 analysis of high-energy scattering data. In the 2004 version,[2] we included Drell-Yan data in the analysis and also studied uncertainties of the nuclear PDFs. Here, we discuss the recent results.[2]

The nuclear PDFs are expressed by the nucleonic ones multiplied by weight functions w_i:

$$f_i^A(x,Q_0^2) = w_i(x,A)\, f_i(x,Q_0^2). \tag{1}$$

The initial scale Q_0^2 is taken as Q_0^2=1 GeV^2. We consider modifications for valence-quark, antiquark, and gluon distributions: w_{u_v}, w_{d_v}, $w_{\bar{q}}$, and w_g. They are expressed by parameters:

$$w_i(x,A) = 1 + \left(1 - \frac{1}{A^\alpha}\right) \frac{a_i + b_i x + c_i x^2 + d_i x^3}{(1-x)^{\beta_i}}. \tag{2}$$

In the recent analysis,[2] α and β_i are fixed at $\alpha = 1/3$ and β_{u_v}=β_{d_v}=$\beta_{\bar{q}}$=β_g=0.1. The parameters a_i, b_i, c_i, and d_i are determined by a χ^2 fit to the experimental data on F_2 structure-function and Drell-Yan cross-section ratios. The total χ^2 is defined by

$$\chi^2 = \sum_j \frac{(R_j^{data} - R_j^{theo})^2}{(\sigma_j^{data})^2}, \tag{3}$$

where R_j indicates a ratio $F_2^A/F_2^{A'}$ or $\sigma_{DY}^{pA}/\sigma_{DY}^{pA'}$, and σ_j^{data} is an experimental error which is calculated by $(\sigma_j^{data})^2 = (\sigma_j^{sys})^2 + (\sigma_j^{stat})^2$. The parametrized distributions are evolved to each experimental Q^2 point by the standard DGLAP evolution equations. Uncertainties of the obtained nuclear PDFs are calculated by the Hessian method:

$$[\delta f^A(x)]^2 = \Delta\chi^2 \sum_{i,j} \left(\frac{\partial f^A(x,\xi)}{\partial \xi_i}\right)_{\xi=\hat{\xi}} \times H_{ij}^{-1} \left(\frac{\partial f^A(x,\xi)}{\partial \xi_j}\right)_{\xi=\hat{\xi}}, \tag{4}$$

where H_{ij} is the Hessian matrix, ξ indicates a parameter set, and $\hat{\xi}$ is the optimum one.

The numbers of F_2 and Drell-Yan data are 899 and 52, respectively, so that the total number is 951. By the χ^2 analysis, we obtain $\chi^2_{min}/d.o.f.$ = 1.58. Typical results are shown for the calcium nucleus in Fig. 1, where the weight functions w_{u_v} (=w_{d_v}), $w_{\bar{q}}$, and w_g are shown at Q^2=1 GeV^2 with their uncertainties. The solid curves are the optimum functions and shaded areas indicate one-σ error ranges.

We find that the valence-quark distributions are well determined by the F_2 data at medium x together with baryon-number and charge conservations. The antiquark distribution is also well determined at small x; however, the uncertainties are large in the medium- and large-x regions. The large uncertainties in w_g suggest that it should be difficult to find the gluon modification in the whole x region. Because the nuclear PDFs are not well investigated, we need further efforts to reduce the uncertainties.

From the analysis results, we proposed nuclear PDFs from the deuteron to a heavy nucleus. A code is available on our web site[2] for calculating the nuclear PDFs at given x and Q^2.

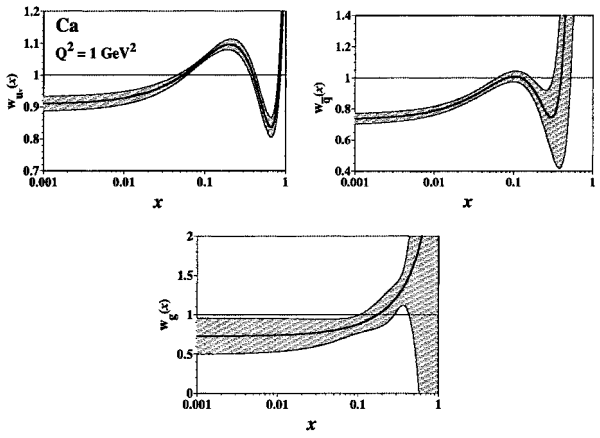

Fig. 1. Modifications of valence, antiquark, and gluon distributions at Q^2=1 GeV^2 in the calcium nucleus.[2]

References

1) M. Hirai, S. Kumano, and M. Miyama: Phys. Rev. D **64**, 034003 (2001).
2) M. Hirai, S. Kumano, and T.-H. Nagai: Phys. Rev. C **70**, 044905 (2004); The NPDF code could be obtained from http://hs.phys.saga-u.ac.jp/nuclp.html.

*1 Institute of Particle and Nuclear Studies, High Energy Accelerator Research Organization (KEK)
*2 Department of Physics, Saga University

Tau polarization in oscillation experiment

M. Aoki,[*1] K. Hagiwara,[*1] K. Mawatari,[*2] and H. Yokoya[*3]

The CNGS project[1] will start in 2006. The project includes two long baseline neutrino oscillation experiments, ICARUS and OPERA. These experiments mainly aim to detect ν_τ which originates from ν_μ through oscillation, propagating from CERN to Gran Sasso in Italy over a distance of 732 km. ν_τ appearance becomes the direct evidence for a three-flavor oscillation scenario. ν_τ is detected through the τ production by charged current interaction. The produced τ, however, decays into several particles immediately. Therefore, it is practically important to observe the decay particle distributions from τ leptons. It is well known that the τ decay distributions significantly depend on the spin polarization, and therefore it is necessary to obtain information on the spin polarization of τ to simulate the realistic decay particle distributions as the observables.

We calculated the polarization vector of τ, as well as the cross section, for the τ production by charged-current neutrino-nucleon scattering[2]:

$$\nu_\tau(\bar{\nu}_\tau) + N \to \tau^-(\tau^+) + X. \tag{1}$$

Quasi-elastic scattering (QE) and Δ-resonance production (RES) are taken into account as identifiable exclusive processes, and we put all other processes inclusively together into the deeply inelastic scattering (DIS) process. The polarization vector has three-dimensional space-like components,

$$\vec{s} = \frac{P}{2}(\sin\theta_P \cos\varphi_P, \sin\theta_P \sin\varphi_P, \cos\theta_P), \tag{2}$$

in the rest frame of τ. P denotes the degree of polarization, which takes 1 for the fully polarized τ and 0 for unpolarized τ. The polarization vector and cross section of τ production are expressed in terms of the charged current structure functions and these functions can be calculated separately for each process. For the QE and RES processes, the form factors of the transition current are known, and for DIS we attempted the tree level calculation of a parton model. During this study, we learned that for the τ production process, the pseudoscalar form factors of the QE and RES processes make a large contribution to both the cross section and polarization, while they make negligibly small contributions for light lepton production.[3]

The obtained τ^- polarizations are shown in the $p_\tau \cos\theta - p_\tau \sin\theta$ plane in Fig. 1. The incoming neutrino energies are fixed to 10 GeV. The gray line shows the kinematical boundary of the phase space and corresponds to the region of the QE process. The contour map denotes the DIS cross section, and between the regions of the QE and DIS processes, the RES process region stands. The vectors in each phase space are the τ^- polarization vectors in the rest frame of τ^- with the direction shown with respect to the scattering angle. We found that both τ^- and τ^+ have large polarization, but that the spin direction varies widely with the energy and scattering angle.

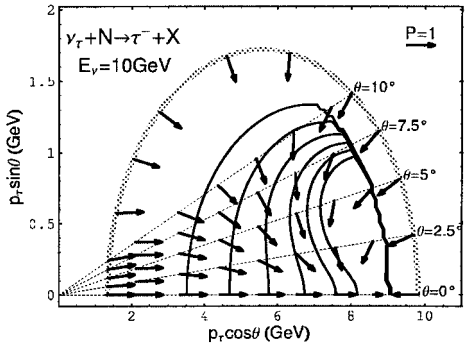

Fig. 1. Contour map of DIS cross section for τ^- production at $E_\nu = 10$ GeV. Polarization vectors are shown by arrows, where the arrow length gives the degree of polarization, and the direction denotes that of in the rest frame of τ with respect to the scattering angle.

To simulate the decay particle distribution through τ, the decay distribution function including the τ polarization is also needed. It has been well investigated for most of the major decay modes analytically and also numerically through experiments.[4] We will soon report on the analysis on the decay particle distribution for CNGS experiments, and its dependence on the τpolarization. Furthermore, in future high-energy neutrino oscillation experiments, τ will be produced in large quantities and the τ decay into e or μ will become a significant background which needs to be clarified in detail.

*1 Theory Group, High Energy Accelerator Research Organization (KEK)
*2 Graduate School of Science and Technology, Kobe University
*3 Department of Physics, Hiroshima University

References

1) The CNGS Project: see *e.g.* http://proj-cngs.web.cern.ch/.
2) K. Hagiwara, K. Mawatari, and H. Yokoya: Nucl. Phys. B **668**, 364 (2003); Erratum-Nucl. Phys. B **701**, 405 (2004).
3) K. Hagiwara, K. Mawatari, and H. Yokoya: Phys. Lett. B **591**, 113 (2004).
4) S. Jadach, Z. Was, R. Decker, and J. H. Kuehn: Comput. Phys. Commun. **76**, 361 (1993).

Density matrix renormalization group in a two-dimensional $\lambda\phi^4$ Hamiltonian lattice model†

T. Sugihara

Hamiltonian diagonalization is a useful method for nonperturbative analysis of many-body quantum systems. If the Hamiltonian is diagonalized, the system can be analyzed nonperturbatively at the amplitude level using the obtained wave functions.[1,2] In addition, one can discuss associated symmetry based on operator algebra.[3,4] However, in general quantum field theories, this method does not work without reducing degrees of freedom, because the dimension of the Hamiltonian increases exponentially as the system size becomes large. There is a severe limitation on numerical diagonalization of the Hamiltonian. To apply the method to quantum field theories, we need to find a way to remove unimportant degrees of freedom and create a small number of optimum basis states.

Wilson's numerical renormalization group in the Kondo problem was a successful consideration along this line.[5] To analyze chain models other than the Kondo Hamiltonian, White proposed the density matrix renormalization group (DMRG) as an extension of the Wilson's method.[6,7] With DMRG, the calculation accuracy of the target state can be controlled systematically using density matrices. White calculated the energy spectra and wavefunctions of Heisenberg chains composed of more than 100 sites using a standard workstation. The DMRG analysis of a 100-site $S = 1/2$ chain corresponds to diagonalization of the Hamiltonian with $2^{100} \sim 10^{30}$ dimensions. DMRG has been applied to various one-dimensional models, such as the Kondo, Hubbard, and t-J chain models, and has achieved great success. A two-dimensional Hubbard model has also been studied with DMRG in both real- and momentum-space representation.[8] DMRG works well on small two-dimensional lattices and new techniques have been proposed for larger lattices. DMRG has also been extended to finite-temperature chain models using the transfer-matrix technique.[9–13] In particle physics, the massive Schwinger model has been studied using DMRG to confirm the well-known Coleman's picture of half-asymptotic particles at a background field $\theta = \pi$.[14] It would be interesting to explore the possibility of applying DMRG to quantum chromodynamics (QCD) in order to study color confinement and spontaneous chiral symmetry breaking based on vacuum wavefunctions.

In fermionic lattice models, the number of particles contained in each site is limited because of the Pauli principle. In contrast, in bosonic lattice models, each site can in principle contain an infinite number of particles. It is not evident whether Hilbert space can be described appropriately with a finite set of basis states in bosonic models. This point becomes crucial when DMRG is applied to gauge theories, because gauge particles are bosons. Before working in lattice gauge theories, we need to test DMRG in a simple bosonic model and recognize how many basis states are necessary for each site to reproduce accurate results.

In this paper, we apply DMRG to a $\lambda\phi^4$ model with (1+1) space-time dimensions. We define a Hamiltonian model on a spatial lattice (only space is discretized) because DMRG is a method based on Hamiltonian formalism. Spontaneous breakdown of discrete Z_2 symmetry is studied numerically using vacuum wavefunctions. We obtain the critical coupling $(\lambda/\mu^2)_{\rm c} = 59.89 \pm 0.01$ and the critical exponent $\beta = 0.1264 \pm 0.0073$, which are consistent with the Monte Carlo[15] $(\lambda/\mu^2)_{\rm c} = 61.56^{+0.48}_{-0.24}$ and the exact[16] $\beta = 0.125$ results, respectively. Our results are based on extrapolation to the continuum limit with lattice sizes $L = 250, 500$, and 1000. The largest lattice size $L = 1000$ is approximately twice that of the latest Monte Carlo lattice size.[15] It is shown that the lattice size $L = 500$ is sufficiently close to the limit $L \to \infty$.

† Condensed from the article in JHEP **0405**, 007 (2004)

References

1) K. Harada, T. Sugihara, M. Taniguchi, and M. Yahiro: Phys. Rev. D **49**, 4226 (1994); T. Sugihara, M. Matsuzaki, and M. Yahiro: Phys. Rev. D **50**, 5274 (1994); T. Sugihara: Phys. Rev. D **57**, 7373 (1998); T. Sugihara and M. Taniguchi: Phys. Rev. Lett. **87**, 271601 (2001).
2) T. Sugihara: Nucl. Phys. B (Proc. Suppl.) **108**, 267 (2002).
3) N. Sakai and M. Sakamoto: Nucl. Phys. B **229**, 173 (1983).
4) P. Fendley, K. Schoutens, and J. de Boer: Phys. Rev. Lett. **90**, 120402 (2003).
5) K. G. Wilson: Rev. Mod. Phys. **47**, 773 (1975).
6) S. R. White: Phys. Rev. Lett. **69**, 2863 (1992).
7) S. R. White: Phys. Rev. B **48**, 10345 (1993).
8) T. Xiang: Phys. Rev. B **53**, R10445 (1996); T. Xiang, J. Lou, and Z. Su: Phys. Rev. B **64**, 104414 (2001).
9) R. J. Bursill, T. Xiang, and G. A. Gehring: J. Phys., Condens. Matter **8**, L583 (1996).
10) X. Wang and T. Xiang: Phys. Rev. B **56**, 5061 (1997).
11) T. Xiang: Phys. Rev. B **58**, 9142 (1998).
12) N. Shibata: J. Phys. Soc. Jpn. **66**, 2221 (1997).
13) I. Peschel, X. Wang, M. Kaulke, and K. Hallberg: *Lecture Notes in Physics*, Vol.528 (Springer, Berlin, 1999).
14) T. Byrnes, P. Sriganesh, R. J. Bursill, and C. J. Hamer: Phys. Rev. D **66**, 013002 (2002).
15) W. Loinaz and R. S. Willey: Phys. Rev. D **58**, 076003 (1998).
16) L. Onsager: Phys. Rev. **65**, 117 (1944).

Impact parameter dependence in Balitsky-Kovchegov equation and Froissart bound

T. Ikeda and L. McLerran*

The impact parameter dependence of parton distribution functions is an old issue. Recently, it has been possible to study this issue quantitatively using the Balitsky-Fadin-Kuraev-Lipatov (BFKL) and Balitsky-Kovchegov (BK) evolution equations. The BFKL equation resums the leading Feynman diagrams in the form of a linear integrodifferential evolution equation for gluon density, and its solution grows exponentially with the rapidity Y, which violates unitarity at large Y values. This is due to the lack of that finite parton density, or the saturation effect. Thus, the BFKL equation is replaced by a nonlinear BK equation including such an effect, which reads

$$\partial_Y N_{\mathbf{xy}} = \int_{\mathbf{z}} K_{\mathbf{xyz}} \left(N_{\mathbf{xz}} + N_{\mathbf{zy}} - N_{\mathbf{xy}} - N_{\mathbf{xz}} N_{\mathbf{zy}}\right),$$

where $\int_{\mathbf{z}} \equiv \int d\mathbf{z}$, the BFKL kernel $K_{\mathbf{xyz}} \equiv \frac{\alpha_S N_c}{2\pi^2} \frac{(\mathbf{x}-\mathbf{y})^2}{(\mathbf{x}-\mathbf{z})^2(\mathbf{z}-\mathbf{y})^2}$, and $N_{\mathbf{xy}} \equiv N_Y(\mathbf{x},\mathbf{y})$ is the scattering amplitude of a quark (q)-antiquark ($\bar{q}$) dipole with a hadronic target. Here, α_S is the strong coupling constant, N_c is the number of colors, and $\mathbf{x}$ ($\mathbf{y}$) is the position of the q ($\bar{q}$) in the transverse space with respect to the center of the target; the dipole vector and impact parameter are defined as $\mathbf{r} = \mathbf{x} - \mathbf{y}$ and $\mathbf{b} = (\mathbf{x}+\mathbf{y})/2$, respectively. The nonlinear term in the r.h.s corresponds to the saturation term responsible for unitarity.

One of the most important issues in saturation physics, in which the BK equation plays an important role, is how fast the black disc radius R_{BD} in which N_Y saturates grows with Y. (We define R_{BD} as $N_Y(r, b = R_{BD}) = 0.5$). This is closely related to the problem of the Froissart bound,[1] that is, the total hadronic cross section is bounded by $\sim \ln^2 s/s_0$ with the energy $s \sim e^Y$. In the saturation regime, the total dipole-nucleus cross section is given by $\sigma \sim 2\pi R_{RB}^2$. If R_{BD} grows at most linearly with Y, the Froissart bound is saturated.

It has been known that a solution of the BK equation at high rapidities has a power law tail in the inverse impact parameter even if the initial distribution has an exponential falling tail and then violates the Froissart bound.[2] This power law tail at high rapidities originates from the long-range Coulomb force generated by an incoherent color source. It is, however, natural for such a long-range force to be screened in a confining theory such as QCD, and we regularize the BFKL kernel by introducing the screening mass scale λ[3]

$$K_{\mathbf{xyz}} \to K_{\mathbf{xyz}} e^{-\lambda|\mathbf{x}-\mathbf{z}|} e^{-\lambda|\mathbf{z}-\mathbf{y}|} \equiv \bar{K}_{\mathbf{xyz}} .$$

With the modified kernel $\bar{K}$ and the initial condition $N_0(r,b) = 1 - \exp(-(cr)^2/(1+cr)e^{-2\mu b})$, the exponential falling tail in the initial condition is found to be maintained at high rapidities as long as $\lambda \geq \mu/2$. Practically, this indicates that a good lowest order approximation should be generated if we ignore the impact parameter diffusion. Doing that, we obtain an equation local in the impact parameter

$$\partial_Y N_{r,b} = \int_{\mathbf{z}} \bar{K}_{\mathbf{xyz}} \left(N_{z-r,b} + N_{z,b} - N_{r,b} - N_{z-r,b} N_{z,b}\right), \quad (1)$$

where $N_{r,b} \equiv N_Y(r,b)$.

We solved numerically Eq. (1) with the parameters $\alpha_S = 0.2$, $N_c = 3$ and $c = 8\mu$. In Fig. 1, R_{BD} for various dipole sizes is plotted as a function of Y. We found that R_{BD} grows linearly with Y for both $\lambda = 0$ and μ, and consequently, the Froissart bound is saturated.[3] One might think it is a natural consequence of the local approximation ignoring the impact parameter diffusion. The important point, however, is that this linear growth of the black disc radius with Y is expected in the full BK equation if its kernel is regulated by the screening mass of gluons.

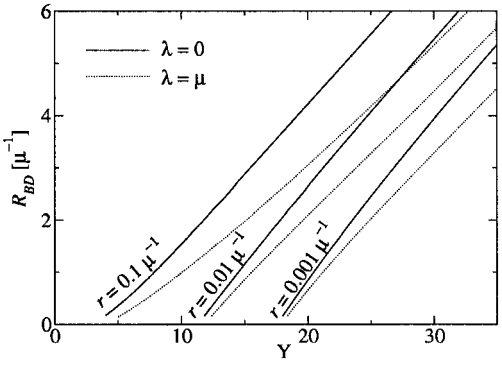

Fig. 1. R_{BD} for $\lambda = 0$ (solid lines) and μ (dotted lines) is plotted as a function of Y at $r = 0.1, 0.01$ and 0.001.

References
1) M. Forissart: Phys. Rev. **123**, 1053 (1961).
2) K. Golec-Biernat and A. M. Stasto: Nucl. Phys. B **668**, 345 (2003).
3) T. Ikeda and L. McLerran: hep-ph/0410345.

* Department of Physics, Brookhaven National Laboratory, USA

Soft modes at the QCD critical point in the chiral quark model

M. Ohtani and H. Fujii*

Theoretical studies of QCD thermodynamics have predicted rich phase structure in the plane of temperature T and the chemical potential for the baryon number. Experiments of high-energy heavy-ion collisions are now ongoing and planned in order to explore these new states of matter experimentally. Based on the lattice QCD as well as the effective model calculations, it is suggested that there exists a critical end point of the first-order transition line, which we call $\mathbb{Z}_2$CP to emphasize the symmetry aspect. Since it is a singular point, we expect to obtain clearer information of it from experiments.

The critical behavior associated with the $\mathbb{Z}_2$CP has been discussed in order to locate its position experimentally. We emphasize that at the $\mathbb{Z}_2$CP, the susceptibilities of the baryon number and energy densities as well as that of the scalar density diverge with the same strength (critical exponent), unlike at the critical point in the chiral limit. This is demonstrated by studying the Ginzburg-Landau (GL) effective potential.[1)] In the chiral limit, the order parameter is identified as the scalar density, and no linear coupling of the scalar density with the baryon number and energy densities can be allowed because of the chiral symmetry. In contrast, near the $\mathbb{Z}_2$CP, the fluctuations of these three densities can be mixed and the proper ordering density becomes a particular linear combination of them. The susceptibilities of these densities contain the singular component and show the same divergence at the $\mathbb{Z}_2$CP.

At a critical point, a soft mode emerges which has a time scale much slower than those of other modes. Here we discuss the soft mode associated with $\mathbb{Z}_2$CP, which causes the critical divergences.[1,2)] It is known that susceptibility χ, obtained in a q-limit of the response function $\chi(\omega, \boldsymbol{q})$, is related to a mode spectrum as

$$\chi = \lim_{\boldsymbol{q}\to 0} \chi(0, \boldsymbol{q}) = \lim_{\boldsymbol{q}\to 0} \frac{\mathcal{P}}{2\pi} \int_{-\infty}^{\infty} d\omega \ \frac{\rho(\omega, \boldsymbol{q})}{\omega} \qquad (1)$$

with the spectral function $\rho(\omega, \boldsymbol{q}) = 2\mathrm{Im}\chi(\omega, \boldsymbol{q})$. The critical divergence is caused by the unintegrable singularity in the integrand at $\omega = 0$ as $\boldsymbol{q} \to 0$.

We show the spectral density $\rho(\omega, \boldsymbol{q})$ of the scalar channel at $\mathbb{Z}_2$CP in the chiral quark model in Fig. 1. The quark-pair creation and annihilation contribute to the timelike spectrum while the spacelike spectrum stems from the Landau-damping-type process possible only in a medium. The gap seen between these two spectra is due to the nonzero quark mass. The divergence at the $\mathbb{Z}_2$CP is caused by the enhancement of the spacelike spectrum at the origin (Fig. 1). Corresponding to the critical enhancement near $\omega \sim 0$, we found a pole of the response function on the pure imaginary axis of the complex ω plane.

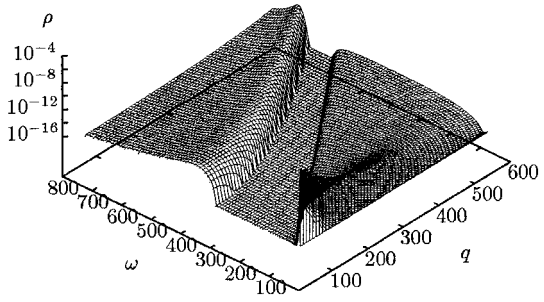

Fig. 1. Spectral function of the scalar channel at $\mathbb{Z}_2$CP.

The baryon number and energy densities are conserved quantities, and their fluctuations are hydrodynamic slow modes of the system. It is known that the fluctuation of a conserved quantity has the spectrum $\propto \delta(\omega)$ as $\boldsymbol{q} \to 0$, which means that it cannot oscillate at $\boldsymbol{q} = 0$. The divergence of their susceptibility can be caused only by the unlimited growth of the strength of this $\delta(\omega)$ spectrum as the critical point is approached. In fact, within the chiral quark model, we obtained the characteristic enhancement near $\omega \sim 0$ in the spectral density of the vector channel, which is related to the baryon number density. This leads us to an important conclusion: the critical slow mode at the $\mathbb{Z}_2$CP, which generates the divergences in the baryon number and energy susceptibilities, must have a hydrodynamic character. The critical mode spectrum seen in Fig. 1 appropriately possesses this property.

At $\mathbb{Z}_2$CP, the quark number and entropy susceptibilities are divergent, wherein only the hydrodynamic spectrum contributes. This means that extra softness or critical slowing of a hydrodynamic mode near $\mathbb{Z}_2$CP is required to give these divergences.

Phenomenological consequences of this observation should be elaborated more carefully, taking into account factors such as the finite size effect in space-time and approximate chiral symmetry. The spectral function in the chiral quark model used here does not satisfy the spectral condition, which also should be improved.

References

1) H. Fujii and M. Ohtani: Phys. Rev. D **70**, 014016 (2004).
2) H. Fujii: Phys. Rev. D **67**, 094018 (2003).

* Institute of Physics, University of Tokyo

Melting pattern of diquark condensates in quark matter†

K. Iida, T. Matsuura,* M. Tachibana, and T. Hatsuda*

Thermal color superconducting phase transitions in high density three-flavor (uds) quark matter are investigated in the Ginzburg-Landau (GL) approach. Effects of nonzero strange quark mass (m_s), electric and color charge neutrality, and direct instantons are considered. Weak coupling calculations show that an interplay between the mass and electric neutrality effects near the critical temperature gives rise to three successive second-order phase transitions as the temperature increases: a modified color-flavor locked (mCFL) phase (ud, ds, and us pairings) → a d-quark superconducting (dSC) phase (ud and ds pairings) → an isoscalar pairing phase (ud pairing) → a normal phase (no pairing). The dSC phase is novel in the sense that while all eight gluons are Meissner screened as in the mCFL phase, three out of nine quark quasiparticles are always gapless. The present anaysis is expected to give a plausible idea of what may occur in the strong coupling regime of physical interest continuously connected to the weak coupling regime.

We adopt the GL approach near the transition temperatures, which was previously used to study the massless three-flavor case.[1] In a realistic situation, the GL potential acquires the following corrections. First of all, nonzero m_s affects the GL potential through reduction in the Fermi momentum of s quarks in such a way as to lower the critical temperature of the pairing involving s quarks. Secondly, the chemical potential shift, $\delta\mu_i = -q_i\mu_e$ ($i = u, d, s$; μ_e: the electron chemical potential), for electrically neutral and beta-equilibrated system with a gas of electrons affects the GL potential so as to lower the critical temperature of the ij pairing with a smaller value of $(\delta\mu_i + \delta\mu_j)/2$. Thirdly, the instanton contribution gives an m_i dependence to the GL potential through the effective four fermion interaction. In the limit of weak coupling in which the diquark pairing arises in the most attractive color-flavor antisymmetric channel with $J^P = 0^+$,[2] the first and second corrections are of the same order, characterized by a small dimensionless parameter,

$$\sigma = \left(\frac{3\pi^2}{8\sqrt{2}}\right)\frac{m_s^2}{g\mu^2}, \tag{1}$$

where g is the color coupling constant, and μ is the quark chemical potential. In this limit the third correction is dominated over by the first and second corrections. We remark that the color neutrality makes negligible correction to the GL potential near the transition temperatures as shown in Ref. 1.

Figure 1 depicts the melting pattern of diquark condensates in weak coupling. We may understand the bifurcation of the transition temperatures as follows. In the massless case (a), T_c is degenerate between the CFL and 2SC phases, the chemical potential is common to all three flavors and colors, and the CFL phase is more favorable than the 2SC phase below T_c. As one goes from (a) to (b), the density of states of the s quarks at the Fermi surface is reduced. Then, the CFL phase becomes anisotropic in flavor space and has the critical temperature lowered. Eventually, the 2SC phase is allowed to appear at temperatures between T_c^s and T_c. As one goes from (b) to (c), the average chemical potential of ds (ud and us) quarks increases (decreases) since $\mu_e \simeq m_s^2/4\mu$. Accordingly, the transition temperatures further change from T_c to $T_c^{\rm III}$ and from T_c^s to $T_c^{\rm I}$ and $T_c^{\rm II}$. We remark that we have analyzed the melting pattern in the mean-field level. Effects of thermally fluctuating color magnetic fields[3] could change the melting pattern.

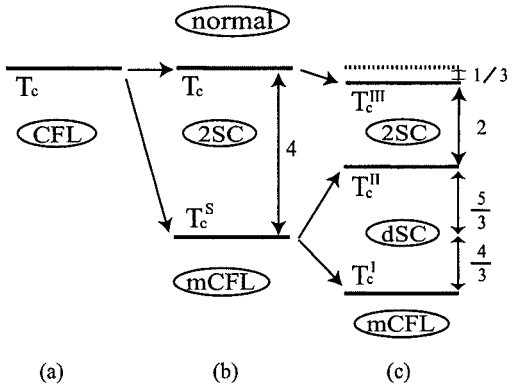

Fig. 1. Transition temperatures of the three-flavor color superconductor in weak coupling: (a) all quarks are massless; (b) nonzero m_s in the quark propagator is considered; (c) electric charge neutrality is further imposed. The numbers attached to the arrows are in units of σT_c.

References
1) K. Iida and G. Baym: Phys. Rev. D **63**, 074018 (2001); Phys. Rev. D **66**, 059903 (E) (2002).
2) W. E. Brown, J. T. Liu, and H. C. Ren: Phys. Rev. D **62**, 054016 (2000).
3) T. Matsuura, K. Iida, T. Hatsuda, and G. Baym: Phys. Rev. D **69**, 074012 (2004).

† Condensed from the article in Phys. Rev. Lett. **93**, 132001 (2004)

* Department of Physics, University of Tokyo

Linking the chiral and deconfinement phase transitions

Y. Hatta and K. Fukushima*

Lattice simulations of finite temperature quantum chromodynamics (QCD) have shown that the chiral phase transition in the chiral limit and the deconfinement phase transition in the quenched limit are continuously connected. In this report we propose a novel scenario which naturally explains this longstanding puzzle.

The deconfinement phase transition has a definite meaning only at an infinite quark mass. In SU(3) pure gluodynamics the transition is known to be of the first order. The expectation value of the Polyakov loop serves as an order parameter and jumps at the deconfinement transition temperature. The first-order phase transition persists at a finite but very large quark mass (solid curve in Fig. 1) and eventually terminates at a second-order phase transition point D where the Polyakov loop becomes massless.

In contrast, chiral symmetry is a true symmetry only at a zero quark mass. The order parameter of the chiral phase transition, the sigma field σ, becomes massless at the end point of the first-order transition C.

A priori, there seems to be no relationship between the chiral and deconfinement phase transitions. However, lattice simulations have revealed a very interesting interplay between the two. Figure 1 is the most commonly accepted phase diagram for QCD in the temperature-quark mass plane. T is the temperature and m is the quark mass. The solid (dotted) curve represents the first-order (crossover) phase transition. This figure shows that, for all values of the quark mass, there is a single (crossover) phase transition which smoothly connects the chiral phase transition in the chiral limit and the deconfinement phase transition in the quenched theory.

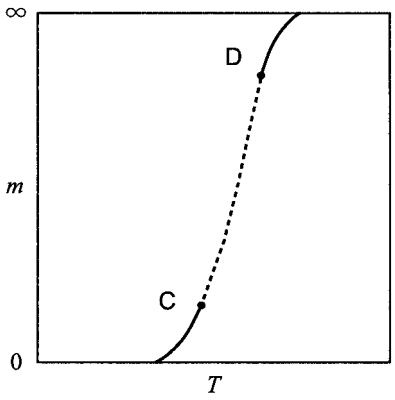

Fig. 1. The phase diagram in the (T, m) plane.

In order to understand this lattice result, first, we propose an alternative characterization of the deconfinement phase transition. We point out that, in the presence of dynamical quarks, the deconfinement phase transition can equivalently be characterized in terms of the glueball field G. Specifically, we have shown[1] that the screening mass of the 0^+ electric glueball vanishes at point D.

Next, we observe that the glueball field G must mix with the sigma field σ so that the correct massless field at D is a linear combination of the two:

$$\phi = G\cos\theta + \sigma\sin\theta, \qquad \sin\theta \approx 0. \tag{1}$$

The orthogonal linear combination with large sigma field content,

$$\phi' = -G\sin\theta + \sigma\cos\theta, \tag{2}$$

is massive. Now the key question concerns the behavior of the mixing angle θ as the quark mass varies. If the mixing angle remains small at small values of quark mass, the ϕ' field, which is massive at D, would become massless at C because the critical field at C is dominantly sigma-like. However, if this were the case, the coincidence of the two critical temperatures for all values of the quark mass would be a pure accident. Figure 1 is most naturally explained by postulating that the critical field at C is again the ϕ field. Namely, the two second-order phase transitions at C and D are driven by the same field. This is possible only if the mixing angle changes from $\theta \approx 0$ to $\approx \pi/2$. Such a continuous variation of the mixing angle is typical of a level repulsion in quantum mechanics. Thus, we have arrived at a novel scenario of the finite temperature QCD phase transition: Due to a level repulsion between the ϕ and the ϕ' fields, the ϕ field continues to be the lightest screening state for all values of quark mass. Simultaneous divergences and peaks in various susceptibilities are simply caused by the dropping of the ϕ field screening mass.

Moreover, we speculate that this scenario is realized at all temperatures. The level repulsion between the scalar glueball and the sigma meson already occurs at zero temperature, as one can easily convince oneself by considering the scalar meson and glueball mass spectrum at zero temperature. Therefore, our scenario can be naturally embedded in the entire phase diagram shown in Fig. 1.

Reference

1) Y. Hatta and K. Fukushima: Phys. Rev. D **69**, 097502 (2004).

* Center for Theoretical Physics, Massachusetts Institute of Technology, USA

Cut-off effects in meson spectral functions

T. Blum*1 and P. Petreczky*2

Temporal meson correlation functions in Euclidean time can be related to meson spectral functions by analytic continuation. Furthermore using the Maximum Entropy Method one can extract the spectral functions from meson correlators calculated on a finite lattice.[1)] The method was applied at zero[1,2)] as well as non-zero temperature.[3–6)] In such an analysis one usually uses all time slices in the correlation function not just the long distance part. Therefore one is sensitive to short distance physics which may be affected by lattice artifacts. The lattice distortion of the correlators at short distances translates into lattice artifacts in the spectral functions for large energies. So far only Wilson gauge action and Wilson (clover) fermion action have been used to study meson spectral functions. The lattice artifacts seen in numerical simulations for this combination of actions turns out to be quite different from what is expected in the free theory. Therefore we study cutoff effects of meson spectral functions using different gauge and fermion actions.

We consider the temporal correlators of local meson operators in the pseudo-scalar and vector channels. We use quenched domain wall fermion correlators on DBW2 gauge configurations from the RBC collaboration. Furthermore, we calculate tree-level clover fermion correlators on quenched 1-loop tadpole-improved Symanzik lattices and on partially-quenched 2+1 flavor Asqtad fermion lattices from the MILC collaboration. To extract the spectral function we use the Maximum Entropy Method. We also parameterize the spectral functions as a sum of delta functions $\sigma(\omega) = \sum_i F_i \delta(\omega^2 - m_i^2)$ and determine the parameters F_i and m_i using constrained curve fitting techniques[7)] which allows for better systematic control of the results.

We start the discussion of our numerical results with the case of domain wall fermions. Here we performed calculations at three different lattice spacings, $a^{-1} = 1.3, 2.0, 3.0\,\mathrm{GeV}$ and valance quark mass around the strange quark mass. For the coarsest lattice we see a two peak structure in the spectral functions with the second peak located around 2 GeV. The positions of the peaks are reasonably reproduced using a two exponential fit. For finer lattices we see a three peak structure. We find that the position of the first peak is independent of the lattice spacing, thus it is clearly correspond to a physical states (the η and ϕ mesons). The position of the second and third peaks on the other is shifted approximately as $1/a$ as the lattice spacing has been changed. Which means that these peaks are lattice artifacts. Similar results were found for the Wilson action.[1,2)] In Ref. 2 they were interpreted as bound states of Wilson doublers. For DWF, however, such an interpretation is more difficult to apply. We have also performed a constrained fit with three exponentials. The ground state mass was obtained from a simple unconstrained fit which was then used as a prior for the constrained fit. We have found a reasonable agreement between the MEM and constrained curve fits.

One may wonder whether the second and third peaks are artifacts of quenching. Absent dynamical quarks, all hadrons are absolutely stable (*i.e.* have zero width) no matter how large their mass is. The situation is different in full QCD where mesons can decay and the lattice artifacts may be absent. To check this we performed calculations in quenched and partially-quenched QCD using the clover action. More precisely we used gauge configurations with Symanzik action generated by the MILC collaboration as well the dynamical 2+1 Asqtad configurations. In both cases the lattice spacing was $a \approx 0.09\,fm$. We use the tree-level value for the clover coefficient, $c_{sw} = 1$, and $\kappa = 0.14$ which corresponds to $m_{PS}/m_V = 0.68$. We have found that the spectral functions for quenched and partially quenched QCD are very similar, indicating that for quark masses around the strange quark mass effects due to quenching are quite small.

References

1) Y. Nakahara et al.: Phys. Rev. D **60**, 091503 (1999); M. Asakawa et al., Prog. Part. Nucl. Phys. **46**, 459 (2001).
2) Yamazaki, et al.: Phys. Rev. D **65**, 014501 (2002).
3) F. Karsch, et al.: Phys. Lett. B **530**, 147 (2002).
4) T. Umeda et al.: hep-lat/0211003.
5) M. Asakawa and T. Hatsuda: Phys. Rev. Lett. **92**, 012001 (2004).
6) S. Datta, et al.: Phys. Rev. D **69**, 094507 (2004).
7) G. P. Lepage, et al.: Nucl. Phys. B (Proc. Suppl.) **106**, 12 (2002).

*1 Physics Department, University of Conneticuit, USA
*2 Physics Department, Brookhaven National Laboratory, USA

Matrix models and lattice simulations for QCD at nonzero density

T. Wettig*

QCD at nonzero density continues to be an important field of current research, in particular because of its relevance to RHIC physics. Nonperturbative studies of the theory by means of unquenched lattice simulations are extremely difficult because of the sign problem. Theoretical arguments[1] show that this sign problem can probably not be overcome by standard methods. It is therefore useful to study the theory using other approaches, *e.g.* low-energy effective theories or random matrix theory (RMT).

In last year's edition of RIKEN Accel. Prog. Rep., G. Akemann and I reported on quenched lattice simulations of QCD at nonzero chemical potential to test the predictions of a random eigenvalue model for the QCD Dirac operator.[2] Akemann's model was formulated and solved in Ref. 3, and the details of our work can be found in Ref. 4. We observed nice agreement between the theoretical predictions and the lattice data.

However, Akemann's model is different from an earlier random matrix model for QCD at nonzero density by Stephanov[5]. The virtue of Akemann's model was that it could be solved analytically for the universal spectral correlation functions of the QCD Dirac operator for which results were not available in Stephanov's model. However, after completion of our work, Splittorff and Verbaarschot[6] as well as Osborn[7] independently derived such results for Stephanov's model. Their results agree with each other but differ from those obtained by Akemann, although the numerical difference is very small.

Since Stephanov's model can be derived from the low-energy effective partition function of QCD at nonzero density, it is believed to provide a correct description of the full theory at sufficiently low energies. It is therefore important to show on the basis of lattice data that Stephanov's model, and not Akemann's, is the correct one. This is not completely trivial because the numerical difference between the results of the two models is so small. Furthermore, since the Dirac spectrum spreads into the complex plane, very high statistics (on the order of 20,000 configurations) is needed to obtain reasonably small error bars.

To be able to resolve the difference between the two models, we concentrate on the spectral density of the Dirac operator for small eigenvalues on the scale of the mean level spacing and consider a domain (sometimes called strong nonhermiticity) in which the results depend only on the absolute value of the Dirac eigenvalue. This allows us to obtain higher statistics by integrating over the phase of the eigenvalues. The corresponding result for Akemann's model is[3]

$$\rho_A(z) = \sqrt{2\pi u}\,|z|\exp(-u|z|^2)I_\nu(u|z|^2)\,, \qquad (1)$$

whereas for Stephanov's model one obtains[8]

$$\rho_S(z) = 2u|z|^2 K_\nu(u|z|^2)I_\nu(u|z|^2)\,. \qquad (2)$$

In both cases the scale is set by a parameter u, and the density is normalized such that the asymptotic value is unity. I and K denote Bessel functions, and the index ν is zero in our case[4].

In Fig. 1 we show fits of the same lattice data to these two equations. While both analytical results are in qualitative agreement with the data, Eq. (2) provides the better fit, which is apparent both by inspection and by the χ^2 values of the fits. We therefore conclude that the results derived in Refs. 6, 7 for Stephanov's model describe lattice data for the QCD Dirac operator at nonzero chemical potential at a quantitative level. Akemann's model, while providing results that are numerically very close to those obtained in Stephanov's model, appears to be ruled out by the lattice data.

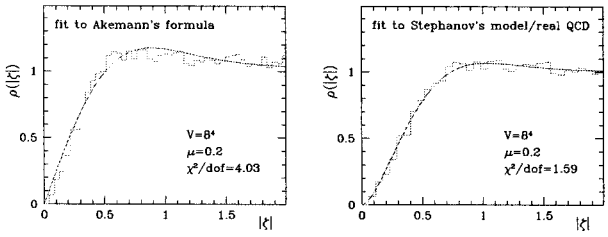

Fig. 1. Density of small Dirac eigenvalues as a function of the absolute value of the eigenvalue. The solid curves represent Eqs. (1) and (2), respectively, with $u = 1$. The histograms represent (identical) lattice data rescaled by the respective fit parameter u. The lattice simulations (20,000 configurations) were done at $\beta = 5.0$ and chemical potential $\mu = 0.2$.

References

1) M. Troyer and U.-J. Wiese: cond-mat/0408370.
2) G. Akemann and T. Wettig: RIKEN Accel. Prog. Rep. **37**, 211 (2004).
3) G. Akemann: Phys. Rev. Lett. **89**, 072002 (2002); J. Phys. A **36**, 3363 (2003).
4) G. Akemann and T. Wettig: Phys. Rev. Lett. **92**, 102002 (2004).
5) M. A. Stephanov: Phys. Rev. Lett. **76**, 4472 (1996).
6) K. Splittorff and J. J. M. Verbaarschot: Nucl. Phys. B **683**, 467 (2004).
7) J. C. Osborn: hep-th/0403131.
8) J. J. M. Verbaarschot: hep-th/0410211, Eq. (481).

* Institute for Theoretical Physics, University of Regensburg, Germany

Two-particle wave function with four-dimension Ising model

T. Yamazaki

The calculation of the scattering phase shift of hadrons is important in understanding a strong interaction. The phase shift in the $I = 2\,\pi\pi$ scattering system[1] was evaluated in lattice QCD with the finite volume method.[2,3] A two-particle wave function plays an important role in the scattering system, because the phase shift can be extracted from the wave function. Recently, Ishizuka and Yamazaki and Aoki *et al.* have numerically studied the wave function in the $I = 2\,\pi\pi$ scattering system.[4] They extracted the scattering length and scattering effective potential from the wave function only for the two-pion ground state. Here, we attempt to calculate the wave functions of the first excited and unstable states in a four-dimensional simple Ising model.[5] We also attempt to evaluate the phase shift from these wave functions.

The wave function $\phi(\vec{r})$ satisfies the Helmholtz equation[2,3] $(\nabla^2 + p^2)\phi(\vec{r}) = 0$ in $r > R$, where $\vec{r}$ is the relative coordinate of two particles and p is the relative momentum. R is the effective range where the effective scattering potential becomes sufficiently small in the exterior region of R. The general solution of the Helmholtz equation in a finite volume under periodic boundary conditions is given by

$$G(\vec{r}) = (1/L^3)\sum_{\vec{k}} e^{i\vec{k}\cdot\vec{r}}/(\vec{k}^2 - p^2) \quad (\vec{r} \neq 0) \qquad (1)$$

where $\vec{k} = (2\pi/L)\cdot\vec{n}$ with $\vec{n}$ being an integer vector. We can extract p^2 by fitting $\phi(\vec{r})$ in $r > R$ with $G(\vec{r})$, and then evaluate the phase shift with the finite volume method.

Our employed model is a simple model where the coupling of a low-mass field (π) to a high-mass field (σ) with three-point coupling is considered. We perform the simulation on the lattice size $L^3 \times T = 20^3 \times 64$ with a large number of configurations, 405×10^3. We calculate three- and four-point functions, $F_i(\vec{r},t) = \langle 0|\mathcal{W}(\vec{r})[\mathcal{O}_i(t) - \mathcal{O}_i(t+1)]|0\rangle$ and $C_{ij}(t) = \langle 0|\mathcal{O}_i(0)[\mathcal{O}_j(t) - \mathcal{O}_j(t+1)]|0\rangle$ for $i,j = 0,1$ and σ, in order to obtain the wave functions. The operators $\mathcal{O}_i(t)$ represent the $\pi\pi$ operator with $p = 0, 2\pi/L$ and the σ operator ($i = \sigma$). The wave function operator $\mathcal{W}(\vec{r})$ is defined by $\mathcal{W}(\vec{r}) = (1/L^3)\sum_{\vec{X}} \pi(\vec{r}+\vec{X})\pi(\vec{X})$. The subtraction $[\mathcal{O}_i(t) - \mathcal{O}_i(t+1)]$ is performed to eliminate the vacuum contribution.

The wave function is defined by $\phi_\alpha(\vec{r}) = \langle 0|\mathcal{W}(\vec{r})|\alpha\rangle$ for the $\alpha = 0,1$ and σ states. Using $\phi_\alpha(\vec{r})$ and overlap $V_{\alpha i} = \langle\alpha|\mathcal{O}_i|0\rangle$, one can calculate $F_i(\vec{r},t) = \sum_\alpha \phi_\alpha(\vec{r})\Delta_\alpha(t)V_{\alpha i}$ and $C_{ij}(t) = \sum_\alpha V^t_{i\alpha}\Delta_\alpha(t)V_{\alpha j}$, where $\Delta_\alpha(t) = (1-e^{-E_\alpha})\,e^{-E_\alpha t} + (1-e^{E_\alpha})\,e^{-E_\alpha(T-t)}$. The overlaps and energies are extracted by the diagonalization method.[6] The wave function $\phi_\alpha(\vec{r})$ is evaluated except the normalization through the appropriate projection $\phi_\alpha(\vec{r}) = \sum_i F_i(\vec{r},t)V^{-1}_{i\alpha}$. In this analysis, we assume that contributions for higher energy states are negligible in the correlation functions.

The fitting of $\phi_\alpha(\vec{r})$ is carried out by assuming the effective ranges $R = 7, 9$ and 8 for the $\alpha = 0, 1$ and σ states. Two fitting parameters correspond to an overall constant of Eq. (1) and the relative momentum p^2. Figure 1 shows the fitting result $G_\alpha(r)$ for each state. The results for all states are consistent with $\phi_\alpha(r)$. This figure illustrates that the wave function in $r > R$, even for the σ state, can be described by the general solution of the Helmholtz equation.

We determine the relative momentum p^2 by two methods in order to calculate the phase shift. The relative momentum p^2 can be evaluated from the wave function. Alternatively, p^2 can be given by the relation $E_\alpha = 2\sqrt{m^2 + p^2}$. Table 1 shows the results obtained by both methods for comparison. It is clear that the results obtained by both methods are reasonably consistent with each other. The results obtained by the former method for the ground and first excited states have smaller errors than those of the latter method. As for the σ state, however, the former method yields a relatively larger error. The reason for this opposite trend is not well understood at present. To clarify this feature, a more detailed study is required particularly for the calculation of the wave function of the σ state.

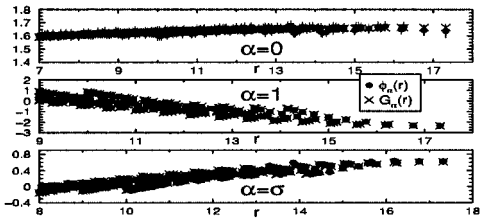

Fig. 1. Fitting result of wave functions.

Table 1. Scattering phase shift (degrees) obtained from wave function and energy.

state	0	1	σ
wave function	−1.48(31)	−15.0(1.1)	39.8(4.9)
energy	−1.96(63)	−14.0(2.1)	47.8(1.2)

References

1) CP-PACS Collaboration, S. Aoki et al.: Phys. Rev. D **67**, 014502 (2003); CP-PACS Collaboration, T. Yamazaki et al.: Phys. Rev. D **70**, 074513 (2004); C. Kim: Nucl. Phys. B (Proc. Suppl.) **129**, 197 (2004).
2) M. Lüscher: Commun. Math. Phys. **105**, 153 (1986).
3) M. Lüscher: Nucl. Phys. B **354**, 531 (1991).
4) N. Ishizuka and T. Yamazaki: Nucl. Phys. B (Proc. Suppl.) **129**, 233 (2004); CP-PACS Collaboration, S. Aoki et al.: hep-lat/0409063.
5) T. Yamazaki: hep-lat/0409099.
6) M. Lüscher and U. Wolff: Nucl. Phys. B **339**, 222 (1990).

Penta-quark baryon in anisotropic lattice QCD

N. Ishii,[*1] T. Doi, H. Iida,[*1] M. Oka,[*1] F. Okiharu,[*2] and H. Suganuma[*1]

The LEPS group at SPring-8[1)] has discovered a narrow resonance Θ^+, with a mass of 1.54(1) GeV and a width smaller than 25 MeV. This resonance has baryon number +1, charge +1 and strangeness +1. Hence, its simplest configuration is $uudd\bar{s}$, *i.e.*, a manifestly exotic penta-quark (5Q) state. After this discovery, many experiments have confirmed the LEPS results where neither spin or parity was determined. On the other hand, a few experiments have reported null results. Therefore, further studies from both experimental and theoretical viewpoints are required concerning its existence and quantum number, particularly, its parity.

In this report, we study the 5Q baryon Θ^+ using lattice QCD, which is a direct nonperturbative calculation from QCD. Although there have been several lattice QCD studies of 5Q,[2–6)] they have not yet reached a consensus, *i.e.*, Refs. 2, 3, and 6 claimed the existence of 5Q resonance in negative parity, whereas Ref. 4 claimed its existence in positive parity. Ref. 5 reported observation of no evidence for narrow resonances. Under these circumstances, we perform high-precision analysis for the 5Q state with the quenched anisotropic lattice QCD. We generate 504 gauge configurations using the standard Wilson gauge action at $\beta = 5.75$ ($a_s^{-1} = 1.1\,\mathrm{GeV}$) on the $12^3 \times 96$ lattice with the renormalized anisotropy $a_s/a_t = 4$. The $O(a)$-improved Wilson quark (clover) action is employed with hopping parameters as $\kappa = 0.1210$–0.1240, where $\kappa_s = 0.1240$ fixed for an s quark, and $\kappa = 0.1210$–0.1240 for u and d quarks. This corresponds to $m_\pi/m_\rho = 0.81$–0.65. We consider a non-NK-type operator for 5Q with $J = 1/2$, $I = 0$ as $O \equiv \epsilon_{abc}\epsilon_{ade}\epsilon_{bfg}\left(u_d^T C\gamma_5 d_e\right)\left(u_f^T C d_g\right)\left(C\bar{s}_c^T\right)$, as an attempt to reduce the overlap with the NK scattering state. This is a crucial difference from Ref. 5, in which a simple NK operator was adopted. To enhance the low-lying spectra, we adopt a smeared source with the gaussian size $\rho \simeq 0.4\,\mathrm{fm}$. For details, see Ref. 7.

We first study the effective mass in both parity channels, where parity projection is performed with $P_\pm \equiv (1 \pm \gamma_4)/2$. For both parity channels, we find plateaus and perform the single-exponential fit. At each κ, we observe that the positive-parity state is much more massive than the negative-parity state. After the chiral extrapolation, the positive-parity state is determined at $m_{5Q} \simeq 2.25\,\mathrm{GeV}$, which is too massive to be identified with the experimentally observed Θ^+. The negative-parity state is found at $m_{5Q} \simeq 1.75\,\mathrm{GeV}$, which is rather close to the empirical value.

In order to identify whether the negative-parity state is a compact 5Q state or just an NK scattering state, we propose the hybrid boundary condition (HBC) method. In this method, we impose the spatial BC on quark fields in a flavor-dependent manner, *i.e.*, antiperiodic BC on u and d quarks, and the periodic BC on the s quark. Under HBC, hadrons are subject to their own spatial BC, *i.e.*, N(uud, udd) and K$(u\bar{s}, d\bar{s})$ are subject to the antiperiodic BC, while $\Theta^+(uudd\bar{s})$ is subject to the periodic BC. Recall that, in a box of size L, the spatial momenta are quantized as $p_i = 2n_i\pi/L$ for periodic BC and $(2n_i+1)\pi/L$ for antiperiodic BC. Therefore, s-wave NK threshold energy is raised as $E_{\mathrm{th}} \simeq \sqrt{m_N^2 + \vec{p}_{\mathrm{min}}^{\,2}} + \sqrt{m_K^2 + \vec{p}_{\mathrm{min}}^{\,2}}, |\vec{p}_{\mathrm{min}}| = \sqrt{3}\pi/L$. In contrast, Θ^+ can have zero spatial momentum and the energy is expected to be unaffected.

In Fig. 1, we show the comparison of the results of standard BC and HBC for each κ. We see that, for all κ, the plateaus are raised a consistent amount with the shift in NK threshold energy. Therefore, we conclude that the observed states in the negative-parity channel are NK scattering states and there are no relevant signals for the compact 5Q resonance.

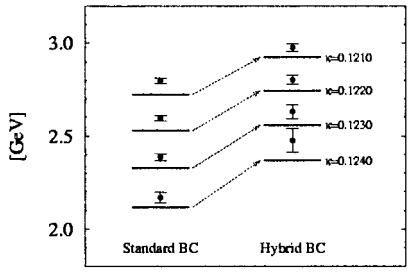

Fig. 1. Comparison of the results of standard BC and HBC for each κ. Dots denote the best-fit mass and the solid lines the corresponding NK threshold energies.

[*1] Department of Physics, Tokyo Institute of Technology
[*2] Department of Physics, Nihon University

References

1) LEPS Collaboration, T. Nakano et al.: Phys. Rev. Lett. **91**, 012002 (2003).
2) F. Csikor, Z. Fodor, S. D. Katz, and T. G. Kovacs: JHEP **0311**, 070 (2003).
3) S. Sasaki: hep-lat/0310014.
4) T. W. Chiu and T. H. Hsieh: hep-ph/0403020; hep-ph/0404007.
5) N. Mathur, F. X. Lee, A. Alexandru, C. Bennhold, Y. Chen, S. J. Dong, T. Draper, I. Horváth, K. F. Liu, S. Tamhankar, and J. B. Zang: hep-ph/0406196.
6) T. T. Takahashi, T. Kunihiro, T. Onogi, and T. Umeda: hep-lat/0410025.
7) N. Ishii, T. Doi, H. Iida, M. Oka, F. Okiharu, and H. Suganuma: hep-lat/0408030; hep-lat/0409121; hep-lat/0410022.

Static quark potential in $N_f = 2$ dynamical domain-wall QCD†

K. Hashimoto* and T. Izubuchi*

We calculate the static quark potential in two-flavor dynamical quark lattice QCD using DBW2 gauge[1] and domain-wall fermion (DWF)[2] actions. One of the purposes is to determine of lattice spacing a from Sommer scale $r_0 = R_0 a \approx 0.5\,\mathrm{fm}$.[3]

The static potential $V(\vec{R})$ between infinitely heavy quark and anti-quark separated by $\vec{R}$ in spatial direction is obtained from the Wilson loop $\langle W(\vec{R},T)\rangle$:

$$\langle W(\vec{R},T)\rangle = C(\vec{R})e^{-V(\vec{R})T} + (\text{“excited states''}), \quad (1)$$

where $C(\vec{R})$ is the overlap with the “ground state.”

We employ DBW2 and $N_f = 2$ DWF actions with $\beta = 0.80$, $L_s = 12$, $M_5 = 1.8$, $m_{\mathrm{dyn}}a = 0.02$, 0.03, 0.04, (941, 559, 473 configurations respectively), corresponding to $m_\pi/m_\rho = 0.54(1)$, 0.60(1), 0.65(1) on $16^3 \times 32$ lattices. Inverse of the lattice spacing from rho meson mass in the chiral limit is $a^{-1}_{m_\rho} = 1.69(5)\,\mathrm{GeV}$.[4]

We implement Bresenham algorithm,[5] which allows us to obtain the geodesic path connecting the ends of $\vec{R} = (N_1, N_2, N_3)$ on lattice, where N_i (i = 1, 2, 3) are any three integers, and APE smearing[6] for spatial links. The smearing coefficient and iteration time are tuned: $(c, n) = (0.50, 20)$ for all m_{dyn} to maximize $C(\vec{R})$.

The static potential $V(\vec{R})$ is obtained from (1):

$$V(\vec{R},T) = \ln\left[\langle W(\vec{R},T)\rangle / \langle W(\vec{R},T+1)\rangle\right] \quad (2)$$

by neglecting the excited states. $T = 5$ is selected as the smallest time at which the excited states contribution becomes negligible in $V(\vec{R})$.

The Sommer scale R_0,

$$R^2 \frac{dV(R)}{dR}\bigg|_{R=R_0} = |\vec{R}|^2 |\nabla V(\vec{R})|\Big|_{|\vec{R}|=R_0} = 1.65, \quad (3)$$

is extracted from $V(\vec{R})$ by the several methods to nail down the systematic errors:
(I) R_0 is obtained from a fitting function:

$$V(\vec{R}) = V_0 - \frac{\alpha}{R} + \sigma R - l\left(\left[\frac{1}{\vec{R}}\right] - \frac{1}{R}\right),$$
$$R_0 = \sqrt{\frac{1.65-\alpha}{\sigma}}, \quad (4)$$

where $[1/\vec{R}]$ is the lattice Coulomb potential,

$$\left[\frac{1}{\vec{R}}\right] = \int_{-\pi}^{\pi} \frac{d^3k}{8\pi^2} \frac{\exp(i\vec{k}\cdot\vec{R})}{\sum_i \left[\sin^2(k_i/2) - 4c_1 \sin^4(k_i/2)\right]}, \quad (5)$$

introduced to correct rotational symmetry breaking ($c_1 = -1.4069$ for DBW2).
(II) R_0 is obtained from calculating the gradient of the potential, $\nabla V(\vec{R})$. To solve Eq. (3), we interpolate by a function: $|\nabla V(\vec{R})| = f_0 + f_1 R^{-2}$, between two neighboring points.

Figure 1 shows the Sommer scale $R_0 = r_0/a$ for dynamical quark mass, $m_{\mathrm{dyn}} + m_{\mathrm{res}}$, where $m_{\mathrm{res}}a = 0.00137(4)$.[4] Our results of the fits are extracted at $T = 5$ and $R \in [\sqrt{3}, 8]$ for all m_{dyn}, and gradient of the potential at same T. R_0 in the chiral limit, $m_{\mathrm{dyn}} + m_{\mathrm{res}} \to 0$, is obtained by a linear extrapolation. $R_0 = 4.24(6)$, 4.28(5) and 4.25(9) from fits with $l \neq 0$, $l = 0$, and $\nabla V(\vec{R})$ respectively. These results are consistent within statistical errors. From $r_0 = 0.5\,\mathrm{fm}$ as an input, our main value is $a^{-1}_{r_0} = 1.69(2)$ from fit with $l = 0$.

Comparing $a^{-1}_{r_0}$ with $a^{-1}_{m_\rho} = 1.69(5)$, these values are consistent within errors. For quenched DBW2 simulation, $a^{-1}_{r_0}$ is about 10% larger than $a^{-1}_{m_\rho}$.[7] The lattice spacings from r_0 and m_ρ become much closer by dyanmical quark effect.

Although we do not show details here, we observe Coulomb term coefficient α becomes larger and the overlap with ground state $C(\vec{R})$ behaves differently by dyanmical quark effect too.[7]

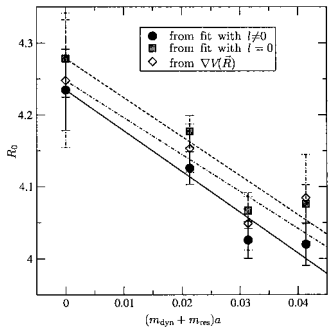

Fig. 1. R_0 *vs.* $(m_{\mathrm{dyn}} + m_{\mathrm{res}})a$ for three types of analysis. “from $\nabla V(\vec{R})$” is preliminary. Error is only statistical.

† Work done with the RBC Collaboration. This work is supported by RIKEN Super Combined Cluster at RIKEN.
* Institute for Theoretical Physics, Kanazawa University

References

1) T. Takaishi: Phys. Rev. D **54**, 1050 (1996); QCD-TARO Collaboration, P. de Forcrand et al.: Nucl. Phys. B **577**, 263 (2000).
2) D. B. Kaplan: Phys. Lett. B **288**, 342 (1992); Y. Shamir: Nucl. Phys. B **406**, 90 (1993); V. Furman and Y. Shamir: Nucl. Phys. B **439**, 54 (1995).
3) R. Sommer: Nucl. Phys. B **411**, 839 (1994).
4) RBC Collaboration, T. Izubuchi: hep-lat/0410034; RBC Collaboration, Y. Aoki et al.: hep-lat/0411006.
5) B. Bolder et al.: Phys. Rev. D **63**, 074504 (2001).
6) M. Albanese et al.: Phys. Lett. B **192**, 163 (1987).
7) RBC Collaboration, K. Hashimoto and T. Izubuchi: hep-lat/0409101.

Nucleon structure in lattice QCD with domain wall fermions†

Y. Aoki,*1 T. Blum,*2 S. Ohta,*3 and K. Orginos*4

This year, numerous new results have been obtained from our lattice QCD numerical investigations of the structure of nucleon with domain wall fermions (DWFs) quark action and DBW2 gauge action.[1] Quenched calculations without virtual creation and annihilation of quark-antiquark pairs are almost complete for the moments of nucleon structure functions[2] and nucleon decay matrix elements,[3] both with nonperturbative renormalizations. Dynamical calculations including virtual creation and annihilation of quark antiquark pairs with two degenerate quark flavors are ongoing for the nucleon axial charge, moments of structure functions, and nucleon decay matrix elements.

In all these calculations, the flavor SU(2)×SU(2) chiral symmetry is very important. In this regard, the use of DWF quarks is indispensable because the more conventional Wilson and staggered quarks badly violate either the flavor or the chiral symmetry or both and makes the use of nonperturbative renormalizations,[4] which is essential for the results reported in this article, impractical. The DBW2 action facilitates the use of DWF.[1]

One of the simplest demonstrations of the power of nonperturbative renormalization combined with the DWF and DBW2 actions is the calculation of nucleon axial charge.[5] Its ratio to the vector charge, g_A/g_V, is naturally renormalized. Since this had been reported in detail in the past years, we simply note here that the new, dynamical calculations are consistent with the quenched ones, although the error is rather large. The quark mass dependence is very mild, and the chiral extrapolation is consistent with the experimental value.

The nucleon structure functions are measured in, for example, the lepton deep inelastic scattering off nucleons. What are accessible in lattice QCD are their moments. We have been calculating some of these moments that do not require finite momentum transfer. This year, their nonperturbative renormalizations in the quenched case have been completed, and found to typically exhibit 10% effects. The quark mass dependence is again mild. Corresponding dynamical calculations are ongoing.

Yasumichi Aoki has been driving our calculations on nucleon decay matrix elements. The grand unified theories generally predict that the nucleon decays into a meson and a lepton. The experiments are now entering the stage where the researchers will be distinguishing among the various supersymmetric versions of these theories. Thus accurate calculations of the associated hadronic matrix elements are increasingly important. Here again, the lattice QCD numerical calculations are the only reliable tools. Two methods have been proposed: direct and indirect. In the direct methods, all the relevant quantities are calculated on the lattice. In the indirect methods, a chiral perturbation is used to reduce the calulations to the derivations of only two coefficients on the lattice. Earlier attempts of calculating the quantities on the lattice resulted in a rather large disagreement between the two methods of up to 50%. The explicit violation of chiral symmetry in these calculations, however, made them inconclusive. Our quenched calculations on this issue are now complete, and are summarized in Fig. 1. It has been confirmed that the direct and indirect methods disagree.

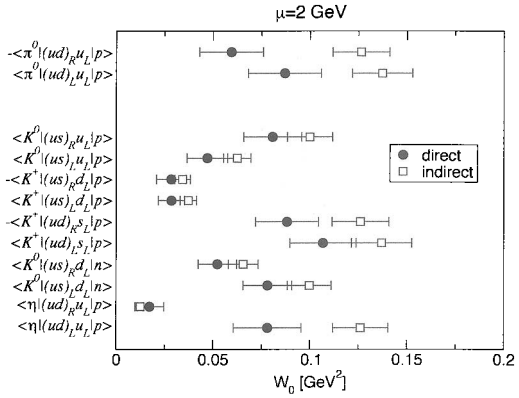

Fig. 1. Nucleon decay matrix elements. The results of direct and indirect methods disagree with each other.

References

1) See for example, Y. Aoki et al.: Phys. Rev. D **69**, 074504 (2004).
2) RBCK Collaboration, S. Ohta and K. Orginos: arXiv:hep-lat/0411008.
3) RBC Collaboration, Y. Aoki: arXiv:hep-lat/0409114.
4) T. Blum et al.: Phys. Rev. D **66**, 014504 (2002).
5) RBCK Collaboration, S. Sasaki, K. Orginos, S. Ohta, and T. Blum: Phys. Rev. D **68**, 054509 (2003).

† Condensed from the presentations at Int. Symp. Lattice 2004, Batavia, USA, 2004-7

*1 Department of Physics, University of Wuppertal, Germany
*2 Department of Physics, University of Connecticut, USA
*3 Theory Division, Institute of Particle and Nuclear Studies, High Energy Accelerator Research Organization (KEK)
*4 Center for Theoretical Physics, Massachusetts Institute of Technology, USA

Neutron electric dipole moment with domain wall quarks

F. Berruto,[*1] T. Blum,[*2] K. Orginos,[*2,*3] and A. Soni[*1]

One of the most intriguing aspects of QCD is that it allows a T- and P-odd, gauge invariant interaction term, $S_\theta = \int d^4x \; i\theta \frac{g^2}{32\pi^2} tr\left[G(x)\tilde{G}(x)\right] = i\theta Q$, where Q is the topological charge of the QCD vacuum. Thus QCD does not respect CP. One of the best ways to monitor this is by searching for the neutron electric dipole moment, d_N. $d_N = |\vec{d}_N| < 6.3 \times 10^{-26}\, e$-cm from current experiments.[1] Using this experimental bound along with various model estimates of d_N[2–4] implies that the CP-odd parameter in the QCD action is *unnaturally* small, $\theta \leq 10^{-10}$. Since there is no reason for this number to be so different from unity, its minuteness requires extraordinary fine-tuning. This is often termed the *Strong CP problem*. To translate the above experimental bound to a constraint on the fundamental θ parameter requires evaluation of nucleon matrix elements, wherein lattice QCD enters.

There are two important elements to our computational strategy: (1) Compute the matrix elements of the electromagnetic current between nucleon states, $\langle p', s|J^\mu|p, s\rangle_\theta = \bar{u}(p', s)\Gamma_\mu(q^2)u(p, s)$, where

$$\begin{aligned}\Gamma_\mu(q^2) \;=\; & \gamma_\mu\, F_1(q^2) + i\,\sigma_{\mu\nu}q^\nu\,\frac{F_2(q^2)}{2m} \\ & + \left(\gamma_\mu\,\gamma_5\,q^2 \;- 2m\gamma_5\,q_\mu\right) F_A(q^2) \\ & + \sigma_{\mu\nu}q^\nu\gamma_5\,\frac{F_3(q^2)}{2m},\end{aligned} \tag{1}$$

and use projectors to obtain linear combinations of F_1 and F_2,

$$G_E(q^2) \;=\; F_1(q^2) + \frac{q^2}{(2m)^2}F_2(q^2) \tag{2}$$

$$G_M(q^2) \;=\; F_1(q^2) + F_2(q^2), \tag{3}$$

and $F_3(q^2)/2m$. By forming ratios of $G_M(q^2)$ and $F_3(q^2)$ with $G_E(q^2)$ and taking $q^2 \to 0$, we find both magnetic and electric dipole moments, respectively: $e(F_1(0) + a_\mu)/2m$ and $d_N = eF_3(0)/2m$ (note, $G_E(0) = F_1(0) = 1$ and 0 for the proton and neutron, respectively, and $a_\mu \equiv F_2(0)$ is the anomalous magnetic moment). In the above $q^2 \leq 0$, and m is the nucleon mass.

(2) Expand $\langle p', s|J^\mu|p, s\rangle_\theta$ to lowest order in θ and compute $F_3(q^2)$ in each topological sector ν, and then average over all sectors with weight Q_ν. Our method requires extrapolation of the form factors to $q^2 = 0$ from non-vanishing values of q^2.

We have calculated the ratios of neutron and proton magnetic to proton electric form factors which become the dipole moment in question in the limit $q^2 \to 0$. These results were computed on 280 $N_f = 2$, $m_{sea} = 0.02$, domain wall fermion configurations (separated by 10–15 trajectories) with $m_{val} = 0.04$ and 0.08.[5] The lattice size is $16^3 \times 32$, $L_s = 12$, and the inverse lattice spacing in the $m_{sea} = 0$ limit is $a^{-1} \approx 1.7\,\text{GeV}$. We have averaged over time slices 14–17 and (equivalent) permutations of momenta, $\vec{p} = (1, 0, 0)$, (1,1,0), and (1,1,1). Q was computed by integrating the topological charge density after APE smearing the gauge fields (20 sweeps with ape weight 0.45).[6] We are also investigating computing the topological charge from the index defined from the domain wall fermion Dirac operator (strictly valid in the limit $L_s \to \infty$).

Approximating the $q^2 \to 0$ value of each with the smallest value of $\vec{p}^2$ ($= (2\pi/16)^2$), taking $m_f = 0.04$ as the physical value of the light quark mass, and $aM_N = aM_P = 0.8989(77)$ at this quark mass, we obtain

$$\begin{aligned} a_\mu^P &\approx 1.45(10) \\ a_\mu^N &\approx -1.50(7) \\ d_N/(e\,a\,\theta) &\approx -0.06(15). \end{aligned}$$

Considering the crude extrapolations just described, these are roughly consistent with the experimental values $a_\mu^P = 1.79$ and $a_\mu^N = -1.91$ (and of course $d_N \sim 0$). The error estimates are statistical uncertainties only. In physical units, $d_N = -7.4(18.0) \times 10^{-16}\,\theta\, e$-cm, so our calculation can not yet exclude any of the model calculations mentioned above. The electric dipole moment of the neutron does not show any significant dependence on the quark mass, within relatively large statistical errors (note, the two valence quark mass calculations are highly correlated). We are striving to reduce the statistical error on our determination of d_N which has already yielded an interesting first-principles bound on the magnitude of d_N. These calculations are in progress.

[*1] High Energy Theory group, Brookhaven National Laboratory, USA
[*2] Physics Department, University of Connecticut, USA
[*3] Center for Theoretical Physics, Massachussets Institute of Technology, USA

References
1) P. G. Harris et al.: Phys. Rev. Lett. **82**, 904 (1999), and references therein.
2) V. Baluni: Phys. Rev. D **19**, 2227 (1979).
3) R. J. Crewther et al.: Phys. Lett. B **88**, 123 (1979).
4) M. Pospelov and A. Ritz: Phys. Rev. Lett. **83**, 2526 (1999).
5) RBC Collaboration, Y. Aoki et al.: hep-lat/0411006.
6) T. DeGrand, A. Hasenfratz, and T. G. Kovacs: Nucl. Phys. B **520**, 301 (1998).

The first results of the dynamical domain wall QCD

T. Izubuchi,* for the RBC Collaboration

We report on the first large-scale study of two flavor QCD with domain wall fermions (DWF). Simulation has been carried out at three dynamical quark mass $m_{sea} = 0.02, 0.03$, and 0.04 which corresponds to about 1/2, 3/4, and 1 $m_{strange}$ on $16^3 \times 32$, or $(1.9\,\mathrm{fm})^3$ box, with $L_s = 12$, domain wall height $M_5 = 1.8$, and $a^{-1} \approx 1.7\,\mathrm{GeV}$. We choose the DBW2 gauge action at $\beta = 0.80$, by which the drastic reduction of the residual mass, m_{res}, for relatively small $L_s \sim O(10)$ was observed in quenched simulation.[1)]

HMC-Φ algorithm is employed to generate $\sim$ 5,000 trajectories for each m_{sea}. We found several interesting and unique technicalities for DWF dynamical simulation such as 1) the acceptance probability kept large for the entire m_{sea} range, 2) improvements of the acceptance by the new lattice action, 3) factor of two to three speed up by forecasting the solution of the Dirac equation.[2)] Although these observations are encouraging for DWF simulations with lighter quark masses in the future, we note that they may only be true for relatively heavy m_{sea}.

For each of three m_{sea}, we measure on 94 lattices separated by 50 trajectories, leaving out the first $\simeq$ 600 trajectories to allow the evolution to be thermalized. All quoted errors are from jackknife estimate of the statistical error, with the correlated fit for hadron propagators using a single covariance matrix computed on the entire ensemble.

By a linear diagonal extrapolation, $m_{sea} = m_{val} \to 0$, we found $m_{res} = 0.00137(4)$ or $\lesssim 5\,\mathrm{MeV}$, which is larger than quenched DBW2 values for the same L_s and a^{-1}, but it is still an order of magnitude smaller than the input quark mass.

Pseudo-scalar decay constant, f_{ps}, was extracted from the wall-point pseudo-scalar correlator and linearly extrapolate to the chiral limit, $m^q_{val} = m^q_{sea} = 0$ with $m^q_{val} \equiv m_{val} + m_{res}$, $m^q_{sea} = m_{sea} + m_{res}$, to obtain an estimation in the chiral limit, $f = 0.078(1)$. The fit to the next-to-leading order (NLO) partially quenched chiral perturbation theory (PQChPT) formula for f_{ps} *did not* describe the data well in the neighborhood of the fit range.[3)] However, the following results depend on the value of f only mildly, so we will use the estimation from the linear fit.

As for the mass of the pseudo-scalar mesons and the vector mesons, it is worth mentioning that a simple linear extrapolation of m^2_{ps} to $m^q_{val,sea} = 0$ is zero within the statistical error. This did not happen in the quenched case: $m^2_{ps} = 0$ at $m_f \approx -(2-3) \times m_{res}$.[1)] This is consistent with the difference between chiral logarithms ($m^2_{ps}/m^q \sim 2B_0 + cm^q \log m^q$) vs the quenched one ($m^2_{ps}/m^q \sim \log m^q$) at small m^q.

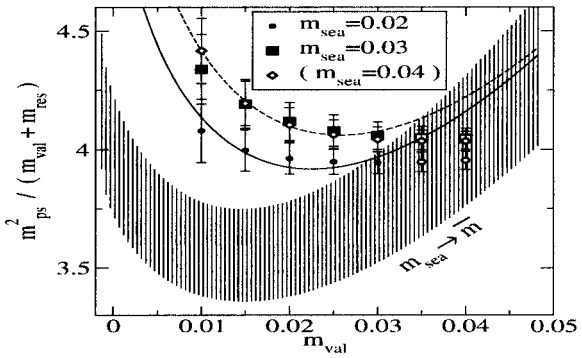

Fig. 1. $m^2_{ps}/(m_{val} + m_{res})$ as a function of m_{val} for each m_{sea}, and the NLO fit curves from $m_{sea,val} \leq 0.03$.

A linear extrapolation of the three vector meson mass points $m_{val} = m_{sea}$, yields a^{-1} =1.69(5) GeV at the quark mass, $m_f = \bar{m} = 0.0002(1)$ corresponding to the neutral pion mass using NLO fit. Similarly, but using the NLO ChPT prediction for non-degenerate valence quarks, $m_s = 0.045(3)$ is obtained from the physical kaon mass. The coefficients in the NLO formula for non-degenerate quarks are determined by the fit of the degenerate quark meson. It is important to note that $\bar{m}$ and m_s as defined above are bare quark masses; the renormalized quark mass is defined as $Z_m m^q = Z_m(m + m_{res})$, where $Z_m \sim 1/0.6$ is a scheme and scale dependent renormalization factor.[4)]

Extrapolating the measured decay constant at the partially quenched points ($m_{val,sea} \leq 0.04$) using the linear ansatz to $\bar{m}$ and m_s, we find $f_\pi = 134(4)\,\mathrm{MeV}$, $f_K = 157(4)\,\mathrm{MeV}$, and $f_K/f_\pi = 1.18(1)$, which agree better with experiment than quenched simulations.[1)]

We have tried the NLO ChPT fit for the mass and a simple linear fit for the decay constant. The results for the physical decay constants are closer than those in quenched DWF simulation. For further details of the simulations and results, we refer the reader to the paper.[3)]

References

1) Y. Aoki et al.: Phys. Rev. D **69**, 074504 (2004); hep-lat/0211023.
2) R. C. Brower et al.: Nucl. Phys. B **484**, 353 (1997); hep-lat/9509012.
3) RBC Collaboration, Y. Aoki et al.: hep-lat/0411006.
4) RBC Collaboration, C. Dawson: Nucl. Phys. B (Proc. Suppl.) **128**, 54 (2004); hep-lat/0310055.

* Institute for Theoretical Physics, Kanazawa University

Perturbative determination of mass-dependent renormalization and improvement coefficients for the heavy-light vector and axial-vector currents with relativistic heavy and domain-wall light quarks†

N. Yamada, S. Aoki,* and Y. Kuramashi*

In the lattice study of heavy-light physics, combining the relativistic heavy (RH) quark[1] and the domain-wall (DW) light quark[2] is a promising choice to successfully describe heavy and light quarks, respectively. The mass-dependent $O(a)$ improvement coefficients for the heavy-light vector and axial-vector currents consisting of this set of quark actions are calculated at the one-loop level. The detailed descriptions for the calculation are available in Ref. 3.

The improvement coefficients for the heavy-light vector current are defined as follows:

$$
\begin{aligned}
&V_\mu^{\overline{\rm MS}} = Z_{V_\mu}^{\overline{\rm MS}-{\rm latt}}\, V_\mu^{\rm lat,imp},\\
&Z_{V_\mu}^{\overline{\rm MS}-{\rm latt}} = Z_{\rm wf}\,\left[1 - g^2\Delta_{V_\mu}\right],\\
&V_\mu^{\rm lat,imp} = \bar{q}\gamma_\mu Q - g^2 c_{V_\mu}^{+}\partial_\mu^{-}\{\bar{q}Q\} - g^2 c_{V_\mu}^{-}\partial_\mu^{+}\{\bar{q}Q\}\\
&\qquad\qquad - g^2 c_{V_\mu}^{L}\{\vec{\partial}_i\bar{q}\}\gamma_i\gamma_\mu Q - g^2 c_{V_\mu}^{H}\bar{q}\gamma_\mu\gamma_i\{\vec{\partial}_i Q\}\\
&\qquad\qquad + O(g^4),
\end{aligned}
$$

where $\partial_\mu^{\pm}=\overrightarrow{\partial}_\mu \pm \overleftarrow{\partial}_\mu$, q and Q denote lattice light and heavy quark fields, respectively, and $Z_{\rm wf}$ is a known factor related to wave function renormalizations. The exact chiral symmetry held by the lattice light quark action provides an exact relationship between the improvement coefficients for the vector and axial-vector currents regardless of the lattice heavy quark action. Thus we do not need to calculate those for the axial-vector current once the above coefficients have been determined.

Figure 1 shows the $m_Q{}^{(0)}$ dependence of Δ_{V_0} (circles) for three different gauge actions, the plaquette, Iwasaki and DBW2. The results for M_5=0.5, 1.1 and 1.7 are shown as examples. The fit (solid lines) reproduces the data very well in the entire ranges of $m_Q^{(0)}$ and M_5 as shown in the figure. The other coefficients, $c_{V_\mu}^{\pm,H,L}$, are also obtained successfully, although we omit the detailed explanations because of limited space.

We examined two methods of improving the perturbation series, namely the mean field improvement (MF) and the quasi nonperturbative improvement with MF (QNP+MF) using the nonperturbative Z-factor for the light-light vector current. The reorganized coefficients of Δ_{V_0}, $\Delta_{V_0}^{\rm MF}$ (triangle-up) and $\Delta_{V_0}^{\rm QNP+MF}$ (triangle-down), are plotted in Fig. 1. It is noted that for the nonimproved coefficients the size

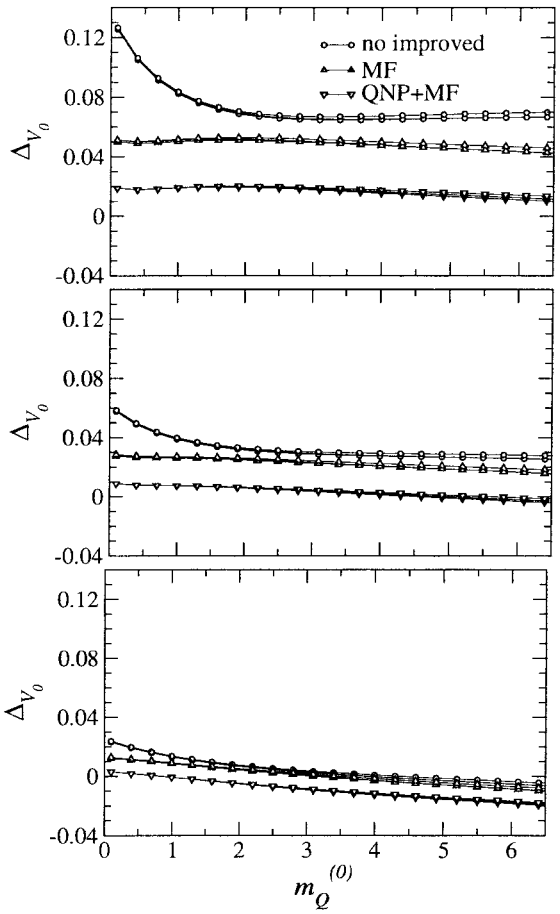

Fig. 1. $m_Q^{(0)}$ dependence of Δ_{V_0}, $\Delta_{V_0}^{\rm MF}$ and $\Delta_{V_0}^{\rm QNP+MF}$ with the plaquette, Iwasaki and DBW2 gauge actions from top to bottom.

of the one-loop coefficient largely depends on the gauge action, whereas when QNP and MF are introduced together, the dependence decreases. It is also interesting to observe that the mean field improvement makes the m_Q dependence smaller. Similar findings were obtained for the improvements of Δ_{V_k} as well.

References

1) S. Aoki, Y. Kuramashi, and S.-I. Tominaga: Prog. Theor. Phys. **109**, 383 (2003).
2) V. Furman and Y. Shamir: Nucl. Phys. B **439**, 54 (1995).
3) N. Yamada, S. Aoki, and Y. Kuramashi: arXiv:hep-lat/0407031.

† Condensed from the Proc. Lattice 2004, Batavia, USA, 2004-7 (Elsevier, 2004), p.719.

* Institute of Physics, University of Tsukuba

Twisted mass QCD, O(a) improvement and Wilson chiral perturbation theory

S. Aoki* and O. Bär*

We point out a caveat in the proof for automatic O(a) improvement in twisted mass lattice QCD at maximal twist angle. With the definition for the twist angle previously given by Frezzotti and Rossi,[1] automatic O(a) improvement can fail unless the quark mass satisfies $m_q \gg a^2\Lambda_{\rm QCD}^3$. We propose a different definition for the twist angle which does not require a restriction on the quark mass for automatic O(a) improvement. In order to illustrate explicitly automatic O(a) improvement we compute the pion mass in the corresponding chiral effective theory. We consider different definitions for maximal twist and show explicitly the absence or presence of the leading O(a) effect, depending on the size of the quark mass.

A crucial assumption for automatic O(a) improvement in twisted mass lattice QCD at maximal twist angle is that the critical mass $M = {\rm cr}$ is odd under $r \to -r$. According to the analysis of the Wilson chiral perturbation theory (WCPT),[2,3] however, the critical mass should have the following structure:

$$M_{\rm cr}(r) = M_{\rm odd}(r) + a^2 c\, M_{\rm even}(r) \equiv M_{\rm cr}^{(1)}(r) \qquad (1)$$

where $M_{\rm odd}(r)$ is odd and $M_{\rm even}(r)$ is even under $r \to -r$. Performing the transformation $r \to -r$ we obtain a second independent critical quark mass:

$$-M_{\rm cr}(-r) = M_{\rm odd}(r) - a^2 c\, M_{\rm even}(r) \equiv M_{\rm cr}^{(2)}(r). \qquad (2)$$

With this form of the critical quark masses, the twisted mass average at the maximal twist becomes

$$\langle O\rangle^{TA}\left(r, m_q, \omega = \frac{\pi}{2}\right) = \frac{1}{2}\Big[\langle O\rangle\left(r, m_q, \omega = \frac{\pi}{2}\right) + \langle O\rangle\left(-r, \hat{m}_q, \omega = \frac{\pi}{2} + \hat{\omega}\right)\Big], \qquad (3)$$

where we have defined

$$\hat{m}_q = \sqrt{m_q^2 + (2a^2 c\, M_{\rm even}(r))^2}, \qquad (4)$$

$$\tan\hat{\omega} = \frac{2a^2 c\, M_{\rm even}(r)}{m_q}, \qquad (5)$$

for the subtracted quark mass m_q and the twisted mass μ. The twist average is therefore no longer equal to the Wilson average. In order to show that the twist average is automatically O(a) improved, the new mass parameter $\hat{m}_q$ and the angle $\hat{\omega}$ must satisfy the conditions

$$\hat{m}_q = m_q + {\rm O}(a^2), \qquad \hat{\omega} = {\rm O}(a^2). \qquad (6)$$

These conditions are met if the quark mass satisfies the bound $m_q \gg a^2\Lambda_{\rm QCD}^3$ where $\Lambda_{\rm QCD}$ is the typical QCD scale.

In order to remove the condition on m_q for the automatic O(a) improvement, we propose an alternative definition for the twist angle. With the definition that $\overline{M}_{\rm cr}(r) = \dfrac{M_{\rm cr}^{(1)}(r) + M_{\rm cr}^{(2)}(r)}{2} = -\overline{M}_{\rm cr}(-r)$ and $\Delta M_{\rm cr}(r) = \dfrac{M_{\rm cr}^{(1)}(r) - M_{\rm cr}^{(2)}(r)}{2} = \Delta M_{\rm cr}(-r)$, we define m_q and μ as

$$m = [m_q + \Delta M_{\rm cr}(r)]\cos\omega' + \overline{M}_{\rm cr}(r), \qquad (7)$$

$$\mu = [m_q + \Delta M_{\rm cr}(r)]\sin\omega'. \qquad (8)$$

Here ω' is an alternative definition of the twist angle. It is easy to see that the automatic O(a) improvement can be proven at $\omega' = \pi/2$ without any restrictions on the size of m_q.[4]

Using the WCPT for the 2 flavor QCD, we have calculated the pion masses to illustrate explicitly the above general argument.[4]

We first consider the original definition of the maximal twist ($\omega = \pi/2$). For $\mu \geq O(a)$ we have

$$m_{\pi^{1,2}}^2 = 2B\mu, \quad m_{\pi^3}^2 = m_{\pi^{1,2}}^2 + 2c_2 a^2 \qquad (9)$$

where B and c_2 are the low energy constants in the WCPT.[2,3] and $\pi^i (i = 1,2,3)$ represents the triplet pion. In this case there is no $O(a)$ scaling violation, so that the automatic $O(a)$ improvement is achieved. For $2B\mu \ll 2c_2 a^2$, on the other hand, we have

$$m_{\pi^{1,2}}^2 = (c_2 a^2)^{1/3}(2B\mu)^{2/3}, \quad m_{\pi^3}^2 = 3m_{\pi^{1,2}}^2. \qquad (10)$$

The above behaviour that $m_\pi^2 = O(\mu^{2/3})$ is different from the behaviour in the continuum theory. Therefore the automatic $O(a)$ improvement does not hold in this case.

At the maximal twist for our alternative definition ($\omega' = \pi/2$), we have

$$m_{\pi^{1,2}}^2 = 2B\mu, \quad m_{\pi^3}^2 = m_{\pi^{1,2}}^2 + 2c_2 a^2 \qquad (11)$$

for all values of μ. Therefore the automatic $O(a)$ improvement holds without any restrictions on the size of the quark mass, as discussed before.

* Graduate School of Pure and Applied Sciences, University of Tsukuba

References
1) R. Frezzotti and G. C. Rossi: JHEP **0408**, 007 (2004).
2) S. R. Sharpe and R. J. Singleton: Phys. Rev. D **58**, 074501 (1998).
3) S. Aoki: Phys. Rev. D **68**, 054508 (2003).
4) S. Aoki and O. Bär: hep-lat/0409006.

Status of the QCDOC computer project

P. A. Boyle,[*1,*2] D. Chen,[*3] N. H. Christ,[*2] M. Clark,[*1] S. D. Cohen,[*2] C. Cristian,[*2] Z. Dong,[*2] A. Gara,[*3] B. Joó,[*1] C. Jung,[*2,*4] C. Kim,[*2] L. Levkova,[*2] X. Liao,[*2] G. Liu,[*2] R. D. Mawhinney,[*2] S. Ohta,[*5] K. Petrov,[*2,*4] T. Wettig,[*6] and A. Yamaguchi[*2]

The QCDOC (QCD On a Chip) computer project[1–5] aims at providing a computational power in the range of tens of TFlops optimized for numerical investigations of lattice QCD (Quantum Chromodynamics). It started in 1999 as a joint research project of Columbia University, IBM Research and RIKEN. The British UKQCD Collaboration joined soon afterwards.

Each QCDOC configuration will involve tens of thousands of computational nodes each communicating with its twelve nearest neighbors in a six-dimensional hypercubic network. A single QCDOC computational node consists of a single application specific integrated circuit (ASIC) with a) a 500 MHz, 32-bit PowerPC 440 processor core, b) a 64-bit, 1 GFlops floating-point unit, c) 4 MBytes of embedded-DRAM memory, d) controllers for embedded and external memories, e) a nearest-neighbor serial communication unit (SCU) with total latencies of 350 ns (550 ns) for supervisor (regular) transfers that will occur simultaneously in the 12 independent directions and an aggregate bandwidth of 12 Gbit/s, and f) other components such as an Ethernet controller. Two such ASICs are mounted on a daughterboard, together with two double data rate (DDR) SDRAM modules (one per ASIC, up to 2 GB each). Thirty-two daughterboards are mounted on a motherboard, and eight motherboards are mounted in a crate with two backplanes. The final machine consists of a certain number of such crates.

Last year, we reported the completion of the ASIC design, the successful production and verification of prototype ASICs, and then the productions and verifications of the daughtercards and motherboards. During the past year we successfully assembled and verified aircooled and watercooled crates that accommodate eight motherboards each. The operating system and application softwares have been developed using these configurations capable of $O(1)$ TFlops computational speeds to the level where physics research can now be undertaken. Indeed an exploratory set of calculations in search of optimal parameters for a very realistic 2+1 flavor dynamical lattice QCD calculation with domain wall fermions (DWFs) quark and DBW2 gluon actions are now under way.

In September, we started assembling a 10-TFlops QCDOC configuration for the UKQCD Collaboration. This configuration was completed and verified by October 22nd, and shipped to Edinburgh, in the United Kingdom. Assembly of another 10-TFlops configuration for the RIKEN BNL Research Center was also started in October, to be completed by the end of the year (see Fig. 1). Both the UKQCD and RBC collaborations are launching several physics research projects using these 10 TFlops computers. In addition, yet another 10-TFlops configuration will be built at Brookhaven National Laboratory for the American lattice QCD research community funded by the US DOE.

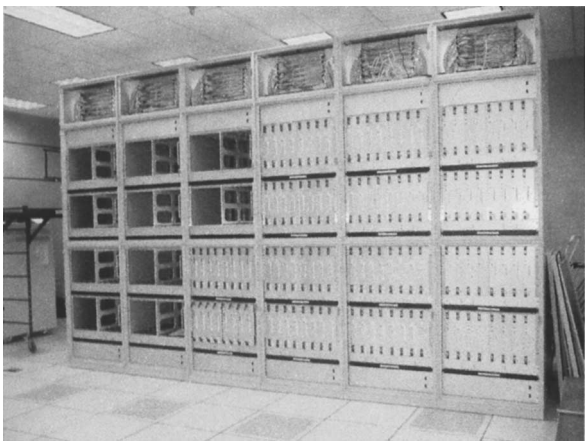

Fig. 1. The 24-crate, 10-TFlops configuration of the QCDOC computer for the RIKEN-BNL Research Center being assembled, as of November 5th, 2004.

*1 Department of Physics and Astronomy, University of Edinburgh, UK
*2 Department of Physics, Columbia University, USA
*3 IBM T. J. Watson Research Center, USA
*4 Department of Physics, Brookhaven National Laboratory, USA
*5 Institute of Particle and Nuclear Studies, High Energy Accelerator Research Organization (KEK)
*6 Institute for Theoretical Physics, University of Regensburg, Germany

References

1) P. A. Boyle et al.: Nucl. Phys. B (Proc. Suppl.) **129**, 838 (2004).
2) QCDOC Collaboration, P. A. Boyle, C. Jung, and T. Wettig: arXiv:hep-lat/0306023.
3) P. A. Boyle et al.: Nucl. Phys. B (Proc. Suppl.) **119**, 1041 (2003).
4) P. A. Boyle et al.: Nucl. Phys. B (Proc. Suppl.) **106**, 177 (2002).
5) D. Chen et al.: Nucl. Phys. B (Proc. Suppl.) **94**, 825 (2001).

PHENIX Run-4 achievments and future prospects

A. Deshpande,* for PHENIX Collaboration

Relativistic Heavy Ion Collider (RHIC) completed its fourth run (Run-4) in May 2004. Before Run-4 RHIC had achieved luminosities of the order of 1–$3 \times 10^{31}\,\mathrm{cm}^{-2}\,\mathrm{sec}^{-1}$ with an average polarization of ∼27%. Both were significantly lower than the design values. However, in Run-3 PHENIX demonstrated for the first time that data collected at a polarized collider at high energy could be used for double spin asymmtry measurements. The principle measurement resulting from Run-3 was the double spin asymmetry in π^0 production in p−p scattering at 200 GeV in Center of Mass (CM) energy. This asymmetry is related to the gluon polarization in the proton and is of great interest as a promising first probe of the gluon spin in the nucleon. Although with large statistical uncertainty, the double spin asymmetries in this process were measured using the PHENIX detector. Further, it was shown that all systematic uncertainties are small enough to plan future spin measurements at RHIC.[1)]

The plan for RHIC Run-4 for polarized proton collisions was mainly accelerator driven: to increase the polarization and luminosity achieved in RHIC. It was hence decided early on that the Run-4 pp would be a commissioning run for polarized protons where the accelerator would strive to achieve a new working point that resulted in higher polarization and luminosity. At the end of 5 weeks of commissioning, both these goals had been reached in short running periods (over fills). However, it was essential that this be demonstrated over long running periods over which the detectors could take data with acceptable background levels. To confirm the collider's ability to provide such a working environment, an extra week of RHIC running was requested and was granted in the period May 7 to May 15, 2004.

Approximately $150\,\mathrm{nb}^{-1}$ were taken during those physics data taking 7-days. Out of which some periods were still used for beam quality improvement and beam studies. Typically evening and night shifts were utilized for data collection at PHENIX in normal running conditions. The PHENIX spin rotators were commissioned early during the commissioning run as such all the data collected were for double longitudinal scattering. The search for the new working point by the CAD was successful and resulted in a successful demonstration of routine delivery of $5 \times 10^{31}\,\mathrm{cm}^{-2}\,\mathrm{sec}^{-1}$ with 40% polarization in the yellow beam and 45% polarization in the blue beam. The relative luminosity at PHENIX was studied and evaluated using the variation of hit multiplicities in the PHENIX Beam Beam Counters (BBCs) and the Zero Degree Calorimeters (ZDCs) w.r.t. each other, as had been successfully done earlier.[1)]

The PHENIX Run-4 pp data were collected from May 10–14, 2004 in 2-shifts-per-day running schedule. They were analyzed and the double spin asymmetries in π^0 production were measured. The results are reported in this volume.[2)] They are consistent with our published results from Run-3[1)] and are consistent with the gluon polarization results from fixed target Deep Inelastic Scatter (DIS) data at ∼30% consistency. The consistency with more exotic expectations of the gluon polarization are at the level of 0.1%.[1)]

So far the beam polarimetry at RHIC had been performed using pC scattering in the Coulomb Nuclear Interference region.[3)] This method presently relies for its absolute calibration on a theoretical calculation which limits the uncertainty with which one can measure the proton beam polarization. One of the most important goals of the RHIC Run-4 was the commissioning of the Hydrogen gas jet target to be used as an absolute calibration for the RHIC pC CNI polarimeters. This was successfully achieved and is described in Ref. 4.

As this articles goes to print, preparations for RHIC Run-5 are well underway. We expect a 9 week physics run at a peak delivered luminosity of $2.7\,\mathrm{pb}^{-1}$ per week. Taking a conservative estimate we expect to write 1/3 of the delivered luminosity to tape for analysis at PHENIX. It is expected that during the physics run we will routinely have 45–50% beam polarization. We will have a first robust measurement of the gluon polarization in the region $p_T^2 = 1$–$5\,\mathrm{GeV}^2$ using the π^0 production asymmetry. A first high statistics measurement of the direct photon cross section in pp scattering will also be possible. We base this confidence on the already attractive results on such a measurement from Run-4[5)] presented in this volume. While it is expected that we will use all available time during the physics run for the investigations of polarized gluon distribution, we will be ready during the beam commissioning period and will request several days of beam with transverse polarization. We believe that the data collected during such times would be exploratory in nature for the beginning of the transverse physics at PHENIX.[6)] With future data analysis needs of PHENIX in mind, we plan to do the Run-5 pp data production at Computing Center in Japan (CCJ) facility at RIKEN, Wako.[7)]

A cold/super-conducting siberian partial snake is being prepared and will be installed in AGS before the pp Run-5 immediately following the heavy ion running. Although the snake will be commissioned, it is not expected to benefit the physics program until Run-

* Department of Physics & Astronomy, State University of New York-Stony Brook, USA

6. With that snake in Run-6, it is expected that the polarization levels will reach $>$ 60–65% and at that time RHIC spin program will reach its peak. Along with this, during the next two years it is also expected that there will be a dedicated test of the 500 GeV in CM energy running. If this is successful, every thing necessary for the W physics program at RHIC will be needed to be in place for a Run-8 or 9 for the first results on quark and anti-quark helicities in proton. This will need an uprgade of the muon trigger capabilities for PHENIX which is now being proposed.[8)]

The expected channels for polarized gluon distribution measurements are (in order of their being expected to be of use:) $\pi^{0,\pm}$ production, inclusive prompt-photon production, open-heavy-quark production and γ-jet production. The last two in this list will require an upgrade of PHENIX with a central Silicon VTX tracker (Si TRK). Si TRK[9)] is being proposed by PHENIX and will be funded by RIKEN and US-DOE. The enhanced tracking capability due to this device will aid the discrimination of heavy-quark and non-heavy-quark events based on their primary and secondary vertices. The multiplicity seen by the Si barrel layers is in addition expected to aid in identification of jet axis allowing for a constraint on the kinematic reconstruction of events with γ-jet final states. This will be a significant enhancement in PHENIX's capability in increasing its ability to measure polarized and un-polarized gluon polarization.

In summary, PHENIX spin program is well on its way. If the expected beam conditions and proposed detector upgrades are realized, exciting new data leading to better understanding of the nucleon spin will be available in near future.

References

1) PHENIX Collaboration: Phys. Rev. Lett., **93**, 202002 (2004).
2) Y. Fukao et al.: RIKEN Accel. Prog. Rep. **38**, 211 (2005).
3) O. Jinnouchi et al.: RIKEN Accel. Prog. Rep. **38**, 226 (2005).
4) H. Okada et al.: RIKEN Accel. Prog. Rep. **38**, 224 (2005).
5) K. Okada et al.: RIKEN Accel. Prog. Rep. **38**, 209 (2005).
6) M. G. Perdekamp et al.: RIKEN Accel. Prog. Rep. **38**, 245 (2005).
7) S. Yokkaichi et al.: RIKEN Accel. Prog. Rep. **38**, 247 (2005).
8) X. Wei et al.: RIKEN Accel. Prog. Rep. **38**, 240 (2005).
9) J. Asai et al.: RIKEN Accel. Prog. Rep. **38**, 235 (2005).

Single transverse-spin asymmetry measurement in neutral pion and charged hadron production at PHENIX

Y. Goto, C. Aidala,[*1] F. Bauer,[*2] M. Grosse Perdekamp,[*3] Y. I. Makdisi,[*4] and K. Okada,
for the PHENIX Collaboration

The single transverse-spin asymmetry (A_N) is the left-right asymmetry of the cross sections in the reactions of a transversely polarized beam on an unpolarized target:

$$A_N = \frac{d\sigma_{Left} - d\sigma_{Right}}{d\sigma_{Left} + d\sigma_{Right}}.$$

In 1990, the Fermilab-E704 experiment showed unexpectedly large A_N of pions[1)] and other particles in reactions of a transversely polarized proton (and antiproton) beam on a proton target at the center of mass energy ($\sqrt{s}$) of 19.4 GeV in the forward-rapidity region. In 2002, the RHIC-STAR experiment also showed large A_N in the neutral pion production of transversely polarized proton collisions at $\sqrt{s} = 200$ GeV in the forward-rapidity region.[2)]

To explain these asymmetries, many possible QCD-based models were developed. One model considers the Sivers effect.[3)] The Sivers effect is a left-right asymmetry in the transverse momentum distribution of partons inside a transversely polarized nucleon. Another model considers the transversity and the Collins effect.[4)] Transversity is a transverse polarization of partons inside a transversely polarized nucleon. The Collins effect is a left-right asymmetry (analyzing power) in the fragmentation of transversely polarized final partons. There is also a model with a higher-twist effect.[5)] It is important to differentiate these possible effects from each other and extract physics implication from the observed asymmetries.

The soft physics effect must also be considered. This is typically evaluated by the cross-sectional measurement of the same reaction. In lower-energy fixed-target experiments such as the Fermilab-E704 experiment, it is questionable whether model calculations based on next-to-leading-order perturbative QCD (NLO pQCD) can explain the measured cross sections. On the other hand, the cross sections measured in collider experiments at RHIC are explained by NLO pQCD calculations very well.[6,7)] This is the great advantage of collider experiments at RHIC.

At PHENIX, we measured A_N of neutral pion and charged hadron production in the mid-rapidity region. In this region, both gluon-gluon and quark-gluon reactions of momentum fraction $x = 0.03 \sim 0.1$ contributed, where quark transversity should be small and gluon transversity should be zero in the leading twist. The contributions of the transversity and Collins effect to the A_N were negligible in this measurement. On the other hand, the measurement at STAR[2)] in the forward-rapidity region was dominated by quark-gluon reactions, where there was a large contribution from quark transversity at $x \sim 0.6$.

Figure 1 shows the results of our measurements. Systematic errors were evaluated by comparing the independent measurements of two polarized beams of the collision and independent measurements of left and right detectors, and comparing minimum-bias and high-energy photon trigger data samples, and store-by-store consistencies of asymmetry values, which were determined to be small. The results of this evaluation were confirmed by the "bunch-shuffling" technique.[8)] The width of the shuffled distribution was compared with the statistical error on the physics asymmetry. The systematic errors were determined to be smaller than the statistical error.

The measured A_N was found to be consistent with zero to $\pm 2\%$ in the mid-rapidity region, which is less than one-tenth the A_N measured at STAR in the forward-rapidity region. The results are expected to be compared with QCD-based model calculations and to be used to determine many possible effects.

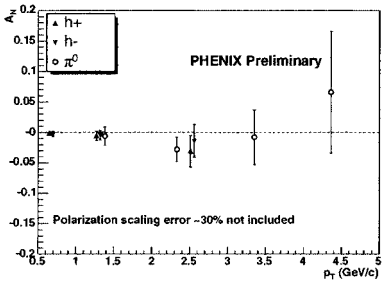

Fig. 1. Results of A_N measurements in neutral pion (π^0) and charged hadron (h^+ and h^-) production in the mid-rapidity region.

*1 Columbia University, USA
*2 University of California-Riverside, USA
*3 University of Illinois at Urbana-Champaign, USA
*4 Brookhaven National Laboratory, USA

References
1) D. L. Adams et al.: Phys. Lett. B **261**, 201 (1991); Phys. Lett. B **264**, 462 (1991).
2) J. Adams et al.: Phys. Rev. Lett. **92**, 171801 (2004).
3) D. W. Sivers: Phys. Rev. D **41**, 83 (1990); Phys. Rev. D **43**, 261 (1991).
4) J. C. Collins: Nucl. Phys. B **396**, 161 (1993).
5) J. W. Qiu and G. Sterman: Phys. Rev. D **59**, 014004 (1999).
6) C. Brourrely and J. Soffer: Eur. Phys. J. C **36**, 371 (2004).
7) S. S. Adler et al.: Phys. Rev. Lett. **91**, 241803 (2003).
8) Y. Fukao et al.: RIKEN Accel. Prog. Rep. 38, 211 (2005).

Measurement of prompt photons in $\sqrt{s} = 200\,\mathrm{GeV}$ pp collisions

K. Okada, Y. Akiba, A. Bazilevsky,[*1] Y. Goto, T. Horaguchi, K. Nakano,[*2] and H. Torii,
for the PHENIX Collaboration

Prompt photon production in proton-proton collisions is a good probe for investigating the parton structure of protons. Its leading subprocess is gluon-quark Compton scattering. In polarized proton-proton collisions at RHIC, it is a golden process for accessing the spin structure function of gluons in protons.

PHENIX is one of two multipurpose detectors at RHIC.[1)] It has electromagnetic calorimeters (EMCal) in the mid-rapidity region ($|\eta| < 0.35$). The EMCal has such a fine granularity ($10 \times 10\,\mathrm{mrad}^2$) that it can identify background photons by reconstructing the π^0 mass effectively. In addition, PHENIX has a tracking system which is useful for rejecting background clusters produced by charged hadrons. Data were collected with a minimum bias trigger provided by the beam-beam counter (BBC) and with an EMCal trigger. By requiring high-energy cluster with the EMCal trigger, event condensation by a factor of 120 was achieved. The EMCal trigger becomes fully efficient for clusters with an energy of above 3 GeV. This report is based on the luminosity of $266\,\mathrm{nb}^{-1}$ obtained in the RHIC proton-proton run in May 2003.

The prompt photon signal is obtained by subtracting known backgrounds from all EMCal clusters. The contribution of hadronic interactions is rejected using a photon shower shape cut and by requiring that no charged track is associated with the cluster. The dominant source of the background is two photon decay of π^0's. This background is estimated by reconstructing π^0's with two photon invariant mass. If only one of the two decay photons from π^0 is detected, it fakes a prompt photon signal. This probability mainly depends on the geometrical acceptance and kinematics of π^0 decays, which can be well reproduced by a Monte-Carlo simulation. The number of photons from hadronic decays other than π^0's is estimated on the basis of the total number of π^0's. Thanks to the highly segmented EMCal, two photon cluster merging for high p_T π^0 is not a problem in our p_T region. Of all photon clusters, 50(20)% are tagged as photons from π^0, and 85(30)% are estimated as photons from hadrons at $p_T = 5(16)\,\mathrm{GeV}/c$. The uncertainties of energy scale, of π^0 extraction, and of the ratio of hadron production to π^0 production are sources of systematic error. After the yield extraction, correction factors such as acceptance, efficiency, luminosity, and BBC trigger bias are applied to calculate the cross section.

Figure 1 shows our measurement results of prompt photon cross section as a function of p_T. Curves

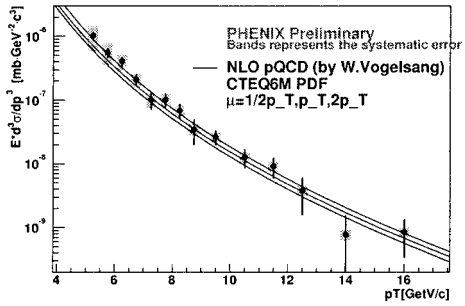

Fig. 1. Prompt photon cross section as a function of p_T.

show NLO pQCD calculations with 3 different scales.[2)] The theory agrees well with our experimental measurements.

Figure 2 shows the same data as a function of $x_T (\equiv 2p_T/\sqrt{s})$ superimposed on other experimental measurements scaled by $\sqrt{s}^5$. The agreement seen in Fig. 2 indicates a consistency among measurements. The index $n = 5$ in the scale $\sqrt{s}^n$ is close to the naive expectation ($n = 4$) for a point-like process. The small deviation from $n = 4$ can be attributed to the scaling violation, and it can be explained by perturbative QCD.

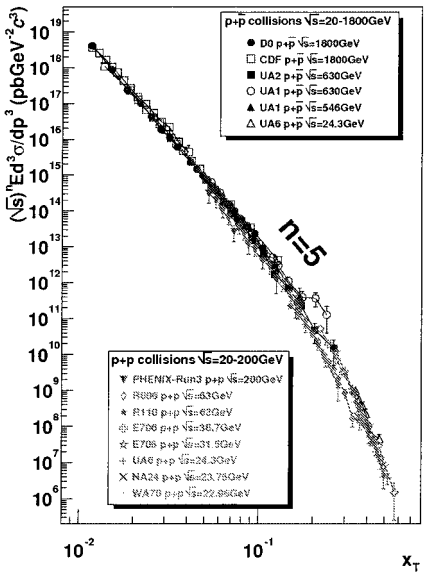

Fig. 2. Our results with other experimental measurements as functions of x_T with a scale of $\sqrt{s}^5$. Our range in x_T is from 0.05 to 0.17.

References

1) K. Adcox et al.: Nucl. Instrum. Methods Phys. Res. A **499**, 469 (2003).
2) Private communication with W. Vogelsang.

*1 Brookhaven National Laboratory, USA
*2 Tokyo Institute of Technology

Measurement of prompt photon cross section in proton-proton collisions at $\sqrt{s} = 200\,\mathrm{GeV}$ by isolation cut method

T. Horaguchi,* Y. Akiba, A. Bazilevsky, Y. Goto, K. Nakano* K. Okada, and H. Torii,
for the PHENIX Collaboration

Polarized proton-proton collisions at the Relativistic Heavy-Ion Collider (RHIC) can provide information on the spin structure of the nucleon. Prompt photons at a high p_T are produced mainly by quark-gluon Compton scattering ($gq \to \gamma q$). The measurement of the direct photon cross section is a testing ground of perturbative QCD, and it provides us the polarized and unpolarized gluon distributions in the nucleon.

In PHENIX,[1] we have collected data with an integrated luminosity of $0.15\,\mathrm{pb}^{-1}$ for transversely polarized proton-proton collisions with 15% average polarization in the run of 2001–2002 and $0.35\,\mathrm{pb}^{-1}$ for longitudinally polarized collisions in the run of 2003 at $\sqrt{s} = 200\,\mathrm{GeV}$ with 27% average polarization.

We analyze the 2003 data collected in PHENIX to measure the prompt photon cross section in proton-proton collisions at RHIC. The electromagnetic calorimeter consists of two subsystems, six sectors of lead scintillator calorimeter and two sectors of lead glass calorimeter. It is located at a radial distance of approximately 5 m from the beam line. Each of these sectors covers the pseudorapidity range of $|\eta| < 0.35$ and the azimuthal angle of $\phi = 0.4$ rad. In this analysis, we use four lead scintillator sectors in the West arm.

To measure the prompt photon cross section, we employ two methods. One is the subtraction method[2] and the other is the isolation cut method. In this paper, we will focus on the isolation cut method. This method requires that the prompt photon candidate is not accompanied by any other particle inside a cone of a certain radius R centered on the photon direction. R is defined as

$$R = \sqrt{\Delta\phi^2 + \Delta\eta^2}, \tag{1}$$

where ϕ is the azimuthal angle and η is the pseudorapidity. We choose $R = 0.5$ which is sufficiently large in PHENIX, and isolation cut conditions as follows;

$$E_{sum} = \sum_{R<0.5} E_i < E_\gamma \times 0.1, \tag{2}$$

where E_{sum} represents the sum of energy inside of a cone with $R = 0.5$ and E_γ represents the energy of the prompt photon candidate in the center of the cone.

We expect that the isolation cut around well-identified photons at a high p_T reduces the background contribution from hadronic dacays from jet. In addition, the isolation cut can separate photon production processes. While the prompt photon from jet fragmentation (Fig. 1 (b)) is suppressed by the cut, most of the prompt photons from quark-gluon Compton scattering (Fig. 1 (a)) can satisfy the cut.

Figure 2 shows the prompt photon cross section as a function of photon p_T measured by the subtraction method (dot) and isolation cut method (open square). The shaded box represents systematic errors. Because the isolation method decreases the background contribution, the systematic uncertainty can be suppressed compared with the subtraction method. We expect that the isolation method suppresses the prompt photon from jet fragmentation, which is predicted to occupy the cross section by 30%. However, the present result obtained by the isolation method is not so different as we expected. This indicates whether the isolation cut does not suppress the prompt photon from jet fragmentation or the cross section of the prompt photon is dominated by quark-gluon Compton scattering. It is critical to decrease the background contribution in the measurement of the polarized gluon distribution function. Further analysis is in progress.

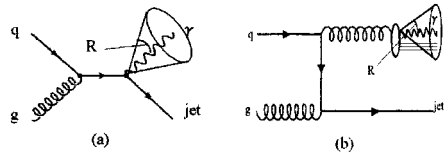

Fig. 1. Main contribution (a) and fragmentation contribution (b) to prompt photon production.

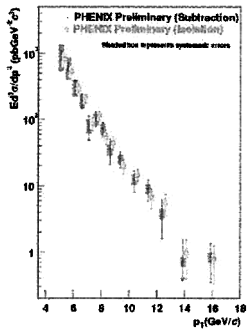

Fig. 2. Prompt photon cross section as a function of photon p_T measured by subtraction method (dot) and isolation cut method (open square).

References

1) K. Adcox et al.: Nucl. Instrum. Methods Phys. Res. A **499**, 469 (2003).
2) K. Okada et al.: RIKEN Accel. Prog. Rep. **38**, 209 (2005).

* Department of Physics, Tokyo Institute of Technology

Measurement of double helicity asymmetry (A_{LL}) in π^0 production in proton-proton collisions at RHIC-PHENIX experiment in Run 4

Y. Fukao,[*1] A. Bazilevsky,[*2] A. Deshpande,[*3] and Y. Goto, for the PHENIX Collaboration

One of the goals of the RHIC-Spin program is to measure gluon polarization in the proton. Double-longitudinal-spin asymmetry (A_{LL}) in high-transverse-momentum (p_T) particle production in polarized proton-proton collisions is a good probe. During the run in 2004 (Run 4), RHIC was operated using longitudinally polarized proton beams with a center of mass energy of 200 GeV. The average beam polarization was improved to be 40%, which is approximately 1.5 times higher than that in the run of last year (Run 3). Integrated luminosity accumulated at PHENIX[1)] was 75 nb^{-1}. This was approximately one third of the Run 3 statistics, however we obtained a higher figure of merit due to a higher polarization. In this report, we present A_{LL} in the π^0 production of the p_T range from 1 GeV/c to 5 GeV/c and at the midrapidity measured in Run 4.

A_{LL} can be calculated using

$$A_{LL} = \frac{1}{|P_B||P_Y|}\frac{N_{++} - RN_{+-}}{N_{++} + RN_{+-}}, \qquad R = \frac{L_{++}}{L_{+-}}, \quad (1)$$

where P_B and P_Y are the beam polarization, N is the yield of π^0, L is the integrated luminosity, $++$ ($+-$) denotes identical (opposite) helicity beams. We adopted a beam-beam counter (BBC) to measure R. Its error was evaluated by comparing the BBC counts with those obtained using a zero-degree calorimeter to be $\delta R = 5.8 \times 10^{-4}$, which corresponds to $\delta A_{LL} = 1.8 \times 10^{-3}$ for a beam polarization of 40%.

Beam polarization was measured using a proton-carbon CNI polarimeter.[2)] The CNI polarimeter assigned 32% to the error of the beam polarization, which affected the scaling error of double helicity asymmetry by 65%. The PHENIX local polarimeter[3)] confirmed that the direction of the proton spin in the PHENIX collision point was more than 99% longitudinal.

High p_T π^0's were collected using a high-p_T photon trigger[4)] based on an electromagnetic calorimeter with a 4×4 tile energy threshold of 1.4 GeV. A charged particle veto was applied to purify photons and to reduce background (BG) to the π^0 signal utilizing a pad chamber in front of the calorimeter. Table 1 shows statistics of π^0 within a ± 25 MeV mass window and fraction of BG under the π^0 peak obtained after the cut for particle identification.

The systematic error of A_{LL} can be evaluated by the bunch shuffling technique. In each shuffle, we randomly assigned a beam helicity sign to each bunch crossing. The number of bunch crossings was ~ 550 since we had 11 fills each containing ~ 50 crossings. This can mimic many experimental data. The fluctuation of A_{LL} generated by a sufficient number of shuffles should be a result of the statistics of π^0 and systematics, which depends on bunch and fill. By comparing the statistical error of A_{LL} with the width of the A_{LL} distribution obtained by bunch shuffling, we found that systematics is negligible compared with statistical uncertainty. Note that the systematic error correlated over all bunches or all fills cannot be evaluated by this bunch shuffling method. The main contributors to these errors are the uncertainty of beam polarization and the relative luminosity described above.

Figure 1 and Table 2 show Run 4 results of π^0 A_{LL} as well as the results of Run 3[5)] and combinations with statistical errors. Two theoretical curves[6)] are also drawn on the figure. Our results favor the GRSV-standard model.

Table 1. Statistics of π^0's and BG fraction.

p_T (GeV/c)	1-2	2-3	3-4	4-5
π^0 statistics ($\times 10^3$)	1151	510	91	17
BG fraction (%)	31	13	7	5

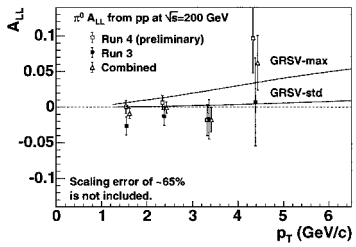

Fig. 1. π^0 A_{LL} as a function of p_T.

Table 2. π^0 A_{LL} in Run 4, Run 3 and combinations.

p_T (GeV/c)	1-2	2-3	3-4	4-5
Run 4 (%)	0.0 ± 0.9	0.7 ± 1.0	-1.8 ± 2.2	9.7 ± 4.9
Run 3 (%)	-2.7 ± 1.3	-1.3 ± 1.3	-1.7 ± 2.8	0.7 ± 6.2
Comb. (%)	-0.9 ± 0.7	0.0 ± 0.8	-1.8 ± 1.7	6.2 ± 3.8

*1 Kyoto University
*2 Brookhaven National Laboratory, USA
*3 Department of Physics and Astronomy, Stony Brook University, USA

References
1) K. Adcox et al.: Nucl. Instrum. Methods Phys. Res. A **499**, 469 (2003).
2) O. Jinnouchi et al.: RHIC/CAD Accel. Phys. Note, 171 (2004).
3) A. Deshpande et al.: RIKEN Accel. Prog. Rep. **37**, 246 (2004).
4) K. Okada et al.: RIKEN Accel. Prog. Rep. **36**, 248 (2003).
5) S. S. Adler et al.: Phys. Rev. Lett. **93**, 202002 (2004).
6) B. Jäger et al.: Phys. Rev. D **67**, 054005 (2003).

J/ψ production in polarized proton-proton collision at $\sqrt{s} = 200\,\mathrm{GeV}$ with PHENIX

N. Kamihara,* for the PHENIX Collaboration

Since a puzzle in the spin structures of nucleons was found by previous lepton deep inelastic scattering experiments, it has become important to measure gluon contributions to the nucleon spin structure (gluon polarization). Although J/ψ production is sensitive to gluon polarization, a theoretical ambiguity in the J/ψ production mechanism at proton-proton collisions makes it difficult to estimate gluon polarization from the double spin asymmetry (A_{LL}) of J/ψ production. Therefore, determination of J/ψ production mechanism is the first step to solving the nucleon spin puzzle. Measuring the J/ψ differential cross sections as functions of the transverse momentum and the rapidity can be a good test to aid in understanding the J/ψ production mechanism.

The PHENIX detector at BNL-RHIC is constructed to investigate the spin structure of protons and the formation of the quark gluon plasma. There are two muon spectrometers in the PHENIX which cover the pseudorapidity range from |1.2| to |2.4|.[1)] Each spectrometer consists of a magnet, a muon tracker (MuTr) and a muon identifier (MuID). The MuID sits behind the MuTr and consists of five layers of steel absorbers and chambers. The MuID is divided into four parts along the azimuth (quadrant) and used for the trigger system. Detailed descriptions of the PHENIX detector and the muon trigger system can be found in references.[1,2)]

The dimuon mass spectrums are obtained after the following criteria are met: i) the event vertex point from the Beam-Beam Counter[3)] is within the detector's fiducial volume, ii) each track hits the different quadrants because the current trigger system cannot distinguish two tracks in the same quadrant, and iii) χ^2 of track fitting is less than 20.

The dimuons fall into three categories. One is an unlike-sign pair contribution (N^{+-}), and the others are like-sign pair contributions (N^{++} and N^{--}). Since the unlike-sign pairs include the J/ψ signals and the combinatorial backgrounds, the like-sign pair spectrum is used for the estimation of the background contributions. The background is estimated from Eq. (1) since the shape of the unlike-sign background is, in principle, identical to the distribution of the geometric average of the like-sign pairs:

$$N_{bg} = 2R_{bg}\sqrt{N^{++}N^{--}}. \quad (1)$$

Here, R_{bg} depends on the correlation between accepted μ^+ and μ^- in each event. If there is no correlation between accepted μ^+ and μ^-, it is expected to be equal to 1.[4)] We determined R_{bg} by comparing N^{+-} and $\sqrt{N^{++}N^{--}}$ within the pure background region from $0.5\,\mathrm{GeV}/c^2$ to $2.5\,\mathrm{GeV}/c^2$. After obtaining R_{bg}, the number of J/ψ signals is deduced.

Figure 1 (A) shows the unlike-sign pair and background mass spectrum. The solid line corresponds to the unlike-sign events. The dashed line is the estimated background from Eq. (1). Figure 1 (B) shows the J/ψ spectrum after the background subtraction. The mass resolution obtained by the Gaussian fit in Fig. 1 (B) is about 140 MeV. The analysis to obtain the differential cross section is ongoing.

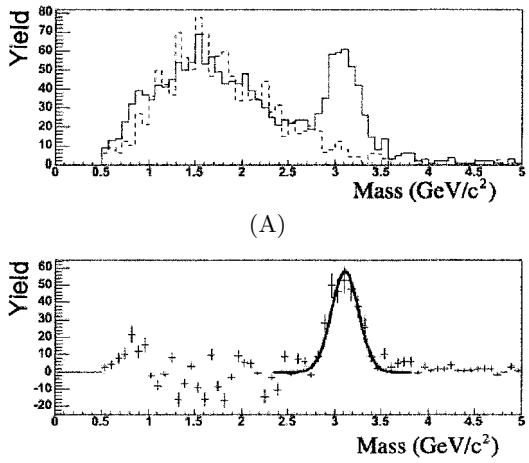

Fig. 1. (A) The unlike-sign pair and background mass spectrum. The solid line is for the unlike-sign events. The dashed line is the background. (B) The J/ψ mass spectrum after background subtraction.

References

1) H. Akikawa et al.: Nucl. Instrum. Methods Phys. Res. A **499**, 537 (2003).
2) N. Kamihara et al.: RIKEN Accel. Prog. Rep. **37**, 224 (2004).
3) M. Allen et al.: Nucl. Instrum. Methods Phys. Res. A **499**, 549 (2003).
4) M. C. Abreu et al.: Phys. Lett. B **438**, 35 (1998).

* Department of Physics, Tokyo Institute of Technology

Measurement of single electron spectrum in $\sqrt{s} = 200\,\mathrm{GeV}$ *p-p* collisions at RHIC-PHENIX

M. Togawa,[*1] Y. Akiba, R. Averbeck,[*2] S. Butsyk,[*2] F. Kajihara,[*3] T. Tabaru, Y. Tsuchimoto,[*3] and W. Xie, for the PHENIX Collaboration

Heavy quarks (charm and beauty) are generated mainly through the gluon-gluon fusion process in $\sqrt{s} = 200\,\mathrm{GeV}$ *proton-proton* collisions at RHIC. Thus, perturbative QCD can be tested and the gluon distribution function can be determined by measuring the heavy quark production. However the production mechanism of heavy quarks is not yet well known. At the Tevatron ($\sqrt{s} = 1.8\,\mathrm{TeV}$ and $1.96\,\mathrm{TeV}$ p-$\bar{p}$ collisions), the measured cross sections of D- and B-mesons were larger than those predicted by pQCD.[1)a)] STAR also measured larger a cross section of D-mesons in $\sqrt{s_{NN}} = 200\,\mathrm{GeV}$ p-p and d-Au collisions.[3)] We consider that these differences result from the uncertainties of the fragmentation and gluon distribution function.

In the PHENIX experiment, heavy quark production can be measured precisely with single electrons from semi-leptonic decays of charm and beauty mesons. These measurements can shed new light to understand the production mechanism of heavy quarks.

Electrons are detected by the two central arms of PHENIX. A central arm is composed of a tracking chamber system, a RICH (Ring Imaging CHerenkov counter) and an EMCal (Electro-Magnetic Calorimeter) system. It covers 90 degrees in azimuthal angle and $|\eta| < 0.35$ in pseudo-rapidity. Electrons are well identified by the RICH detector (Cherenkov threshold for $\pi^{\pm}$ being $4.9\,\mathrm{GeV}/c$) and the EMCal. The raw spectrum is corrected for the geometrical acceptance, the reconstruction and identification efficiencies as determined by a detailed GEANT simulation.

The yield of electrons can be categorized into *nonphotonic* and *photonic* sources. *Nonphotonic* electrons are mainly from semi-leptonic decays of charm and beauty. *Photonic* electrons include electrons from the gamma conversion and Dalitz decays of neutral mesons such as π^0 and η. To decompose these two sources, we installed a thin brass photon converter around the beam pipe and took data as a converter run. The converter increases electrons only from the gamma conversion by a fixed factor which is determined by the radiation length of the converter (1.7%). The effect of the converter was studied using the GEANT simulation of the PHENIX detector. By comparing the real data with the simulation with and without the converter, the *nonphotonic* electrons could be extracted. We analyzed $30\,\mathrm{nb}^{-1}$ of the nonconverter data and $47\,\mathrm{nb}^{-1}$ of the converter data. These data were taken with a special electron trigger, which requires a RICH hit and an associated energy deposit in EMCal of more than $400\,\mathrm{MeV}$.

Figure 1 shows the invariant p_{T} spectra of electrons from semi-leptonic decays of charm and beauty. Small remaining *nonphotonic* backgrounds such as K_{e3} decay were subtracted from the spectra. Present results (RUN3 data) are plotted as filled circle points together with the preliminary result from the previous RUN period (RUN2: statistics $\sim 20\,\mathrm{nb}^{-1}$) shown by triangles. They are consistent within the error. The curves show the expected spectra from a pythia calculation[4,5)] which is tuned to reproduce the charm production at SPS and FNAL.[6)] In our result, the cross section is larger than that of the tuned pythia calculation in the high-p_{T} region.

We have used $\sim$1/10 of all available statistics in this analysis. In the near future, comparison of the experimental data with the tuned pythia calculation can be made with smaller statistical error and the spectrum can be extended to the higher-p_{T} region with high statistics.

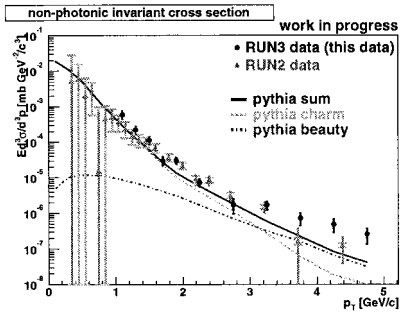

Fig. 1. The invariant p_{T} spectra of electrons from semi-leptonic decays of charm and beauty. The filled circles and triangles show the data corrected in 2003 (RUN3) and 2002 (RUN2), respectively. The curves show the expected spectra from the tuned pythia calculation.

*1 Department of Physics, Kyoto University
*2 Department of Physics, State University of New York-Stony Brook, USA
*3 Center for Nuclear Study, Graduate School of Science, University of Tokyo
*4 Graduate School of Science, Hiroshima University

a) Recently, NLO QCD calculation has been improved to agree with CDF data.[2)]

References

1) D. Acosta et al.: Phys. Rev. Lett. **91**, 241804 (2003).
2) CDF Collaboration: hep-ex/0408020 (2004).
3) J. Adams et al.: nucl-ex/0407006.
4) T. Sjostrand: Comput. Phys. Commun. **82**, 74 (1994).
5) K. Adcox et al.: Phys. Rev. Lett. **88**, 192303 (2002).
6) G. A. Alves et al.: Phys. Rev. Lett. **77**, 2388 (1996).

J/Ψ production in p-p, d-Au and Au-Au and collisions in the PHENIX muon arms

D. E. Fields*

Muons are an important probe for both the heavy ion physics program (focusing on the generation, detection, and subsequent characterization of the quark-gluon plasma (QGP) as well as studying the gluon distribution in nuclear matter) and the spin physics program (measuring the helicity distributions of flavor-separated quarks and antiquarks, as well as the first *direct* measurement of the gluon polarization in the nucleon[1]). For these purposes, the most interesting muons originate from vector meson (J/Ψ, Υ, *etc.*) decays, Drell-Yan decays, W-decays, and heavy flavor (c and b) meson decays. PHENIX has implemented a two-arm (North and South) muon spectrometer at high rapidity to supplement the photon, electron and hadron identification around mid-rapidity.[2] Although these muon arms are performing well, several upgrades are planned to improve the trigger rejection power and to discriminate based on coincident particles ($\chi_c \to J/\Psi + \gamma$) or offset vertices (c, b $\to e, \mu$).

The muon arms have now been operational through three separate RHIC runs, where data was taken with p-p, d-Au and Au-Au collisions. PHENIX has published the results of the J/Ψ analysis for the di-muons and di-electrons from Run02,[3,4] and is in preparation for the publication of the d-Au and p-p J/Ψ analysis from Run03. For RHIC Run03, both the North and South muon arms were operational and took nominal integrated luminosities of $\mathcal{L}_{\rm int} = 2.74\,{\rm nb}^{-1}$ in d-Au running and $\mathcal{L}_{\rm int} = 352\,{\rm nb}^{-1}$ in longitudinally polarized p-p running. The p-p data will increase our statistics for J/Ψs by approximately one order of magnitude over the published Run02 results. The d-Au analysis will provide insight into the nuclear and initial state effects on J/Ψ production since measurements were made simultaneously in the low- and high-x regimes with respect to the gold nucleus. Preliminary results for the ratio of d-Au to p-p are shown in Fig. 1. In addition to this important upcoming paper, analysis of the Run04 Au-Au data has proceeded and the first good measurement of the J/Ψ cross section as a function of centrality in relativistic heavy-ion collisions is forthcoming. A sample of the data quality is shown in Fig. 2 for a small subset of the total Run04 data set. The Run04 data anlalysis is nearing completion.

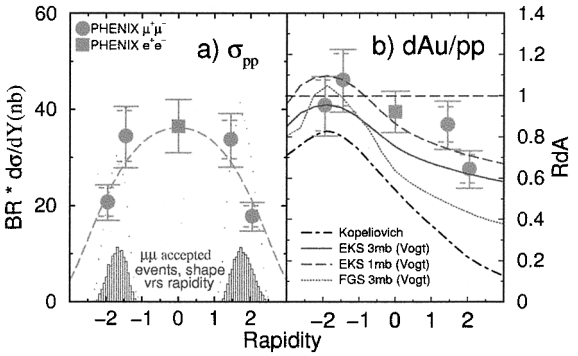

Fig. 1. Deuteron-Au J/Ψ cross section *vs.* rapidity (left panel) and the ratio of d-Au to p-p cross sections (right panel).

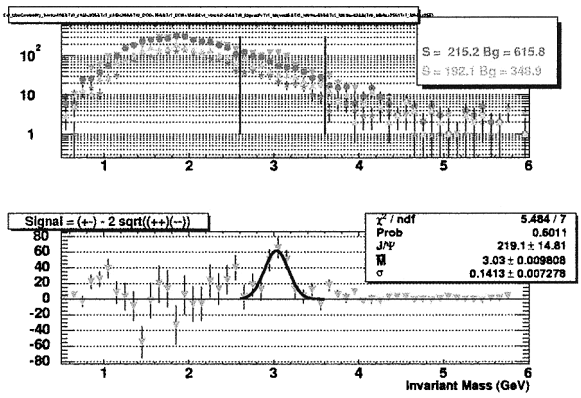

Fig. 2. Like-sign and unlike-sign di-muon invariant mass distributions (top panel) and thedifference between them (bottom panel) for peripheral Au-Au collisions showing a clear J/Ψ peak.

References

1) G. Bunce, N. Saito, J. Soffer, and W. Vogelsang: Annu. Rev. Nucl. Part. Sci. **50**, 525 (2000).
2) K. Adcox et al.: Nucl. Instum. Methods Phys. Res. A **499**, 602 (2003).
3) S. S. Adler et al.: Phys. Rev. Lett. **92**, 051802 (2004).
4) S. S. Adler et al.: Phys. Rev. C **69**, 014901 (2004).

* University of New Mexico, USA

Single electron measurement in the PHENIX Run3 *d*+Au experiment

F. Kajihara,[*1] Y. Akiba, R. Averbeck,[*2] S. Butsyk,[*2] H. Hamagaki,[*1] K. Ozawa,[*1] T. Tabaru, M. Togawa,[*3] Y. Tsuchimoto,[*4] and W. Xie,[*5] for the PHENIX Collaboration

Heavy-quark (charm and bottom) measurements provide valuable information for testing perturbative QCD (pQCD) predictions.[1] The measurements also impose significant conditions on uncertainties in the Leading Order (LO) and the Next-to-Leading Order (NLO) pQCD calculations of heavy-quark productions which considerably depend on the gluon distribution function.[2] In heavy-ion collisions, non-pQCD effects, such as conventional cold nuclear effects can also modify the gluon distribution, *i.e.*, heavy-quark production. Since such nuclear effects are unknown in high-energy region, it is important to investigate these influences on the heavy-quark measurements.

Heavy-quark production also has an important role in the investigation of the hot and dense matter created in heavy-ion collisions. The heavy-quark momentum spectrum may be affected by final state interactions such as its energy loss in the dense medium. However, the energy loss is predicted to be small compared with that of light quarks with high transverse momentum (p_{T}) due to the larger quark masses.[3] The measurement of high-p_{T} heavy quarks will verify the flavor dependence of energy loss. For precise measurements, it is essential to estimate and to subtract the influence of the above-mentioned nuclear effects.

The RHIC-PHENIX experiment measured d+Au collisions at $\sqrt{s_{NN}} = 200\,\mathrm{GeV}$ in 2003 (called Run3). We can study cold nuclear effects since no high-energy-density matter is formed. The measurement of single electrons (e^+ or e^-) from semileptonic decays of heavy quarks is a useful way to investigate heavy-quark production. Inclusive electrons can be categorized into two groups. The first group consists of "*photonic*" electrons mainly from (1) Dalitz decays of mesons (π^0, *etc.*) and (2) photon conversion. The second group is termed "*nonphotonic*" electrons. The decays of charm and bottom quarks are the dominant sources of the second group. This report presents the status of the *nonphotonic* electron measurements.

In the PHENIX, the electron measurements are performed by two central arm spectrometers. Each arm is composed of a Drift Chamber (DC), Pad Chambers (PC), a Ring-Imaging Čerenkov counter (RICH) and ElectroMagnetic Calorimeters (EMCal), covering pseudo-rapidity $|\eta| < 0.35$ and $\pi/2$ in azimuth (ϕ).[4] The RICH and EMCal are used for electron identification (eID) in the off-line analysis. They are also used to form an electron trigger system, called the EMCal-RICH Trigger (ERT).[5] To evaluate the ERT efficiency for electrons, a trigger simulator was developed in the PHENIX simulation framework. The simulator was also used for the low-mass-vector meson analysis.[6]

To extract *nonphotonic* yield $N(p_{\mathrm{T}})$ by subtracting *photonic* yield $P(p_{\mathrm{T}})$, the "converter subtraction" method is applied.[7] The Run3 experiment was performed with/without the installation of a brass photon-converter (1.68 radiation length) around the beam pipe. It can enhance *photonic* yield by a certain factor R_{sim}. The measured inclusive yield $I(p_{\mathrm{T}})$ can be expressed as $I(p_{\mathrm{T}}) = P(p_{\mathrm{T}}) + N(p_{\mathrm{T}})$ without the converter and $I'(p_{\mathrm{T}}) = R_{\mathrm{sim}}P(p_{\mathrm{T}}) + N(p_{\mathrm{T}})$ with the converter. Since (1)'s branching ratios and form factors, (2)'s probability, and the materials in the PHENIX environment are well known, R_{sim} can be evaluated with a GEANT-based simulation. $N(p_{\mathrm{T}})$ is given by these two equations. Figure 1 shows $N(p_{\mathrm{T}})$. The error bars indicate only statistic errors. The yield is fully corrected for the trigger efficiency, geometrical acceptance, reconstruction and eID efficiency that were determined by the simulation.

Presently, a more precise simulation is being developed to study systematic errors. The *nonphotonic* electrons in the high-p_{T} region ($\geq 5\,\mathrm{GeV}/c$) will be analyzed for the study of bottom quarks.

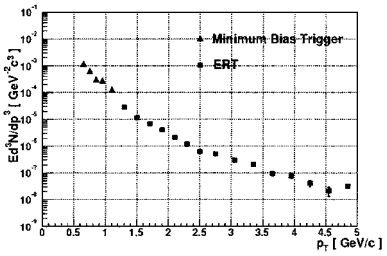

Fig. 1. The p_{T} distribution of *nonphotonic* invariant yield (triangle; minimum bias trigger, square; ERT).

*1 Center for Nuclear Study, University of Tokyo
*2 Department of Physics and Astronomy, State University of New York-Stony Brook, USA
*3 Department of Physics, Kyoto University
*4 Department of Physics, Hiroshima University
*5 Brookhaven National Laboratory, USA

References
1) S. Frixione et al.: hep-ph/9702287 (1997).
2) R. Vogt et al.: Z. Phys. C **71**, 475 (1996).
3) Y. L. Dokshitzer et al.: Phys. Lett. B **519**, 199 (2001).
4) K. Adcox et al.: Nucl. Instrum. Methods Phys. Res. A **499**, 469 (2003).
5) F. Kajihara et al.: CNS Annu. Rep. **2003**, 49 (2004).
6) Y. Tsuchimoto et al.: RIKEN Accel. Prog. Rep. **38**, 217 (2005).
7) S. S. Adler et al.: nucl-ex/0409028 (2004).

Radial flow study via identified hadrons spectra in Au+Au collisions at RHIC-PHENIX

A. Kiyomichi, for the PHENIX Collaboration

Heavy-ion collisions at relativistic energy offer the possibility of producing highly compressed strongly interacting matter, which may form the quark gluon plasma (QGP). An identified hadron provides important information on collision dynamics. The momentum spectra of pions, kaons, and protons are sensitive to the dynamical evolution of the system and carry information on the radial flow velocity and thermal freeze-out condition.

PHENIX[1] is one of the major experiments at RHIC for measuring a variety of signals from heavy-ion collisions. We have measured the transverse momentum spectra for $\pi^{\pm}$, $K^{\pm}$, p and $\overline{p}$ at mid-rapidity in Au+Au collisions at $\sqrt{s_{NN}} = 200\,\mathrm{GeV}$ over a broad momentum range with various centrality selections.[2] We have also measured ϕ meson production in the K^+K^- decay channel and compared it with identified charged hadron data.[3]

In order to deduce radial flow velocity and thermal freeze-out temperature, particle spectra were compared to a functional form, which describes a boosted thermal source, based on relativistic hydrodynamics.[4] A two–parameter model, termed the "blast-wave" model is used in this analysis, in which the surface radial flow velocity (β_T) and freeze-out temperature (T_{fo}) are free parameters,

$$\frac{dN}{m_T\,dm_T} \propto \int_0^R r\,dr\,m_T I_0\Big(\frac{p_T \sinh\rho}{T_{\mathrm{fo}}}\Big) \times K_1\Big(\frac{m_T \cosh\rho}{T_{\mathrm{fo}}}\Big),$$

where I_0 and K_1 represent modified Bessel functions with ρ being the transverse boost which depends on the radial position according to $\rho(r) = \tanh^{-1}(\beta_T)\cdot r/R$. To study the parameter correlations, a grid of $(T_{\mathrm{fo}}, \beta_T)$ pairs is generated and then a χ^2 minimization is performed for each particle type. The experimental data include the decay of resonance; we add the decay of mesonic $(\rho, \eta, \omega, K^*, , ,)$ and baryonic $(\Delta, \Lambda, \Sigma, , ,)$ resonance effects. The detailed analysis methods are described in Ref. 5.

The first fit attempt is performed simultaneously for the six particle species $\pi^{\pm}$, $K^{\pm}$, p and $\overline{p}$ in the range $(m_T - m_0) < 1.0\,\mathrm{GeV}/c^2$. The two–dimensional grid search results obtained in this analysis for each centrality bin are shown in Fig. 1. The expansion velocity parameter is seen to decrease moderately toward peripheral collisions and the kinetic freeze-out temperature increases significantly, approximately 40%. If one takes these parameters literally, then radial flow is weak in the peripheral collisions and the particles decouple kinetically from each other at temperatures close to the chemical freeze-out temperature. This is a physically reasonable scenario given the small number of participants in the initial expansion phase.

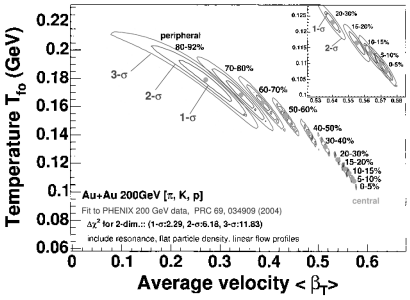

Fig. 1. Contour plots for hydrodynamical fit to 200 GeV single particle transverse momentum spectra. The contour lines are in standard deviation steps.

Figure 2 shows the 10% central spectra and blast-wave model fit results. The line drawn through the ϕ meson spectrum is the model's prediction obtained after fitting all other particle species. The shape of the ϕ meson spectrum is reproduced by the same flow parameters. As a result, the ϕ meson participates in the collective flow motion similar to other hadrons.

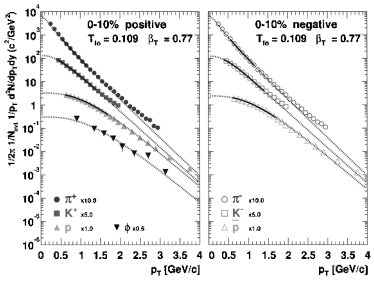

Fig. 2. Transverse momentum data and best-fit hydrodynamical results for 0–10% centrality bin for 200 GeV $\pi^{\pm}$, $K^{\pm}$, p and $\overline{p}$, along with prediction for ϕ transverse momentum spectrum.

References

1) PHENIX Collaboration, K. Adcox et al.: Nucl. Instrum. Methods Phys. Res. A **499**, 469 (2003).
2) PHENIX Collaboration, S. S. Adler et al.: Phys. Rev. C **69**, 034909 (2004).
3) PHENIX Collaboration, S. S. Adler et al.: to appear Phys. Rev. C, [nucl-ex/0410012].
4) E. Schnedermann, J. Sollfrank, and U. Heinz: Phys. Rev. C **48**, 2462 (1993).
5) A. Kiyomichi et al.: RIKEN Accel. Prog. Rep. **37**, 235 (2004).

Measurement of low-mass vector mesons in nuclear collisions at PHENIX

Y. Tsuchimoto* and Y. Akiba, for the PHENIX Collaboration

It is predicted that in nuclear matter at high baryon density and/or high temperature, chiral symmetry will be restored and consequently, the masses and the widths of the low-mass vector mesons (ρ, ω and ϕ) will be modified. If this phenomenon is observed, it will be one of the most interesting observations in high-energy nuclear physics. Some interesting results that suggest the modification of the properties of hadrons in ordinary nucleus matter have been reported.[1,2)]

The Relativistic Heavy Ion Collider at Brookhaven National Laboratory provides a great opportunity to study the properties of mesons in hot and dense matter. We have programs of $p+p$, $d+\mathrm{Au}$ and $\mathrm{Au}+\mathrm{Au}$ collisions at $\sqrt{s_{NN}} = 200\,\mathrm{GeV}$. Comparison of data in different collision systems is important to distinguish in-medium effects. The PHENIX experiment can measure the low-mass vector mesons in both e^+e^- and hadronic decay channels within the same acceptance at mid-rapidity. The e^+e^- decay channel carries information on mesons deep inside the hot and dense matter since an electron is not subject to strong interactions. Thus, comparison of the two decay modes is sensitive to the modification of the properties of the mesons. In this report, we present the measurement of the low-mass vector mesons in the dielectron channels in $d+\mathrm{Au}$ collisions at $\sqrt{s_{NN}} = 200\,\mathrm{GeV}$.

The PHENIX experiment at RHIC recorded about $1\,\mathrm{nb}^{-1}$ of $d+\mathrm{Au}$ collisions in the year 2003 run period. The PHENIX detector is described in detail elsewhere.[3)] Charged particle tracks were reconstructed by drift chambers and pad chambers. Electron identification was carried out using Ring Imaging Cerenkov detectors (RICHs) and electromagnetic calorimeters (EMC). The dielectron pair data were recorded mainly by an electron trigger, called ERT (EMC-RICH Trigger), which required a hit in the RICH and an associated energy deposit in the EMC. The data were taken in two running periods with different thresholds of EMC energy, 600 MeV and 800 MeV. The integrated luminosity of the two periods was approximately the same.

Figure 1 shows the dielectron invariant mass distribution. The data from the two running periods are combined in this figure. A high background due to the random combination of unrelated e^+ and e^- was subtracted by an event mixing method. One can clearly observe narrow peaks of ϕ (at 1020 MeV) and ω (at 780 MeV) in the mass distribution. To determine the production cross section of the vector mesons, the observed ϕ and ω yields should be corrected for the detector acceptance, electron ID efficiency, and the trigger efficiency. A simulator of the ERT trigger has been developed and incorporated into the GEANT-based PHENIX simulation program framework.[4)] We calculated the combined acceptance and efficiency using the simulation program. The results of the acceptance/efficiency calculation are shown in Fig. 2. In the next step, we will determine the invariant cross sections of ω and ϕ as a function of p_T using the acceptances shown in Fig. 2.

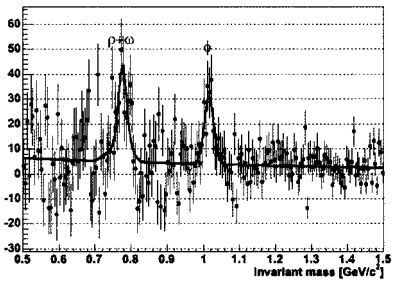

Fig. 1. Low-mass dielectron mass distribution in $d+\mathrm{Au}$ collision at $\sqrt{s_{NN}} = 200\,\mathrm{GeV}$.

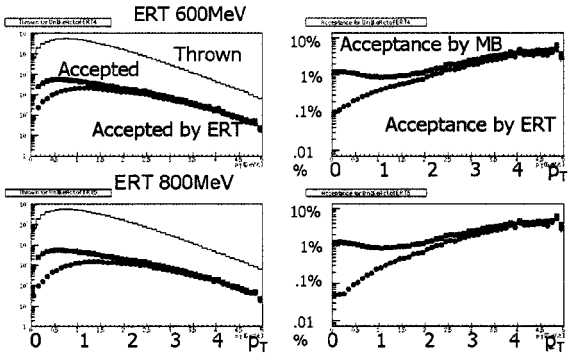

Fig. 2. Acceptances for $\phi \to e^+e^-$ in the PHENIX detector. The top and bottom panels are for the ERT thresholds of 600 MeV and 800 MeV, respectively. The upper acceptance curves (MB) are for minimum bias triggers.

References

1) K. Ozawa et al.: Phys. Rev. Lett. **86**, 5019 (2001).
2) K. Suzuki et al.: Phys. Rev. Lett. **92**, 072302 (2004).
3) K. Adcox et al.: Nucl. Instrum. Methods Phys. Res. A **499**, 469 (2003).
4) F. Kajihara et al.: RIKEN Accel. Prog. Rep. **38**, 215 (2005).

* Department of Physics, Hiroshima University

Charm Production in Au + Au collisions at $\sqrt{s_{NN}} = 200\,\mathrm{GeV}$†

T. Hachiya* and Y. Akiba, for the PHENIX Collaboration

Charm quark production is an important probe of the hot and dense medium created in high-energy heavy-ion collisions. Due to its large mass, the charm cross section is calculable *via* pQCD and the yield is sensitive to the initial gluon density. In the central Au + Au collisions at RHIC, π^0's and charged hadrons are strongly suppressed at high transverse momentum (p_T)[1] due to parton energy loss in the medium produced in the collisions. It has been predicted that charm quarks suffer less energy loss than light quarks due to the "dead cone" effect.[2] This effect can be studied through systematic measurement of open charm p_T spectra.

The measurement of single electrons resulting from semi leptonic decays of open heavy flavors ($D \to e+X$ and $B \to e+X$) at low p_T is a useful way to study charm production. The PHENIX experiment[3] has a unique ability to measure electrons with a wide momentum range using the ring imaging Čerenkov detector and the electromagnetic calorimeter. We measured single-electron production in Au + Au collisions at $\sqrt{s_{NN}} = 200\,\mathrm{GeV}$.

Inclusive electrons contain two components: "non-photonic" — primarily semi leptonic decays of open heavy flavor (charm and bottom), and "photonic" — Dalitz decays of light neutral mesons (π^0, η, η', ρ, ω and ϕ) and photon conversions in the detector material. To separate these two components, a thin (1.7% X_0) photon converter was installed around the beam pipe during a part of the run period. Since the photon converter multiplies the photonic component of electrons by a fixed factor determined by its radiation length, we can separate these two components by comparing the dataset with and without the converter.

Figure 1 shows fully corrected p_T spectra of non-photonic electrons for minimum-bias collisions and five centrality bins. PHENIX has also measured the heavy flavor electron spectrum in $p+p$ collisions at $\sqrt{s} = 200\,\mathrm{GeV}$.[4] The lines in Fig. 1 show the best-fit curve of this spectrum scaled by T_{AA} for each Au + Au centrality bin. Here, T_{AA} is the nuclear overlap function calculated using a Glaubar model.[1] Au + Au spectra are in reasonable agreement with the $p+p$ fit in all centrality bins.

To quantify the centrality dependence of charm production, we calculated the integrated yield dN_e/dy ($0.8< p_T <4.0\,\mathrm{GeV}/c$) and fit it to $AN_{\mathrm{coll}}^{\alpha}$, where N_{coll} and A are the number of nucleon-nucleon collisions and a normalization parameter, respectively, and $\alpha = 1$ is the expectation in the absence of the medium effects. Figure 2 shows dN_e/dy ($0.8< p_T <4.0$) / N_{coll} *vs.* N_{coll} for minimum-bias and five centrality bins in Au + Au collisions and $p+p$ collisions. We find that $\alpha = 0.938 \pm 0.075(\mathrm{stat.}) \pm 0.018(\mathrm{sys.})$. This shows that the total yield of charm electrons for all centralities is consistent with N_{coll} scaling. Our current statistics are too small to conclude charm suppression at high p_T.

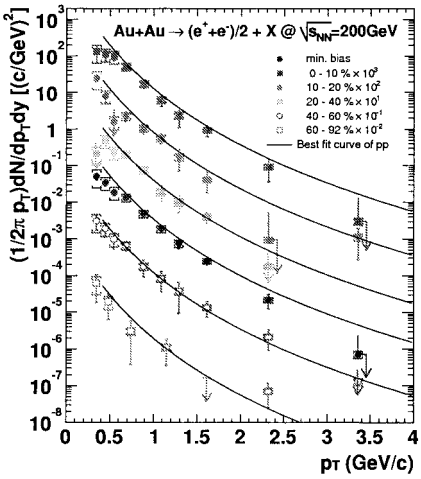

Fig. 1. Fully corrected p_T spectra of heavy flavor electrons for minimum-bias collisions and five centrality bins.

In conclusion, we have measured single electrons from heavy flavor decays in Au + Au collisions at $\sqrt{s_{NN}} = 200\,\mathrm{GeV}$. We observe that the centrality dependence of charm production is consistent with N_{coll} scaling, as is expected for hard processes.

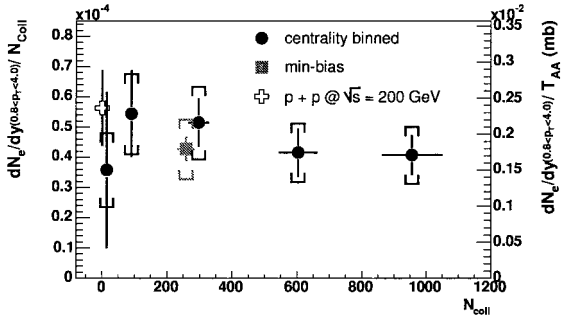

Fig. 2. Charm electron yield ($0.8< p_T <4.0\,\mathrm{GeV}/c$) scaled by N_{coll} as a function of centrality given by N_{coll}.

† Condensed from the article in arXiv:nucl-ex/0409028

* Hiroshima University

References

1) S. S. Adler et al.: Phys. Rev. Lett. **89**, 072301 (2003).
2) Y. L. Dokshitzer and D. E. Kharzeev: Phys. Lett. B **519**, 199 (2001).
3) K. Adcox et al.: Nucl. Instrum. Methods. Phys. Res. A **499**, 469 (2003).
4) S. Kelly et al.: J. Phys. G **30**, S1189 (2004).

Muon trigger upgrade with muon cathode strip chambers

K. Aoki,* for the PHENIX Collaboration

One of the major goals for the PHENIX detector[1] at the Relativistic Heavy Ion Collider (RHIC) is to enable the understanding of the spin structure of the proton. The proton consists of quarks and gluons, and its structure should be explained in terms of them. It has been discovered that only 10–30% of the proton spin is carried by quark spin,[2] which is much smaller than our naive expectation. The rest of the proton spin should be carried by gluon spin and orbital angular momentum. It has also been shown that s quarks, which exist as sea quarks in the proton, have spin anti-parallel to that of the proton. Sea quarks were thought to carry no quantum number before, thus it is also important to measure the other sea quark spin contributions as well as that of s quarks.

W production in pp collisions is a powerful tool to investigate the sea quark spin contribution because the reaction depends on both quark flavor and helicity.[3] The process is advantageous because it is a pure electroweak process and free from fragmentation functions. These features make W production a unique probe for the sea quark spin measurement.

PHENIX can detect W via the muon decay channel with the forward Muon Arm, which consists of the Muon Tracker (MuTr) and Muon IDentifier (MuID). The MuTr is a set of cathode strip chambers that are used for momentum measurement with a magnetic field. The MuID is a set of five chamber layers with alternating layers of steel walls which can distinguish muons from hadrons. The MuID also serves as a first-level muon trigger.

The RHIC design luminosity at $\sqrt{s} = 500\,\mathrm{GeV}$ is $2 \times 10^{32}\,\mathrm{cm^{-2}s^{-1}}$. When this is achieved, the reaction rate is 12 MHz. With the existing MuID trigger, whose rejection factor (RF) is about 250, the trigger rate is as high as 48 kHz. However, the maximum allowed trigger rate is 2 kHz, so we need a new trigger with the RF of at least 6 k to record all the W signals.

In MuID triggered events observed to date, low-momentum muons dominate while most of the muons that decayed from W have momentum above $40\,\mathrm{GeV}/c$. By selecting high-momentum muons at the trigger level, the desired RF can be achieved. However, the threshold of the MuID trigger is determined by the absorber thickness of the MuID steel, thus it is not easy to change the threshold. Therefore, we propose a new trigger with existing MuTr to select high-momentum muons. Figure 1 shows the concept of the new trigger. A muon has its trajectory bent in a magnetic field, thus the distance between the straight interpolation and the actual track (which is called the sagitta) is larger if the muon momentum is low. Thus, MuTr hit matching in the trigger level can be used to select high-momentum muons. This trigger also rejects unnecessary events in which muons are outside the MuTr acceptance but are in the MuID acceptance.

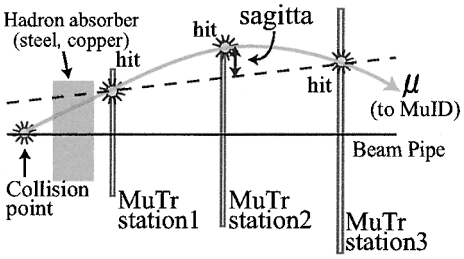

Fig. 1. The new trigger concept.

We performed simulations to estimate both the RF and efficiency for the W signal of the proposed trigger. The simulations were performed with the CCJ. Table 1 shows the estimated RF and efficiency. "Δstr" denotes a sagitta which is expressed in terms of the number of MuTr strips (= 10 mm). The efficiency of 66% is due to the acceptance (75%) and trigger plane efficiency (96%)^3. Sufficient RF is achieved while almost maximum efficiency is realized. Figure 2 shows the trigger logic efficiency in terms of muon momentum (trigger plane efficiency is not included).

To realize this idea, we are developing the fast readout electronics for the MuTr so that hit infomation can be used at the trigger level. We hope to finalize the first prototype soon.

Table 1. Estimated Rejection Factor and efficiency for W. Δstr is a sagitta in terms of the number of MuTr strips.

	MuID only	Δstr ≤ 1	Δstr ≤ 2	Δstr ≤ 3
RF	250	24 k	11 k	7 k
eff.	95	66	66	66

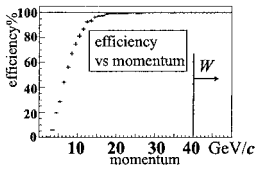

Fig. 2. Trigger logic efficiency for muons in the acceptance. Simulation.

References

1) K. Adcox et al.: Nucl. Istrum. Methods Phys. Res. A **499**, 469 (2003).
2) J. Ashman et al.: Phys. Lett. B **206**, 364 (1988).
3) G. Bunce et al.: Annu. Rev. Nucl. Part. Sci. **50**, 525 (2001).

* Department of Physics, Kyoto University

Multiparticle analysis for jet identification at PHENIX

K. Nakano* and Y. Goto

One of the goals of the PHENIX experiment is to obtain the polarized gluon distribution function in nucleon. With longitudinally polarized proton-proton collisions at RHIC, particles produced with high transverse momentum (p_T) are measured. Until recently, we have mainly focused on single-particle productions.[1] Here, we expand our scope and start analyses of multiple particles for the measurement of jet production. We need detailed studies of better jet-identification methods using the limited acceptance of the PHENIX Central Arms which cannot detect all the particles from a jet. The multiparticle measurement will provide us with higher statistics in the high-p_T region than the single-particle measurements.

We used RHIC-PHENIX RUN3 polarized proton-proton collision data, which was obtained at $\sqrt{s} = 200\,\mathrm{GeV}$ with an average beam polarization of $\sim 26\%$. For event selection, we required that at least one photon had a p_T of $> 2\,\mathrm{GeV}/c$. There are two Central Arms at PHENIX, each of which covers the pseudorapidity region $|\eta| < 0.35$ and 90-degree azimuthal angle, and are positioned almost back-to-back on their azimuth. We measured the total transverse momentum, $p_T^{\mathrm{sum}} \equiv |\sum_i \vec{p_T}_i|$, by summing p_T of photons and charged particles in one of the Central Arms which involves photons with $p_T > 2\,\mathrm{GeV}/c$. For $2 \to 2$ hard scattering events, we expect that one of the arms detects photons and charged particles from one scattered parton, and we can evaluate p_T and shape of a jet. Photons were detected with electromagnetic calorimeters and identified with shower-shape and charged-track veto conditions. Charged particles were detected with drift chambers and pad chambers and identified with a track-quality condition. Photons with $p_T > 0.4\,\mathrm{GeV}/c$ and charged particles with $0.4\,\mathrm{GeV}/c < p_T < 5\,\mathrm{GeV}/c$ were used to calculate the total transverse momentum.

To study the structure of events detected in one arm, we used a thrust variable, which represents the topology of particles. The thrust T is defined as

$$T \equiv \max_{\vec{u}} \frac{\sum_i |\vec{p}_i \cdot \vec{u}|}{\sum_i |\vec{p}_i|}. \quad (1)$$

Here, $\vec{u}$ is a unit vector, which is called thrust axis and is directed to maximize T, and $\vec{p}_i$ is the momentum of each particle in one arm. T is equal to one when all $\vec{p}_i$ are collinear, and T decreases as the jet cone size increases. In the PHENIX Central Arm acceptance, the mean value of the thrust of high-multiplicity isotropic events is equal to 0.88.

Figures 1 and 2 show the thrust distributions for events which have three particles in one arm and $6 < p_T^{\mathrm{sum}} < 7\,\mathrm{GeV}/c$ and $8 < p_T^{\mathrm{sum}} < 9\,\mathrm{GeV}/c$, respectively. They are compared with high-p_T QCD (hard scattering) events simulated with the PYTHIA event generator and isotropic events simulated by simply assuming that the particle production cross section is proportional to $\exp(-p_T)$. We used PYTHIA with tuned Multi-Parton Interaction (MPI) parameters because it reproduces event structures better than with the default parameters.[2,3] The measured thrust distributions show a rough agreement with the PYTHIA simulation, and this agreement indicates that the selected events are dominated by hard scattering events. The thrust values of both the real data and the PYTHIA calculation are generally larger than those of isotropic calculation, particularly in the high-p_T^{sum} range, and the distributions become sharper as p_T^{sum} increases. This is a characteristic of the shape of the jet. Therefore, we can conclude that jet structures are observed with the acceptance of the PHENIX Central Arms.

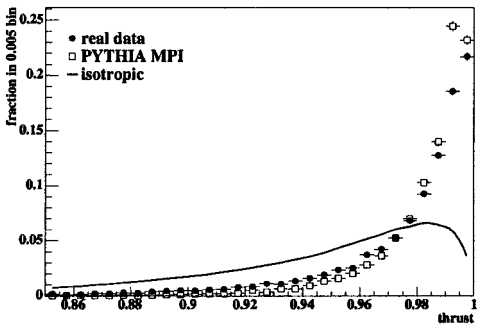

Fig. 1. Thrust distribution ($6 < p_T^{\mathrm{sum}} < 7\,\mathrm{GeV}/c$).

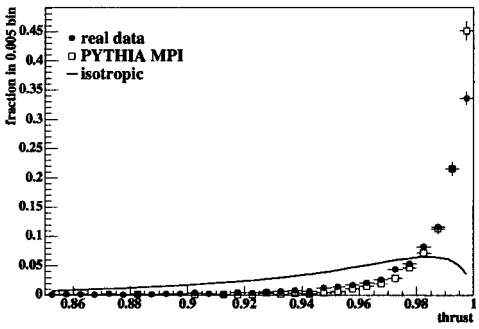

Fig. 2. Thrust distribution ($8 < p_T^{\mathrm{sum}} < 9\,\mathrm{GeV}/c$).

References

1) S. S. Adler et al.: Phys. Rev. Lett. **93**, 202002 (2004).
2) T. Affolder et al.: Phys. Rev. D **65**, 092002 (2002).
3) R. Field: Acta Phys. Pol. B **36**, 167 (2005).

* Department of Physics, Tokyo Institute of Technology

Pentaquark search in $\sqrt{s_{NN}} = 200\,\mathrm{GeV}$ Au+Au collisions at RHIC-PHENIX

M. Kaneta and H. Torii, for the PHENIX Collaboration

The Relativistic Heavy Ion Collider (RHIC) at Brookhaven National Laboratory is the largest heavy-ion collider and provides the highest energy heavy-ion collisions in the world. There are two areas of research at RHIC. The first one is the Quark-Gluon Plasma (QGP) search and the other is investigating the origin of the proton spin. The PHENIX experiment is one of the largest experiments at RHIC. The important issue in the QGP search is to measure several signals simultaneously. To accomplish that, PHENIX is designed to measure photons, identified hadrons, electrons (at the mid-rapidity region) and muons (at the forward-rapidity region).

The LEPS collaboration has reported an evidence for a narrow $S = +1$ baryon resonance state.[1] It is a candidate for $\Theta^+(uudd\bar{s})$ of which existence is predicted with mass 1.540 GeV. Θ^+ has two decay modes, $K^+ + n$ and $K^0 + p$. Additionally, the NA49 experiment at CERN-SPS has reported the other penta quark states, called $\Xi^{--}_{\frac{3}{2}}$ $(ssdd\bar{u})$ and $\Xi^{0}_{\frac{3}{2}}$ $(ssud\bar{d})$.[2]

Since the antibaryon to baryon ratio is more than 0.75 at mid-rapidity in $\sqrt{s_{NN}} = 200\,\mathrm{GeV}$ $p+p$ and Au+Au collisions,[3–6] we expect that antipentaquark to pentaquark ratio is a similar to or larger than 0.75. We have been attempting pentaquark searches using antineutrons, that is, $\bar{\Theta}^- \to K^- + \bar{n}$. PHENIX has an advantage in antineutron measurements with the Electro-Magnetic Calorimeter (EMCal). The $K^- + \bar{n}$ channel (two-body decay) has a larger acceptance than the $K^0_S + p(\bar{p})$ (which will decay three particles finally, i.e., $\pi^+ + \pi^- + p(\bar{p})$. Hence, $K^- + \bar{n}$ is a better channel than $K^0_S + p(\bar{p})$ for the PHENIX measurement.

The main purpose of PHENIX EMCal is photon and electron measurement. An antibaryon makes a larger energy deposit and different energy shower shape than photons and electrons. We identified an antineutron requiring three conditions: (1) an energy deposit on EMC is larger than 1 GeV, (2) the energy deposit not due to charged particles, (3) the shower shape is different from those produced by photons and electrons. K^- is identified by a cut of combinations of momentum and the EMCal Time-of-Flight.

The data we used is a set of minimum bias trigger data in $\sqrt{s_{NN}} = 200\,\mathrm{GeV}$ Au+Au collisions. The invariant mass distribution of the K^- and $\bar{n}$ pair is calculated for each event. The distribution has a combinatorial background and we estimate it by event mixing. The event mixing is performed by combining similar conditions of the event vertex and the centrality. The background distribution obtained is normalized to the data in a mass range of 1.6–1.8 GeV/c^2. Figure 1 shows the invariant mass distribution of the K^- and $\bar{n}$ pair with the background distribution (solid histogram) in each centrality bin. The centrality range is shown in each histogram.

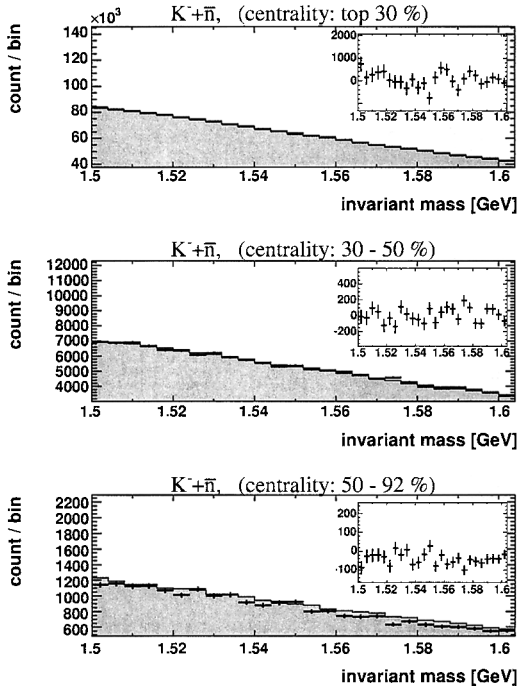

Fig. 1. Invariant mass distributions of K^- and $\bar{n}$ pair and combinatorial background distribution (solid histograms) are shown for each centrality bin. The plot after background subtraction is shown on top-right in each plot.

The results show no significant pentaquark peak around the expected mass ($\sim 1.540\,\mathrm{GeV}/c^2$) in any centrality bin. The estimation of the upper limit is in progress.

References

1) LEPS Collaboration, T. Nakano et al.: Phys. Rev. Lett. **91**, 012002 (2003).
2) NA49 Collaboration, C. Alt et al.: Phys. Rev. Lett. **92**, 042003 (2003).
3) BRAHMS Collaboration, I. G. Bearden et al.: nucl-ex/0409002.
4) PHENIX Collaboration, S. S. Adler et al.: Phys. Rev. C **69**, 034909 (2004).
5) PHOBOS Collaboration, B. B. Back et al.: nucl-ex/0409003.
6) STAR Collaboration, J. Adams et al.: Phys. Rev. Lett. **92**, 112301 (2004).

Pentaquark search in $\sqrt{s_{NN}} = 200\,\mathrm{GeV}$ $p+p$ and d+Au collisions at RHIC-PHENIX

H. Torii and M. Kaneta, for the PHENIX Collaboration

Since the first experimental evidence of a narrow $S = +1$ baryon (Θ^+) was reported by T. Nakano *et al.*,[1] further lines of evidence of Θ have been published by other researchers.[2] The mass of Θ^+ is close to the theoretical value predicted using a quark-soliton model[3] as the ground state of antidecuplet baryon. According to the model, Θ is predicted to confine five quarks ($uudd\bar{s}$) unlike three quarks. In addition to the ground state, the model predicts a higher excited state ($\Xi_{3/2}$), whose candidates were observed by NA49 collaboration.[4] The obtained evidence for the ground state Θ^+ is either from low-energy experiments at $\sqrt{s} < 10\,\mathrm{GeV}$ or from a photoproduction process. However, no positive evidence of Θ^+ has been found[5] in hadron collisions at a high energy.

Here, we report on the search for $\bar{\Theta}^-$ at RHIC-PHENIX in $\sqrt{s_{NN}} = 200\,\mathrm{GeV}$ $p+p$ and d+Au collisions obtained during 2002–2003. The numbers of events analyzed for $p+p$ and d+Au collisions are 35M and 91M, respectively.

The PHENIX experiment[6] has the advantage of being able to search the anti-pentaquark state through the $\bar{\Theta}^- \to \bar{n} + K^-$ channel rather than $\bar{\Theta}^+ \to p + K^0_s$. To identify $\bar{n}$, we used the PHENIX electromagnetic calorimeters (EMCal), which have an azimuthal coverage of $90° + 90°$ and a pseudorapidity coverage of ± 0.35. Because of the fine segmented structure and annihilation process of baryon and anti-baryon, EMCal can identify $\bar{n}$. For each cluster detected by EMCal, we require 1) a deposited energy of more than 1 GeV, 2) the absence of a charged particle near the candidate, and 3) larger shower size than photon. The charged particles of $\pi^\pm$ and $K^\pm$ are identified from the time-of-flight measured by EMCal. As proof that $\bar{n}$ is well identified, we utilize a decay process of $\bar{\Sigma}^\pm \to \bar{n} + \pi^\pm$. Figure 1 shows the invariant mass spectra of $\bar{n} + \pi^\pm$ with clear peaks at approximately 1.2 GeV. The shaded area represents an expected contribution of combinatorial background. In the $\bar{n} + \pi^+$ distribution, a deviation from the background at mass region lower than the peak position can be explained by the background process of $\bar{\Lambda} \to \bar{p} + \pi^+$. The two peak positions are consistent with expectations from the known masses of $\Sigma^\pm$.[2] The difference between the two peak positions is explained by the difference in the nominal mass.

Figure 2 shows the invariant mass spectra of $\bar{n} + K^-$ in $p+p$ and d+Au collisions with the expected background distribution depicted as a shaded area. The average mass[2] of Θ^+ observed by other experiments is indicated by the arrow in the figure. No clear peaks

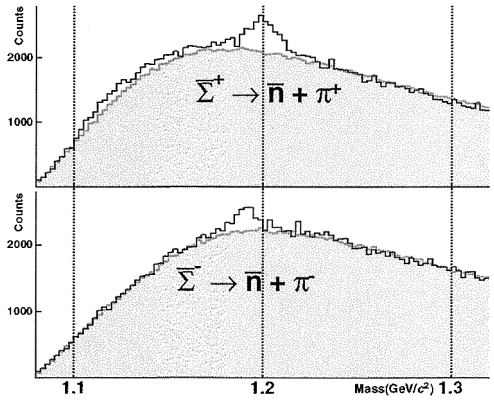

Fig. 1. Invariant mass spectra of $\bar{n} + \pi^\pm$. The shaded area shows the expected contribution of the background. The positions of the peaks are consistent with those expected from the decay of $\bar{\Sigma}^\pm$.

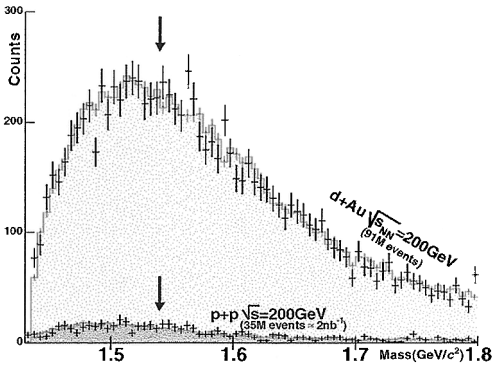

Fig. 2. Invariant mass spectra of $\bar{n} + K^-$ in $p+p$ and d+Au collisions. The shaded area shows the estimated background. The arrows represent the expected mass of the pentaquark.

at the expected region are observed. The estimate of the upper limit of the production cross section is in progress.

References

1) LEPS Collaboration, T. Nakano et al.: Phys. Rev. Lett. **91**, 012002 (2003).
2) For a recent review, Particle Data Group Collaboration, S. Eidelman et al.: Phys. Lett. B **592**, 1 (2004).
3) D. Diakonov et al.: Z. Phys. Lett. A **359**, 305 (1997).
4) NA49 Collaboration, C. Alt et al.: Phys. Rev. Lett. **92**, 042003 (2003).
5) See references in HyperCP Collaboration, M. J. Longo et al.: hep-ex/0410027.
6) K. Adcox et al.: Nucl. Instrum. Methods Phys. Res. A **499**, 469 (2003).

Measurement of single electrons in $\sqrt{s_{NN}} = 62.4\,\mathrm{GeV}$ Au-Au collisions at RHIC PHENIX

T. Tabaru, Y. Akiba, R. Averbeck,[*1] S. Butsyk,[*1] F. Kajihara,[*2] M. Togawa,[*3] and Y. Tsuchimoto,[*4]
for the PHENIX Collaboration

There is growing evidence that a new hot and/or dense matter is formed in heavy ion collisions at the RHIC energy. This state is considered to consist of deconfined partons. Heavy quarks are produced in the early stage of collisions, mainly from hard gluon-gluon fusions, and travel through the matter consisting of partons. Consequently, their yields are sensitive to the initial gluon density.[1] In addition, the heavy quarks experience interactions with the medium in a way different from light quarks, due to their heavy mass,[2] providing important information on the nature of the matter created at the RHIC energy.

In high-energy nuclear collisions, a large portion of electrons with transverse momentum (p_{T}) larger than $1\,\mathrm{GeV}/c$ comes from the decays of open heavy quarks (charm and bottom). Therefore, one can measure heavy quark production via electrons. This measurement also provides the baseline for the analysis of the J/ψ meson, which is predicted to be either suppressed[3] or enhanced[4] in the presence of deconfined quarks and gluons. In the RHIC-PHENIX experiment,[5] we measured electrons at mid-rapidity ($|\eta| < 0.35$) in the p_{T} range of 0.5 to $5\,\mathrm{GeV}/c$ in Au-Au, d-Au and p-p collisions at $\sqrt{s_{NN}} = 200\,\mathrm{GeV}$, and in Au-Au collisions at $\sqrt{s_{NN}} = 62.4\,\mathrm{GeV}$. In this article, we focus on the new data at $\sqrt{s_{NN}} = 62.4\,\mathrm{GeV}$.

During the 2004 run period, we recorded 2.6×10^7 events of Au-Au collisions at $\sqrt{s_{NN}} = 62.4\,\mathrm{GeV}$ with the minimum bias trigger, which was defined as a coincidence of two beam-beam counters. The paths of the charged particles were reconstructed with drift chambers and pad chambers. The electrons were identified by Ring Imaging Čerenkov counters (RICH) and electromagnetic calorimeters. We evaluated a large background of electrons from γ-conversion and from Dalitz decays of π^0 and η mesons using "converter subtraction method" as described in the literature.[6] For this purpose, we performed a dedicated run with additional conversion material (converter run) and collected 2.1×10^6 events. After subtracting the Dalitz and conversion backgrounds, there remained small backgrounds from kaon decays and light vector meson decays. These remaining background components were estimated using a Monte Carlo simulation. We found that the yield of these two components was approximately 10% of electrons form π^0 Dalitz decays in the range of $p_{\mathrm{T}} > 1\,\mathrm{GeV}/c$.

Subtracting all backgrounds, the only remaining source of electrons is heavy quark decays. Figure 1 shows the fully corrected electron spectrum from heavy quark decays. In the figure, the ISR single electron data[7–9] are also plotted after being scaled using the number of binary nucleon collisions for comparison. There is no significant difference between these data, which means that heavy quark production scales with the number of binary collisions. This is also consistent with the result of the Au-Au data at $\sqrt{s_{NN}} = 200\,\mathrm{GeV}$.[6]

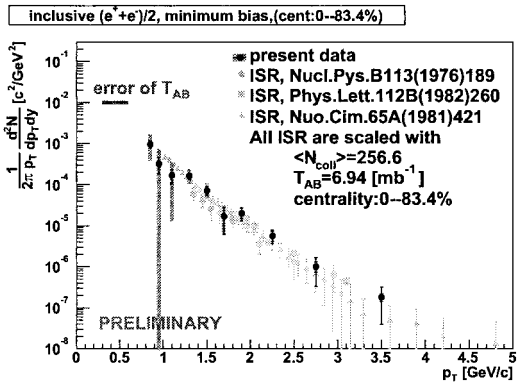

Fig. 1. Comparison of single electron p_{T} spectra between present data and the ISR data taken at same $\sqrt{s_{NN}}$.

References

1) B. Muller and X. N. Wang: Phys. Rev. Lett. **68**, 2437 (1992).
2) Y. L. Dokshitzer and D. E. Kharzeev: Phys. Lett. B **519**, 199 (2001).
3) T. Matsui and H. Satz: Phys. Lett. B **178**, 416 (1986).
4) R. L. Thews, M. Schroedter, and J. Rafelski: Phys. Rev. C **63**, 054905 (2001).
5) K. Adcox et al.: Nucl. Instrum. Methods Phys. Res. A **499**, 469 (2003).
6) S. S. Adler et al.: nucl-ex/0409028.
7) F. W. Büsser et al.: Nucl. Phys. B **113**, 189 (1976).
8) P. Perez et al.: Phys. Lett. B **112**, 260 (1982).
9) M. Basile et al.: Nouvo Cimento A **65**, 421 (1981).

*1 Stony Brook University, State University of New York, USA
*2 Center for Nuclear Study, University of Tokyo
*3 Kyoto University
*4 Hiroshima University

Measurement of analyzing power in *pp* elastic scattering in peak CNI region with polarized hydrogen gas jet target

H. Okada,[*1] I. Alekseev,[*2] A. Bravar,[*3] G. Bunce,[*3] S. Dhawan,[*4] R. Gill,[*3] W. Haeberli,[*5] O. Jinnouchi, A. Khodinov,[*3] A. Kponou,[*3] K. Kurita,[*6] Z. Li,[*3] Y. Makdisi,[*3] A. Nass,[*3] S. Rescia,[*3] N. Saito,[*1] H. Spinka,[*7] E. Stephenson,[*8] D. Svirida,[*2] T. Wise,[*5] and A. Zelenski[*2]

The elastic scattering of nucleons has been studied for a long time as the most fundamental information on the reaction of the elementary building blocks of the matter, nucleons. Five independent helicity amplitudes (ϕ_i; $i = 1\sim5$) are required to describe this process, assuming parity conservation. For example, the total cross section is described with ϕ_1 and ϕ_3. For spin-dependent asymmetry, analyzing power (A_N) is expressed with ϕ_5, which represents the hadronic spin flip amplitude. Particularly in very small momentum transfer in the $-t$ range of 0.001–0.02 $(\mathrm{GeV}/c)^2$, the helicity amplitudes of hadronic and electromagnetic components become similar and interfere with each other. A_N is expected to reach $\sim$4.5% at $-t$ of $\sim$0.003 $(\mathrm{GeV}/c)^2$ and is expected to change dynamically. We call this phenomenon Coulomb Nuclear Interference (CNI), and the shape of A_N is related to the hadronic amplitude.[1)] The only A_N data in the CNI region is from E704 at Fermilab, but the accuracy is limited to see the peak structure of A_N.

The CNI process is ideal in applications to a polarimeter for a high-energy proton beam, and to determine the RHIC beam polarization,[2)] we installed the RHIC Absolute Polarimeter this spring.[3)] The polarimeter comprises a polarized hydrogen gas jet target which includes a Breit-Rabi polarimeter to obtain a precise absolute measurement of the target polarization[4,5)] and a silicon spectrometer which counts the elastic scattering event yield. Both beam and target are protons; precise measurements of absolute beam polarization and A_N are completed simultaneously.

Figure 1 shows the schematic of the setup. To reduce systematic errors, the target polarization was flipped (up and down) every 8 minutes. We measured the energy (T_R), time of flight (tof) and angle (θ_R) of the recoil particles using silicon detectors, as shown.

To determine A_N, we count the elastic event yields from the left (N_{left}) and right (N_{right}) detectors, and divide their difference-to-sum ratio by the target polarization.

$$A_N = \frac{1}{P_{target}} \frac{N_{left} - N_{right}}{N_{left} + N_{right}}$$

*1 Department of Physics, Kyoto University
*2 Institute for Theoretical and Experimental Physics, Russia
*3 Brookhaven National Laboratory, USA
*4 Yale University, USA
*5 Department of Physics, University of Wisconsin, USA
*6 Rikkyo University
*7 Argonne National Laboratory, USA
*8 Indiana University Cyclotron Facility, USA

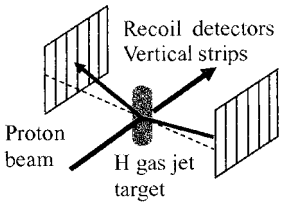

Fig. 1. Setup.

The key features of this experiment are high and accurate target polarization and correct selection of the elastic events. The target polarization was considerably high, accurate (0.924 ± 0.018)[4)] and stable during the entire running time. For the correct selection of elastic events, we confirmed that both recoil particle mass and forward-scattered particle mass were consistent with those of the proton, using two correlations. The correlation of T_R and tof confirms that the recoil particle is a proton (see Fig. 2). The correlation of T_R and θ_R confirms that the forward-scattered particle is a proton (see Fig. 3). In Fig. 3, T_R decreases at recoil angles of more than 5 mrad because the recoil protons penetrated through the silicon detector. To avoid this effect, we have focused on a smaller T_R region, $T_R < 5\,\mathrm{MeV}$, which corresponds to the $-t$ region of 0.0015–0.01 $(\mathrm{GeV}/c)^2$.

In this manner, we selected the elastic events correctly and counted event yield asymmetry. We obtained then finally A_N. Figure 4 shows our results as black points and E704 data as open circles. The errors on the y-axis are statistical only. The systematic errors of our data points are 0.0015 for all bins.

We measured A_N in the peak CNI region for the first time. The asymmetry is large and consistent with that without hadronic spin-flip (Fig. 4). However, the

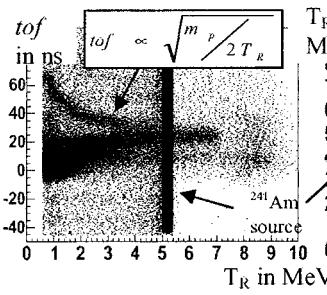

Fig. 2. Correlation of T_R and tof.

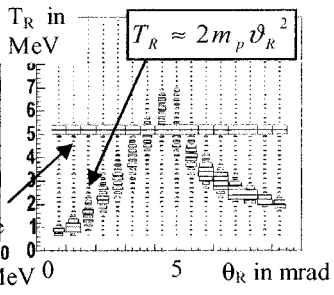

Fig. 3. Correlation of T_R and θ_R.

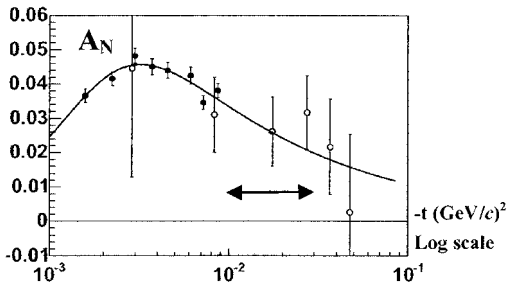

Fig. 4. A_N data for pp elastic scattering as a function of $-t$. Black circles depict our data obtained this spring and open circles depict E704 data. The solid line is fitted with nonhadronic spin flip. The analysis is in progress in the region marked by the arrow.

sensitivity to the hadronic spin flip is higher for $|t| > 0.01$. Further analysis is in progress.

References

1) L. Trueman: Proc. 16th Int. Spin Physics Symp. (SPIN 2004), Torieste, Italy, 2004-10 (To be published).
2) O. Jinnouchi et al.: RIKEN Accel. Prog. Rep. **37**, 245 (2004).
3) H. Okada et al.: RIKEN Accel. Prog. Rep. **37**, 243 (2004).
4) A. Zelenski: Nucl. Instrum. Methods Phys. Res. A **536**, 248 (2005).
5) A. Nass et al.: Proc. 16th Int. Spin Physics Symp. (SPIN 2004), Torieste, Italy, 2004-10 (To be published).

Measurement of the analyzing power of proton-carbon elastic scattering in the CNI region at RHIC

O. Jinnouchi, I. G. Alekseev,[*1] A. Bravar,[*2] G. Bunce,[*2] S. Dhawan,[*3] R. Gill,[*2] H. Huang,[*2] W. Haeberli,[*4] G. Igo,[*5] V. P. Kanavets,[*1] K. Kurita,[*6] A. Khodinov,[*7] Z. Li,[*2] Y. Makdisi,[*2] A. Nass,[*2] W. Lozowski,[*8] W. W. Mackay,[*2] H. Okada,[*9] S. Rescia,[*2] T. Roser,[*2] N. Saito,[*9] H. Spinka,[*10] D. N. Svirida,[*1] D. Underwood,[*10] C. Whitten,[*5] T. Wise,[*4] J. Wood,[*5] and A. Zelenski[*2]

The proton-carbon elastic scattering process in the Coulomb Nuclear Interference (CNI) region of very low momentum transfer, $-t$, has been used for the polarization measurment of the relativistic heavy-ion collider (RHIC) proton beam. This polarimeter has proven to be reliable, and has a high performance in measuring the beam polarization. In addition, the systematic errors, which were detailed in the annual reports,[1–3] are now mostly understood from the recent years of running. In spite of these advantages, the absolute normalization, *i.e.*, the analyzing power (A_N) of the process, has been known with 30% uncertainty[4] only near the RHIC injection energy (24 GeV). During the run 2004, data were collected simultaneously with the Polarized Hydrogen Jet target, which measure the beam polarization[5] for calibrating the p-carbon process at 24 and 100 GeV. The carbon ions recoil from the ultrathin carbon target and are detected by the silicon strip detectors (SSDs). The invariant mass is reconstructed with the measured time of flight and kinetic energy of carbon. The carbon mass peak ($\sigma = 1.7\,\mathrm{GeV/c^2}$) is clearly distinguished from background, and the carbon events are defined as the events within 3 standard deviations. The asymmetry is calculated with the square-root formula[6] to take full advantage of the alternating spin pattern in RHIC. The details of the setup and DAQ system are described in the previous article.[7] $-t$ is approximated as $-t = 2 \times M_C E_{kin}$, where M_C is the carbon mass and E_{kin} is the recoil energy; thus energy measurement is essential to precisely determine $-t$. For the energy calibration, the signal of 5.486 MeV α-particles from the ^{241}Am source is monitored throughout the run. Although SSDs were manufactured to have a very thin nonactive surface, the energy loss in this surface layer has a significant effect on low-energy spectroscopy. The layer thickness is assessed from the deformation of the carbon kinetic curve (tof *vs.* energy correlation). The thickness of $57\,\mu\mathrm{g/cm^2}$ is obtained with the uncertainty of $\pm 12\,\mu\mathrm{g/cm^2}$, which is the major systematic error of this measurement. 1.2×10^9 carbon events were collected with the Jet polarimeter running in parallel. Figure 1 shows the obtained $A_N^{pC}(t)$ at 100 GeV. The thin line on top of the data points is the fitting result with the model function which allows hadronic spin flip.[8] The error bars on data points represent the quadratic sum of the statistical error and the systematic error from the cut dependence on the invariant mass of carbon. Other major systematic errors are due to (i) the $-t$ ambiguity from the uncertainty in inactive surface layer thickness, and (ii) the error of the beam polarization measured with the Jet polarimeter, and these are shown by the shaded band in the figure. The major goal ($\delta P/P < 10\%$ calibration) of the Run-04 commissioning was successfully achieved. The $A_N(t)$ of the pC polarimeter at 100 GeV is obtained with good precision. The data at 24 GeV are under analysis, and we are looking forward to obtaining the new 24 GeV result fairly soon.

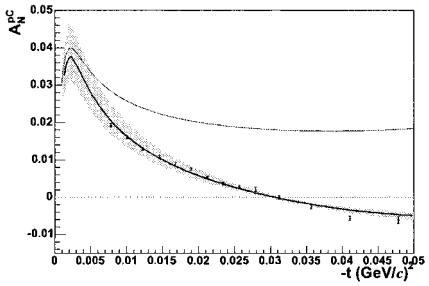

Fig. 1. Measured $A_N^{pC}(t)$ at RHIC 100 GeV. The calibration is carried out with jet measurement. The best-fit result obtained using hadronic spin-flip model significantly departs from the result of the non-spin-flip calculation (top curve). The shaded band represents the systematic uncertainty of the measurement.

*1 Institute for Theoretical and Experimental Physics, Russia
*2 Brookhaven National Laboratory, USA
*3 Yale University, USA
*4 University of Wisconsin, USA
*5 University of California, Los Angeles, USA
*6 Rikkyo University
*7 Stony Brook University, USA
*8 Indiana University Cyclotron Facility, USA
*9 Kyoto University
*10 Argonne National Laboratory, USA

References

1) O. Jinnouchi et al.: RIKEN Accel. Prog. Rep. **35**, 228 (2002).
2) O. Jinnouchi et al.: RIKEN Accel. Prog. Rep. **36**, 237 (2003).
3) O. Jinnouchi et al.: RIKEN Accel. Prog. Rep. **37**, 245 (2004).
4) J. Tojo et al.: Phys. Rev. Lett. **89**, 052302 (2002).
5) H. Okada et al.: RIKEN Accel. Prog. Rep. **38**, 224 (2005).
6) G. G. Ohlsen and P. W. Keaton: Nucl. Instrum. Methods **109**, 41 (1973).
7) O. Jinnouchi et al.: AIP Conf. Proc. **675**, 817 (2003).
8) T. L. Trueman: hep-ph/0305085 (2003).

PHENIX silicon vertex detector upgrade project

Y. Akiba, J. Asai, H. En'yo, K. Fujiwara,[*1] Y. Goto, J. M. Heuser, H. Kano, T. Kawasaki,[*1] Z. Li,[*2] H. Ohnishi, V. L. Rykov, N. Saito,[*3] T. Tabaru, A. Taketani, M. Tanaka,[*4] M. Togawa,[*3] J. Tojo, Y. Watanabe, and PHENIX VTX Collaboration

We propose the construction of a silicon vertex tracker (VTX) for the PHENIX experiment at RHIC. The VTX will substantially enhance the physics capabilities of the PHENIX central arm spectrometer. Our primary aim is to enable the precision measurements of heavy-quark production (charm and beauty) in $A+A$, $p(d)+A$, and polarized $p+p$ collisions. These are key measurements that are required for the future RHIC program, both for the study of high-density partonic matter created in heavy ion collisions and for the exploration of the nucleon spin structure function.

The main physics topics addressed by the VTX are as follows.

- Probing high-density partonic matter
  - open charm production
  - open beauty production
  - energy loss of charm in the dense matter
  - Thermal dilepton radiation
- Gluon spin structure of nucleon
  - $\Delta G/G$ measurement with charm
  - $\Delta G/G$ measurement with beauty
  - $\Delta G/G$ with γ-jet measurement
- Nucleon structure in nuclei
  - Gluon shadowing over broad x-range

The proposed VTX detector is shown in Fig. 1. The detector consists of two layers of silicon pixel detectors at the radii of 2.5 cm and 5 cm from the beam pipe and two layers of silicon strip detectors at the radii of 10 and 14 cm. The silicon pixel detector[1,2] has been developed in collaboration with the ALICE group at CERN (RIKEN–ALICE collaboration). The PHENIX pixel sensor and read-out chip are based on those of ALICE. The pixel chips were used andworked very well in the NA60 experiment. The silicon strip detector uses a novel "stripixel" sensor developed at BNL.[3] The sensor is to be read out using the SVX4 chip developed at FNAL.

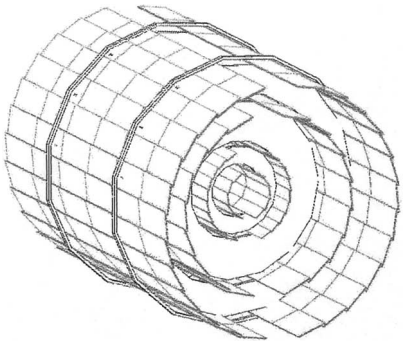

Fig. 1. The PHENIX VTX detector.

The main points of progress in this year are as follows.

- The configuration of the detector is upgraded to two pixel and two strip layers. The new configuration enables much more robust vertex tracking as well as better stand-alone momentum measurement.
- QA of the pixel chips at CERN[4]
- Development of "pilot" ASIC for the pixel layers[5]
- Development of thin data bus for the pixel layers[6]
- Development of the strip sensor[7]
- QA of the strip sensors at BNL[8]
- R&D of the strip ROCs using SVX4 chip at ORNL
- Software development for VTX[9]

With the aim of gaining the approval of the PHENIX silicon upgrade project as a construction plan, the "Proposal for a Silicon Vertex Tracker (VTX) for the PHENIX Experiment" was submitted to the U.S. Department of Energy through BNL in August 2004.[10]

*1 Niigata University
*2 Brookhaven National Laboratory, USA
*3 Kyoto University
*4 High Energy Accelerator Research Organization (KEK)

References

1) H. Ohnishi et al.: RIKEN Accel. Prog. Rep. **38**, 230 (2005).
2) J. M. Heuser et al.: RIKEN Accel. Prog. Rep. **38**, 139 (2005).
3) Z. Li et al.: Nucl. Instrum. Methods Phy. Res. A **518**, 300 (2004)
4) K. Fujiwara et al.: RIKEN Accel. Prog. Rep. **38**, 228 (2005).
5) H. Kano et al.: RIKEN Accel. Prog. Rep. **38**, 237 (2005).
6) A. Taketani et al.: RIKEN Accel. Prog. Rep. **38**, 233 (2005).
7) J. Tojo et al.: RIKEN Accel. Prog. Rep. **38**, 231 (2005).
8) J. Asai et al.: RIKEN Accel. Prog. Rep. **38**, 235 (2005).
9) V. L. Rykov et al.: RIKEN Accel. Prog. Rep. **38**, 236 (2005).
10) Y. Akiba et al.: Proposal for a Silicon Vertex Tracker (VTX) for the PHENIX Experiment (BNL, Upton, NY, 2004).

Evaluation of pixel read outchip of PHENIX silicon vertex upgrade

K. Fujiwara*, J. M. Heuser, H. En'yo, T. Iwabuti*, H. Kano, T. Kawasaki*, H. Ohnishi, and A. Taketani

The PHENIX experiment at the Brookhaven National Laboratory has been running since the year 2000, and it is planned to be upgraded by the year 2007 to enhance its physical capability in both heavy ion collisions (Au-Au) and polarized proton-proton collisions at the Relativistic Heavy Ion Collider. The purpose of the upgrade is to enable the precise measurement of heavy quarks, which carry direct signals from a Quark Gluon Plasma in heavy ion collisions and fundamental information of gluon polarizartion in polarized proton-proton collisions. Thus, the RIKEN group is developing a novel Silicon Pixel Detector (SPD) with the ALICE collaboration at CERN. A vertex tracker is planned with four cylindrical layers surrounding a beam pipe and each layer is placed 2.5 cm, 5 cm, 8 cm and 10 cm from the collision point, such that the tracker is exposed to very high radiation during the experiment period because of the high particle multiplicity. The inner two layers are constituted by an SPD and the outer two layers are constituted by a Silicon Strip Detector. The inner two layers are installed in a particularly high radiation environment. Therefore, we decided to construct these devices with radiation hardness technology, which was developed by the ALICE group at the CERN Large Hadron Collider.[1)]

This device is a hybrid device consisting of a silicon pixel sensor and a readout chip, which are interconnected by bump bonding technology with microscopic solder balls. The sensor chip is based on 200-μm-thick P^+N silicon produced by CANBERA and has 32 columns $\times$ 256 rows of pixels of 425 μm (z) $\times$ 50 μm (ϕ) size; the total size of the readout chip is 15.5 $\times$ 13.6 mm^2. The ALICE1LHCb readout chip is designed using a commercial 0.25 μm radiation hardness process, functions as an amplifier of a raw signal from each pixel, discriminates with configurable threshold levels, and stores this discriminated binary information to be read out downstream by a data acquisition system. The chip has 42 internal 8 bit Digital-to-Analog Converters (DACs) for controling the threshold of discriminators and various timings.[2)] All configurations are set via the JTAG serial interface (IEEE std. 1149.1-1990). The chip can be operated with a 10 MHz clock; therefore, the readout speed can be 25.6 μsec/chip with a 32 bit line.

Four hundred eighty ALICE1LHCb readout chips are required for the construction of the PHENIX Silicon Vertex Tracker. They are produced using a special method, which is radiation tolerance technology, as 8″ silicon wafers. In addition, the yield rate of the readout chips is not always 100%; therefore, it is necessary to probe the chip on the wafer. To identify fully functional chips, we have two tests which are carried out before and after bump bonding. They were developed at CERN.[3)] One is a quality assurance (QA) test of the ALICE1LHCb readout chip on a wafer. The other is the QA test of interconnected hybrid ladders with a radioactive source to check the interconnection of both the sensor substrate and readout chips. This report describes the first QA test. Each procedure is performed using a semiautomatic probe station at CERN, which is shown in Fig. 1. One wafer contains 86 readout chips. In the first test, all chips are touched with a dedicated probe card and connected to the testing equipment. Then, test pulses and control signals are injected into the chip and digital information is read out for evaluation. Initially, all chips are tested for the following common parameters.

- Measurement
  - Both digital and analog current consumptions are measured.
- Confirmation
  - JTAG functionality.
  - The internal DAC functionality is tested. In the test, the linearlity of the changed DAC value is measured.
  - The minimum threshold and noise level on a chip are measured. Initially, a global threshold on a chip is set. Then, the reference pulse is sent to each pixel as the pulse height is changed. The minimum threshold is defined as the dispersion from the global level for all pixels and also the minimum noise level is defined as the dispersion of each pixel threshold.

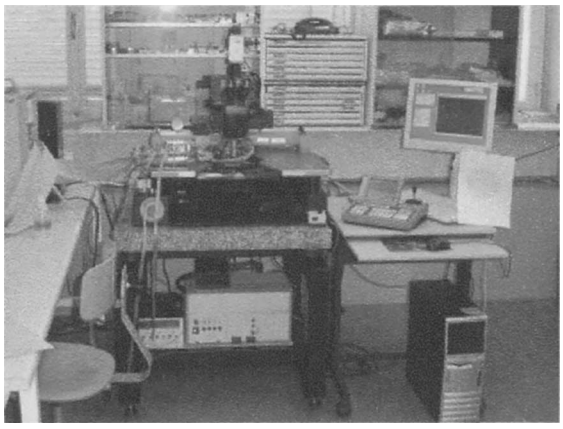

Fig. 1. Semiautomatic prober.

* Science and Technology, Niigata University

The classification of the wafer probe is divided into three classes (Classes 1, 2, 3), which is described later. Class 1 chips are of sufficiently good quality for the construction of a ladder. Chips that have more than 82 defect pixels or that have a minimum threshold higher than 30 mV (1980 e^-) become Class 2. Finally, chips that have too much current for the digital or analog circuit or that do not respond to the test pulse are put into Class 3.

- Class 1 (Chips for ladder)
  - JTAG and DAC are functional.
  - The consumption current for the analog circuit is less than 350 mA.
  - The consumption current for the digital circuit is less than 270 mA.
  - Less than 82 defect pixels on a chip.
  - The minimum threshold is less than 30 mV (1980 e^-).

At present, 860 chips (10 wafers) have been probed, and we have obtained 303 Class 1 chips. The average yield is shown in Table 1. The average yield is 35% for Class 1 chips.

Figure 2 shows a typical minimum threshold and mean noise value. The minimum threshold is 1868 e^-, the standard deviation is 350 e^-, and the mean noise value is 205 e^-. Usually, the number of electrons induced by the minimum ionizing particles in the silicon sensor of the thickness of 200 μm is around 15000 e^-. Consequently, the signal-to-noise ratio is more than 10. Figure 3 shows an example of the probing result. It seems that Class 1 chips are in the middle region of a wafer.

In summary, 303 Class 1 chips were obtained. Two probed wafers have already been sent to a factory for the bump bonding process. The number of chips is sufficient for the production of 75 ladders for the PHENIX experiment, indicating that we can construct most of the inner tracker with these chips. The tracker requires 480 chips and some spares; we expect to finish probing by the end of December 2004. The first production ladders for PHENIX will arrive from the factory in Jannuary 2005, and we will start probing these ladders soon after.

Table 1. The total yield rate of wafer probing.

Class 1	35%	303 chips
Class 2	13%	108 chips
Class 3	52%	449 chips

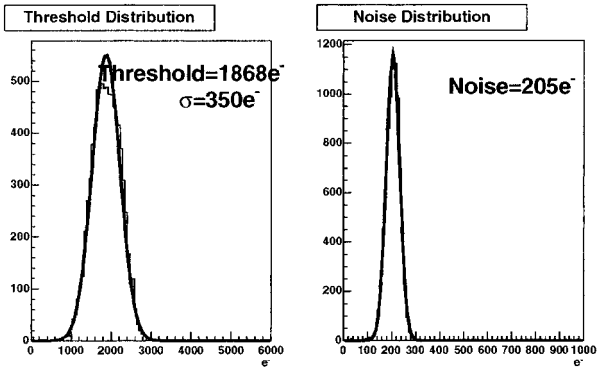

Fig. 2. Typical minimum threshold dispersion and minimum noise dispersion on a readout chip (Wafer Name: AVA4LJT, Chip ID: 6).

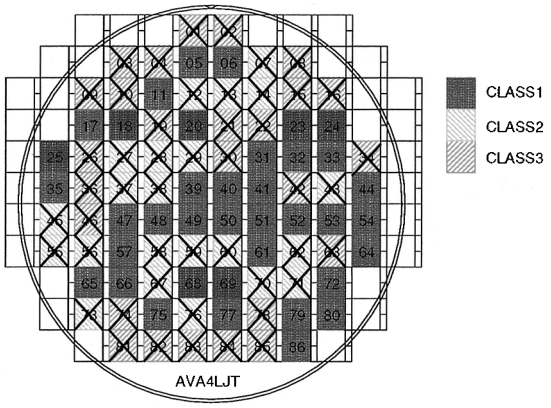

Fig. 3. Example of probing result.

References
1) Y. Akiba: RIKEN Accel. Prog. Rep. **38**, 227 (2005).
2) J. M. Heuser: RIKEN Accel. Prog. Rep. **38**, 139 (2005).
3) P. Riedler et al.: Nucl. Phys. A **501**, 111 (2003).

Development of silicon pixel detectors for PHENIX at CERN

H. Ohnishi, H. En'yo, K. Fujiwara, J. M. Heuser, H. Kano, and A. Taketani

The Silicon Vertex Tracker (SiVTX) has been proposed as a detector upgrade for the PHENIX experiment at the Brookhaven National Laboratory's Relativistic Heavy Ion Collider. The prime motivation for this new detector system is to provide precision measurements of heavy-quark production (charm and beauty) in A-A, p(d)-A, and polarized p-p collisions. For these measurements, the new detector needs to satisfy the following requirements:

- The SiVTX needs to operate over a wide dynamic range, from particle multiplicities with a few tracks in the case of p-p collisions up to several hundred tracks in central heavy-ion collisions.
- The origin of an electron from a heavy-quark decay has an offset of the order of 100 μm with respect to the primary vertex position, due to the life time of the heavy quark. In order to separate the electron from the background that mainly originates from the primary vertex, the resolution of the track offset measurement must be equal to or less than 50 μm.

The SiVTX realizes the desired performance with four layers of silicon detectors. It will consist of two internal layers of silicon pixel detectors and two outer layers of silicon strip-pixel detectors. For the pixel detectors, we decided to utilize the technology developed for the ALICE experiment at the Large Hadron Collider (LHC) at CERN. Two activities are ongoing at CERN for the PHENIX pixel detector project. Firstly, we have established a collaboration with the ALICE experiment, with the goal of actually constructing important componets for PHENIX silicon pixel detector modules[1] in a partnership with the ALICE Pixel Detector Group. Secondly, we are working with the NA60 experiment at the CERN-SPS which applies the same silicon pixel detectors in its Vertex Tracker. The purpose of this collaboration is to learn the operation and basic functionality of the silicon pixel detectors.

A more detailed description of the NA60 Vertex Tracker is given elsewhere.[2] The Vertex Tracker was constructed and installed in 2003 and operated during two beam periods: Indium-Indium collisions in 2003 and proton-nucleus collisions in 2004. One of the challenges of this experiment is the operation of the silicon pixel detector in a high-radiation environment. The particle fluence at the silicon pixel detector, which is very inhomogeneous with radius from the beam axis, is up to 10^{12} 1 MeV equivalent neutron flax per cm per week (1 MeV $n_{eq.}/cm^2$/week). It should be noted that the radiation dose expected for the silicon pixel detector of ALICE is much lower, approximately 1.75×10^{12} 1 MeV $n_{eq.}/cm^2/10$ y. The conditions for PHENIX are similar. Therefore, five weeks of NA60 data taking corresponds to approximately 30 years of data taking with ALICE or PHENIX. The measurements performed with NA60 will be unique reference for determining the detector performance, particularly concerning the radiation damage of the silicon sensors. The performance of the detector was closely monitored during the run. Figure 1 shows an example of the tests performed with one of the tracking planes. The left panel presents an integrated hit map obtained with the sensors biased at 150 V after five weeks of irradiation. The right panel shows the situation at 30 V bias. Note that new sensors deplete typically between 9 V and 30 V bias. The dead area in the central region of the plane indicates that at 30 V the silicon sensors were no longer fully depleted; radiation damage and type inversion had occured where the sensors were exposed to the largest particle fluences. Further analysis of the systematic measurements is ongoing and will give us a unique view of the evolution of the radiation damage.

In summary, the silicon pixel detectors that we plan to use for the PHENIX Vertex Tracker have been successfully operated in a high-radiation environment. In five weeks, the detectors sustained fluences up to 5×10^{12} 1 MeV $n_{eq.}/cm^2$, which is equivalent to three decades of PHENIX running. These results justify the selection of the pixel detector for PHENIX in terms of radiation hardness.

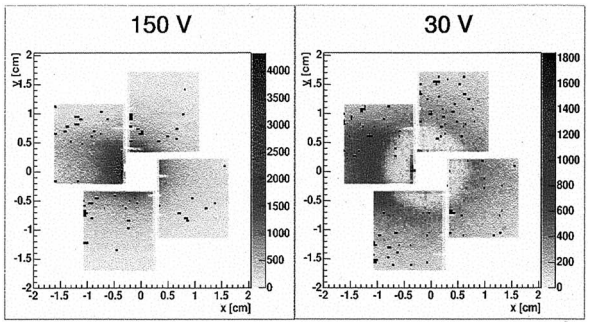

Fig. 1. Hit maps of an irradiated NA60 Pixel Detector tracking plane at different bias voltages. At low bias voltage, the central area with reduced hits identifies type-inverted silicon.

References

1) J. M. Heuser et al.: RIKEN Accel. Prog. Rep. **38**, 139 (2005).
2) H. Ohnishi et al.: Nucl. Phys. A **734**, 49 (2004).

Development of silicon stripixel detector for PHENIX silicon vertex tracker

J. Tojo, Y. Akiba, J. Asai, H. En'yo, Y. Goto, Z. Li,* and A. Taketani

The use of a silicon vertex tracker (VTX) for the PHENIX experiment in the Brookhaven National Laboratory (BNL) has been proposed to enhance the physics capability of the baseline detector system.[1] The VTX consists of four barrel layers of silicon detectors that cover the acceptance of almost $2\,\pi$ in an azimuthal angle and $|\eta| < 1.2$ in pseudo-rapidity. An overview of the PHENIX VTX project is given in Ref. 2. In this article, we report the development of a stripixel detector for the outer two barrel layers of the VTX.

The stripixel detector concept innovated by the BNL Instrumentation Division has a novel feature of two-dimensional position sensitivity with single-sided processing, which is achieved by charge sharing between two interleaved electrodes in one pixel. The details of the detector concept are given in Ref. 3. The stripixel detector for the PHENIX experiment has been designed and prototyped in collaboration with the BNL Instrumentation Division. The detailed performance of the prototype detector has been studied in static electrical tests[4] and beam/source tests.[5] On the basis of the results obtained, we decided to apply the stripixel detector technology to the outer barrel layers of the VTX.

The outer two barrel layers of the VTX are planned to be constructed with 246 stripixel sensors that cover a $2000\,\mathrm{cm}^2$ area in the third layer and a $3400\,\mathrm{cm}^2$ area in the fourth layer.[6] The production of such a large number of silicon sensors has to be performed in a company that has an appropriate silicon wafer processing technology with an acceptable production yield. The processing technology of the very fine pattern and many through holes in the stripixel sensor is nontrivial. Two companies, SINTEF in Norway and Hamamatsu in Japan, were selected as candidate companies for sensor mass production. In these two companies, sensor preproduction has been carried out in order to evaluate the mass production capability of the company technologies.

The sensor preproduction processes carried out are summarized in Table 1. There are five types of preproduction sensor, distinguished in terms of the company process, wafer mask design, wafer size and wafer thickness. The main difference between the SINTEF and Hamamatsu processes is in the double-metal process required to form strip electrodes in the stripixel sensor. The insulation layer between two metal layers is made of 2-μm-thick polyimide in the SINTEF process or 1-μm-thick SiO_2 in the Hamamatsu process. Three mask designs in Table 1 were produced to meet the process and detector design requirements. In all the designs, the stripixel structure was designed with five-turn spiral p^+ electrodes of $5\,\mu$m lines and $3\,\mu$m gaps. The "v2b" mask design is the same as the prototype sensor design[4] with two sensors on a $4''$ silicon wafer. The "v2c" mask design is the same as the prototype sensor design except for the guard ring and additional aluminum pads for testing, with three sensors on a $6''$ silicon wafer. The "v3a" mask design was modified from the v2c design to be optimum for the construction of a ladder-shaped detector module in the VTX. The sensor design is shown in Fig. 1. The readout pads were placed in the longer edges of the sensor and designed to match the SVX4 readout chip[7] for use in the VTX. The dead space in the middle of the sensor, which existed in the v2c design for the arrangement of the readout pads, was eliminated. A photograph of the "H-3a-500" type wafer is shown in Fig. 2. The number of wafers processed and delivered is listed in Table 1.

In the first stage of the evaluation, the fabricated preproduction sensors will be tested in a newly built clean room at the RIKEN BNL Research Center and in the silicon detector facility at the University of New Mexico.[8] The static electrical properties (leakage current and capacitance) and the wafer/sensor production yield in each type of sensor will be measured on a wafer with a semiautomatic probe station. The tested wafers will be laser-diced at the BNL Instrumentation Division. In the second stage, the sensors will be wire-bonded to the readout electronics with SVX4 chips at RIKEN and evaluated by reading out signals with the

Table 1. Stripixel sensor preproduction processes.

Type	Process	Mask design	Wafer size [in.]	Wafer thickness [μm]	# Wafer	# Sensor
S-2b-500	SINTEF	v2b	4	500	17	34
H-2c-500	Hamamatsu	v2c	6	500	6	18
H-2c-625	Hamamatsu	v2c	6	625	6	18
H-3a-500	Hamamatsu	v3a	6	500	11	33
H-3a-625	Hamamatsu	v3a	6	625	12	36

* Brookhaven National Laboratory, USA

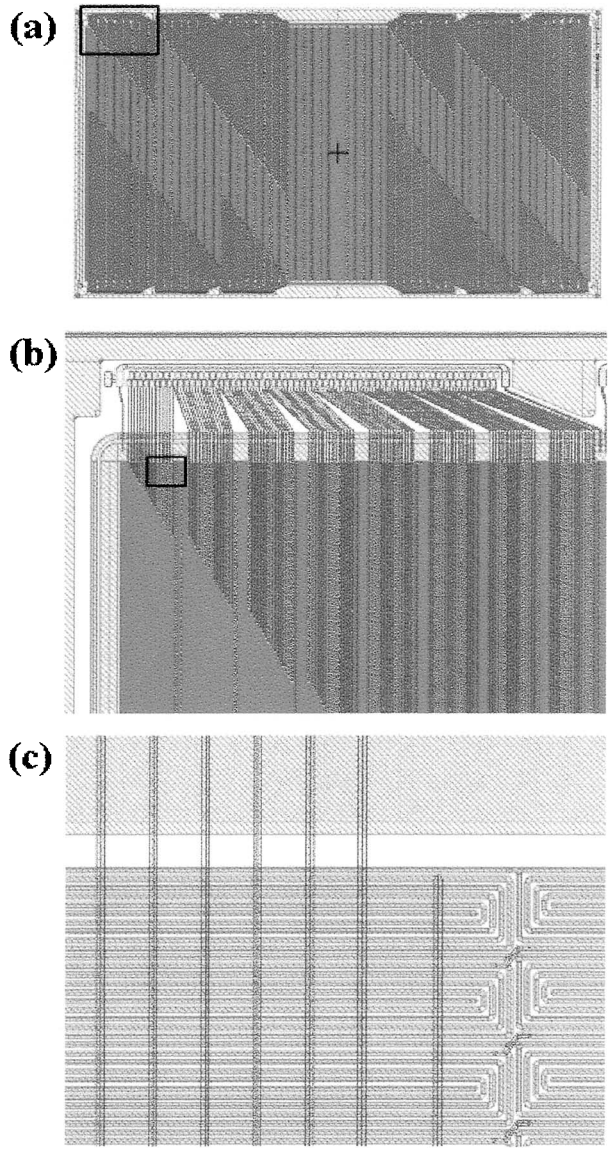

Fig. 1. (a) Layout of the v3a mask design sensor, (b) enlarged view of the square area in (a), and (c) enlarged view of the square area in (b).

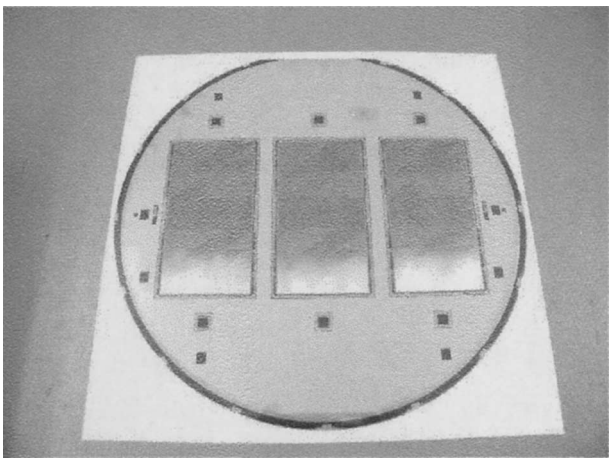

Fig. 2. Photograph of the silicon stripixel sensor wafer. The wafer type is H-3a-500 in Table 1.

injected nanosecond pulsed laser lights. On the basis of the results of the evaluation, the processing company for the stripixel sensor mass production will be determined.

References

1) K. Adcox et al.: Nucl. Instrum. Methods Phys. Res. A **499**, 469 (2003).
2) J. M. Heuser: Nucl. Instrum. Methods Phys. Res. A **511**, 210 (2003); Y. Akiba et al.: RIKEN Accel. Prog. Rep. **38**, 227 (2005).
3) Z. Li: BNL Internal Report, BNL Rep., No. 67527 (2000); Nucl. Instrum. Methods Phys. Res. A **518**, 738 (2004).
4) Z. Li et al.: RIKEN Accel. Prog. Rep. **36**, 250 (2003); Nucl. Instrum. Methods Phys. Res. A **518**, 300 (2004).
5) J. Tojo et al.: RIKEN Accel. Prog. Rep. **36**, 252 (2003); RIKEN Accel. Prog. Rep. **37**, 251 (2004); IEEE Trans. Nucl. Sci. **51**, 2337 (2004).
6) Y. Akiba et al.: Proposal for a Silicon Vertex Tracker (VTX) for the PHENIX Experiment (Brookhaven National Laboratory, Upton, NY, 2004), unpublished.
7) http://www-cdf.lbl.gov/users/mweber/svx4
8) J. Asai et al.: RIKEN Accel. Prog. Rep. **38**, 235 (2005).

Aluminum bus development for silicon vertex detector

A. Taketani, H. En'yo, K. Fujii,[*1] K. Fujiwara, J. M. Heuser, H. Kano, Y. Inoue,[*2] H. Maeta,[*1] H. Ohnishi, M. Tanaka,[*3] K. Tanida, and J. Tojo

A silicon vertex detector is planned to be implemented at the RHIC PHENIX experiment in order to identify heavy flavor quark decays by measuring a displaced vertex.[1)] One of the major physics goal for this new detector is the investigation of proton spin structure and quark gluon plasma by identifying open heavy flavor production. The silicon vertex detector will be located just outside of a beam pipe, where proton-proton or heavy ion collisions occur. The detector consists of two major parts; the inner two layers are pixel-type sensors[2)] and the outer two layers are strip-type sensors.[3)]

The detailed structure of pixel detector is described in Ref. 2. Signals from the sensor are fed into bump-bonded readout chips. The readout chips are connected to the readout bus, which is a printed circuit board, with wire bondings. The readout bus is connected to front-end electronics[4)] that serve as interfaces to the PHENIX data acquisition system. We have been developing a thin printed circuit board with fine pitch patterns.

The silicon vertex detector is located at most inner part of the PHENIX central arm. To avoid the generation of electrons by photon conversions resulting from collisions, the silicon vertex tracker is required to be fewer radiation length on the detector material budget. In addition to the thin silicon sensor, the readout bus should be fewer radiation length. Due to the high charged particle multiplicity from heavy-ion collisions, the pixel sensor is segmented into 32×256 pixels of $50 \times 425\,\mu\mathrm{m}^2$ size. Four hundred and eighty sensors will be used in total and 3.9 M channels will be read out. Therefore the readout bus has to include 190 signal lines and several control lines as well power supply and ground layers. The size of the bus is $1.4 \times 40\,\mathrm{cm}^2$. Thus, the signal and control lines will be of 70 μm pitch if we a choose double-layer bus. If we choose the triple-layer option, lines should be of 140 μm pitch.

In order to satisfy these two requirements, a thin kapton-film base and Al conductor are used, instead of Cu, which is widely used for printed circuit boards. A comparison of radiation length among the Cu and Al conductor boards is shown in Table 1. We assume 7-μm-thick bus line conductors, 50-μm-thick power/ground layers and 22-μm-thick kapton layers between conducting planes. The radiation length of the pixel sensor and readout chip is 0.36%. So the Al conductor is desirable. However, the use of Al is not common in the printed circuit board industry.

*1 Hiroshima Kokusai Gakuin University
*2 Rikkyo University
*3 High Energy Accelerator Research Organization (KEK)

Table 1. Expected radiation length for the bus.

Configuration	Al+Kapton		Cu+Kapton	
Num. of signal layers	2	3	2	3
Radiation length	0.17%	0.20%	0.9%	1.0%

Thus, we started to develop a fine-pitch Al-kapton-base board by ourselves.

The board is manufactured by four major processes. [1] Pattern etching, [2] formation of through-holes connecting conducting lines among different layers, [3] stacking layers, and [4] plating with Ni-Au on wire-bonding pads.

The pattern etching process proceeds in the following way. (1) The Al foil and kapton film are attached; (2) they are pressed with heat so that they adhere together; (3) photoresist is painted on the Al plane; (4) the line patterns are exposed; (5) unnecessary Al is dissolved with acid or alkali; (6) the photoresist is removed. The etching result is shown in Fig. 1. The white lines are 12-μm-thick Al conductor and the black plane is 12-μm-thick kapton-film base. The lines are 40 μm in width and 120 μm in pitch. They are inspected using a microscope. Most of lines have good shape. Some of lines show defects. It is expected that this problem can be avoided by washing the surface with sodium hydroxide before step (3). We are currently trying to fabricate a finer pitch pattern.

After the etching of one side of the Al plane, an Al foil is adhered to the other side. The formation of through holes consists of two steps before the etching of the new Al plane: (1) the formation of holes through the single Al-kapton layer, but not through the new Al plane, by a laser drilling method, and (2) the plating with the Cu. 500-μm-diameter through holes are

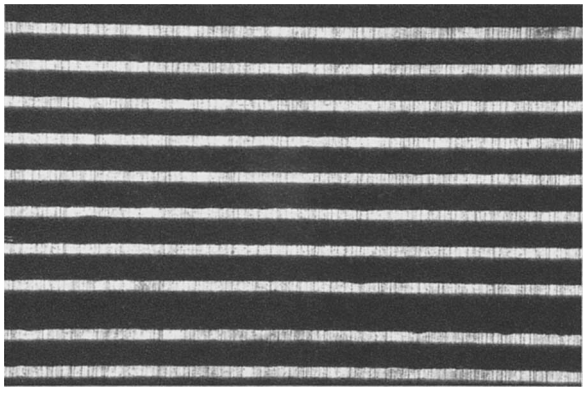

Fig. 1. Etched pattern of the bus.

formed since the Cu in the through holes is a very small amount of material relative to the entire board material. Figure 2 shows a cross-sectional view of the through hole. The white line is Cu plating which connects an Al conductor on the upper and a lower plane.

After the through-hole formation and the painting of the photoresist on the newly adhered Al foil, new line patterns are aligned with the line patterns on the other side and etched. This technique is established well for the popular Cu fine-pitch board.

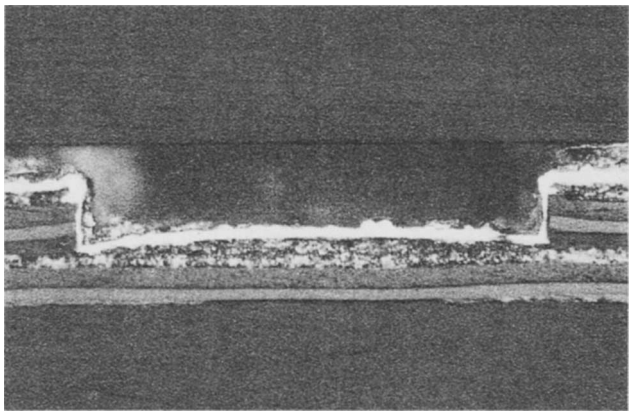

Fig. 2. Cross-sectional view of through hole.

Subsequently, the steps of [1], [2], and [3] are repeated to build a multilayer board, Ni-Au plating is carried out. Because kapton-Al-Au structure is too soft for wire bonding, Ni is plated between Al and Au. We tested the wire bonding on the Al-Ni-Au plated pad using the Kulicke&Soffa Model 8060 automatic wedge bonder with 25.4-μm-diameter Al wire. The bonding strength is measured as 4.7 ± 1.6 g. Although it is necessary to tune the bonding parameter, the Al-Ni-Au plating is satisfactory.

We have been developing a fine-pitch Al-kapton bus for the PHENIX pixel detector. We established major key techniques for its fabrication.

References

1) Y. Goto et al.: RIKEN Accel. Prog. Rep. **37**, 249 (2004).
2) J. M. Heuser et al.: RIKEN Accel. Prog. Rep. **37**, 250 (2004).
3) J. Tojo et al.: RIKEN Accel. Prog. Rep. **37**, 251 (2004).
4) H. Kano: RIKEN Accel. Prog. Rep. **37**, 253 (2004).

Evaluation of silicon strip sensor for PHENIX upgrade

J. Asai, K. Boyle,[*1] Y. Akiba, A. Deshpande, D. E. Fields, Y. Goto, M. Hoeferkamp,[*2] A. Taketani, and J. Tojo

We are studying the characteristics of a quark gluon plasma (QGP) and the spin structure of a proton using a relativistic heavy ion collider (RHIC) at the Brookhaven National Laboratory (BNL). The PHENIX is a device for detecting photons, electrons, muons, and hadrons with a high-rate data acquisition capability from the collision of 100 GeV or 250 GeV polarized protons. We plan to build the silicon vertex tracker (VTX) in the PHENIX detector.[1)] The VTX can identify the decay of heavy flavor mesons by the precise measurement of the decay vertex. It can also work function as a large solid angle charged particle tracker.

The performance of silicon sensors decreases due to radiation damage during a detector running period. Due to the damage, the leakage current also increases gradually. The leakage current I [A] depends on the temperature T [K].

$$I(T) = AT^2 \exp(-E_g/2k_BT). \quad (1)$$

Here, A is the sensor constant; E_g is the gap energy in silicon ($E_g = 1.2\,\mathrm{eV}$); and k_B is the Boltzmann constant ($k_B = 8.6 \times 10^{-5}\,\mathrm{eV/K}$). We measured the leakage current for the operation temperature. Figure 1 shows the temperature dependence of the leakage current of the sensor, which was measured for the first prototype strip sensor tested with a beam at KEK 2002 in the temperature and humidity control chamber at RIKEN. Each line shows a measurement for one bias-voltage setting. It is constant from 263 [K] to 283 [K] at a full depletion voltage (∼100 V). The operation temperature does not need to be less than 283 [K], because the intensity of the noise signal from the leakage current does not decrease with the temperature.

Quality assurance (QA) for the VTX silicon stripixel sensor will be carried out at BNL, University of New Mexico and Stony Brook University. The main purposes of the QA program are the visual inspection of each sensor and the characterization measurements of each sensor. The bias-voltage dependences of the leakage current (I-V) and the capacitance (C-V) will be measured. In a clean room, they are measured using a semiautomatic probe station. Figures 2 and 3 show the measurement system consisting of a probe station, a picoammeter/voltage source (Keithley 6487), an LCR meter (HP 4263 B), and a switch scanner system (Keithley 7002), which are controlled using the LabVIEW software through GPIB interface cables.

Now we are studying two sensors fabricated by Hamamatsu Photonics and SINTEF. We will decide the vender and the design of the sensors from the results of characterization measurements. As the next step of the QA program, we will evaluate approximately 400 production sensors for PHENIX upgrade.

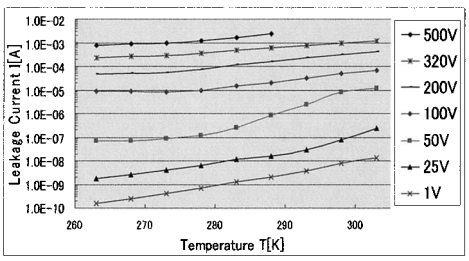

Fig. 1. Leakage current distribution plotted against temperature T [K] dependence on bias voltage.

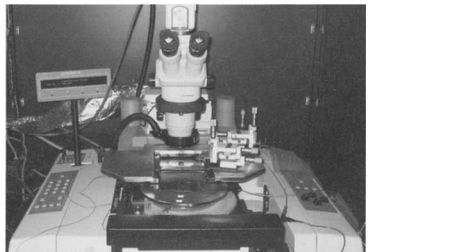

Fig. 2. Semiautomatic probe station.

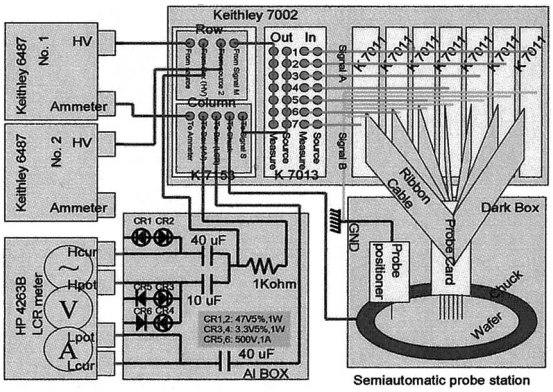

Fig. 3. Measurement system diagram.

*1 Department of Physics and Astronomy, Stony Brook University, USA
*2 Department of Physics and Astronomy, University of New Mexico, USA

References
1) Y. Akiba et al.: Proposal for a Silicon Vertex Tracker (VTX) for the PHENIX Experiment (Brookhaven National Laboratory, Upton, NY, 2003).
2) Z. Li et al.: Nucl. Instrum. Methods Phys. Res. A **518**, 300 (2004).

PHENIX VTX simulation and reconstruction software (Status report)

V. L. Rykov and J. T. Mitchell*

The simulation software for the PHENIX Silicon Vertex Tracker (VTX) upgrade[1,2] currently consists of two main pieces:

- The VTX part of the GEANT based PHENIX simulation framework called *PISA*.
- The VTX hit simulation and reconstruction *svx* package.

Since March 2004, both pieces for the VTX barrel are publicly available from the PHENIX CVS repository. In October 2004, the VTX endcaps have also been implemented in *PISA* by the Los Alamos PHENIX group.

The currently implemented barrel VTX geometry in *PISA* emulates the main physics properties of the active parts of the detector as close to expectations as is possible at the current design stage. On the other hand, it is still flexible enough for easy geometry modifications by changing a few parameters in the data file without editing and recompiling the *PISA* code. This flexibility was very helpful, when in May 2004, the VTX was significantly redesigned, switching from 1 pixel + 3 strip to 2 pixel + 2 strip layers with the overall increase of dimensions.

Each VTX barrel layer represents a set of rotated ladders with adjustable overlap in azimuth of the neighboring ladders in order to recover the insensitive areas at the sensor edges (see fig. 1 of reference[2]). In turn, each ladder consists of either silicon pixel[3] or strip[4] sensors. At this stage of the project, the "add-ons" (electronic chips, buses, cooling pipes, support, etc.) are emulated with a passive aluminum layer of adjustable thickness on top of each silicon sensor. Later on, as the design evolves, all passive VTX elements will be implemented according to the engineering drawings, which are not available yet.

In a *PISA* run, GEANT hits in the VTX sensors are written into the PHENIX standard *PISAEvent.root* file along with the hits from other PHENIX detectors. At the next simulation stage, VTX hits are read by the *svx* package code, and the "rawhits" and "clusters" are built. "Rawhits" are the digitized electric signals in the VTX pixels and strips, and "clusters" are reconstructed from rawhits candidates of particles crossing areas in the VTX sensors, which then are used for reconstructing charged particle trajectories (tracks).

The current version of the *svx* package consists of the following branches of *C++* classes:

SvxHit hierarchy is represented by the GEANT hit ("ghit") class *SvxGhit*,[a] rawhit class *SvxRawhit*, and cluster class *SvxCluster*.

Hit relater branch is represented by three classes: *SvxGhitRawhit*, *SvxRawhitCluster* and *SvxGhitCluster*. Each of these classes is a pair of *hit ID* numbers, which relates two hits of different types and tells which hit of one type (e.g. ghit) contributed to the generation of the other type of hit in the pair (e.g. cluster).

Data nodes *SvxGhitList*, *SvxRawhitList*, *SvxClusterList*, *SvxGhitRawhitList*, *SvxRawhitClusterList*, and *SvxGhitClusterList*, are the collections of the respective hits and their relaters in an event. After processing each event, these data nodes are written into the output file and/or directly submitted to the tracking code.

SvxSensor hierarchy consists of a number of classes for the sensors of different types.[b] These are the most complex classes in the *svx* package, which are doing the real job of generating rawhits from ghits and then finding clusters, using algorithms and methods specific for a particular sensor type.

SvxReco class is the *svx* code run manager, which also implements the interface to the PHENIX analysis framework *Fun4All*.

The current version of the *svx* package covers only the VTX barrel with no processing of endcap hits yet, and in general, still should be treated as the "1st iteration" of the VTX simulation and reconstruction software. Nevertheless, it is already widely used in the collaboration for the VTX performance simulations with important contributions to the proposal[1] on electronic channel occupation, ghost hits, resolutions, etc. The package is also used for the VTX tracking code development.

References

1) Y. Akiba et al.: Proposal for a Silicon Vertex Tracker (VTX) for the PHENIX Experiment (BNL, Upton, NY, 2004).
2) Y. Akiba et al.: RIKEN Accel. Prog. Rep. **38**, 227 (2005).
3) H. Ohnishi et al.: RIKEN Accel. Prog. Rep. **38**, 230 (2005).
4) J. Tojo et al.: RIKEN Accel. Prog. Rep. **38**, 231 (2005).

* Brookhaven National Laboratory, USA.

a) *SvxGhit* objects are the reformatted copies of VTX GEANT hits from *PISAEvent.root* file.

b) Currently, 1 type of pixel and 3 types of strip sensors are implemented.

Development of digital-pilot ASIC and data link system for PHENIX pixel detector

H. Kano, A. Taketani, H. Ohnishi, M. Tanaka,[*1] J. M. Heuser, K. Fujiwara,[*2] and H. En'yo

The PHENIX collaboration has started a study for an upgraded experiment for the eighth physics run at RHIC in 2007/2008. Several new detector systems will provide extended detection capabilities in collisions of heavy ion and polarized-proton beams when RHIC reaches full operation at the design luminosity in the next few years. The main PHENIX upgrade is a new vertex spectrometer installed between the pole faces of the central magnet. It combines high-precision tracking for jet and heavy-flavor decay vertex measurements, electron identification and charged-particle tracking in its subsystem silicon vertex detector, micro-TPC, and compact hadron blind detector. The silicon vertex detector comprises pixel and novel microstrip sensors. The pixel detectors in the internal layer are essential for resolving the high track densities in heavy-ion collisions.

The block diagram of the PHENIX pixel detector readout system is shown in Fig. 1. The right-hand side shows the control-room-located electronics, whereas the left-hand side shows the on-detector electronics. Comunication between the control room and the detector is via two optical fibers, one carrying clock, the other carrying trigger, configuration, and control. Data transmission from the detector to the control room is performed via 1.6 Gbps optical fiber-link.

The main components of the on-detector readout electronics are ASICs. All the ASICs have been developed by IBM 0.25 μ CMOS technology with radiation-hardening techniques. Precautions have been taken to reduce malfunction due to single-event upset. The digital-pilot ASIC (shown in Fig. 2.) performs the optical to electrical conversion of the incoming clock and data signals, initiates the readout sequence in the readout chips, and sends data to the 1.6 Gbps ethernet-like serializer chip GOL.[1)] We modified the digital-pilot ASIC based on the ALICE chip architecture,[2,3)]

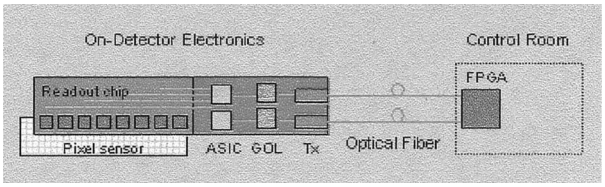

Fig. 1. Block diagram of PHENIX pixel detector readout system.

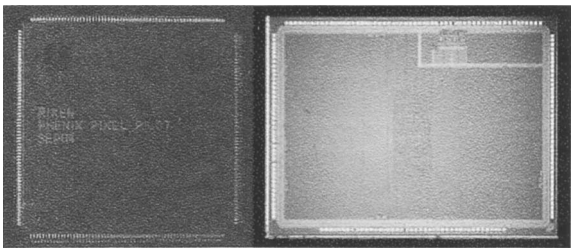

Fig. 2. Pictures of PHENIX digital pilot chip and internal core (core size: 8 mm × 6 mm).

which has extended data bus width (16 bit to 32 bit) for PHENIX. This modification reduces the area of the on-detector readout board and the number of chips.

In the PHENIX optical link between the control-room and on-detector electronics, a serializer is used to encode 32 bit words in a serial stream. The frequency of input words is 40 MHz, while that of the output stream is up to 1.6 Gbps. In this system, we chose to use GOL (transmitter) and Vertex-2 pro (receiver). The latest FPGA, Vertex-2 pro is suitable for our link system due to its built-in support for high-speed serial links. The block diagram of the test setup is shown in Fig. 3. The test signals generated by FPGA are sent to the GOL test board through an optical transmitter and an optical fiber. The FPGA includes an encoder (8 b/10 b and gigabit ethernet) and a serializer. An FPGA source code for the GOL has been developed, and we are checking speed (1.6 Gbps), error rate ($< 10^{-15}$), and temperature in a long term test.

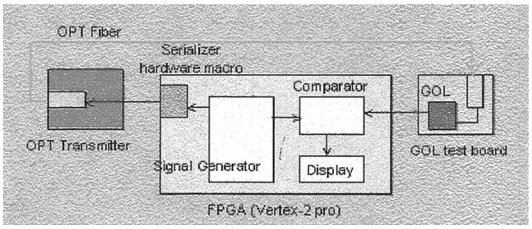

Fig. 3. Block diagram of test setup for link system.

References

1) http://proj-gol.web.cern.ch/proj-gol/proj%2Dgol/manuals/gol_manual.pdf
2) P. Chochula et al.: Nucl. Phys. A **715**, 849 (2003).
3) A. Kluge et al.: CERN 2001-005, 95 (2001).

*1 High Energy Accelerator Research Organization (KEK)
*2 Niigata University

Field measurements in AGS warm snake†

J. Takano,[*1] M. Okamura, T. Hattori,[*1] R. Alforque,[*2] R. Belkin,[*2] G. Ganetis,[*2] A. Jain,[*2] W. W. MacKay,[*2] T. Roser,[*2] R. Thomas,[*2] and J. E. Tuozzolo[*2]

A new warm snake has been produced by RIKEN for the alternating gradient synchrotron (AGS) at Brookhaven National Laboratory (BNL). The AGS had a solenoidal Siberian snake for overcoming all imperfection depolarizing resonance, but the solenoidal field had caused transverse coupling resonance. This warm snake is the world's first normal conducting helical dipole partial snake for overcoming all imperfection resonance and decreasing transverse coupling resonance. The relative heavy-ion collider has some superconducting Siberian snakes. These snakes have a helical coil but no helical pole piece. A warm snake has both a helical coil and a helical pole pieces made of lamination steel. The magnetic field of the warm snake had been measured and compared with that obtained by 3D finite element calculations.

It is very important to calculate the magnetic field in 3D because the Siberian snake magnet has a helical magnetic field. OPERA-3D/TOSCA[a)] was used to simulate the field of the warm snake. The simulation models are shown in Figs. 1 and 2.

As shown in Fig. 1, the warm snake has three sections with different pitches called a double-pitch structure. The pitches were optimized as the beam in the warm snake has no position offset at each end of the warm snake or no deflection angle at the extraction of the warm snake. The optimized pitches are 132 cm long with a pitch of 185 cm in the center slow-pitch region and 39 cm long with a pitch of 90 cm at each end of the rapid regions. The simulated proton beam trajectory in the warm snake is shown in Figs. 3 and 4.

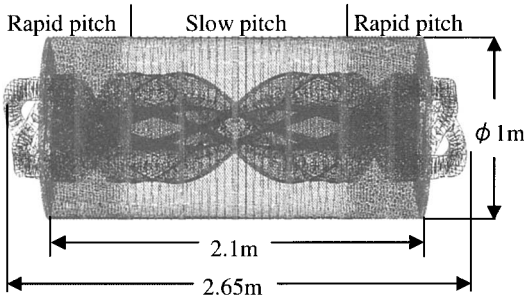

Fig. 1. 3D simulation model of the warm snake on the OPERA-3D/TOSCA.

Fig. 2. Helical coil in the simulation model of the warm snake.

The warm snake had been designed and fabricated in Japan. The picture of the completed warm snake is shown in Fig. 5.

The high-quality measurement of the magnetic field had been carried out in BNL. The probe for this measurement is a 51-mm-long harmonic coil.[1)] The longitudinal magnetic field distribution in the warm snake had been measured with a short harmonic coil. The distribution is shown in Fig. 6. The transfer functions at the center of the slow-pitch and rapid-pitch regions had been measured. The graph of the transfer function is shown in Fig. 7.

As shown in Fig. 6, the graph of 95% operating cur-

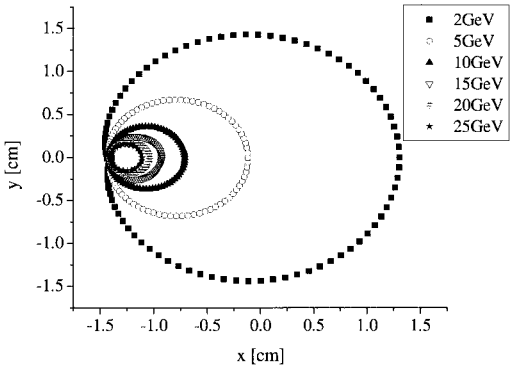

Fig. 3. Transverse trajectory from 2 GeV to 25 GeV proton beam.

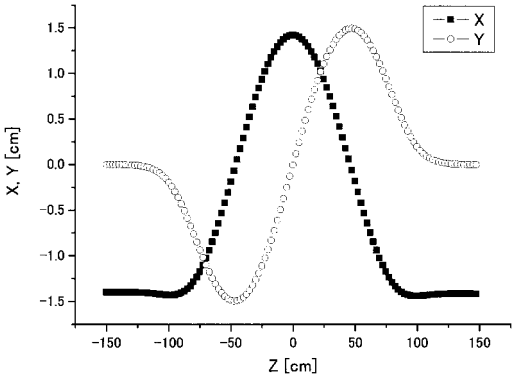

Fig. 4. Longitudinal trajectory of 2 GeV proton beam in calculated magnetic field of warm snake.

† Condensed from the Proc. EPAC 2004 (2004), p. 2116.
*1 Tokyo Institute of Technology
*2 Brookhaven National Laboratory, USA
a) Vector Fields Inc.

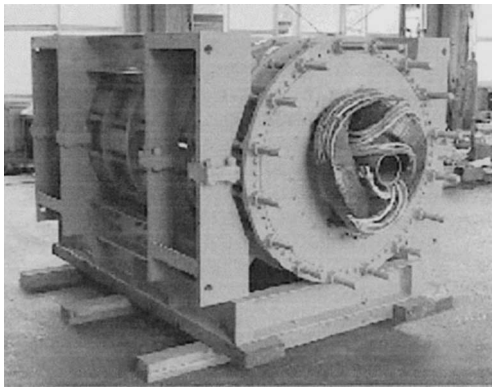

Fig. 5. Photograph of completed warm snake.

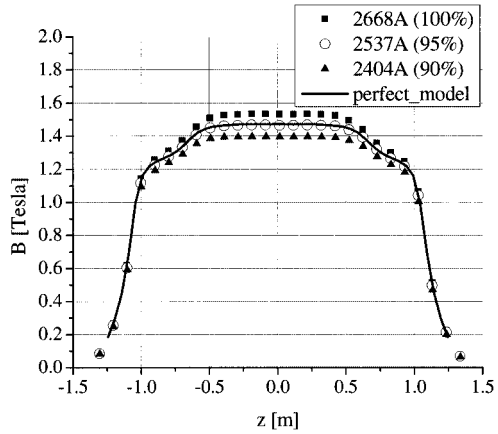

Fig. 6. Dipole field distribution measured at three different currents and simulation data of perfect model (no deflection or offset).

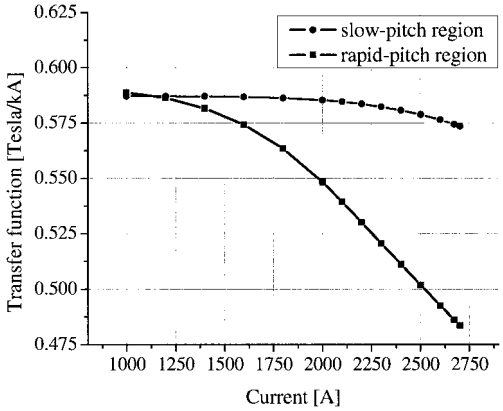

Fig. 7. Measured transfer functions.

rent is similar to that of the perfect model. The distribution at 2668A (100%) is higher than that of the perfect model. This result suggests the warm snake has some fabrication errors. The reason for this increase in magnetic field within the slow-pitch region is a decrease in the packing factor in the rapid-pitch region because the end plates are bending out ward caused by the weight of the yoke itself and the magnetic force. Therefore, the rapid-pitch region yoke saturates faster than the slow-pitch region as shown in Fig. 7.

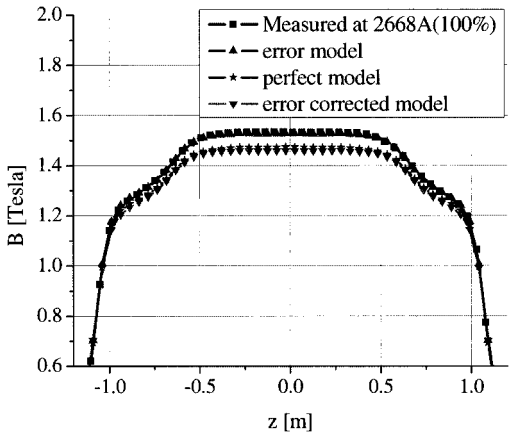

Fig. 8. Field profiles before and after error correction.

To correct this error, a simulation model which includes the fabrication error was required. The magnetic field of this error model is shown in Fig. 8 as plots of the error model. This model has almost the same distribution as the perfect model. The parameters that were optimized were operating current and the number of 6-mm-thick iron shims added to each end plate. The results of the optimization indicate that the operating current should be 2538A and one shim should be added to each end plate.[2)]

The fabrication error of the warm snake was corrected by adjusting operating current and adding shims. Several Siberian snakes had been measured already and they are used in RHIC. However, this measurement for the warm snake is unique because this magnet has the world's first double-pitch structure. Therefore, this measurement and the error correction method will be useful for Siberian snakes that have a double-pitch structure. There is a plan to install AGS with a cold snake which is a superconducting helical dipole partial snake with a double-pitch structure. Therefore, we have a chance to measure a snake by the same method using cold snake.

References

1) A. Jain: Proc. CERN Accelerator School on Measurement and Alignment of Accelerator and Detector Magnets, Anacapri, Italy, 1997-4 (CERN, Geneva, 1998), p. 1.
2) J. Takano: Master's Thesis, Tokyo Institute of Technology (2004).

Forward muon trigger upgrade for PHENIX experiment at RHIC

W. Xie, M. Grosse Perdekamp,* and D. Kawall, for PHENIX Collaboration

The measurement of the proton spin structure is one of the main physics programs for the PHENIX experiment at RHIC. The early deep-inelastic-scattering experiment shows that quarks contribute about 20% of the proton spin. The other contribution should come from gluon and parton orbital angular momenta. The PHENIX experiment is able to determine the gluon contribution to the proton spin by measuring the asymmetry of π^0, direct photon, etc, and it is also able to determine quark and antiquark spin contributions by the measurement of single spin asymmetry of decay leptons from W bosons produced *via* V-A interactions.[1] In PHENIX, we plan to measure W in the coming $\sqrt{s} = 500\,\mathrm{GeV}$ run by detecting electrons and muons.

The luminosity of the coming $\sqrt{s} = 500\,\mathrm{GeV}$ run is expected to be as high as $2 \times 10^{32}\,\mathrm{cm}^{-2}\mathrm{sec}^{-1}$, resulting in a 12 MHz collision rate. The total number of events, produced from W boson decay in the PHENIX muon arm, is expected to be approximately 10^4. One critical issue is whether the current the PHENIX muon trigger has a sufficient rejection power to preselect all of these events because the PHENIX data-acquisition system bandwidth has the upper limit of 12 KHz. A simulation study shows that the maximum rejection factor of the current single-muon trigger is only about 500, assuming the absence of beam-related backgrounds. This corresponds to 24 KHz. A reasonable assignment of bandwidth resources for this specific trigger is 1–3 KHz. Therefore, we need at least tenfold increase in the rejection power of the current muon trigger to be able to accept all events from W boson decay. An upgraded muon trigger is required.

After testing many different ideas, two methods were found to be effective in achieving a high enough rejection power for the W measurement. One is the installation of two new pad chambers with one in front of muon tracker station 1, and the other either behind the fifth gap of the muon identifier or between the muon tracker and the muon identifier. The algorithm requires first that hits from the two new pad chambers be associated with the muon candidate of the existing muon trigger followed by the application of the angle cut between the two pad-chamber hits to reject low-momentum muons. The other method is similar to the first one but the hits from the existing muon tracker stations are utilized instead of building new detectors. In this method, one has to redesign the existing muon tracker front-end electronics. The ideas are shown in Fig. 1. Both provide a sufficient rejection power for preselecting all the events from W boson decay.

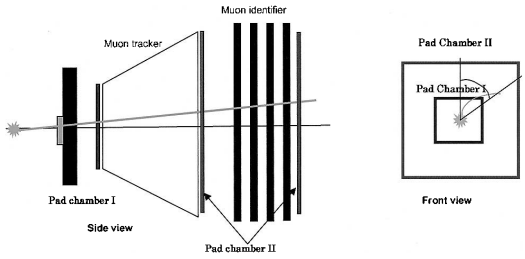

(a) New pad-chamber method

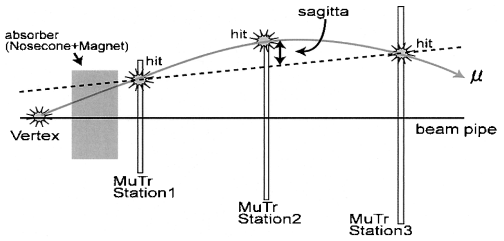

(b) Redesign existing muon tracker electronics

Fig. 1. Two possible methods of muon trigger upgrade.

We have not fixed the final scheme of the trigger because there are many issues to be clarified, such as the effect of the beam-related background. The new pad chamber method is expected to reject most of the background through the timing cut and may also improve PHENIX muon-arm pattern recognition in most central Au+Au collisions. The method of replacing muon tracker electronics can take advantage of the high granularity in the muon tracker but it will not improve pattern recognition and its performance might also be degraded by the beam-related background. The combination of the two methods is expected to provide even higher rejection power to enable PHENIX to do the same physics in higher luminosity environment. Anyway, the simulation study is still on the way to check different scenarios before the final decision.

Various R&D projects related to the trigger upgrade have been carried out or are ongoing. In Kyoto University and University of New Maxico, one muon-tracker chamber prototype has been fabricated for a fast readout front-end electronic test. During the p+p run in year 2003, at Riken-BNL Research Center and University of Illinois at Ubrana Champaign, a successful measurement of the beam background has been carried out and a more comprehensive new measurement will be carried out in the p+p run in year 2005. All these will help determine the final configuration of the upgraded trigger which will start to be installed in year 2007.

Reference

1) G. Bunce et al.: Annu. Rev. Nucl. Part. Sci. **50**, 525 (2000).

* University of Illinois at Ubrana Champaign, USA

New scaler boards based on LBL/STAR design for PHENIX

M. Wagner,[*1] R. Bennett,[*2] A. Deshpande,[*2] Y. Goto, D. Kawall, and N. Saito,[*1]

Within the measurement program at RHIC is an effort to understand the origins of the nucleon spin.[1)] At RHIC, collisions of polarized protons at energies up to sqrt(s) = 200 GeV have been realized, and the cross sections required to produce various final states have been measured with the PHENIX detector, and analysed for their dependence on the polarization directions of the colliding bunches.[2,3)] This requires that the production rates of particular final states are normalized to the luminosities of the colliding bunches so that any remaining differences in production rates may be ascribed to the spin-dependent effects of interest. Since the longitudinal profiles and numbers of protons in the colliding bunches are typically different, a reliable measurement of the relative luminosities of the colliding bunches is required. In the PHENIX data acquisition (DAQ), an additional board has been introduced into the Global Level 1 Trigger (GL-1), with scalers to monitor the luminosity of each bunch crossing number (BCN) separately.[2)] Minimum-bias collisions are detected by a coincidence between the beam-beam counters (BBC), or with lower efficiency, by a coincidence between the zero degree calorimeters (ZDC).[2)]

After hardware cuts are performed on the reconstructed vertex position, these GL-1P scalers count the triggers from the BBC and ZDC as a measure of the luminosity for each BCN separately. For run01 through run04 the scalers performed sufficiently well to obtain the relative luminosities at the accuracy required for first measurements of asymmetries in inclusive π^0 production.[3)] Figure 1 shows a typical distribution for the currently used scaler systems with the clearly visible variation of the counts (and hence luminosity) depending on the BCN.

Run04 was also used to obtain test data at very high intensities in order to evaluate future hardware requirements for a relative luminosity accuracy down to 10^{-5}. For this issue, new scaler boards based on a LBL/STAR design have been tested. For this test and for the future use of these scalers, an interface board which converts the RBIB signals from the GL-1 backplane into the required PECL signals was developed. The central unit of the interface board is a programmable Lattice ispXPDL 51024 MX chip, which ensures the simultaneous distribution of possible 130 RBIB signals to four 25-pin outputs, which will be connected to the four available scaler boards in the final operation mode. The new scaler boards are significantly different from the currently used boards: while the currently used scalers are not able to measure correlations between ZDC and BBC (*e.g.*, applying conditions to ZDC while plotting BBC-distributions), the new boards are designed on the basis of an 80 Mbyte memory. This memory is required due to the input design, which uses 24 inputs (*i.e.*, 17 different detector signals + 7 bits for 120 BCN applied simultaneously per board) as a bit pattern which reproduces 2^{24} memory addresses at a 40-bits depth per address. Each address represents a specific signal combination including the BCN. The 24 detector signals are gated by a 25th input, which is fed by the RHIC clock at 9.8 MHz. One board was tested using signals from ERT triggers, muon trigger and the aforementioned BBC and ZDC signals. Since the boards are being tested for the very first time, a comparison with the GL-1P modules is essential. A typical BBC distribution from the new scaler boards — similar to that shown in Fig. 1 — is shown in Fig. 2. The beam abort gaps between BCN 30 and 40 are clearly reproducible, although there is a clear BCN shift. The origins of this shift may be an improperly timed fiducial signal from the V124 module, which is possibly also responsible for a significantly higher background, which is visible in the empty BCN, while an expected electronic jitter or different transition times within the interface board could be excluded as shown in Fig. 3.

For future measurements an internal reset signal in the interface board will be used instead of the external V124 fiducial signal. Despite these problems, the test measurement could be used to analyse possible saturation effects at high intensities, which have been detected with the GL-1P scalers, as shown in Fig. 4. This effect can be reproduced clearly by the new scaler

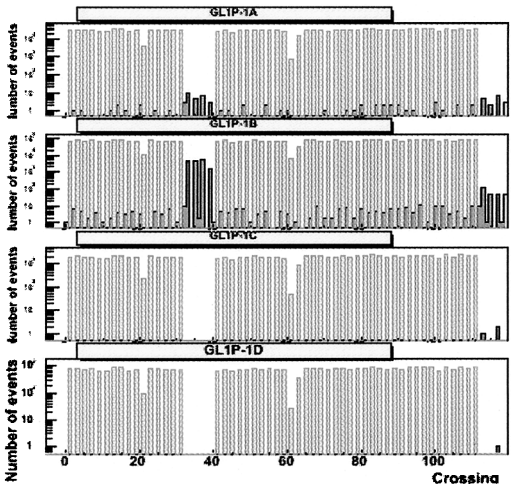

Fig. 1. GL-1P scaler entries *vs.* BCN (upper 2 panels: BBC, lower 2 panels: ZDC).

*1 Department of Physics, Kyoto University
*2 State University of New York at Stony Brook USA

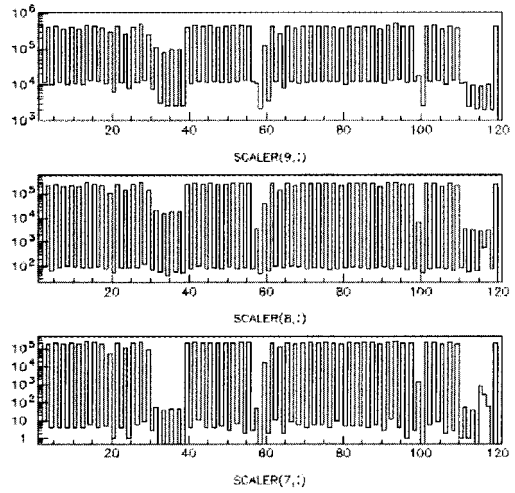

Fig. 2. Results from the new scaler boards, showing BBC trigger signals *vs.* BCN. Top: BBC N or S, center: BBC wide vertex cut, bottom: BBC narrow cut.

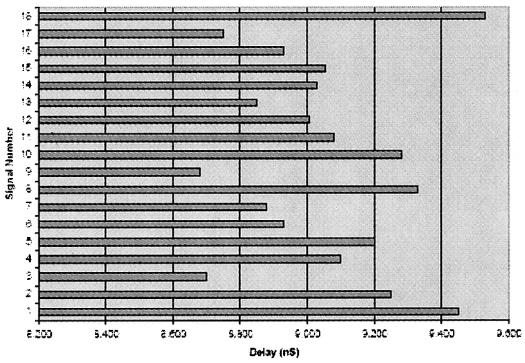

Fig. 3. Transition times for 18 signals through the interface board. The small size of these variations excludes them as the source of the background.

boards, as shown in Fig. 5. Moreover, the correlation between other trigger signals (in Fig. 5: ertg1) and BBC or ZDC, respectively, is shown. This important comparison was not possible with the GL-1P scalers, due to their restriction to ZDC and BBC signals and it could indicate a nonlinearity problem of the ZDC instead of the BBC at high beam intensities.

References

1) G. Bunce et al.: Annu. Rev. Nucl. Part. Sci. **50**, 525 (2000).
2) S. S. Adler et al.: Nucl. Instrum. Methods Rhys. Res. A, **499**, 560 (2003).
3) S. S. Adler et al. : Phys. Rev. Lett. **93**, 202002 (2004).

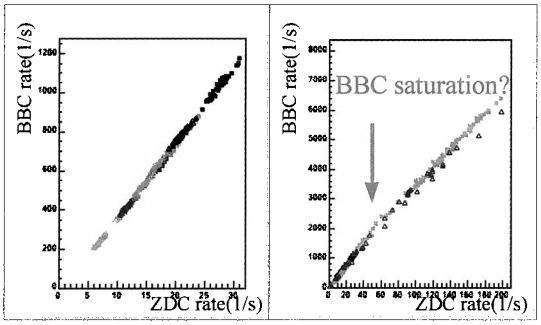

Fig. 4. BBC rate *vs.* ZDC rate measured with GL-1P scalers. Left: low beam intensity, right: high beam intensity.

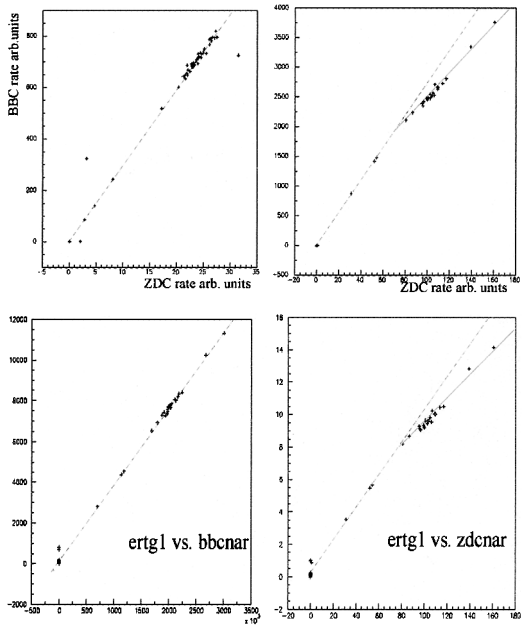

Fig. 5. Correlations with the new scaler boards. Upper panels: same as Fig. 3. Lower panels: ertg1 trigger signal *vs.* BBC (left) and ertg1 *vs.* ZDC (right), both at high beam intensities (consider: arbitrary units).

DAQ system upgrade of optical alignment system at PHENIX muon tracker

H. Kanoh,[*1] T. Watanabe,[*1] T.-A. Shibata,[*1] A. Taketani, N. Kamihara,[*1]
T. Horaguchi,[*1] and M. J. Kweon[*2]

The optical alignment system (OASYS) is one of the subdevices for the PHENIX muon tracker. The muon tracker has threes layer of chambers termed station. Each station is moved 200 to 300 micrometers by a magnetic field or temperature excursion during the experiment period. In order to achieve better momentum resolution, we correct these relative movements. The purpose of the OASYS is the real-time monitoring of the relative alignment among stations.

The OASYS consists of a light source at the 1st station, a convex lens at the 2nd station, and a CCD camera at the 3rd station, as shown in Fig. 1.[1,2)] When an individual station moves, the image on the CCD camera moves. There are 7 sets of optics on each section of each station, and there are $7 \times 8 \times 2 = 112$ optics in total. By observing the position of the light spot on the image of the CCD camera, we can monitor each station's relative movement.

We have already modelled the relationship between the CCD image movement and each station's relative movement.[3)] This model contains the 2nd station's parallel translation along the x and y axes and its rotation around the z axis. The accuracy of relative alignment using our model is estimated to be approximately 50 μm.

Figure 2 shows a block diagram of the current DAQ system. Fifty-six signals from the CCD cameras are fed into a multiplexor and one signal is fed into the PCI capture board of a Windows PC. In the Windows PC, histograms are generated, which are projected images

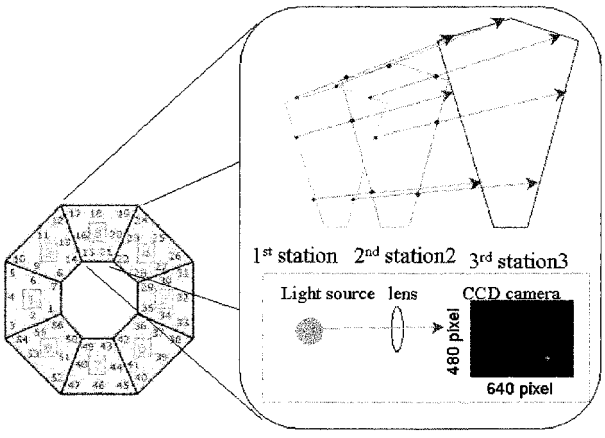

Fig. 1. Optical alignment system.

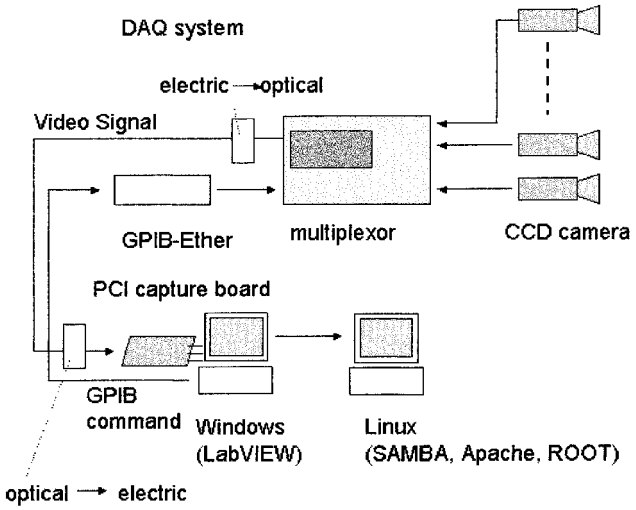

Fig. 2. Schematic of DAQ system.

along the vertical or horizontal axis, and then stored on the hard disk of the Windows PC and a Linux server through SAMBA. Then, on the Linux server, we obtain the position of the light spot via a Gaussian fit, using ROOT. We replaced the old GUI base DAQ system with the LabVIEW base system this summer. LabVIEW is commercially available software, which is widely used in the monitor and control industry. The stability of the system is improved and the data taking speed increased from 1 image/30 min/camera to 1 image/10 min/camera.

As another upgrade, the image processing procedure is improved as detailed below. In the old method, data from all vertical pixels in the CCD image are used for generating horizontally projected histograms and vice versa. Only the vertical pixels that contribute to the peak image are selected. In this way, the sharpness of the peak images is improved. Second, we superimpose images that are sequentially taken over approximately 1 second (16 at least and 128 maximum), and the background noise is averaged and statistical fluctuations are minimized. Thus, the peak position accuracy is improved. Figure 3 shows the effect of these improvements. The two raw sets of the date on the top are histograms produced by the old system and, the two raw sets of date on the bottom are histograms produced by the new one. The same CCD cameras are used for each histogram. It is difficult to find the peak in the histograms produced by the old system, but very easy in that prodeced by the new system.

*1 Department of Physics, Tokyo Institute of Technology
*2 Department of Physics, Korea University, Korea

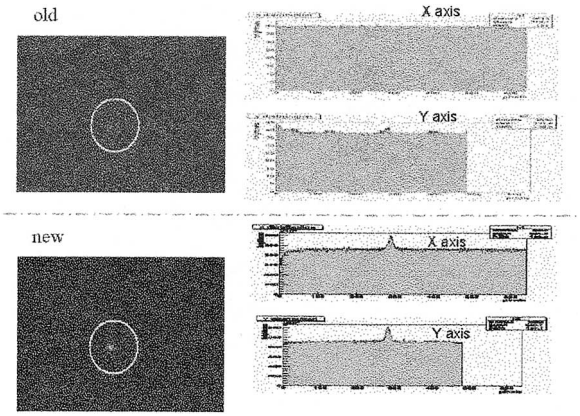

Fig. 3. Comparison of old DAQ and upgraded DAQ.

As a result of this upgrade, the number of cameras that can be used for relative alignment increases from 75 to 96. In addition, the S/N ratio increases from 1.4 to 12 at maximum (S/N = 0.2 is taken as a cut threshold for image analysis).

References

1) J. Murata et al.: Nucl. Instrum. Methods Phys. Res. A **500**, 309 (2003).
2) N. Kamihara: Master Thesis, Tokyo Institute of Technology (2002).
3) T. Watanabe: Master Thesis, Tokyo Institute of Technology (2004).

Status of fragmentation function analysis at BELLE

D. Gabbert,[*1,*3] M. Grosse Perdekamp,[*1] K. Hasuko, A. Ogawa,[*2] and R. Seidl[*1]

The BELLE experiment at the asymmetric e^+e^- collider KEK-B in Tsukuba, Japan, is mainly dedicated to investigate CP violation in B meson decays. It is tuned to the $\Upsilon(4S)$ resonance at 10.58 GeV, whereas background studies are performed at 10.52 GeV. These continuum events are studied in order to measure spin-dependent and precise spin-independent fragmentation functions.

Spin-independent fragmentation functions are measured as normalized cross sections $\frac{1}{\sigma_{tot}}\frac{d\sigma_h}{dz}$. The available global data on the normalized hadronic cross section[1)] in the high region of the fractional energy z is limited. In particular, at low center of mass energies, precision fragmentation function data is not available. Consequently, the behavior of fragmentation functions at a large z is only poorly understood and its separation into different parton flavors involves significant uncertainties, which particularly affect the understanding of semi-inclusive measurements in HERMES, COMPASS and RHIC experiments. Fragmentation functions for identified hadrons h will, for instance, enter a global QCD analysis of double-spin-polarized asymmetries A_{LL}^h at RHIC with the goal of extracting gluon polarisation. Presently, such an analysis suffers from uncertainties in the gluon fragmentation in current fragmentation parameterizations.[2,3)] One can extract the gluon fragmentation functions from QCD evolution by combining fragmentation functions at higher center of mass energies from LEP and SLAC with data at lower energies, at which BELLE can contribute significantly with its good detector performance and high statistics of more than 30 fb^{-1} in the off-resonance sample.

Unpolarized fragmentation functions and their systematic effects are presently being investigated at BELLE. We have made significant progress in the study of momentum smearing and particle identification. Momentum smearing was studied in order to select an appropriate binning and to estimate the resulting error. Corrections for particle identification (pid) were studied using Monte Carlo techniques, see Fig. 1 and data: A study using pions and kaons from the D* decay revealed a good agreement between the pid efficiencies derived from Monte Carlo and data.

A second analysis adresses the fragmentation of transversely polarized quarks into pseudoscalar hadrons, also known as the Collins function.[4)] This function is necessary to access the transversity quark distribution function, which, due to its chiral-odd nature, can only be measured in conjunction with a chiral-odd fragmentation function in semi-inclusive channels. The quark-antiquark pair created as a result of electron-positron annihilation can possess a net antialignment in their transverse spins. During the fragmentation, these transversely polarized (anti) quarks pick up transverse momenta. One can then measure the resulting azimuthal distributions of two hadrons in opposite hemispheres along the thrust axis, relative to the production plane, to obtain a combination of quark and antiquark Collins functions.

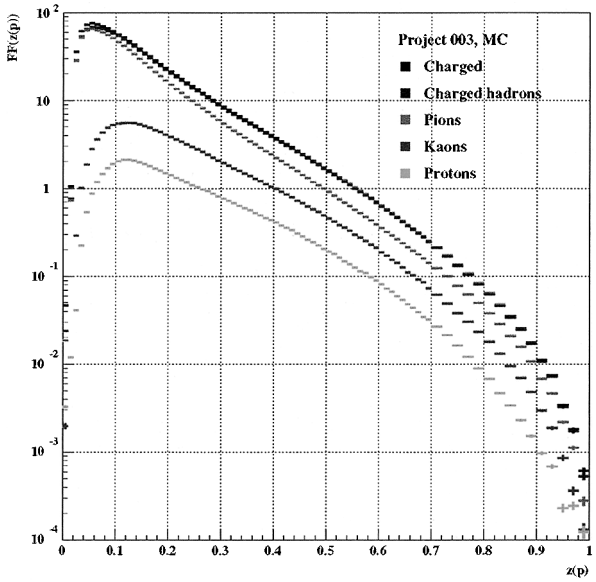

Fig. 1. Fragmentation functions for identified hadrons in MC after performing pid corrections, errors indicate statistics for 1.4 fb^{-1}.

References

1) O. Biebel, P. Nason, and B. R. Webber: Phys. Rev. D **66**, 010001 (2002).
2) S. Kretzer: Phys. Rev. D **62**, 054001 (2000).
3) B. A. Kniehl, G. Kramer, and B. Potter: Nucl. Phys. B **582**, 514 (2000).
4) J. C. Collins: Nucl. Phys. B **396**, 161 (1993).

*1 University of Illinois, USA
*2 Brookhaven National Laboratory, USA
*3 Technische Universität München, Germany

Spin transfer to Λ_c^+ hyperons in polarized proton collisions at RHIC

V. L. Rykov and K. Sudoh

Helicity transfer to inclusive charmed Λ_c^+ hyperons in polarized proton collisions has been recently proposed as a probe for the polarized gluon distribution $\Delta G/G$ of proton.[1] It has been estimated that, with the integrated luminosity of 320 (800) pb^{-1} at $\sqrt{S}$=200 (500) GeV, the achievable at RHIC statistical errors for the helicity transfer parameter D_{LL}[a] could be small enough for distinguishing, for example, the popular AAC[2] and $GSRV$[3] models for $\Delta G/G$.

Compared to the usually considered for these purposes cross-section asymmetry $A_{LL} = \frac{\sigma^{++}-\sigma^{+-}}{\sigma^{++}+\sigma^{+-}}$, where σ^{++} and σ^{+-} are the cross sections for the same and opposite helicities of colliding protons, spin transfers are linear with $\Delta G/G$ while $A_{LL} \propto (\Delta G/G)^2$. This means that spin transfers might become more sensitive probes for polarized gluon distribution if $\Delta G/G$ appeared to be unexpectedly small. The other difference is that, unlike A_{LL}, measuring spin transfers generally does not require monitoring the relative luminosity of collisions with different polarizations of initial protons, which is always considered as a potential source of systematic errors. And, in general, measuring a number of sensitive characteristics rather than one and comparing them to the predictions of theoretical models could serve as a good consistency check of the model's assumption.

In report,[4] we extended the analyses[1] to the proton helicity correlations with the Λ_c^+ transverse polarization component in the production plane (parameter D_{LS}). The D_{LS} is also expected to be nonzero at Λ_c's transverse momenta P_T of a few GeV/c due to the large c-quark mass. Moreover, for each spin transfer, LL and LS, we evaluated two more observables, $D_{L\Pi}^{++}$ and $D_{L\Pi}^{+-}$, $\Pi = L, S$, which will actually be measured at RHIC in collisions of *two* polarized protons of the same and opposite helicities, respectively. Then, parameters $D_{L\Pi}$ for collisions of polarized protons at unpolarized can be determined as the weighted averages of $D_{L\Pi}^{++}$ and $D_{L\Pi}^{+-}$:

$$D_{L\Pi} = \frac{1}{2}[D_{L\Pi}^{++}(1 + A_{LL}) + D_{L\Pi}^{+-}(1 - A_{LL})] \qquad (1)$$

In turn, if all three D's for the same final spin component were measured, then A_{LL} can be derived, using Eq. (1), with the result, as it mentioned above, potentially free from systematics due to monitoring the relative luminosity of collisions with different beam polarizations. With this approach, the A_{LL} statistical errors would usually be larger than of "direct" measurements. However, if the systematics rather than statistic is an issue, then using spin transfers and Eq. (1) could be an option.

In Fig. 1, the leading order calculations for pseudorapidity dependences of 6 spin transfer parameters, averaged over P_T interval from 2 to 5 GeV/c, are shown. These results have been obtained, using the assumptions and techniques of the papers.[1] The same spin dependent fragmentation function $\Delta\mathcal{D}(z) = \mathcal{C}(z) \cdot \mathcal{D}(z)$ have been used for both the longitudinal and transverse spin transfers from c-quark to Λ_c^+, where $\mathcal{D}(z)$ is the "unpolarized" quark fragmentation function. For the $\mathcal{C}(z)$, two option are compared: $\mathcal{C}(z) = 1$ and $\mathcal{C}(z) = z$. One can observe that, in the central region of $|\eta| < 1$, both, D_{LL}'s and D_{LS}'s are of about the same size ∼5–15%. As η increases, all D_{LL}'s grow up to ∼20–30% for the AAC model, while D_{LS}^{+-} stays virtually flat. The achievable at RHIC statistical errors of about 1% are small enough to clearly separate predictions for the shown models.

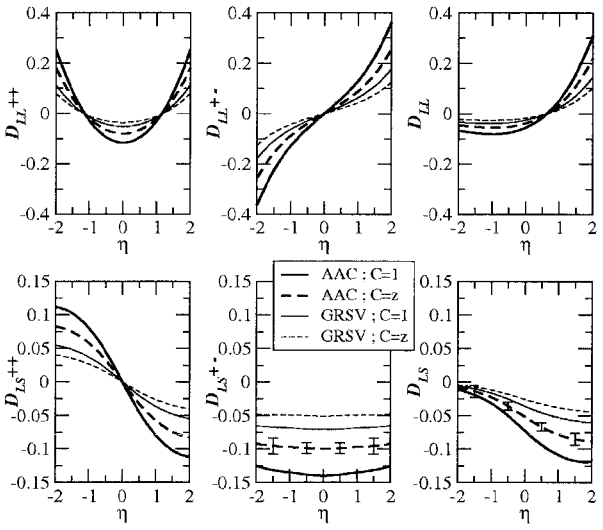

Fig. 1. η-dependences of spin transfer parameters for inclusive Λ_c^+ production in polarized proton collisions at $\sqrt{S}$= 200 GeV. The statistical errors are for the integrated luminosity of 320 pb^{-1} and beam polarization 70%. See text for details.

References

1) K. Ohkuma, K. Sudoh, and T. Mori: Phys. Lett. B **491**, 117 (2001); K. Ohkuma and T. Mori: hep-ph/0306285.
2) Y. Goto et al.: Phys. Rev. D **62**, 034017 (2000).
3) M. Glück et al.: Phys. Rev. D **63**, 094005 (2001).
4) V. L. Rykov and K. Sudoh: Proc. 16th Int. Spin Physics Symp. (SPIN2004), Trieste, Italy, 2004-10 (to be published); hep-ph/0412244.

[a] A_{LL} in the notations of papers.[1]

CCJ operation in 2003–2004

S. Yokkaichi, Y. Goto, H. Hamagaki,* T. Ichihara, O. Jinnouchi, A. Kiyomichi, Y. Watanabe, and H. En'yo

The operation of CCJ,[1–3] RIKEN Computing Center in Japan for RHIC[4] physics, started in June 2000 as the largest off-site computing center for the PHENIX[5] experiment at RHIC. CCJ performs, in PHENIX computing, the three roles of 1) the simulation center, 2) the Asian regional center and 3) the center of spin physics. Recently, DST (Data Summary Tape) production from raw data has become more important.

Many analysis and simulation projects are being carried out at CCJ, including some PHENIX official projects. They are shown on the web page: http://ccjsun.riken.go.jp/ccj/proposals/. The report from each project is described in this volume.

We have approximately 180 PC nodes operated using Linux, 166 are calculation nodes and the others are service nodes. Each calculation node has 1 GB of memory, 2 GB of swap area, 10–31 GB of local work area and dual CPUs (Pentium III 700 MHz–1.4 GHz, Pentium 4 2.0 GHz). Red Hat 8.0/kernel 2.4.20 is operated on the calculation nodes, the same as at the RCF (RHIC computing facility),[6] which is the main analysis facility for the PHENIX. The upgrade to Red Hat 8 was carried out in Jan. 2004.

We also have six SUN servers operated using Solaris, one is a service node and five are data servers, which are connected to large RAID systems (38 TB in total) and operated as NFS servers. Service nodes are used for various purposes such as a login server from WAN, a database server for analysis, an AFS client to share the PHENIX computing environment. Calculation nodes are connected with 100Base-T and data servers are connected with 1000Base-SX *via* a gigabit switch. Gigabit switch Alteon ACE 180 was replaced by Cisco Catalyst 4506 in Feb. 2004.

HPSS[7] 4.5 is used as a mass-storage system in CCJ, the same as RCF. Approximately 180 TB/650000 files of data have been stored in CCJ-HPSS as of Oct. 2004. Five IBM p630 servers operated using AIX are used as the HPSS core server and data/tape movers. Eight 9940B tape drives (30 MB/s I/O & capacity 200 GB/cartridge) and 3000 tape cartridges in a StorageTek PowderHorn 9310 tape robot are available. The robot can handle approximately 5000 tapes, thus we can extend the total tape capacity to 1 PB. The upgrade to the current HPSS system was carried out in Nov. 2003, as a part of the RIKEN Super Combined Cluster System (RSCC),[8] which is explained in the following section. We also have a tape duplication facility at BNL which consists of an IBM p630 server and two 9940B tape drives.

On the calculation nodes, the batch queueing system LSF[9] 4.2 was operated and upgrading to LSF 5.1 was carried out in Apr. 2004.

In Mar. 2004, the AFS client was upgraded from a SUN WS to a PC (Pentium III 1.4 GHz/memory 1 GB) using OpenAFS on Linux. In Jun. 2004, a PC (dual Xeon 2.6 GHz/memory 2 GB) functioning as an NFS server was deployed which was connected to an 8 TB FC RAID system.

The DB system for PHENIX analysis was gradually being changed from Objectivity/DB (OBJY) to PostgreSQL this year. The last OBJY update at PHENIX was in Jun. 2004. The limited support of PostgreSQL in CCJ started in Apr. 2004.

RSCC was deployed in Mar. 2004 by the RIKEN Advanced Center for Computing and Communication. Integrated operation between RSCC and CCJ was investigated from 2003, and opened for users in May 2004. RSCC includes 1024 nodes/2048 CPUs of PC clusters and HPSS as a mass-storage device, which is shared with CCJ.

As calculation nodes, 128 PC nodes (dual Xeon 3.06 GHz/2 GB memory/100 GB local disk), forming the 'pc2c' cluster in RSCC are dedicated to CCJ. Our data servers and HPSS can also be accessed by these nodes the same as for our old PC nodes. In particular, the user's home area and the PHENIX computing environment are shared using NFS.

As a batch queueing system, NQSII/ERSII (made by NEC) is operated in the pc2c cluster. For the time being, the performance of the system is insufficient for our usage in experimental nuclear physics, e.g., to process up to 1000–10000 jobs per day. The redundancy of the system is also worse than that of LSF. Improvement or replacement should be planned.

To estimate how appealing our CPU power is to users, we examine the 'obsolescence index (OI)', which is defined as the 'total CPU power in the cluster' divided by the 'fastest desktop CPU power available in that year'. In other words, the cluster is equivalent to the fastest desktop PC × OI for that year. If there is no CPU upgrade, the OI decreases because CPUs become faster year by year. Here, the 'effective CPU power' is measured using a typical PHENIX software and normalized with respect to 1 GHz Pentium III.

The trend of the OI of CCJ (building commenced in 1999) is shown in Fig. 1. It shows that, at the end of JFY 2004, the fastest Intel CPU is estimated to be 4.2 GHz (solid triangles), CCJ (with RSCC pc2c) have calculation power equivalent to approximately 1100 Pentium III 1 GHz CPUs (solid squares) and equivalent to approximately 250 of the fastest available CPUs

* Center for Nuclear Study, University of Tokyo

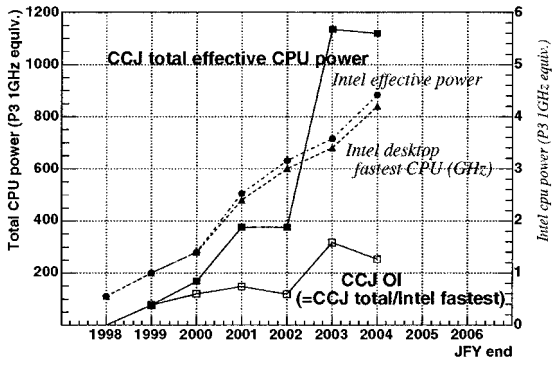

Fig. 1. Obsolescence index (OI) of CCJ.

(open squares) for the PHENIX software. RSCC made CCJ very appealing in terms of CPU power.

Here, we report hardware problems that occurred in the term of Dec. 2003–Nov. 2004. Concerning the PC nodes, 10% of nodes were down due to various problems involving the cooling fan, disk, memory, CPU and power supply. In total, 25% of calculation nodes has been down because 15% were down in the previous year.[2] The problems occurred in the older (and slower) node group purchased in JFY 1999–2001. There were almost no problems with the newer (and faster) node group purchased at the end of JFY 2001 including Linux Networx R-Cluster and IBM xSeries 330. Concerning the SUN servers, M/B replacement in Mar. and memory & CPU replacement in Oct. were the only two problems that required the shutdown.

Concerning the RAID systems, the controller, cable, FC-hub and I/F card problems which caused a disk-offline are approximately 10 times including two cases that required the shutdown of the servers. Simple disk failure is not included because disks comprising RAID are hot swappable. The old problematic 3.2 TB SCSI RAID purchased in JFY 1999 was retired in Mar. 2004. The disk-failure rate of the old 6 TB FC RAID purchased in JFY 2000 became very high (4 times/month or more) this year. We could not neglect the probability of the simultaneous failure of two disks, which could cause the loss of data, therefore we retired the RAID in Dec. 2004.

The air-conditioning system in the machine room was down on Mar. 9, 2004, which was caused by a mistake by the building maintenance staff. A high room temperature for 6–8 hours could have damaged the hardware, although data were not lost in this case.

The most serious problem occurred in Feb. 2004, that is, an operational error of the disk caused a loss of data in the user's home area. Although backup data was restored, the data updated in the previous 7 days were lost. (Backup using the *dump* command was operated once a week. Unfortunately, the accident occurred on the 7th day.) Backup using *rsync* once a day was also started after the accident.

In PHENIX Run4 (2003/11–2004/5), approximately 200 TB of raw data for the heavy-ion collision experiment and 20 TB for the p-p collision experiment were recorded. The transfer of the p-p data from BNL to RIKEN *via* WAN was carried out and a transfer rate of approximately 100 Mbps (12 MB/sec) for 24 hours (or more) was achieved using *bbftp*.[10] In the test, approximately 70 MB/s was achieved using *GridFTP*.[11]

The project to transfer the Run5 (2004/11 ∼) data *via* WAN is planned to produce DST in CCJ, particularly for the p-p collision data. The amount of data of Run5 will be approximately 200–400 TB for just the p-p data for 2–3 months. If a transfer rate of 70 MB/s (= 6 TB/day = 180 TB/month) cannot be maintained continuously, transfer using tape will also be required.

The following tasks should be processed in the next several months: upgrade to Scientific Linux 3 (and LSF 6.0) on the calculation node, reinforcement of the DB server for PHENIX, improvement of the batch queueing system of the pc2c cluster in RSCC, establishment of the (semi-)automatic data-transfer procedure from the PHENIX counting house and the efficient data-I/O procedure for the p-p DST production at CCJ.

References

1) http://ccjsun.riken.go.jp/ccj/
2) S. Yokkaichi et al.: RIKEN Accel. Prog. Rep. **37**, 257 (2004).
3) Y. Watanabe et al.: RIKEN Accel. Prog. Rep. **36**, 262 (2003); T. Ichihara et al.: RIKEN Accel. Prog. Rep. **35**, 236 (2002).
4) http://www.bnl.gov/rhic
5) http://www.phenix.bnl.gov
6) http://www.rhic.bnl.gov/RCF/
7) http://www.hpss-collaboration.org/
8) http://rscc.riken.jp
9) http://www.platform.com/products/LSF/
10) http://doc.in2p3.fr/bbftp/
11) http://www.globus.org/datagrid/gridftp.html

Pumping ^{229m}Th by hollow-cathode discharge [II]

S. Enomoto, H. Haba, M. Hara,[*1] T. T. Inamura, Y. Kasamatsu,[*2] H. Kikunaga,[*3] T. Mitsugashira,[*1] T. Nakanishi,[*3] T. Ohtsuki,[*4] A. Shinohara,[*2] K. Takamiya,[*5] A. Yokoyama,[*3] and H. Yuki[*4]

We proposed a new method for pumping ^{229m}Th by hollow-cathode discharge and built a hollow-cathode tube that was specially designed to measure α particles from ^{229m}Th.[1)] After making a small but decisive alternation around the insulation between the anode and the hollow cathode, we successfully made Ar-gas discharge stable as long as we wanted with ^{229}Th (0.1–0.2 μg) loaded into the hollow cathode. Usually, we use Ar gas at a pressure of 200 Pa, a discharge current of 100 mA or 200 mA and a voltage of about 300 V (constant current mode). These discharge conditions are comparable to the standard conditions in the hollow-cathode tube for atomic spectroscopy, and we can excite atomic states up to about 10 eV in Th I (neutral atom) and Th II (singly charged atom). This was confirmed by preliminary experiment with natural Th using the UV spectrograph at the Poznan University of Technology in 2002.[2)]

From the level systematics in this mass region, the ground state of ^{229}Th has been assigned to the Nilsson orbital $5/2^+$ [633],[3)] and similarly, the so-called 3.5-eV isomer[4)] is considered to be $3/2^+$ [631] if it exists. Consequently, as we reported at an international workshop this year,[5)] one can expect four significant α transitions from ^{229m}Th to the known levels of ^{225}Ra: 4930-keV α transition to the $I^\pi = 3/2^+$ ($3/2^+$[631]) level at 149.96 keV, 5036-keV to $3/2^+$ ($1/2^+$[631]) at 42.77 keV, 5053-keV to $5/2^+$ ($1/2^+$[631]) at 25.41 keV, and 5079-keV to $1/2^+$ ($1/2^+$[631]) at the ground state. The first two transitions are expected to be strongly favored.[6)] Although we started this experiment by assuming its half-life to be about 14 hours according to Ref. 6, measurements were performed successively for a period of 10 minutes, 20 minutes after switching off the discharge that was kept at 100 mA for 3 hours. Figure 1 shows α spectra observed 20 minutes (●) and 17 hours (□) after switching off the discharge. The observed four distinct peaks mainly come from the α decay of the ground state of ^{229}Th ($T_{1/2} = 7340$ y). As indicated in Fig. 1, however, there seems to be a trace of 5036-keV transition only in the first spectrum (●), which is likely to have a decay half-life shorter than 20 minutes. At present, it is hard to make a definite statement about whether the isomer was really pumped. To confirm this, we will perform an in-beam measurement, *i.e.*, a measurement during the discharge. The half-life of the isomer could be even shorter than a few minutes.

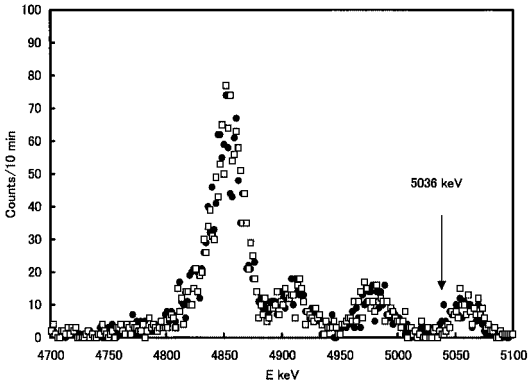

Fig. 1. Alpha spectra observed 20 minutes (●) and 17 hours (□) after switching off the discharge in the hollow-cathode tube loaded with ^{229}Th (0.1 μg or about 1 kBq). An arrow indicates an energy of 5036 keV that is likely to coincide with the probable α transition from ^{229m}Th.

The in-beam measurement will be made at the Oarai Branch of the Institute for Materials Research, Tohoku University.

References

1) H. Haba et al.: RIKEN Accel. Prog. Rep. **37**, 263 (2004).
2) B. Arcimowicz, S. Chojnacki, and T. T. Inamura: Annu. Rep. **2002**, Heavy Ion Laboratory, Warsaw University (2003), p. 43.
3) R. B. Firestone, V. S. Shirley, C. M. Baglin, S. Y. F. Chu, and J. Zipkin: *Table of Isotopes*, 8th ed. (Wiley and Sons, New York, 1996).
4) R. G. Helmer and C. W. Reich: Phys. Rev. C **49**, 1845 (1994).
5) T. T. Inamura, T. Mitsugashira, and the Oarai Collaboration: Int. Workshop on Laser Methods in the Study of Nuclei, Atoms and Molecules, Poznan, Poland, May 23-27, 2004; the proceedings will be published in Hyperfine Interact. in 2005.
6) T. Mitsugashira et al.: J. Radioanal. Nucl. Chem. **255**, 63 (2003).

*1 Oarai Branch, Institute for Materials Research, Tohoku University
*2 Graduate School of Science, Osaka University
*3 Graduate School of Science, Kanazawa University
*4 Laboratory of Nuclear Science, Tohoku University
*5 Research Reactor Institute, Kyoto University

Carbon-nanoparticle formation from Teflon through rf-discharge processes

O. Kamigaito and T. Kobayashi

It was found that carbon-nanoparticles are formed from Teflon (PTFE: polytetrafluoroethylene) through rf-discharge processes in the atmosphere. This phenomenon was formerly observed in an rf breakdown in a feeder line of a RILAC cavity, where vast amounts of black ashes were generated from a small portion of the Teflon insulator. We confirmed the formation in an experiment using an rf resonator, as described below.

Figure 1 (a) shows a schematic drawing of the experimental set-up. A coaxial resonator, which was used for testing the flat-topping system of the AVF cyclotron,[1] has been modified by attaching a spark gap at the open end. The resonant frequency, Q-value and shunt impedance of the resonator are 80 MHz, 5200 and 615 kΩ, respectively. The pulsed rf signal from a signal generator (Agilent E4436B) is amplified through a wide-band amplifier (Thamway A145-6767A), which has a gain of 60 dB with a maximum power output of 5 kW, and fed into the resonator with a capacitive coupler. The gap voltage is monitored by a capacitive pickup probe.

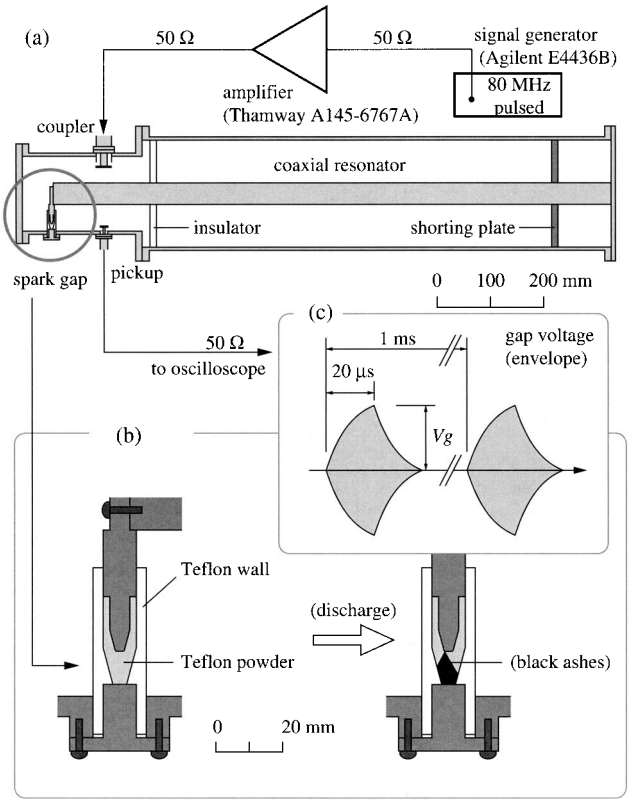

Fig. 1. (a) Schematic drawing of experimental set-up. (b) Spark gap and Teflon cylinder containing Teflon powder. (c) Time sequence of gap voltage.

The spark gap is shown in Fig. 1 (b). The gap between the two copper electrodes is surrounded by a Teflon cylinder, which contains Teflon powder in it.

The pulse width and the repetition rate of the signal generator were set to be 20 μs and 1 kHz, respectively, as shown in Fig. 1 (c). When the gap voltage V_g, shown in Fig. 1 (c), exceeded 35 kV, discharge occurred in the Teflon cylinder. Soon the gap became conductive and it was found that some portion of the Teflon powder had burned; black ashes were generated between the gap as shown in Fig. 1 (b).

A typical SEM image of the ashes is shown in Fig. 2, where clusters of fine particles of 30–80 nm in diameter are observed. Analyses using TEM/EDX have shown that these nanoparticles mainly consist of carbon. A smaller amount of fluorine is also observed in the nanoparticles.

It has been shown by TEM and electron-diffraction analyses that the nanoparticles have an amorphous structure. Further investigation on the structure as well as their formation process is under way.

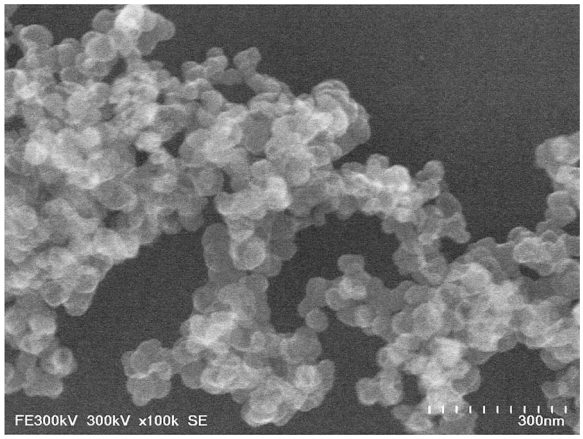

Fig. 2. SEM image of nanoparticles formed from Teflon, taken using Hitachi 300 kV FE-STEM. A single unit of the scale corresponds to 30 nm.

Reference

1) S. Kohara et al.: Proc. 12th Symp. on Accelerator Science and Technology, Wako, 1999-10 (1999), p. 227.

Effects of plasma electrode position on beam intensity and emittance of RIKEN 18 GHz ECRIS

Y. Higurashi, T. Nakagawa, M. Kidera, T. Aihara,* M. Kase, and Y. Yano

To improve the performance of the RIKEN 18 GHz ECRIS, we intensively studied the effect of the plasma electrode position on the beam intensity of heavy ions during the past several years.[1,2] In previous experiments, we investigated the effect of the plasma electrode position on the beam intensity of $Ar^{8+,9+}$ and increased the beam intensities up to the order of mA.[3] However, the effect of plasma electrode position on the beam intensities of heavier ions (Kr and Xe ions) is still not clear. Furthermore, such a beam intensity should affect the beam quality (emittance, brightness and so on).[4] In this paper, we report on the effects of the plasma electrode position on the beam intensity of Ar, Kr and Xe ions, and the emittance of intense heavy ion beam.

Figure 1 shows the position of the movable plasma electrode and beam extraction side. The diameter of the plasma electrode hole was 10 mm. The distance between the extraction electrode and the plasma electrode was $\sim$ 15 mm. The hole diameter of the extraction electrode was 12 mm.

In a previous paper,[3] the plasma electrode position for maximizing the beam intensities of $Ar^{8+,9+}$ was found to be at electrode position C (see Fig. 1). To investigate the effect of electrode position on the beam intensities of Kr and Xe ions, we measured the beam intensities as functions of plasma electrode position. We chose four positions (position A (edge of hexapole magnet), B, C, and D (within 2.5 cm from the edge of the hexapole magnet) as shown in Fig. 1. The other parameters (magnetic field, gas pressure, biased disc position, and negative bias voltage of disc) were tuned to maximize the beam intensity.

Figure 2 shows the charge distributions of Ar, Kr and Xe ions produced from the RIKEN 18 GHz ECRIS at plasma electrode position C. The ion source was tuned to produce Ar^{8+}, $Kr^{13+}$and Xe^{18+} ion beams. Beam intensities of $Xe^{18,20+}$ increased from 0.2 to 0.3 emA, when the plasma electrode was moved from position A to C. At plasma electrode position C, beam intensities of 0.6 mA of Kr^{13+}, 0.5 emA of Kr^{14+} and 0.3 emA of $Xe^{18,20+}$ were extracted at the RF power of $\sim$ 700 W.

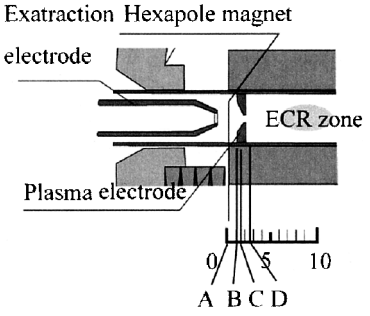

Fig. 1. Cross-sectional view of movable plasma electrode and beam extraction side of RIKEN 18 GHz ECRIS.[5]

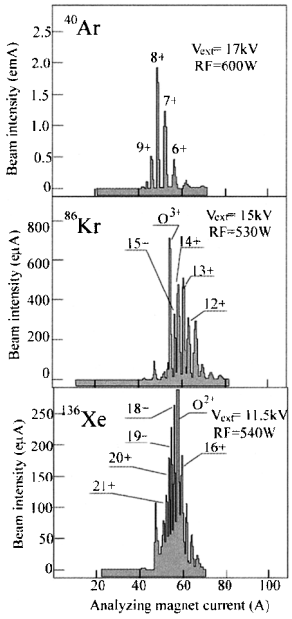

Fig. 2. Charge distribution of the Ar, Kr and Xe ions.

Figure 3 shows the beam intensities of Ar, Kr and Xe ions at plasma electrode positions A and C. We observed that the beam intensities of medium charge state Kr and Xe ions were strongly enhanced at plasma electrode position C, which is the same tendency observed in Ar ion production. Figure 4 shows the beam intensities of Ar, Kr and Xe ions as functions of plasma electrode position. It is clearly seen that beam intensities of lower charge state heavy ions increased as was plasma electrode moved toward the ECR zone.

Figure 5 shows the beam intensities of Ar, Kr and Xe ions as functions of RF power at plasma electrode position C. The ion source was tuned with 600 W of RF power and then the RF power was changed without changing any other parameters. It should be stressed that the beam intensity is not saturated at the maximum RF power in this experiment. This means that higher beam intensities can be realized at higher RF powers.

Measurements of the emittance both horizontally and vertically were performed over a wide range of the

* SHI Accelerator Service, Ltd.

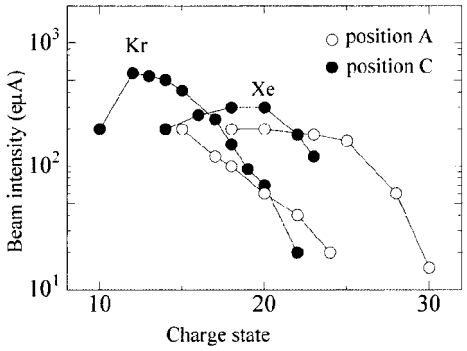

Fig. 3. Beam intensities Ar, Kr and Xe ions at plasma electrode positions A and C.

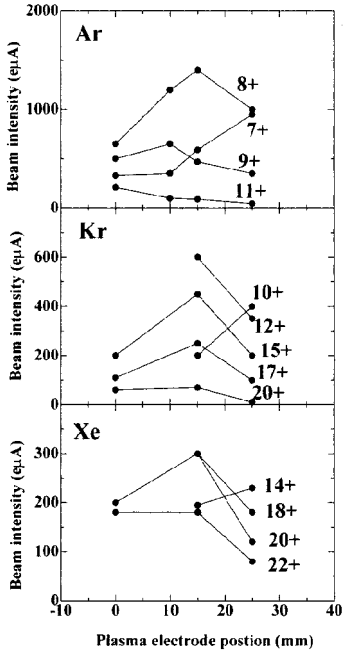

Fig. 4. Beam intensities of Ar, Kr and Xe ions as functions of plasma electrode position.

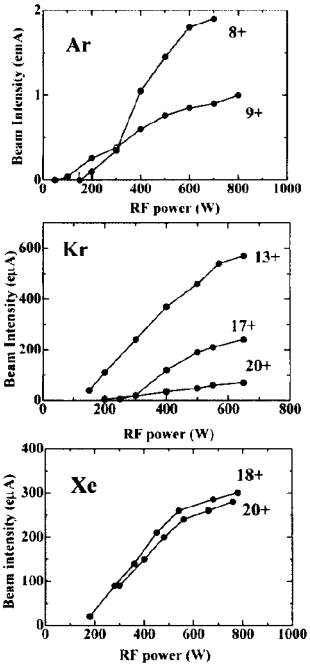

Fig. 5. Beam intensities of Ar, Kr and Xe ions as functions of RF power at plasma electrode position C.

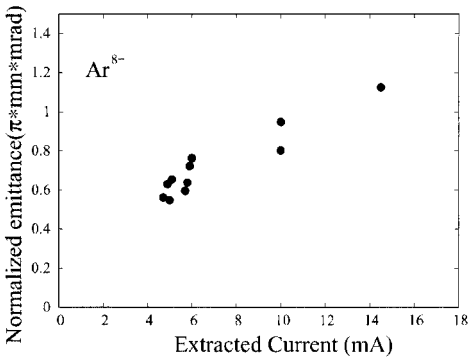

Fig. 6. Normalized 99% emittance of Ar^{8+} as a function of drain current.

drain current of the RIKEN 18 GHz ECRIS. Figure 6 shows the normalized 99% emittance of Ar^{8+} as a function of drain current. It is clearly seen that the emittance gradually increased from 0.5 to 1.1π mm mrad with increasing the drain current from 4 to 15 mA. At the highest drain current, the beam intensity of Ar^{8+} was 1.5 emA at the extraction voltage of 17 kV. In this case, the unnormalized emittance was 420π mm mrad, which is 3 times as large as the acceptance of our RFQ linac (acceptance is 150π mm mrad).[6] To accelerate the full beam of 1.5 mA Ar^{8+} under this condition, we require the extraction voltage of 60 kV. At a low drain current, 90% of the Ar^{8+} beam will be accepted by the RFQ linac at the extraction voltage of 20 kV. The emittances of the Xe^{20+} beam were 0.45 and 0.47π mm mrad for the drain currents of 3.5 and 1.5 mA, respectively. It seems that the emittance is almost constant at low drain current. In this test experiment, other effects (such as beam instability) may be larger than the space charge effect. To understand these phenomena, we need to conduct further investigations.

References

1) Y. Higurashi, T. Nakagawa, M. Kidera, T. Aihara, M. Kase, and Y. Yano: Rev. Sci. Instrum. **73**, 598 (2002).
2) Y. Higurashi, T. Nakagawa, M. Kidera, T. Aihara, M. Kase, and Y. Yano: Jpn. J. Appl. Phys. **42**, 3656 (2003).
3) Y. Higurashi, T. Nakagawa, M. Kidera, T. Aihara, M. Kase, and Y. Yano: Nucl. Instrum. Methods Phys. Res. A **510**, 206 (2003).
4) S. Gamino et al.: Rev. Sci. Instrum. **75**, 1637 (2003).
5) T. Nakagawa and Y. Yano: Rev. Sci. Instrum. **71**, 637 (2000), and references therein.
6) O. Kamigaito et al.: Rev. Sci. Instrum. **70**, 4523 (1999).

Improvements in Hyper-ECR ion source for production of metallic ions and extraction of ion beams

Y. Ohshiro,* S. Yamaka,* and S. Watanabe*

A Hyper-ECR ion source[1] and a 10 GHz ECR ion source have been operated alternatively to supply beams to the RIKEN AVF cyclotron. Various highly charged gaseous ions are produced by the Hyper-ECR ion source. Metallic ions are routinely produced by a rod insertion method, which is adopted in the 10 GHz ECR ion source. A solid material insertion system (called a rod insertion system) and a beam extraction system (called an ion decelerator) were installed in the Hyper-ECR ion source this year. With these devices, metallic ion beams, for example, $^{24}Mg^{7+}$ and $^{7}Li^{2+}$ ion beams, were extracted from the Hyper-ECR ion source, which enabled the supply of intense metallic ion beams to a CRIB separator[2].

A schematic drawing of the rod insertion system in the Hyper-ECR ion source is shown in Fig. 1. A rod-shaped solid material is inserted near the ECR zone on the right-hand side of the gas inlet. The solid material was heated and ionized by hitting the ECR plasma. The specifications of the rod insertion system are shown in Table 1.

First, we inserted the rod into the ECR plasma and subsequently heated the inside of the plasma chamber, for about 4 hours, to remove residual gases. When the vacuum in the plasma chamber was of the order of 10^{-7} Torr, metallic ions were generated by the rod located 1.7 cm away from the boundary of the ECR zone. The metallic ions $^{24}Mg^{7+}$ and $^{24}Mg^{5+}$ were produced by the 6-cm-long MgO rod. The metallic ion $^{7}Li^{2+}$was produced by the 5-cm-long LiF rod.

The operating conditions of the ECR ion source are as follows: the supporting gas used for generating magnesium ions was oxygen and that for generating lithium ones was helium. The RF (14.2 GHz) power was about 100 W. Two peaks of the mirror fields were 10.5 kG and 11.5 kG. The length of the ECR zone was about 7 cm. The beam intensities obtained in the initial test are summarized in Table 2.

For extraction, we replaced the extraction system of the present electrode with the ion decelerator in order to increase the extraction voltage up to 20 kV, but without changing the injection voltage.

Figure 2 shows the new ion decelerator consisting of electrodes arranged in the following order from the right-hand side: plasma, extraction, and ground electrodes. The gap between the plasma and extraction electrodes is about 4.5 cm. Beams are supplied from right to left.

We investigated the dependence of voltage on the beam intensity at the extraction electrode, while the voltage of the plasma electrode was 10 kV. In cases of $^{14}N^{6+}$and $^{14}N^{5+}$ ions, the maximum beam intensity was obtained at −5 kV (15 kV total acceleration) for the $^{14}N^{6+}$ ion and −7 kV (17 kV total acceleration) for the $^{14}N^{5+}$ ion on the extraction electrode. For ions, the beam intensity increased roughly by a factor of two.

We completed the installation of the rod insertion system and the ion decelerator in the Hyper-ECR ion source. This enabled the extraction of metallic ion beams from the Hyper-ECR ion source.

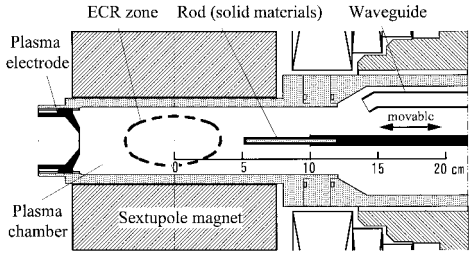

Fig. 1. Rod insertion system in Hyper-ECR ion source.

Table 1. Specifications of rod insertion system.

Maximum rod cross section	0.16 cm^2
Attachable rod length	5 cm to 20 cm
Minimum speed	0.1 mm/h
Maximum speed	1.0 mm/h

Table 2. Metallic beam intensities obtained in initial test.

Ion species	$^{24}Mg^{7+}$	$^{24}Mg^{5+}$	$^{7}Li^{2+}$
Beam intensity (eμA)	3	5	10

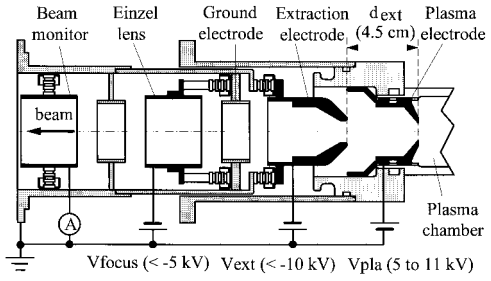

Fig. 2. Ion decelerator of Hyper-ECR ion source.

* Center for Nuclear Study, Graduate School of Science, University of Tokyo

References

1) Y. Ohshiro et al.: RIKEN Accel. Prog. Rep. **36**, 279 (2003).
2) Y. Yanagisawa et al.: RIKEN Accel. Prog. Rep. **34**, 183 (2001).

A broadband cavity with magnetic alloy cores as buncher of ion beams†

M. Watanabe,*1 Y. Chiba, T. Koseki, Y. Ohshiro,*2 and S. Watanabe*2

Presented in this paper is a broadband cavity that has been installed in a beam transport line of an ion source, HiECR, in the Center for Nuclear Study of The University of Tokyo.

The HiECR ion source[1] is intensively used for ion source research and also used for R&D's of ion beam monitors, which are applicable to existing and future cyclotrons in RIKEN. For the latter purpose, ion beams having a bunched structure corresponding to the frequencies of the cyclotrons are required. We have developed a broadband and compact size cavity using magnetic alloy (MA) cores as a buncher of HiECR ion beams.

The cavity has a low Q-value less than 1 and operates in the wide frequency range between 18 and 45 MHz without any tuning systems. It is the first MA-loaded cavity used in a frequency higher than 18 MHz in the world.

As one of the R&D's of the RIBF project, we studied the characteristics of MA-loaded cavities in the frequency range from 20 to 40 MHz.[2,3] On the basis of such studies, we adopted the cut-core configuration of Finemet (FT-3M) for the buncher cavity. Finemet is an iron-based nanocrystalline MA made by Hitachi Metals, Ltd.[4] The core is made of thin tape, which is coated with SiO_2 and wound into a toroidal shape. The cut-core configuration is cutting the troidal core and setting it with appropriate air gaps between two circular halves.[5,6] Since the inductance of the cavity depends on the air gap length of the cut core, the resonance frequency can be properly choosen with the gap length.[3]

Figure 1 shows a cross-sectional view of the buncher cavity. To obtain a resonance frequency of approximately 30 MHz, the air gaps of the cut core are set to be 0.5 mm. A Macor ring is attached to the acceleration gap for insulation. Because the present extraction voltage of the HiECR ion source is 10 keV, two mesh plates made of copper are placed in parallel at the acceleration gap to increase the transit time factor. Each mesh is hexagonal and the distance between the centers of adjacent meshes is 2 mm. The width and thickness of the mesh wires are 0.1 mm. The distance between the mesh plates is 5 mm.

The rf characteristics of the cavity were measured using a network analyzer (HP4195A) with an impedance test kit (HP41951A). The measured resonance frequency is 29.5 MHz. The measured Q-value, shunt impedance R_s and inductance at the resonance frequency are 0.7, 150 Ω and 0.7 μH, respectively. The total gap capacitance including the parasitic capacitance is 40 pF at the resonance frequency.

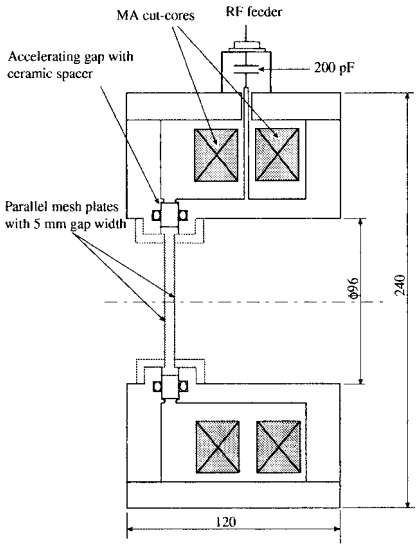

Fig. 1. Cross-sectional view of the buncher cavity.

We carried out a high-power test using a 3 kW rf power amplifier, which feeds the power to the cavity through a 50 Ω coaxial cable. To match the input impedance of the cavity to 50 Ω, a capacitor of 200 pF is connected in series with the cavity, and the cut cores are set in parallel as shown in Fig. 1.

Figure 2 shows the frequency dependence of the input voltage standing wave ratio (VSWR). Input and reflection powers were measured using a vector volt-

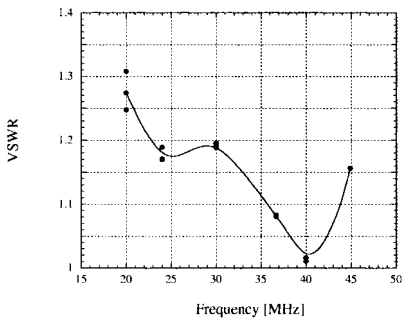

Fig. 2. Frequency dependence of the voltage standing wave ratio (VSWR) of the buncher cavity.

† Condensed from the article in the Proc. 17th Int. Conf. on Cyclotrons and Their Applications, Tokyo, 2004-10, in print.

*1 J-PARC, Japan Atomic Energy Research Institute
*2 Center for Nuclear Study (CNS), Graduate School of Science, The University of Tokyo

meter (HP8508A). The VSWR is kept at less than 1.3 in the frequency range from 20 to 45 MHz.

The relationship between the peak gap voltage V and the cavity dissipation power P for several frequencies is shown in Fig. 3. The gap voltages were measured using a high-voltage probe (Tektronix, P5102). Each curve shows the fitted results of the square function of the voltage. The calculated shunt impedance ($R_s = V^2/2P$) of the cavity is 133 Ω at 30 MHz.

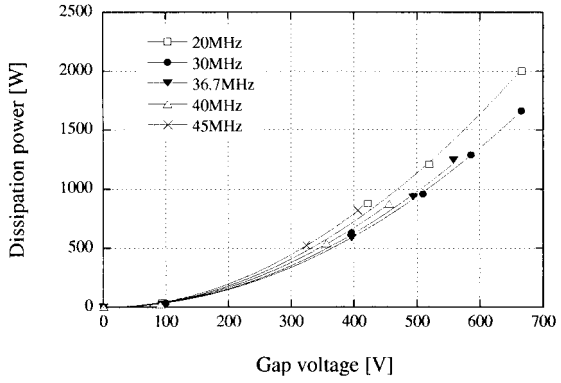

Fig. 3. Relationship between the peak gap voltage and dissipation power of the buncher cavity.

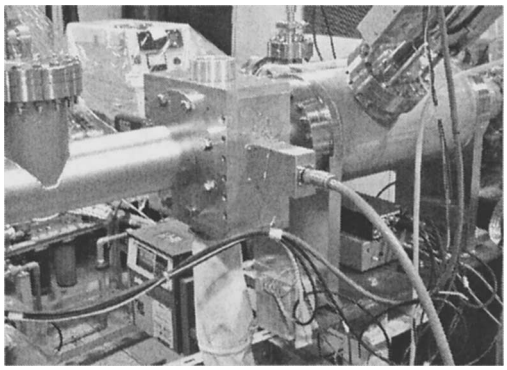

Fig. 4. Buncher cavity installed in the beam transport line of the HiECR ion source.

The buncher cavity was installed in the beam transport line of the HiECR ion source system. Figure 4 shows a photograph of the cavity in the beam line. The Finement cores were cooled by an electric fan.

Figure 5 shows the typical beam current waveform observed using the buncher cavity. The beam current was measured using a Faraday cup at 2.3 m downstream of the cavity. In this case, a 10 keV H^+ beam with an average current of 20 μA was used. The frequency and peak voltage of the cavity were 30 MHz and 150 V, respectively. As shown in the figure, a beam structure of 30 MHz was successfully obtained.

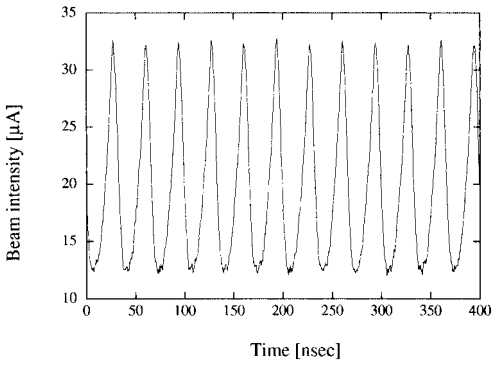

Fig. 5. Typical bunched beam current waveform.

References

1) S. Watanabe et al.: CNS Rep. **45**, 47 (2002).
2) M. Watanabe et al.: RIKEN Accel. Prog. Rep. **36**, 325 (2003).
3) M. Watanabe et al.: Nucl. Instrum. Methods Phys. Res. A **532**, 503 (2004).
4) Y. Yoshizawa et al.: J. Appl. Phys. **64**, 6044 (1988).
5) M. Yoshii et al.: Proc. EPAC2000 (2000), p.984.
6) J. Dey et al.: Proc. PAC2001 (2001), p.882.

Status of control system for RARF and RIBF

M. Kobayashi-Komiyama, I. Yokoyama, M. Fujimaki, J. Odagiri,* and M. Kase

The structure of the current control system of the RIKEN Accelerator Research Facility (RARF) is shown in Fig. 1. Our control system is based on the Experimental Physics and Industrial Control System (EPICS),[1] and we have been using the CAMAC-CIM/DIM system as a low-level control system for more than 20 years. The basic operations of RARF are currently carried out without any serious problems. However, our control system includes one fundamental problem; a phototransceiver module in the U-Port Adopter, which is an essential module in our CAMAC system based on a CAMAC Serial HWY loop, is no longer available. This means that it will be difficult to continue using the current CAMAC-CIM/DIM system when a U-Port Adopter is out of order.

To take measures to resolve the difficult situation to continue using our old CAMAC control system in the future, we have applied two improvements to the control system. One is the introduction of our original control device, Network-DIM (N-DIM). As mentioned in the last report,[2] we have already started to control nine sets of the new vacuum control unit in RILAC using N-DIMs for the R/D of the N-DIM system. This year, we increased the number of the new vacuum control units in RARF up to approximately twenty. Furthermore, we replaced the control system of the beam profile monitor in RILAC from the CAMAC-CIM/DIM system with N-DIM. We developed an EPICS device support for a beam profile monitor control with a control group of KEK, and developed high-level control software based on it for the CAMAC-CIM/DIM system on a Linux PC. Therefore, an operator can control a beam profile monitor as before, and the same type of graph can be obtained. Furthermore, we can obtain equal performance of beam profile measurement as before. Thus, there is no confusion during beam operation due to the difference in the type of controller. We have controlled about twenty beam profile monitors using N-DIM from the same Linux server PC as the vacuum control since this summer. Beam operation has been carried out without any serious problems.

It is planned to replace the CAMAC-CIM/DIM system in RILAC with N-DIM gradually because the number of DIMs is small and we have a plan to simplify the complex low-level control system of RILAC. However, it is difficult to replace the entire CAMAC-CIM/DIM system in RARF with N-DIM because of the following three reasons. One is that it becomes too costly because there would be too many DIMs in the RARF. We currently are using approximately 170 DIMs for RARF control. The second reason is that RARF is in operation. The last reason is that the existing control commands in N-DIM are prepared to control only beam diagnostic equipment such as a beam profile monitor. Therefore, we have to develop control commands when we replace the CAMAC-CIM/DIM control system with N-DIM. This

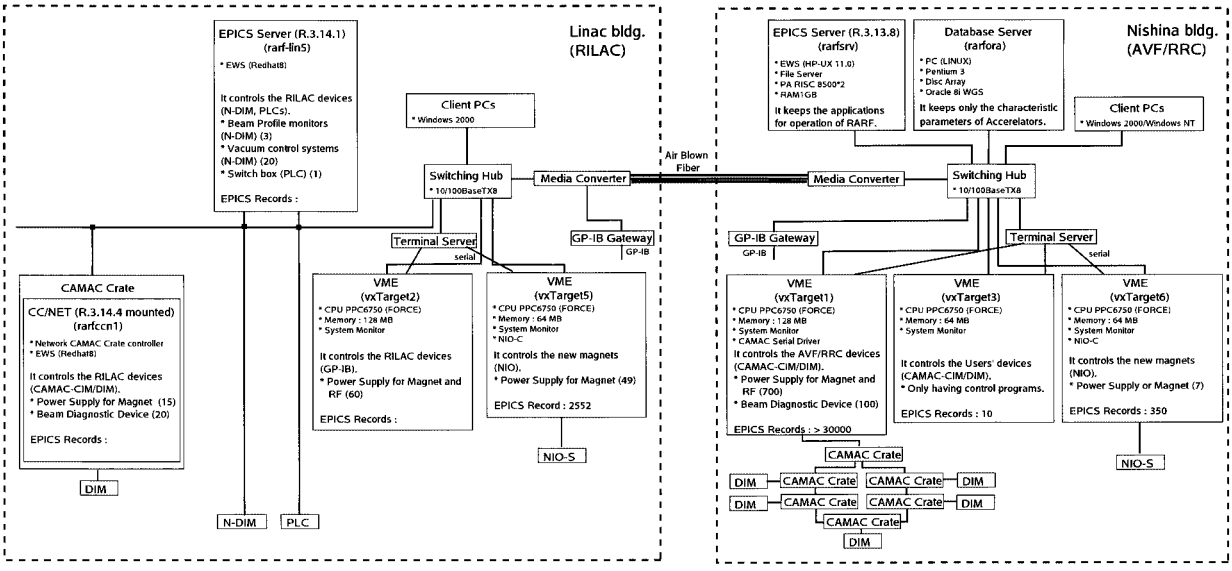

Fig. 1. Structure of RARF control system.

* High Energy Accelerator Research Organization (KEK)

is not easy. Thus, we investigated a way to support the CAMAC-CIM/DIM system in the future, and decided to employ the Pipeline CAMAC Controller with a PC104plus Single-Board Computer, CC/NET,[3] as another improvement to maintain our old CAMAC-CIM/DIM system in RARF.

The important features of CC/NET are as following.
- CC/NET is a network-based intelligent controller.
- System disk: flash disk (512 MB).
- OS: Debian/GNU Linux (kernel version 2.4).
- Includes original device driver and library.

According to the first feature, we can replace the CAMAC Serial HWY loop with the Ethernet using CC/NET, and we can continue using the CIM/DIM system in the future. More specifically, we can remove a U-Port Adopter and CAMAC Serial HWY loop from our control system and control the CIM/DIM system through the Ethernet directly from a high-level control system using CC/NET instead of the former CAMAC crate controller. Furthermore, since Debian/GNU Linux is running on CC/NET, CC/NET can also function as a high-level control system. We developed the control software of CC/NET with the control group of KEK as well as the N-DIM control software. We derived it from the existing software camacLib.c, in EPICS R3.13, and developed a wrapper over the CC/NET driver from TOYO to enable ISONE Standard CAMAC APIs to be able to use our original EPICS CAMAC-CIM/DIM device support modules as well as the standard EPICS CAMAC device support modules without major changes. There is no difference between the former CAMAC-CIM/DIM system and the CC/NET-CIM/DIM system in terms of the operator interface such as GUIs for beam operation. Since the control system of RILAC is easy to renew because the number of components is small, we installed CC/NET to run parallel to the installed N-DIM, and have started to use it in the system since this spring, as shown in Fig. 1. The same control performance as with the old system has been obtained to date.

As a next step, we have the following plans.
- Control Faraday cup by N-DIM.
- Replace the CAMAC-CIM/DIM system of AVF/RRC, the other system in RARF, with the system using CC/NET.

For the first plan, since we have already been able to control the Faraday cup using a test GUI, we can proceed to develop the same type of control software as the existing one as a next step. For the second plan, in the CAMAC-CIM/DIM system of AVF/RRC including 6 sets of CAMAC crates, we are going to replace the CAMAC crate controllers in use with CC/NET one by one, while checking for effects of radiation.

References

1) http://www.aps.anl.gov/epics/
2) M. Kobayashi-Komiyama et al.: RIKEN Accel. Prog. Rep. **37**, 277 (2003).
3) http://www-online.kek.jp/~yasu/Parallel-CAMAC/

Field test of N-DIM

M. Fujimaki, M. Kobayashi-Komiyama, and M. Kase

In the RIBF project, we have decided to use N-DIM (Network Device Interface Module)[1] as interface circuits which control beam monitoring devices like a Farady-Cup and beam profile monitor, and also control vacuum pump sets installed along beam transport lines.

After a prototype of N-DIM circuit boards were tested, twenty sets of N-DIM circuit boards were made in spring 2003. Then we started a field test of N-DIM to manipulate a vacuum pomp sets in RILAC (RIken Linear ACcelerator). In summer 2003, we installed twenty two N-DIM for vacuum pump set on the beam transport lines of RILAC (Fig. 1). These are remotely controlled by the host control system (EPICS)[2] through Ether-net.

In spring 2004, we make 105 N-DIM which were upgraded performance of analog circuits and clock lines on CPU board. In summer 2004, we replaced CIM/DIM[1] control devices for the beam profile monitors with the N-DIM that we have been testing from spring 2004 at the beam line for GARIS (Gas-filled Recoil Ion Separator) at RILAC. In addition, we have also installed a number of N-DIM to test the radiation effect near the RRC (Riken Ring Cyclotron).

We consider that the N-DIM has controlled the beam profile monitors and vacuum pump sets nearly satisfactorily, but their performance was not sufficient in hot environments. We have found that the network interface chip on the CPU board of the N-DIM stopped over about 45°C. N-DIM overheat when they are installed densely in a 19 inches standard cabinet at EIA (Electronic Industries Association). The case of N-DIM is 1 U size of 19 inches standard cabinet at EIA, which contains a 40 W power supply and an N-DIM circuit board. The heat of this power supply causes this problem. We avoid this problem by temporarily using a large fun or installing N-DIM with an enough cooling interval gap. We are currently developing a cooling system that requires no maintenance. This situation is shown in Figs. 2 and 3.

When N-DIM is exposed to radiation, we feel that the N-DIM is not better than the DIM (old control device used before N-DIM). We have not made a measurement yet, but we have already observed the presence of some errors for N-DIM installed near the RRC. We need to select the location of N-DIM considering radiation level.

If a large number of N-DIM are connected to a network, it would causes a bad effect on the network traffic because each N-DIM transmits a large amount of

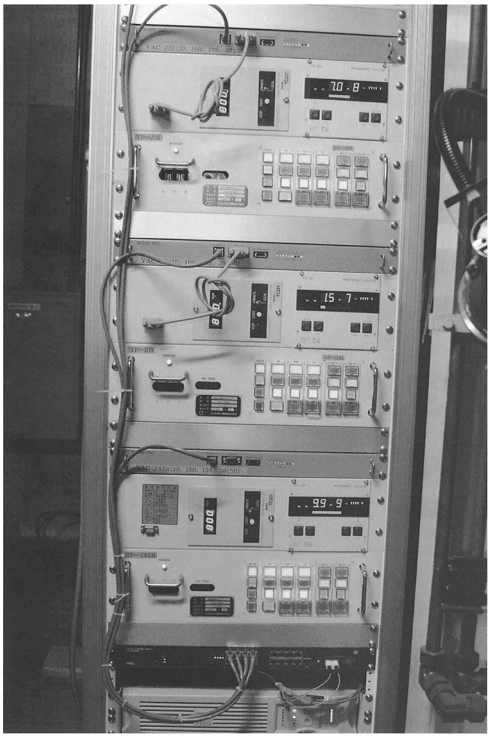

Fig. 1. Vacuum control system.

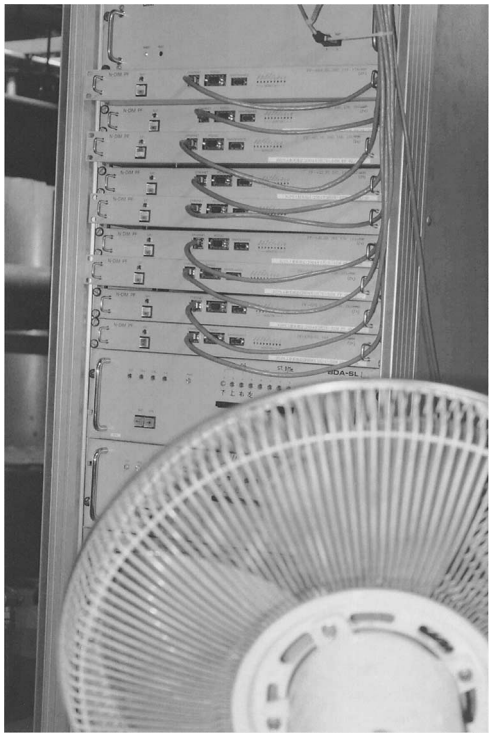

Fig. 2. N-DIM for profile-monitors.

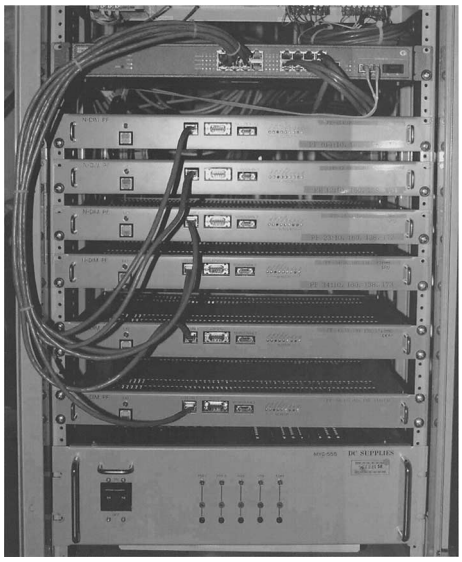

Fig. 3. N-DIM for profile-monitors.

data to the network once every 64 milliseconds during the measurement of a beam profile. Therefore, we have employed a fast network using optical fibers. As shown in Fig. 4, the network for N-DIM consists of one optical HUB and six media converters.

Now we operate totally 42 N-DIM, twenty for beam profile monitors and twenty two for vacuum pump sets. Faraday-cups are not controlled yet by N-DIM.

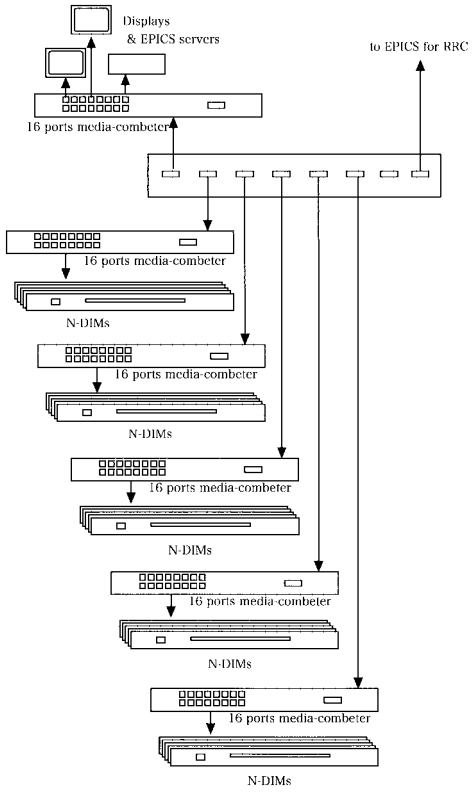

Fig. 4. Network construction.

References
1) M. Fujimaki et al.: RIKEN Accel. Prog. Rep. **37**, 279 (2004).
2) M. Kobayashi-Komiyama et al.: RIKEN Accel. Prog. Rep. **37**, 277 (2004).

Remodeling of linear accelerator building for uranium acceleration

Y. Uwamino, N. Fukunishi, T. Nakagawa, M. Kidera, Y. Higurashi, H. Haba, S. Fujita, E. Ikezawa, H. Sakamoto, S. Ito, M. Kase, and Y. Yano

For the RIBF Project, uranium acceleration is essential in obtaining unstable nuclei efficiently. However, uranium has not yet been accelerated in Japan, and a number of its technical aspects remain unexplored. Therefore, it is necessary for us to master uranium acceleration in our present facilities. Actually, we are remodeling our facilities so that we can use uranium in safety and in conformity to the requirements of laws and regulations.

Because uranium is a nuclear fuel material, its use is regulated by the Nuclear Reactor and Fuel Regulation Law, whereas radioisotopes other than nuclear fuel materials must be used in conformity to the Law Concerning Prevention of Radiation Hazards. The use of an accelerator is however regulated by the Law Concerning Prevention of Radiation Hazards. To gain regulatory approval to accelerate uranium, we must therefore meet all the conditions required by these two laws.

The Law Concerning Prevention of Radiation Hazards specifies in detail the requirements concerning the equipment (*e.g.*, draft), floor, walls and ceiling of laboratories where unsealed radioisotopes are used. On the other hand, the Nuclear Reactor and Fuel Regulation Law is silent on these matters. However, because uranium emits highly hazardous α-rays, we decided that the rooms where uranium will be used should be designed and equipped in the same manner as the Class 1 radiation controlled area, which is an area in RIKEN where unsealed radioisotopes are used.

There are two methods of introducing uranium into an ion source: the slow supply of UF_6 gas from an airtight container owing to vapor pressure at room temperature and the vaporization of a solid or powder uranium compound placed inside an ion source chamber. At the Hot Lab of the Nishina Building, we will repack a small portion of UF_6 from our stock into airtight containers. The solid or powder uranium compound will be prepared at the Hot Lab for the chemical formula adjustment. Uranium will be handled at the Ion Source Room of the Linear Accelerator Building and at the Hot Lab of the Nishina Building. This impels us to prepare these two rooms accordingly.

At the Linear Accelerator Building, we partitioned the Accelerator Room (Class 2 radiation controlled area) to create the Ion Source Room (Class 1 radiation controlled room). We coated the floor and walls to facilitate decontamination. Figure 1 shows the plan of the new Ion Source Room. In area 1, we installed a ventilator equipped with HEPA filters. The exhaust will be controlled by an α-dust monitor. We are currently planning to install a draft in area 1 for a simple treatment of uranium. Area 2 houses ion sources. The Ion Source Room will remain accessible even during beam acceleration. Area 3 is the contamination control room equipped with access control devices. Access control information can be monitored not only at the Linear Accelerator Building but also at the Nishina Building.

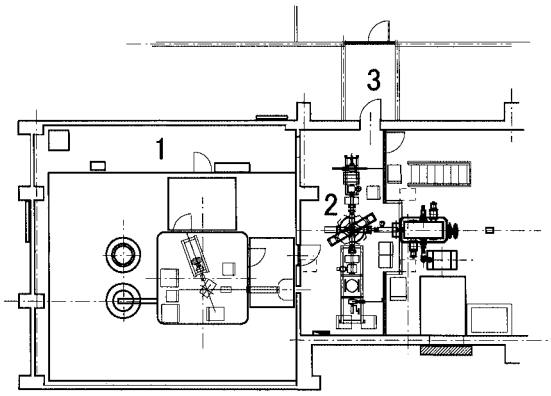

Fig. 1. Plan of Ion Source Room at Linear Accelerator Building. In area 1, we installed a filter unit and an exhaust fan. Area 2 houses two ion sources, whereas area 3 is a contamination control room equipped with an HFC monitor and sinks.

At the Hot Lab, we installed two new drafts that will be exclusively used to treat uranium (Fig. 2). At the same time, two old drafts were replaced by new

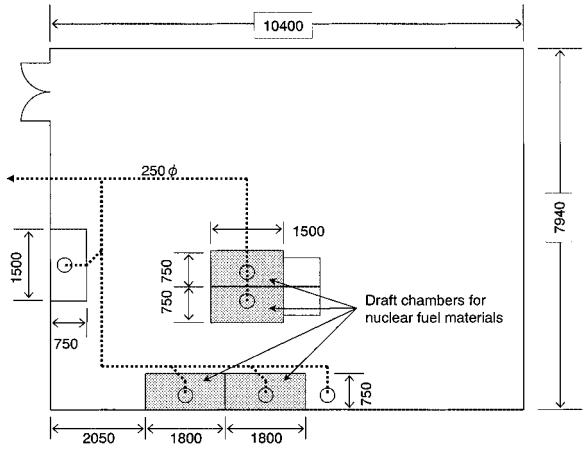

Fig. 2. Plan of Hot Lab at Nishina Building. Gray-colored devices are four drafts (2 newly installed ones and 2 replacements ones). The uncolored draft has not been replaced. We made an aeration hole covered with a filter on the entrance door to increase the ventilation rate.

ones. Because these four new drafts are equipped with scrubbers that can locally treat toxic gas or scattered uranium, exhaust from the draft chambers will be purified by the HEPA filters of the ventilation system. We increased the ventilation capacity due to the installation of new draft chambers.

Measurements of long-term phase stability of RRC rf-system

O. Kamigaito, N. Sakamoto, and Y. Chiba

The phase-control system of the RIKEN ring cyclotron (RRC: $K = 540$ MeV), based on a heterodyne technique, is designed to have a stability of less than ± 0.5 degrees in the rf-phase.[1] In the RI-beam factory (RIBF) project, a better phase-stability of less than ± 0.1 degrees is required since the RRC will be used as the injector for a cascade of ring cyclotrons: fixed-frequency ring cyclotron (fRC: $K = 510$ MeV), intermediate-stage ring cyclotron (IRC: $K = 930$ MeV), and superconducting ring cyclotron (SRC: $K = 2500$ MeV).[2]

The long-term stability of the rf-phase has been measured with vector voltmeters (VVM), which had been commercially available. However, the measurement accuracy is limited by the stability of the VVM itself; it is very difficult to achieve an accuracy better than ± 0.2 degrees in long-term measurements. On the other hand, it has been reported that the phase detectors using a hybrid coupler exhibit excellent characteristics.[3,4] We fabricated a similar phase detector using a 180° hybrid coupler and measured the long-term stability of the RRC rf-system.

The circuit drawing is shown in Fig. 1.[3] When rf-signals of the same frequency are applied to the input ports of the 180° hybrid coupler, as shown in Fig. 1, the output voltage V_{out} of the op-amp is proportional to $a \cdot b \cdot \Delta\phi$, where a and b are the amplitudes of the input signals, and the phase difference of the two signals is assumed to be $\pi/2 + \Delta\phi$ with $|\Delta\phi| \ll 1$.[4] When the amplitudes are constant, the output voltage is sensitive only to $\Delta\phi$.

It is important to maintain the temperature of the detector circuit constant, because the circuit elements, particularly the diodes, are sensitive to the temperature. Therefore, we housed the entire circuit in a small oven, where the temperature is stabilized through a sensor AD590.[5]

Figure 2 shows the setup of the performance test

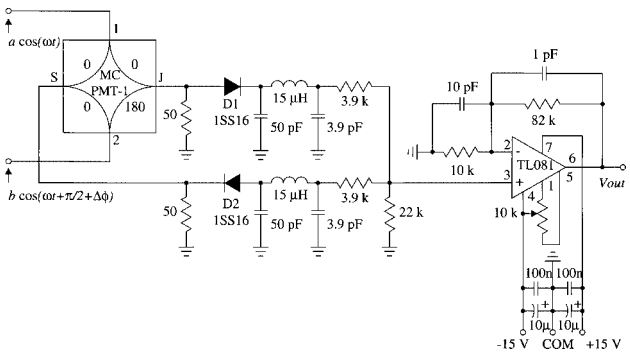

Fig. 1. Circuit drawing of phase detector.

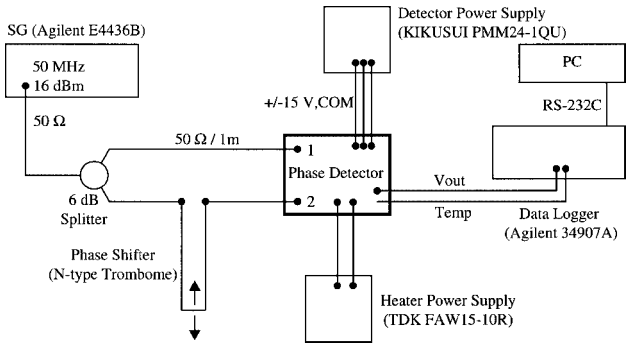

Fig. 2. Setup for performance test of phase detector.

of the phase detector. Two rf-signals of 50 MHz with 10 dBm, divided from a single output of a signal generator, are fed into the input ports of the detector. In one of the transmission lines, a phase shifter (coaxial trombone) is inserted which varies the electric length continuously and precisely. The total length of the line is chosen so that the the phase difference of $\pi/2$ falls into the stroke of the trombone. It was deduced from the measurement that the sensitivity to the phase difference is approximately 70 mV/degree for this input level.

The oven temperature measured with a thermocouple and the output voltage were tracked from the start of the oven heating. The result shown in Fig. 3 indicates the stability of the phase detector.

With this detector, the rf-phase of the RRC resonator was measured at the rf-frequency of 36.66 MHz. The reference signal from a synthesizer was fed into

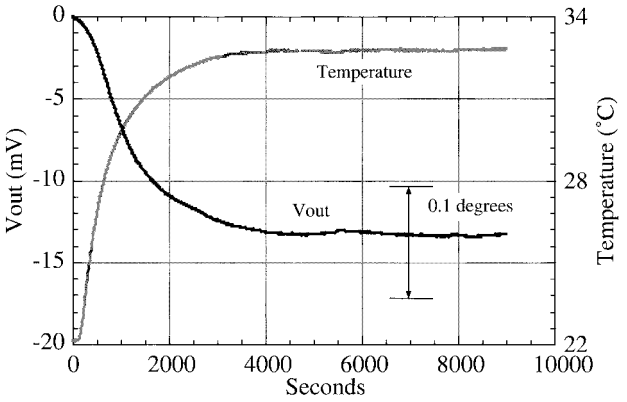

Fig. 3. Output voltage and oven temperature measured with thermocouple. The heater was switched on at the origin of the horizontal scale in seconds. The output voltage corresponding to the phase difference of 0.1 degrees is also indicated.

port 1, while the pick-up signal from the resonator was fed into port 2. The electric length of the pick-up signal was adjusted using the trombone, so that the phase

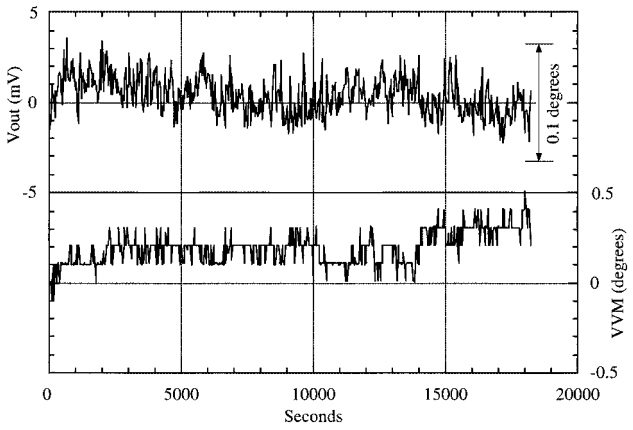

Fig. 4. Phase of the RRC rf-system No. 2 measured with the phase detector (upper curve) and that with VVM (HP8508A/lower curve). The measurement with the VVM shows a large drift in contrast with the upper curve.

difference was almost $\pi/2$. At the same time, both input signals were adjusted to be approximately 10 dBm, and their amplitude variations were maintained within 10^{-3} during the measurements.

The result is shown in Fig. 4; it has been confirmed that the rf-phase is well controlled within less than ± 0.1 degrees for a long period.

The phase stability of the RIKEN heavy-ion linac will be measured soon with the same detector. Further developments on the phase detector of this type are required for the RIBF project, where severe rf-phase control is required in the cascade operation of the cyclotrons.

References

1) T. Fujisawa, K. Ogiwara, S. Kohara, Y. Oikawa, I. Yokoyama, M. Nagase, and Y. Chiba: Nucl. Instrum. Methods Phys. Res. A **292**, 1 (1990).
2) Y. Yano, A. Goto, M. Kase, and T. Katayama: AIP Conf. Proc. **600**, 167 (2001).
3) E-mail from P. Sigg (PSI) to A. Goto, January 2001.
4) J. Cherix: TRIUMF Design Note, TRI-DN-86-17 (1986).
5) Data sheet of AD590: http://www.analog.com.

Rotating carbon disk stripper

H. Ryuto, S. Yokouchi, N. Fukunishi, H. Hasebe, N. Inabe, A. Goto, M. Kase, and Y. Yano

In the RIKEN RI-beam factory (RIBF), four stripper sections are under investigation. The stripper discussed here is the one referred to as the third stripper in Ref. 1. The third stripper is the last stripper the beam experiences before the beam is bombarded onto the target, when the fixed-frequency ring cyclotron (fRC) is employed. In the typical acceleration scheme under investigation, a 3 pμA $^{238}U^{72+}$ beam at 50.5 MeV/nucleon is stripped to 88+ by the third stripper, a 14 mg/cm^2 thick carbon plate. The thickness of the third stripper was estimated using the theoretical calculation code GLOBAL,[2] and the extraction radius of the fRC was determined as the energy of the uranium beam behind the third stripper which became 46 MeV/nucleon, the injection energy of the intermediate-stage ring cyclotron. The uranium ion supplies approximately 8% of its kinetic energy to the third stripper.[3] Therefore, the power supplied by the typical beam is expected to be 3 kW, which easily evaporates a carbon plate placed in a vacuum chamber. To cope with such a high power supply, the carbon plate is rotated, enlarging the area from which thermal radiation is emitted.

A thermal calculation for the carbon disk irradiated with a uranium beam was performed using a finite element method code, ANSYS, by a method similar to that in Ref. 4. In the calculation, a 3 pμA uranium beam was bombarded onto a 120-mm-diameter 14 mg/cm^2 thick carbon disk rotating at 1000 rpm. The uranium ion supplies its kinetic energy to the carbon disk following a Bragg curve, and heats the doughnut-shaped area of the rotating carbon disk. The energy supplied to the disk is mainly released as thermal radiation from the surface of the disk because of the thinness of the disk, and a small amount of energy is absorbed by the rotating shaft. The maximum temperature reached equilibrium after approximately 1 sec of irradiation. Figure 1 shows the result of the calculation after approximately 3 sec of irradiation. The disk was rotated clockwise. The beam was bombarded onto the head part of the dark band at the left middle of Fig. 1. The maximum temperature was calculated to be 1549°C, which was sufficiently lower than the evaporation temperature of carbon.

Figure 2 shows the schematic of the rotating carbon disk stripper. A 120-mm-diameter carbon disk is placed in a vacuum chamber that is connected to the beam pipes. The disk is connected to an AC servo motor, whose maximum rotation frequency is 3000 rpm, placed outside of the vacuum chamber by a water-cooled ferrofluid-sealed rotary motion feedthrough. The mechanism of disk rotation is the same as that of liquid film stripper in Ref. 5. The disk stripper

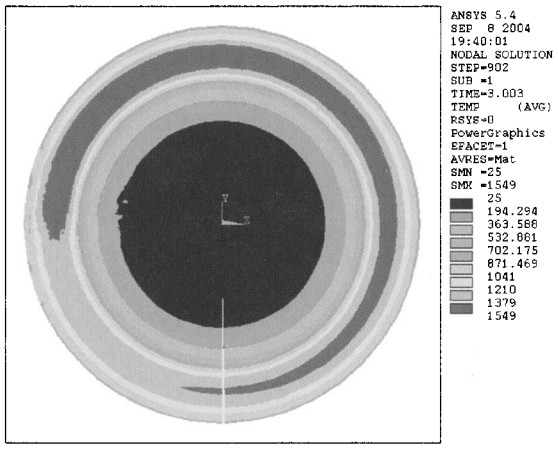

Fig. 1. Calculation of temperature increase of carbon disk bombarded with 3 pμA uranium beam. This calculation was performed using ANSYS.

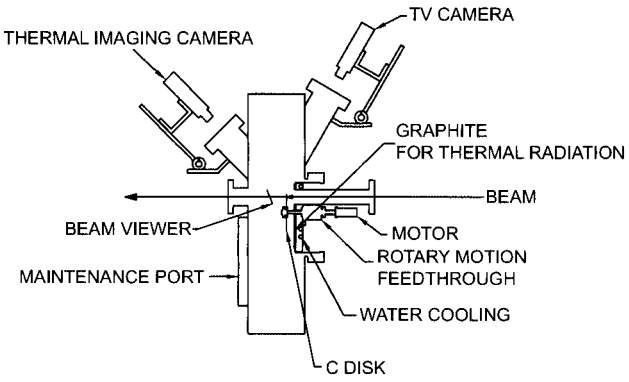

Fig. 2. Schematic of rotating carbon disk stripper.

is designed such that the beam bombards the disk at 8 mm from its outer edge. An array of graphite plates is soldered to a water-cooled copper plate close to the carbon disk for the purpose of absorbing the thermal radiation emitted from the carbon disk. A sheet of ZnS (Ag) is placed at the position of the beam using a pneumatic linear motion feedthrough as a beam viewer, and the beam spot on the sheet is observed using a TV camera placed outside the vacuum chamber through a viewing port. Another viewing port facing the beam spot on the carbon disk is prepared for a thermal imaging camera.

The geometrical thickness distribution of the disk was measured using a micrometer, and revealed that the thickness was uniform within 0.9%. Therefore, if the density of the carbon disk is uniform, the energy of the uranium beam is expected to vibrate within

approximately 0.07%, which is comparable to the energy straggling (one sigma) calculated using ATIMA in LISE++[6] of 0.03%. The angular straggling (one sigma) is expected to be 0.9 mrad.[7]

A beam test was performed using a 0.1 pμA $^{86}Kr^{26+}$ beam at 46 MeV/nucleon accelerated by the RIKEN heavy-ion linac and the RIKEN ring cyclotron with the same acceleration scheme that is planned to be used for a krypton beam in the RIBF. The krypton beam was bombarded onto a 12 mg/cm^2 thick carbon disk rotating at 1000 rpm. The charge-stripped ions were separated using a 90° bending dipole magnet according to the charge states, and the beam currents were measured using a Faraday cup. The beam spot on the beam viewer had an approximately spherical shape, and the diameter was approximately 5 mm. The power supplied to the carbon disk was approximately 18 W, which is much smaller than the expected power supplied by the typical beam in the RIBF, a 3 pμA uranium beam. A dim image of the beam shape on the carbon disk was observed using a TV camera. No visible damage to the carbon disk caused by the beam test was observed.

Figure 3 shows the charge state fractions of ^{86}Kr at 46 MeV/nucleon. The data for a 12 mg/cm^2 thick carbon disk rotating at 1000 rpm are plotted with the data for carbon foils, aramid films and a polyimide film. The results obtained using the GLOBAL code for estimating the thickness of the third stripper are also plotted. These results well reproduced the data points of higher charge states, and naturally, the data points for the rotating carbon disk also showed a consistent tendency with the other data points.

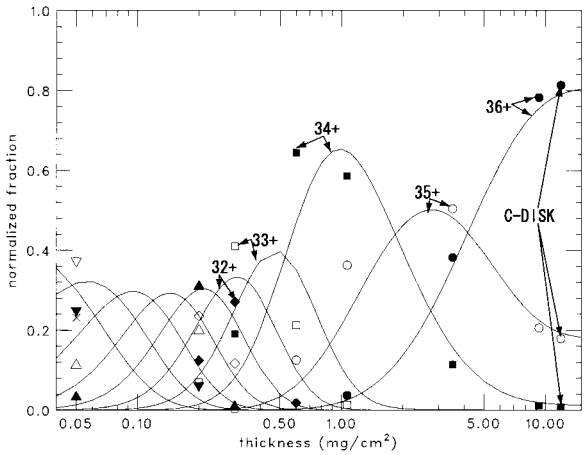

Fig. 3. Charge state fractions of ^{86}Kr at 46 MeV/nucleon. The horizontal axis indicates the thickness of the stripper and the vertical axis indicates the charge state fractions. The charge state fractions are normalized using the sum of the measured charge state distributions. The rightmost points are the data for the 12 mg/cm^2 thick carbon disk rotating at 1000 rpm. The other points are the data for carbon foils, aramid films and a polyimide film. Solid lines indicate the results obtained using the GLOBAL code.

References

1) H. Ryuto, N. Inabe, N. Fukunishi, H. Hasebe, S. Yokouchi, M. Kase, A. Goto, and Y. Yano: RIKEN Accel. Prog. Rep. **37**, 283 (2004).
2) C. Scheidenberger, Th. Stöhlker, W. E. Meyerhof, H. Geissel, P. H. Mokler, and B. Blank: Nucl. Instrum. Methods Phys. Res. B **142**, 441 (1998).
3) J. F. Ziegler, J. P. Biersack, and U. Littmark: *The Stopping and Range of Ions in Solids*, vol. 1 (Pergamon, New York, 1985).
4) A. Yoshida, K. Morita, K. Morimoto, D. Kaji, T. Kubo, Y. Takahashi, A. Ozawa, and I. Tanihata: Nucl. Instrum. Methods Phys. Res. A **521**, 65 (2004).
5) H. Ryuto, T. Chiba, H. Hasebe, M. Kase, and Y. Yano: Jpn. J. Appl. Phys. **43**, 7753 (2004).
6) D. Basin, O. Tarasov, M. Lewitowicz, and O. Sorlin: Nucl. Instrum. Methods Phys. Res. A **482**, 307 (2002).
7) R. Anne, J. Herault, R. Bimbot, H. Gauvin, G. Basin, and F. Hubert: Nucl. Instrum. Methods Phys. Res. B **34**, 295 (1988).

Preparation of carbon foils by cracking using of methane gas

H. Hasebe,* H. Ryuto, M. Kase, and Y. Yano

Long-lived carbon stripper foils are strongly and urgently required for charge strippers of the RIKEN RI-Beam Factory (RIBF) project. We have decided to produce carbon foils (C-foils) ourselves because commercially available foils do not satisfy our requirements.

At the end of 1999, a high-vacuum evaporation system (EBX-2000C by ULVAC) was purchased and installed in the RILAC building. We started to produce C-foils by an arc discharge evaporation method.[1] We successfully produced C-foils with a lifetime 120 times longer than that of commercially available foils (Arizona Carbon Foil Co.).[2]

For the further development of a long-life C-foil production, we started to use a chemical vapor deposition (CVD) apparatus with a methane (CH_4) gas cracking system from June 2004.

Figure 1 shows the CVD apparatus with the CH_4 gas cracking system. It consists of a vacuum chamber, a cold-water supply system, a DC power supply system for filament heating, an oil-sealed pump for exhausting the chamber, a radiation thermometer for filament temperature measurement, and a CH_4 gas supply system. At the center of the chamber, a mount for the filament, which is connected to the DC power supply system via a vacuum feed through with a 38 mm^2 cable, is located. Before the vacuum chamber is opened, it is filled with N_2 gas in order to avoid explosion and damaging the C-foils.

As the filament, a tantalum plate with dimensions of 26 mm × 76 mm × 0.1 mm was used for a preliminary test. It was found that a C-foil with a thickness of 100–200 $\mu g/cm^2$ was generated on the surface of the filament heated at approximately 1200°C after it was exposed to the CH_4 gas with a pressure of 4000 Pa for 20 min. The thickness of the C-foil was estimated from the difference between the weights of the filament before and after CVD.

Next, CVD was systematically investigated in nickel filaments. Nickel plates of 26 mm × 76 mm with thicknesses of 0.05 mm, 0.08 mm and 0.1 mm were used as filaments. The temperature of these filaments was maintained from 1100°C to 1200°C during CVD for as long as 45 min. Figure 2 shows the thickness of the C-foil as a function of CH_4 gas pressure for the three different filaments. CVD starts at pressures higher than 200 Pa. The thickness of the C-foil gradually increases for pressures 200–10000 Pa. The change is small for pressures higher than 10000 Pa.

The C-foil is separated from the Ni filament in a solution of chloride and nitric acid. It is very difficult to separate a C-foil with a thickness less than 100 $\mu g/cm^2$, because it easily cracks. Thus, we could not stick the foil on the holder. Figure 3 shows the photograph of C-foils mounted on aluminum holders.

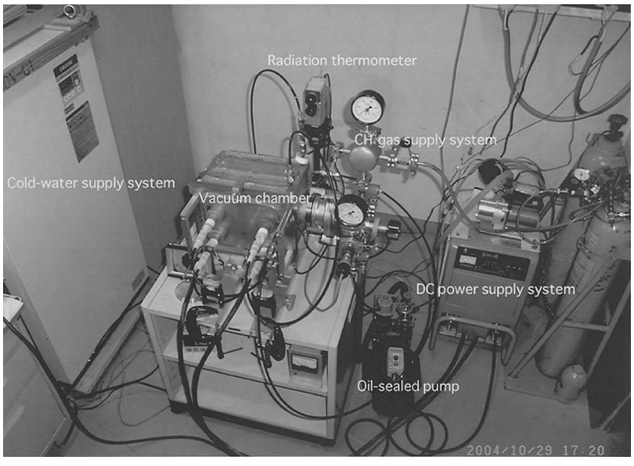

Fig. 1. Photograph of the CVD apparatus with the CH_4 gas cracking system.

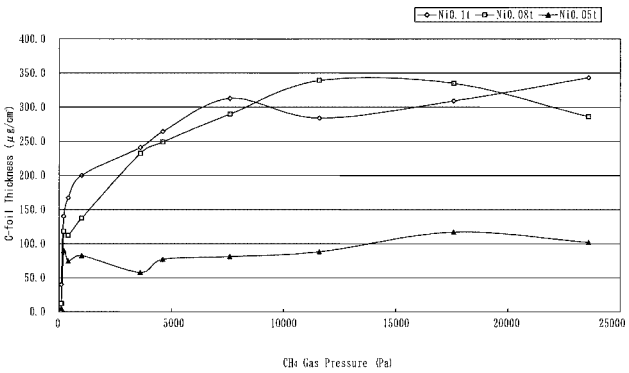

Fig. 2. Thickness of C-foil as a function of CH_4 gas pressure for three different filaments.

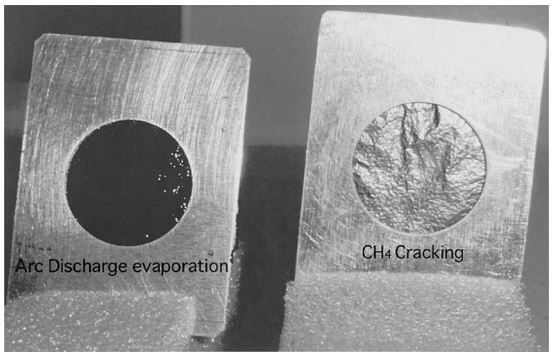

Fig. 3. Photograph of C-foils mounted on aluminum holders.

* Katagiri Engineering Co., Ltd.

The right-hand side of the C-foil of 200 μg/cm^2 thickness was formed by cracking, while its left-hand side of 100 μg/cm^2 thickness was formed by arc discharge evaporation. The C-foil formed by cracking has metallic bright gloss, while that formed by arc discharge evaporation has a blackish color.

The foils will be tested as charge strippers by intense heavy ion beam irradiation and their lifetimes will be compared with those of the foils formed by other methods.

References

1) H. Hasebe, I. Sugai, and M. Kase: RIKEN Accel. Prog. Rep. **34**, 313 (2001).
2) H. Hasebe, H. Ryuto, M. Kase, and Y. Yano: Proc. The 17th Int. Conf. on Cyclotrons and Their Applications, Tokyo, 2004-10, in press.

Response of imaging plate and X-ray film to heavy-ion beam irradiation

H. Ryuto, T. Yamane,* S. Kubota,* N. Fukunishi, M. Kase, and Y. Yano

Imaging plates and X-ray films are utilized in various fields, e.g., biological research and nondestructive inspection. To examine the possibility of using imaging plates and X-ray films as detectors for beam diagnostics or radiation biology experiments in the RIKEN Accelerator Research Facility (RARF), a neon beam was bombarded on imaging plates and X-ray films.

The irradiation was performed at the E5B beam line in the RARF. An approximately 5-mm-diameter ^{20}Ne beam at 133 MeV/nucleon was transformed into an approximately 10-cm-diameter uniform radiation field at the target position of the automated irradiation system for radiation biology experiments[1] by wobbler magnets and a scatterer foil.[2] The surface dose was calibrated by an ionization chamber according to the procedure described in Ref. 2. Because the range of the ^{20}Ne beam at 133 MeV/nucleon in water is 25 mm,[3] which is much larger than the thicknesses of the imaging plates or X-ray films, the stopping power only slightly changes while passing through the imaging plates or the X-ray films. The dose rate was approximately 0.004 Gy/sec. A 0.5-mm-thick imaging plate or a 0.2-mm-thick X-ray film was placed on a movable table at the target position, and long and narrow leaves were placed on it for the purpose of simulating biological samples. The imaging plates used were Fujifilm BAS-III, and the X-ray films, Fujifilm IX50 EPII or IX50 LP (with a lead sheet). The imaging plates were scanned by a Fujifilm BAS2500 phosphor imaging plate scanner. The uniformity of the beam was examined by analyzing the image obtained by the imaging plate, revealing that the standard deviation of the pixel density was 0.8%.

Figure 1 shows the pixel density of the imaging plate irradiated by a neon beam. The data show excellent linearity. The response exceeded the dynamic range of the imaging plate when the imaging plate was irradiated with a surface dose of more than 0.016 Gy.

Figure 2 shows the optical density of the X-ray films irradiated by a neon beam. Both data of the IX50 EPII films and the IX50 LP films show linearity. The optical density did not exceed the dynamic range of the X-ray film when the film was irradiated with a surface dose of 2 Gy.

The pixel density of the imaging plate had an excellent linear dependence on the surface dose of neon beam less than 0.008 Gy. The response exceeded the dynamic range of the imaging plate when the dose was more than 0.016 Gy. Therefore, the imaging plate can be a sensitive detector for use in a beam diagnostics or low-dose radiation biology experiment. The optical density of the X-ray films had a linear dependence on the surface dose of neon beam from 0.004 Gy to 2 Gy, and still did not exceed the dynamic range, indicating that the X-ray films can be applied to a radiation biology experiment with a typical surface dose of 10 Gy.

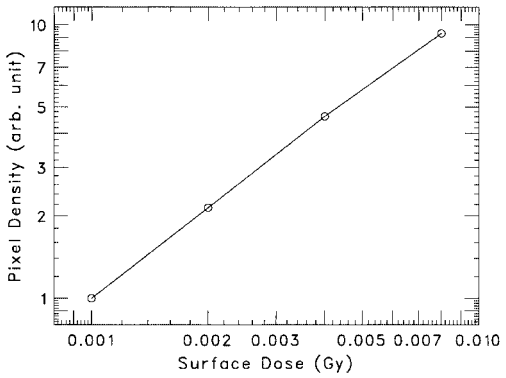

Fig. 1. Response of imaging plate to neon beam irradiation. Horizontal and vertical axes show the surface dose and the pixel density of the imaging plate, respectively.

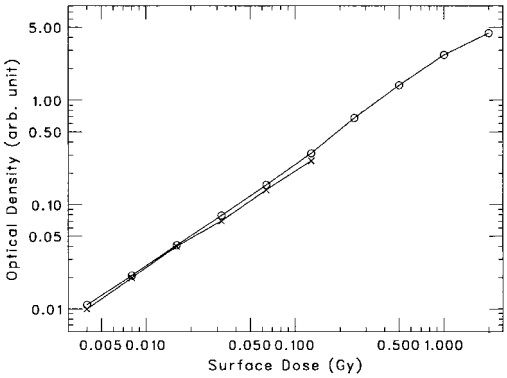

Fig. 2. Response of X-ray film to neon beam irradiation. Horizontal and vertical axes show the surface dose and the optical density of the film, respectively. Circles indicate the data of IX50 EPII, and crosses indicate the data of IX50 LP shielded by thin lead sheets.

References

1) H. Akiyoshi et al.: RIKEN Accel. Prog. Rep. **36**, 291 (2003).
2) T. Kanai et al.: RIKEN Accel. Prog. Rep. **25**, 103 (1991).
3) J. F. Ziegler et al.: *The Stopping and Range of Ions in Solids*, vol. 1 (Pergamon, New York, 1985).

* Fuji Photo Film Co., Ltd.

Electrical power supply system for RI beam factory

T. Fujinawa, Y. Sekiguchi, A. Sakamoto,* H. Ikawa,* M. Kase, and Y. Yano

The RI Beam Factory (RIBF) has required a large amount of electrical power after its commission. In order to provide the necessary electrical power, the Gas Insulated Substation (GIS), which is the No. 2 high-voltage substation in RIKEN, was constructed on the Accelerator building roof in spring 2003 specifically for the use of the RIBF. In this substation, 66 kV vacuum circuit breakers (VCB) are used instead of gas circuit breakers (GCB). The GIS uses VCBs, which require less maintenance, space, and cost than GCBs.

At the same time, a medium-voltage metal-clad Switch gear, which is called an alternative power source, was provided in the bidding. A diagram of the electric power system for the RIBF as shown in Fig. 1.

The No. 2 high-voltage substation is connected to the No. 1 high-voltage substation located near the West Gate by two 66 kV XLPE underground cables. The cross–sectional area and length of the cables are 325 mm^2 and 750 ms respectively. One is for normal use and the other is for use as a spear. Each cable has sufficient capacity for the expected volume increase in the future.

The capacity of a 66/6.6 kV transformer was determined as 25 MVA. Its percent impedance (%TZ) was selected as 11% (actual 10.67%) on the basis of voltage regulation and the capacity of the cogeneration system (CGS).[1)]

The rating of each VCB in 6.6 kV lines was determined as 25 kA from the short-circuit current. The

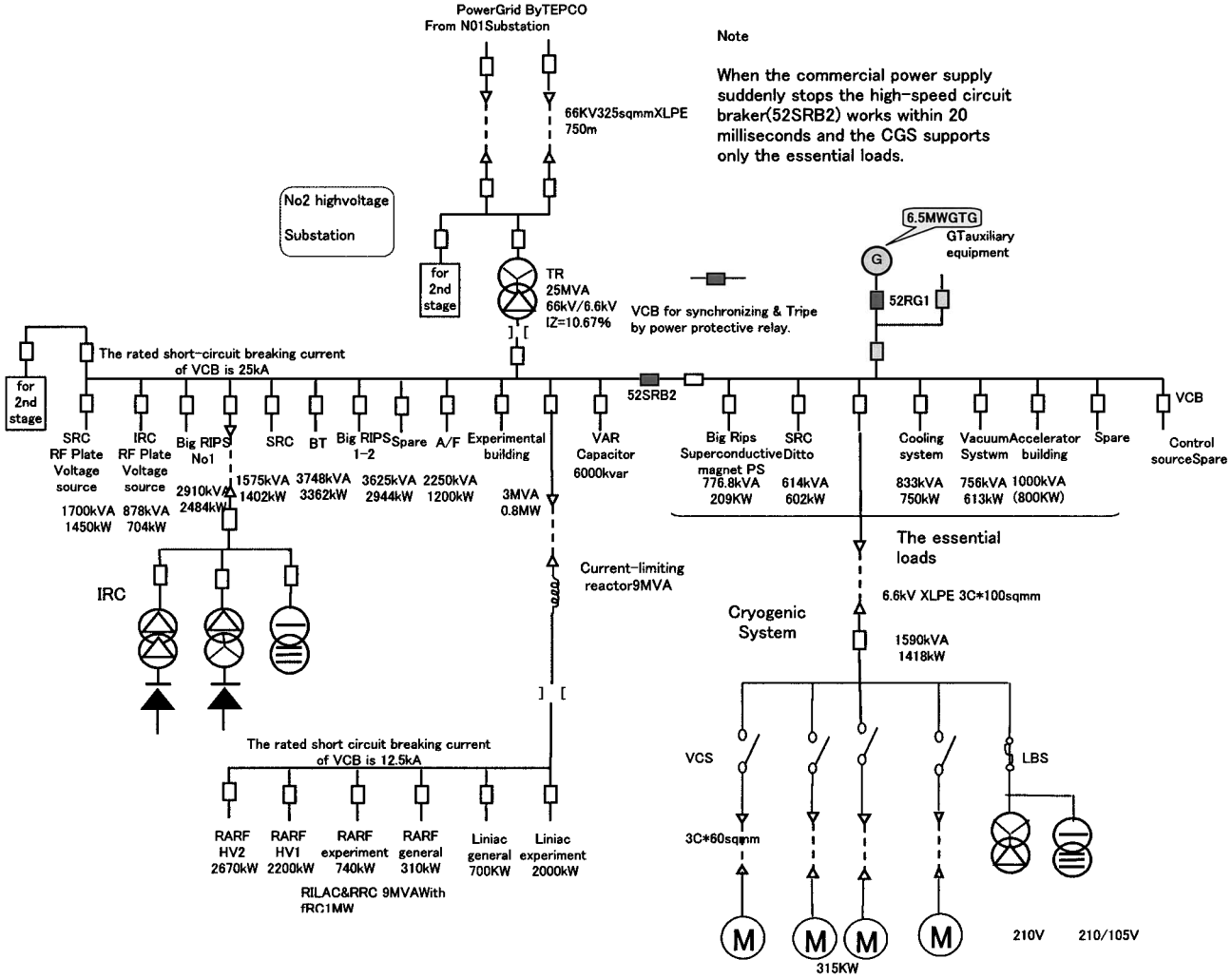

Fig. 1. Single-line diagram of electrical power supply system for RIBF.

* Mitsubishi Electric.

short-circuit current in the medium-voltage system is calculated as follows.

The impedance map is shown in Fig. 2.

The %TZ at 10 MVA base is

$$\%\mathrm{ZT} = \frac{10000}{25000} \times 10.67 = 4.268,$$
$$\therefore\ \%\mathrm{ZT} = 4.268 \quad (\text{at } 10\,\mathrm{MV}),$$

The total percent impedance (%Z) of the power source from the load side is

$$\%\mathrm{Z} = \frac{(0.7167 + 0.0093 + 4.268) \times 17.85}{(0.7167 + 0.0093 + 4.268) + 17.85} = 3.90$$

at 10 MVA,

There for the short-circuit current (IF) is

$$\mathrm{IF} = \mathrm{Capacity}(10\,\mathrm{MVA})/\sqrt{3} \times \mathrm{voltage}\,(\mathrm{kV}) \times 100/\%\mathrm{Z},$$
$$\mathrm{IF} = \frac{10000}{\sqrt{3} \times 6.6} \times \frac{100}{3.90} = 22.43\,\mathrm{kA},$$

The maximum permissible short-circuit current of a 60 mm^2 cable is

$$\mathrm{Is} = (3.4 \times \mathbf{60}/0.00393 \times 0.309 \times 0.125 \log_e 180)^{1/2} = 25.26\,(\mathrm{kA}); 25.26 > 22.43\,(\mathrm{kA}).$$

Here 3.4 is the specific heat of copper ($\mathrm{J/cm^3/^\circ C}$), **60** is the cross-sectional area of the conductor (mm^2), 0.00393 is the temperature coefficient of copper, 0.309 is the alternative resistance (Ω/cm at 20°C), 0.125 is fault duration (sec) and 180 is the temperature increase from 54.42 to 230°C (conductor temperature in the nominal current: 54.2°C, short time permissible temperature of XLPE: 230°C).

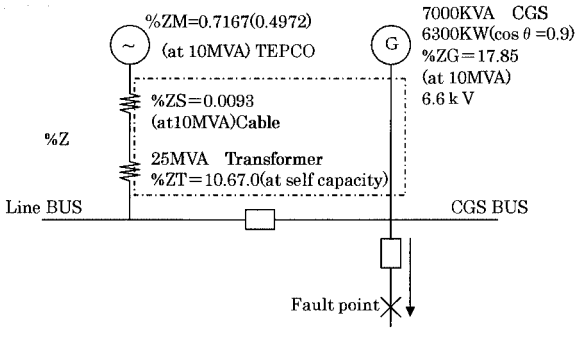

Fig. 2. Impedance map.

The CGS system is separated within 20 msec with a high-speed breaker (52SRB2), as shown in Fig. 1, when the commercial power supply suddenly stops. Then, the CGS only supports essential loads such as the cryogenic system and superconducting magnets and works as a 5 MW UPS.

A current-limiting reactor with a capacity of 9 MVA was installed in the line to the existing facility (RARF) because the capacity of each circuit breaker (VCB) in the RARF substation is 13.8 kA and thus they cannot withstand a short-circuit current of 22.84 kA.

The newly constructed switch gear with a capacity of 20 MW is of a metal-clad type according to the JEM (Japan Electrical Manufacturers) standard and is very compact. Its volume is almost the same as that of the RARF 7 MW cubicles. This M/C can be operated in a power outage because the DC power supply is used for its control. This feature makes the M/C much safer than existing cubicles.

The DC power source used for the accelerators produces undesirable harmonic currents. To prevent this from happing, two transformers with the △-△ and △-Y connections were used for the IRC and others as shown in Fig. 1. This makes same effect as multi phase rectifiers. Since transformers are placed inside of a building, dry-type ones are used. The dry-type transformers require no insulation oil; therefore, they satisfy the Fire Defense Law. In addition, all transformers in the experimental building are highly efficient and meet the law concerning the Rational Use of Energy Policy.

In the RIBF, more than 50 electrical motors are installed, including four 315 kW cryogenic system compressors. All motor starters are direct connection type which enables a quick start and an efficient restart. Also, they are more reliable and economical than Y-△ and/or reactor starters. The direct-type starters can only be used when the transformer's capacity is sufficiently large.

The amount of equipment for the experimental building will be increased in the future, and more power will be required. The space for the 2nd bank has been prepared for the expansion.

Reference

1) T. Fujinawa et al.: RIKEN Accel. Prog. Rep. **36**, 310 (2003).

Cooling water system in RIKEN RI beam factory

T. Kageyama, N. Inabe, M. Kase, and Y. Yano

A cooling water system for the RIBF[1] has been completed in the RIBF building. This cooling system is used for removing heat originating from sources such as magnets, RF systems, power supplies, liquid He systems and the vacuum systems of accelerators (IRC[2] and SRC[3]), beam transport lines and the BigRIPS.[4] Moreover, the cooling water plays an important role in the stable operation of the above-mentioned devices by maintaining the temperature of the cooling water constant.

Figure 1 shows a flowchart of the cooling water system. As shown in Fig. 1, the cooling system is divided into two stages by heat exchangers to prevent cooling water used in rooms where radiation is generated from flowing out of the radiation control area. The first stage consists of closed-loop channels between the heat sources and heat exchangers. In each channel, electrical pure water (> 1 MΩ cm) is supplied for insulation of the heat sources. The second stage consists of channels between the heat exchangers and cooling towers or headers of cold water sent from refrigerators. In terms of the quality (temperature, pressure, and so on) of supplied water, the first and second stages are separated into eight branches and four branches, respectively. As shown in Fig. 1, one branch with no heat exchanger also exists in the cooling system.

In Table 1, the heat removal conditions of each branch are summarized. As shown in Table 1, fine temperature control is required for the branches of the IRC trim, IRC main and SRC trim. The average temperature of the inlet and outlet ismaintained at 30 ± 0.1°C for the IRC trim and IRC main and 30 ± 0.5°C for the SRC trim even if the consumption power of the magnet changes. The middle-temperature branch removes heat from the vacuum pumps of the IRC and the SRC and the liquid He system for the quadrupoles in the BigRIPS. This branch requires cooling water of low temperature (< 30°C at inlet) and low pressure (< 0.7 MPa). The low-temperature branch supplies cold water of 20°C to the magnetic channels of the SRC with a large temperature increase and magnets and target of the BigRIPS to prevent the room temperature from rising. The low-pressure branch supplies cooling water of 0.6 MPa to the amplifiers of RF systems in the IRC and SRC. The room-temperature-1 and room-temperature-2 branches supply a large amount of cooling water at room temperature to the magnets and power supplies of the IRC, the SRC, beam transport lines and the BigRIPS.

The branches of the second stage connect with those of the first stage according to the temperature of supplied water. The CR1 and CR2 can supply cold wa-

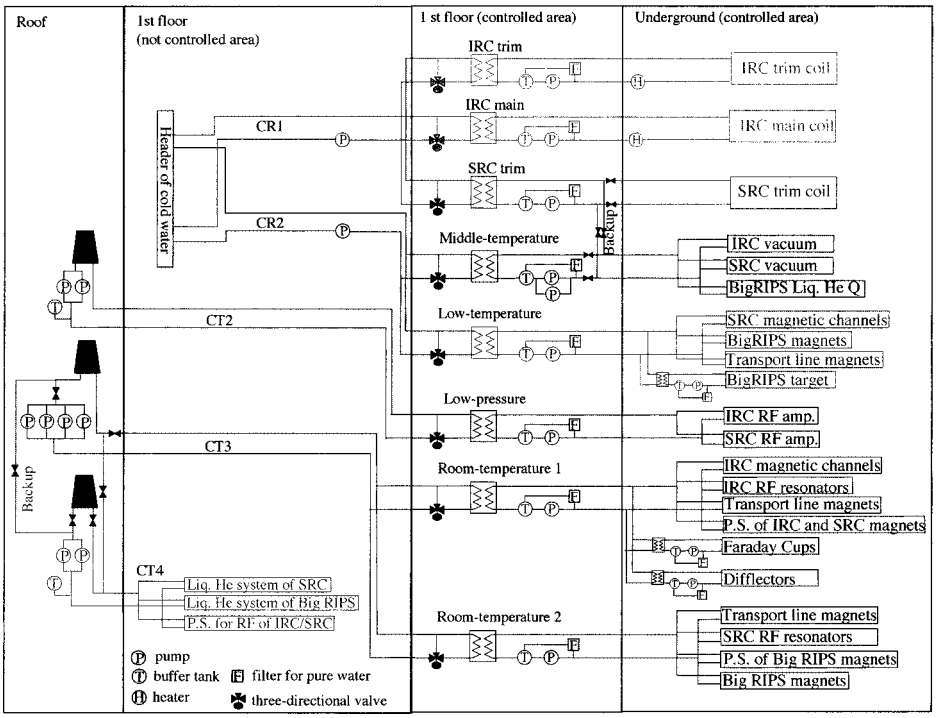

Fig. 1. Flow chart of cooling water system in RIBF.

Table 1. Heat removal conditions of each branch.

Branch	Heat (kW)	Flow (l/min)	Pressure (Mpa)	Temperature (°C)
(1 st stage)				
IRC trim	150	350	1	30 ± 0.1
IRC main	370	550	1	30 ± 0.1
SRC trim	780	670	1	30 ± 0.5
Middle-temperature	520	1100	0.7	< 30
Low-temperature	2450	4100	1	< 20
Low-pressure	600	1450	0.6	30∼35
Room-temperature-1	3030	4500	1	30∼35
Room-temperature-2	3840	5580	1	30∼35
(2nd stage)				
CR1	1300	1750	-	7
CR2	2970	5280	-	7
CT2	600	1450	0.35	30∼35
CT3	6870	10160	0.38	30∼35
(other)				
CT4	1370	4220	0.4	30∼35

ter at approximately 7°C all year. The CR1 connects with the three branches of the IRC trim, IRC main and SRC trim. The CR2 connects with branches of middle- and low-temperature. The CT2 (1500 kW) and CT3 (8000 kW) have cooling towers and connect with the low-pressure and the room-temperature-1 and room-temperature-2 branches, respectively. The CT4 (1500 kW) directly connects with the liquid He systems of the SRC and BigRIPS with no heat exchanger. The channels of the CT2 and CT4 are of closed-loop type while that of the CT3 is not because the CT3 is a cooling tower of open-air type.

The cooling system has two bypasses for backup in case of emergency or maintenance because the liquid He system cannot be stopped anytime during the year. One is used to exchange the CT4 for the CT3 and another to exchange the middle-temperature branch for the SRC trim branch.

Almost all the devices, such as pumps, heat exchangers and buffer tanks in the cooling system are located on the first floor and connected to heat sources underground by pipes for pure water. Headers and pumps in the CR1 and CR2 are also located on the first floor connected by pipes with heat insulators.

Cooling towers and pumps in CT2, CT3 and CT4 are located on the roof and are connected to heat exchangers or heat sources on the first floor.

Pumps are installed in all branches with consideration of the amount of water flow and pressure. The first-stage pumps are for pure water. The CT2, CT3, CT4 have one additional pump for backup. The middle-temperature branch also has a backup pump since the liquid He system cannot be stopped. Buffer (expansion) tanks are installed in all closed-loop channels to absorb the change in water volume due to temperature. Filters to produce pure water are installed in all the branches of the first stage. To locate filters, each branch has a small loop separated from main channel. Heat exchangers are installed not only at boundary between the first and second stages but also in the low-temperature and room-temperature branches as shown in Fig. 1. The reason why there are three additional heat exchangers located in the first stage is that cooling water passes through heat sources with very strong radiation. These heat exchangers are located near heat sources. Three-directional valves are installed near heat exchangers in the second stage for temperature control. In branches needing fine temperature control (IRC trim and main), heaters are installed in the first stage. Temperature is automatically controlled by a loop composed of the three-directional valve, the heater and thermometers. Constant flow valves are equipped for the branch with additional limbs so as to maintain constant flow even if the operation of other limbs is changed. Flowmeters, pressure gauges, and thermometers are installed in all branches. Ohmmeters are also installed in all branches of the first stage. A PC monitor is installed to allow the observation of the cooling system status and to enable the switching on/off of pumps, cooling towers and certain valves. Exchange of backup can also be carried out from the PC.

We examined the system by bypassing with U pipes at connecting points to heat sources and confirmed that the amount of water flow and pressure required in each branch were realized. A check of the loop for temperature control was also performed. At present, the CT4, IRC trim and IRC main branches and a part of CR1, CR2, CT3, middle-temperature and room-temperature-1 branches have already been used. Near-future fine temperature control will be checked using heat sources of the IRC trim and main branches.

References

1) Y. Yano: Proc. 17th Int. Conf. Cyclotrons and Their Applications, Tokyo, 2004-10, to be published.
2) J. Ohnishi et al.: Proc. 17th Int. Conf. Cyclotrons and Their Applications, Tokyo, 2004-10, to be published.
3) H. Okuno et al.: Proc. 17th Int. Conf. Cyclotrons and Their Applications, Tokyo, 2004-10, to be published.
4) T. Kubo: Nucl. Instrum. Methods Phys. Res. B **204**, 97 (2003).

Improvements of a current and position monitor using HTS SQUIDs aiming at the measurements of a 1 nA DC beam

T. Watanabe, M. Kase, Y. Sasaki,[*1] S. Watanabe,[*2] T. Ikeda, T. Kawaguchi,[*3] and Y. Yano

A highly sensitive current and position monitor with HTS (High-Temperature Superconducting) SQUIDs (Superconducting QUantum Interference Device) and an HTS magnetic shield for the measurement of the intensity of faint heavy ion beams was developed for the RIKEN RI beam factory project.[1–7] We abbreviate this monitor to "SQUID monitor" here. The HTS magnetic shield and the HTS current sensor including the HTS SQUID[8] are cooled by a low-vibration pulse-tube refrigerator. Both the HTS magnetic shield and the HTS current sensor were fabricated by dip-coating a thin Bi_2-Sr_2-Ca_2-Cu_3-O_x (Bi-2223) layer on 99.9% MgO ceramic substrates. The HTS technology enabled us to develop a system equipped with a downsized and highly sensitive current monitor. Recently, a prototype system was completed and installed in the beam transport line of the RIKEN Ring Cyclotron for the measurement of the DC- current of high-energy heavy-ion beams. As a result, we succeeded in measuring the intensity of the 600 nA $_{40}Ar^{17+}$ beam (95 MeV/u).

The purposes of the SQUID monitor are an accurate and nondestructive measurement of the current and position of the DC beam. This monitor is expected to be used for the high-energy heavy-ion beam, because if the beam were stopped by a destructive monitor such as a Faraday cup, the beam could no longer be used, and there would be a danger of activation and melting which could be caused by a miss-handling operation. Also, we are currently studying how to use this monitor for ion implantation in semiconductor production, particularly the nondestructive and real time dose measurements of drift and discharge caused by an ion source. In this paper, we report the progress of the SQUID monitor used as a position monitor and the research towards improving the resolution by more than two orders of magnitude.

We investigated whether the principle of a conventional beam position monitor could be applied to the SQUID monitor. The beam position pick up has a pair of isolated electrodes (or two pairs, if two beam position coordinates are being measured). The deviation of the beam center with respect to the vacuum chamber can be monitored by measuring the difference in voltage of each electrode induced by the beam.[9] Then we fabricated a smaller version of the position sensor, as shown in Fig. 1 (a). The HTS current sensor is divided into two parts by the slit and setting an HTS SQUID on each bridge. To measure the position dependence on the output voltage of each SQUID, we converted a measurement system which was used to measure the field distribution inside an HTS magnetic shield[10] into the position measurement system. This system is composed of an X-Y stage driven by stepping motors, and a Cu-rod which is fixed on the X-Y stage and simulates a beam. Figure 2 shows the schematic drawing of the position sensor, where D is the width of the sensor, Δx is the beam position from the center, and V_R and V_L represent the output voltage on each SQUID. If the position of the beam is center, the output of each SQUID should be equal. However, if the beam is shifted to the right-hand side, it is to be expected that the output signal V_R will be larger than that of V_L. Usually, a beam position Δx is obtained by the following relationship:

$$\Delta x = \frac{1}{\varepsilon}\frac{D}{2}\frac{\Delta}{\Sigma} = \frac{1}{\varepsilon}\frac{D}{2}\frac{V_R - V_L}{V_R + V_L},$$

where ε is the position sensitivity of the monitor. The measured values of Δ/Σ are plotted versus the Cu-rod position in Fig. 3 where a sine of simulated current (1 mA, 5 Hz) was used, and thus we discovered that the beam position and the beam current can be measured simultaneously in real time by dividing the current sensor into two parts and setting a SQUID on each

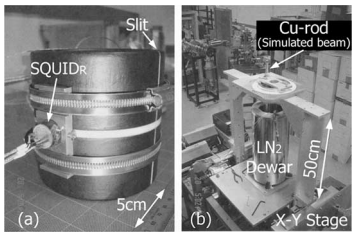

Fig. 1. (a) Smaller version of position sensor which is divided into two parts by the slit; a SQUID is set on each bridge. (b) Position measurement system which is composed of an X-Y stage driven by stepping motors, and a Cu-rod which is fixed on the X-Y stage and which plays the role of a simulated beam.

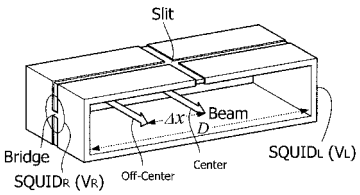

Fig. 2. Schematic drawing of the current sensor of the HTS SQUID monitor.

*1 Matsushita Electric Industrial
*2 Center for Nuclear Study, Graduate School of Science, University of Tokyo
*3 KT Science Ltd.

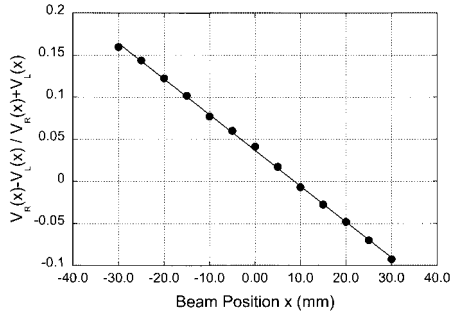

Fig. 3. Measured values of Δ/Σ are plotted versus the wire position where a sine of simulated current (1 mA, 5 Hz) was used.

bridge. The output voltage on the right SQUID V_R is not equal to that on the left SQUID V_L when the position of the simulated beam is center in Fig. 3 because the output voltage of the SQUID is very sensitive to the setting accuracy, but it was difficult to install each SQUID on the bridge accurately because each SQUID was bound by two stainless bands (Fig. 1).

Next, we describe the research to improve the current resolution. Although we can measure the intensity of the sub-microampere beam, a current resolution that is higher by more than two orders of magnitude is required. Therefore, we are now attempting to improve the bridge of the current (position) sensor (Fig. 4). The principle of the SQUID monitor is based on the cryogenic current comparator. The MgO ceramic tube used as the substrate is coated on both sides with a thin layer of Bi2223. While a beam is passing through the tube, a shielding current produced by the Meissner effect flows in the opposite direction along the wall, so as to screen the magnetic field generated by the beam (Fig. 4 (a)). Because the outer surface is designed to have a bridge circuit, the current concentrates in the bridge circuit and forms an azimuthal magnetic field Φ. The HTS SQUID is located close to the bridge circuit and can detect the azimuthal magnetic field. Figure 4 (b) shows the close view of the improved bridge circuit. The high-permeability material is placed into the hole in the bridge (c) and an HTS SQUID with a high-permeability core is placed on the bridge circuit (d). Finally, both materials are

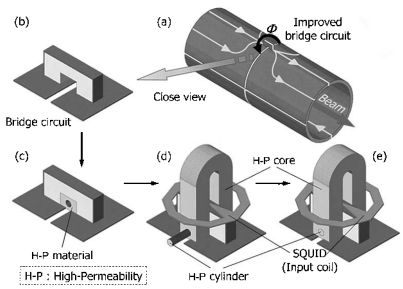

Fig. 4. Schematic drawing of the improved bridge of the current (position) sensor.

fixed by this high-permeability cylinder (e). The magnetic field generated by the beam is covered by the high-permeability materials completely. In addition, because the ridge circuit must be fabricated precisely, the substrate made of MgO is changed to one made of silver (Ag). Figure 5 shows a comparison of enlargements of surfaces of HTS material between Bi2223 coated on the MgO substrate (a) and Bi 2212 coated on the Ag substrate (b). These pictures were observed using a EPMA (Electron Probe (X-ray) Micro Analyzer) in RIKEN and clearly showed that the surface of the HTS material Bi2212 was smooth and the Bi2212 was adhered strongly on the Ag substrate compared with the Bi2223. Finally, the calculation of the static magnetic field by the MAFIA program showed a 1000-fold improvement because the coupling efficiency of transferral of the magnetic field produced by the beams to a SQUID can be improved. We aim to measure the beam current and position of a 1 nA beam to render the system applicable to physics and biology experiments as well as to an ion implanter. The authors are grateful to R. L. Fagaly of Tristan Technologies for valuable insights into the HTS SQUID system and to K. Watanabe of RIKEN for the support and advice regarding the EPMA.

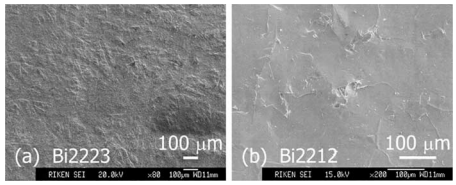

Fig. 5. Comparison of enlargements surfaces of HTS material between Bi2223 coated on the MgO substrate (a) and Bi 2212 coated on the Ag substrate (b).

References

1) T. Watanabe et al.: RIKEN Accel. Prog. Rep. **35**, 314 (2002).
2) T. Watanabe et al.: Proc. 8th European Particle Accelerator Conf., Paris, France, 2002-6 (EPS-IGA, 2002), p. 1995.
3) T. Watanabe et al.: RIKEN Accel. Prog. Rep. **36**, 331 (2003).
4) T. Watanabe et al.: CNS Annu. Rep. **59**, 71 (2003).
5) T. Watanabe et al.: Proc. 14th Symp. on Accelerator Science and Technology, Tsukuba, 2003-11 (KEK, 2003), p. 99.
6) T. Watanabe et al.: RIKEN Accel. Prog. Rep. **37**, 310 (2004).
7) T. Watanabe et al.: Supercond. Sci. Technol. **17**, S450 (2004).
8) M. I. Faley et al.: IEEE Trans. Appl. Supercond. (ASC2000) **11**, 1383 (2001).
9) T. Watanabe et al.: Nucl. Instrum. Methods Phys. Res. A **336**, 194 (1996).
10) S. Watanabe et al.: Proc. 8th European Particle Accelerator Conf., Paris, France, 2002-6 (EPS-IGA, 2002), p. 1992.

Beam quality estimation of RIBF accelerator complex

N. Fukunishi, A. Goto, O. Kamigaito, M. Kase, H. Ryuto, N. Sakamoto, M. Wakasugi, R. Taki,* and Y. Yano

Beam qualities in the RIKEN RI Beam Factory[1] (RIBF) were estimated based on the measured longitudinal emittance of beams accelerated by the RIKEN Ring Cyclotron.[2] The RIBF is a project to upgrade the present RIKEN Accelerator Research Facility (RARF) and is aimed at producing the world's most intense RI beams. The accelerator complex used in the RIBF consists of three existing accelerators and three new ring cyclotrons. The existing three accelerators are the RIKEN Linear Accelerator (RILAC), an AVF-type cyclotron (AVF) and the RIKEN Ring Cyclotron (RRC). The three new ring cyclotrons under construction are a fixed-frequency Ring Cyclotron[3] (fRC), an Intermediate-stage Ring Cyclotron[4] (IRC) and a Superconducting Ring Cyclotron[5] (SRC). Three acceleration modes will be available in the RIBF. The first mode involves the use of five accelerators in series: the RILAC, the RRC, the fRC, the IRC and the SRC. In this mode, every element from hydrogen to uranium can be accelerated up to 350 MeV/nucleon. However, the beam energy will be fixed because the fRC is a fixed-frequency machine. The second is a variable-energy mode involving four frequency-variable accelerators, i.e., the RILAC, the RRC, the IRC and the SRC. This acceleration mode will be able to produce, for example, a 400 MeV/nucleon ^{40}Ca beam and a 350 MeV/nucleon ^{86}Kr beam. The last mode is aimed at producing an 880 MeV polarized deuteron beam. The accelerators employed here are the AVF, the RRC and the SRC. Beam quality estimations were performed for the first two modes. Details are shown in Ref. 6.

A series of longitudinal emittance measurements were performed using the high-resolution magnetic spectrometer SMART placed in the E4 experimental vault in the RARF.[2] An example of measured longitudinal phase space distributions is shown in Fig. 1 for a 95 MeV/u $^{40}Ar^{17+}$ beam. The energy spread and the time spread of the beam were determined to be 1.3×10^{-3} (FWHM) and 700 ps (FWHM), respectively. Based on the measured longitudinal emittance shown in Fig. 1, longitudinal phase space distributions were estimated at every stage of the RIBF from the extraction point of the RRC to the injection point of the SRC. The transverse emittance at the injection point of the RRC was chosen to be 16π mm mrad. In the simulations, we neglected the imperfections of isochronous fields, instabilities of the power supplies of magnets, instabilities of the RF acceleration systems and other effects originating from poor tunings in energy matching, dispersion matching and transverse emittance matching when injecting a beam into the cyclotrons. We investigated these effects and found that they did not seriously deteriorate beam qualities when accelerators were carefully tuned. We also did not include the space-charge effects in these simulations. The space-charge effects become serious, for example, in the case of a 350 MeV/nucleon 1 pμA $^{238}U^{88+}$ beam, as reported in Ref. 7. Hence, the present results hold for the low-intensity (< 0.1 pμA) cases.

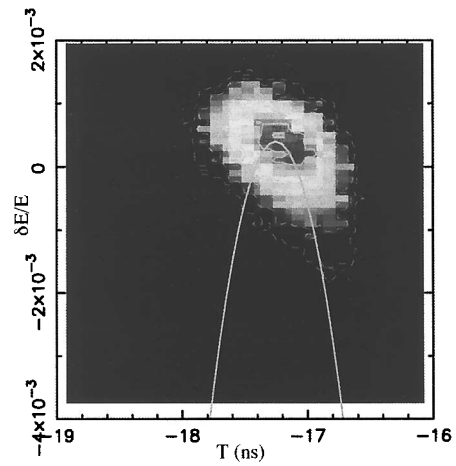

Fig. 1. Measured longitudinal phase space distributions at the extraction point of the RRC for a 95 MeV/nucleon ^{40}Ar beam. The vertical axis shows the relative deviation of the kinetic energy (E) and the horizontal axis shows the extraction time of each particle.

We chose a 350 MeV/nucleon ^{86}Kr beam as an example of the variable-energy mode. Ions extracted from the RRC will be injected directly into the IRC, which is 114 meters away from the RRC. The long drift space between the RRC and the IRC will expand a beam bunch markedly. However, the IRC, which has a flat-topping acceleration system, can accept almost all the ions transferred to it. The SRC will further accelerate the IRC beam. The longitudinal phase space distribution estimated at the injection point of the SRC is shown in Fig. 2. The longitudinal emittance is sufficiently small compared with the longitudinal acceptance of the SRC, as shown in Fig. 2. High-quality beams are expected after acceleration by the SRC.

A 350 MeV/nucleon ^{136}Xe beam was chosen as an example of the fixed-energy mode. In this mode, ions accelerated by the RRC will be transferred to the fRC through a beam rebuncher to be installed in the RIBF and further accelerated by the remaining three cy-

* Department of Accelerator Science, School of High Energy Accelerator Science, The Graduate University for Advanced Studies

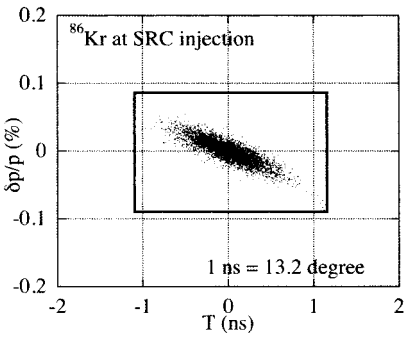

Fig. 2. Longitudinal phase space distribution at the injection point of the SRC for ^{86}Kr beam accelerated in the variable energy mode. The box shows the acceptance of the SRC.

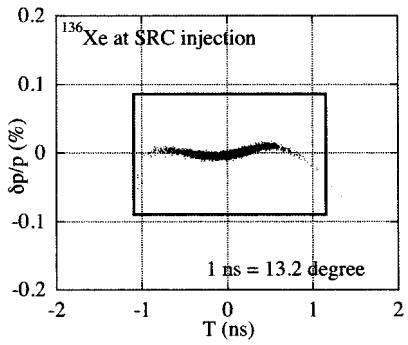

Fig. 4. Longitudinal phase space distribution for ^{136}Xe in the fixed-energy mode. The box in the figure shows the acceptance.

clotrons. As shown in Fig. 3, a beam rebunching system between the RRC and the fRC is essential because the operating frequency of the RF system in the fRC is chosen to be three times that of the RRC. The fRC cannot accept beams accelerated by the RRC without a rebuncher. The distance between the fRC and the IRC is more than 140 meters, therefore we should widen the phase acceptance of the IRC to 30 degrees by increasing the operating voltage of the flat-topping cavity. The phase space distribution expected at the injection point of the SRC is shown in Fig. 4 with the SRC acceptance. We also expect fairly good beam qualities.

Beam quality after acceleration by the RRC depends on the injector. The AVF cyclotron was employed for the 95 MeV/nucleon ^{40}Ar beam, the longitudinal emittance of which was used for input data in the simulations. In contrast, the RILAC will mainly be used as the injector in the RIBF. We also compared the measured longitudinal emittance of the 95 MeV/nucleon ^{40}Ar beam with the results of a numerical simulation. We found that the measured emittance was larger than that given by the simulation under the assumption that the momentum and phase spreads at the injection point of the RRC were 0.3% (FWHM) and ± 9 degrees (2σ), respectively. One possible explanation for the discrepancy is that the momentum spread at the injection point of the RRC was much larger than that assumed. To eliminate the discrepancy and understand the injector dependence, we plan to measure the longitudinal emittance of RILAC beams before and after acceleration by the RRC.

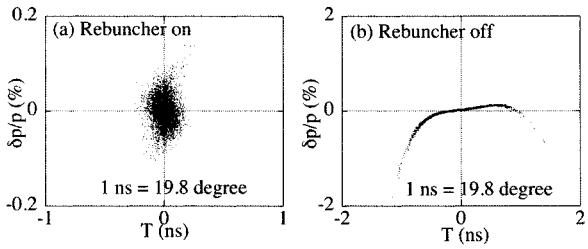

Fig. 3. Longitudinal phase space distribution for ^{136}Xe at the extraction point of the fRC (a) with and (b) without a rebuncher.

References

1) Y. Yano et al.: Proc. 17th Int. Conf. on Cyclotrons and Their Applications, Tokyo, 2004–10, to be published.
2) R. Taki: Master Thesis of Michigan State University (2003).
3) N. Inabe et al.: 17th Int. Conf. on Cyclotrons and Their Applications, Tokyo, 2004–10, to be published; T. Mitsumoto et al.: 17th Int. Conf. on Cyclotrons and Their Applications, Tokyo, 2004–10, to be published.
4) J. Ohnishi et al.: 17th Int. Conf. on Cyclotrons and Their Appilications, Tokyo, 2004–10, to be published.
5) H. Okuno et al.: 17th Int. Conf. on Cyclotrons and Their Applications, Tokyo, 2004–10, to be published.
6) N. Fukunishi et al.: 17th Int. Conf. on Cyclotrons and Their Applications, Tokyo, 2004–10, to be published.
7) S. B. Vorojtsov, A. S. Vorozhtsov, T. Mitsumoto, A. Goto, and Y. Yano: RIKEN-AF-AC-36 (2002).

Status of fixed-frequency Ring Cyclotron (fRC) in RIBF

N. Inabe N. Fukunishi A. Goto M. Kase H. Ryuto N. Sakamoto S. Yokouchi T. Mitsumoto,* and Y. Yano

A fixed-frequency Ring Cyclotron is used as a booster to obtain very heavy ions (> Xe) of 350 MeV/u with a high intensity in the RIBF.[1] Figure 1 shows an acceleration scheme in the RIBF. As shown in Fig. 1, middle heavy ions (< Xe) are stripped to high-charge states by a charge stripper[2] upstream of the RRC and accelerated up to 46.3 MeV/u by the RRC to be sent into the IRC directly. In the case of very heavy ions (> Xe), however, a high-intensity beam cannot be expected in the above-mentioned acceleration scheme because efficiency to produce the required high-charge state using the charge stripper is very small due to the low beam energy. For this reason very heavy ions are accelerated up to 11 MeV/u by the RRC without using the stripper upstream of the RRC and are boosted up by the fRC after passing through a charge stripper downstream of the RRC in order to obtain sufficient energy for acceleration by the IRC. These beams are then sent to the IRC via a charge stripper again. In the case of the U ion beam as illustrated in Fig. 1, $^{238}U^{35+}$ obtained from an 18 GHz ECR ion source is accelerated up to 11 MeV/u by the RRC and boosted up to 50.7 MeV/u by the fRC and 115 MeV/u by the IRC after charge-stripping to each favourable charge state at the charge strippers upstream of each cyclotron. Furthermore, this beam is also accelerated up to 350 MeV/u by the SRC. The charge states in the fRC and IRC are 71+ and 88+, and the expected fractions are 1/5 and 1/3, respectively.

The fRC is a four-sector ring cyclotron operated at a fixed frequency unlike other cyclotrons in the RIBF to reduce the construction cost. Moreover, to make the correction of magnetic field small, only ion beams with very similar charge-to-mass ratios can be accelerated.

The main specifications of the fRC are summarized in Table 1. The injection and extraction energies (11.0 and 50.7 MeV/u) of the fRC are determined by considering the energy losses in the charge strippers upstream and downstream of the fRC. The K-value of the fRC is 570, which corresponds to an acceleration of 50.7 MeV/u for $^{238}U^{71+}$. The frequency of the fRC is determined as 55 MHz, which is three times those of the RILAC and the RRC, so as to obtain a high voltage in the main RF cavity that is small with a low power. The harmonic number and injection radius of the fRC are chosen to be 12 and 1.55 m, respectively to match the beam structure from the RRC. The extraction radius is determined as 3.30 m from the velocity gain (2.13) in the fRC. A sector angle is chosen to be 58° taking into consideration beam focusing in the fRC, and the determined maximum magnetic field is 1.68 T. The acceleration voltage per turn is 0.7–1 MV using two RF cavities to obtain a large turn separation. Since the fRC is operated at a frequency three times that of the RRC, a flat-top cavity is equipped to enlarge phase acceptance (± 10°).

Table 1. Specifications of fRC.

K Value	570
Energy (MeV/u)	
Injection	10.5
Extraction	50.7
Frequency (MHz)	55
Harmonics	12
Radius (m)	
Injection	1.55
Extraction	3.30
No. of sectors	4
Sector angle (degrees)	58
Max. magnetic field (T)	1.68
Acceleration voltage (MV/turn)	0.7–1
Phase acceptance (degrees)	±10

The layout of the fRC is shown in Fig. 2. As shown in Fig. 2, the fRC is composed of four sector magnets,[3] two main RF cavities, one flat-top cavity, injection and extraction channels, beam diagnostics, and one vacuum system. Each sector magnet consists of a pair of main coils, ten pairs of trim coils, poles and a yoke. The weight of the sector magnet is approximately 370 t and the height is 4.38 m. The gap of the magnet is 50 mm and the medium plane is 1.7 m from floor to match the existing beam line.

The isochronous magnetic field of the fRC is produced by the main and trim coils in the magnet. The

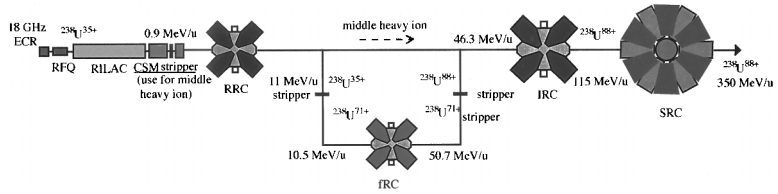

Fig. 1. Acceleration scheme in RIBF.

* Sumitomo Heavy Industries, Ltd.

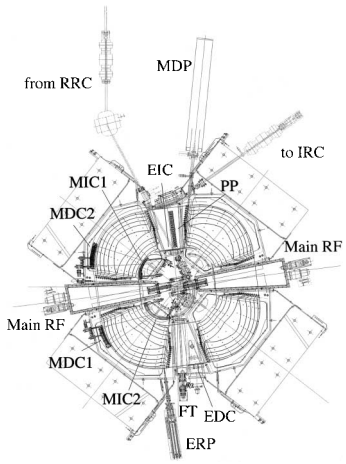

Fig. 2. Layout of fRC.

number of turns of the main coil is 70 and the maximum ampere-turn of the main coil is 90 kAT. The main coils of the sector magnets are connected to a power supply in series. The trim coils of one sector magnet consist of six pairs with a maximum current of 200 A and four pairs with one of 100 A. The power supplies of the trim coils are prepared, 24 for 200 A and 8 for 100 A, to carry out small corrections of A/q difference as well as construction and alignment errors.

The upper and bottom poles of the sector magnet form part of a vacuum chamber due to the limitation of construction height. For this reason the surface of each pole is coated with thin Ni to avoid outgas from iron.

An RF system is composed of two main RF cavities and one flat-top cavity located at valley sections, as shown in Fig. 2. The main cavity has a single acceleration gap and its maximum voltage is 350–500 kV (depending on radius) with the maximum consumption power of 100 kW. The flat-top cavity is of 3f-type and driven at 165 MHz. The maximum consumption power of the flat-top cavity is 30 kW. Each cavity has a fine tuner to correct changes in frequency originating from construction errors and changes in temperature.

The vacuum system is composed of six cryopumps used for main evacuation and two sets of turbomolecular and rotary pumps and two sets of mechanical booster and rotary pumps used for rough evacuation. In each valley box with the main RF cavity, two cryopumps are located and in the other two valley boxes, two cryopumps are located. The evacuation speed of one cryopump is 13000 l/s to achieve 4×10^{-5} Pa.[4)]

In the fRC, one main radial probe (MDP), one phase probe (PP), one extraction radial probe (ERP), some slits and Faraday cups are prepared, mainly for beam diagnostics. The MDP is a distractive probe that can move almost over the entire range from the injection radius to the extraction radius and can measure the beam current cut in steps of 0.5 mm for radial direction. The MDP can also measure the remaining part. The PP consists of 14 pairs of parallel plate pickups with a gap of 30 mm. In one pair of pickups, approximately 10 turns of beam pass through. The PP measures phase by timing the beam passing through the pickups. This information is used for fine tuning to produce the isochronous magnetic field. Slits are located at the entrance of each magnetic channel. These slits are separated into four parts (up, down, left, and right) that can read beam current approximately.

As shown in Fig. 2, the injection and extraction channels are composed of two magnetic channels and one electrostatic channel, respectively. The main specifications of each channel are summarized in Table 2. In Table 2, the minus sign shows that the magnetic field is in the direction opposite to that of the sector magnet. Each magnetic channel has correction coils to avoid the appearance of the magnetic field in the acceleration orbit. The EIC has a hole for the injection beam. The position of each channel can be changed.

The fRC is now under construction. The sector magnet is almost completed. The valley boxes including the main RF cavity will be completed by March 2005. Installation in the E4 room of the Nishina building will start from June 2005. The first commission is planned for September 2006.

Table 2. Main specifications of injection and extraction channels.

Magnetic channels			
Name	Radius (m)	Max. magnetic field (T)	Bending angle (degree)
MIC2	0.72	0.16	80
MIC1	0.87	0.16	40
MDC1	2.15	−0.06	19
MDC2	2.30	−0.14	20
Electrostatic channels			
Name	Gap (mm)	Max. Voltage (kV)	Length (m)
EIC	12	120	0.5
EDC	12	120	0.55

References

1) Y. Yano: Proc. 17th Int. Conf. on Cyclotrons and Their Applications, Tokyo, 2004-10, to be published.
2) H. Ryuto et al.: Proc. 17th Int. Conf. on Cyclotrons and Their Applications, Tokyo, 2004-10, to be published.
3) T. Mitsumoto et al.: Proc. 17th Int. Conf. on Cyclotrons and Their Applications, Tokyo, 2004-10, to be published.
4) S. Yokouchi et al.: RIKEN Accel. Prog. Rep. **38**, 279 (2005).

Design of vacuum system for RIKEN fRC

S. Yokouchi, N. Fukunishi, A. Goto, N. Inabe, M. Kase T. Mitsumoto,* H. Ryuto, N. Sakamoto, and Y. Yano

We aim at producing a beam transmission of more than 99% for $^{238}U^{71+}$ in the fixed-frequency ring cyclotron (fRC).[1] The pressure required to achieve this goal was estimated using the beam transmission (η) equation $\eta = \exp(-Cp\sigma_T L)$, where $C = 2.5 \times 10^{14}$ molecules/cm$^3 \cdot$ Pa, p the beam chamber pressure in Pa, σ_T the sum of the electron capture and loss cross section in cm^2, and L the path length of a beam in cm. By using Bezt-Schmelzer approximations for the low energy range,[2] the capture and loss cross sections are calculated to be 2.9×10^{-18} and 2.0×10^{-19} cm^2, respectively. In the high energy range of the fRC, the loss cross section above should be corrected because of underestimation. Therefore, the σ_T would be estimated to be 3.9×10^{-18} with a correction factor 5.[2] The L of $^{238}U^{71+}$ is calculated to be 2.6×10^5 cm for specifications of the fRC.[1] Consequently, the pressure required in the fRC vacuum system is calculated to be less than 4×10^{-5} Pa from the above equation.

Figure 1 shows a schematic diagram of the vacuum pumping system for the fRC. The vacuum pumping system consists of two rough evacuation systems, two high-vacuum pumping systems, and six main pumps. The rough evacuation system having a roots vacuum pump of 400 m^3/h is installed at each valley chamber. The high-vacuum pumping system having a turbomolecular pump of 2200 L/s is installed at each RF resonator. A cryopump of 13 m^3/s is used as the main pump. Two cryopumps are installed at each RF resonator, and one cryopump is installed at each valley chamber.

The total volume of the vacuum chamber is 16 m^3. The main materials used in the vacuum system are stainless steel, copper, Ni-plated iron, and fluoroelastomer. These inner surface areas and outgassing rates are summarized in Table 1. The total throughput outgassed from the vacuum chamber is calculated by summing those outgassed from all materials. The calculated total throughput is approximately $4.6 \times 10^{-2} t^{-1.2}$ Pa$\cdot$m^3/s, where t is the pumping down time in hours. The total effective pumping speed of the main pump is 49 m^3/s.

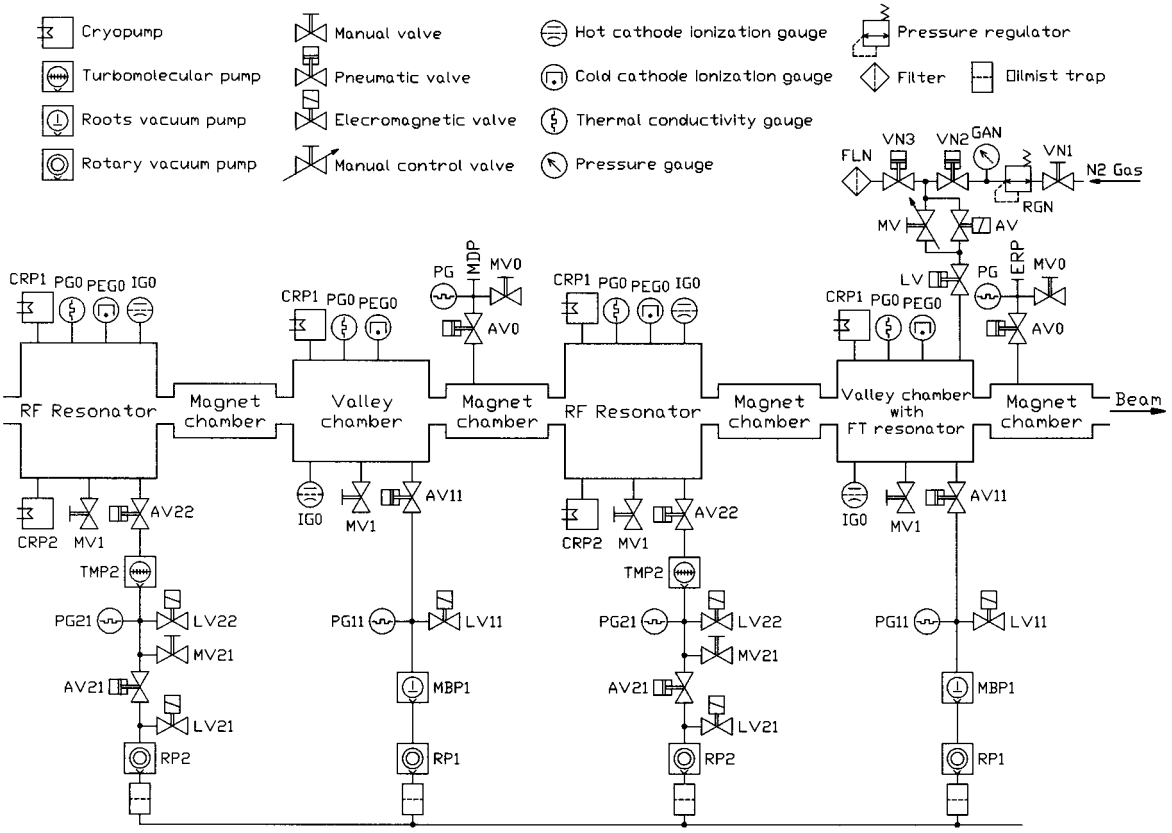

Fig. 1. Schematic diagram of vacuum pumping system for fRC.

* Sumitomo Heavy Industries, Ltd.

Table 1. Inner surface area and outgassing rate of the fRC vacuum chamber. The outgassing rate (Throughput which is outgassed at a given time from a material, divided by the area of the surface of the material.) is approximated by a continued product of pumping down time t (h). The throughput outgassed from each material is the product of its outgassing rate by its inner surface area.

Material	Inner surface area (m^2)	Outgassing rate ($Pa \cdot m^3/s \cdot m^2$)
Stainless steel	70	$2.0 \times 10^{-5} t^{-1.0}$
Copper	92	$5.3 \times 10^{-5} t^{-1.0}$
Ni-plated iron	45	$8.7 \times 10^{-4} t^{-1.5}$
fluoroelastomer	2.0	$1.3 \times 10^{-3} t^{-0.64}$

The pumping down time from an atmospheric pressure of the vacuum chamber to 50 Pa by rough evacuation is estimated to be about 26 min. The pumping down time from 50 Pa to 1×10^{-2} Pa by high-vacuum evacuation is estimated to be about 1.7 h. The cryopump is started at 1×10^{-2} Pa and normally operated after its cooling down time of 2 h. It takes 10 h after a normal operation of the cryopump to reach the required pressure of 4×10^{-5} Pa. Figure 2 shows an outline of the pumping down curve. As shown in this figure, the goal of about 14 h and a pressure in the range of 10^{-6} Pa, about 50 h after starting the vacuum pumping system, are expected. The pressure is estimated to reach the very low range of 10^{-6} Pa in the long term.

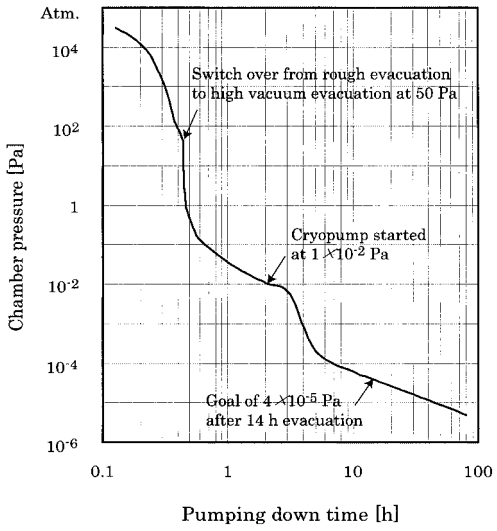

Fig. 2. Outline of pumping down curve.

The vacuum pumping system will be installed in 2006.

References

1) N. Inabe et al.: RIKEN Accel. Prog. Rep. **38**, 277 (2005).
2) The K500⊗K1200 — A Coupled Cyclotron Facility at the National Superconducting Cyclotron Laboratory: NSCL Report MSUCL-939, 64 (1994).

Construction status of IRC

J. Ohnishi, M. Kase, N. Sakamoto, K. Ikegami, S. Yokouchi, M. Nagase, M. Fujimaki,
H. Mikami,* H. Okuno, N. Fukunishi, A. Goto, and Y. Yano

A plan view of the intermediate-stage ring cyclotron (IRC) is shown in Fig. 1.[1)] Four sector magnets were installed at the RIBF accelerator building in 2003.[2)] The magnet and the vacuum systems were completed by November, 2004. A brief outline of the construction carried out in 2004 is as follows. A work schedule is shown in Fig. 2.

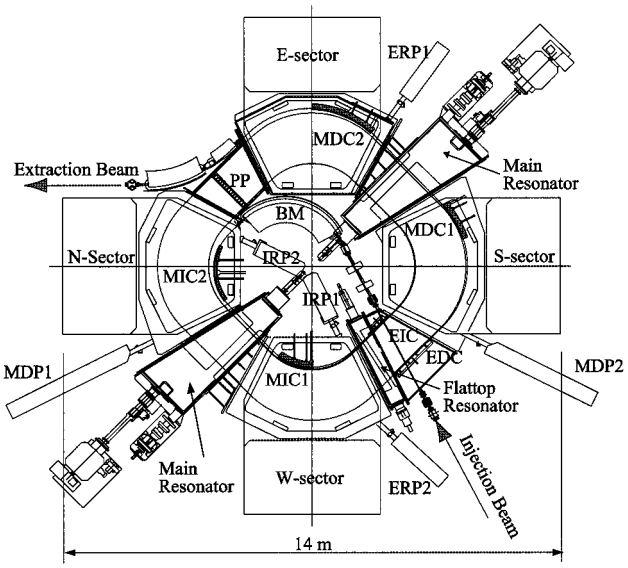

Fig. 1. Plan view of the IRC.

(1) Piping for the cooling water in the IRC room.

The cooling water system for the IRC consists of five routes for the cooling of the following: main coils, trim coils, RF resonators and the magnets for the beam injection and extraction, RF amplifiers, equipment for the vacuum pumping system. After the piping and flow tests, the operation of the cooling water system started for the magnet and the vacuum pumping systems.

(2) Installation of the RF resonators and the valley chambers.

The RF resonators and the valley chambers were placed and aligned with the positional accuracy of better than 0.5 mm in the horizontal and the vertical directions. A photograph of the installed main RF resonators is shown in Fig. 3. The resonators are connected to the beam chambers in the sector magnets with pneumatic seal joints.

(3) Assembly of the vacuum pumping system.

A layout of the vacuum pumping system is shown in Fig. 4. It consists of two rouging pumping lines, four main pumping lines with turbo molecular pumps of 3,200 L/s, twelve cryopumps of 10,000 L/s and two of 4,000 L/s. Further twelve differential pumping lines are used for the subvacuum of the RF resonators and the beam chambers for the sector magnets.

(4) Installation of the magnetic channels.

The magnetic channels for the beam injection and extraction system (MIC1, MIC2, MDC1, and MDC2) were placed with the positional accuracy of better than 1 mm.

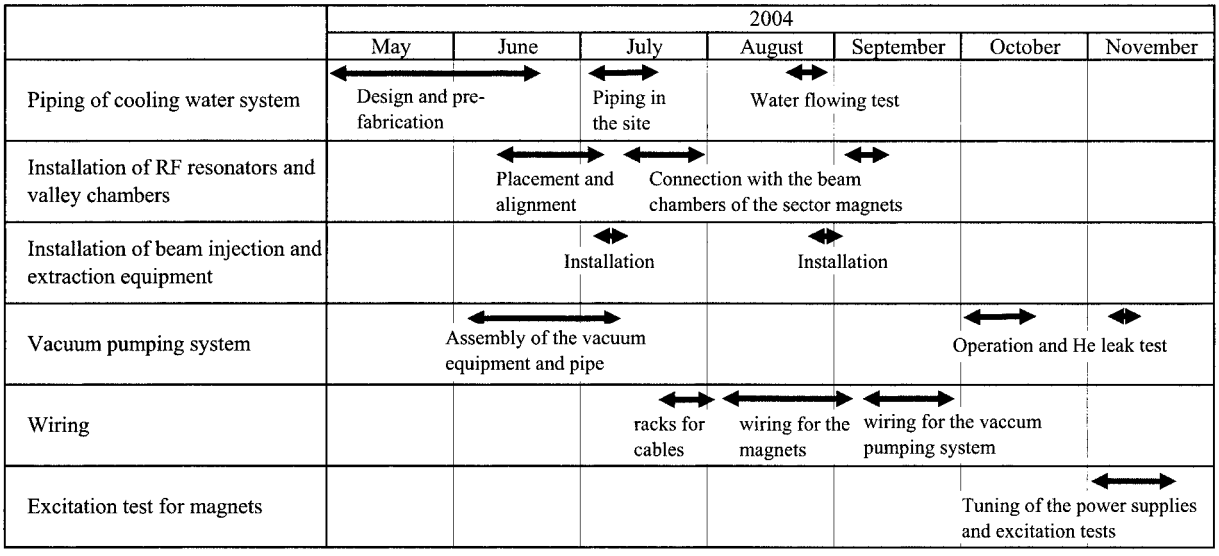

Fig. 2. Work schedule of the IRC construction in 2004.

* Sumitomo Heavy Industries, Ltd.

(5) Wiring for the magnet system.

The magnets and their 52 power supplies were wired with approximately 400 cables. The magnet system consists of four sector magnets, each of which has two pairs of main coils and 20 pairs of trim coils, and seven magnets for the beam injection and extraction system.

(6) Operation start for the vacuum pumping system.

Evacuation of the vacuum chambers started after the wiring and checking of the pumps, valves, gauges and safety system. The helium leak test was carried out while the pressure was lowered. First operation of the cryopumps started on November 10 and the design pressure of 10^{-5} Pa was achieved on November 15.

(7) First excitation of the magnets.

After tuning of the power supplies for the magnets, all the magnets were excited at their respective maximum current. As a result, the magnets, the power supplies and the cooling water system were confirmed to be good.

The wiring and the power test for the RF system and the installation of the beam diagnostic system will be carried out and the whole IRC will be completed in 2005.

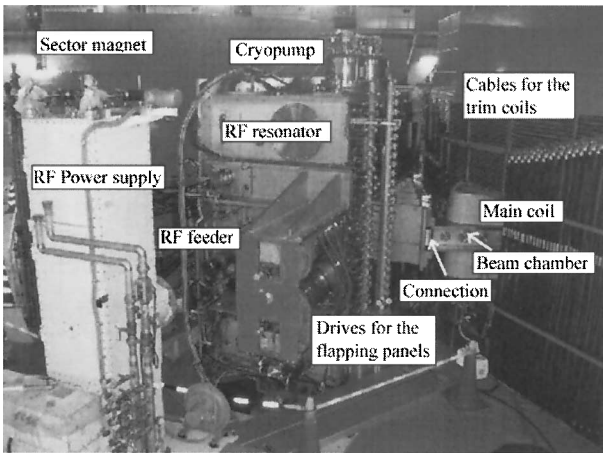

Fig. 3. The installed main RF resonator.

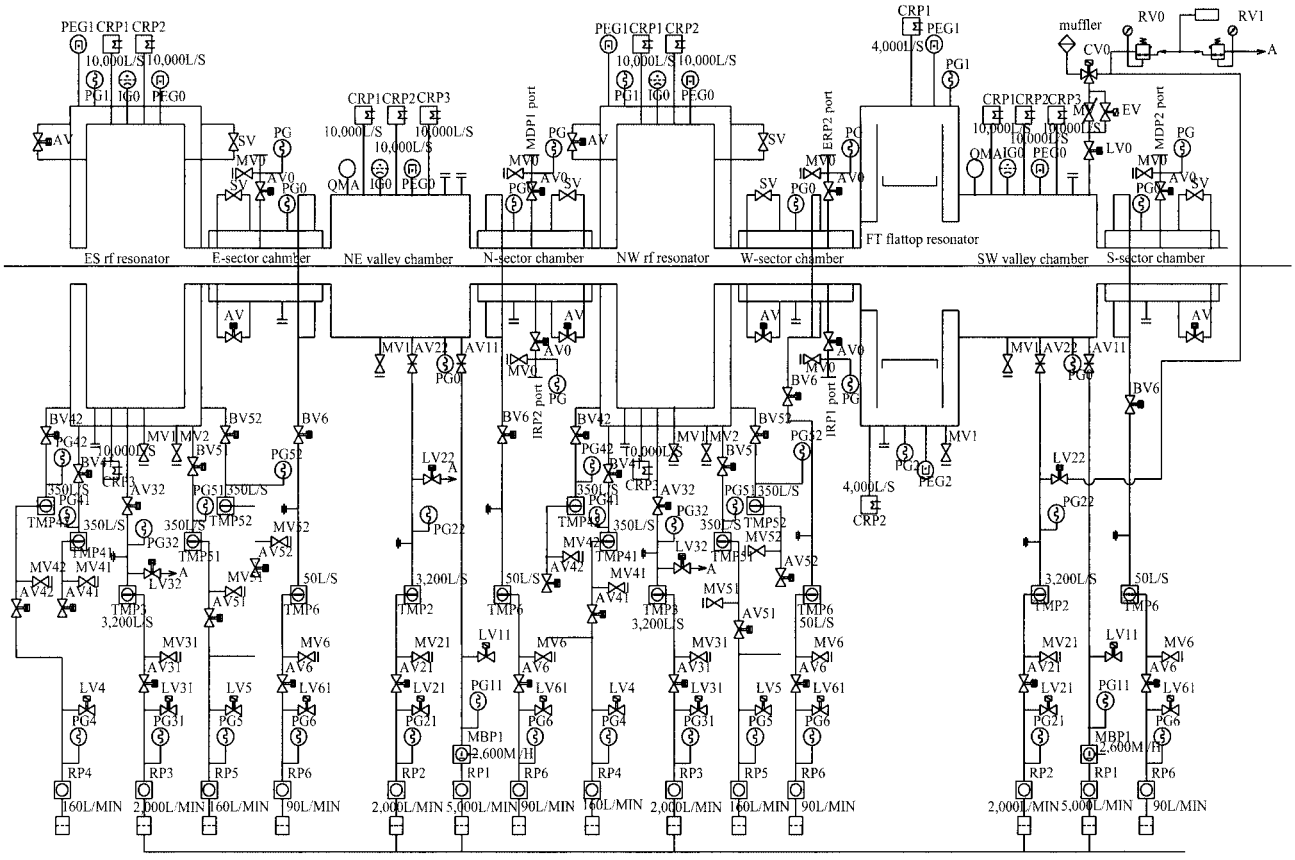

Fig. 4. Layout of the vacuum pumping system.

References

1) T. Mitsumoto et al.: AIP Conf. Proc. **600**, 167 (2001).
2) J. Ohnishi et al.: Proc. 1st Annual Meeting of Particle Accelerator Society of Japan, Funabashi, 2004-8 (Institute of Quantum Science, Nihon University, 2004), p.224.

Status of magnets for the SRC

H. Okuno, N. Fukunishi, J. Ohnishi, K. Ikegami, T. Tominaka,
S. Yokouchi, T. Fujinawa, A. Goto, and Y. Yano

In January of 2004 the assembly of the SRC sector magnet began in the SRC vault with the goal of having the first beam operable by the autumn of 2006. This paper is a report on its progress for this year.

Figure 1 shows cross-sectional and plan views of the sector magnet. Its length and height are 7.2 m and 6 m, respectively. The weight is about 800 tons per sector. Its main components are a pair of superconducting main coils, four sets of superconducting trim coils, a radiation shield, a cryostat chamber, thermal insulation support links, twenty-two pairs of normal conducting trim coils, warm poles and a yoke. The details of its structure are described in Ref. 1. Figure 2 shows a bird's-eye view of the vertically expanded sector magnet explaining the assembly procedure. The assembly in the SRC vault proceeds in the following order: the lower yoke, the lower cold mass assembly, the side wall of the cryostat, the upper cold mass assembly and the upper yoke. The cold mass assemblies consist of the superconducting coils, the radiation shields, the poles and other parts. They were assembled in the factories to improve the quality of assembly.

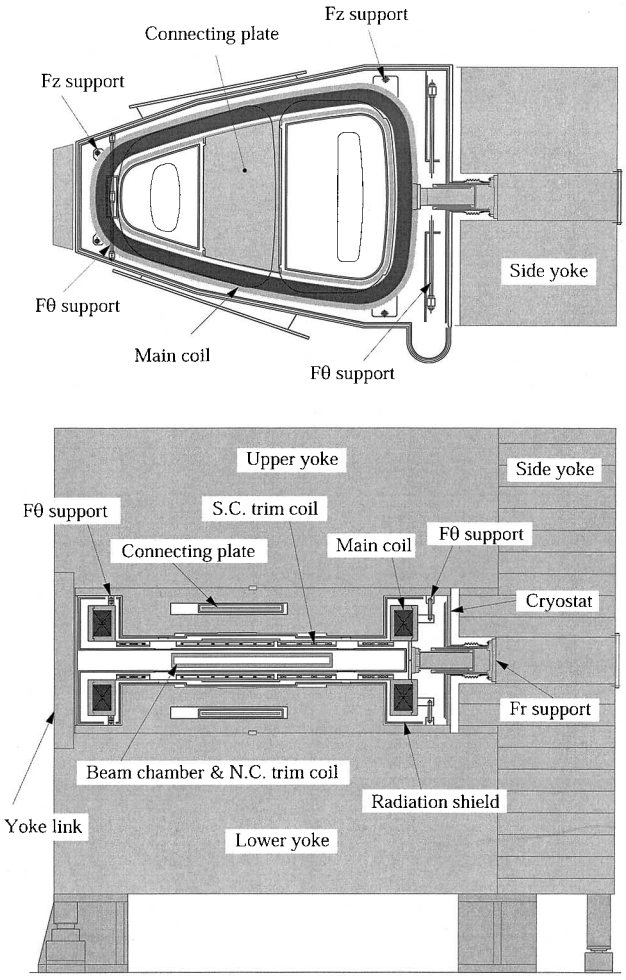

Fig. 1. Cross-sectional view of the sector magnet.

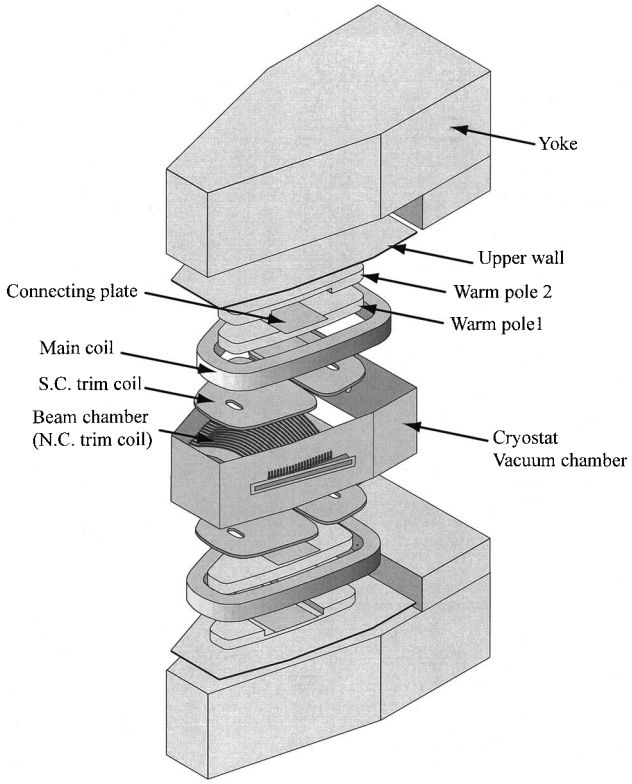

Fig. 2. Expanded view of the sector magnet for the SRC.

Figure 3 shows the SRC vault at the present time (Nov. 2004). The canning of the entire cryostat has almost been completed. The assembly of the upper yoke is ongoing. Alignment accuracy of all parts was typically 0.1–0.2 mm. Before the welding of the cryostat, a high sensitivity total leak test of all the He vessels and pipes was carried out. These tests will decrease the risks that cold leaks will occur during cooling-down of the superconducting coils.

The level of the floor and sector magnet of the SRC has been monitored, as shown in Fig. 4, to see how much the floor subsides due to the heavy weight of the sector magnet. The data suggest that the floor around the east wall has subsided by 2 mm and remained so for several months. The level of the lower yoke was readjusted before the cold mass assemblies were installed on the yoke. They were measured again two months

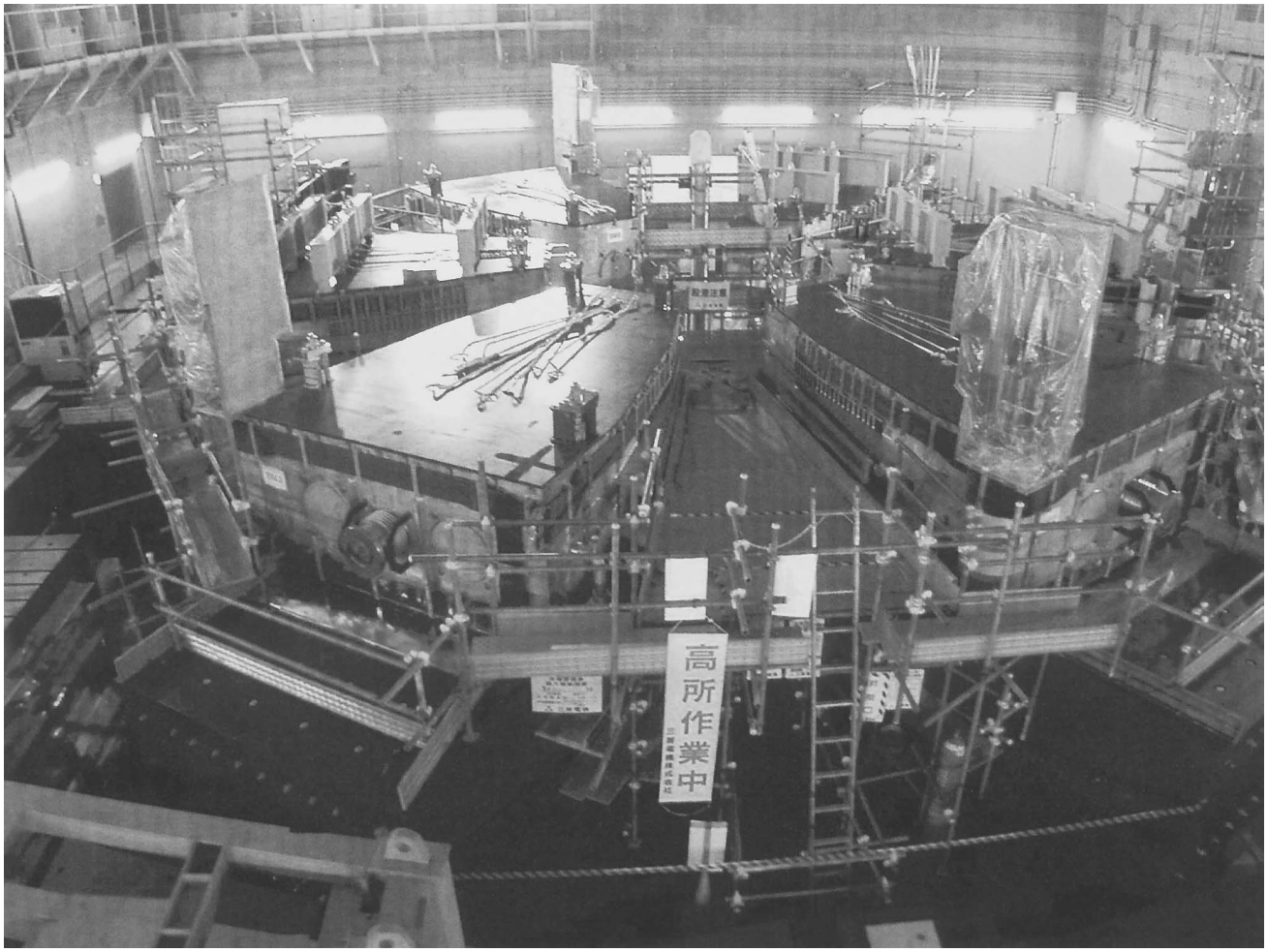

Fig. 3. Photograph of the SRC during assembling.

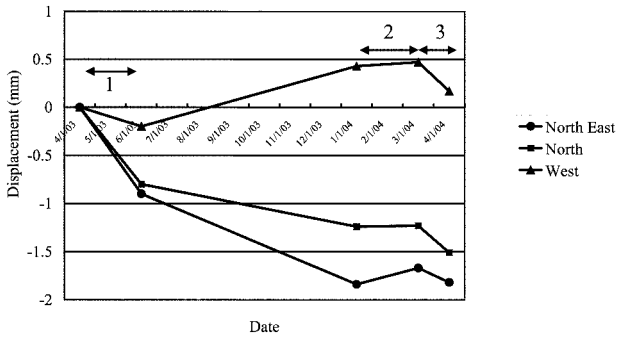

Fig. 4. Subsidence of the floor level in the SRC. Periods 1, 2, and 3 indicate the following. 1: Delivery of slabs for the yoke and the shield into the SRC and Big-RIPS vaults, 2: Assembly of the lower yokes and 3: Transfer of most slabs from the Big-RIPS vaults into the SRC vaults.

later, and the base plane of the sector magnet was found to be tilted by 0.4 mm/20 m. The mode of the level change is not thought to be harmful to the performance of the SRC. The floor level will be monitored until beam commissioning.

Assembly of the sector magnet, which is ongoing, will be finished in July of 2005. The superconducting coils will be cooled from the middle of August and will be excited in October. The magnetic field maps will be taken until the end of January 2006. The other components will be installed by the end of April 2006 for the power test of the rf-system. Finally, beam commissioning is scheduled to be performed in the autumn of 2006.

Reference

1) A. Goto, H. Okuno, J. Ohnishi, T. Tominaka, S. Fujishima, K. Ikegami, N. Fukunishi, Y. Miyazawa, T. Mitsumoto, and Y. Yano: IEEE Trans. Appl. Supercond. **14**, 300 (2004).

Development of liquid helium flow meter for the SRC magnets

H. Okuno, T. Tominaka, J. Ohnishi, K. Ikegami, A. Goto, and Y. Yano

The SRC has two types of superconducting coils: the main coils and superconducting trim coils. The main coils are cooled in the liquid helium bath and the superconducting trim coils are indirectly cooled by a forced two-phase helium flow. The cooling circuit is divided into three parallel circuits to cool 48 sets of superconducting trim coils. It is very important to tune individually flow rate in the three parallel circuits using control valves installed in lines to uniformly cool all the trim coils. Flow meters of liquid helium are necessary to tune flow rate. In any cases, orifice plates are inserted to the line to monitor flow rate. It measures the difference in pressures upstream and downstream of the orifice plate. To have some sensitivity for liquid helium, the diameter of the orifice should be sufficiently small so that pressure decrease at the orifice is very large during the initial cooling at room temperature. Therefore, we need to install many additional bypass valves, which are expensive low-temperature valves and render the cooling system complex. So, we developed a cup-type liquid helium flow meter instead of the standard orifice flow meter, to realize a system less expensive and simpler. We adopted multihole cups to widen their available ranges. In the next section the details of the flow meter will be described.

The flow meter is composed of a cup with some holes and a level indicator for liquid helium as shown in Fig. 1. The discharge rate of liquid helium from a hole is proportional to the square root of pressure exerted by liquid helium filling the cup. When discharge rate is equal to pouring rate, the liquid surface remains at an appropriate level, which can be measured using a level indicator. The available range of flow rate for a singe-hole cup is insufficiently small because flow rate is proportional to the square root of liquid column height. To obtain a wide range, we adopted a multihole cup, which shows approximately the linear dependence of flow rate on the height of liquid in an appropriate range.

We performed experiments to determine the relationship between flow rate and liquid helium level. First, liquid helium was transferred from the dewar and to the cup. Secondly, after completing the transfer, the level of liquid helium was monitored as a function of time. Flow rate can be plotted as a function of liquid helium level from the measurements. Figure 2 shows the data in the case of using cups with four 4-mm-diameter holes at the levels of 1.3, 8.8, 16.3 and 23.8 cm from the bottom. Their relationships agree well with the expectation and the cups can measure flow rate in a required range (5–40 cc/s). We tested three cups that have the same structure. Obtained data also coincided with each other. The tested flow meters were installed in the helium vessel for the SRC to monitor flow rate in the cooling lines for the superconducting trim coils.

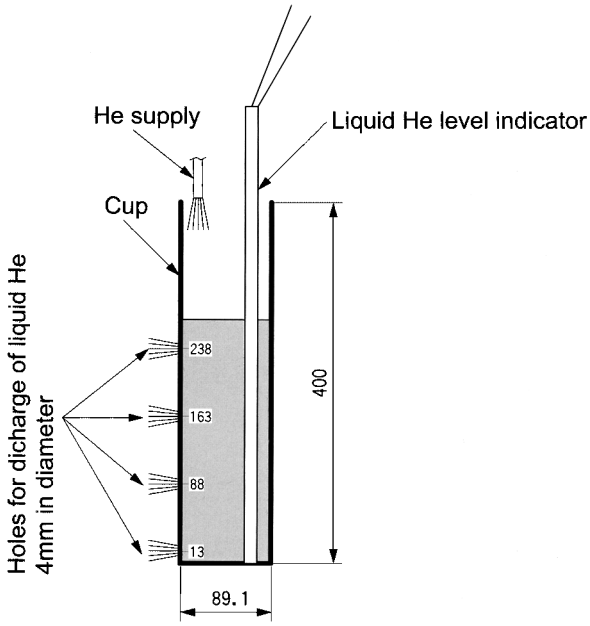

Fig. 1. Conceptual drawing of cup-type flow meter for liquid helium.

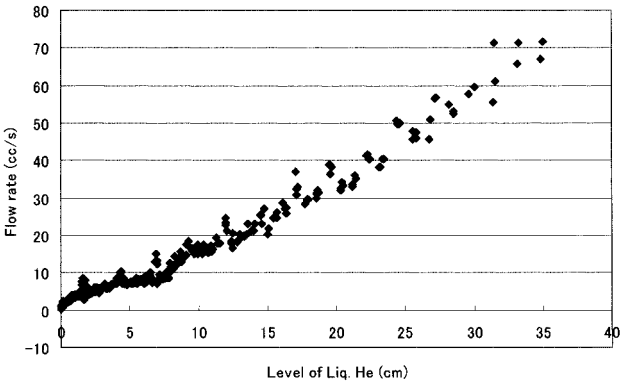

Fig. 2. Measured relationship between flow rate and liquid He level.

Present status of liquid-helium supply and recovery system

K. Ikegami, M. Ohtake, T. Tominaka, and Y. Yano

The liquid-helium supply and recovery system[1] at the Wako campus can generate liquid helium at a rate of 200 ℓ/h from pure helium gas. It has been stably operated since the beginning of April 2001. Volumes of liquid helium supplied per year are listed in Table 1. The volume supplied has gradually increased over the years and it will soon be more than twice that supplied in 2001. This is due to the increase in the number of users for nanoscience projects such as the advanced device laboratory, the nanomaterial laboratory, and the low-temperature physics laboratory.

The recovery system consists of a recovery compressor, a gas bag and three recovery stations. The recovery compressor has a blow rate of 130 m^3/h at a pressure of 15 MPa. The gas bag has a volume of 100 m^3 and is placed in the liquid-helium supply and recovery building. The first recovery station has a gas container with a volume of 20 m^3 and a blower with a blow rate of 80 m^3/h. It is placed near the cooperation building for the advanced device laboratory located on the south side of the RIKEN campus. The second recovery station has a gas container with a volume of 40 m^3 and a blower with a blow rate of 80 m^3/h. It is placed in the RIKEN main research building and is connected to the frontier research building and the frontier material research facilities building. The third recovery station is placed behind the east brain science building located on the east side of the RIKEN campus and connected to the Nishina memorial building. In the near future, the new RIBF accelerator building will also be connected to it through a recovery pipe. In March 2005, a new recovery station that has one gas container with a volume of 30 m^3 and one blower with a blow rate of 80 m^3/h will be installed in front of the chemistry and material physics building for the nanoscience project. At the same time, impure gas cadres with a volume of 1800 m^3 will be added to the system to compensate for the increase in the volume of recovered helium gas.

Table 1. Volumes of liquid helium supplied per year from 2001 to 2003.

Year	Volumes of supplied liquid helium (kℓ)
2001	28
2002	40
2003	52

For approximately one year, problems with impurity in the system have occurred. The recovered helium gas contained 1–2 ppm of hydrogen gas. The gas is liquefied after purification with an internal device installed in the refrigerator. However, about 0.06 ppm hydrogen had entered the liquid helium storage vessel because the capacity of the 20 K adsorber in the refrigerator was not sufficient to remove all the hydrogen gas in the helium. As a result, the hydrogen in the liquid helium caused a blockages in the dilution refrigerators which are used for the nanoscience project. In order to remove the hydrogen and the impure gases in the liquid helium storage vessel, The temperature of the vessel had to be raised to room temperature. After replacing the pure helium gas, the storage vessel was cooled back to 4.2 K.

Reference

1) K. Ikegami et al.: RIKEN Accel. Prog. Rep. **34**, 349 (2001).

Status of the BigRIPS separator project

T. Kubo, K. Kusaka, K. Yoshida, A. Yoshida, Y. Mizoi,[*1] N. Fukuda,
N. Aoi, H. Sakurai,[*2] T. Motobayashi, and Y. Yano

The large-acceptance superconducting in-flight RI beam separator BigRIPS[1)] is under construction for phase I of the RI beam factory (RIBF) project. The BigRIPS separator is characterized by two major features: large acceptances and a two-stage separator scheme. The large acceptances are achieved by using large-aperture superconducting triplet quadrupoles (STQ), allowing the efficient production of RI beams by the in-flight fission of uranium beams. The two-stage separator scheme allows one to deliver tagged RI beams: The first stage of BigRIPS serves to produce and separate RI beams using the technique called momentum-loss achromat, while the second stage works as an analyzing section to identify RI-beam species in an event-by-event mode. Since the RI-beam purity is poor in our energy domain, the present scheme significantly facilitates RI-beam experiments such as secondary reaction studies of unstable nuclei. The integrated capability of the BigRIPS and RIBF cyclotrons is expected to enlarge the scope of RI-beam experiments significantly, promoting studies on the properties and reactions of unstable nuclei further from the stability.

The BigRIPS separator is followed by the phase-I RI-beam delivery line, which transports the tagged RI beams to experimental setups placed downstream. Figure 1 shows a schematic layout of the phase-I RIBF project, in which two RIBF cyclotrons, the BigRIPS separator, and the RI-beam delivery line are shown. Part of the delivery line, as shown in the figure, has been designed to also serve as a zero-degree forward spectrometer which we call ZDS spectrometer. This was made possible by adopting the same quadrupoles and dipoles as those of BigRIPS for the delivery line. A secondary target surrounded by γ-ray array detectors is placed in the starting focus point of ZDS spectrometer, while projectile residues from secondary reactions are analyzed and identified by the ZDS spectrometer. In-beam γ-ray secondary reaction studies will be extensively made for a variety of unstable nuclei using

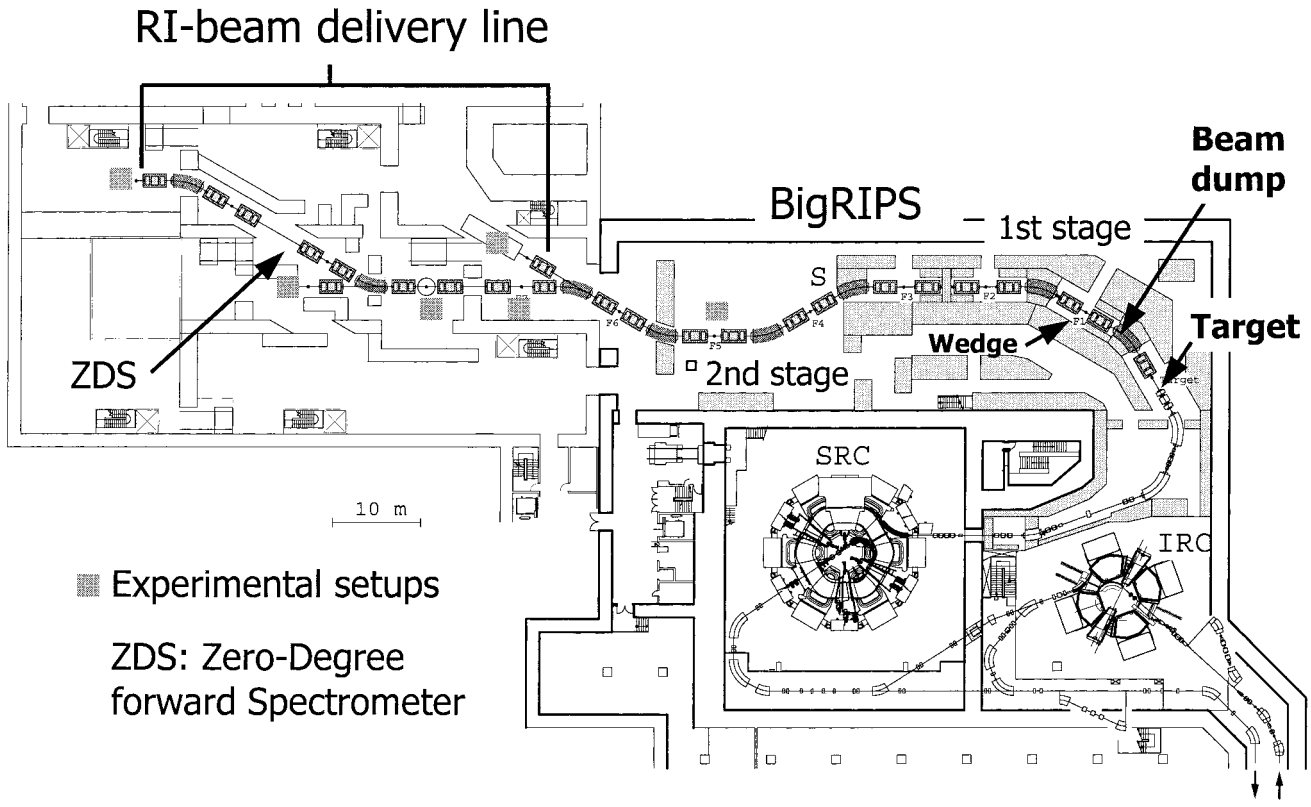

Fig. 1. A schematic layout of the RI beam factory project in 2007 (RIBF phase I).

*1 Osaka Electro-Communication University
*2 Department of Physics, University of Tokyo

the ZDS spectrometer.

The construction schedule for the BigRIPS separator project is shown in Fig. 2, along with that of the RI-beam delivery line. Most of the BigRIPS construction will be finished in early 2006. The construction of the delivery line will start in 2005, its completion being scheduled for early 2007. The first RI-beam production using BigRIPS is scheduled in late 2006, while RI-beam experiments will start in April, 2007.

Fabrication of the BigRIPS magnets consisting of fourteen superconducting triplet quadrupoles (STQ) and six room-temperature dipoles was finished in March, 2004. In the case of the first-stage magnets consisting of five STQs and two dipoles, their installation has also been finished, along with the cryogenic plant to be used for the cooling of STQs.[2] Stand-alone test operation of the cryogenic plant was carried out in April, 2004, in order to measure the heat loads of the transfer line as well as the cooling capacity of the cryogenic plant.[3] A cooling capacity higher than the design value has been obtained.

The second-stage magnets consisting of nine STQs and four dipoles are currently being stored in the BigRIPS hall until their installation in 2005. The fabrication of the delivery-line magnets consisting of ten STQs and two dipoles will also begin in 2005.

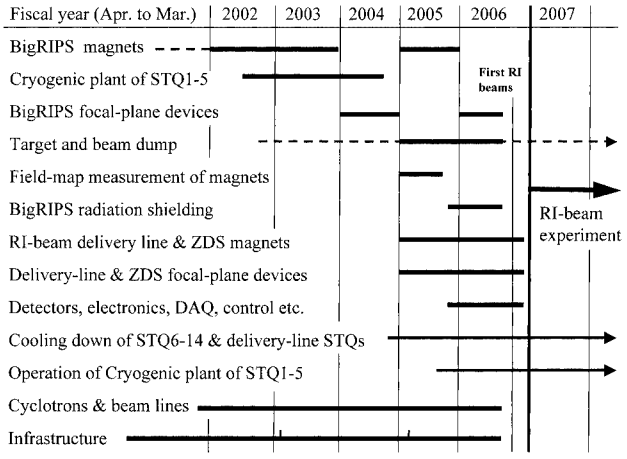

Fig. 2. Schedule of the BigRIPS separator project.

The design and fabrication of the focal plane devices, such as vacuum chambers, degrader control, slit control, collimator, stopper and detector tables, are currently being carried out.[4] The focal plane devices will be placed in a vacuum chamber at each focus of BigRIPS, being employed to tune not only the production and separation of RI beams but also the RI-beam tagging. The fabrication will be finished in March, 2005.

In order to cope with the beam power of 100 kW at RIBF, the design, study and development of the high-power water-cooled rotating-disk production target[5] and the high-power water-cooled swirl-tube beam dump[6] are progressing. As for the beam dump, a water-cooled swirl tube has been tested by irradiating a high-power laser beam. Recent analysis of the data indicates that the swirl-tube beam dump can withstand the expected power density at BigRIPS.[6]

The ZDS spectrometer has been designed to have different optics mode, which allows one to choose the appropriate mode depending experimental requirements.[7]

Test operation of the cryogenic plant started in October, 2004, to cool the first-stage STQs, and is still in progress as of November.

References

1) T. Kubo: Nucl. Instrum. Methods Phys. Res. B **204**, 97 (2003).
2) K. Kusaka et al.: RIKEN Accel. Prog. Rep. **38**, 291 (2005).
3) T. Kubo et al.: RIKEN Accel. Prog. Rep. **38**, 289 (2005).
4) K. Yoshida et al.: RIKEN Accel. Prog. Rep. **38**, 293 (2005).
5) A. Yoshida et al.: RIKEN Accel. Prog. Rep. **38**, 296 (2005).
6) Y. Mizoi et al.: RIKEN Accel. Prog. Rep. **38**, 295 (2005).
7) Y. Mizoi et al.: RIKEN Accel. Prog. Rep. **38**, 297 (2005).

Stand-alone test operation of the BigRIPS liquid-helium cryogenic plant and heat-load measurement of its cryogenic-temperature transfer line

T. Kubo, K. Kusaka, K. Yoshida, A. Yoshida, Y. Mizoi,[*1] N. Kakutani,[*2] T. Tsuchihashi,[*2] M. Shimada,[*2] K. Sato,[*2] M. Nagami,[*3] T. Kumaki,[*3] M. Nobutoki,[*3] and Y. Katou[*3]

The five surpeconducting triplet quadrupoles (STQ) on the first stage of the BigRIPS separator[1] are cooled by a large liquid-helium cryogenic plant, the main components of which are a Linde-TCF50S refrigerator, a Maekawa 315 kW compressor, and a 50-m-long cryogenic-temperature helium-transfer line. The cryogenic plant supplies liquid helium and 70 K gas helium in a refrigeration mode to the STQs through the transfer line. Each STQ is connected to the transfer line by way of its valve box unit and U-shaped cryogenic-temperature tubes. The 70 K gas helium is used to cool 70 K shields of the transfer line as well as those of STQ cryostats. More details are described in Ref. 2.

The system, including the STQs and the cryogenic plant, was fabricated by Toshiba Corporation and Taiyo Nippon Sanso Corporation, and were installed in the RIBF building in March 2004. Some photographs of the BigRIPS cryogenic plant are shown in Ref. 3.

Stand-alone test operation of the BigRIPS cryogenic plant was carried out in April 2004, in order to measure not only the cooling capacity of the refrigerator but also the heat loads of the transfer line. In the operation, the STQs were disconnected from the system by closing the cryogenic-temperature valves in the valve box units, and liquid nitrogen, which can enhance the cooling capacity, was not employed in the first heat exchanger of the refrigerator.

In the measurement of the cooling capacity, cryogenic-temperature valves at the cold end of the refrigerator were closed so that the transfer line was disconnected. The cooling capacity to supply liquid helium, which we call the 4.3 K cooling capacity, was measured by saving liquid helium in the phase separator dewar inside the refrigerator and keeping the liquid-helium level constant by switching on a heater in the phase separator. The measured input power to the heater corresponds to the 4.3 K cooling capacity of the refrigerator. In the measurement of the cooling capacity to supply 70 K gas helium, which we call the 70 K cooling capacity, heat loads to the 70 K shields were simulated by switching on a heater installed at the inlet position of the first turbine.

The operation conditions of the refrigerator, such as pressure, temperature, conductance of control valves, rotation speed of two turbines and so on, were adjusted, so that the cooling capacities could be optimized. The results are listed in Table 1 along with the design cooling capacities. Fortunately, the measured values are higher than the design values for both cooling capacities. This may be because the efficiency of the heat exchangers as well as that of the turbines in the refrigerator are higher than what is expected in the design.

In measuring the heat loads to the transfer line, liquid helium and 70 K gas helium were supplied to the transfer line by opening the supply and return valves at the cold end of the refrigerator. End valves located at the end of the transfer line were also opened, so that the liquid and gas helium could return to the refrigerator. The supplied liquid helium returns in two phases to the phase separator, while the 70 K gas helium returns to the inlet of the first turbine as in the usual operation mode. During this operation mode, the operation conditions of the refrigerator were kept the same as those in the stand-alone operation, including the temperature of water that cools the compressor. The heater power at the inlet of the first turbine was adjusted such that the same operation conditions could be attained. The heater power to the phase separator was also adjusted so as to keep the liquid level constant.

The difference in the heater power between the stand-alone and heat-load measurement operations indicates the heat loads to the transfer line: 4.3 K heat loads and 70 K heat loads. The measured values are listed in Table 1 along with the design values. Unfortunately, the measured 4.3 K heat loads are higher than the design value. This is because 70 K shields in some parts of the transfer line were not actually installed. On the other hand, the measured 70 K heat loads were smaller than expected, for the same as above.

Table 2 summarizes the cooling capacity, measured

Table 1. Measured cooling capacities and transfer-line (T.L.) heat loads.

	Measured	Design
4.3 K cooling capacity	509 W	390 W
70 K cooling capacity	907 W	700 W
4.3 K heat loads to T.L.	114 W	62 W
70 K heat loads to T.L.	408 W	440 W

Main operation conditions: 1.59 MPaG at the exit of compressor, 1.33 MPaG at the inlet of first turbine, water temperature 19°C.

*1 Osaka Electro-Communication University
*2 Toshiba Corporation
*3 Taiyo Nippon Sanso Corporation

Table 2. Summary of measured and expected performance of the BigRIPS cryogenic plant.

4.3 K performance		
Cooling capacity	509 W	(measured)
Extra cooling capacity	267 W	
Total heat loads	242 W	
Transfer line	114 W	(measured)
Valve boxes and U-shaped pipes	40 W	(estimated)
STQs (STQ1-5)	18 W	(measured off line)
Power leads	70 W	(estimated)
70 K performance		
Cooling capacity	907 W	(measured)
Extra cooling capacity	212 W	
Total heat loads	695 W	
Transfer line	408 W	(measured)
Valve boxes and U-shaped pipes	62 W	(estimated)
STQs (STQ1-5)	225 W	(measured off line)

and expected heat loads, and expected extra cooling capacity. The extra cooling capacity is expected to be 267 W for 4.3 K heat loads and 212 W for 70 K heat loads. These capacities will be used for radiation heat loads due to fast neutrons that are emitted from the production target and the beam dump located near the STQs.

Test operation of the cryogenic plant, including the first-stage STQs, began in October 2004, and was still in progress as of November 2004.

References

1) T. Kubo: Nucl. Instrum. Methods Phys. Res. B **204**, 97 (2003).
2) T. Kubo et al.: RIKEN Accel. Prog. Rep. **36**, 316 (2003).
3) K. Kusaka et al.: RIKEN Accel. Prog. Rep. **38**, 291 (2005).

First stage of BigRIPS separator

K. Kusaka, T. Kubo, K. Yoshida, A. Yoshida, Y. Mizoi,[*1]
N. Kakutani,[*2] T. Tsuchihashi,[*2] and K. Sato[*2]

An in-flight RI beam separator named BigRIPS[1] is being built for the RIBF phase-I project. Large acceptances and a two-stage separator scheme characterize the BigRIPS separator. While the large acceptances are achieved by the use of superconducting quadrupoles with large apertures, the two-stage separator scheme allows tagged RI beams to be delivered. The first stage of the BigRIPS separator serves to produce and separate RI beams, while the second stage serves to identify RI-beam species in an event-by-event mode. Here we report the current status of the first stage of the BigRIPS separator.

Figure 1 shows a schematic layout of the first stage of the BigRIPS separator. The main magnetic components are five superconducting quadrupole triplets (STQ) and two room-temperature dipoles. The five STQs are cooled by liquid helium (LHe) which is supplied by a large-scale, integrated cryogenic system through a transfer line. The transfer line and valve boxes are also shown in Fig. 1.

While the STQs and the dipole magnets were fabricated by Toshiba Corporation and completed in the beginning of 2004, the large cryogenic system was fabricated by Nippon Sanso Ltd. and some of its components, such as the cold box (Fig. 2), buffer tanks (Fig. 3), and compressors (Fig. 4), were installed in the RIBF building in 2003. The design of the cryogenic system has been reported elsewhere.[2] Installation of the magnet system of the first stage, the five STQs including the cryogenic system and the two dipoles, was complete by the end of March 2004 (Fig. 5). A stand-alone test of the cold box and measurements of heat loads of the transfer line were also performed in 2004.[3]

Table 1 summarizes the main parameters of STQs.

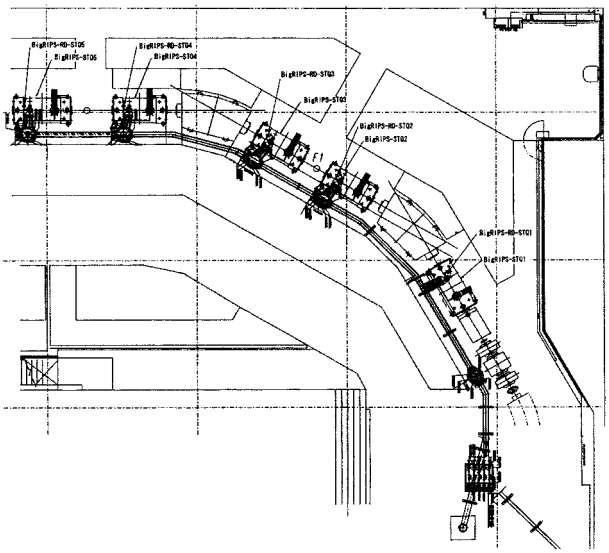

Fig. 1. Schematic layout of the first stage of BigRIPS separator.

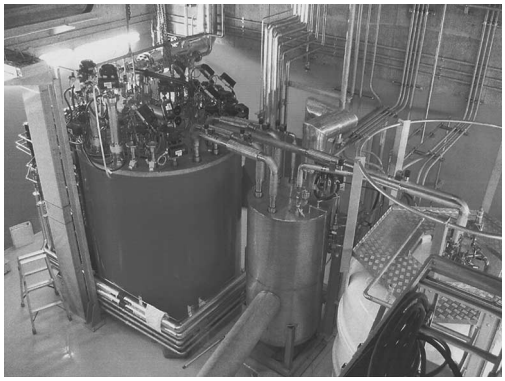

Fig. 2. Cold box (TCF50S), joint box, and, LHe dewar.

Fig. 3. Buffer tanks.

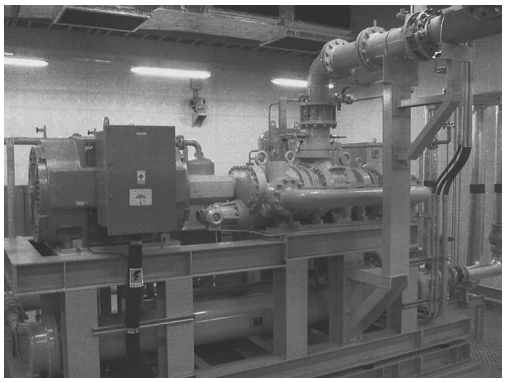

Fig. 4. Main compressor.

*1 Osaka Electro-Communication University
*2 Toshiba Corporation

Table 1. Specifications of STQs.

	STQ1	STQ2	STQ3	STQ4	STQ5
Type	air-core	superferric	←	←	←
Effective length [m]	0.5, 0.8, 0.5	←	←	←	0.5, 1.0, 0.5
Max. field gradient [T/m]	24, 20, 20	14.1 all	←	←	←
Warm bore radii [mm]	90, 120, 120	120 all	←	←	←
Cold mass weight [Ton]	4	8	←	←	←
Hexapole coil	downstream	upstream	downstream	upstream	no

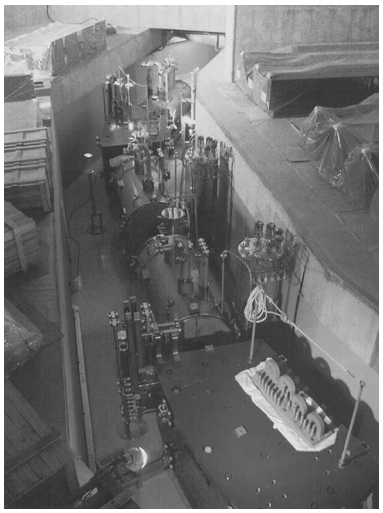

Fig. 5. BigRIPS cave.

STQ1 is an air-core superconducting quadrupole triplet and its maximum field gradients are 24, 20, and 20 T/m.[4] These strong gradients enable us to collect rapidly diverging radioactive isotopes created at the target. The remainder (STQ2-STQ5) are of a superferric type in which quadrupole field distribution is mainly generated by hyperbolic shaped cold iron poles, and the maximum field gradient is 14.1 T/m.[5] In both types, three quadrupoles are rigidly connected to each other and stored in a single LHe vessel and cooled by LHe supplied through the transfer line. The 80 K shields surrounding the LHe vessels are also cooled by gas helium supplied from the cold box, so that no liquid nitrogen shield is used. To cool the current leads, which connect the cold coils and the room-temperature busbar, newly developed a gas-cooled current leads have been used. Toshiba developed the gas-cooled current lead with multiple electrodes in a single cooling gas channel, so no multi channel gas control is required.[6]

Since neutron radiation from the production target and the beam dump, installed in the first dipole, is expected to give radiation damage to nearby components, we have carefully selected materials used to built the magnets and cryogenic system. For the coils of superconducting quadrupoles, we use a NbTi superconducting wire with polyester-imide (PEI) insulator. PEI is chosen for the insulation material, since it is less sensitive to radiation than polyvinyl formal enamel (PVF) which is widely used as the insulation material of superconducting wire. In the cryogenic system we have used a radiation-resistant superinsulator (SI) made of aluminized polyimide film and an aramid fiber net these materials are considered to be less sensitive to radiation damage than polyester (PET) sheets and nets, which are widely used for SI. The radiation-resistant SI is used in the cryostats of STQ1, STQ2, and STQ3, part of the transfer line, namely, the U-tubes, some valve boxes, and, a part of the main transfer tubes.

In addition to the radiation damage, a large flux of neutron radiation causes significant heat loads to the cold mass of the STQ1 and STQ2 cryostats. We have designed our cryogenic system with extra cooling capacity in order to cope with radiation heat loads.[2] Furthermore, a heater system controlled by the LHe level in the cryostats is installed in each STQ. The maximum heater powers of each cryostat are 100 W for STQ1 and STQ2 and 20 W for STQ3, STQ4, and STQ5. This heater system ensures stable operation of the cold box and the compressor.

The license required to operate our cryogenic system was issued in October 2004 by the Saitama municipal goverment. The first cool-down operation of the total cryogenic system began in October. After 10 days of a purification run, about 20 days were required for precooling and about 10 days to fill LHe into all the STQ cryostats. Measurements of extra-cooling capacity, heat loads of the each part of cryogenic system, and tests of heater control will be reported in the near future.

References

1) T. Kubo: Nucl. Instrum. Methods Phys. Res. B **204**, 97 (2003).
2) T. Kubo et al.: RIKEN Accel. Prog. Rep. **36**, 316 (2003).
3) T. Kubo et al.: RIKEN Accel. Prog. Rep. **38**, 287 (2005).
4) K. Kusaka et al.: RIKEN Accel. Prog. Rep. **37**, 297 (2004).
5) T. Hirumachi et al.: IEEE Trans. Appl. Supercond. **10**, 236 (2000); K. Kusaka et al.: IEEE Trans. Appl. Supercond. **14**, 310 (2004).
6) N. Kakutani et al.: RIKEN Accel. Prog. Rep. **37**, 299 (2004).

Design of focal-plane devices for BigRIPS

K. Yoshida, T. Kubo, N. Fukuda, N. Aoi, K. Kusaka, and A. Yoshida

A design has been developed for the focal-plane devices of fragment separator BigRIPS.[1] Figure 1 shows the BigRIPS beam line, consisting of 6 normal conducting dipole magnets and 15 super conducting triplet quadrupole magnets. There are 8 focus along the beam line as shown in Fig. 1. A rectangular vacuum chamber is placed at each focus, which is equipped with devices necessary for beam selections and beam diagnoses as well as a vacuum pump.

The first focus F1 is a dispersive focus where the horizontal position of the beam depends on its magnetic rigidity. Therefore, the slit at F1 can be used to select the magnetic rigidity of secondary beams. Slit blades are designed to use 40-mm-thick copper blocks with water cooling. The material and the thickness of the blades are chosen with the consideration of the stopping power and the weight. While the blades can stop secondary beams with $Z \geq 7$, lighter secondary beams with $Z \leq 6$ may pass through the slit blades. However, these beams are swiped out by the dipole magnet downstream of the separator. After the slit, a wedge-shaped energy degrader is placed to produce mass dispersion. In the design, 4 types of degrader are installed and can be changed without breaking the vacuum of the F1 chamber. Two of these types have the mechanism for adjusting the wedge angle. The required change in wedge angle is accomplished by the combination of the rotation and the horizontal shift of the wedge in the following manner. The rotation of the wedge leads to the changes in angle and thickness, while the horizontal shift compensates the change in thickness. Two Joker slits, which stop a part of the beam within the acceptance of the separator, are also placed in order to prevent the mixture of charge states of primary beams entering to the downstream of the separator. Two position-sensitive parallel plate avalanche counters (PPACs)[2] are provided to observe the position and angular distributions of the beams at F1.

The second focus F2 is an achromatic focus where the position of the beam does not depend on the momentum of the secondary beam. With the help of the

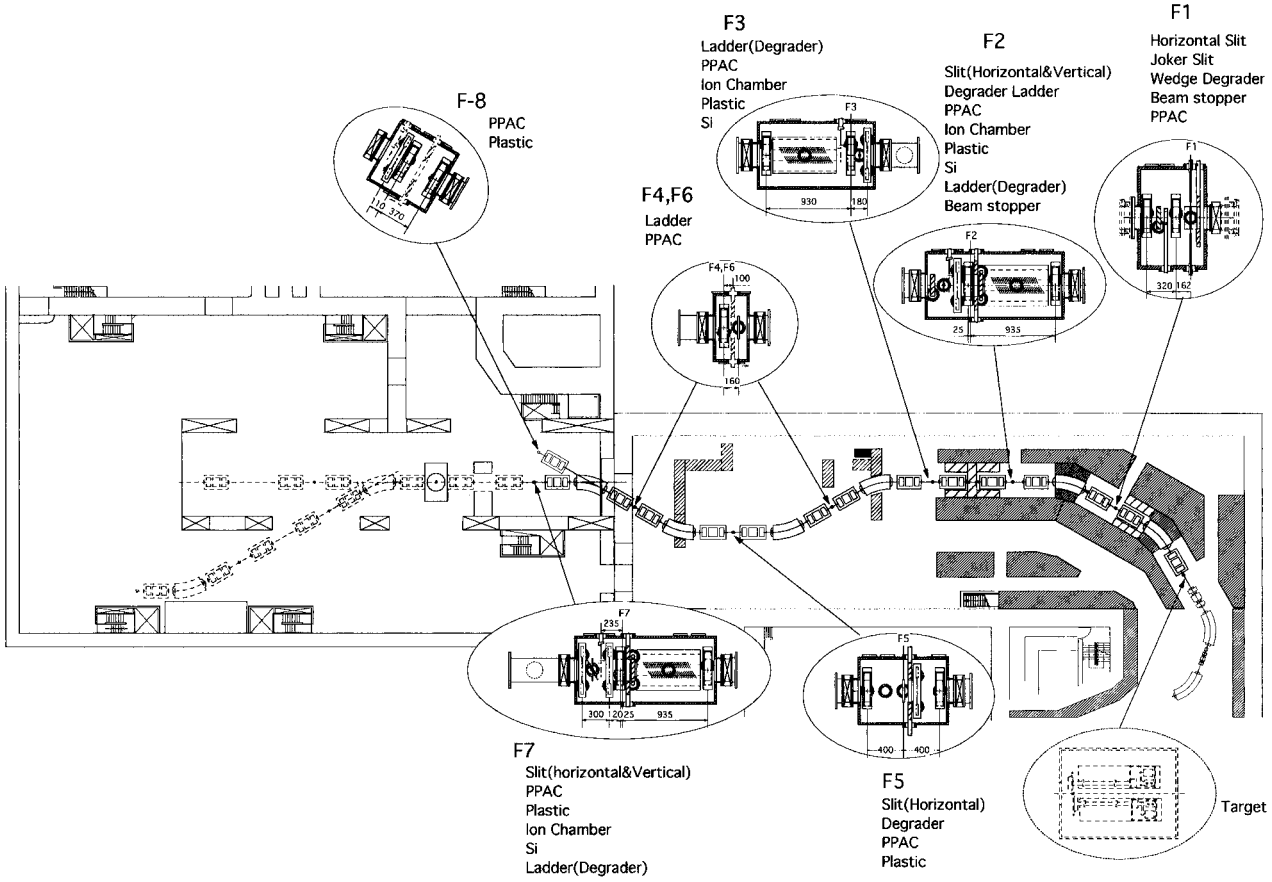

Fig. 1. Focal-plane devices of BigRIPS separator.

wedge degrader at F1, isotope separation is attained at F2. The slits and detectors in the F2 chamber are respectively used for the isotope selection and rough identification of the beam species. The two PPACs installed in the F2 chamber monitor the beam position and angle. The ion chamber (IC)[3] and Si detector are used to measure the energy loss of the beam, which is related to Z of the secondary beam. The plastic scintillator (PL) gives the beam arrival time. From this beam arrival time, the time of flight (TOF) of the beam between the production target and F2 is obtained together with the rf signal of the accelerator. Since the TOF is related to A of the beam, the identification of the beam isotope is accomplished using the abovementioned detectors. A beam stopper is also placed in the F2 chamber to stop the beam when we need to access the downstream of the BigRIPS.

The section of the BigRIPS between the third focus F3 to the seventh focus F7 is used for beam tagging. Secondary beam species and their momentum are measured in an event-by-event mode. The positions and angles of the beam are measured using the PPACs in the F3, F5, and F7 chambers. Since the F5 is a dispersive focus, the position of the beam at F5 corresponds to the momentum of the beam with the correction of the position of the beam at F3. The energy loss of the beam is measured using the IC in the F3 or F7 chamber. The IC has been specifically developed to handle a high beam rate.[3] The TOF of the beam is obtained using the PLs in the F3 and F7 chambers. The precise measurement of TOF with the correction of the flight pass difference due to the position, angle and momentum of the beam makes it possible to identify the Z, A, and charge state q of the beam species when A/q is not close to an integer number.[1] The PPACs in the F4 and F6 chambers are used to check the beam position. The slit and the degrader in the F5 chamber can be used for the second-stage isotope selection. The ladders in the F3, F4, and F6 chamber can be used to mount the collimator. The degrader ladder in the F7 chamber can be rotated and used for the energy adjustment of the secondary beam.

The eighth focus F8 is provided for experiments using dispersive secondary beams. PL for TOF measurement and PPACs for position monitoring are installed in the F8 chamber.

Based on the above conceptual design, the mechanical design and fabrications of these chambers and devices are now in progress, and their installation will be performed in 2005.

References

1) T. Kubo: Nucl. Instrum. Methods Phys. Res. B **204**, 97 (2003).
2) H. Kumagai et al: Nucl. Instrum. Methods Phys. Res. A **470**, 562 (2001).
3) K. Kimura et al.: Nucl. Instrum. Methods Phys. Res. A **538**, 608 (2005).

Laser-beam testing of prototype swirl-tube beam dump for BigRIPS separator

Y. Mizoi,[*1] N. Fukuda, T. Kubo, K. Yoshida, K. Kusaka, A. Yoshida, N. Kakutani,[*2] T. Okuyama,[*2] and K. Sato[*2]

We have performed a laser-beam irradiation test for the prototype beam dump, and confirmed that the present design of the beam dump appeared to have a sufficient ability to cool the 100-kW beam heat expected at the RIBF.

Details of a prototype of the beam dump are described in Ref. 1. A test measurement using a CO_2 laser-beam was performed at Toshiba Co. Ltd.

We measured the change in temperature at the surface of a sample piece, on which carbon powder was sprayed and the laser-beam was subseqently irradiated. Since we know the specific heat capacity, the density and the volume of the sample, we can estimate the absorbed heat under adiabatic conditions. Although this measurement was performed in atmosphere, it is well known that the adiabatic approximation is very reliable for estimating the absorbed power.

The laser-beam spot size was measured in two ways; measurement of the size of a melted hole on a Lucite surface and direct measurement using a laser-power monitoring device. The spot sizes obtained by these measurements were both approximately 4 mm in diameter.

A water pump was tuned so that the water flowed at the required velocity. Water pressure was estimated by the relationship between the pressure and the flow, which is a characteristic of the pump. The laser-beam irradiation and the temperature were measured using an IR camera and a thermocouple, which was soldered at a distance of 6 mm from the center of the beam spot. The temperature was measured by changing the water flow velocity and the laser power. The water velocity was changed to 8, 10 and 12 m/s, and the laser power was also changed to 0.5, 1.0, 1.3 and 1.5 kW for each water velocity.

Figure 1 shows the thermograph image obtained under the condition of a water velocity of 12 m/s and a laser power of 1.5 kW which corresponds to a heat density of about 70 MW/m^2. The maximum temperature on the tube surface was about 360°C. Figure 2 shows the result of the ANSYS calculation, which can reproduce the temperature distribution shown in Fig. 1. The detailed analyses are now in progress.

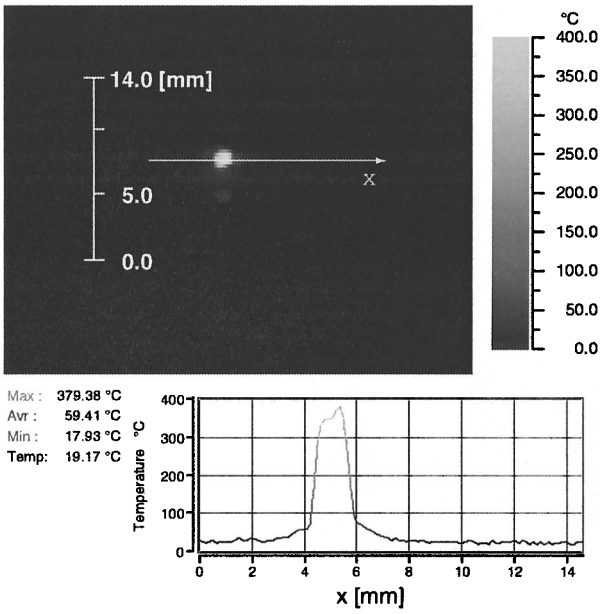

Fig. 1. Thermograph image obtained under the condition of water velocity of 12 m/s and laser power of 1.5 kW.

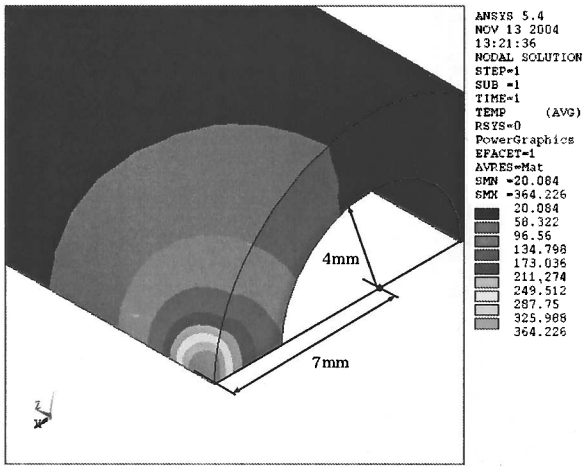

Fig. 2. Result of the ANSYS calculation.

Reference

1) Y. Mizoi et al.: RIKEN Accel. Prog. Rep. **36**, 318 (2003).

*1 Osaka Electro-Communication University
*2 Toshiba Corporation

Development of production target for BigRIPS separator

A. Yoshida, Y. Mizoi, Y. Takahashi, T. Kubo, K. Yoshida, and K. Kusaka

A conceptual design of the water-cooled rotating target system for the projectile fragment separator (BigRIPS) is investigated (Fig. 1). To facilitate the maintenance of the target system in a high radiation environment, an all-in-one structure is considered. That is, two sets of rotating target mechanics and other beam diagnostic detectors, such as a beam viewer, a Faraday cup and a beam profile monitor, are planned to be mounted on one vacuum flange. Each set of the target mechanics slides perpendicular to the beam axis to change the effective target thickness. For maintenance, it is planned that the all-in-one flange will be removed using a remote-controlled handling transportation system.

A part of a mockup for the target system was constructed (Fig. 2) on the basis of the design studies of this target system.[1–4] A rotating target wheel with a diameter of 30 cm and a maximum rotation speed of 1krpm was applied, which are acceptable target parameters even for the severest operating condition of a ^{238}U primary beam with an energy of 350 MeV/nucleon and an intensity of 1 particle μA. A sample target wheel was mounted on a water-cooled disk. Cooling water

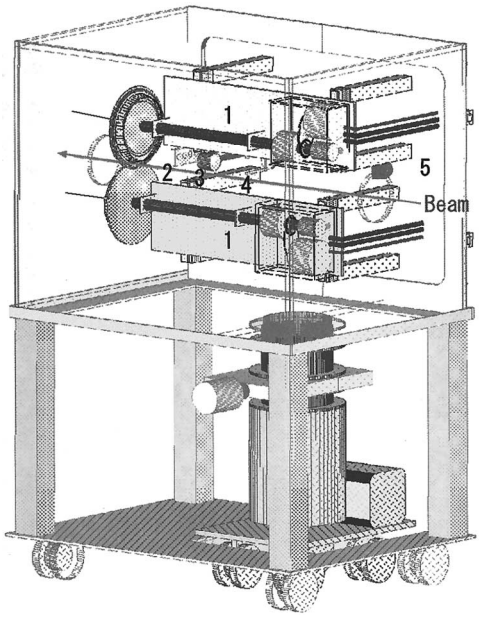

Fig. 1. A conceptual design of the target chamber. Two sets of rotating target mechanics (1), a beam viewer (2), a Faraday cup (3) and a beam profile monitor (4) are planned to be mounted on one vacuum flange (5).

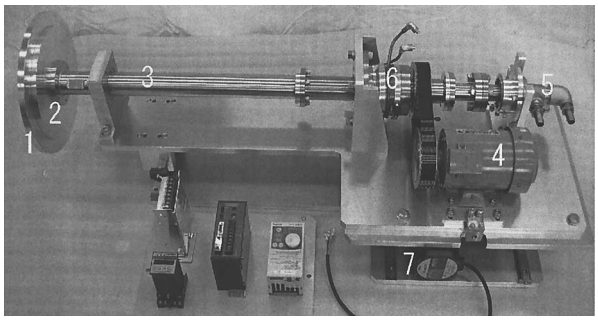

Fig. 2. Mockup of the target system. A sample target wheel (1) and a water-cooled disk (2) connected to a double-piped shaft (3) were rotated using a motor (4). The motor, a rotary joint (5) and a ferromagnetic feedthrough (6) are planned to be placed in a small vacuum tight box. All the target mechanics can slide perpendicular to the beam axis using a vacuum motor (7).

was introduced in to the disk through a double-piped shaft. The wheel and the disk were rotated using a motor. This motor and the rotary joint used for the cooling-water inlet are planned to be placed in a small vacuum tight box, and the ferromagnetic feedthrough used here isolates the vacuum region. The length of the double-piped shaft was designed to be 60 cm to satisfy the radiation hardness of the ferromagnetic feedthrough, which was measured and estimated to be larger than 0.5–1.5 MGy.[5]

A high-speed rotation test was performed under air pressure. The target wheel was smoothly rotated at a speed of 1 krpm and its oscillation was as small as $\pm$0.5 mm in the radial direction. In the next step of this mockup test, the above-mentioned small vacuum tight box will be introduced and an endurance test under vacuum pressure will soon be performed.

References

1) A. Yoshida et al.: RIKEN Accel. Prog. Rep. **34**, 188 (2001).
2) A. Yoshida et al.: RIKEN Accel. Prog. Rep. **35**, 152 (2002).
3) A. Yoshida et al.: Nucl. Instrum. Methods Phys. Res. A **521**, 65 (2004).
4) A. Yoshida et al.: RIKEN Accel. Prog. Rep. **37**, 295 (2004).
5) A. Yoshida et al.: Research Report of Laboratory of Nuclear Science, Tohoku University, **36**, 111 (2003).

Design of RI-beam delivery line and zero-degree recoil separator

Y. Mizoi,[*1] T. Kubo, H. Sakurai,[*2] K. Kusaka, K. Yoshida, and A. Yoshida

We have designed an RI-beam delivery line and a zero-degree recoil separator (ZDS) to be located after the BigRIPS separator for the RIBF project in phase I. Figure 1 shows a schematic top view of them. The RI-beam delivery line and ZDS are being built in the experimental hall. Magnetic devices used in the RI-beam delivery line and ZDS are a normal-conducting dipole magnet, and a superconducting triplet-quadrupole magnet with a small refrigerator. The designs of these magnets are same as those of the BigRIPS separator.

There are four experimental ports, denoted as P1 to P4 on the RI-beam delivery line. P1 is placed on a dispersive focal plane, and the others are placed on the double-achromatic focal plane.

The beam line from P2 to P4 is designed to operate not only as the delivery line but also as a double-achromatic spectrometer system for use as a ZDS. The ZDS has the configuration of TQ-D-TQ-TQ-TQ-TQ-D-TQ, where TQ and D denote a triple-quadrupole magnet and a dipole magnet, respectively. The secondary-reaction experiments can be carried out on the P2 port in corporation with the ZDS, and we expect that the ZDS will be used in three modes, a high-resolution mode, a large-acceptance mode, and a dispersive mode, depending on the experimental conditions. A promising experiment for the high-resolution and large-acceptance modes is γ-ray spectroscopic measurement. A secondary target and a γ-ray detector array are installed at P2. The γ rays are measured with a γ-ray detector array by tagging a recoil particle with the ZDS in the high-resolution mode or the large-acceptance mode. A promising experiment for the dispersive mode is secondary-reaction spectroscopy with precise recoil-momentum analysis.

The beam envelopes of the high-resolution mode, the large-acceptance mode, and the dispersive mode are shown in Figs. 2, 3, and 4, respectively. The optical parameters of the different modes are also summarized in Table 1.

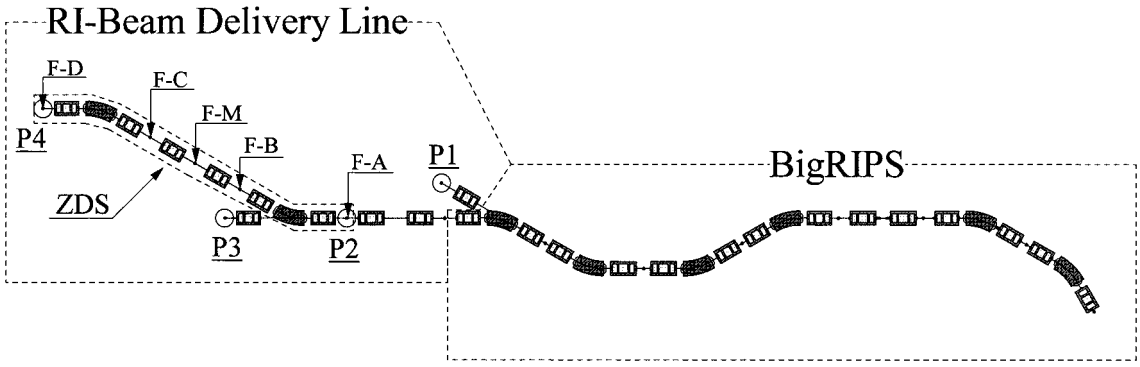

Fig. 1. Schematic top view of BigRIPS separator, RI-beam delivery line and ZDS. There are four experimental ports indicated by P1 to P4. The focal planes of ZDS are indicated by F-A to F-D.

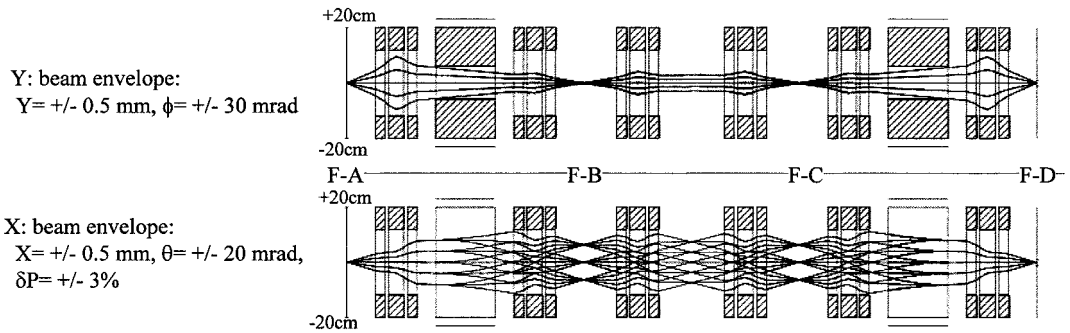

Fig. 2. Beam envelopes of high-resolution mode.

[*1] Osaka Electro-Communication University
[*2] Department of Physics, University of Tokyo

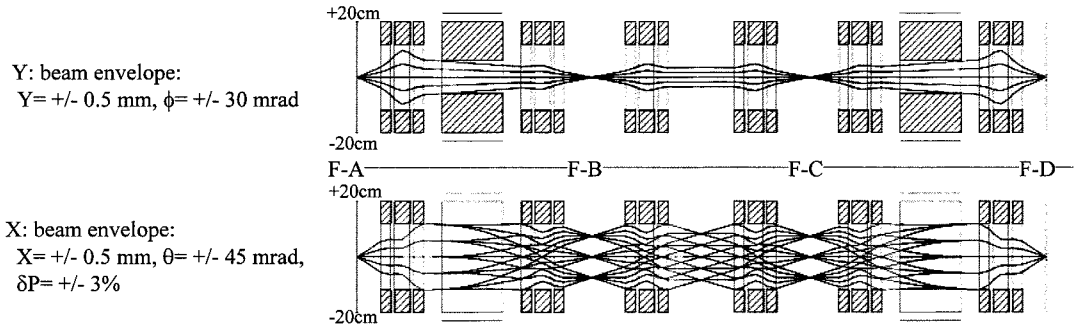

Fig. 3. Beam envelopes of large-acceptance mode.

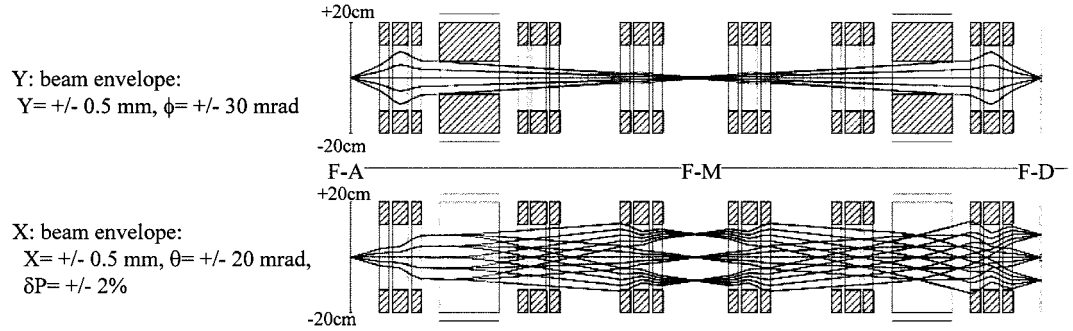

Fig. 4. Beam envelopes of dispersive mode.

Table 1. Optical parameters are listed. The parameters of the high-resolution mode and the large-acceptance mode are summarized in the left-hand table. Those of the dispersive mode are summarized in the right-hand table. F-B, F-D, and F-M denote focal planes indicated in Figs. 2, 3 and 4. x and y denote the horizontal and vertical lengths in meters, respectively. θ and ϕ denote the horizontal and vertical angles in radians, respectively. δp denotes the ratio of momentum spread (dp) to momentum (p), $\delta p = dp/p$.

Plane	Parameter	High resolution	Large acceptance
F-B	$(x\|x)$	−1.00	−2.00
	$(x\|\theta)$	0.00	0.00
	$(x\|\delta p)$	2.12	2.48
	$(\theta\|x)$	0.00	0.23
	$(\theta\|\theta)$	−1.00	−0.50
	$(\theta\|\delta p)$	0.00	0.00
	$(y\|y)$	−2.68	−2.24
	$(y\|\phi)$	0.00	0.00
	$(\phi\|y)$	0.00	0.00
	$(\phi\|\phi)$	−0.37	−0.45
F-D	$(x\|x)$	−1.00	−1.00
	$(x\|\theta)$	0.00	0.00
	$(x\|\delta p)$	0.00	0.00
	$(\theta\|x)$	0.00	0.93
	$(\theta\|\theta)$	−1.00	−1.00
	$(\theta\|\delta p)$	0.00	0.00
	$(y\|y)$	−1.00	−1.00
	$(y\|\phi)$	0	0.00
	$(\phi\|y)$	0	0.00
	$(\phi\|\phi)$	−1.00	−1.00

Plane	Parameter	Dispersive mode
F-M	$(x\|x)$	−2.03
	$(x\|\theta)$	0.00
	$(x\|\delta p)$	4.20
	$(\theta\|x)$	0.00
	$(\theta\|\theta)$	−0.49
	$(\theta\|\delta p)$	0.00
	$(y\|y)$	−5.82
	$(y\|\phi)$	0.00
	$(\phi\|y)$	0.00
	$(\phi\|\phi)$	−0.17
F-D	$(x\|x)$	1.00
	$(x\|\theta)$	0.00
	$(x\|\delta p)$	−4.13
	$(\theta\|x)$	0.00
	$(\theta\|\theta)$	1.00
	$(\theta\|\delta p)$	0.00
	$(y\|y)$	1.00
	$(y\|\phi)$	0
	$(\phi\|y)$	0
	$(\phi\|\phi)$	1.00

The construction of the RI-beam delivery line and ZDS will be started in 2005, and they will be ready for experiments by the end of FY 2006.

Rf cavity with parallel-plate radial lines

T. Koseki and M. Izawa*

For modern electron storage rings such as high-luminosity colliders and high-brilliance synchrotron radiation sources, the suppression of the coupled-bunch instability due to higher-order modes (HOMs) in rf cavities is one of the most important issues for achieving a high beam current limit. In this paper, we present a new HOM damper for rf cavities in electron storage rings.

The design of the new HOM damper is based on the rf cavity of the Photon Factory (PF) storage ring in KEK.[1–3] The PF cavity has beam ducts of silicon carbide (SiC) that are 140 mm in diameter. All HOMs having a frequency higher than the cutoff frequency of the 140 mmϕ duct (1.64 GHz and 1.26 GHz for TM01 and TE11 modes, respectively) are dissipated by the SiC duct.

The HOM damper, proposed in this paper, employs parallel-plate radial transmission lines on the beam duct instead of the SiC duct. Figure 1 shows a schematic view of the cavity with a radial line. The outer end of the radial line is terminated by the sintered SiC, the same material as the beam duct absorber of the PF cavity. The HOMs, extracted from the center of the cavity through the beam duct, couple the radial waves in the radial line and are dissipated in the SiC absorber. The design of the center part of the cavity is the same as that of the present PF cavity, and the property of the accelerating mode is not changed.

The choke mode cavity developed in KEK also employs the radial transmission line to extract HOMs.[4] Since the lowest radial transmission line mode does not have a cutoff frequency, the radial line requires a choke structure to block the accelerating mode. However, the cavity shown in Fig. 1 does not need any filters in the radial line because the frequency of the accelerating mode is sufficiently less than the 140 mmϕ cutoff frequency.

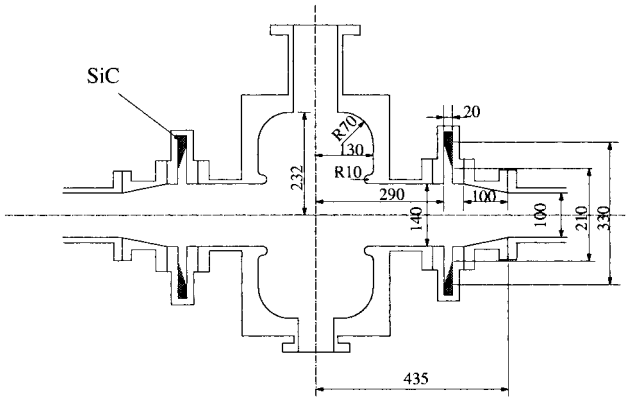

Fig. 1. The damped cavity with radial line damper.

The calculated characteristics of the accelerating mode and HOMs are summarized in Table 1. R_s and R_t in the table are the longitudinal and transverse impedances, respectively. The resistivity of the SiC absorber was assumed to be 20 Ω cm in this calculation. As shown in this table, HOMs with a frequency higher than the cutoff frequency of the 140 mm ϕ duct are dissipated well. Only a certain number of HOMs, whose frequencies are lower than the cutoff frequency, are trapped in the cavity and continue to have a high impedance. To avoid instabilities due to the "trapped modes", the frequency-shift method using two fixed tuners should be applied, as in the case of the present PF cavity.[2] The fixed tuner is a blank flange, which has an appropriately chosen block length to adjust the trapped-mode frequencies so that they do not coincide with the coupled-bunch mode frequencies. Since the frequency-shift method is effective for the modes with a high Q-value, the radial line damper is positioned keeping the appropriate distance from the center of the cavity so as not to dampen the Q-values of trapped modes halfway. To maintain the high Q-value of the TM111-like mode (transverse 0.99 GHz), it is preferable that the radial line damper is not positioned closer to the center of the cavity than the position shown in Fig. 1.

One of the notable features of the cavity using the radial line damper is its short length in the longitudinal direction. For the cavity shown in Fig. 1, the total length between the taper transition flanges is 870 mm, which is 490 mm smaller than that of the original PF cavity.

In order to estimate the wall heating in the radial line damper, we calculated the longitudinal wake field induced by a Gaussian bunched beam using the time domain solver of MAFIA. The loss parameter k is defined by the total energy loss ΔU and total charge in the bunch Q as follows:[5]

$$k = \frac{\Delta U}{Q^2} = \frac{1}{Q}\int_{-\infty}^{\infty} \rho(s)W(s)ds,$$

where s is the longitudinal coordinate, $\rho(s)$ is the longitudinal charge distribution of the bunch and $W(s)$ is the longitudinal wake potential. The bunch length dependence of k is shown in Fig. 2. Power loss in the radial line damper is not so serious and heat problems due to large bunch current can be easily avoided using the simple water-cooling system in the same manner as the SiC duct of the present PF cavity.[6]

* High Energy Accelerator Research Organization (KEK)

Table 1. Summary of accelerating mode and HOMs of the cavity.

Longitudinal modes			Transverse modes		
Frequency [GHz]	Q	R_s [kΩ]	Frequency [GHz]	Q	R_t [kΩ/m]
0.5005	41958	7394.20	0.7059	45191	339.08
0.7941	36514	1899.63	0.7924	49024	13491.64
1.0567	4	0.21	0.9906	21981	9910.39
1.0567	4	0.03	1.1915	309	13.08
1.1625	38439	0.95	1.2242	210	2.02
1.3121	56659	525.66	1.2611	5	1.75
1.3725	27859	245.59	1.2612	6	0.01
1.7022	88	0.03	1.2898	40	2.83
1.7195	50	0.03	1.3319	65	0.49
1.7617	74	0.53	1.3695	349	1.77
1.7916	109	0.11	1.4581	1264	30.22
1.8158	89	0.01	1.5173	942	10.18
1.8808	42	0.05	1.5450	777	2.09
1.9062	56	0.02	1.5781	321	9.83
2.0352	2009	0.24	1.6214	204	0.64
2.0983	794	0.00	1.6999	174	0.11
2.1646	100	0.02	1.7570	451	3.22
2.1718	286	1.07			
2.2267	39	0.00			

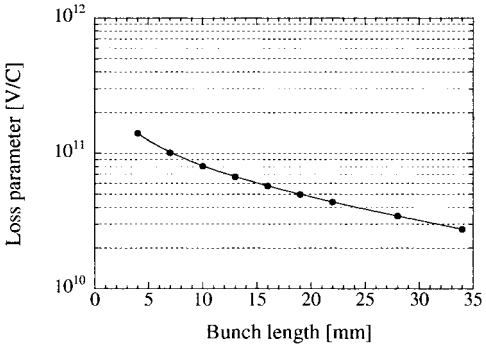

Fig. 2. Bunch length dependence of the loss parameter of the radial line damper.

References

1) T. Koseki, M. Izawa, and Y. Kamiya: Rev. Sci. Instrum. **66**, 1926 (1995).
2) M. Izawa et al.: J. Synchrotron Radiat. **5**, 369 (1998).
3) T. Koseki: RIKEN Accel. Prog. Rep. **37**, 306 (2004).
4) T. Shintake: Jpn. J. Appl. Phys. **31**, L1567 (1992).
5) A. W. Chao: *Physics of Collective Beam Instabilities in High Energy Accelerators* (John Wiley & Sons, New York, 1993).
6) M. Izawa, T. Koseki, Y. Kamiya, and T. Toyomasu: Rev. Sci. Instrum. **66**, 1910 (1995).

High current RFQ linac

M. Okamura, J. Takano,* K. Yamamoto,* T. Hattori,* and N. Hayashizaki*

Since 2001, we have been conducting experiments to verify the direct plasma injection scheme (DPIS) using an existing RFQ in TITech, Tokyo. The obtained maximum current of carbon beam was 9.2 mA, which agreed well with our simulation value.[1] With this achievement, we decided to construct a new RFQ to attain a higher current using the DPIS. We believe this new technique will have great impact on the heavy-ion accelerator field.

To demonstrate the intrinsic performance of the DPIS, the new RFQ was constructed at the Institute for Applied Physics (IAP), Goethe University, Frankfurt. This RFQ was designed to accelerate carbon 4+ and 6+. The target current was set at 100 mA with C^{4+}. The chosen operation frequency was 100 MHz since it is available using an RF amplifier system. The resonant structure is the 4-rod type, which is well established in IAP and suited for this frequency region and low-duty factor operation. It has a reasonably small diameter, and the field distribution is easy to tune. Moreover it is not difficult to replace vanes in future modifications. The total vane length was set at 2 m considering future modifications however, the output beam energy is 100 keV/u, which is limited by a radiation safety regulation. The beam is accelerated up to 100 keV/u within the first 1.42 m section and then transported through nonmodulated vanes to the end of the RFQ. In the nonmodulated section, the accelerated beam is completely debunched and this will reduce the space charge effect in an analyzing section, which will be constructed in the near future. The input energy of the beam is a very important value, because in DPIS a high-voltage-biased slit is located at the entrance of the RFQ and might cause discharges. Part of the very high intensity plasma is guided through the several mm diameter hole in the biased slit and enter the RFQ. To minimize the beam size emitted from the hole, the slit needs to be close to the vanes. At the same time, we have to prevent sparking and an effect on the resonant condition of the cavity. We adopted 60 kV as the total input beam energy based on our experience. In case of C^{4+}, the value corresponds to 20 keV/u as the injection energy. The position of the slit can be adjusted. A picture and summarized design parameters of the RFQ are shown in Fig. 1 and Table 1, respectively. The vane parameters of the RFQ were designed to maximize beam acceptance. To confirm the particle dynamics in the RFQ, PteqHI was used. This code was developed by one of authors and can simulate multiple charge states simultaneously.

We have been investigating two types of laser system for plasma production. Currently a CO_2 laser is used for our experiment. The maximum output energy of the CO_2 laser is 8 J. However, the emitted energy to the carbon target was measured to be 1.2 J with a pulse width of 85 ns (FWMS). Our plasma measurement experiment showed that, under this condition of the laser system, C^{4+} (50%) is mainly produced and the rest of the ions are C^{5+} (35%) and C^{3+} (15%). We can assume that these three-charged state ions are injected to the RFQ. We also measured the property of the plasma induced by a Nd-YAG laser system. This laser has an output energy of 300 mJ and can produce mainly C^{6+} (50%).[2] This laser system is now planned to be used in the next DPIS experiment. The measured result also shows that the Nd-YAG laser plasma can provide sufficient beam current to the RFQ.

Ion sources parts, including the plasma production solid target and the space which will be filled by the ablated plasma, have to be isolated electrically and maintained at a high voltage corresponding to the beam injection energy of the RFQ. Sixty kilovolts is applied to

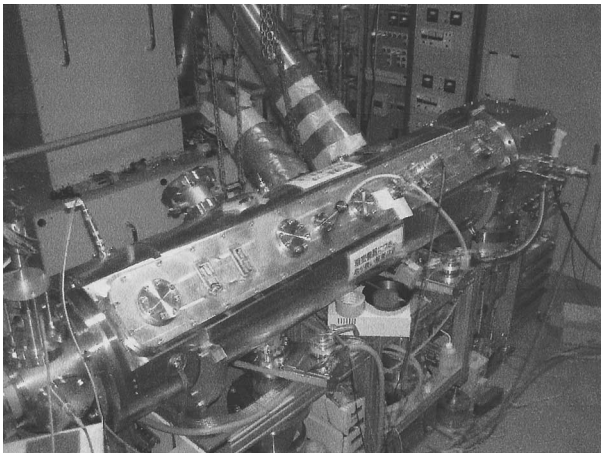

Fig. 1. 100 MHz RFQ. The cube box behind the RFQ is the ion source.

Table 1. Basic design parameters of the RFQ.

Frequency	100 MHz
Total length	2.0 m
Modulated vane length	1.42 m
Limit of intervane voltage	120 kV
I_{out} at 100 mA C^{4+} in	76 mA
Saturated I_{out}, C^{4+} only	155 mA
I_{in} for saturated I_{out}	$\sim$ 300 mA
Acceptance	0.14 cm·rad
Aperture	0.655 cm

* Tokyo Institute of Technology

the ion source part which is too high to insulate in an atmosphere. Therefore, high-voltage parts are located in a vacuum. The high-voltage connector is at the bottom of the TEFLON sleeve that is 30 cm long, and a cable from the high-voltage power supply is inserted to the sleeve. The high-voltage parts are not shown from outside of the vacuum box. As we mentioned above, all the energy fed to the plasma is provided by laser shot. This means that both a large terminal stage and a safety fence are not required and the ion source part can be made extremely compact and simple. Behind the vacuum box, the laser beam is injected through double NaCl windows and guided to the high voltage region. A concave mirror reflects and focuses the laser beam on to the carbon target. Plasma is then induced and expanded towards the RFQ. Finally, the expanding plasma that can be accommodated in the high-voltage slit is injected to the RFQ.

We obtained the first beam in June 2004 after overcoming the sparking problem. The measured peak current reached 30 mA with a slit having 4-mm-diameter hole. We optimized various parameters for the C^{4+} beam and obtained a maximum peak current of more than 50 mA. Under this condition, the inner diameter of the slit is 6 mm. A typical beam shape is shown in Fig. 2. This signal was from a Faraday cup immediately after the RFQ. The applied repetition rate was 1 Hz, which was limited by the laser system.

The input current and emittance have not been measured. At the C^{4+} peak, a tracking analysis of beam extraction indicate that with a 4-mm-diameter extraction slit, ∼100 mA with an emittance of ∼0.45 cm·rad enters the RFQ. The RFQ simulation then showed that ∼40% is transmitted. With a 6-mm-diameter extraction slit, ∼200 mA with an emittance of ∼0.6 cm·rad enters the RFQ and ∼25% is transmitted. In this regime, output current saturation is expected.

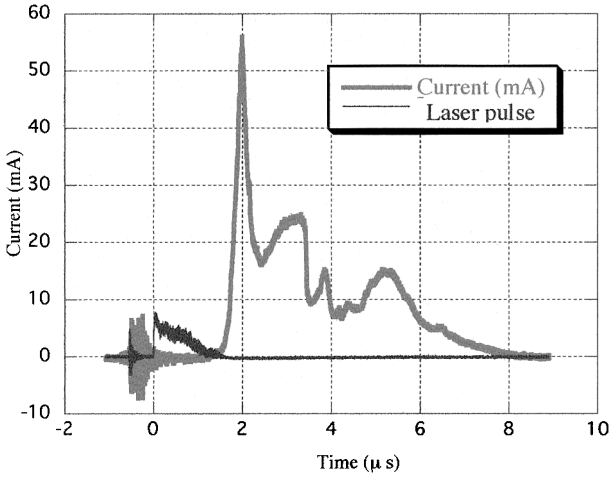

Fig. 2. Accelerated beam out of RFQ. The laser pulse is drawn using arbitrary unit.

References

1) M. Okamura et al.: Laser Part. Beams **20**, 451 (2002).
2) H. Kashiwagi et al.: Rev. Sci. Instrum. **75**, 1569 (2004).

Proof examination of alternating-phase focusing

K. Yamamoto,* M. Okamura, T. Hattori,* N. Hayashizaki, and J. Takano

Recently, cancer therapy has been one of the major applications of hadron accelerators. In a typical conventional design, a chain of linacs occupies a large area in cancer-therapy facilities. For example, an injector of HIMAC (heavy ion medical accelerator in chiba) consisting of an RFQ linac and an Alvarez linac accelerates C^{4+} ions up to 6 MeV/u; the length is more than 30 m.[1] Particularly in such a medical accelerator complex, not only machine performance, but also cost performance is very important. Therefore, a compact and reliable linac has been highly required. For this purpose, we designed an Interdigital-H mode linac with alternating-phase focusing as a high-efficiency injector. The IH structure has an advantage of a high shunt impedance in the low-energy region. The APF has not yet successfully accelerated beams, although it has been proposed for the design of short low-beta structures due to the elimination of the external transverse focusing by drift-tube quadrupoles.[2–5]

The basic parameters were determined for O^+ acceleration, which were mainly an injection energy of 10 keV/u, an acceleration energy of 77 keV/u and an operation frequency of 63.3 MHz. For stable operation and efficient acceleration, the electric-field strength in the gaps and the effective acceleration voltage were determined to be twice the Kirpatric limit and 4 MV/m, respectively. On the basis of these conditions, the linac was designed to be 0.53 m in length. The number of cells is 16, which ware determined by the linac length divided by the average cell length. Gap voltage and length was designed as follows, (1) The first gap length was determined to be half of the first cell length. (2) The nth gap voltage distribution was determined to maintain the total acceleration voltage. (3) All of the gap length was determined to be twice the Kilpatric limit of the electric-field strength. On the basis of the above design conditions, we optimized the phase pattern for APF to work effectively using the thin-lens approximation.

Next, we constructed a half-scale cold model to determine the length of an end-ridge tuner to obtain the required electric-field distribution. The measurement was carried out by a perturbation method; a small aluminium ball was placed onto the acceleration axis, and the electric field at this position was obtained by measuring the variation in the frequency. The electric-field distribution was obtained by changing the ball position. The optimum electric-field distribution was obtained at a cut-area length of 150 mm. The result is shown in Fig. 1 and the final parameters are summarized in Table 1. On the basis of these parameters, the beam dynamics was re-calculated.

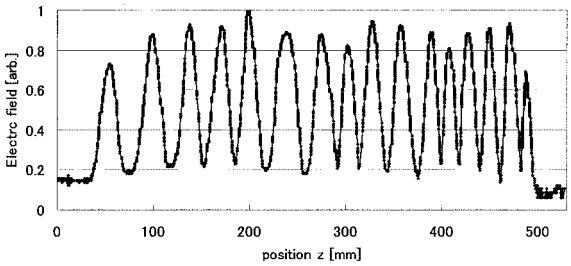

Fig. 1. Measurement results of electric-field distribution of linac.

Table 1. Design parameters of linac.

Q / A	1/16
Input Energy	10.8 keV/u
Output Energy	77.2 keV/u
Frequency	63.3 MHz
Number of cells	16
Cavity length	530 mm
Diameter	630 mm
Transverce Acceptance	88π mm·mrad
Phase Acceptance	30 degree
Gap voltage	74–145 kV

The cavity was processed within an accuracy of $\pm$0.1 mm. After plating Cu on the cavity, the drift tubes and the length of each gap were aligned at an accuracy of $\pm$1% (Fig. 2). The vacuum was checked after assembling the side plates. The frequency and Q-values were 63.32 MHz and approximately 15370, respectively.

An acceleration test of a proton beam was carried out in the test bench as shown in Fig. 3. A PIG ion source with an extraction voltage of 10.8 kV was utilized to supply protons. For a low-energy beam transport, a solenoid lens was prepared. Acceleration energy after the IH linac was analyzed by a bending mag-

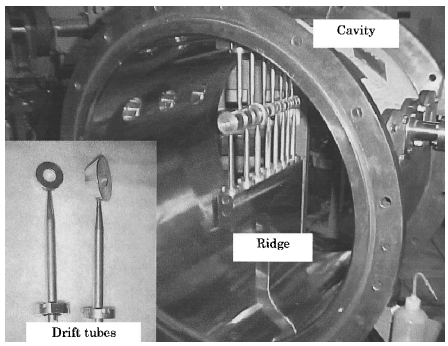

Fig. 2. Photograph of IH linac with APF.

* Tokyo Institute of Technology

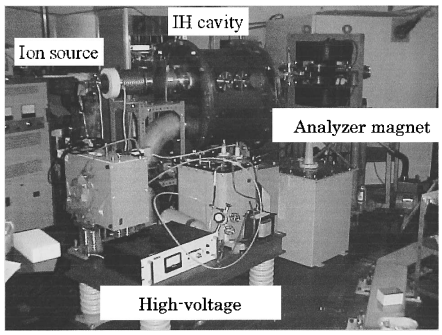

Fig. 3. Photograph of the experimental set-up.

net after focusing by an electric-quadrupole lens. Slits were placed after the magnet to improve the resolution (Fig. 4).

Figure 5 shows the energy spectrum of accelerated ions. The figure clearly shows that the protons were accelerated up to the design energy. During this measurement, the focusing-lens strength was adjusted so that the accelerated-ion current would be maximum at the Faraday cup (FCN3) after the bending magnet. Since the slit in front of the FCN3 was fully opened, the signal widths in the energy spectrum do not indicate energy dispersal. Figure 6 shows accelerated energy and ion current as a function of RF power. The gap voltage, obtained from the measured Q-value, corresponds to an RF power of 45 W. The acceleration efficiency of the IH linac was approximately 6%. It should be noted that the PIG ion source supplied beams under DC operation whereas the phase acceptance of the linac was 30 degrees. By pulsing the beam with a buncher so that the beam-pulse length matches the acceptance, the efficiency is expected to be eventually approximately 70%. Moreover, by improving the transverse matching, the acceleration efficiency is estimated to be improved up to 8% even during the DC operation of the PIG ion source.

A proof test of the IH linac with APF was successfully completed, which is the first acceleration of a beam by using the APF principle in the world. The

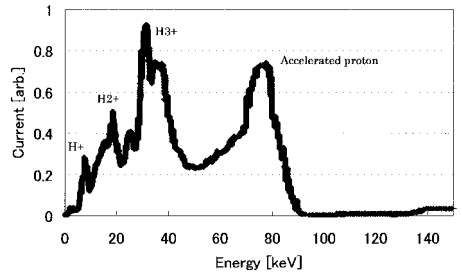

Fig. 5. Energy spectrum of accelerated beam. The accelerated proton is shown at an energy of 77 keV.

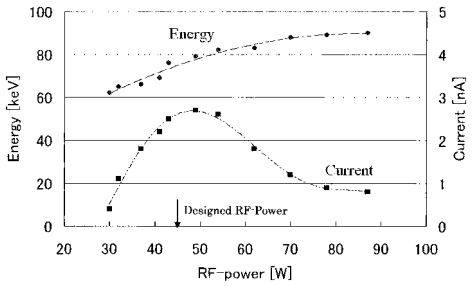

Fig. 6. Current and energy of accelerated proton beam as function of RF-power.

results of the proof examination using low-current proton beams are in good agreement with the numerical prediction. In order to evaluate the performance of the IH linac with APF, however, high-current and high-energy acceleration tests are highly required. We are planning to accelerate C^{4+} ions up to a several MeV/u with a several mA using a new linac and a new ECR ion source.

References

1) S. Yamada et al.: Proc. APAC98, p.885 (1998).
2) T. Hattori et al.: Nucl. Instrum. Methods Phys. Res. B **161**, 1174 (2000).
3) N. Hayashizaki et al.: Rev. Sci. Instrum. **71**, 990 (2000).
4) V. V. Kushin et al.: Proc. PAC 1993, p.1798 (1993).
5) D. A. Swenson: Part. Accel. **7**, 61 (1976).

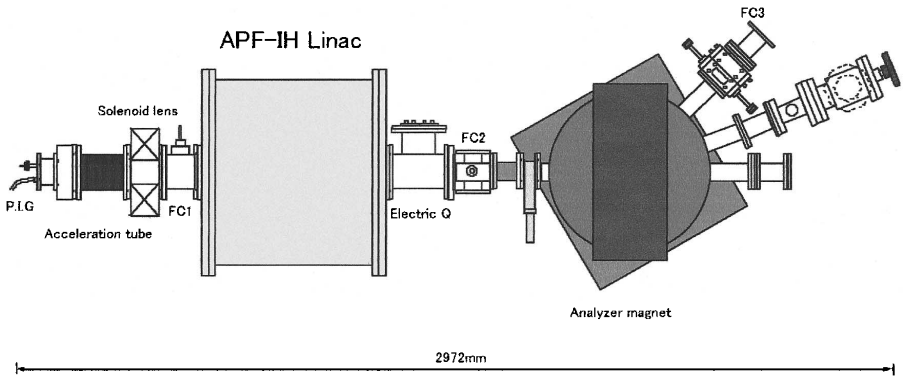

Fig. 4. Layout of experimental setup.

Inductance calculation of helical conductors†

T. Tominaka

The self- and mutual inductances for infinitely long coaxial helical conductors are investigated over the entire available range, from solenoids with an infinitesimal pitch length to straight conductors with an infinite pitch length. The principal terms, apart from the logarithmically divergent term due to the infinite length of the self- and mutual inductances, are rigorously obtained, using the analytical expressions for the vector potential of a single helical thin conductor.[1)]

Generally, the self- and mutual inductances of infinitely long conductors can be described with the double integrals of Neumann's formula in the following form:[2)]

$$L_{ik} = \frac{\mu_0}{4\pi} \oint_i \oint_k \frac{\vec{dl}_i \cdot \vec{dl}_k}{r_{ik}} = \frac{1}{I_i} \oint_k \vec{A}_i(r,\theta,z) \cdot \vec{dl}_k, \tag{1}$$

where L_{ik} $(= M_{ik})$ is the mutual inductance between the ith and kth conductors, L_{ii} is the self-inductance, and $A_i(r,\theta,z)$ is the divergence-free vector potential due to an infinitely long helical conductor, which is expressed in the form of the infinite series of modified Bessel functions of the first and second kinds, $I_n(nkr)$, $K_n(nkr)$, where k $(= 2\pi/L_p)$ is the pitch parameter, and L_p is the twist pitch length.

The self-inductance per unit length along the central axis (z axis), L/l, of a long solenoid or a single helical thin conductor, located at $(r_1, \varphi_1, z = 0)$ of the circular cylindrical coordinate system with a pitch length L_1 $(= 2\pi/k_1)$, as shown in Fig. 1, can be calculated as follows:

$$\begin{aligned}\frac{L}{l} = &-\frac{\mu_0}{2\pi}\ln r_1 + \frac{\mu_0}{\pi}\sum_{n=1}^{\infty} K_n(nk_1r_1)I_n(nk_1r_1) \\ &+ \frac{\mu_0}{2L_1}k_1r_1^2 + \frac{\mu_0 k_1 r_1^2}{L_1}\sum_{n=1}^{\infty}\{K_{n+1}(nk_1r_1) \\ &\cdot I_{n+1}(nk_1r_1) + K_{n-1}(nk_1r_1)I_{n-1}(nk_1r_1)\}. \end{aligned} \tag{2}$$

In the limit of $k_1 \to \infty$ (or $L_1 \to 0$), the self-inductance per unit length coincides with the well-known result calculated with the assumption of a uniform interior magnetic field.

$$\lim_{k_1\to\infty} \frac{L}{l} \approx \frac{\mu_0}{2L_1}k_1r_1^2 = \frac{\mu_0}{L_1^2}\pi r_1^2 = \mu_0 n_1^2 \pi r_1^2, \tag{3}$$

where n_1 $(= 1/L_1)$ is the number of turns per unit length and πr_1^2 is the cross-sectional area of the solenoid. The self-inductance of Eq. (3) does not contain the infinite contribution of the exterior azimuthal field. On the other hand, in another limit of $k_1 \to 0$ (or $L_1 \to \infty$), the self-inductance does not converge, consistently with the inductance of a straight thin conductor. Therefore, we cannot neglect the cross section of the helical conductor, at least for the inductance calculation near the limit of $k_1 \to 0$ (or $L_1 \to \infty$) corresponding to a straight conductor.

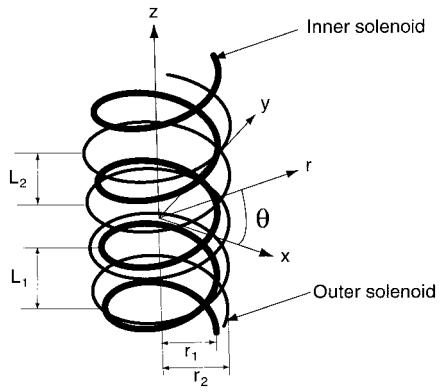

Fig. 1. Schematic view of two coaxial solenoids.

The calculated results for the self-inductance of a helical thin conductor with the winding radius of 10 mm are shown in Fig. 2. The self-inductance calculated using the analytical expression of Eq. (2) up to the first one hundred terms ($n = 100$) is shown as the solid line, and the conventional expression of Eq. (3) is shown as the dashed line. In Fig. 2, it is clearly shown that the conventional approximate expression is applicable up to approximately where the pitch length is equal to the winding radius.

In order to calculate the accurate self-inductance for a helical conductor, including that at the limit of $k \to 0$ (or $L_p \to \infty$), it is necessary to take into account the finite cross section of the helical conductor.

The calculated results from a numerical surface integration for the self-inductance of a helical conductor

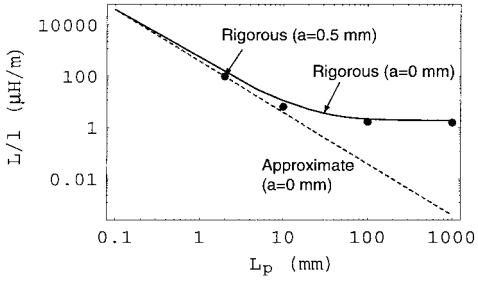

Fig. 2. Self-inductance per unit length for infinitely long helical conductor with winding radius of 10 mm, and conductor radii of infinitesimally thin and 0.5 mm.

† Condensed from the article in Supercond. Sci. Technol. **18**, 214 (2005)

with the radius of 0.5 mm and the winding radius of 10 mm are shown as dots in Fig. 2. In this calculation, the analytical expressions up to the first fifty terms ($n = 50$) are taken into account. When the radius of the helical conductor decreases, more terms within the analytical expression of the infinite series are needed.

The mutual inductance per unit length, M/l of the secondary solenoid, located at $(r_2, \varphi_2, z = 0)$, with a pitch length L_2 $(= 2\pi/k_2)$, due to the first solenoid at $(r_1, \varphi_1, z = 0)$ with L_1 $(= 2\pi/k_1)$, as shown in Fig. 1, can also be calculated. Specifically, for case of $k_1 = k_2 = k$, and $r_1 < r_2$, the following expression of mutual inductance is obtained:

$$\begin{aligned}\frac{M}{l} &= -\frac{\mu_0}{2\pi}\ln r_2 + \frac{\mu_0}{\pi}\sum_{n=1}^{\infty} I_n(nkr_1)K_n(nkr_2) \\ &\quad \cdot \cos[n(\varphi_2 - \varphi_1)] + \frac{\mu_0}{4\pi}k^2 r_1^2 + \frac{\mu_0}{2\pi}k^2 r_1 r_2 \\ &\quad \cdot \sum_{n=1}^{\infty}\{I_{n+1}(nkr_1)K_{n+1}(nkr_2) \\ &\quad + I_{n-1}(nkr_1)K_{n-1}(nkr_2)\}\cos[n(\varphi_2 - \varphi_1)]. \quad (4)\end{aligned}$$

In the limit of $k_1, k_2 \to \infty$ (or $L_1, L_2 \to 0$), it is shown that the mutual inductance per unit length coincides with the well-known result

$$\begin{aligned}\lim_{k_1,k_2\to\infty}\frac{M}{l} &\approx \frac{\mu_0}{4\pi}k_1\frac{r_1^2}{r_2}\frac{2\pi r_2}{L_2} \\ &= \frac{\mu_0}{2L_2}k_1 r_1^2 = \frac{\mu_0}{L_1 L_2}\pi r_1^2 = \mu_0 n_1 n_2 \pi r_1^2. \quad (5)\end{aligned}$$

where n_2 $(= 1/L_2)$ is the number of turns per unit length of the secondary solenoid and πr_1^2 is the cross-sectional area of the inner solenoid. On the other hand, in another limit of $k_1, k_2 \to 0$ (or $L_1, L_2 \to \infty$), the mutual inductance coincides with that of an infinitely long straight conductor.

The calculated results for the mutual inductance between two coaxial helical thin conductors of $k_1 = k_2 = k$ $(= 2\pi/L_p)$ with the winding radii of 10 mm and 12 mm and the angular difference of $\Delta\varphi = \varphi_2 - \varphi_1 = \pi/6$ are shown in Fig. 3. The mutual inductance calculated using Eq. (4) up to the first one hundred terms ($n = 100$), is shown as the solid line, and the approximated expression of Eq. (5) is also shown as the dashed line. In addition, the calculated results up to the first fifty terms ($n = 50$) for two coaxial solenoids or helical conductors with the radius of 0.5 mm are also shown as dots in Fig. 3.

Furthermore, it is shown that the calculations of the self- and mutual inductances for helical conductors of a twisted bifilar lead and a twisted superconducting multistrand cable are consistent with the magnetic energy calculation.[3,4]

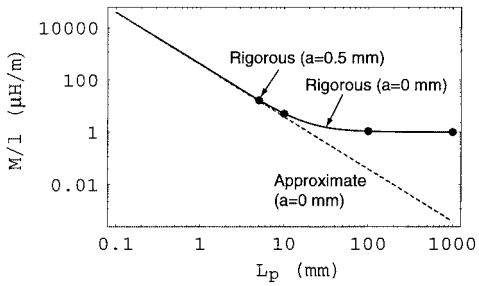

Fig. 3. Mutual inductance per unit length between two coaxial solenoids of the same pitch lengths with winding radii of 10 and 12 mm and the azimuthal angular difference of $\Delta\varphi = \pi/6$, and conductor radii of infinitesimally thin and 0.5 mm.

References

1) T. Tominaka: Nucl. Instrum. Methods Phys. Res. A **523**, 1 (2004).
2) A. Sommerfeld: in *Electrodynamics, Lectures on Theoretical Physics*, Vol. III, (Academic Press, New York, 1952), p. 104.
3) T. Tominaka and Y. Chiba: J. Phys. D **37**, 1592 (2004).
4) T. Tominaka: Supercond. Sci. Technol. **18**, 214 (2005).

Routine work for radiation safety in the ring cyclotron facility

Y. Uwamino, S. Fujita, S. Ito, H. Sakamoto, R. Hirunuma, T. Yamaki, H. Mukai,[*1] A. Sato,[*2] and Y. Yano

We report here the residual radioactivity and leakage radiation level at the Riken Ring Cyclotron (RRC) facility.

Residual radioactivities in the RRC facility were measured at various locations using ionization-chamber survey meters. The measurements were performed after almost every beam experiment as well as during the routine overhaul period. This year, the overhaul was suddenly started at the end of June, because a serious failure of the contact fingers of the RF cavity was occurred during an experiment using an 80-MeV/u alpha beam in the E3 room.

The dose rates at the deflector in the injector AVF cyclotron were found to be 1.1 mSv/h on Aug. 18, 2004. The dose rates at the RRC deflector were not measured in this period, although those at magnetic deflection channel 1 (MDC1) were measured. The highest rate was 1.85 mSv/h on Aug. 9.

In addition to the above routine measurements, dose rates inside the injector AVF cyclotron were measured when its acceleration chamber was opened on Dec. 23, 2003, due to an insulation failure of the deflector. The highest dose rate at the deflector was 4.2 mSv/h.

During the period from Oct. 1, 2003 to Sept. 30, 2004, the dose rates were measured along the beam lines. The spots **a**–**v**, marked by bullets in Fig. 1, are the places where the dose rates exceeded 30 μSv/h. Table 1 summarizes the observed dose rates and the dates when the measurements were performed. The maximum dose rate was found to be 1.4 mSv/h (1400 μSv/h) at the beam duct in the beam distribution corridor denoted by **h** in Fig. 1. When we observed

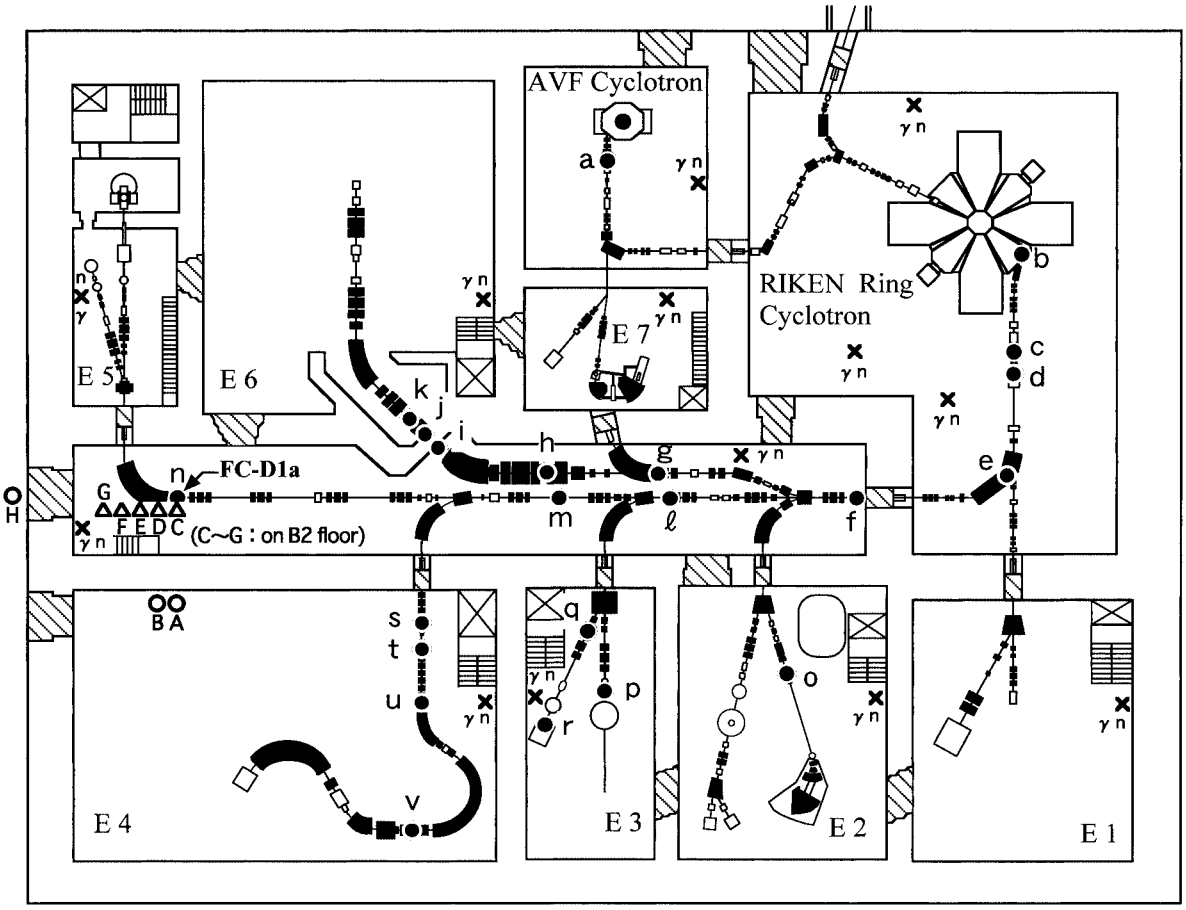

Fig. 1. Layout of the RIKEN Ring Cyclotron facility at the 1st basement floor as of 2004. Measured locations of residual radioactivities along the beam lines are indicated by solid circles **a**–**v**. Locations of the neutron and γ-ray measurements when the ^{86}Kr beam was on are indicated by open circles A, B and H which are on the beam line level in the 1st basement and by open triangles of C to G which are on the 2nd basement floor.

*1 Japan Environment Research Corporation
*2 Tokyo University of Science

Table 1. Summary of dose rates measured along the beam lines with ionization-chamber survey meters. Detection points **a**–**v** indicate measured locations shown in Fig. 1.

Detection point	Measured dose rate (μSv/h)	Date	Particle	Energy (MeV/u)	Intensity (enA)	Period (days)
a	130	Apr 16,'04	Ne-20	135	10	1
b	400	Apr 16,'04	Ne-20	135	10	1
c	1100	Apr 16,'04	Ne-20	135	10	1
d	450	Apr 16,'04	Ne-20	135	10	1
e	150	Apr 16,'04	Ne-20	135	10	1
f	65	Apr 16,'04	Ne-20	135	10	1
g	225	Jan 6,'04	Ar-40	95	1360	4
h	1400	Jan 6,'04	Ar-40	95	1360	4
i	200	Jan 6,'04	Ar-40	95	1360	4
j	85	May 13, '04	Ar-40	95	1000	6
k	30	May 13, '04	Ar-40	95	1000	6
l	170	Apr 16,'04	Ne-20	135	10	1
m	230	Apr 16,'04	Ne-20	135	10	1
n	100	Apr 16,'04	Ne-20	135	10	1
o	35	Mar 15, '04	He-4	26	80	1
p	35	May 13, '04	Ar-40	95	20	1
q	360	Apr 26,'04	N-14	135	2450	1
r	350	Apr 26,'04	N-14	135	2450	1
s	1200	May 24, '04	d	65	110	4
t	600	May 24, '04	d	65	110	4
u	50	May 24, '04	d	65	110	4
v	45	Jan 6,'04	Ar-40	95	17	1

Table 2. Measured dose rates in and around the RRC facility when a 46-MeV/u 54-pnA ^{86}Kr beam was stopped by a Faraday cup, FC-D1a, without any local shield. Measured points are shown in Fig. 1.

Measured point	Neutron dose rate (μSv/h)	Gamma dose rate (μSv/h)	Remark
A	0.03	LTD[§]	90 degree, 13 cm from the E4 wall surface, beam line height
B	0.04	LTD	1 m west from A
C	0.06	LTD	directly below the Faraday cup, on floor B2
D	0.16	LTD	1 m west from C
E	0.15	LTD	2 m west from C
F	0.23	LTD	3 m west from C
G	0.05	LTD	4 m west from C
H	LTD	LTD	outside the shielding door on the beam distribution corridor

[§]lower than the detection limit

a high dose rate, we cordoned off the area and posted a warning sign to indicate that it was dangerous to remain for a long period in that place.

We paid particular attention to measuring the leakage radiations in and around the RRC facility when a 46-MeV/u ^{86}Kr beam of 54 pnA intensity was stopped by a Faraday cup, FC-D1a, in the beam distribution corridor, without any local shield. Aloka TPS-451BS neutron rem counters and AE133 V ionization-chamber γ-ray survey meters from Applied Engineering Inc. were used. The measured results were shown in Table 2. The leakage was found to be small, and was below the detection limit outside the RRC building.

We also continuously monitored the leakage radiation from the RRC facility. Having analyzed the data collected on leakage neutrons, we found that the radiation levels in the controlled area were much lower than the allowable dose limit. The leakage of γ-rays and neutrons was below the detection limit of the environmental monitors. We evaluated the radiation level at the boundary of the accelerator facility by using a monitor installed in the computer room on the ground floor immediately above a bending magnet which guided the beams from the RRC vault to the distribution corridor. As a result, we obtained a radiation level of approximately 8.2 μSv/year which was much lower than the allowable dose limit (1 mSv/year).

VI. LIST OF PUBLICATIONS

1. Accelerator development and accelerator physics

A. Bandyopadhyay, O. Kamigaito, A. Chakrabarti, V. Banerjee, P. Ghosh, A. Goto, and Y. Yano: "Design of the RFQ and the LINAC postaccelerator for the VEC-RIB facility", J. Phys. G **24**, 1367–1370 (1998).

M. Komiyama, I. Yokoyama, M. Fujimaki, J. Odagiri, M. Nagase, T. Tanabe, and M. Kase: "Expansion of the control system for RARF", Proc. 14th Symp. on Accelerator Science and Technology, (The Japanese Accelerator Researchers Association and KEK), Tsukuba, 2003–11, KEK, pp. 272–274 (2003).

D. Tomono, S. Nakamura, Y. Matsuda, M. Iwasaki, G. Mason, K. Ishida, T. Matsuzaki, I. Watanabe, S. Sakamoto, and K. Nagamine: "Precise measurement of the positive muon lifetime at the RIKEN-RAL muon facility ", AIP Conf. Proc. **721**, 293–296 (2004).

Y. Matsuda, P. Bakule, P. Strasser, K. Ishida, T. Matsuzaki, M. Iwasaki, Y. Miyake, K. Shimomura, S. Makimura, and K. Nagamine: "Recent development of a point positive muon source at the RIKEN-RAL muon facility", AIP Conf. Proc. **721**, 313–316 (2004).

A. Goto, H. Okuno, J. Ohnishi, T. Tominaka, S. Fujishima, K. Ikegami, N. Fukunishi, Y. Miyazawa, T. Mitsumoto, and Y. Yano: "Sector magnets for the RIKEN superconducting ring cyclotron", IEEE Trans. Appl. Supercond. **14**, 300–305 (2004).

T. Tominaka, H. Okuno, J. Ohnishi, N. Fukunishi, H. Ryuto, M. Ohtake, K. Ikegami, A. Goto, and Y. Yano: "Radiation effects on cryogenic temperature sensors of Cernox, CGR and PtCo", IEEE Trans. Appl. Supercond. **14**, 1802–1805 (2004).

T. Tominaka: "Analytical field calculations for various helical conductors", IEEE Trans. Appl. Supercond. **14**, 1838–1841 (2004).

T. Tominaka: "Calculations using the helical filamentary structure for current distributions of a six around one superconducting strand cable and a multifilamentary composite", J. Appl. Phys. **96**, 5069–5080 (2004).

T. Tominaka and Y. Chiba: "Low frequency inductance for a twisted bifilar lead", J. Phys. D **37**, 1592–1595 (2004).

H. Amemiya, T. Tanabe, and T. Katayama: "Cooling of ions by cold electrons through coulomb collisions", J. Phys. Soc. Jpn. **73**, 617–626 (2004).

H. Ryuto, T. Chiba, H. Hasebe, M. Kase, and Y. Yano: "Liquid film stripper for intense heavy-ion beams", Jpn. J. Appl. Phys. Pt.1 **43**, 7753–7755 (2004).

S. Kohara, A. Goto, N. Sakamoto, O. Kamigaito, S. Watanabe, T. Teranishi, T. Katayama, Y. Chiba, M. Kase, and Y. Yano: "Flattop acceleration system in the RIKEN AVF cyclotron", Nucl. Instrum. Methods Phys. Res. A **526**, 230–238 (2004).

A. Chakrabarti, V. Naik, O. Kamigaito, S. Dechoudhury, D. Bhowmik, D. Sanyal, A. Bandyopadhyay, T. K. Chakraborty, M. Mondal, S. Nayak, H. Pandey, T. K. Bhaumik, A. Giri, D. Bhattacharya, T. J. Sen, S. Bhattacharya, A. Goto, and Y. Yano: "The design of a four-rod RFQ LINAC for VEC-RIB facility", Nucl. Instrum. Methods Phys. Res. A **535**, 599–605 (2004).

T. Watanabe, S. Watanabe, T. Ikeda, M. Kase, Y. Sasaki, T. Kawaguchi, and T. Katayama: "A prototype of a highly sensitive cryogenic current comparator with a HTS SQUID and HTS magnetic shield", Supercond. Sci. Technol. **17**, 450–455 (2004).

T. Tominaka: "Inductance calculation for helical conductors", Supercond. Sci. Technol. **18**, 214–222 (2005).

2. Nuclear physics and nuclear instrumentation

S. Sugimoto, K. Ikeda, and H. Toki: "Relativistic mean field theory with pion field for finite nuclei", Prog. Theor. Phys. Suppl., No. 146, pp. 437–441 (2002).

R. Kanungo, M. Chiba, S. Adhikari, D. Fang, N. Iwasa, K. Kimura, K. Maeda, S. Nishimura, Y. Ogawa, T. Ohnishi, A. Ozawa, C. Samanta, T. Suda, T. Suzuki, Q. Wang, C. Wu, Y. Yamaguchi, K. Yamada, A. Yoshida, T. Zheng, and I. Tanihata: "Possibility of a two-proton halo in ^{17}Ne", Phys. Lett. B **571**, 21–28 (2003).

K. Ishida: "Non-particle physics with intense muon beams", AIP Conf. Proc. **721**, 77–82 (2004).

P. Strasser, K. Nagamine, T. Matsuzaki, K. Ishida, Y. Matsuda, K. Itahashi, and M. Iwasaki: "Radioactive muonic atom studies with intense muon beams", AIP Conf. Proc. **721**, 309–312 (2004).

N. Dinh Dang: "Reply to the Comment by A. Rabhi on "Energies of the ground state and first excited 0^+ state in an exactly solvable pairing model" ", Eur. Phys. J. A **20**, 281–282 (2004).

K. Morita, K. Morimoto, D. Kaji, H. Haba, E. Ideguchi, R. Kanungo, K. Katori, H. Koura, H. Kudo, T. Ohnishi, A. Ozawa, T. Suda, K. Sueki, I. Tanihata, H. Xu, A. V. Yeremin, A. Yoneda, A. Yoshida, Y. Zhao, and T. Zheng: "Production and decay of the isotope ^{271}Ds(Z=110)", Eur. Phys. J. A **21**, 257–263 (2004).

K. Morita, K. Morimoto, D. Kaji, H. Haba, E. Ideguchi, J. L. Peter, R. Kanungo, K. Katori, H. Koura, H. Kudo, T. Ohnishi, A. Ozawa, T. Suda, K. Sueki, I. Tanihata, H. Xu, A. V. Yeremin, A. Yoneda, A. Yoshida, Y. Zhao, T. Zheng, S. Goto, and F. Tokanai: "Production and decay properties

of ^{272}111 and its daughter nuclei", J. Phys. Soc. Jpn. **73**, 1738–1744 (2004).

K. Morita, K. Morimoto, D. Kaji, T. Akiyama, S. Goto, H. Haba, E. Ideguchi, R. Kanungo, K. Katori, H. Koura, H. Kudo, T. Ohnishi, A. Ozawa, T. Suda, K. Sueki, H. Xu, T. Yamaguchi, A. Yoneda, A. Yoshida, and Y. Zhao: "Experiment on the synthesis of element 113 in the reaction ^{209}Bi(^{70}Zn,n)^{278}113", J. Phys. Soc. Jpn. **73**, 2593–2596 (2004).

A. Yoshida, K. Morita, K. Morimoto, D. Kaji, T. Kubo, Y. Takahashi, A. Ozawa, and I. Tanihata: "High-power rotating wheel targets at RIKEN", Nucl. Instrum. Methods Phys. Res. A **521**, 65–71 (2004).

Y. Ishida, M. Wada, Y. Matsuo, I. Tanihata, A. Casares, and H. Wollnik: "A time-of-flight mass spectrometer to resolve isobars", Nucl. Instrum. Methods Phys. Res. B **219/220**, 468–472 (2004).

C. Signorini, A. Yoshida, Y. Watanabe, D. Pierroutsakou, L. Stroe, T. Fukuda, M. Mazzocco, N. Fukuda, Y. Mizoi, M. Ishihara, H. Sakurai, A. Diaz-Torres, and K. Hagino: "Subbarrier fusion in the systems ^{11,10}Be+^{209}Bi", Nucl. Phys. A **735**, 329–344 (2004).

R. Kanungo: "Two-proton halo in ^{17}Ne", Nucl. Phys. A **738**, 293–297 (2004).

S. V. Stepantsov, M. Golovkov, A. Fomichev, A. Rodin, S. Sidorchuk, R. Slepnev, G. Ter-Akopian, M. Chelnokov, V. Gorshkov, Y. T. Oganessian, R. Wolski, A. A. Korsheninnikov, E. Nikolski, and I. Tanihata: "^{5}H and ^{5}He nuclear systems studied by means of the ^{6}He+^{2}H reaction", Nucl. Phys. A **738**, 436–439 (2004).

H. Jeppesen, R. Kanungo, B. A. Ibrahim, S. Adhikari, M. Chiba, D. Fang, N. Iwasa, K. Kimura, K. Maeda, S. Nishimura, T. Ohnishi, A. Ozawa, C. Samanta, T. Suda, T. Suzuki, I. Tanihata, Q. Wang, C. Wu, Y. Yamaguchi, K. Yamada, A. Yoshida, and T. Zheng: "One- and two-proton removal from ^{15}O", Nucl. Phys. A **739**, 57–66 (2004).

M. Chiba, R. Kanungo, B. A. Ibrahim, S. Adhikari, D. Fang, N. Iwasa, K. Kimura, K. Maeda, S. Nishimura, T. Ohnishi, A. Ozawa, C. Samanta, T. Suda, T. Suzuki, I. Tanihata, Q. Wang, C. Wu, Y. Yamaguchi, K. Yamada, A. Yoshida, and T. Zheng: "Neutron removal studies on ^{19}C", Nucl. Phys. A **741**, 29–41 (2004).

S. Sidorchuk, D. Bogdanov, A. Fomichev, M. Golovkov, Y. Oganessian, A. Rodin, R. Slepnev, S. Stepantsov, G. Ter-Akopian, R. Wolski, A. A. Korsheninnikov, E. Nikolski, A. Yukhimchuk, V. Perevozchikov, Y. Vinogradov, F. Hanappe, T. Materna, L. Stuttge, A. Ninane, P. Roussel-Chomaz, and W. Mittig: "Experimental study of ^{4}H in the reactions ^{2}H(t,p) and ^{3}H(t,d)", Phys. Lett. B **594**, 54–60 (2004).

K. Iida and K. Oyamatsu: "Surface tension in a compressible liquid-drop model: Effects on nuclear density and neutron skin thickness", Phys. Rev. C **69**, 037301-1–037301-4 (2004).

A. Kohama, K. Iida, and K. Oyamatsu: "Nuclear radius deduced from proton diffraction by a black nucleus", Phys. Rev. C **69**, 064316-1–064316-4 (2004).

T. Matsuura, K. Iida, T. Hatsuda, and G. Baym: "Thermal fluctuations of gauge fields and first order phase transitions in color superconductivity", Phys. Rev. D **69**, 074012-1–074012-10 (2004).

K. Iida, T. Matsuura, M. Tachibana, and T. Hatsuda: "Melting pattern of diquark condensates in quark matter", Phys. Rev. Lett. **93**, 132001-1–132001-4 (2004).

A. Kohama: "Determination of matter surface distribution of neutron-rich nuclei ", Proc. Int. Symp. on A New Era of Nuclear Structure Physics (NENS03), (Niigata University), Kurokawa-cho, Niigata Pref., 2003–11, edited by Y. Suzuki and others, World Scientific, Singapore, pp. 272–276 (2004).

K. Iida, G. Baym, T. Matsuura, and T. Hatsuda: "Ginzburg-Landau approach to color superconductivity", Prog. Theor. Phys. Suppl., No. 153, pp. 230–240 (2004).

T. Matsuzaki, K. Nagamine, K. Ishida, N. Kawamura, Y. Matsuda, H. Imao, M. Iwasaki, S. Nakamura, M. Kato, H. Sugai, M. Tanase, K. Kudo, N. Takeda, and G. H. Eaton: "Strong n-α correlations observed in muon catalyzed t-t fusion reactions", Prog. Theor. Phys. Suppl., No. 154, pp. 225–232 (2004).

N. Kawamura, K. Nagamine, T. Matsuzaki, K. Ishida, S. Nakamura, Y. Matsuda, M. Tanase, M. Kato, H. Sugai, K. Kudo, N. Takeda, and G. H. Eaton: "Anomalous temperature-dependent phenomena of muon catalyzed fusion in solid deuterium and tritium mixtures", Prog. Theor. Phys. Suppl., No. 154, pp. 233–240 (2004).

S. Ozawa and M. Hamagaki: "Preparation of self-supporting boron films by sputtering with electron-beam-excited plasma", Vacuum **74**, 417–421 (2004).

3. Atomic and solid-state physics

F. L. Pratt, S. J. Blundell, T. Jestadt, B. W. Lovett, R. M. Macrae, and W. Hayes: "Muon radical states in some electron donor and acceptor molecules", Magn. Reson. Chem. **38**, S27–S32 (2000).

B. Webster and R. M. Macrae: "A theoretical investigation of the effect of a sodium cation on the proton-electron hyperfine coupling constants of the cyclohexadienyl radical and some consequences for the muonium-substituted cyclohexadienyl radical, C_6H_6Mu, formed in zeolites", Physica B **289/290**, 598–602 (2000).

R. M. Macrae, I. D. Reid, J.-U. von Schutz, and K. Nagamine: "Order-disorder transition in anthracene/tetracyanobenzene probed by muonium-

substituted radicals", Physica B **289/290**, 616–619 (2000).
Y. Iwai, Y. Kanai, H. Oyama, K. Ando, H. Masuda, K. Nishio, M. Nakao, K. Komaki, and Y. Yamazaki: "High-resolution soft X-ray spectroscopy of 2.3 keV/u N^{7+} ions through a highly ordered Au microcapillary target", At. Collision Res. Jpn., No. 28, pp. 27–28 (2002).
Y. Nakai, Y. Kanai, Y. Iwai, K. Nishio, and H. Masuda: "Coincidence measurement of L X-ray and final charge state of Ar ions transmitted through a microcpaillary", At. Collision Res. Jpn., No. 28, pp. 42–43 (2002).
Y. Chimi, A. Iwase, N. Ishikawa, and T. Kambara: "Defect production induced by electronic excitation in iron", Nucl. Instrum. Methods Phys. Res. B **193**, 248–252 (2002).
N. Ishikawa, A. Iwase, Y. Chimi, O. Michikami, H. Wakana, T. Hashimoto, T. Kambara, C. Mueller, and R. Neumann: "S_e-scaling of lattce parameter change in high ion-velocity region ($v \geq 2.6 \times 10^9$ cm/s) in ion-irradiated $EuBa_2Cu_3O_y$", Nucl. Instrum. Methods Phys. Res. B **193**, 278–282 (2002).
Y. Iwai, Y. Kanai, Y. Nakai, T. Ikeda, H. Oyama, K. Ando, H. Masuda, K. Nishio, H. Torii, K. Komaki, and Y. Yamazaki: "High-resolution soft X-ray spectroscopy of slow highly charged ions transmitted through a Ni microcapillary target using a single photon counting method", At. Collision Res. Jpn., No. 29, pp. 19–20 (2003).
Y. Kanai, Y. Nakai, Y. Iwai, T. Ikeda, K. Nishio, H. Masuda, and Y. Yamazaki: "Coincidence measurements of X-rays and final charge state of highly charged ions transmitted through a microcapillary", At. Collision Res. Jpn., No. 29, pp. 25–26 (2003).
F. Ono, Y. Hamatani, Y. Mukumoto, S. Komatsu, N. Ishikawa, Y. Chimi, A. Iwase, T. Kambara, C. Mueller, and R. Neumann: "Modification of Fe-Ni Invar alloys by high-energy ion beams", Nucl. Instrum. Methods Phys. Res. B **206**, 295–298 (2003).
A. Iwase, Y. Hamatani, Y. Mukumoto, N. Ishikawa, Y. Chimi, T. Kambara, C. Mueller, R. Neumann, and F. Ono: "Anomalous shift of Curie temperature in iron-nickel Invar alloys by high-energy heavy ion irradiation", Nucl. Instrum. Methods Phys. Res. B **209**, 323–328 (2003).
R. Kadono, R. M. Macrae, and K. Nagamine: "Charge dynamics of muonium centers in Si revealed by photoinduced muon spin relaxation", Phys. Rev. B **68**, 245204-1–245204-17 (2003).
P. Bakule and E. Morenzoni: "Generation and applications of slow polarized muons", Contemp. Phys. **45**, 203–225 (2004).
E. Yagi, T. Iwata, T. Urai, and K. Ogiwara: "Channelling studies on the lattice location of B atoms in graphite", J. Nucl. Mater. **334**, 9–12 (2004).
N. Oshima, M. Niigaki, M. Inoue, T. M. Kojima, A. Mohri, Y. Kanai, Y. Nakai, K. Komaki, and Y. Yamazaki: "Project to produce cold highly charged ions using positron and electron cooling techniques", J. Phys.: Con. Ser. **2**, 127–133 (2004).
A. Igarashi and I. Shimamura: "Time-delay matrix analysis of resonances: application to the positronium negative ion", J. Phys. B **37**, 4221–4237 (2004).
Y. Matsuda and Y. Miyake: "Ultra slow muon beam leads to novel applications of the μSR technique", Kotai Butsuri **39**, 599–605 (2004).
N. Yamanaka, Y. Kino, Y. Takano, H. Kudo, and A. Ichimura: "Direct positron annihilation and positronium formation", Mater. Sci. Forum **445/446**, 449–451 (2004).
Y. Fukuyama, Y. Moriwaki, and Y. Matsuo: "Laser-induced fluorescence spectra of Ba^{+*}-He exciplexes produced in cold He GAS", Phys. Rev. A **69**, 042505-1–042505-6 (2004).
A. Igarashi and I. Shimamura: "Stable complex-rotation eigenvalues that correspond to no full resonances in scattering: Examples in positron scattering by the helium ion ", Phys. Rev. A **70**, 012706-1–012706-5 (2004).
Y. Morishita, R. Hutton, H. Torii, K. Komaki, T. Brage, K. Ando, K. Ishii, Y. Kanai, H. Masuda, M. Sekiguchi, F. B. Rosmej, and Y. Yamazaki: "Direct observation of the initial-state distribution of the first electron transferred to slow highly charged ions interacting with a metal surface", Phys. Rev. A **70**, 012902-1–012902-6 (2004).
H. Higaki, N. Kuroda, Y. K. Franzen, Z. Wang, M. Hori, A. Mohri, K. Komaki, and Y. Yamazaki: "Radial compression of protons and H_3^+ ions in a multiring trap for the production of ultralow energy antiproton beams", Phys. Rev. E **70**, 026501-1–026501-5 (2004).
N. Oshima, T. M. Kojima, M. Niigaki, A. Mohri, K. Komaki, and Y. Yamazaki: "New scheme for positron accumulation in ultrahigh vacuum", Phys. Rev. Lett. **93**, 195001-1–195001-4 (2004).
Y. Yamazaki: "Intense ultra slow $\bar{p}$ beam and its application", Phys. Scr. T **110**, 286–291 (2004).
N. Nakamura, Y. Nakai, Y. Kanai, K. Komaki, A. Endo, and Y. Yamazaki: "Compact electron beam ion source with high-T_C bulk superconductors", Rev. Sci. Instrum. **75**, 3034–3038 (2004).

4. Radiochemistry, radiation chemistry, and radiation biology

M. Suzuki, C. Tsuruoka, T. Kanai, T. Kato, F. Yatagai, and M. Watanabe: "Qualitative and quantitative difference in mutation induction between carbon- and neon-ion beams in normal human cells", Biol. Sci. Space **17**, 302–306 (2003).
H. Haba, K. Akiyama, K. Tsukada, M. Asai, A. Toyoshima, T. Yaita, M. Hirata, K. Sueki, and Y.

Nagame: "Chloride complexation of rutherfordium: X-ray absorption fine structure spectroscopy of Zr and Hf in HCl", Advances in Nuclear and Radiochemistry (Reihe Allgemeines und Interdisziplinares Vol. 3), (Forschungszentrum Julich), Aachen, Germany, 2004–8〜9, Forschungszentrum Julich, Julich, pp. 150–152 (2004).

A. Toyoshima, K. Tsukada, M. Asai, H. Haba, K. Akiyama, I. Nishinaka, D. Saika, K. Matsuo, W. Sato, H. Ishidu, M. Ito, J. Saito, S. Goto, H. Kudo, H. Kikunaga, N. Kinoshita, C. Kato, A. Yokoyama, K. Sueki, Y. Nagame, and A. Shinohara: "Elution behavior of rutherfordium (Rf) in anion-exchange chromatography in a hydrofluoric acid system", Advances in Nuclear and Radiochemistry (Reihe Allgemeines und Interdisziplinares Vol. 3), (Forschungszentrum Julich), Aachen, Germany, 2004–8〜9, Forschungszentrum Julich, Julich, pp. 153–154 (2004).

K. Tsukada, H. Haba, M. Asai, A. Toyoshima, K. Akiyama, I. Nishinaka, M. Hirata, K. Hashimoto, S. Ichikawa, Y. Nagame, K. Yasuda, Y. Miyamoto, Y. Tani, H. Hasegawa, W. Sato, A. Shinohara, S. Goto, M. Ito, J. Saito, H. Ishidu, H. Kudo, Y. Oura, H. Nakahara, K. Sueki, N. Kinoshita, H. Kikunaga, and A. Yokoyama: "Sorption on anion-exchange resin of dubnium and its homologues in HF solution", Advances in Nuclear and Radiochemistry (Reihe Allgemeines und Interdisziplinares Vol. 3), (Forschungszentrum Julich), Aachen, Germany, 2004–8〜9, Forschungszentrum Julich, Julich, pp. 155–157 (2004).

H. Haba, K. Igarashi, D. Kaji, R. Hirunuma, and S. Enomoto: "Development of a gas-jet-coupled multitarget system for multitracer production", Advances in Nuclear and Radiochemistry (Reihe Allgemeines und Interdisziplinares Vol. 3), (Forschungszentrum Julich), Aachen, Germany, 2004–8〜9, Forschungszentrum Julich, Julich, pp. 333–335 (2004).

S. Komiyama, S. Taniguchi, Y. Matsumoto, E. Tsunoda, T. Ohto, Y. Suzuki, L. H. Yin, M. Tomita, A. Enomoto, A. Morita, T. Suzuki, K. Ohtomo, Y. Hosoi, and N. Suzuki: "Potentiality of DNA-dependent protein kinase to phosphorylate Ser46 of human p53", Biochem. Biophys. Res. Commun. **323**, 816–822 (2004).

H. Haba and Y. Nagame: "Chemical Properties of Superheavy Elements", Gendai Kagaku **12**, No. 405, pp. 32–38 (2004).

H. Haba, K. Tsukada, M. Asai, A. Toyoshima, K. Akiyama, I. Nishinaka, M. Hirata, T. Yaita, S. Ichikawa, Y. Nagame, K. Yasuda, Y. Miyamoto, T. Kaneko, S. Goto, S. Ono, T. Hirai, H. Kudo, M. Shigekawa, A. Shinohara, Y. Oura, H. Nakahara, K. Sueki, H. Kikunaga, N. Kinoshita, N. Tsuruga, A. Yokoyama, M. Sakama, S. Enomoto, M. Schaedel, W. Bruechle, and J. V. Kratz: "Fluoride complexation of element 104, rutherfordium", J. Am. Chem. Soc. **126**, 5219–5224 (2004).

K. Igarashi, H. Inage, Y. Nakanishi, T. Nakadai, M. Okayasu, R. Hirunuma, S. Enomoto, and S. Kimura: "Efficacy of sodium iron etylenediaminetetraacetic acid as a food fortifier for improving the iron-deficient status of anemic rats", J. Jpn. Soc. Nutr. Food Sci. **57**, 89–97 (2004).

T. Abe, Y. Miyazawa, H. Saito, Y. Yamamoto, H. Ryuto, and N. Fukunishi: "Development of plant mutational breeding by heavy ions", JAERI-Conf, No. 2004-001, pp. 44–47 (2004).

H. Haba: "Chemistry of the heaviest elements in RIKEN: Present status and future plans", JAERI-Conf, No. 2004-004, pp. 105–118 (2004).

H. Haba, K. Morita, S. Enomoto, K. Morimoto, D. Kaji, and Y. Nagame: "Development of a novel heavy element chemistry apparatus using the RIKEN gas-field recoil separator as a pre-separator", JAERI-Conf, No. 2004-014, pp. 67–71 (2004).

H. Haba, K. Tsukada, M. Asai, A. Toyoshima, K. Akiyama, I. Nishinaka, M. Hirata, T. Yaita, S. Ichikawa, Y. Nagame, K. Yasuda, Y. Miyamoto, T. Kaneko, S. Goto, S. Ono, T. Hirai, H. Kudo, M. Shigekawa, A. Shinohara, Y. Oura, H. Nakahara, K. Sueki, H. Kikunaga, N. Kinoshita, N. Tsuruga, A. Yokoyama, M. Sakama, S. Enomoto, W. Bruechle, M. Schaedel, and J. V. Kratz: "Fluoride complexation of Rf", JAERI-Rev., No. 2004-027, pp. 43–44 (2004).

K. Tsukada, A. Toyoshima, M. Asai, H. Haba, K. Akiyama, I. Nishinaka, Y. Nagame, D. Saika, K. Matsuo, W. Sato, A. Shinohara, H. Ishizu, M. Ito, J. Saito, S. Goto, H. Kudo, H. Kikunaga, N. Kinoshita, C. Kato, A. Yokoyama, and K. Sueki: "Anion-exchange chromatographic behavior of rutherfordium(Rf) in hydrofluoric acid", JAERI-Rev., No. 2004-027, pp. 45–46 (2004).

H. Haba: "Chemical properties of the super heavy element 112", Kagaku to Kogyo **57**, 440 (2004).

T. Abe: "Development of mutant induction method using heavy-ion irradiation", Noukouken Tsushin **4**, No. 132, pp. 2–8 (2004).

T. Abe: "Application of ion beam irradiation for mutation breeding", Nuclear Viewpoints **50**, No. 5, pp. 42–45 (2004).

N. Yamanaka, Y. Kino, and A. Ichimura: "Wave-packet analysis of multichannel resonances in positron scattering by a helium ion", Phys. Rev. A **70**, 62701-1–062701-5 (2004).

T. Kagawa, M. Kasahara, T. Abe, S. Yoshida, and M. Wada: "Function analysis of phototropin2 using fern mutants deficient in blue light-induced chloroplast avoidance movement", Plant Cell Physiol. **45**, 416–426 (2004).

H. L. Yin, Y. Suzuki, Y. Matsumoto, M. Tomita, Y.

Furusawa, A. Enomoto, A. Morita, M. Aoki, F. Yatagai, T. Suzuki, Y. Hosoi, K. Ohtomo, and N. Suzuki: "Radiosensitization by hyperthermia in the chicken B-lymphocyte cell line DT40 and its derivatives lacking nonhomologous end joining and/or homologous recombination pathways of DNA double-strand break repair", Radiat. Res. **162**, 433–441 (2004).

5. Material Analysis

Z. Liu, J. Kawamura, M. Nagasono, K. Maeda, and J. Kawai: "Determination of the structure of boron subphosphide by P Kβ X-ray fluorescence spectra", J. Electron Spectrosc. Relat. Phenom. **135**, 73–81 (2004).

K. Maeda, H. Hamanaka, M. Maeda, K. Ogiwara, and K. Hasegawa: "Time-resolved chemical state analysis by highly sensitive high-resolution PIXE", Proc. 10th Int. Conf. on Particle Induced X-ray Emission and its Analytical Applications (PIXE 2004), (Jozef Stefan Institute, University of Ljubljana and others), Portoroz, Slovenia, 2004–6, edited by M. Budnar and M. Kavcic, Jozef Stefan Institute, Ljubljana, pp. 815.1–815.3 (2004).

6. RIKEN-BNL Collaboration

Y. Goto and PHENIX Collaboration: "Prospects of the gluon polarization measurement at PHENIX", AIP Conf. Proc. **675**, 493–503 (2003).

Y. Akiba and PHENIX Collaboration: "Silicon vertex detector upgrade for the PHENIX experiment at RHIC", AIP Conf. Proc. **698**, 785–788 (2003).

Y. Goto and PHENIX Collaboration: "Neutral pion measurements in polarized proton collisions from PHENIX at RHIC", Nucl. Phys. A **721**, 360c–363c (2003).

Y. Akiba and H. Hamagaki: "The beginning of high energy nucleus-nucleus collision experiment at RHIC", Butsuri **59**, 291–299 (2004).

J. Tojo, K. Aoki, H. Enyo, Y. Fukao, Y. Goto, J. Heuser, Z. Li, H. Onishi, H. Okada, V. Radeka, V. Rykov, N. Saito, F. Sakuma, M. Sekimoto, K. Tanida, M. Togawa, and Y. Watanabe: "Development of a novel silicon stripixel detector for RHIC-PHENIX detector upgrade", IEEE Trans. Nucl. Sci. **51**, 2337–2340 (2004).

T. Tominaka: "Vector potential for a single helical current condutor", Nucl. Instrum. Methods Phys. Res. A **523**, 1–8 (2004).

Z. Li, H. Enyo, Y. Goto, V. Radeka, R. H. Beuttenmuller, W. Chen, D. Elliott, Y. H. Guo, T. Kawabata, M. Togawa, N. Saito, V. Rykov, K. Tanida, and J. Tojo: "Development of 2nd prototype of novel silicon stripixel detector for PHENIX upgrade", Nucl. Instrum. Methods Phys. Res. A **535**, 404–409 (2004).

M. Hirai: "Uncertainty of polarized gluon distribution from prompt photon production", Phys. Lett. B **596**, 287–292 (2004).

M. Hirai, S. Kumano, and T. Nagai: "Nuclear parton distribution functions and their uncertainties", Phys. Rev. C **70**, 044905-1–044905-10 (2004).

M. Hirai, S. Kumano, and N. Saito: "Determination of polarized parton distribution functions and their uncertainties", Phys. Rev. D **69**, 054021-1–054021-10 (2004).

T. Ikeda: "Effect of memory on relaxation in a scalar field theory", Phys. Rev. D **69**, 105018-1–105018-10 (2004).

H. Fujii and M. Ohtani: "Sigma and hydrodynamic modes along the critical line", Phys. Rev. D **70**, 014016-1–014016-18 (2004).

Y. Hidaka, O. Morimatsu, T. Nishikawa, and M. Ohtani: "Two-pion bound state in the sigma channel at finite temperature", Phys. Rev. D **70**, 076001-1–076001-5 (2004).

M. Ohtani and K. Ohta: "Skyrmions coupled to the electromagnetic field via the gauged Wess-Zumino term", Phys. Rev. D **70**, 096014-1–096014-7 (2004).

Y. Akiba: "Experimental results from RHIC", Proc. Int. Conf. on Color Confinement and Hadrons in Quantum Chromodynamics: Confinement 2003, (Tokyo Institute of Technology and RIKEN), Wako, 2003–7, World Scientific, Singapore, pp. 361–372 (2004).

H. Fujii and M. Ohtani: "Soft modes at the critical end point in the chiral effective models", Prog. Theor. Phys. Suppl., No. 153, pp. 157–164 (2004).

A. Iwazaki, O. Morimatsu, T. Nishikawa, and M. Ohtani: "Quantum Hall states of gluons in quark matter", Prog. Theor. Phys. Suppl., No. 153, pp. 198–203 (2004).

M. Ohtani and H. Fujii: "Sigma and hydrodynamic modes near the critical end point", Prog. Theor. Phys. Suppl., No. 156, pp. 167–168 (2004).

T. Nishikawa, A. Iwazaki, O. Morimatsu, and M. Ohtani: "Color ferromagnetic states and quantum hall states of gluons in quark matter", Prog. Theor. Phys. Suppl., No. 156, pp. 178–179 (2004).

VII. LIST OF PREPRINTS

2004

RIKEN-AF-NP

456 M. Hirai and K. Sudoh: "Effect of polarized gluon distribution on π^0 spin asymmetry"

457 T. Yamazaki, A. Dote, and Y. Akaishi: "Quest for dense and cold nuclear bound systems mediated by K^- mesons"

458 Y. Yanagisawa, S. Kubono, T. Teranishi, K. Ue, S. Michimasa, M. Notani, J. J. He, Y. Ohshiro, S. Shimoura, S. Watanabe, N. Yamazaki, H. Iwasaki, S. Kato, T. Kishida, T. Morikawa, and Y. Mizoi: "Low-energy radioisotope beam separator CRIB"

459 Y. Kondo, T. Nakamura, N. Aoi, H. Baba, D. Bazin, N. Fukuda, T. Gomi, H. Hasegawa, N. Imai, M. Ishihara, T. Kobayashi, T. Kubo, M. Miura, T. Motobayashi, A. Saito, H. Sakurai, S. Shimoura, T. Sugimoto, K. Watanabe, Y. X. Watanabe, T. Yakushiji, Y. Yanagisawa, and K. Yoneda: "In-beam γ-ray spectroscopy of the neutron-rich boron isotopes ^{15,17}B via inelastic scattering on ^{12}C"

460 N. Dinh Dang: "Nuclear giant resonances"

461 N. Dinh Dang: "Particle-number conservation within self-consistent random-phase approximation"

RIKEN-AF-AC

44 H. Amemiya, H. Tsutsui, and T. Katayama: "Electron cooling by electron beam of flattened velocity distribution with variable coulomb logarithm"

45 M. Nishiura, T. Tanabe, T. Katayama, E. Syresin, A. Sidorin, A. Smirnov, and I. Watanabe: "Study on the electron cooler for the accumulator cooler ring at RIKEN"

46 M. Serata, M. Takanaka, T. Ohkawa, M. Watanabe, and T. Katayama: "Design and bench test of a planner slotline pick-up for stochastic cooling"

VIII. PAPERS PRESENTED AT MEETINGS

1. Accelerator development and accelerator physics

M. Komiyama, I. Yokoyama, M. Nagase, M. Fujimaki, T. Tanabe, M. Kase, and J. Odagiri: "Current status of the control system for the RIKEN Accelerator Research Facility", 9th Int. Conf. on Accelerator and Large Experimental Physics Control Systems (ICALEPCS 2003), (Pohang University of Science and Technology), Gyeongju, Korea, Oct. (2003).

M. Komiyama: "Device interface module at RIKEN", EPICS Collaboration Meet., Gyeongju, Korea, Oct. (2003).

M. Komiyama, M. Kase, T. Tanabe, M. Fujimaki, M. Nagase, I. Yokoyama, and J. Odagiri: "Expansion of the control system for RARF", 14th Symp. on Accelerator Science and Technology (SAST03), (The Japanese Accelerator Researchers Association and KEK), Tsukuba, Nov. (2003).

T. Watanabe: "A highly sensitive current and position monitor with HTS SQUIDs and an HTS magnetic shield", Nihon Gakujyutu Shinkoukai Choudendou Electronics Dai 146 Iinkai, Kouseinou SQUID System Bunkakai, Dai 59 Kai Kenkyuukai, Japan, May (2004).

J. Ohnishi, T. Mitsumoto, A. Goto, M. Kase, M. Nagase, and Y. Yano: "Construction status of the magnet system for the RIKEN intermediate-stage ring cyclotron", 1st Ann. Meet. of Particle Accelerator Soc. of Japan/29th Linear Accelerator Meet. in Japan, Funabashi, Aug. (2004).

A. Goto: "Study on accelerators at RIKEN", Workshop on Research and Development of Accelerators in Atomic Energy Science, (Kyoto University Research Reactor Institute), Kyoto, Aug. (2004).

T. Watanabe, T. Ikeda, M. Kase, Y. Yano, S. Watanabe, Y. Sasaki, and T. Kawaguchi: "Development of a highly sensitive current and position monitor with HTS SQUIDs and an HTS magnetic shield", 17th Int. Conf. on Cyclotrons and Their Applications (Cyclotrons 2004), (RIKEN), Tokyo, Oct. (2004).

A. Goto, Y. Chiba, N. Fukunishi, O. Kamigaito, M. Kase, S. Kohara, N. Sakamoto, Y. Yano, T. Katayama, T. Teranishi, and S. Watanabe: "Status of the flattop acceleration system in the RIKEN AVF cyclotron", 17th Int. Conf. on Cyclotrons and Their Applications (Cyclotrons 2004), (RIKEN), Tokyo, Oct. (2004).

O. Kamigaito, T. Chiba, Y. Chiba, M. Fujimaki, A. Goto, M. Hemmi, E. Ikezawa, M. Kase, S. Kohara, Y. Miyazawa, N. Fukunishi, N. Sakamoto, and Y. Yano: "Upgrade of RILAC injector", 17th Int. Conf. on Cyclotrons and Their Applications (Cyclotrons 2004), (RIKEN), Tokyo, Oct. (2004).

2. Nuclear physics and nuclear instrumentation

H. Madokoro, T. Shimizu, and Y. Motizuki: "Effects of small-scale fluctuations of neutrino flux in supernova explosions", IAU Colloq. 192 on Supernovae (10 years of SN1993J), Valencia, Spain, Apr. (2003).

A. Kohama, K. Iida, and K. Oyamatsu: "Fraunhofer diffraction and nuclear matter radii", 59th Ann. Meet. of Physical Soc. of Japan, Fukuoka, Mar. (2004).

Y. Motizuki: "Supernovae and solar activity enshrined in Antarctic ice core", Special Colloq. at Natl. Institute of Polar Research, Tokyo, Mar. (2004).

H. Ueno: "Measurements of nuclear moments: Current status and future trend", Physics of Unstable Nuclei: Past Decade and the Future, (RIBF-UEC and RIKEN), Wako, June (2004).

Y. Ishida, M. Wada, Y. Matsuo, and H. Wollnik: "Precise mass measurement of unstable nuclei using a multi-reflection time-of-flight mass spectrometer", 52nd Ann. Conf. on Mass Spectrometry, (The Mass Spectrometry Society of Japan), Nagoya, June (2004).

K. Iida: "Ginzburg-Landau approach to color superconductivity", University of Washington Institute for Nuclear Theory Program (INT-04-1): QCD and Dense Matter: From Lattices to Stars, Seattle, USA, June (2004).

T. Gomi, T. Motobayashi, Y. Ando, N. Aoi, H. Baba, K. Demichi, Z. Elekes, N. Fukuda, Z. Fulop, U. Futakami, H. Hasegawa, Y. Higurashi, K. Ieki, N. Imai, M. Ishihara, K. Ishikawa, N. Iwasa, H. Iwasaki, S. Kanno, Y. Kondo, T. Kubo, S. Kubono, M. Kunibu, K. Kurita, Y. Matsuyama, S. Michimasa, T. Minemura, M. Miura, H. Murakami, T. Nakamura, M. Notani, S. Ota, A. Saito, H. Sakurai, M. Serata, S. Shimoura, T. Sugimoto, E. Takeshita, S. Takeuchi, Y. Togano, K. Ue, K. Yamada, Y. Yanagisawa, K. Yoneda, and A. Yoshida: "Coulomb dissociation of ^{23}Al for the ^{22}Mg(p,γ)^{23}Al reaction", 8th Int. Symp. on Nuclei in the Cosmos (NIC8), (TRIUMF), Vancouver, Canada, July (2004).

K. Ishida: "Muon catalyzed fusion", 6th Int. Workshop on Neutrino Factories and Superbeams (NuFact 04), Osaka, July–Aug. (2004).

D. Tomono: "Muon lifetime measurement with pulsed muon beam", 6th Int. Workshop on Neutrino Factories and Superbeams (NuFact 04), Osaka, July–Aug. (2004).

K. Morimoto: "Recent results of superheavy element research using GARIS at RIKEN", 3rd Workshop on Recoil Separator for Superheavy Element Chemistry, (GSI), Darmstadt, Germany, Aug. (2004).

K. Yamada, T. Motobayashi, N. Aoi, H. Baba, K.

Demichi, Z. Elekes, J. D. Gibelin, T. Gomi, H. Hasegawa, N. Imai, H. Iwasaki, S. Kanno, T. Kubo, K. Kurita, Y. Matsuyama, S. Michimasa, T. Minemura, M. Notani, T. Onishi, H. Ong, S. Ota, A. Ozawa, A. Saito, H. Sakurai, S. Shimoura, E. Takeshita, S. Takeuchi, M. Tamaki, Y. Togano, Y. Yanagisawa, K. Yoneda, and I. Tanihata: "B(E2) measurement of the proton-rich ^{46}Cr,^{50}Fe, and ^{54}Ni nuclei studied by Coulomb excitation", 2004 Autumn Meet. of the Physical Soc. of Japan, Kochi and Aomori, Sept. (2004).

M. Takashina: "Direct reaction dynamics of unstable nucleus", 2004 Autumn Meet. of the Physical Soc. of Japan, Kochi and Aomori, Sept. (2004).

H. Masui: "Dynamics of halo nuclei, and the role of the resonant and continuum states", 2004 Autumn Meet. of the Physical Soc. of Japan, Kochi and Aomori, Sept. (2004).

N. Aoi, W. F. Mueller, D. Bazin, M. D. Bowen, C. M. Campbell, J. M. Cook, D. C. Dinca, A. Gade, T. Glasmacher, T. Kubo, H. Iwasaki, H. Sakurai, T. Motobayashi, T. Nakamura, H. Olliver, S. Takeuchi, J. R. Teryy, H. Suzuki, and K. Yoneda: "Inelastic scattering on ^{74}Ni", 2004 Autumn Meet. of the Physical Soc. of Japan, Kochi and Aomori, Sept. (2004).

R. Mutou, J. Chiba, H. Enyo, Y. Fukao, H. Funahashi, H. Hamagaki, M. Ieiri, M. Ishino, H. Kanda, M. Kitaguchi, S. Mihara, T. Miyashita, K. Miwa, T. Murakami, T. Nakura, M. Naruki, M. Nomachi, K. Ozawa, F. Sakuma, O. Sasaki, M. Sekimoto, T. Tabaru, K. Tanaka, M. Togawa, S. Yamada, S. Yokkaichi, and Y. Yoshimura: "Measurement of in-medium mass modification of vector mesons in 12 GeV p+A $\rightarrow \rho/\omega/\phi$ + X interactions (KEK-PS E325)", 2004 Autumn Meet. of the Physical Soc. of Japan, Kochi and Aomori, Sept. (2004).

K. Ishida, K. Nagamine, T. Matsuzaki, N. Kawamura, Y. Matsuda, M. Iwasaki, H. Imao, M. Kato, H. Sugai, and G. H. Eaton: "Muon catalyzed fusion experiment in D-T system at RIKEN-RAL Muon Facility: magnetic field effect 2", 2004 Autumn Meet. of the Physical Soc. of Japan, Kochi and Aomori, Sept. (2004).

H. Imao, K. Nagamine, T. Matsuzaki, K. Ishida, N. Kawamura, Y. Matsuda, A. Toyoda, M. Kato, H. Sugai, A. Uritani, and H. Harano: "Ortho-para effect on μCF in condensed D_2", 2004 Autumn Meet. of the Physical Soc. of Japan, Kochi and Aomori, Sept. (2004).

Y. Ishida, M. Wada, and H. Wollnik: "Precise mass measurement of short-lived nuclei using a compact time-of-flight mass spectrometer", 2004 Autumn Meet. of the Physical Soc. of Japan, Kochi and Aomori, Sept. (2004).

K. Iida, A. Kohama, and K. Oyamatsu: "Reaction cross section described by a "black" nucleus", 2004 Autumn Meet. of the Physical Soc. of Japan, Kochi and Aomori, Sept. (2004).

A. Kohama, K. Iida, and K. Oyamatsu: ""Black" nucleus picture and nuclear matter radii", 2004 Autumn Meet. of the Physical Soc. of Japan, Kochi and Aomori, Sept. (2004).

S. Michimasa, S. Shimoura, H. Iwasaki, M. Tamaki, S. Ota, N. Aoi, H. Baba, N. Iwasa, S. Kanno, S. Kubono, K. Kurita, M. Uesaka, T. Minemura, T. Motobayashi, M. Notani, H. Ong, A. Saito, H. Sakurai, S. Takeuchi, E. Takeshita, Y. Yanagisawa, and A. Yoshida: "Study of single-particle states in ^{23}F using a proton transfer reaction", 4th Int. Conf. on Exotic Nuclei and Atomic Masses (ENAM 04), Pine Mountain, USA, Sept. (2004).

Y. Ishida, M. Wada, and H. Wollnik: "A multi-reflection time-of-flight mass spectrometer for mass measurements of short-lived nuclei", 18th Int. Conf. on the Application of Accelerators in Research and Industry (CAARI 2004), (American Physical Society), Fort Worth, USA, Oct. (2004).

H. Ueno: "Design of the beam transport line from IRC to RIPS", RIKEN Symp. on Research Projects Dedicated to RIPS in the RIBF Configuration, Wako, Oct. (2004).

N. Dinh Dang: "Nuclear giant resonances", 9th Asia Pacific Physics Conf. (APPC 2004), (Association of Asia Pacific Physical Societies and others), Hanoi, Vietnam, Oct. (2004).

T. Matsuzaki: "Recent researches at the RIKEN-RAL Muon Facility; Muon catalyzed d-t fusion", 9th Asia Pacific Physics Conf. (APPC 2004), (Association of Asia Pacific Physical Societies and others), Hanoi, Vietnam, Oct. (2004).

K. Sekiguchi: "Nucleon-deuteron scattering at intermediate energies and three nucleon force", Workshop on Light Ion and Polarization Phenomena 2004, (Tsukuba University), Tsukuba, Nov. (2004).

T. Gomi, T. Motobayashi, Y. Ando, N. Aoi, H. Baba, K. Demichi, Z. Elekes, N. Fukuda, Z. Fulop, U. Futakami, H. Hasegawa, Y. Higurashi, K. Ieki, N. Imai, M. Ishihara, K. Ishikawa, N. Iwasa, H. Iwasaki, S. Kanno, Y. Kondo, T. Kubo, S. Kubono, M. Kunibu, K. Kurita, Y. Matsuyama, S. Michimasa, T. Minemura, M. Miura, H. Murakami, T. Nakamura, M. Notani, S. Ota, A. Saito, H. Sakurai, M. Serata, S. Shimoura, T. Sugimoto, E. Takeshita, S. Takeuchi, Y. Togano, K. Ue, K. Yamada, Y. Yanagisawa, K. Yoneda, and A. Yoshida: "Coulomb dissociation for astrophysics", Japanese-German Nuclear Structure and Astrophysics Workshop, (GSI and RIKEN), Darmstadt, Germany, Dec. (2004).

A. Kohama, K. Iida, and K. Oyamatsu: "Extensive view of nuclei in black sphere picture", Workshop on Recent Progress and Future Prospects of Few Body System Physics, (RCNP), Osaka, Dec. (2004).

T. Gomi, T. Motobayashi, Y. Ando, N. Aoi, H.

Baba, K. Demichi, Z. Elekes, N. Fukuda, Z. Fulop, U. Futakami, H. Hasegawa, Y. Higurashi, K. Ieki, N. Imai, M. Ishihara, K. Ishikawa, N. Iwasa, H. Iwasaki, S. Kanno, Y. Kondo, T. Kubo, S. Kubono, M. Kunibu, K. Kurita, Y. Matsuyama, S. Michimasa, T. Minemura, M. Miura, H. Murakami, T. Nakamura, M. Notani, S. Ota, A. Saito, H. Sakurai, M. Serata, S. Shimoura, T. Sugimoto, E. Takeshita, S. Takeuchi, Y. Togano, K. Ue, K. Yamada, Y. Yanagisawa, K. Yoneda, and A. Yoshida: "Coulomb dissociation experiment for explosive hydrogen burning: study of the ^{22}Mg(p,γ)^{23}Al reaction", Nuclear Structure, Astrophysics and Reactions (NUSTAR 05), (University of Surrey), Guildford, UK, Jan. (2005).

3. Atomic and solid-state physics

M. Hoshino, T. Kambara, Y. Kanai, S. Madzunokov, R. Schuch, and Y. Yamazaki: "Multi-electron processes in close single collisions of slow highly charged ions with atoms", 28th Ann. Meet. of the Soc. for Atomic Collision Research, Hachioji, Aug. (2003).

M. Hoshino, Y. Kanai, Y. Nakai, M. Kitajima, H. Tanaka, and Y. Yamazaki: "State-selective angular distribution measurements of charge transfer processes for slow X^{4+}(X = C, N, O) - He collisions", 28th Ann. Meet. of the Soc. for Atomic Collision Research, Hachioji, Aug. (2003).

M. Fujiwara: "Confronting CPT with cold antihydrogen", New Direction of Particle Physics (TEA03), (Yukawa Institute for Theoretical Physics), Kyoto, Oct. (2003).

N. Oshima, T. M. Kojima, M. Niigaki, M. Inoue, K. Komaki, and Y. Yamazaki: "Plans for improvement of positron accumulation efficiency", Specialist Research Meet. on Positron Beam Techniques and Their Applications, (Research Reactor Institute, Kyoto University), Kyoto, Dec. (2003).

Y. Kanai: "Development of a new method to prepare a polarized antihydrogen", RIKEN Symp. on Studies on Condensed Matter Physics, Atomic Physics, Nuclear Chemistry, and Biology and Medicine Using RIKEN Accelerators, Wako, Jan. (2004).

N. Oshima: "Development of a positron accumulator for cooling of highly charged ions", RIKEN Symp. on Int. Workshop on Atomic Collisions of Slow/Trapped Highly-Charged Ions, Wako, Feb. (2004).

M. Hoshino: "The study of double-electron capture processes for C^{4+} - He collisions in the energy range of 60–110 eV/q", RIKEN Symp. on Int. Workshop on Atomic Collisions of Slow/Trapped Highly-Charged Ions, Wako, Feb. (2004).

M. Wada: "Universal slow radioactive beams and their application", RIKEN Symp. on Int. Workshop on Atomic Collisions of Slow/Trapped Highly-Charged Ions, Wako, Feb. (2004).

S. Masugi, A. Ishikawa, T. Muranaka, T. Azuma, C. Kondo, A. Hatakeyama, K. Komaki, Y. Yamazaki, E. Takada, and T. Murakami: "Channeling and resonant coherent excitation of high energetic ions using thin crystals", 59th Ann. Meet. of Physical Soc. of Japan, Fukuoka, Mar. (2004).

Y. Kanai, Y. Nakai, Y. Iwai, T. Ikeda, H. Masuda, K. Nishio, and Y. Yamazaki: "Coincidence measurements of L X-rays and final charge state of Ar ions transmitted through a microcapillary (2)", 59th Ann. Meet. of Physical Soc. of Japan, Fukuoka, Mar. (2004).

M. Niigaki, M. Inoue, N. Oshima, T. M. Kojima, A. Mohri, and Y. Yamazaki: "Cooling of highly-charged ions by utilizing a high density electron plasma: An attempt", 59th Ann. Meet. of Physical Soc. of Japan, Fukuoka, Mar. (2004).

N. Yamanaka and Y. Kino: "Development of a time-dependent coupled channel method and its application to antiproton-hydrogen atom collisions", 59th Ann. Meet. of Physical Soc. of Japan, Fukuoka, Mar. (2004).

N. Kuroda, H. Torii, M. Inoue, A. Mohri, D. Barna, K. Komaki, and Y. Yamazaki: "Diagnostics of antiproton-electron mixed plasma and extraction of ultra-slow antiprotons of from a strong magnetic field", 59th Ann. Meet. of Physical Soc. of Japan, Fukuoka, Mar. (2004).

Y. Nakai, M. Wada, T. Kambara, I. Katayama, and Y. Yamazaki: "Electronic response in nuclear decay of an ion with an unstable nucleus trapped in vacuum", 59th Ann. Meet. of Physical Soc. of Japan, Fukuoka, Mar. (2004).

A. Mohri, Y. Kanai, Y. Nakai, and Y. Yamazaki: "Experiment on electron plasma confinement in a cusped high magnetic field and an electric octupole", 59th Ann. Meet. of Physical Soc. of Japan, Fukuoka, Mar. (2004).

M. Niigaki, T. M. Kojima, N. Oshima, A. Mohri, M. Inoue, K. Komaki, and Y. Yamazaki: "Formation of a high-density electron plasma in a multi-ring trap", 59th Ann. Meet. of Physical Soc. of Japan, Fukuoka, Mar. (2004).

M. Fujiwara: "Fundamental physics with cold antihydrogen", 59th Ann. Meet. of Physical Soc. of Japan, Fukuoka, Mar. (2004).

M. Inoue, N. Oshima, T. M. Kojima, M. Niigaki, A. Mohri, K. Komaki, and Y. Yamazaki: "Improvement of a positron accumulator", 59th Ann. Meet. of Physical Soc. of Japan, Fukuoka, Mar. (2004).

H. Kanamitsu, S. Komatsu, Y. Hamatani, A. Iwase, N. Ishikawa, Y. Chimi, T. Kambara, and F. Ono: "Ion induced Fe-Pt alloy magnetic property change", 59th Ann. Meet. of Physical Soc. of Japan, Fukuoka, Mar. (2004).

A. Igarashi and I. Shimamura: "Positron scattering

by the He ion: Examples of complex rotation eigenvalues corresponding to no full resonances", 59th Ann. Meet. of Physical Soc. of Japan, Fukuoka, Mar. (2004).

T. Kambara, Y. Nakai, T. Ikeda, Y. Kanai, N. Fukunishi, K. Komaki, T. Azuma, C. Kondo, and Y. Yamazaki: "Resonant Coherent Excitation (RCE) observed for 2s electrons of Li-like Fe and Ni ions", 59th Ann. Meet. of Physical Soc. of Japan, Fukuoka, Mar. (2004).

C. Kondo, T. Muranaka, S. Masugi, A. Ishikawa, T. Azuma, A. Hatakeyama, K. Komaki, Y. Yamazaki, E. Takada, and T. Murakami: "Resonant coherent excitation of relativistic highly charged ion 4: Stark effect of He-like Ar and Fe ions", 59th Ann. Meet. of Physical Soc. of Japan, Fukuoka, Mar. (2004).

H. Torii, N. Kuroda, M. Inoue, M. Hori, A. Mohri, D. Barna, K. Komaki, and Y. Yamazaki: "Status and Perspective of the ASACUSA antiproton trap "MUSASHI"", 59th Ann. Meet. of Physical Soc. of Japan, Fukuoka, Mar. (2004).

M. Terada, N. Nakamura, Y. Kanai, Y. Nakai, K. Komaki, S. Ohtani, and Y. Yamazaki: "Surface modification by highly charged ions: STM/AFM observation of irradiated surface (2)", 59th Ann. Meet. of Physical Soc. of Japan, Fukuoka, Mar. (2004).

M. Fukuzumi, R. Taniguchi, N. Ishikawa, Y. Chimi, T. Kambara, S. Komatsu, F. Ono, F. Hori, and A. Iwase: "Swift heavy ion induced magnetic phase transition of Fe-Rh alloy", 59th Ann. Meet. of Physical Soc. of Japan, Fukuoka, Mar. (2004).

Y. Fukuyama, Y. Moriwaki, and Y. Matsuo: "Temperature dependence of the formation and dissociation cross section of Ba^{+*}-He", 59th Ann. Meet. of Physical Soc. of Japan, Fukuoka, Mar. (2004).

M. Hoshino, Y. Kanai, Y. Nakai, M. Kitajima, H. Tanaka, and Y. Yamazaki: "The study of electron capture processes for slow X^{4+}(X=C, N, O)-He collisions", 59th Ann. Meet. of Physical Soc. of Japan, Fukuoka, Mar. (2004).

Y. Iwai, Y. Kanai, Y. Nakai, T. Ikeda, H. Oyama, K. Ando, H. Masuda, K. Nishio, H. Torii, K. Komaki, and Y. Yamazaki: "X-ray measurement from N ions transmitted through a microcapillary target", 59th Ann. Meet. of Physical Soc. of Japan, Fukuoka, Mar. (2004).

T. Ikeda, Y. Nakai, Y. Kanai, Y. Iwai, H. Oyama, H. Sato, Y. Takizawa, S. Shiki, C. Otani, H. M. Shimizu, H. Masuda, K. Nishio, and Y. Yamazaki: "X-ray spectroscopy of highly-charged ions using STJ detectors and X-ray lens", 59th Ann. Meet. of Physical Soc. of Japan, Fukuoka, Mar. (2004).

Y. Kanai: "Spectroscopic study of ions transmitted from microcapillary tube", China-Japan Symp. on Atomic and Molecular Processes in Plasma (AMPP), (National Natural Science Foundation of China and JSPS), Lanzhou, China, Mar. (2004).

N. Oshima, M. Niigaki, A. Mohri, T. M. Kojima, Y. Kanai, Y. Nakai, K. Komaki, and Y. Yamazaki: "Cold highly charged ion production with positron/electron cooling techniques", 9th Int. Symp. on Electron Beam Ion Sources and Traps and Their Applications (EBIS/T 2004), Hachioji, Apr. (2004).

Y. Fukuyama, Y. Moriwaki, and Y. Matsuo: "Laser-induced fluorescence spectra of Ba^{+*}-He exciplexes in cold He gas of 3 – 30 K", 59th Ohio State University Int. Symp. on Molecular Spectroscopy, Columbus, USA, June (2004).

T. Kambara: "Detection of acoustic signals induced by heavy-ion impact: Ion-beam seismology", 21st Int. Conf. on Atomic Collisions in Solids (ICACS 21), (Instituto Nazionale per la Fisica della Materia and Dipartimento di Fisica dell Universita di Genova), Genova, Italy, July (2004).

Y. Nakai, T. Ikeda, Y. Kanai, T. Kambara, N. Fukunishi, K. Komaki, C. Kondo, T. Azuma, and Y. Yamazaki: "Resonant coherent excitation of 2s electron of Li-like Fe ions to the n=3 states", 21st Int. Conf. on Atomic Collisions in Solids (ICACS 21), (Instituto Nazionale per la Fisica della Materia and Dipartimento di Fisica dell Universita di Genova), Genova, Italy, July (2004).

T. Kambara: "Heavy-ion irradiation of solids at RIKEN accelerator facility", 24th Werner Brandt Workshop on Particle Penetration Phenomena and Excitations of Solids (WBW 24), Berlin, Germany, July (2004).

N. Oshima, M. Niigaki, A. Mohri, T. M. Kojima, Y. Kanai, Y. Nakai, K. Komaki, and Y. Yamazaki: "Application of a positron (electron) plasma for cooling of highly charged ions", 41st Ann. Meet. on Radioisotopes and Radiation in the Physical Science and Industries, (Japan Radioisotope Association), Tokyo, July (2004).

M. Niigaki, N. Oshima, A. Mohri, T. M. Kojima, K. Komaki, and Y. Yamazaki: "Current status and improvement plans of a positron accumulator", 41st Ann. Meet. on Radioisotopes and Radiation in the Physical Science and Industries, (Japan Radioisotope Association), Tokyo, July (2004).

Y. Kanai, A. Mohri, Y. Nakai, and Y. Yamazaki: "Development of a new method to prepare a polarized antihydrogen", 29th Ann. Meet. of the Soc. for Atomic Collision Research, Sendai, Aug. (2004).

Y. Iwai, Y. Kanai, Y. Nakai, T. Ikeda, M. Hoshino, H. Oyama, K. Ando, H. Masuda, K. Nishio, H. Torii, K. Komaki, and Y. Yamazaki: "X-ray measurement from N ions transmitted through a microcapillary target", 29th Ann. Meet. of the Soc. for Atomic Collision Research, Sendai, Aug. (2004).

N. Oshima, M. Niigaki, A. Mohri, T. M. Kojima, Y. Kanai, Y. Nakai, K. Komaki, and Y. Yamazaki: "Co-cooling scheme of highly charged ions with

positrons and electrons", 12th Int. Conf. on the Physics of Highly Charged Ions (HCI 2004), (VU Research Institute of Theoretical Physics and Astronomy), Vilnius, Lithuania, Sept. (2004).

Y. Kanai, Y. Nakai, Y. Iwai, T. Ikeda, K. Nishio, H. Masuda, and Y. Yamazaki: "Coincidence measurements of L X-ray and final charge state of highly charged Ar ions passing through a microcapillary", 12th Int. Conf. on the Physics of Highly Charged Ions (HCI 2004), (VU Research Institute of Theoretical Physics and Astronomy), Vilnius, Lithuania, Sept. (2004).

Y. Iwai, Y. Kanai, Y. Nakai, T. Ikeda, M. Hoshino, H. Oyama, K. Ando, H. Masuda, K. Nishio, H. Torii, K. Komaki, and Y. Yamazaki: "X-rays emitted from N ions transmitted through a thin Ni microcapillary target", 12th Int. Conf. on the Physics of Highly Charged Ions (HCI 2004), (VU Research Institute of Theoretical Physics and Astronomy), Vilnius, Lithuania, Sept. (2004).

Y. Matsuda: "Development of slow muon beam line at RIKEN-RAL muon facility (3)", 2004 Autumn Meet. of the Physical Soc. of Japan, Kochi and Aomori, Sept. (2004).

Y. Iwai, Y. Kanai, Y. Nakai, T. Ikeda, M. Hoshino, H. Masuda, K. Nishio, and Y. Yamazaki: "L X-ray measurement from Ar ions transmitted through microcapillaries 3", 2004 Autumn Meet. of the Physical Soc. of Japan, Kochi and Aomori, Sept. (2004).

I. Shimamura, A. Igarashi, and J. F. McCann: "Relation between the time-delay matrix and the eigenphase sum: Application to resonance analysis theory", 2004 Autumn Meet. of the Physical Soc. of Japan, Kochi and Aomori, Sept. (2004).

A. Igarashi and I. Shimamura: "Resonances in the positronium negative ion: Analysis in terms of the time-delay matrix", 2004 Autumn Meet. of the Physical Soc. of Japan, Kochi and Aomori, Sept. (2004).

Y. Fukuyama, Y. Moriwaki, and Y. Matsuo: "Temperature dependence of the formation and dissociation cross section of Ba^{+*}-He (2)", 2004 Autumn Meet. of the Physical Soc. of Japan, Kochi and Aomori, Sept. (2004).

Y. Kanai, Y. Nakai, Y. Iwai, T. Ikeda, M. Hoshino, K. Nishio, H. Masuda, and Y. Yamazaki: "X-ray measurements of highly charged Ar ions passing through a Ni microcapillary: coincidence of L X-ray and final charge state", 8th Workshop on Fast Ion-Atom Collisions, (Institute of Nuclear Research of the Hungarian Academy of Sciences), Debrecen, Hungary, Sept. (2004).

Y. Iwai, Y. Kanai, Y. Nakai, T. Ikeda, M. Hoshino, H. Oyama, H. Masuda, K. Nishio, H. Torii, K. Komaki, and Y. Yamazaki: "X-rays emitted from 2 keV/u N ions passing through Ni microcapillaries", 8th Workshop on Fast Ion-Atom Collisions, (Institution of Nuclear Research of the Hungarian Academy of Science), Debrecen, Hungary, Sept. (2004).

E. Yagi, S. Koike, T. Sugawara, T. Shishido, T. Urai, and K. Ogiwara: "Site change of hydrogen in Nb on alloying with high concentration of undersized Mo atoms", Int. Symp. on Metal-Hydrogen Systems: Fundamentals & Applications (MH2004), Cracow, Poland, Sept. (2004).

Y. Sakamaki, M. Hashimoto, Y. Fukai, K. Morita, J. Yuhara, M. Kato, S. Koike, and E. Yagi: "Stress-induced states of hydrogen and deuterium in vanadium by channeling experiments", Int. Symp. on Metal-Hydrogen Systems: Fundamentals & Applications (MH2004), Cracow, Poland, Sept. (2004).

Y. Matsuda: "Development of slow muon beam line at the RIKEN-RAL muon facility and new applications of mSR technique", 9th Asia Pacific Physics Conf. (APPC 2004), (Association of Asia Pacific Physical Societies and others), Hanoi, Vietnum, Oct. (2004).

4. Radiochemistry, radiation chemistry, and radiation biology

T. Shimada, M. Otani, H. Saito, and T. Abe: "Induction of mutations in sweet potato plants by heavy-ion beam irradiation", 105th Ann. Congr. of the Breeding Soc. of Japan, Tokyo, Mar. (2004).

K. Osawa, T. Abe, K. Maruta, S. Kadota, and H. Yamanishi: "Effect of heavy-ion beam irradiation on the survival and growth of japanese pear", 35th Ann. Meet. of Naganoken Engei Kenkyukai, Minamiminowa-mura, Nagano Pref., Mar. (2004).

M. Miyasaka, T. Abe, K. Seki, and T. Usui: "Effects of heavy-ion beam irradiation on dry seeds of eustoma.", 35th Ann. Meet. of Naganoken Engei Kenkyukai, Minamiminowa-mura, Nagano Pref., Mar. (2004).

T. Abe: "Mutation breeding using heavy-ion beam irradiation", 59th Ann. Meet. of Physical Soc. of Japan, Fukuoka, Mar. (2004).

S. Motomura, H. Takeichi, S. Enomoto, M. Kibe, Y. Gono, and Y. Yano: "Gamma-ray Compton imaging by strip germanium telescope", CNS-RIKEN Joint Symp. on Frontier of Gamma-Ray Spectroscopy and Its Application, Wako, Mar. (2004).

Y. Hase, S. Fujioka, S. Yoshida, K. Son, M. Umeda, and A. Tanaka: "Analyses of frill1 mutant induced by carbon-ion beam", 1st Meet. of the Ion Beam Breeding Soc., Takasaki, Apr. (2004).

K. Suzuki, Y. Takatsu, T. Gonai, Y. Miyazawa, H. Saito, T. Abe, S. Yoshida, and M. Kasumi: "Induction of new flower color mutant in spray-type chrysanthemum", 1st Meet. of the Ion Beam Breeding Soc., Takasaki, Apr. (2004).

M. Sugiyama, T. Terakawa, H. Saito, T. Abe, and S. Yoshida: "Mutation induction by heavy-ion beams in Pelargonium", 1st Meet. of the Ion Beam Breed-

ing Soc., Takasaki, Apr. (2004).

H. Saito, T. Abe, N. Fukunishi, H. Ryuto, K. Miyazaki, T. Kusumi, K. Suzuki, and S. Yoshida: "Sterile verbena mutants induced by heavy-ion beam irradiation", 1st Meet. of the Ion Beam Breeding Soc., Takasaki, Apr. (2004).

T. Morishita, H. Yamagichi, K. Debana, Y. Hase, N. Shikazono, A. Tanaka, T. Abe, N. Fukunishi, Y. Miyazawa, K. Sakamoto, and S. Yoshida: "Tartary backwheat mutants obtained by ion beams and gamma rays irradiation", 1st Meet. of the Ion Beam Breeding Soc., Takasaki, Apr. (2004).

M. Tomita, M. Aoki, and Y. Furusawa: "Molecular response of DNA double-strand break repair proteins", Heisei15nendo HIMAC Kyodo Riyo Kenkyu Seika Hapyokai, (National Institute of Radiological Sciences), Chiba, Apr. (2004).

S. Motomura, H. Takeichi, M. Kibe, Y. Gono, S. Enomoto, and Y. Yano: "Fourier analysis of back-projected images obtained by Compton camera composed of segmented Ge detectors", 87th Scientific Meet. of Japanese Soc. of Medical Physics, Yokoyama, Apr. (2004).

K. Igarashi, R. Hirunuma, H. Haba, S. Enomoto, and S. Kimura: "Influence of carnosine on the absorption of iron and other trace elemetns in rats using multitracer technology", 58th Ann. Meet. of Japanese Soc. of Nurtrition and Food Science, Sendai, May (2004).

M. Tomita, A. Naruto, Y. Matsumoto, Y. Hosoi, N. Suzuki, M. Izumi, and F. Yatagai: "Response of DNA repair proteins to heavy ion induced DNA damages", 8th Int. Workshop on Radiation Damage to DNA, Banff, Canada, May (2004).

K. Igarashi, R. Hirunuma, S. Kimura, and S. Enomoto: "Effect of polyphenol on the absorption of trace elements in rats", 21st Symp. on Trace Nutrients Research, (Japan Trace Nutrients Research Society), Kyoto, May (2004).

H. Haba, K. Morita, S. Enomoto, K. Morimoto, and D. Kaji: "Development of a novel heavy element chemistry apparatus using the RIKEN gas-field recoil separator as a pre-separator", 8th Symp. on REIMEI Research Resources, (JAERI), Tokai-mura, Ibaraki Pref., June (2004).

Y. Kanayama, R. Amano, H. Haba, and S. Enomoto: "Brain uptake behavior of the ^{24}Na, ^{28}Mg, ^{43}K and ^{47}Ca by intranasal administration", 15th Ann. Meet. of the Japan Soc. for Biomedical Reserch on Trace Elements, Tokyo, July (2004).

K. Igarashi, R. Hirunuma, S. Kimura, and S. Enomoto: "Effect of carnosine on the iron absorption in rats", 15th Ann. Meet. of the Japan Soc. for Biomedical Reserch on Trace Elements, Tokyo, July (2004).

H. Eto, T. Abe, Y. Saito, S. Yoshida, and O. Saijo: "Floating farm—hydroponics of salt-tolerant rice plants 1st report: Outline for facilities", Ann. Meet. of Architectural Institute of Japan 2004, Sapporo, Aug. (2004).

Y. Saito, T. Abe, H. Eto, S. Yoshida, and O. Saijo: "Floating farm—hydroponics of salt-tolerant rice plants 2nd report: Two case studies", Ann. Meet. of Architectural Institute of Japan 2004, Sapporo, Aug. (2004).

H. Haba, K. Igarashi, D. Kaji, R. Hirunuma, and S. Enomoto: "Development of a gas-jet-coupled multitarget system for multitracer production", 6th Int. Conf. on Nuclear and Radiochemistry, (Forschungszentrum Julich), Aachen, Germany, Aug.–Sept. (2004).

A. Toyoshima, K. Tsukada, M. Asai, H. Haba, K. Akiyama, I. Nishinaka, D. Saika, K. Matsuo, W. Sato, H. Ishidu, M. Ito, J. Saito, S. Goto, H. Kudo, H. Kikunaga, N. Kinoshita, C. Kato, A. Yokoyama, K. Sueki, Y. Nagame, and A. Shinohara: "Elution behavior of rutherfordium (Rf) in anion-exchange chromatography in a hydrofluoric acid system", 6th Int. Conf. on Nuclear and Radiochemistry, (Forschungszentrum Julich), Aachen, Germany, Aug.–Sept. (2004).

K. Tsukada, H. Haba, M. Asai, A. Toyoshima, K. Akiyama, I. Nishinaka, M. Hirata, K. Hashimoto, S. Ichikawa, Y. Nagame, K. Yasuda, Y. Miyamoto, Y. Tani, H. Hasegawa, W. Sato, A. Shinohara, S. Goto, M. Ito, J. Saito, H. Ishidu, H. Kudo, Y. Oura, H. Nakahara, K. Sueki, N. Kinoshita, H. Kikunaga, and A. Yokoyama: "Sorption on anion-exchange resin of dubnium and its homologues in HF solution", 6th Int. Conf. on Nuclear and Radiochemistry, (Forschungszentrum Julich), Aachen, Germany, Aug.–Sept. (2004).

T. Abe and M. Arai: "Induction of mutations on carnation by ion beam radiation and comparison to other treatments", 106th Ann. Congr. of Breeding Soc. of Japan, Tsu, Sept. (2004).

H. Takeichi, S. Motomura, Y. Gono, Y. Yano, and S. Enomoto: "Concurrent imaging of multiple radioactive tracers with a Compton camera", 27th Ann. Meet. of the Japan Neuroscience Soc./47th Ann. Meet. of the Japan Soc. for Neurochemistry Joint Meet. (Neuro2004), Osaka, Sept. (2004).

K. Igarashi, Y. Nakanishi, R. Hirunuma, S. Enomoto, and S. Kimura: "Nutritional study on efficacy of sodium iron ethylenediaminetetraacetic acid as a food fortificant", 28th the Japan BioIron Soc., Tokyo, Sept. (2004).

T. Matsuyama, H. Ichida, K. Koike, H. Saito, T. Abe, T. Asami, T. Ebisuzaki, and S. Yoshida: "A DNA polymorphism detection system by computer simulation using the Arabibidopsis genome sequences: A virtual imaging restriction landmark genomic scanning", 68th Ann. Meet. of the Botanical Soc. of Japan, Fujisawa, Sept. (2004).

Y. Yamamoto, Y. Shimada, M. Kimura, H. Ryuto, N.

Fukunishi, T. Abe, and S. Yoshida: "Global classification of transcriptional responses to light stress in *Arabidopsis thaliana*", 9th Int. Congr. of Endocytobiology and Symbiosis, Jena, Germany, Sept. (2004).

K. Osawa, I. Maruta, T. Abe, S. Tsunoda, and H. Yamanishi: "Effects of heavy-ion beam irradiation on in vitro shoot growht in japanese pear 'Nansui'", Ann. Meet. 2004 of Japan Soc. for Horticultural Science, Shizuoka, Sept. (2004).

Y. Matsumoto, M. Tomita, A. Morita, Y. Hosoi, and N. Suzuki: "XRCC4 as the genuine target of DNA-PK in DNA double-strand break repair and the maintenance of genomic stability", 63rd Ann. Meet. of the Japanese Cancer Assoc., Fukuoka, Sept.–Oct. (2004).

K. Tsukada, A. Toyoshima, H. Haba, M. Asai, K. Akiyama, I. Nishinaka, Y. Nagame, D. Saika, K. Matsuo, W. Sato, A. Shinohara, H. Ishizu, M. Ito, J. Saito, S. Goto, H. Kudo, H. Kikunaga, N. Kinoshita, C. Kato, A. Yokoyama, and K. Sueki: "Anion-exchange chromatographic behavior of Rutherfordium (Rf) in hydrofluoric acid", 2004 Ann. Meet. on Japan Soc. of Nuclear and Radiochemical Sciences and 48th Symp. on Radiochemistry, Tokyo, Oct. (2004).

Y. Tani, H. Hasegawa, D. Saika, Y. Kitamoto, K. Matsuo, W. Sato, N. Takahashi, T. Yoshimura, H. Haba, and A. Shinohara: "Development of liquid scintillation counting system for the on-line alpha-ray measurement of heavy elements", 2004 Ann. Meet. on Japan Soc. of Nuclear and Radiochemical Sciences and 48th Symp. on Radiochemistry, Tokyo, Oct. (2004).

D. Saika, Y. Kitamoto, K. Matsuo, Y. Tani, H. Hasegawa, W. Sato, N. Takahashi, T. Yoshimura, K. Takamiya, S. Shibata, H. Haba, S. Enomoto, and A. Shinohara: "Development of online solvent extraction system for heavy actinide chemistry", 2004 Ann. Meet. on Japan Soc. of Nuclear and Radiochemical Sciences and 48th Symp. on Radiochemistry, Tokyo, Oct. (2004).

K. Akiyama, H. Haba, K. Tsukada, M. Asai, K. Sueki, A. Toyoshima, T. Yaita, and Y. Nagame: "EXAFS study of the 4th and 5th group of elements in hydrofluoric acid", 2004 Ann. Meet. on Japan Soc. of Nuclear and Radiochemical Sciences and 48th Symp. on Radiochemistry, Tokyo, Oct. (2004).

A. Toyoshima, K. Tsukada, M. Asai, H. Haba, K. Akiyama, Y. Ishii, I. Nishinaka, T. Sato, M. Hirata, Y. Nagame, W. Sato, K. Matsuo, Y. Tani, D. Saika, Y. Kitamoto, H. Hasegawa, A. Shinohara, S. Goto, M. Ito, J. Saito, H. Kudo, M. Sakama, A. Yokoyama, K. Morishita, K. Sueki, H. Nakahara, and M. Schaedel: "Formation of anionic fluoride complex of Rutherfordium (Rf): Anion-exchange behavior in hydrofluoric acid/nitric acid mixed solution system", 2004 Ann. Meet. on Japan Soc. of Nuclear and Radiochemical Sciences and 48th Symp. on Radiochemistry, Tokyo, Oct. (2004).

Y. Kanayama, R. Hirunuma, H. Haba, S. Enomoto, and R. Amano: "Olfactory transport of alkaline metal ions by intranasal administration (2): Uptake behavior of Na+ and K+", 2004 Ann. Meet. on Japan Soc. of Nuclear and Radiochemical Sciences and 48th Symp. on Radiochemistry, Tokyo, Oct. (2004).

H. Haba, K. Tsukada, K. Akiyama, M. Asai, A. Toyoshima, Y. Ishii, S. Enomoto, and Y. Nagame: "Reversed-phase extraction chromatography of Zr and Hf in the TBP/HCl system: Model experiments for chemical characterization of element 104, rutherfordium", 2004 Ann. Meet. on Japan Soc. of Nuclear and Radiochemical Sciences and 48th Symp. on Radiochemistry, Tokyo, Oct. (2004).

H. Kikunaga, Y. Kasamatsu, K. Takamiya, T. Mitsugashira, M. Hara, T. Ohtuki, H. Yuki, H. Haba, A. Shinohara, S. Shibata, N. Kinoshita, A. Yokoyama, and T. Nakanishi: "Search for the extremely low energy isomer of Th-229 by alpha-spectrometry", 2004 Ann. Meet. on Japan Soc. of Nuclear and Radiochemical Sciences and 48th Symp. on Radiochemistry, Tokyo, Oct. (2004).

Y. Kasamatsu, H. Kikunaga, K. Takamiya, T. Mitsugashira, T. Nakanishi, T. Ohtuki, H. Yuki, H. Haba, W. Sato, H. Yamana, Y. Ohkubo, M. Hara, K. Ninomiya, S. Shibata, and A. Shinohara: "Visible and ultraviolet light measurement from the ultra low-lying isomer 229mTh", 2004 Ann. Meet. on Japan Soc. of Nuclear and Radiochemical Sciences and 48th Symp. on Radiochemistry, Tokyo, Oct. (2004).

H. Takeichi, S. Motomura, Y. Gono, H. Haba, R. Hirunuma, K. Igarashi, Y. Yano, and S. Enomoto: "Concurrent tomography of multiple radioactive tracers with a Compton camera", 34th Ann. Meet. of Soc. for Neuroscience (Neuroscience 2004), San Diego, USA, Oct. (2004).

S. Motomura, H. Takeichi, R. Hirunuma, H. Haba, K. Igarashi, S. Enomoto, Y. Gono, and Y. Yano: "Gamma-ray compton imaging of multitracer in biosamples by strip germanium telescope", IEEE Rome 2004, Nuclear Science Symp., Rome, Italy, Oct. (2004).

Y. Yamamoto, C. Bae, H. Saito, H. Ryuto, N. Fukunishi, T. Abe, and S. Yoshida: "Heavy ion beam mutagenesis of Arabidopsis thaliana and screening for light stress mutants", Joint Meet. of 14th Crucifer Genetics Workshop and 4th ISHS Symp. on Brassicas (BRASSICA 2004), Daejeon, Korea, Oct. (2004).

H. Takeichi, S. Motomura, Y. Gono, H. Haba, R. Hirunuma, K. Igarashi, Y. Yano, and S. Enomoto: "Development of γ-ray emission imaging", 17th Int. Conf. on Cyclotrons and Their Applications (Cy-

clotrons 2004), (RIKEN), Tokyo, Oct. (2004).

T. Abe, S. Yoshida, N. Fukunishi, H. Ryuto, and K. Suzuki: "The ion-beam breeding makes great success in plant business", 17th Int. Conf. on Cyclotrons and Their Applications (Cyclotrons 2004), (RIKEN), Tokyo, Oct. (2004).

L. H. Yin, Y. Suzuki, Y. Matsumoto, M. Tomita, Y. Furusawa, A. Enomoto, A. Morita, M. Aoki, F. Yatagai, T. Suzuki, Y. Hosoi, K. Ohtomo, and N. Suzuki: "Molecular mechanisms of hyperthermic radiosensitization: Roles of DNA double-strand break pathways", 47th Ann. Meet. Japan Radiation Research Soc., Nagasaki, Nov. (2004).

M. Tomita, Y. Yano, F. Yatagai, N. Suzuki, Y. Hosoi, and Y. Matsumoto: "Response of DSB repair proteins to accelerated iron ion induced DSBs", 47th Ann. Meet. Japan Radiation Research Soc., Nagasaki, Nov. (2004).

Y. Matsumoto, M. Tomita, L. H. Yin, A. Morita, A. Enomoto, T. Suzuki, Y. Hosoi, K. Ohtomo, and N. Suzuki: "The significance of protein-phosphorylating function of DNA-PK in DNA double-strand break repair: XRCC4 as the genuine target", 47th Ann. Meet. Japan Radiation Research Soc., Nagasaki, Nov. (2004).

H. Takeichi, S. Motomura, and S. Enomoto: "A multi-nuclide gamma-ray emission imaging system (GREI)", 44th Ann. Meet. of Japanese Society of Nuclear Medicine, Kyoto, Nov. (2004).

M. Tomita: "Response of DNA double-strand break repair proteins to low dose ionizing radiations", PF Seminar: Microbeam saibou shousha souti wo motiita teisenryo houshasen eikyou kenkyu ni kansuru workshop, (Institute of Materials Structure Science, KEK), Tsukuba, Dec. (2004).

5. Material Analysis

K. Maeda, k. Hasegawa, M. Maeda, K. Ogiwara, and H. Hamanaka: "Time-resolved chemical state analysis by highly sensitive high-resolution PIXE", 10th Int. Conf. on Particle-induced X-ray Emission and Its Analytical Applications, (Jozef Stefan Institute and others), Portoroz, Slovenia, June (2004).

K. Mochiki, K. Okada, T. Toriyama, K. Kawasaki, K. Sanetoshi, K. Maeda, and K. Hasegawa: "Development of an x-ray detecting system for WDX PIXE", 21st PIXE Symp., (The Japan Society for Particle Induced X-ray Emission (PIXE) Research), Tokyo, Nov. (2004).

K. Maeda, K. Hasegawa, H. Hamanaka, K. Ogiwara, M. Tsuji, and S. Murao: "In-air chemical state analysis of Cr and Fe by PIXE using a position-sensitive crystal spectrometer", 21st PIXE Symp., (The Japan Society for Particle Induced X-ray Emission (PIXE) Research), Tokyo, Nov. (2004).

H. Hamanaka, K. Atsumi, F. Nagase, and K. Maeda: "PIXE analysis of ancient pottery (middle Jomon period) excavated at Unasawa Shimonohara in Tokyo (1)", 21st PIXE Symp., (The Japan Society for Particle Induced X-ray Emission (PIXE) Japan), Tokyo, Nov. (2004).

6. RIKEN-BNL Collaboration

Y. Goto: "Transversity and transverse-spin asymmetry measurements at PHENIX", 5th European Research Conf. on Electromagnetic Interactions with Nucleons and Nuclei (EINN 2003), Parallel Pre-Conf. Workshops B: Transversity, (Institute of Accelerating Systems and Applications), Athens, Greece, Oct. (2003).

M. Ohtani: "Soft mode near the critical end point in the chiral quark model", 59th Ann. Meet. of Physical Soc. of Japan, Fukuoka, Mar. (2004).

M. Hirai: "Polarized parton distributions and their uncertainties", RIKEN-TODAI Mini-Workshop on "Topics in Hadron Physics at RHIC", Wako, Mar. (2004).

T. Ikeda: "The effect of memory on relaxation in ϕ^4 theory", RIKEN-TODAI Mini-Workshop on "Topics in Hadron Physics at RHIC", Wako, Mar. (2004).

M. Ohtani: "Charge distribution of spin polarized Skyrmion and the gauged Wess-Zumino term", 2004 Autumn Meet. of the Physical Soc. of Japan, Kochi and Aomori, Sept. (2004).

T. Tabaru, Y. Akiba, R. Averbeck, S. Butsyk, F. Kajihara, M. Togawa, and Y. Tsuchimoto: "Measurement of single electrons in $\sqrt{s_{NN}} = 62.4\,\mathrm{GeV}$ Au-Au collisions at RHIC PHENIX", 2004 Autumn Meet. of the Physical Soc. of Japan, Kochi and Aomori, Sept. (2004).

A. Kiyomichi: "Radial flow study via identified hadron spectra in Au+Au collisions", 2004 Autumn Meet. of the Physical Soc. of Japan, Kochi and Aomori, Sept. (2004).

T. Ikeda and L. McLerran: "Understanding impact parameter in Balitsky-Kovchegov equation", 2004 Autumn Meet. of the Physical Soc. of Japan, Kochi and Aomori, Sept. (2004).

M. Ohtani: "Spin polarized Skyrmions in the $\mathrm{U_{EM}}(1)$ gauged Wess-Zumino action", 10th Int. Conf. on the Structure of Baryons (Baryons 2004) , (L'Institut de Physique Nucleaire d'Orsay), Palaiseau, France, Oct. (2004).

M. Ohtani: "Spin polarized Skyrmions and the $\mathrm{U_{EM}}(1)$ gauged Wess-Zumino term", YITP Workshop on Fundamental Problems and Applications of Quantum Field Theory, (Yukawa Institute for Theoretical Physics), Kyoto, Dec. (2004).

IX. LIST OF SYMPOSIA

(Jan.–Dec. 2004)

1) "Post Cluster'03" Cluster Project Workshop
7 Jan., Wako, Heavy Ion Nuclear Physics Lab., RIKEN

2) Studies on Condensed Matter Physics, Atomic Physics, Hyperfine Interactions and Biomedical Sciences Using RIKEN Accelerators
19 Jan., Wako, Muon Science Lab., Atomic Physics Lab., Nuclear Chemistry Lab., and Cellular Physiology Lab., RIKEN

3) Workshop on Cyclotron Mutagenesis (II)
20 Jan., Wako, Plant Functions Lab., RIKEN

4) RHIC Spin Collaboration Meeting XXI
22 Jan., New York, USA, RBRC, RIKEN

5) Lattice QCD at Finite Temperature and Density
8–12 Feb., New York, USA, RBRC, RIKEN

6) Int. Workshop on Atomic Collisions of Slow/Trapped Highly-Charged Ions
19–21 Feb., Wako, Atomic Physics Lab., RIKEN

7) Workshop on Super Heavy Element Synthesis
26 Feb., Wako, Beam Technology Division, Cyclotron Center, RIKEN

8) RHIC Spin Collaboration Meeting XXII
27 Feb., New York, USA, RBRC, RIKEN

9) CNS-RIKEN Joint Symp. on Frontier of Gamma-ray Spectroscopy and Its Application
18–19 Mar., Wako, Heavy Ion Nuclear Physics Lab., RIKEN and CNS

10) RHIC Spin Collaboration Meeting XXIII
19 Mar., New York, USA, RBRC, RIKEN

11) RIKEN-TODAI Mini-Workshop on "Topics in Hadron Physics at RHIC"
23–24 Mar., Wako, Radiation Lab., RIKEN and University of Tokyo

12) Status Report of RIKEN Cluster Project
14–15 May, Wako, Heavy Ion Nuclear Physics Lab., RIKEN

13) New Discoveries at RHIC
14–15 May, New York, USA, RBRC, RIKEN

14) RHIC Spin Collaboration Meeting XXIV
21 May, New York, USA, RBRC, RIKEN

15) RHIC Spin Collaboration Meeting XXV
27 May, New York, USA, RBRC, RIKEN

16) The Present and Future of Muon Sciences at the RIKEN-RAL Muon Facility
27–28 May, Wako, Advanced Meson Science Lab., RIKEN

17) RHIC Spin Collaboration Meeting XXVI
1 June, New York, USA, RBRC, RIKEN

18) 1st Summer School on QCD Spin Physics
5–12 June, New York, USA, RBRC, RIKEN

19) RIBF-UEC/RIKEN Joint Workshop "Physics of Unstable Nuclei: These 10 years and From Now On"
15–17 June, Wako, Heavy Ion Nuclear Physics Lab., RIBF-UEC and RIKEN

20) Physics of Unstable Nuclei in This Decade and the Future
15–17 June, Wako, Heavy Ion Nuclear Physics Lab., RIKEN

21) Int. Symp. on Exotic Nuclei (EXON 2004)
5–12 July, Peterhof, Russia, Heavy Ion Nuclear Physics Lab., JINR, RIKEN, GSI and GANIL

22) RHIC Spin Collaboration Meeting XXVII
22 July, New York, USA, RBRC, RIKEN

23) Int. Summer School on Subatomic Physics
26–30 Aug., Beijing, China, Heavy Ion Nuclear Physics Lab., RIKEN, PKE, IMP and others

24) RHIC Spin Collaboration Meeting XXVIII
2 Sep., New York, USA, RBRC, RIKEN

25) RIBF Nuclear Physics Workshop "Mean Field and Collective Motion of Unstable Nuclei"
5–7 Sep., Wako, Heavy Ion Nuclear Physics Lab., RIKEN

26) Theory Summer Program on RHIC Physics
28 Sep., New York, USA, RBRC, RIKEN

27) Lectures on Hadron Physics
7–9 Oct., Wako, Radiation Lab., RIKEN, Tokyo Institute of Technology and University of Tokyo

28) RHIC Spin Collaboration Meeting XXIX
8–9 Oct., Torino, Italy, RBRC, University of Torino

29) 15th Inelastic Ion Surface Collision Workshop (IISC-15)
17–22 Oct., Shima, Atomic Physics Lab., JSAP

30) RIKEN Symp. on Development of Science with RI-beam below than 100 MeV/u
20 Oct., Wako, Applied Nuclear Physics Lab., RIKEN

31) High Performance Computing with BlueGene/L QCDOC Architectures
27–28 Oct., New York, USA, RBRC, RIKEN

32) 5th Italy-Japan Symp. on Recent Achievements and Perspectives in Nuclear Physics
3–7 Nov., Napoli, Italy, Heavy Ion Nuclear Physics Lab., RIKEN

33) Workshop on the Physics Programme of the RBRC and UKQCD QCDOC Machines
12–13 Nov., New York, USA, RBRC, RIKEN

34) Interim Report of RIKEN Cluster Project
15 Nov., Wako, Heavy Ion Nuclear Physics Lab., RIKEN

35) RBRC Scientific Review Committee
16–17 Nov., New York, USA, RBRC, RIKEN

36) RIKEN, Joint Workshop for Nuclear Reaction Theory and Experiment
26–27 Nov., Wako, Heavy Ion Nuclear Physics Lab., RIKEN

37) Japanese-Russian Workshop on Studies of Exotic Nuclei
3–4 Dec., Wako, Heavy Ion Nuclear Physics Lab., RIKEN

38) Physics at RHIC and Related Topics
6–7 Dec., Wako, Radiation Lab., RIKEN

39) RHIC-SPIN-J Physics Discussion
15 Dec., Kyoto , Radiation Lab., RIKEN

40) Strongly Coupled Plasmas: Electromagnetic, Nuclear & Atomic
16–17 Dec., New York, USA, RBRC, RIKEN

41) Japanese-German Workshop on Nuclear Structure and Astrophysics
16–18 Dec., Darmstadt, Germany, Heavy Ion Nuclear Physics Lab., RIKEN and GSI

X. LIST OF SEMINARS

(Jan.–Dec. 2004)

RIKEN Nuclear-Physics Seminar

1) R. Seki, California State University (USA), 21 Jan.
"Thermal properties of simple nucleon matter on a lattice"

2) W. G. Lynch, Michigan State University (USA), 3 Mar.
"Towards the equation of state of dense asymmetric matter"

3) W. Shen, Shanghai Institute of Applied Physics (China), 11 Mar.
"Radioactive ion beam physics and nuclear astrophysics in China"

4) Y. T. Oganessian, Flerov Laboratory of Nuclear Reactions, JINR (Russia), 12 Mar.
"Heavy element research in Dubna"

5) K. Summerer, GSI (Germany), 6 Apr.
"High-energy Coulomb dissociation of ^{8}B"

6) H.-J. Schulze, Catania University (Italy), 14 June
"Hyperons in nuclear matter, neutron stars, and finite nuclei"

7) S. Yoshida, Hosei University (Tokyo), 5 Aug.
"Neutron skin thickness and equation of state in neutron matter"

8) H. Nakada, Chiba University (Chiba), 12 Aug.
"New method, new interaction for mean-field approximations and structure of unstable nuclei"

9) K. Iida, RBRC (USA), 21 Sep.
"Nuclear radius and the equation of state of nuclear matter"

10) H. Witala, Jagiellonian University (Poland), 6 Oct.
"Relativistic effects in the elastic Nd scattering"

11) R. A. Gherghescu, National Institute for Nuclear Physics and Engineering Bucharest (Romania), 1 Nov.
"Two center model for binary processes fusion and fission"

12) W. Q. Shen, Shanghai Institute of Applied Physics (China), 16 Nov.
"New machine for nuclear physics in China"

13) G. Shirkov, JINR (Russia), 24 Nov.
"JINR and JINR basic facilities"

14) A. Ono, Tohoku University (Sendai), 14 Dec.
"Symmetry energy in multifragmentation"

Radiation Lab.

1) K. Ohnishi, University of Tokyo (Tokyo), 3 Feb.
"Mode coupling theory for the dynamic aspect of the chiral phase transition"

2) G. Bunce, RBRC/BNL (USA), 24 Mar.
"The new muon g-2 result"

3) M. Nio, RIKEN (Wako), 24 Mar.
"Theory of muon g-2: Overview"

4) Y. En'yo, KEK (Tsukuba), 25 May
"AMD study of pentaquark in a quark model"

5) S. Digal, University of Tokyo (Tokyo), 31 May
"Induced critical behavior"

6) T. Inagaki, KEK (Tsukuba), 23 July
"Experiment on the rare decay $K_L \to \pi^0\nu\nu$"

7) J. Noaki, RIKEN (Wako), 23 July
"Lattice QCD calculation of kaon matrix elements"

8) H. Lipkin, Weizmann Institute (Israel)/Argonne National Laboratory (USA), 28 July
"What can we learn from QCD about pentaquarks and vice versa?"

9) A. Hayashigaki, Kyoto University (Kyoto), 3 Aug.
"High-p_T leading hadron suppression in heavy-ion collisions"

10) K. Fukushima, MIT (USA), 3 Aug.
"Heating (Gapless) color-flavor locked quark matter"

11) T. Wettig, University of Regensburg (Germany), 9 Aug.
"Color-flavor transformation and application to lattice QCD"

12) T. Yamazaki, RBRC/BNL (USA), 5 Oct.
"I = 2 S-wave pion scattering phase shift with two flavor full QCD"

13) T. Sugihara, RBRC/BNL (USA), 12 Oct.

"Matrix product variational formulation for lattice gauge theory"

Applied Nuclear Physics Lab.

1) P. F. Mantica, Michigan State University (USA), 18 Feb.
"Low-energy structure of exotic nuclei studied at the NSCL using β-delayed γ ray and β-NMR spectroscopies"

2) R. Neugart, University of Mainz (Germany), 24 Feb.
"Recent experiments at ISOLDE on the laser spectroscopy and β-NMR spectroscopy with optically polarized beams"

3) E. Stachowska, Poznan University of Techbology (Poland), 24 Feb.
"Laser spectroscopic investigations on atoms with open 3d and 4f shells: elements with high nuclear spins"

4) F. Mareschal, Strasbourg University (France), 1 Mar.
"The beta decay of the heavy calcium isotopes"

5) H. H. Bertschat, Hahn-Meitner-Institut, Berlin (Germany), 23 Mar.
"Basic research on the atomic scale towards magnetic terabit memories: investigations with radioactive probe atoms"

Atomic Physics Lab.

1) A. V. Solov'yov, A. F. Ioffe Physical-Technical Institute/Russian Academy of Sciences (Russia), 14 Apr.
"Fission, fusion and collision processes of atomic clusters: ab initio and model approaches"

2) E. D. Donets, JINR (Russia), 23 Apr.
"Electron string phenomenon: physics and use"

3) S. L. Chin, Laval University (Canada), 17 June
"Self-guided hot light pulse"

4) A. Bai, National Institute of Advanced Industrial Science and Technology (Tsukuba), 17 Sep.
"Atomic images of the defects on graphite by scanning probe microscopy"

5) K. M. Aggarwal, Queen's University (UK), 15 Oct.
"Atomic data for plasma diagnostics"

6) R. Oiwa, "ULVAC PHI Incorporated (Tokyo), 3 Dec.
"Developing small area trends in surface analysis"

Heavy Ion Nuclear Physics Lab.

1) N. Otsuka, JCPRG (Sapporo)/JAERI (Tsukuba), 16 Jan.
"Introduction to nuclear data base"

2) A. Ono, Tohoku University (Sendai), 14 Dec.
"Nuclear equation of state and liquid-gas phase transition"

Advanced Meson Science Lab.

1) H. Goka, IMR, Tohoku University (Sendai), 19 Nov.
"A universal spin excitation in high-Tc superconductor"

Plant Functions Lab.

1) S. Y. Kang, KAERI (Korea), 24 Feb.
"New development of mutation breeding in Korea"

2) S. Ohno, Theoretical Radiation Research Laboratory (Yokohama), 21 May
"An ion-track structure model to understand cross-sections for ion-induced DNA bond breaks"

3) A. Iwase, Research Institute for Advanced Science and Technology, Osaka Prefecture University (Osaka), 21 May
"Structures and production mechanisms of GeV-ion induced tracks in inorganic materials"

RIBF Project Group, Accelerator Sub-Group

1) L. Conradie, iThemba LABS (South Africa), 26 Oct.
"Status of the iThemba LABS accelerators"

2) P. Sigg, PSI (Switzerland), 5 Nov.
"Status of the PSI accelerators"

RIKEN BNL Research Center

1) Z. Sep, Hungarian Academy of Sciences (Hungary), 23 Jan.
"The T-mu phase diagram in the chiral quark model from a large flavor number expansion"

2) T. Sugihara, RBRC (USA), 5 Feb.
"Vector and chiral gauge theories on the lattice"

3) T. Kaneko, KEK (Japan), 11 Feb.
"Light hadron spectrum and quark masses in three-flavor dynamical QCD"

4) H. Meyer, Oxford University (UK), 12 Feb.
"Glueball Regge trajectories"

5) A. Gouvea, Northwestern University (USA), 18 Feb.
"What have we really learned from neutrino oscillation experiments?"

6) A. Gal, Hebrew University (Israel), 20 Feb.
"Indication of chiral symmetry restoration from deeply bound pionic atoms?"

7) W. Kinney, SUNY at Buffalo (USA), 25 Feb.
"Inflation after WMAP"

8) S. Kretzer, RBRC (USA), 26 Feb.
"Strangeness asymmetry of the nucleon and other QCD aspects of the NuTeV anomaly"

9) T. Falter, Universitaet Giessen (Germany), 27 Feb.
"High energy electroproduction off complex nuclei"

10) N. A. Perez, Cern (Switzerland), 10 Mar.
"Effects of medium-induced gluon radiation on jet shapes and heavy flavors"

11) K. Tuchin , BNL (USA), 11 Mar.
"Cosmology inside hadrons"

12) S. Mrowczynski, Soltan Institute of Nuclear Studies (Poland), 12 Mar.
"Equilibration of the quark gluon plasma"

13) M. Piai, Yale University (USA), 17 Mar.
"A class of extended technicolor models"

14) G. Brown, SUNY at Stonybrook (USA), 19 Mar.
"What hath RHIC wrought?"

15) J. Giedt, University of Toronto (Canada), 7 Apr.
"Lattice (super) Yang-Mills and the dynamical lattice spacing"

16) Y. Dokshitzer, LPTHE (France), 15 Apr.
"Heavy quark physics"

17) C. Quigg, FNAL (USA), 21 Apr.
"Charmonium: The next wave"

18) A. Shoshi, Columbia University (USA), 22 Apr.
"Small-x physics beyond the Kovchegov equation"

19) K. Holland, UC San Diego (USA), 28 Apr.
"Triviality and the Higgs mass lower bound"

20) S. Gupta, Tata Institute of Advanced Research (India), 29 Apr.
"Transport and fluctuations in finite-temperature QCD"

21) D. Boyanovsky, University of Pittsburgh (USA), 30 Apr.
"Dynamical renormalization group approach to relaxation and transport"

22) T. Baltz, RBRC/BNL (USA), 6 May
"Calculation of heavy-ion e^+e^- pair production to all orders in $Z\alpha$"

23) G. Zaharijas, New York University (USA), 12 May
"Phenomenology of a stable or long-lived H di baryon"

24) A. Gonzalez-Arroyo, Madrid/Rutgers (Spain), 26 May
"Constructing vortices and instantons by expansion methods"

25) R. Venugopalan, BNL (USA), 27 May
"k_t factorization and beyond in gluon and quark-pair production in high energy hadronic collisions"

26) H. Logan, University of Wisconsin (USA), 2 June
"The littlest higgs boson at a photon collider"

27) F. Petriello, Johns Hopkins University (USA), 9 June
"Differential distributions in QCD at NNLO"

28) B. Kerbikov, ITEP (Russia), 10 June
"BCS-Bose crossover for quarks"

29) U. Florian, GSI (Germany), 22 June
"Strange particle production at SIS and GSI"

30) M. Tokarev, JINR, Dubna (Russia), 25 June
"New Verification of Z-scaling at RHIC and the Tevatron"

31) K. Iida, RBRC (USA), 15 July
"Nuclear radius and the equation of state of nuclear matter"

32) T. Krupovnickas, Florida State University (USA), 21 July
"Collider reaches in SUSY"

33) T. Yamazaki, RBRC (USA), 22 July
"I = 2 π-π scattering phase shift with two flavors dynamical quark effect"

34) S. Munier, CPHT of the Ecole Polytechnique (France), 23 July
"New insights in high energy QCD from general tools of statistical physics (contracted from 07/16/04)"

35) C. Marquet, SPhT-CEA, Saclay (France), 28 July
"Testing saturation with forward jets"

36) T. Doi, RBRC (USA), 29 July
"Pentaquark baryons from the QCD sum rule"

37) T. D. Lee, Columbia University/RBRC (USA), 5 Aug.
"New ways to solve the schrodinger equation"

38) A. Muronga, Frankfurt University (Germany), 6 Aug.
"Nom-ideal fluid dynamics for nuclear collisions"

39) D. Suprun, University of Chicago (USA), 11 Aug.
"Phenomenology of charmless hadronic B decays"

40) G. Nayak, Stony Brook University (USA), 2 Sep.
"Gluon propagator in non-equilibrium and non-zero magnetic screening in QED and QCD at one loop level"

41) D. Antonov, Humboldt University (Germany), 8 Sep.
"3D Georgi-Glashow model and confining strings at zero and finite temperatures"

42) R. Glauber, Harvard University (USA), 11 Sep.
Quantum optics and heavy-ion physics"

43) H. J. Pirner, Heidelberg University (Germany), 11 Sep.
"Low-x scattering as a critical phenomenon"

44) Y. Markov, Institut of System Dynamics and Control Theory Siberian Branch of Academy of Sciences (Russia), 17 Sep.
"Nonlinear dynamics of soft boson collective excitations in hot QCD plasma: Bremsstrahlung and energy losses"

45) E. Iancu, CEA Saclay (France), 8 Oct.
"Stochastic aspects of high energy QCD"

46) A. Dumitru, University of Frankfurt (Germany), 15 Oct.
"Deconfinement in matrix models and the Gross-Witten point"

47) U. Heller, BNL (USA), 20 Oct.
"Light hadrons in $2+1$ flavor lattice QCD"

48) A. Stasto, BNL (USA), 21 Oct.
"Resummation at small x"

49) S. Sasaki, RBRC (USA), 28 Oct.
"Pentaquarks: Status and perspectives for lattice calculations"

50) M. Lublinsky, University of Connecticut (USA), 29 Oct.
"High energy evolution beyond the Balitski-Kovchegov equation"

51) D. Semikoz, UCLA (USA), 4 Nov.
"Ultra-high energy cosmic rays"

52) I. Low, Institute for Advanced Study (USA), 10 Nov.
"The little hierarchy problem"

53) S. Bass, Duke University (USA), 18 Nov.
"RHIC physics with the parton cascade model"

54) B. Gelman, Stony Brook University (USA), 19 Nov.
"What QGP at RHIC and cold dense atomic clouds may have in common?"

55) J. Pati, University of Maryland (USA), 1 Dec.
"Tying in CP and flavor violations with fermion masses and neutrino oscillations"

56) K. Petrov, BNL (USA), 2 Dec.
"Quarkonium correlators and spectral functions at zero and finite temperature"

57) G. Sterman, Stony Brook University (USA), 3 Dec.
"Single-particle production near the edge of phase space"

58) H. Warringa, Free University (The Netherlands), 9 Dec.
"Thermodynamics of QCD inspired theories"

XI. LIST OF PERSONNEL

Supervisor for RIKEN Accelerator Research Facility

Supervisor	Hiromichi KAMITSUBO

Cyclotron Center

Director	Yasushige YANO

Accelerator-based Research Group

Director	Tohru MOTOBAYASHI

Experimental Equipment Sub-Group

Sub-Group Leader	Masayuki KASE
Deputy Sub-Group Leader	Tadashi KAMBARA

Leader

GARIS	Kosuke MORITA
Atomic Collision Experiment	Tadashi KAMBARA
Radioisotope Production	Shuichi ENOMOTO
SMART	Naruhiko SAKAMOTO
Plant Irradiation Technology	Tomoko ABE
Experimental Animal Irradiation	Fumio YATAGAI
RIPS	Toshiyuki KUBO
Experimental Support	Tadashi KAMBARA
Computing and Networking Management	Takashi ICHIHARA

Experimental Research Sub-Group

Sub-Group Leader (*Non Nuclear Physics*)	Yasunori YAMAZAKI
Deputy Sub-Group Leader (*Nuclear Physics*)	Koichiro ASAHI

Leader

Nuclear Structure	Tohru MOTOBAYASHI
Nuclear Reaction	Tohru MOTOBAYASHI
Applied Nuclear Physics	Koichiro ASAHI
Atomic Science	Yasunori YAMAZAKI
Animals and Cultured Cells Irradiation Research	Fumio HANAOKA
Plant Mutation Research	Shigeo YOSHIDA
Storage Ring	Takeshi KATAYAMA
Analysis on Trace Elements	Yasushige YANO
Detectors Development	Hideto EN'YO

Collaborative Research Sub-Group

Sub-Group Leader	Tohru MOTOBAYASHI

RIBF Project Group

Director	Yasushige YANO Masayasu ISHIHARA

Process Management

Leader	Nobuhisa FUKUNISHI Hiromu OKAZOE

Construction Safety

Leader	Atsushi YAMANAKA

Accelerator Sub-Group

Sub-Group Leader	Akira GOTO

Deputy Sub-Group Leader Nobuhisa FUKUNISHI

Leader

Project Management	Nobuhisa FUKUNISHI
Ion-source Development	Takahide NAKAGAWA Hiromitsu HABA
RRC-system Upgrade	Osamu KAMIGAITO
Frc	Naohito INABE
Irc	Jun-ichi OHNISHI
SRC	Hiroki OKUNO
Cryogenics	Kumio IKEGAMI

Equipment Development Sub-Group

Sub-Group Leader Tohru MOTOBAYASHI
Deputy Sub-Group Leader Toshiyuki KUBO

Leader

Counter System Development	Toshimi SUDA
RIB Generator	Toshiyuki KUBO Naoki FUKUDA
RI Spin Probe Facility Development	Koichiro ASAHI
SLOWRI	Michiharu WADA
SCRIT	Masanori WAKASUGI
RI Ring	Tohru MOTOBAYASHI
Zero-degree Spectrometer	Tohru MOTOBAYASHI
Daimajin	Tohru MOTOBAYASHI
p-RIPS	Tohru MOTOBAYASHI
Networking and Data Processing Development	Takashi ICHIHARA
Data Acquisition Technique Development	Yasushi WATANABE

Safety Sub-Group

Sub-Group Leader Yoshitomo UWAMINO

Cosmic Radiation Laboratory

Head
Kazuo MAKISHIMA

Members

Hiroshi KATO	Toru TAMAGAWA
Yukikatsu TERADA	Tatehiro MIHARA
Mitsuhiro KOHAMA*	

* Special Postdoctoral Researcher

Visiting Members
Yasushi FUKAZAWA (Dept. Phys., Hiroshima Univ.)
Tateo GOKA (JAXA)
Soojing HONG (Dept. Phys., Saitama Univ.)
Madoka KAWAHARADA (Dept. Phys., Univ. Tokyo)
Yugo KIMOTO (JAXA)
Motohide KOKUBUN (Dept. Phys., Univ. Tokyo)
Hideki KOSHIISHI (JAXA)
Haruhisa MATSUMOTO (JAXA)
Takefumi MITANI (JAXA)
Hiromasa MIYASAKA (Cal. Inst. Technol., USA)
Mio MURAKAMI (Dept. Phys., Univ. Tokyo)
Motoki NAKAJIMA (Coll. Sci. Technol., Nihon Univ.)
Kazuhiro NAKAZAWA (JAXA)
Masanori OHNO (Dept. Phys., Hiroshima Univ.)

Yuu OKADA (Dept. Phys., Univ. Tokyo)
Tadayuki TAKAHASHI (JAXA)
Kazutaka YAMAOKA (Aoyama Gakuin Univ.)

Radiation Laboratory

Head

Hideto EN'YO

Members

Yasuyuki AKIBA
Yuji GOTO
Yoshie OTAKE
Kiyoshi TANIDA
Hiroaki OHNISHI[*1]
Ryotaro MUTO[*1]
Junji TOJO[*1]
Kazumi HASUKO[*2]
Masanori HIRAI[*2]
Akio KIYOMICHI[*2]
Munehisa OTANI[*2]
Kazutaka SUDO[*2]
Takashi ICHIHARA
Masayasu OKAMURA
Atsushi TAKETANI
Yasushi WATANABE
Tetsuya OHNISHI[*1]
Hiroyuki TAKEDA[*1]
Hisayuki TORII[*1]
Johann HEUSER[*2]
Hiroyuki KANO[*2]
Junichi NOAKI[*2]
Vladimir L. RYKOV[*2]
Satoshi YOKKAICHI[*2]

[*1] Special Postdoctoral Researcher
[*2] Contract Researcher

Visiting Members

Masayuki ASAKAWA (Grad. Sch. Sci., Osaka Univ.)
Wolfgang BENTZ (Dept. Phys., Sch. Sci., Tokai Univ.)
Muriel Jane BURWARD-HOY (Dept. Phys., State Univ. New York, Stony Brook, USA)
Yoshihide FUCHI (KEK)
Hirotsugu FUJII (Grad. Sch. Arts Sci., Univ. Tokyo)
Tetsuo HATSUDA (Dept. Phys., Grad. Sch. Sci., Univ. Tokyo)
Toshiyuki HATTORI (Tokyo Inst. Technol.)
Kensuke HOMMA (Fac. Sci., Hiroshima Univ.)
Kenichi IMAI (Fac. Sci., Kyoto Univ.)
Katsuya ISHIGURO (Kanazawa Univ.)
Noriyoshi ISHII (Tokyo Inst. Technol.)
Takeo KAWASAKI (Fac. Sci., Niigata Univ.)
Jirou KODAIRA (Fac. Sci., Hiroshima Univ.)
Yuji KOIKE (Fac. Sci., Niigata Univ.)
Shunzo KUMANO (Fac. Sci. Eng., Saga Univ.)
Teiji KUNIHIRO (YITP, Kyoto Univ.)
Youngil KWON (Dept. Phys., Seoul Natl. Univ., Korea)
Yajun MAO (Sch. Phys., Peking Univ., China)
Yasuo MIAKE (Inst. Phys., Univ. Tsukuba)
Shoichi MIDORIKAWA (Fac. Eng., Aomori Univ.)
Toshiyuki MORII (Fac. Human Dev., Kobe Univ.)
Osamu MORIMATSU (KEK)
Shoji NAGAMIYA (KEK)
Kenichi NAITO (Hokkaido Univ.)
Shogo NAKAMURA (Fac. Educ., Yokohama Natl. Univ.)
Akio OGAWA (Phys. Dept., BNL, USA)
Jameson ROBERT (Institut Angewandth Physik, Goethe Universität Frankfurt)
Naohito SAITO (Fac. Sci., Kyoto Univ.)
Koichi SAITO (Fac. Sci. Technol., Tokyo Univ. Sci.)
Harutaka SAKAGUCHI (Fac. Sci., Kyoto Univ.)
Fuminori SAKUMA (Fac. Sci., Kyoto Univ.)
Digal SANATAN (Dept. Phys., Grad. Sch. Sci., Univ. Tokyo)
Shinya SAWADA (KEK)
Michiko SEKIMOTO (KEK)

Toshiaki SHIBATA (Tokyo Inst. Technol.)
Kenta SHIGAKI (Fac. Sci., Hiroshima Univ.)
Toru SUGITATE (Fac. Sci., Hiroshima Univ.)
Tsuneo SUZUKI (Kanazawa Univ.)
Manobu TANAKA (KEK)
Satoru TERASHIMA (Fac. Sci., Kyoto Univ.)
Thomas THROWE (Phys. Dept., BNL, USA)
Marcus WAGNER (Fac. Sci., Kyoto Univ.)
Yoshiaki YASUI (Tokyo Manage. Coll.)
Koichi YAZAKI (Tokyo Women's Chr. Univ.)

Trainees

Kazuya AOKI (Fac. Sci., Kyoto Univ.)
Hisato EGUCHI (Fac. Sci., Niigata Univ.)
Kouhei FUJIWARA (Fac. Sci., Niigata Univ.)
Yoshinori FUKAO (Fac. Sci., Kyoto Univ.)
Takashi HACHIYA (Fac. Sci., Hiroshima Univ.)
Koichi HASHIMOTO (Kanazawa Univ.)
Yoshimasa HIDAKA (Fac. Sci., Univ. Tokyo)
Takuma HORAGUCHI (Tokyo Inst. Technol.)
Yasuyoshi INOUE (Coll. Sci., Rikkyo Univ.)
Fukutarou KAJIHARA (CNS)
Nobuyuki KAMIHARA (Tokyo Inst. Technol.)
Hiroki KANO (Tokyo Inst. Technol.)
Masahiro KONNO (Inst. Phys., Univ. Tsukuba)
Kentarou MAWATARI (Fac. Hum. Dev., Kobe Univ.)
Takahiro NAGAI (Fac. Sci. Eng., Saga Univ.)
Junji NAGASHIMA (Fac. Sci., Niigata Univ.)
Tomoaki NAKAMURA (Fac. Sci., Hiroshima Univ.)
Yoshifumi NAKAMURA (Kanazawa Univ.)
Kenichi NAKANO (Tokyo Inst. Technol.)
Megumi NARUKI (Fac. Sci., Kyoto Univ.)
Hiromi OKADA (Fac. Sci., Kyoto Univ.)
Shinsuke OOTA (CNS)
Toru SEKIDO (Kanazawa Univ.)
Maya SHIMOMURA (Inst. Phys., Univ. Tsukuba)
Kohei SHOJI (Fac. Sci., Kyoto Univ.)
Noriyuki SUGITA (Fac. Sci., Hiroshima Univ.)
Satoshi TAKAGI (Inst. Phys., Univ. Tsukuba)
Junpei TAKANO (Tokyo Inst. Technol.)
Akira TAKANO (Tokyo Inst. Technol.)
Manabu TOGAWA (Fac. Sci., Kyoto Univ.)
Yuji TUCHIMOTO (Fac. Sci., Hiroshima Univ.)
Takashi WATANABE (Tokyo Inst. Technol.)
Kazuo YAMAMOTO (Tokyo Inst. Technol.)
Hiroshi YOKOYA (Fac. Sci., Hiroshima Univ.)
Choong-Jae YOON (Fac. Sci., Kyoto Univ.)

Applied Nuclear Physics Laboratory

Head

Koichiro ASAHI

Members

Yoshio KOBAYASHI
Akihiro YOSHIMI
Hideki UENO
Tomohito HASEYAMA*

* Special Postdoctoral Researcher

Visiting Members

Minoru ADACHI

Hisazumi AKAI (Grad. Sch. Sci., Osaka Univ.)
Yasuaki EINAGA (Fac. Sci. Eng., Keio Univ.)
Koji HIGASHIYAMA (Grad. Sch. Sci., Univ. Tokyo)
Hideaki IZUMI (Grad. Sch. Sci. Eng., Osaka Univ.)
Norimichi KOJIMA (Grad. Sch. Arts Sci., Univ. Tokyo)
Kenya M. KUBO (Div. Natl. Sci., Int. Chr. Univ.)
Takuya KURAHASHI (Inst. Mol. Sci.)
Jiro MURATA (Fac. Sci., Rikkyo Univ.)
Masaki MURATA (Grad. Sch. Sci., Univ. Tokyo)
Kazuo MUTO (Grad. Sch. Sci. Eng., Tokyo Inst. Technol.)
Yujiro NAGATA (Coll. Sci. Technol., Aoyama Gakuin Univ.)
Hiromichi NAKAHARA (Grad. Sch. Sci., Tokyo Metrop. Univ.)
Jin NAKAMURA (Dept. Appl. Phys. Chem., Univ. Electro-Commun.)
Saburo NASU (Grad. Sch. Eng. Sci., Osaka Univ.)
Hiroshi OGAWA (Natl. Inst. Adv. Ind. Sci. Technol.)
Takuya OKADA
Hiroyuki SAGAWA (Math. Sci., Univ. Aizu)
Kenji SAKAI (JAERI, CEPAF, Neutron Facility G.)
Wataru SATO (Grad. Sch. Sci., Osaka Univ.)
Kenzi SHIMADA (Grad. Sch. Sci. Eng., Tokyo Inst. Technol.)
Tadashi SHIMODA (Grad. Sch. Sci. Eng., Osaka Univ.)
Satoshi TUTUI (Jpn. Syn. Rad. Res. Inst.)
Makoto UCHIDA (Grad. Sch. Sci. Eng., Tokyo Inst. Technol.)
Masahiko UTSURO (RCNP, Osaka Univ.)
Hiroshi WATANABE (Dept. Nucl. Phys., Australian Natl. Univ.)
Eiichi YAGI (Sch. Sci. Eng., Waseda Univ.)
Yasuhiro YAMADA (Fac. Sci., Tokyo Univ. Sci.)
Yutaka YOSHIDA (Fac. Sci. Technol., Shizuoka Inst. Sci. Technol.)

Trainees
Takamasa ARAI (Fac. Sci., Tokyo Inst. Technol.)
Syoken EMORI (Grad. Sch. Sci. Eng., Tokyo Inst. Technol.)
Shinya FUKAGAI (Sch. Sci. Eng., Waseda Univ.)
Shinichi HAGIWARA (Grad. Sch. Sci. Eng., Waseda Univ.)
Masaki HAYASHI (Sch. Sci. Eng., Waseda Univ.)
Tatsuya HAYASHI (Sch. Sci. Eng., Waseda Univ.)
Naota HIGAMI (Sch. Sci. Eng., Waseda Univ.)
Kazuhiro HIRABAYASHI (Sch. Sci. Eng., Waseda Univ.)
Yuichi HIRAISHI (Sch. Sci. Eng., Waseda Univ.)
Sayaka HORIE (Fac. Sci. Technol., Shizuoka Inst. Sci. Technol.)
Takashi ITO (Fac. Sci., Tokyo Inst. Technol.)
Shimon JINBO (Coll. Sci. Technol., Aoyama Gakuin Univ.)
Daisuke KAMEDA (Grad. Sch. Sci. Eng., Tokyo Inst. Technol.)
Go KATO (Grad. Sch. Sci. Eng., Tokyo Inst. Technol.)
Yoshihiro KAWAGUCHI (Div. Natl. Sci., Int. Chr. Univ.)
Go KIJIMA (Grad. Sch. Sci. Eng., Tokyo Inst. Technol.)
Hiroshi MATSUBA (Grad. Sch. Sci. Eng., Waseda Univ.)
Jun MIYAZAKI (Grad. Sci., Tokyo Univ. Sci.)
Hisanori MIYOSHI (Grad. Sch. Sci. Eng., Tokyo Inst. Technol.)
Katsuhito MORI (Grad. Sch. Sci. Eng., Waseda Univ.)
Daisuke NAGAE (Grad. Sch. Sci. Eng., Tokyo Inst. Technol.)
Tetsuya NAKAGAWA (Fac. Sci., Tokyo Univ. Sci.)
Akio NAKAMOTO (Grad. Sch. Arts Sci., Univ. Tokyo)
Takanori NAKAYAMA (Fac. Sci. Technol., Shizuoka Inst. Sci. Technol.)
Yuki NEMOTO (Fac. Sci., Tokyo Univ. Sci.)
Hiroshi NONAKA (Fac. Sci., Tokyo Univ. Sci.)
Masashi OHKUBO (Grad. Sch. Arts Sci., Univ. Tokyo)
Yoshinori OKADA (Grad. Sch. Sci. Eng., Waseda Univ.)
Yuuki ONO (Grad. Sch. Arts Sci., Univ. Tokyo)
Sachiko OSHIMA (Grad. Sch. Sci. Eng., Tokyo Inst. Technol.)

Kiwamu SAKUMA (Grad. Sch. Sci. Eng., Waseda Univ.)
Chika SUGI (Grad. Sch. Sci. Eng., Waseda Univ.)
Kunifumi SUZUKI (Fac. Sci. Technol., Shizuoka Inst. Sci. Technol.)
Kaori TAGUCHI (Div. Natl. Sci., Int. Chr. Univ.)
Makoto TAKEMURA (Fac. Sci., Tokyo Inst. Technol.)
Masato TSUKUI (Fac. Sci., Tokyo Inst. Technol.)
Yoji TURUOKA (Div. Natl. Sci., Int. Chr. Univ.)
Motoyasu YOSHII (Grad. Sch. Sci. Eng., Waseda Univ.)

Atomic Physics Laboratory

Head

Yasunori YAMAZAKI

Members

Tadashi KAMBARA
Hitoshi OYAMA
Takao M. KOJIMA
Takane KOBAYASHI
Masaki OURA
Nobuhiro YAMANAKA[*1]
Masamitsu HOSHINO[*1]
Yoshihisa ISHIDA[*2]
Naofumi KURODA[*2]
Yasuyuki KANAI
Michiharu WADA
Yoichi NAKAI
Tokihiro IKEDA
Yoshio IWAI[*1]
Makoto C. FUJIWARA[*1]
Masahiro SHIBATA[*1]
Nagayasu OSHIMA[*2]

[*1] Special Postdoctoral Researcher
[*2] Contract Researcher

Visiting Members

Kozo ANDO
Takeo ARUGA (Tokai Res. Estab., JAERI)
Yohko AWAYA (Coll. Art Design Gen. Ed., Musashino Art Univ.)
Toshiyuki AZUMA (Dept. Phys., Tokyo Metrop. Univ.)
Joachim BURGDÖRFER (Vienna Univ. Technol., Austria)
Yasuhiro CHIMI (Tokai Res. Estab., JAERI)
Jörg EICHLER (Hahn-Meiter-Inst. Berlin, Germany)
Atsushi HATAKEYAMA (Grad. Sch. Arts Sci., Univ. Tokyo)
Akira HITACHI (Kochi Med. Sch.)
Atsushi ICHIMURA (Inst. Space Astro. Sci.)
Akinori IGARASHI (Fac. Eng., Miyazaki Univ.)
Keishi ISHII (Fac. Sci. Eng., Ritsumeikan Univ.)
Norito ISHIKAWA (Tokai Res. Estab., JAERI)
Akio ITOH (Dept. Nucl. Eng., Kyoto Univ.)
Yoh ITOH (Fac. Sci., Josai Univ.)
Akihiro IWASE (Res. Inst. Adv. Sci. Technol., Osaka Pref. Univ.)
Kensuke KAGEYAMA (Fac. Eng., Saitama Univ.)
Ichiro KATAYAMA (KEK)
Kenji KIMURA (Fac. Eng., Kyoto Univ.)
Mineo KIMURA (Grad. Sch. Sci., Kyushu Univ.)
Masashi KITAJIMA (Fac. Sci. Technol., Sophia Univ.)
Tetsuo KOIZUMI (Dept. Phys., Rikkyo Univ.)
Ken-ichiro KOMAKI (Grad. Sch. Arts Sci., Univ. Tokyo)
Kenichi KOWARI (Dept. Appl. Phys. Chem., Univ. Electro-Commun.)
Kenro KUROKI (Natl. Res. Inst. Police Sci.)
Michio MATSUZAWA (Dept. Appl. Phys. Chem., Univ. Electro-Commun.)
Koichiro MITSUKE (Inst. Mol. Sci.)
Akihiro MOHRI
Kanetada NAGAMINE (Inst. Mater. Struc. Sci., KEK)
Nobuyuki NAKAMURA (Inst. Laser Sci., Univ. Electro-Commun.)
Takashi NAKAMURA (KEK)
Tetsuya NAKAZAWA (Tokai Res. Estab., JAERI)

Megumi NIIGAKI (Dept. Phys., Grad. Sch. Sci., Univ. Tokyo)
Tamio NISHIMURA (Dept. Chim., Univ. Roma, Italy)
Shunsuke OHTANI (Inst. Laser Sci., Univ. Electro-Commun.)
Kunihiro OKADA (Fac. Sci. Technol., Sophia Univ.)
Satoru OKAYASU (Tokai Res. Estab., JAERI)
Kazuhiko OKUNO (Dept. Phys., Tokyo Metrop. Univ.)
Fumihisa ONO (Fac. Sci., Okayama Univ.)
Lukas PICHL (Found. Comput. Sci. Lab., Univ. Aizu)
Frank B. ROSMEJ (Univ. Provence, France)
Syuiti SAKAGUTI (Fac. Eng., Yamaguchi Univ.)
Akio SAKAI (Vacuum Products Co.)
Reinhold SCHUCH (Phys. Dept., Stockholm Univ., Sweden)
Hans A. SCHUESSLER (Texas A & M Univ., USA)
Hiroyuki SHIMADA (Dept. Phys., Grad. Sch. Sci., Univ. Tokyo)
Noriyuki SHIMAKURA (Fac. Sci., Niigata Univ.)
Isao SHIMAMURA
Hiroya SUNO (NIFS)
Aiko TAKAMINE (Dept. Phys., Grad. Sch. Sci., Univ. Tokyo)
Michiya TAKEKAWA (Inst. Pure Appl. Phys.)
Hiroyuki TORII (Grad. Sch. Arts Sci., Univ. Tokyo)
Nobuyuki TOSHIMA (Inst. Appl. Phys., Univ. Tsukuba)
Hidetsugu TSUCHIDA (Dept. Nucl. Eng., Kyoto Univ.)
Kazuyuki UEDA (Toyota Technol. Inst.)
Kiyoshi UEDA (Res. Inst. Sci. Meas., Tohoku Univ.)
Victor VARENTSOV (V. G. Khlopin Radium Inst., Russia)
Tsutomu WATANABE
Akira YAGISHITA (KEK)
Yaming ZOU (Fudan Univ., China)

Trainees
Yoshinori ENOMOTO (Coll. Art Sci., Univ. Tokyo)
Masafumi FUKUZUMI (Grad. Sch. Eng., Osaka Pref. Univ.)
Matthew GARDNER (Univ. Birmingham, UK)
Masato INOUE (Dept. Phys., Grad. Sch. Sci., Univ. Tokyo)
Hiroaki KANEMITSU (Dept. Phys., Okayama Univ.)
Seiji KOMATSU (Dept. Phys., Okayama Univ.)
Chikara KONDOU (Dept. Phys., Grad. Sch. Sci., Univ. Tokyo)
Matthieu LEBOIS (Univ. Paris-Sud Orsay, France)
Vladimir LIOUBIMOV (Texas A&M Univ., USA)
Takuya MAJIMA (Grad. Sch. Eng., Kyoto Univ.)
Saburou MASUGI (Dept. Phys., Tokyo Metrop. Univ.)
Yuji MIYAMOTO (Grad. Sch. Sci. Eng., Sophia Univ.)
Tomoko MURANAKA (Dept. Phys., Tokyo Metrop. Univ.)
Yugo NAGATA (Dept. Phys., Grad. Sch. Sci., Univ. Tokyo)
Yuji NAKANO (Dept. Phys., Tokyo Metrop. Univ.)
Tetsu SONODA (Grad. Sch. Sci., Tohoku Univ.)
Nozomi TANAKA (Dept. Phys., Sophia Univ.)
Masashi TERADA (Inst. Laser Sci., Univ. Electro-Commun.)
Kouhei YAMASHITA (Dept. Phys., Sophia Univ.)

Heavy Ion Nuclear Physics Laboratory

Head
Tohru MOTOBAYASHI

Members
Takashi ICHIHARA
Takashi KISHIDA
Yasushi WATANABE
Akihisa KOHAMA
Nori AOI
Toshimi SUDA
Alexei A. KORSHENINNIKOV
Yukari MATSUO
Shunji NISHIMURA
Yoshiyuki YANAGISAWA

Tomoko GOMI[*1]
Masaaki KIMURA[*1]
Toshiyuki SUMIKAMA[*1]
Masaaki TAKASHINA[*1]
Masayuki YAMAGAMI[*1]
Evgueni NIKOLSKI[*2]
Satoshi TAKEUCHI[*2]
Toshimitsu YAMAZAKI[*2]
Nobuaki IMAI[*1]
Hiroshi MASUI[*1]
Kanenobu TANAKA[*1]
Kazunari YAMADA[*1]
Yoshimitsu FUKUYAMA[*2]
Parihawadana Aloy PERERA[*2]
Meiko UESAKA-KUROKAWA[*2]

[*1] Special Postdoctoral Researcher
[*2] Contract Researcher

Visiting Members

Yasuhisa ABE (Yukawa Inst. Theor. Phys., Kyoto Univ.)
Yasuo AOKI (Fac. Sci., Univ. Tsukuba)
Shigeyoshi AOYAMA (Kitami Inst. Technol.)
Yoshihiro ARITOMO (JINR, Russia)
Daniel BAZIN (Natl. Supercond. Cycl. Lab., Michigan State Univ., USA)
Didier BEAUMEL (Paris-XI Univ., IPN-Orsay, France)
Francis A. BECK (CRN, Strasbourg, France)
Mottelson R BEN (NORDITA, Copenhagen, Denmark)
Shawn BISHOP (JSPS)
Yorick BLUMENFELD (Paris-XI Univ., IPN-Orsay, France)
Peter von BRENTANO (Inst. fur Kern Phys., Univ. Koeln, Germany)
Rangacharyulu CHILAKAMARRI (Univ. Saskatchewan, Canada)
Zsolt DOMBRADI (Inst. Nucl. Res., Hung. Acad. Sci., Hungary)
Zoltan ELEKES (Inst. Nucl. Res., Hung. Acad. Sci., Hungary)
Yoshiko ENYO (KEK)
Yoshitaka FUJITA (Fac. Sci., Osaka Univ.)
Mamoru FUJIWARA (RCNP, Osaka Univ.)
Mitsunori FUKUDA (Grad. Sch. Sci., Osaka Univ.)
Zsolt FÜLÖP (Inst. Nucl. Res., Hung. Acad. Sci., Hungary)
Zoltan GACSI (Inst. Nucl. Res., Hung. Acad. Sci., Hungary)
Janos GAL (Inst. Nucl. Res., Hung. Acad. Sci., Hungary)
Yu-Cheng GE (Peking Univ., China)
Adrian GELBERG (Inst. Kern Phys., Univ. Koeln, Germany)
Nobuyuki HASEBE (Sci. Eng. Res. Lab., Waseda Univ.)
Nguyen Thuc HIEN (Hanoi Univ., Vietnam)
Satoru HIRENZAKI (Fac. Sci., Nara Women's Univ.)
Khiem LE HONG (Inst. Phys., Natl. Cen. Sci. Technol., Vietnam)
Shen HONG (Dept. Phys., Nankai Univ.)
TakatoshiI HORIBATA (Fac. Sci., Aomori Univ.)
Hisashi HORIUCHI (Fac. Sci., Kyoto Univ.)
Hui HUA (Michigan State Univ., USA)
Munetake ICHIMURA (Univ. Air)
Kazuo IEKI (Coll. Sci., Rikkyo Univ.)
Shigeru ISHIMOTO (KEK)
Naoyuki ITAGAKI (Fac. Sci., Univ. Tokyo)
Makoto ITO (Fac. Sci., Univ. Tsukuba)
Akira IWAMOTO (JAERI)
Naohisa IWASA (Fac. Sci., Tohoku Univ.)
Hironori IWASAKI (Grad. Sch. Sci., Univ. Tokyo)
Takuji IZUMIKAWA (Fac. Sci., Niigata Univ.)
Dang-Xing JIANG (Peking Univ., China)
Toshiki KAJINO (Natl. Astron. Obs.)
Nasser KALANTAR-NAYESTANAKI (Univ. Groningen, The Netherland)
Gabor KALINKA (Inst. Nucl. Res., Hung. Acad. Sci., Hungary)
Shoko KANNO (Coll. Sci., Rikkyo Univ.)
Kiyoshi KATO (Fac. Sci., Hokkaido Univ.)
Jun KIKUCHI (Sci. Eng. Res. Lab., Waseda Univ.)

Kikuo KIMURA (Fac. Sci., Nagasaki Inst. Appl. Sci.)
Masanori KOBAYASHI (Sci. Eng. Res. Lab., Waseda Univ.)
Takeshi KOIKE (Nucl. Struct. Lab., State Univ. New York, Stony Brook, USA)
Tetsuro KOMATSUBARA (Univ. Tsukuba)
Evgueni KOUZMINE (Kurchatov Inst., Russia)
Attila KRASZNAHORKAY (Inst. Nucl. Res., Hung. Acad. Sci., Hungary)
Kazuyoshi KURITA (Coll. Sci., Rikkyo Univ.)
Guan-Hua LIU (Inst. Modern Phys., China)
William LYNCH (Michigan State Univ., USA)
Kazushige MAEDA (Fac. Sci., Tohoku Univ.)
Kensaku MATSUTA (Fac. Sci., Osaka Univ.)
Kenichi MATSUYANAGI (Grad. Sch. Sci., Kyoto Univ.)
Jie MENG (Peking Univ., China)
Alberto MENGONI (ENEA, Italy)
Johannes G. MESSCHENDORP (Univ. Groningen, The Netherland)
Mototugu MIHARA (Fac. Sci., Osaka Univ.)
Toshiyuki MINEMURA (KEK)
Takashi MIYACHI (Fac. Sci. Eng., Waseda Univ.)
Yasuo MIYAKE (Fac. Sci., Univ. Tsukuba)
Hiroari MIYATAKE (KEK)
Takahiro MIZUSAKI (Fac. Sci., Univ. Tokyo)
Sadao MOMOTA (Kochi Univ. Technol.)
Peter MOLLER (Los Alamos Natl. Lab., USA)
Hiroyuki MURAKAMI (Coll. Sci., Rikkyo Univ.)
Atsushi MUTA (Inst. Phys., Univ. Tsukuba)
Takayuki MYO (RCNP, Osaka Univ.)
Yasuki NAGAI (RCNP, Osaka Univ.)
Takashi NAKAMURA (Fac. Sci., Tokyo Inst. Technol.)
Takashi NAKATSUKASA (Fac. Sci., Univ. Tsukuba)
Masahiro NOTANI (Argonne Natl. Lab., USA)
Atsuko ODAHARA (Nishinippon Inst. Technol.)
Alexei A. OGLOBLIN (Kurchatov Inst., Russia)
Masahisa OHTA (Fac. Sci., Konan Univ.)
Hideaki OHTSU (Fac. Sci., Tohoku Univ.)
Takashi OHTSUBO (Fac. Sci., Niigata Univ.)
Takeo ONISHI (Grad. Sch. Sci., Univ. Tokyo)
Kazuhiro OYAMATSU (Aichi Shukutoku Univ.)
Chilakamarri RANGACHARYULU (Univ. Saskatchewan, Canada)
Zhou Zhang REN (Nanjing Univ., China)
Hiroyuki SAGAWA (Univ. Aizu)
Harutaka SAKAGUCHI (Fac. Sci., Kyoto Univ.)
Yoshinori SAKURAGI (Fac. Sci., Osaka City Univ.)
Kimikazu SASA (Univ. Tsukuba)
Hiroyuki SASADA (Keio Univ.)
Yoshiteru SATOU (Fac. Sci., Tokyo Inst. Technol.)
Ryoichi SEKI (Cal. State Univ., Northridge, USA)
Caiwan SHEN (Dept. Nucl. Phys., China Inst. Atom. Energy, China)
Yoshifumi SHIMIZU (Fac. Sci., Kyushu Univ.)
Cosimo SIGNORINI (INEN, Italy)
Dorottya SOHLER (Inst. Nucl. Res., Hung. Acad. Sci., Hungary)
Takashi SUGIMOTO (Fac. Sci., Tokyo Inst. Technol.)
Kohsuke SUMIYOSHI (Numazu Coll. Technol.)
Akihiro SUZUKI (Shinshu Univ.)
Masaru SUZUKI (Grad. Sch. Sci., Univ. Tokyo)
Shoji SUZUKI (KEK)
Toshio SUZUKI (Fac. Eng., Fukui Univ.)
Yasuyuki SUZUKI (Fac. Sci., Niigata Univ.)
Naoki TAJIMA (Fac. Eng., Fukui Univ.)
Tadayuki TAKAHASHI (Inst. Space Astronaut. Sci.)
Yutaka TAKAHASHI (RCNP, Osaka Univ.)

Masatoshi TAKANO (Sci. Eng. Res. Lab., Waseda Univ.)
Noboru TAKIGAWA (Fac. Sci., Tohoku Univ.)
Atsushi TAMII (RCNP, Osaka Univ.)
Kazuko TANABE (Otsuma Women's Univ.)
Manyee TSANG (Michigan State Univ., USA)
Yutaka UTSUNO (Tokai Res. Estab., JAERI)
Takahiro WADA (Fac. Sci., Konan Univ.)
Herman WOLLNIK (Oak Ridge. Lab., USA)
Shuwei XU (Inst. Modern Phys., Chin. Acad. Sci., China)
Kazuhiro YABANA (Fac. Sci., Univ. Tsukuba)
Hirosuke YAGI (Fac. Sci., Univ. Tsukuba)
Kentarou YAKOU (Grad. Sch. Sci., Univ. Tokyo)
Takayuki YAMAGUCHI (Fac. Sci., Univ. Saitama)
Yanlin YE (Peking Univ., China)
Ken-ichirou YONEDA (Natl. Supercond. Cycl. Lab., Michigan State Univ., USA)
Naotaka YOSHINAGA (Fac. Sci., Saitama Univ.)
Shan-Gi ZHOU (Peking Univ., China)

Trainees

Akiko CHIBA (Fac. Sci., Univ. Tsukuba)
Masami CHIBA (Fac. Sci., Tohoku Univ.)
Jonathan Michael COOK (Michigan State Univ., USA)
Pham N. DINH (Michigan State Univ., USA)
Natsumi ENDO (Fac. Sci., Tohoku Univ.)
Hiroki FUJIWARA (Fac. Sci., Osaka Univ.)
Yasuro FUNAKI (Fac. Sci., Kyoto Univ.)
Takeshi FURUKAWA (Fac. Sci., Osaka Univ.)
Julien J. GIBELIN (Coll. Sci., Rikkyo Univ.)
Ryosuke HADATE (Coll. Sci., Rikkyo Univ.)
Yoshiko HASHIMOTO (Fac. Sci., Tokyo Inst. Technol.)
Naho HOKOIWA (Fac. Sci., Kyushu Univ.)
Yuichi ICHIKAWA (Grad. Sch. Sci., Univ. Tokyo)
Kazuhiro ISHIKAWA (Fac. Sci., Tokyo Inst. Technol.)
Ikuko KANAZAWA (Fac. Sci., Saitama Univ.)
Tomomi KATO (Fac. Sci., Niigata Univ.)
Shoko KAWAI (Coll. Sci., Rikkyo Univ.)
Yoshie KAWAMURA (Fac. Sci., Niigata Univ.)
Takayuki KINOSHITA (Coll. Sci., Rikkyo Univ.)
Mituhisa KITAYAMA (Fac. Sci., Tohoku Univ.)
Kei KOBAYASHI (Fac. Sci., Saitama Univ.)
Yousuke KONDOU (Fac. Sci., Tokyo Inst. Technol.)
Ryo KOYAMA (Fac. Sci., Niigata Univ.)
Hironori KUBOKI (Grad. Sch. Sci., Univ. Tokyo)
Shinichi KUMASHIRO (Fac. Sci., Osaka Univ.)
Chie KUROKAWA (Fac. Sci., Hokkaido Univ.)
Michitarou KUSAKA (Fac. Sci., Tohoku Univ.)
Yukie MAEDA (Grad. Sch. Sci., Univ. Tokyo)
Takashi MAEMURA (Fac. Sci., Saitama Univ.)
Tetsuya MASUDA (Coll. Sci., Rikkyo Univ.)
Yohei MATSUDA (Fac. Sci., Tohoku Univ.)
Nobuyuki MATSUI (Coll. Sci., Rikkyo Univ.)
Taizo MATSUMASA (Fac. Sci., Osaka Univ.)
Ryohei MATSUMIYA (Fac. Sci., Osaka Univ.)
Takafumi MATSUYAMA (Fac. Sci., Niigata Univ.)
Yuichi MATSUYAMA (Coll. Sci., Rikkyo Univ.)
Toshiya MIKI (Fac. Sci., Tohoku Univ.)
Kazutaka MIYAKAWA (Fac. Sci., Univ. Tsukuba)
Michal MOCKO (Michigan State Univ., USA)
Kensuke MORIMOTO (Coll. Sci., Rikkyo Univ.)
Konomi MURAKAMI (Fac. Sci., Saitama Univ.)

Takashi NAGATOMO (Fac. Sci., Osaka Univ.)
Takumi NAKABAYASHI(Fac. Sci., Tokyo Inst. Technol.)
Shinpei NAKAJIMA (Fac. Sci., Saitama Univ.)
Ryoko NAKAMURA (Coll. Sci., Rikkyo Univ.)
Taro NAKAO (Grad. Sch. Sci., Univ. Tokyo)
Hiroyuki NAKAYAMA (Grad. Sch. Sci., Univ. Tokyo)
Yuki NAOI (Fac. Sci., Tohoku Univ.)
Khai Thuan NGYEN (Hanoi Univ., Vietnam)
Haruki NISHINO (Grad. Sch. Sci., Univ. Tokyo)
Koremitsu OGATA (Fac. Sci., Saitama Univ.)
Masako OGURA (Fac. Sci., Osaka Univ.)
Masafumi OIZUMI (Grad. Sch. Sci., Univ. Tokyo)
Takashi OKUDA (Fac. Sci., Tohoku Univ.)
Toshifumi OKUMURA (Fac. Sci., Tokyo Inst. Technol.)
Hooi Jin ONG (Grad. Sch. Sci., Univ. Tokyo)
Kazutaka OZEKI (Fac. Sci., Tohoku Univ.)
Andrew ROGERS (Michigan State Univ., USA)
Hiroshi SAENMA (Grad. Sch. Sci., Univ. Tokyo)
Takaaki SAITO (Grad. Sch. Sci., Univ. Tokyo)
Shouta SAITO (Coll. Sci., Rikkyo Univ.)
Hazuki SAKAI (Coll. Sci., Rikkyo Univ.)
Takashi SAKO (Grad. Sch. Sci., Univ. Tokyo)
Tomoyuki SAKURADA (Coll. Sci., Rikkyo Univ.)
Makoto SASAKI (Fac. Sci., Osaka Univ.)
Masaki SASANO (Grad. Sch. Sci., Univ. Tokyo)
Junichi SATO (Coll. Sci., Rikkyo Univ.)
Kazunori SATO (Fac. Sci., Niigata Univ.)
Yoko SEKI (Fac. Sci., Tohoku Univ.)
Masatugu SEKIGUCHI (Fac. Sci., Tohoku Univ.)
Mayukko SHINOHARA (Fac. Sci., Tokyo Inst. Technol.)
Tokukazu SHINOHARA (Fac. Sci., Tohoku Univ.)
Daisuke SHINOJIMA (Fac. Sci., Niigata Univ.)
Wakako SHINOZAKI (Fac. Sci., Niigata Univ.)
Edward SMITH (Ohio Univ., USA)
Ryohei SUGO (Coll. Sci., Rikkyo Univ.)
Daisuke SUZUKI (Grad. Sch. Sci., Univ. Tokyo)
Hiroshi SUZUKI (Grad. Sch. Sci., Univ. Tokyo)
Ryusuke SUZUKI (Fac. Sci., Hokkaido Univ.)
Kensaku TAKAHASHI (Fac. Sci., Saitama Univ.)
Yoshiyuki TAKAHASHI (Grad. Sch. Sci., Univ. Tokyo)
Maya TAKECHI (Fac. Sci., Osaka Univ.)
Hideki TANAKA (Fac. Sci., Niigata Univ.)
Yasutaka TANIGUCHI (Fac. Sci., Kyoto Univ.)
Shinya TAZAWA (Fac. Sci., Tohoku Univ.)
Satoru TERASAWA (Fac. Sci., Kyoto Univ.)
Yasuhiro TOGANO (Coll. Sci., Rikkyo Univ.)
Kazuma TSURUSAKI (Grad. Sch. Sci., Univ. Tokyo)
Hirotaka UENO (Coll. Sci., Rikkyo Univ.)
Naori UMEZAWA (Coll. Sci., Rikkyo Univ.)
Kazuya URUSHIBARA (Coll. Sci., Rikkyo Univ.)
Toru UZIIE (Fac. Sci., Tohoku Univ.)
Yasuo WAKABAYASHI (Fac. Sci., Kyushu Univ.)
Mark WALLACE (Michigan State Univ., USA)
Kiwamu WATANABE (Fac. Sci., Tohoku Univ.)
Shigeo WATANABE (Fac. Sci., Niigata Univ.)
Takeshi WATANABE (Coll. Sci., Rikkyo Univ.)
Takuya YAGI (Grad. Sch. Sci., Univ. Tokyo)
Takashi YAKUSHIJI (Fac. Sci., Tohoku Univ.)
Koji YAMAGUCHI (Coll. Sci., Rikkyo Univ.)
Takuma YASUNO (Fac. Sci., Univ. Tsukuba)

Advanced Meson Science Laboratory

Head

Masahiko IWASAKI

Members

Teiichiro MATSUZAKI
Haruhiko OUTA
Yasuyuki MATSUDA
Takahisa KOIKE[*1]
Pavel BAKULE[*2]
Katsuhiko ISHIDA
Isao WATANABE
Kenta ITAHASHI
Shinji OKADA[*1]
Seiko OHIRA[*2]

[*1] Special Postdoctoral Researcher
[*2] Contract Researcher

Visiting Members

Tadashi ADACHI (Grad. Sch. Eng., Tohoku Univ.)
Yoshitami AJIRO (Grad. Sch. Sci., Kyoto Univ.)
Yoshinori AKAISHI
Jun AKIMITSU (Coll. Sci. Eng., Aoyama Gakuin Univ.)
Juichiro ARAI (Fac. Sci., Tokyo Univ. Sci.)
Shingo ARAKI (Grad. Sch. Sci., Osaka Univ.)
Kunio AWAGA (Grad. Sch. Sci., Nagoya Univ.)
George A. BEER (Univ. Victoria, Canada)
Hyoung Chan BHANG (Seoul Natl. Univ., Korea)
Ludmila N. BOGDANOVA (Inst. Theor. Exp. Phys., Russia)
Tara P. DAS (State Univ. New York, USA)
Mark P. FAIFMAN (Kurchatov Inst., Russia)
Yutaka FUJII (Fac. Eng., Fukui Univ.)
Masaki FUJITA (IMR, Tohoku Univ.)
Hideto FUKAZAWA (Grad. Sch. Sci. Eng., Chiba Univ.)
Makoto HAGIWARA (Fac. Eng. Design, Kyoto Inst. Technol.)
Emiko HIYAMA (Fac. Sci., Nara Women's Univ.)
Susumu IKEDA (KEK)
Yutaka IKEDO (KEK)
Shigeru ISHIMOTO (KEK)
Tomoichi ISHIWATARI (Stefan Meyer Inst., Austria)
Atsuko ITO
Ryosuke KADONO (KEK)
Masayasu KAMIMURA
Mineo KATO (Tokai Res. Estab., JAERI)
Naritoshi KAWAMURA (KEK)
Yasushi KINO (Fac. Sci., Tohoku Univ.)
Yoh KOHORI (Fac. Sci., Chiba Univ.)
Youji KOIKE (Grad. Sch. Eng., Tohoku Univ.)
Yoshitaka KUNO (Grad. Sch. Sci., Osaka Univ.)
Syunsuke MAKIMURA (KEK)
Goro MARUTA (Grad. Sch. Sci., Hokkaido Univ.)
Yasuhiro MIYAKE (KEK)
Satoshi N. NAKAMURA (Grad. Sch. Sci., Tohoku Univ.)
Takashi NAKAMURA (Grad. Sch. Sci. Eng., Tokyo Inst. Technol.)
Takayoshi NAKAMURA (Res. Inst. Electron. Sci., Hokkaido Univ.)
Takehito NAKANO (Grad. Sch. Sci., Osaka Univ.)
Nobuhiko NISHIDA (Fac. Sci., Tokyo Inst. Technol.)
Kusuo NISHIYAMA (KEK)
Yasuo NOZUE (Grad. Sch. Sci., Osaka Univ.)
Vassili V. PEREVOZCHIKOV (Russ. Fed. Nucl. Cen., Russia)
Leonid I. PONOMAREV (Kurchatov Inst., Russia)
Francis L. PRATT (RAL, UK)
Shinichi SAKAMOTO (Tokai Res. Estab., JAERI)
Ryoichi SEKI (California State Univ., USA)

Koichiro SHIMOMURA (KEK)
Patrick STRASSER (KEK)
Hiroyuki SUGAI (Tokai Res. Estab., JAERI)
Keiji TAKEDA (Res. Inst. Electron. Sci., Hokkaido Univ.)
Hiroyuki TANAKA (Univ. Cal., Riverside, USA)
Eiko TORIKAI (Grad. Sch. Med. Eng. Sci., Univ. Yamanashi)
Akihisa TOYODA (KEK)
Kazuo UEDA (Inst. Solid State Phys., Univ. Tokyo)
Kazuyoshi YAMADA (IMR, Tohoku Univ.)
A. A. YUKHIMCHUK (Russ. Fed. Nucl. Cen., Russia)
Johann ZMESKAL (Stefan Meyer Inst., Austria)

Trainees
Soichiro ARIMURA (Grad. Sch. Sci., Osaka Univ.)
Ken GOTO (Grad. Sch. Sci., Osaka Univ.)
Kenichi HACHITANI (Grad. Sch. Sci., Chiba Univ.)
Aya HINO (Grad. Sch. Sci., Tohoku Univ.)
Hiroshi IMAO (Grad. Sch. Sci., Univ. Tokyo)
Junho JEONG (State Univ. New York, USA)
Mijung KIM (Seoul Natl. Univ., Korea)
Yoshihiro KUBOTA (Grad. Sch. Sci., Tohoku Univ.)
Sougo KUROIWA (Grad. Sch. Sci. Eng., Aoyama Gakuin Univ.)
Haruo MIYADERA (Grad. Sch. Sci., Univ. Tokyo)
RISDIANA (Grad. Sch. Eng., Tohoku Univ.)
Masaharu SATO (Grad. Sch. Sci. Eng., Tokyo Inst. Technol.)
Ralph SCHEICHER (State Univ. New York, USA)
Yoko TOMITA (Coll. Sci. Eng., Aoyama Gakuin Univ.)
Maki YAMAZAWA (Grad. Sch. Sci. Eng., Aoyama Gakuin Univ.)
Heejoong YIM (Seoul Natl. Univ., Korea)

Magnetic Materials Laboratory

Head
Hidenori TAKAGI

Members
Masayuki HAGIWARA
Hiroki YAMAZAKI
Koshi TAKENAKA
Seiji NIITAKA[*1]
Hiroko KATORI
Tetsuo HANAGURI
Katsuya IWAYA[*1]
Petra JONSSON[*2]

[*1] Special Postdoctoral Researcher
[*2] Contract Researcher

Visiting Members
Masaaki MATSUDA (JAERI-ASRC)
Hirokazu TSUNETSUGU (Yukawa Inst. Theor. Phys., Kyoto Univ.)
Kunimitsu UCHINOKURA

Trainees
Hideo NISHIKUBO (Dept. Supercond., Univ. Tokyo)
Seiichi SATO (Adv. Mater. Sci., Univ. Tokyo)
Tomohiro TAKAYAMA (Adv. Mater. Sci., Univ. Tokyo)

Cellular Physiology Laboratory

Head
Fumio HANAOKA

Members
Fumio YATAGAI

Visiting Members

Koichi ANDO (Natl. Inst. Radiol. Sci.)
Yoshiya FURUSAWA (Natl. Inst. Radiol. Sci.)
Yoshimasa HAMA (Sci. Eng. Inst., Waseda Univ.)
Hisao ITOH (Fac. Med., Chiba Univ.)
Tatsuaki KANAI (Natl. Inst. Radiol. Sci.)
Kiyomi KASAI (Natl. Inst. Radiol. Sci.)
Yasuhiko KOBAYASHI (JAERI)
Hiroshi WATANABE (JAERI)
Masami WATANABE (Fac. Pharm. Sci., Nagasaki Univ.)
Shoji YAMASHITA (Natl. Saitama Hosp.)

Plant Functions Laboratory

Head

Shigeo YOSHIDA

Members

Tomoko ABE
Hiroyuki SAITO*1
Tomoki MATSUYAMA
Yoshiharu YAMAMOTO*2

*1 Special Postdoctoral Researcher
*2 Contract Researcher

Visiting Members

Chang-Hyu BAE (Sunchon Natl. Univ., Korea)
Koji FURUKAWA (Mukoyama Orchids Co., Ltd.)
Misako HAMATANI (Hiroshima City Agric. Forest. Promot. Cen.)
Yasuhide HARA (Kanagawa Inst. Agric. Sci.)
Masanori HATASHITA (Wakasa Wan Energy Res. Cen.)
Atsushi HIGASHITANI (Grad. Sch. Life Sci., Tohoku Univ.)
Akiko HOKURA (Fac. Sci., Tokyo Univ. Sci.)
Ichiro HONDA (Natl. Agric. Res. Cen., Min. Agric. Forest. Fish.)
Mitsugu HORITA (Hokkaido Green-bio Inst.)
Yuji ITO (Inst. Rad. Breeding, Natl. Inst. Agric. Res.)
Hiroshi KAGAMI (Shizuoka Citrus Exp. Station)
Toshiaki KAMEYA (Grad. Sch. Life Sci., Tohoku Univ.)
Takeshi KANAYA (Suntory Flowers, Ltd.)
Si-Yong KANG (Dep. Rad. Plant Breed. Genet., KAERI, Korea)
Takeo KITAURA (Kanagawa Inst. Agric. Sci.)
Tsutomu KUBOYAMA (Fac. Agric., Ibaraki Univ.)
Yutaka MIYAZAWA (Grad. Sch. Life Sci., Tohoku Univ.)
Kazumitsu MIYOSHI (Fac. Bioresour. Sci., Akita Pref. Univ.)
Toshikazu MORISHITA (Inst. Rad. Breeding, Natl. Inst. Agric. Res.)
Kenji Osawa (Nagano Agric. Res. Cen.)
Jin Heui PARK (Coll. Life Environ., Sci., Korea Univ., Korea)
Koichi SAKAMOTO (JAERI, Takasaki Rad. Chem. Res. Est.)
Tadashi SATO (Grad. Sch. Life Sci., Tohoku Univ.)
Takiko SHIMADA (Res. Inst. Agric. Resour., Ishikawa Agric. Coll.)
Masao SUGIYAMA (Hokko Chemical Ind. Co., Ltd.)
Kazunori SUZUKI (Plant Biotech. Inst. Ibaraki Agric. Cen.)
Kenichi SUZUKI (Suntory Flowers, Ltd.)
Ken TOKUHARA (Dogashima Orchid Cen.)
Hisashi TSUJIMOTO (Fac. Agric., Tottori Univ.)
Takuji YOSHIDA (Takii Seed Co., Ltd.)
Masao WATANABE (Fac. Agric., Iwate Univ.)

Trainees

Hideki ASAUMI (Ehime Agric. Exp. Station)
Hiroyuki ICHIDA (Fac. Agric., Meiji Univ.)

Tomojiro KOIDE (RIKEN Vitamin Co., Ltd.)
Hiroyuki NAGAYAMA (Fac. Sci., Tokyo Univ. Sci.)
Ryoko ONUMA (Fac. Sci., Tokyo Univ. Sci.)
Eikou OOYABU (Saga Agric., Exp. Station)
Minoru SAITO (Fukui Agric. Exp. Station)
Tsukasa SHIRAO (Kagoshima Biotech. Inst.)
Chisato SUZUKI (Fac. Agr., Meiji Univ.)
Hinako TAKEHISA (Grad. Sch. Life Sci., Tohoku Univ.)
Kei-ichiro UENO (Kagoshima Biotech. Inst.)
Tetsuya UMEKI (Miyazaki Agric. Exp. Station)
Kenji WATANABE (Fac. Agric., Meiji Univ.)

Cyclotron Center

Head

Yasushige YANO

Members

Satoru SUGIMOTO[*1]
Hideki MADOKORO[*2]
Nguyen Dinh DANG[*2]
Yuko MOCHIZUKI[*2]

[*1] Special Postdoctoral Researcher
[*2] Contract Researcher

Visiting Members

Michio HONMA (Univ. Aizu)
Kiyomi IKEDA
Takashi INAMURA
Ken-ici KATO
Shoushichi MOTONAGA
Takaharu OTSUKA (Sch. Sci., Univ. Tokyo)
Mutsuko SASAKI
Noritaka SHIMIZU (Sch. Sci., Univ. Tokyo)
Takahiro TACHIBANA (Waseda High Sch., Waseda Univ.)
Kouji TAKAHASHI (Max Planck Inst., Germany)
Shuhei YAMAJI
Yumin ZHAO (Dept. Phys, Shanghai Jiao-Tong Univ., China)

Beam Dynamics Division

Head

Akira GOTO

Members

Takashi EMOTO
Jun-ichi OHNISHI
Tadashi KOSEKI
Osamu KAMIGAITO
Nobuhisa FUKUNISHI
Kimiko SEKIGUCHI[*1]
Toshiyuki KUBO
Masanori WAKASUGI
Kouichi YOSHIDA
Atsushi YOSHIDA
Naruhiko SAKAMOTO
Kensuke KUSAKA[*2]

[*1] Special Postdoctoral Researcher
[*2] Contract Researcher

Visiting Members

Yoshiaki CHIBA
Mitsuhiro FUKUDA (Takasaki Res. Estab., JAERI)
Hironori KUBOKI (Dept. Phys., Sch. Sci., Univ. Tokyo)
Shinji MACHIDA (KEK)
Toshinori MITSUMOTO (Sumitomo Heavy Ind., Ltd.)
Hiroari MIYATAKE (KEK)

Hirofumi MIYAZAKI (Sumitomo Heavy Ind., Ltd.)
Yutaka MIZOI (Osaka Electro-Commun. Univ.)
Yoshiharu MORI (KEK)
Hiroyuki OKAMURA (Cycl. Radioisot. Cen., Tohoku Univ.)
Tsutomu SHINOZUKA (Cycl. Radioisot. Cen., Tohoku Univ.)
Eri TAKESHITA (Dept. Phys., Rikkyo Univ.)

Trainees

Takahiro AKIYAMA (Grad. Sch. Sci. Eng., Saitama Univ.)
Takashi HASEGAWA (Grad. Sch. Sci. Eng., Tohoku Univ.)
Keisuke ITOH (Grad. Sch. Sci. Eng., Saitama Univ.)
Youhei SHIMIZU (Grad. Sch. Sci. Eng., Osaka Univ.)
Kousuke SUGAHARA (Grad. Sch. Sci. Eng., Saitama Univ.)
Naoya SUGIMOTO (Grad. Sch. Sci. Eng., Tohoku Univ.)
Yuji TAMESHIGE (Grad. Sch. Sci. Eng., Osaka Univ.)

Beam Technology Division

Head

Masayuki KASE

Members

Kiyoshi OGIWARA
Makoto NAGASE
Kosuke MORITA
Kiminori USHIDA
Keiko KUMAGAI
Tamaki WATANABE
Masaki FUJIMAKI
Kohji MORIMOTO
Daiya KAJI[*1]
Akiko MASUDA[*2]
Tadashi FUJINAWA[*3]
Shigeru YOKOUCHI[*3]
Jiro FUJITA[*4]
Tadashi KAGEYAMA
Shigeo KOHARA
Takahide NAKAGAWA
Eiji IKEZAWA
Naohito INABE
Toshiya TANABE
Sachiko ITO
Yoshihide HIGURASHI[*1]
Masanori KIDERA[*2]
Hiromichi RYUTOU[*2]
Misaki KOBAYASHI-KOMIYAMA[*3]
Akira YONEDA[*3]
Kenichi YAMAGUCHI[*4]

[*1] Special Postdoctoral Researcher
[*2] Contract Researcher
[*3] Contract Technical Assistant
[*4] Temporary Employee

Visiting Members

Hiroaki ASAI (JAXA)
Keisuke ASAI (Fac. Eng., Tohoku Univ.)
Toshiya CHIBA
Shin-ichi GOTO (Niigata Univ.)
Naoyuki HASEBE (Adv. Res. Inst. Sci. Eng., Waseda Univ.)
Hiroo HASEBE (Katagiri Eng. Co., Ltd.)
Masatake HEMMI
Yoshiya IIDE (JAXA)
Naomi IKEDA (JAXA)
Masayuki ITO (Adv. Res. Inst. Sci. Eng., Waseda Univ.)
Toshiji ITOH
Chihiro KAMEZAWA (JAXA)
Kenji KATORI
Kazuie KIMURA
Masanori KOSHIMIZU (Fac. Eng., Tohoku Univ.)
Hiroyuki KOURA (JAERI, Tokai)
Satoshi KUBOYAMA (JAXA)
Hisaaki KUDO (Fac. Sci., Niigata Univ.)
Sumio MATSUDA (JAXA)

Takehiro MATSUSE (Fac. Textile Sci. Technol., Shinshu Univ.)
Hideo MIKAMI (SHI Accel. Serv., Ltd.)
Takashi MIYACHI (Adv. Res. Inst. Sci. Eng., Waseda Univ.)
Yoshitoshi MIYAZAWA
Tetsuya MURAKAMI (Grad. Sch. Sci., Kyoto Univ.)
Toru NOMURA
Ryusuke NOZAKI (Dept. Phys., Hokkaido Univ.)
Junichi ODAGIRI (KEK)
Hideharu OHIRA (JAXA)
Koji OISHI (Shimizu Constr. Co., Ltd.)
Katsumi OKA (JAXA)
Osamu OKUDAIRA (Adv. Res. Inst. Sci. Eng., Waseda Univ.)
Hiromitsu OOTOMO (JAXA)
Yuichiro SASAKI (Matsushita Electr. Ind. Co., Ltd.)
Hiroki SATO (JAXA)
Osamu SHIMADA (JAXA)
Hiroyuki SHINDO (JAXA)
Keisuke SUEKI (RI Cen., Univ. Tsukuba)
Fuyuki TOKANAI (Dept. Phys., Yamagata Univ.)
Ryoichi WADA (Texas A & M Univ., USA)
Masakazu WASHIO (Adv. Res. Inst. Sci. Eng., Waseda Univ.)
Ichiro YOKOYAMA
Kenji YOSHINO (Fac. Eng., Miyazaki Univ.)

Trainees
Kentaro ASAI (Grad. Sch. Sci. Eng., Waseda Univ.)
Takehiko KURIBAYASHI (Grad. Sch. Sci. Eng., Waseda Univ.)
Naoyuki YAMASHITA (Grad. Sch. Sci. Eng., Waseda Univ.)

Liquid Helium Service Division

Head
Yasushige YANO

Members
Kumio IKEGAMI
Hiroki OKUNO
Toshiharu TOMINAKA[*1]
Masato NAKAMURA
Masao OTAKE
Tatsuhiko YOSHIDA[*2]

[*1] Contract Researcher
[*2] Temporary Employee

Radioisotope Technology Division (∼2004. 5. 31)

Head
Fumio YATAGAI (∼2004. 3. 31)
Yasushige YANO (2004. 4. 1∼2004. 5. 31)

Visiting Members
Masamitsu HONMA (Natl. Inst. Health Sci.)
Atsushi ITO (Sch. Eng., Tokai Univ.)
Osamu KAWAGUCHI (Sch. Med., Keio Univ.)
Tetsuya KAWATA (Fac. Med., Chiba Univ.)
Hideaki MAEKAWA (Natl. Inst. Infect. Dis.)
Hiroshi MAEZAWA (Fac. Med. Technol., Univ. Tokushima)
Takehiko NOHMI (Natl. Inst. Health Sci.)
Takeo OHNISHI (Fac. Biol., Nara Med. Univ.)
Toshihiro OHTA (Fac. Life Sci., Tokyo Univ. Pharm. Life Sci.)
Akihisa TAKAHASHI (Fac. Biol., Nara Med. Univ.)
Kaoru TAKAKURA (Div. Natl. Sci., Int. Chr. Univ.)

Trainees

Tsutomu MATSUO (Fac. Sci. Eng., Waseda Univ.)
Aiko NARUTO (Fac. Life Sci., Tokyo Univ. Pharm. Life Sci.)
Toshitaka OKA (Fac. Sci. Eng., Waseda Univ.)
Momoko TAKAHASHI (Div. Natl. Sci., Int. Chr. Univ.)

Application Development Division (2004. 6. 1∼)

Head

Yasushige YANO

Members

Kazuya TAKAHASHI
Hiroshige TAKEICHI
Teruyo TSUKADA
Kaori IGARASHI*2
Masanori TOMITA*2
Shuichi ENOMOTO
Masako IZUMI
Shinji MOTOMURA*1
Akihiro NAKAYAMA*2

*1 Special Postdoctoral Researcher
*2 Contract Researcher

Visiting Members

Ryohei AMANO (Fac. Med., Kanazawa Univ.)
Sachiko AMARI (Washington Univ., USA)
Wenjun DING (Colorado State Univ., USA)
Kazutoyo ENDO (Showa Pharm. Univ., USA)
Tatsunori FUKUMAKI (Japan NUS Co., Ltd.)
Mika FUKUOKA (Tokyo Univ. Fish.)
Yasuyuki GONO
Hiroshi HIDAKA (Fac. Sci., Hiroshima Univ.)
Seiichiro HIMENO (Fac. Pharm. Sci., Tokushima Bunri Univ.)
Eiko HIRANO (Japan NUS Co., Ltd.)
Takako IKEDA (Showa Women's Univ.)
Hiroko INAGE (Int. Life Sci. Inst.)
Nobuyoshi ISHII (Natl. Inst. Radiol. Sci.)
Toshiaki ISHII (Natl. Inst. Radiol. Sci.)
Hiroyuki KAGI (Grad. Sch. Sci., Univ. Tokyo)
Yousuke KANAYAMA (Grad. Sch. Med. Sci., Kanazawa Univ.)
Kenji KAWABE (Kyoto Pharm. Univ.)
Shuichi KIMURA
Masuo KONDOH (Showa Pharm. Univ.)
Kuniko MAEDA
Ken-ichiro MATSUMOTO (Natl. Inst. Health, USA)
Yoshitaka MINAI (Cen. Art. Sci., Musashi Univ.)
Takeshi MINAMI (Dept. Life Sci., Sch. Sci. Eng., Kinki Univ.)
Tomohiro NABEKURA (Fac. Pharm. Sci., Niigata Univ. Pharm. Appl. Life Sci.)
Yuichiro NAGAME (JAERI)
Tomoko NAKANISHI (Grad. Sch. Agric. Life Sci., Univ. Tokyo)
Yukiko NAKANISHI (Int. Life Sci. Inst.)
Van Chuyen NGUYEN (Jpn. Women's Univ.)
Yasumitsu OGURA (Grad. Sch. Pharm. Sci., Chiba Univ.)
Jun SAITO (Iwatsu Test Instrum. Corp.)
Tomofumi SAKURAGI (Natl. Inst. Radiol. Sci.)
Hiromu SAKURAI (Kyoto Pharm. Univ.)
Sadao SHIBATA (Nucl. Safety Technol. Cen.)
Hiroshi SHIMIZU (Fac. Sci., Hiroshima Univ.)
Atsushi SHINOHARA (Dept. Chem., Grad. Sch. Sci., Osaka Univ.)
Hiroyuki SUZUKI (RI Res. Cen., Chiba Univ.)
Kazuo T. SUZUKI (Grad. Sch. Pharm. Sci., Chiba Univ.)
Mikiko SUZUKI (Showa Women's Univ.)

Toshihiro SUZUKI (Meiji Pharm. Univ.)
Keiko TAGAMI (Natl. Inst. Radiol. Sci.)
Masaaki TAKAHASHI (Grad. Sch. Agric. Biol. Sci., Osaka Pref. Univ.)
Miho TAKAHASHI (Tokyo Univ. Fish.)
Yoshio TAKAHASHI (Grad. Sch. Sci., Hiroshima Univ.)
Atsushi TAKEDA (Sch. Pharm. Sci., Univ. Shizuoka)
Haruna TAMANO (Sch. Pharm. Sci., Univ. Shizuoka)
Shinzo TANABE (Meiji Pharm. Univ.)
Tadayasu TOGAWA (Meiji Pharm. Univ.)
Takehiro TOMITANI (Natl. Inst. Radiol. Sci.)
Shigeo UCHIDA (Natl. Inst. Radiol. Sci.)
Kohshin WASHIYAMA (Fac. Med., Kanazawa Univ.)
Mineo YAMASAKI (Nara Med. Univ.)
Makoto YANAGA (Fac. Sci., Shizuoka Univ.)
Hiroyuki YASUI (Kyoto Pharm. Univ.)
Akihiko YOKOYAMA (Fac. Sci., Kanazawa Univ.)
Shigekazu YONEDA (Natl. Sci. Museum)
Shozo YOSHIDA (Nara Med. Univ.)
Takashi YOSHIMURA (Grad. Sch. Sci., Osaka Univ.)

Trainees

Yusuke ADACHI (Grad. Sch. Pharm. Sci., Kyoto Pharm. Univ.)
Tomoko ANDO (Sch. Hum. Life Sci., Showa Woman's Univ.)
Masako HASAMA (Grad. Sch. Hum. Life Sci., Showa Woman's Univ.)
Hiroko HASEGAWA (Grad. Sch. Sci., Osaka Univ.)
Ryoichi HIRAYAMA (Grad. Sch. Sci. Technol., Chiba Univ.)
Kenichi ISHIBASHI (Meiji Pharm. Univ.)
Yoshiharu ISOBE (Dept. Radiol. Sci., Ibaraki Pref. Univ.)
Hanako KAJIYA (Grad. Sch. Hum. Life Sci., Showa Woman's Univ.)
Yoshitaka KASAMATSU (Grad. Sch. Sci., Osaka Univ.)
Nobuyuki KINUGAWA (Grad. Sch. Sci. Technol., Shizuoka Univ.)
Yusuke KITAMOTO (Grad. Sch. Sci., Osaka Univ.)
Keiko MANABE (Grad. Div. Hum., Ochanomizu Univ.)
Keiji MATSUO (Grad. Sch. Sci., Osaka Univ.)
Akiko MIDORIKAWA (Grad. Div. Hum., Ochanomizu Univ.)
Ryuji MINAYOSHI (Grad. Sch. Sci. Technol., Shizuoka Univ.)
Takanori OGI (Grad. Sch. Sci. Technol., Shizuoka Univ.)
Shigeki OHATA (Meiji Pharm. Univ.)
Mizue OZAKI (Grad. Sch. Pharm. Sci., Meiji Pharm. Univ.)
Daisuke SAIKA (Grad. Sch. Sci., Osaka Univ.)
Naoko SATOU (Meiji Pharm. Univ.)
Tomomasa TAKABE (Sch. Sci., Osaka Univ.)
Yuuki TANI (Grad. Sch. Sci., Osaka Univ.)
Yuki TASHIRO (Sch. Sci., Osaka Univ.)
Makoto YATSUKAWA (Grad. Sch. Sci., Osaka Univ.)
Atsushi YUMOTO (Grad. Sch. Pharm. Sci., Meiji Pharm. Univ.)

Safety & Security Office

Head

Yasushige YANO

Members

Shin FUJITA
Hisao SAKAMOTO[*2]
Hiroki MUKAI[*4]
Rieko HIRUNUMA[*1]
Tsutomu YAMAKI[*3]

[*1] Contract Researcher
[*2] Contract Technical Scientist
[*3] Temporary Employee
[*4] Visitng Contract Officer

ADVANCED DEVELOPMENT AND SUPPORTING CENTER

Beam Application Team

Head
Takashi MEGURO

Members
Tomohiro KOBAYASHI
Aiko NAKAO
Kowashi WATANABE

RESEARCH UNIT

Image Information Research Unit

Head
Hirohiko M. SHIMIZU

Members
Hiromi SATO
Seiichiro ARIYOSHI[*1]
Kazuaki IKEDA[*1]
Masashi OHNO[*1]
Tomohiro ADACHI[*2]
Mario E. BERTAINA[*2]
Katsuya HIROTA[*2]
Masahiko KURAKADO[*2]
Kenji MISHIMA[*2]
Takahiro MORISHIMA[*2]
Shigetomo SHIKI[*2]
Takenao SHINOHARA[*2]

[*1] Special Postdoctoral Researcher
[*2] Contract Researcher

Visiting Members
Tadashi KIFUNE (Fac. Eng., Shinshu Univ.)
Hiroaki MYOREN (Fac. Eng., Saitama Univ.)
Takayuki OKU (JAERI)
Kenji SAKAI (Dept. Phys., Tokyo Inst. Technol.)
Tohru TAINO (Fac. Eng., Saitama Univ.)
Fuyuki TOKANAI (Dept. Phys., Yamagata Univ.)
Satoru YAMADA (JAERI)

Trainees
Ran NAKANO (Dept. Electr. Syst., Saitama Univ.)
Masayo YOSHIDA (Dept. Electr. Syst., Saitama Univ.)
Shota YOSHIMURA (Dept. Electr. Syst., Saitama Univ.)

RIKEN BNL Research Center

Head
Nicholas P. SAMIOS (Director)
Hideto EN'YO (RBRC Associate Director)
Tsung-Dao LEE (Director Emeritus)

Experimental

Group Leader
Hideto EN'YO

Deputy Group Leader
Gerry M. BUNCE

Members
Yuji GOTO
Takashi ICHIHARA
Atsushi TAKETANI
Yasushi WATANABE
Kiyoshi TANIDA
Yasuyuki AKIBA

Abhay DESHPANDE[*1]
Matthias GROSS PERDEKAMP[*1]
Tsuguchika TABARU[*3]
Kensuke OKADA[*2]
Wei XIE[*4]
Douglas Edward FIELDS[*1]
Masashi KANETA[*2]
Osamu JINNOUCHI[*2]
Junkichi ASAI[*3]
David KAWALL[*4]

Visiting Members

Yoshinori FUKAO (Kyoto Univ.)
Takuma HORAGUCHI (Tokyo Inst. Technol.)
Kazuyoshi KURITA (Rikkyo Univ.)
Naohito SAITO (Kyoto Univ.)
Zheng LEE (BNL, USA)
Viktor SIEGLE (Univ. Heidelberg, Germany)
Akio OGAWA (BNL, USA)
Dominik GABBERT (Univ. Illinois, USA)
Kenichi NAKANO (Tokyo Inst. Technol.)

Theory

Group Leader

Larry MCLERRAN

Deputy Group Leader

Anthony J. BALTZ

Members

Steffen A. BASS[*1]
Takashi IKEDA[*3]
Sangyong JEON[*1]
Yukio NEMOTO[*2]
Stefan KRETZER[*2]
Mikhail A. STEPHANOV[*1]
Ubirajara van KOLCK[*1]
Tilo WETTIG[*1]
Norikazu YAMADA[*2]
Sinya AOKI[*1]
Takeshi YAMAZAKI[*2]
Takumi DOI[*3]
Shoichi SASAKI[*4]
Christopher DAWSON[*4]
Thomas BLUM[*4]
Alexander KUSENKO[*1]
Jun-ichi NOAKI[*2]
Thomas SCHAEFER[*1]
Takanori SUGIHARA[*3]
Peter PETRECZKY[*4]
Werner VOGELSANG[*4]
Taku IZUBUCHI[*1]
Kei IIDA[*4]
Yoshitaka HATTA[*3]
Feng YUAN[*1]

Visiting Members

Miklos GYULASSY (Columbia Univ., USA)
Robert L. JAFFE (Massachusetts Inst. Technol., USA)
Robert MAWHINNEY (Columbia Univ., USA)
Edward SHURYAK (State Univ. New York, Stony Brook, USA)
Shigemi OHTA (KEK)
Hiroshi YOKOYA (Hiroshima Univ.)
Konstantinos ORGINOS (Massachusetts Inst. Technol., USA)
Koichi HASHIMOTO (Kanazawa Univ.)
Tetsufumi HIRANO (Columbia Univ., USA)

Administration

Pamela ESPOSITO (Secretary)
Rae GREENBERG (Assistant)
Tammy Anne STEIN (Secretary)
Taeko ITO (Secretary)
Linda SALLUSTIO (Secretary)

Administrative Manager

Kiyofumi TSUTSUMI

Deputy Administrative Manager

Chiharu SHIMOYAMADA
Jun NAKAMURA

---

*1 RHIC Physics Fellow, *2 Research Associate,
*3 Special Postdoctoral Researcher, *4 RIKEN BNL Fellow

SAFETY DIVISION

Head

Hiroshi SAWA

Deputy Director

Masayuki SHIMAGAKI
Yasuhide MATSUZAWA
Makoto MIYAGAWA

Laboratory Safety Section

Head

Yoshitomo UWAMINO

Members

Yuji NAKASHIMA
Hajime YOSHIKI
Shigemi SHINOHARA

Research Ethics Section

Head

Satoru KAGAYA

Members

Akira OZAKI
Kazunori TAGUCHI
Ritsuko NAKAGAWA
Hiroko KATOU
Shigeki ASAKAWA

AUTHOR INDEX